Title

The Faint, the Poor, and the Steady: studies of low-luminosity, metal-poor, and non-pulsating populations of high-mass X-ray binaries

Author

Fornasini, Francesca Maria

Publication Date

2016

Peer reviewed|Thesis/dissertation

The Faint, the Poor, and the Steady: studies of low-luminosity, metal-poor, and non-pulsating populations of high-mass X-ray binaries

By

Francesca Maria Fornasini

A dissertation submitted in partial satisfaction of the

requirements for the degree of

Doctor of Philosophy

in

Astrophysics

in the

Graduate Division

of the

University of California, Berkeley

Committee in charge:
Professor Mariska Kriek, Co-chair
Dr. John Tomsick, Co-chair
Professor Joshua Bloom
Professor Steven Boggs
Professor Aaron Parsons

Fall 2016

The Faint, the Poor, and the Steady:
studies of low-luminosity, metal-poor, and non-pulsating populations of high-mass X-ray binaries

Francesca Maria Fornasini

Abstract

The Faint, the Poor, and the Steady:
studies of low-luminosity, metal-poor, and non-pulsating populations of high-mass X-ray binaries

by

Francesca Maria Fornasini

Doctor of Philosophy in Astrophysics

University of California, Berkeley

Professor Mariska Kriek, Co-chair
Dr. John Tomsick, Co-chair

High-mass X-ray binaries (HMXBs) consist of a black hole or neutron star accreting material from a high-mass stellar companion. Although these systems are very rare, with only about 100 having been discovered in the Milky Way Galaxy, they provide crucial insights into the evolution of high-mass stars and may have played an important role in the early Universe, heating the gas in the intergalactic medium and facilitating its reionization by the ultraviolet light produced by the first stars and galaxies. The advent of gravitational wave astronomy further motivates a more thorough understanding of HMXB populations, since HMXBs are the likely progenitors of many of the double compact binaries whose mergers will be detected by gravitational wave observatories. This dissertation presents three studies of HMXB populations, addressing open questions about the faint end of the HMXB luminosity function, the metallicity dependence of HMXB evolution, and the nature of compact objects in non-pulsating HMXBs.

In order to identify low-luminosity HMXBs and study their properties and Galactic number density, we surveyed a square-degree region in the direction of the Norma spiral arm with the *Chandra* and *NuSTAR* X-ray telescopes. We discovered three low-luminosity HMXB candidates, all of which have main-sequence Be/B-type counterparts and X-ray luminosities equal to $0.1 - 1$ solar luminosities. The *Chandra* and *NuSTAR* surveys of the Norma region also provided the opportunity to study other low-luminosity X-ray populations in the Galaxy. We found that the majority of sources detected at energies above 2 keV are cataclysmic variables (CVs), which likely dominate the hard X-ray component of the Galactic Ridge X-ray Emission. The CV candidates in the Norma region have plasma temperatures of $kT = 10 - 20$ keV, whereas the CVs found in similar surveys of the Galactic Center region have temperatures of $kT = 20 - 50$ keV. The lower temperatures of Norma CVs may result

from a significant number of them being nonmagnetic CVs, polars, or symbiotic binaries whereas the Galactic Center CVs are likely dominated by intermediate polars.

The second part of this dissertation discusses the X-ray emission of star-forming galaxies at redshifts between $z = 1.4$ and $z = 2.6$. Simulated models of HMXB populations predict that luminous HMXBs should be more numerous in low-metallicity environments. Studies of nearby galaxies have found an excess of luminous HMXBs in very metal-poor blue compact dwarf galaxies, and it has been suggested that the observed increase of the X-ray luminosity per star formation rate (SFR) of star-forming galaxies at higher redshifts is a result of the metallicity dependence of HMXBs. In order to test this hypothesis, we divided a sample of high-redshift galaxies from the MOSDEF survey into different metallicity bins, and stacked the X-ray data from deep *Chandra* extragalactic surveys to measure the average X-ray luminosity of the galaxies in each bin. Our preliminary results confirm the increase of the X-ray luminosity per SFR with redshift but do not find a significant correlation between the X-ray luminosity per SFR and the metallicity of galaxies.

The third part of this dissertation investigates the nature of the compact object in a non-pulsating HMXB. X-ray pulsations provide strong evidence that an HMXB hosts a neutron star (NS), but the absence of pulsations does not rule out the possibility that an HMXB hosts a NS. Using *XMM-Newton* and *NuSTAR* observations of IGR J18214-1318, we study the timing and spectral properties of this supergiant HMXB in detail. Our analysis rules out the presence of pulsations with periods shorter than an hour and detects an exponential cutoff to the power-law spectrum of the source with e-folding energy lower than 25 keV. This low cutoff energy indicates that the compact object in this HMXB is most likely a NS. This study exemplifies the powerful diagnostics provided by the combination of *XMM-Newton* and *NuSTAR* observations for the identification of compact objects in HMXBs.

For Michele.

"There are stars
whose light reaches Earth long after they have disintegrated and are no more.
And there are people
whose scintillating memory lights the world after they have passed from it.
These lights,
which shine brightest in the darkest night, illumine for us the path."
– Hannah Senesh

Contents

List of Figures

List of Tables

Acknowledgments

This dissertation[1] is not merely the fruit of six years of work, but a testament to the support, mentorship, and education I have been fortunate to receive throughout my life. I want to express my gratitude to the vast number of people who have helped me to pursue my studies in astrophysics.

At the most practical level, my graduate research would not have been possible without funding and without X-ray observatories, so I would like to acknowledge the support I have received from the United States taxpayers. I am grateful to have received financial support from the National Science Foundation Graduate Research Fellowship, the University of California, Berkeley, and the National Aeronautics and Space Administration[2]. The scientific results in this thesis are based on observations made by the *Chandra X-ray Observatory*, the *Nuclear Spectroscopic Telescope Array*, the European Space Agency's *XMM-Newton*, the Keck Observatory, and the SOAR telescope at the Cerro-Tololo Inter-American Observatory[3]. All of these observatories receive public support, and I feel privileged to have been been able to use some of these resources to expand our knowledge of the Universe just a little further.

I owe a special debt of gratitude to my primary thesis advisor, John Tomsick. John – thank you for entrusting me with such a large and significant data set as soon as I started working with you, and for giving me the opportunity to be a part of an exciting, new mission through the *NuSTAR* science team. I really appreciate the time and effort you spent to guide me as a student, the patience with which you explained concepts and methods to me while I was still learning the ropes, and the feedback you provided at all stages of my research to make me a better scientist. I feel fortunate to have had you as mentor, and I look forward to our future collaborations.

My second advisor, Mariska Kriek, also deserves special recognition. During my fourth

[1]This dissertation was typeset using the ucastrothesis LaTeX template, courtesy of Peter Williams.

[2]This work was partly supported by NASA under *XMM* Guest Observer grant NNX15AG31G and through *Chandra* Award Number G01-12068A issued by the *Chandra X-Ray Observatory Center*, which is operated by the Smithsonian Astrophysical Observatory for and on behalf of NASA under contract NAS8-03060.

[3]Thank you to the numerous scientists and engineers involved in the development and operations of these observatories, and to those who helped create the software packages and data products that facilitate the analysis of data from these telescopes. This research has made use of software provided by the Chandra X-ray Center (CXC) in the application packages CIAO and Sherpa, as well as the *NuSTAR* Data Analysis Software (NuSTARDAS), which was jointly developed by the ASI Science Data Center (ASDC, Italy) and the California Institute of Technology (USA). This work also made use of data products from observations made with ESO Telescopes at the Paranal Observatories under ESO programme ID 179.B-2002.

year, while I was preparing for my qualifying exam, I approached her with the idea for a research project to test the metallicity depedence of HMXBs. Even though this project was somewhat extraneous to her science interests, she agreed to work with me and became increasingly enthusiastic about the project; I hope to maintain that same openness to new research areas as I continue in my scientific career. Mariska – thank you for bringing me into the MOSDEF collaboration, and for providing with me with encouragement, advice, and perspective during the very stressful job application process.

During my graduate studies, I have enjoyed the support of additional mentors. Many thanks to Steve Boggs, Aaron Parsons, and Josh Bloom, who served on both my qualifying and thesis committees, providing valuable feedback on my dissertation projects. I also want to express my appreciation to the co-authors of my published papers for their insights and suggestions. In particular, I would like to thank Arash Bodaghee, Roman Krivonos, Farid Rahoui, Daniel Stern, Jaesub Hong, and Eric Gotthelf for the pieces of analysis they contributed, and the many useful discussions we had. I feel privileged to have had the opportunity to be both a student and a teaching assistant of Eugene Chiang, whose classes were meticulously crafted, peppered with humor, and among the most challenging I've taken. Eugene – thank you for pushing me to strive for excellence, and for sharing some of your favorite short stories and history of science books, to the delight of the English major in me.

I also want to thank all the staff members who have helped me to sort through administrative or technical problems, both thorny and mundane, especially Rayna Helgens, Nina Ruymaker, Bill Boyd, Lochland Trotter, and, most of all, Dexter Stewart. Dexter – not only are you an incredibly effective student affairs officer, but your beaming smile and personal engagement with each person make the department a much more cheerful, welcoming place.

I am very grateful for the research experiences I had prior to grad school, which inspired and prepared me to undertake this thesis research. I want to thank my undergraduate thesis research advisors, Seth Aubin and Irina Novikova, who taught me the fundamentals of carrying out scientific research, my REU program advisor, Lisa Kewley, who guided me through the research experience that convinced me I wanted to study astrophysics, and family friend Massimo Robberto, who let me shadow him for a few weeks at the Space Telescope Science Institute and work with *Hubble* data.

I would not have made it through grad school without the solid educational foundation and encouragement given to me by the many excellent teachers I had from elementary school through high school. To my high school physics teacher and mentor in the school of life, Fr. José Medina – thank you for introducing me to the challenge, frustration, and fascination that is the study of physics, and for showing me that, when it comes to both physics and the Mystery, there is joy to be found in the struggle. Many thanks are due to my high school math teachers, Mrs. Feinstein and Mrs. Haas, paragons of friendship who imparted memorable life advice along with fundamental math skills, including the importance of taking mental health days which proved to be sound advice during grad school. I feel indebted to my high school English teacher Mrs. Mattingly, whom I try to emulate while I edit scientific papers in order to imbue them with grace of form in addition to accuracy of content. I am also very grateful to my third grade teacher Mrs. Stopak, who showered me with patience

and affection while I was struggling to learn English during my first year in the US, and my fourth grade teacher Mr. Millner, who introduced me to the fun of science experiments.

Throughout grad school, I was fortunate to belong to a tight-knit community of grad students. In particular, I want to thank Carolyn, Clio, Michelle, and Alex, with whom I shared an office at SSL as well as the daily frustrations and small victories of research, Aaron Lee, my "partner-in-crime" when it came to organizing publich outreach, teaching Astro 375, and discussing pedagogy, and Sedona Price, who patiently and expertly answered my questions when I started working in a new field. I feel especially lucky to have had wonderful classmates, whose support helped to stave off the attrition of grad school. Casey Stark and Erik Petigura, your friendship has been a beautiful, unexpected gift, and Garrett "Karto" Keating, I never imagined that my most significant discovery in grad school would be my spouse (but more on that later). I treasure the experiences we've shared together (and with "classmates-in-law" Alana and Lindsay), especially those spent around a grill, a table, or a brewing bucket of hops, and I look forward to sharing many more, despite the geographical distances that may separate us. After all, what are a few thousand miles when you've studied the Universe together?

Finally, I am filled with gratitude for my family and friends who are sources of constant love, unwavering support, and often-needed perspective. In particular, to my friends Ana Carolina, Juliet, Maria Elena, Jorge Nicolas, and Alejandra – thank you for being sources of inspiration, captive audiences, companions in difficulties, fellow wonderers[4], and anchors to what makes life meaningful. To Zia Lucia, Nonna Ninetta, and Nonna Evelina – a thousand thanks for your love and for being so proud of me that you periodically Google search my name to keep track of my accomplishments, no matter how small. [5] To my brother Giachi – thanks for keeping me grounded and level, as any good engineer should. To Mi and Papi, who always want to see what's on the other side of that ridge and passed on that curiosity to me – I cannot thank you enough for all the ways you've supported me and guided me through the years, which are too many to enumerate. I want to thank you especially for prioritizing my education and for taking me to so many national parks while I was growing up where I could experience wonder in front of the beauty and vastness of the natural world; I will never forget when we visited the canyons in Arizona and Utah, where, for the first time, I saw a night sky so full stars that it was difficult to identify the constellations. Last but certainly not least, I am profoundly grateful to my husband, Garrett, brilliant radio astronomer, expert grill master, thoughtful spouse, and awesome friend. Even before we were dating, you were my favorite person to talk to about statistics – thank you for all the conversations that contributed to this thesis. But even more so, thank you for rejoicing with me in the ups, supporting me in the downs, and re-energizing me in the flats I experienced over the past six years, and for bringing laughter to all of them. Above all, thank you for showing me, with a certainty greater than statistics can provide, that this adventure is worth the risk.

[4]Not a typo.

[5]Per Zia Lucia, Nonna Ninetta, e Nonna Evelina – grazie infinite per il vostro amore e per essere così fiere di me che cercate per il mio nome sull'internet per tenere conto di tutti i miei successi, anche se siano piccoli.

Chapter 1

Introduction

1.1 High-Mass X-ray Binaries

In 1962, Riccardo Giacconi, Bruno Rossi, and their collaborators launched a rocket carrying three large area Geiger counters and detected the first source of X-rays outside the solar sytem (Giacconi et al. 1962). Their discovery marks the beginning of X-ray astronomy. The bright X-ray source they detected, Scorpius X-1, was eventually identified as a neutron star accreting material from a low-mass stellar companion ($M \lesssim 1 M_{\odot}$; Lamb 1989). Such systems, containing either a neutron star (NS) or black hole (BH) accreting from a low-mass companion, are referred to as low-mass X-ray binaries (LMXBs). Giacconi et al. (1962) also suggested that a secondary peak of X-ray emission was located in the direction of the Cygnus constellation, although its count rate was too low to ascertain whether it was likely to be a single well collimated source or an anisotropy of the diffuse X-ray background. Using data gathered by Geiger counters on two rocket flights in 1964, Bowyer et al. (1965) identified two discrete sources in the direction of the Cygnus constellation. The brighter of the two, Cygnus X-1, was later determined to be black hole with a mass of $14.8 \pm 1.0 M_{\odot}$ accreting material from a supergiant stellar companion (Bolton 1975; Bahcall 1978; Orosz et al. 2011 and references therein). An artistic illustration of Cyg X-1 is shown is Figure 1.1.

During the fifty years since the discovery of Cyg X-1, several hundred additional high-mass X-ray binaries (HMXBs) have been discovered. HMXBs consist of a NS or BH accretor and a high-mass stellar donor ($M \gtrsim 10 M_{\odot}$). It is estimated that about 1% of binaries consisting of two main-sequence high-mass stars will evolve into HMXBs (Postnov & Yungelson 2014). In order for a high-mass binary to become an HMXB, the binary must survive two critical evolutionary phases. The first critical phase occurs when the more massive star in the system, the primary, expands into a supergiant. At this point, in binaries with short initial orbital periods, the primary will engulf the secondary, forming a common envelope; the secondary will lose angular momentum due to frictional drag and spiral inwards. Depending on the binding energy of the envelope of the primary and the efficiency of the transfer of orbital energy into the envelope, the secondary may either unbind the envelope and end up as a close binary or it may continue to spiral inwards and merge with the primary (Ivanova et al. 2013).

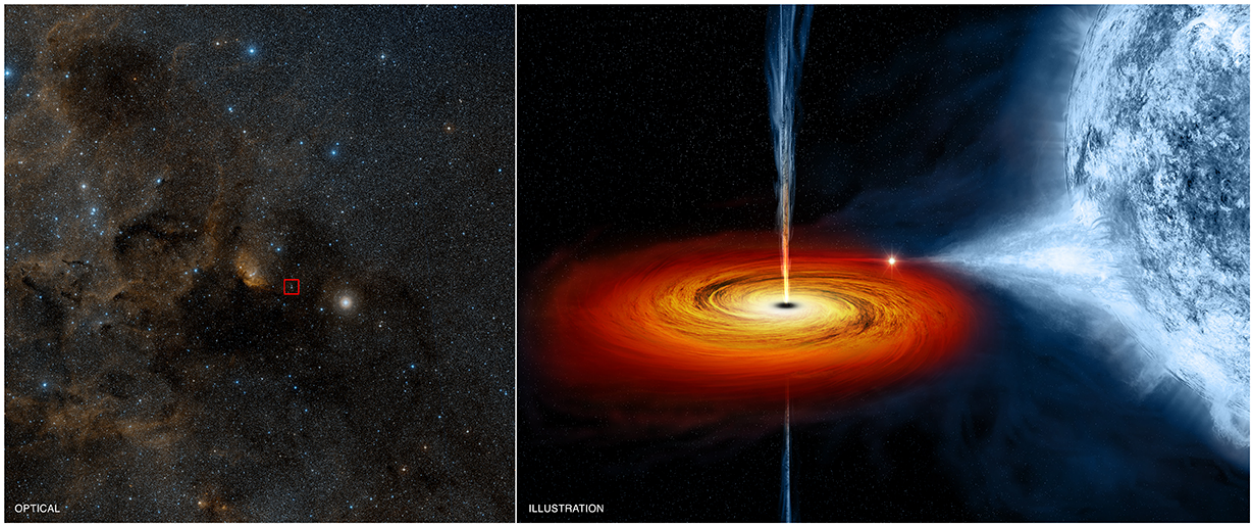

Figure 1.1: *Left*: An optical image from the digitized sky survey of Cyg X-1, which is shown in the red box. *Right*: An artist's illustration of Cyg X-1, a black hole accreting via Roche-lobe overflow from a high-mass companion. During the high soft spectral state, the X-ray emission of BH HMXBs is dominated by the accretion disk. During the low hard spectral state, the X-ray emission is dominated by the jets and hot corona. (Credit: Optical - DSS; Illustration - NASA/CXC/M.Weiss)

About 25% of high-mass binaries are expected to merge together (Sana et al. 2012). The second critical phase occurs when the primary explodes as a supernova (SN). Only 4–10% of high-mass binaries are estimated to survive the core-collapse SN explosion depending on the amount of mass lost relative to the pre-SN binary mass and the strength of the kick imparted to the compact object due to an asymmetric explosion (Postnov & Yungelson 2014). Even if a binary survives both these phases, its orbit may be too wide for appreciable accretion onto the NS or BH to take place and be detected as an HMXB.

The HMXB phase typically starts $\approx 4 - 40$ Myr after the formation of the high-mass binary and lasts $\sim 10^7$ years (Iben et al. 1995; Bodaghee et al. 2012c; Antoniou & Zezas 2016). The donor stars in HMXBs tend to either be supergiant (Sg) O/B stars or Oe/Be stars; the latter are rapidly rotating main-sequence or giant O/B stars which exhibit one or more Balmer lines in emission arising from an outwardly diffusing gaseous disk often referred to as a decretion disk (Rivinius et al. 2013). The spectral type of the donor star and the type of compact object that an HMXB harbors impact the X-ray properties it displays. Therefore HMXBs are typically divided into different categories based on the classification of their binary components.

1.1.1 Classes of HMXBs

In the Milky Way Galaxy, about 60% of the ≈ 100 known HMXBs have Be donors [1], 35% have Sg donors, and 5% have main-sequence or giant stellar donors which are not Oe/Be stars (Liu et al. 2006; Walter et al. 2015). In the Large Magellanic Cloud (LMC), only 4 out of 40 HMXBs have Sg donors (Antoniou & Zezas 2016), and in the Small Magellanic Cloud (SMC), only one of ≈ 100 HMXBs has been identified as a Sg HMXB (Haberl & Sturm 2016). Since Sg HMXBs have shorter lifetimes than Be HMXBs, the different ratios of Sg/Be HMXBs in the Milky Way, LMC, and SMC point to differences in the ages of the most recent episodes of star formation in each galaxy (Antoniou & Zezas 2016). It has also been suggested that the production of HMXBs per star formation rate (SFR) is highest in the SMC and lowest in the Milky Way (Grimm et al. 2003; Antoniou & Zezas 2016), a trend which may driven by differences in the metallicities of these galaxies (Dray 2006).

The vast majority of HMXBs in the Milky Way and the Magellanic Clouds harbor neutron stars. In the Milky Way, there are three known BH HMXBs: Cyg X-1 and Cyg X-3[2] are Sg-BH HMXBs while MWC 656 is the only known Be-BH binary (Casares et al. 2014). In the Magellanic Clouds, there are three BH-Sg HMXBs: LMC X-1, LMC X-3, and SMC X-1 (Hutchings et al. 1983; Cowley et al. 1983; Bahcall 1978). While BH HMXBs are rare, Sg-BH binaries are among the most luminous HMXBs because they are short period systems where the supergiant companion is (or is close to) overflowing its Roche lobe overflow[3], and thus the mass accretion rates in these systems are high compared to wind-fed systems. In contrast, the only known Be-BH binary has one of the lowest measured X-ray luminosities due to its wide orbit(Munar-Adrover et al. 2014).

Accretion onto the compact object in Sg HMXBs and Be HMXBs proceeds through different processes. Since most HMXBs possess NS accretors, we focus our description of accretion processes on NS binaries. In Sg HMXBs, the NS either accretes material directly from the stellar wind or from an accretion disk that is formed when the donor star overflows its Roche lobe (Chaty 2011). In most Be HMXBs, the NS is on a wide and eccentric orbit; as it reaches periastron, the NS passes near or through the dense decretion disk of the Be star and accretes mass (Reig 2011). Many Be HMXBs exhibit periodic X-ray outbursts where the X-ray flux increases by a factor of ~ 10 as the NS passes through the decretion disk; these type I outbursts, caused by thermonuclear burning of accreted material on the NS surface, are followed by longer periods of low accretion rate or even quiescence as the NS continues along the remainder of its orbit (Reig 2011). In some cases, as the NS travels through the decretion disk, an accretion disk is formed around it which can persist into quiescence (Doroshenko et al. 2014), while in other systems, no accretion disk forms or it forms but dissipates during quiescence (Klus et al. 2014; Elshamouty et al. 2016).

[1] Throughout this dissertation, HMXBs with Oe donor stars are included in the category of Be HMXBs.

[2] The radio and X-ray variability of Cyg X-3 favors a microquasar nature for the compact object in this source, but the estimated mass of the compact object is too uncertain to definitively rule out a neutron star nature (Zdziarski et al. 2016).

[3] The Roche lobe is the equipotential surface bounding the region around a star within which material is gravitationally bound to that star.

The differences in accretion processes and stellar wind properties between Sg and Be HMXBs are reflected in their distinct locations in the Corbet diagram, which presents the NS spin period ($P_{\rm spin}$) versus the binary orbital period ($P_{\rm orb}$) (Corbet 1984). Disk-fed Sg HMXBs have short spin and orbital periods of $\lesssim 10$ seconds and $\lesssim 3$ days. The spin and orbital periods appear to be anti-correlated for these HMXBs, but since only a few disk-fed Sg HMXBs have been identified, it is unclear whether this trend is a selection effect or the effect of torques tending to synchronize the spin and orbital periods (Corbet 1986). Wind-fed Sg HMXBs tend to have $10 \lesssim P_{\rm spin} \lesssim 10^4$ s and $3 \lesssim P_{\rm orb} \lesssim 60$ days, and they do not exhibit any correlation between their spin and orbital periods, as is expected when wind accretion is very inefficient at transferring angular momentum from the stellar wind to the NS (Chaty 2011). In contrast, the spin and orbital periods of Be HMXBs are positively correlated and span the ranges of $1 \lesssim P_{\rm spin} \lesssim 10^3$ s and $20 \lesssim P_{\rm orb} \lesssim 500$ days (Corbet 1984). Even though accretion in Be HMXBs is often wind-fed, the equatorial decretion disks of Be stars tend to have lower velocities and steeper density gradients than Sg winds, resulting in a more efficient transfer of angular momentum in Be HMXBs than Sg HMXBs (Waters & van Kerkwijk 1989). Since neutron stars in HMXBs have strong magnetic fields ($B \sim 10^{12}$ G; Coburn et al. 2002), in order for matter from the stellar wind to accrete onto the NS, the pressure from the infalling material must exceed the centrifugal barrier posed by the magnetosphere, which corotates with the NS. If the angular velocity of the magnetosphere at the magnetospheric radius[4] is higher than the Keplerian angular velocity (which is an estimate of the angular velocity of the infalling material), the propeller mechanism will fling away the material, reducing the angular momentum of the NS. If the angular velociity of the magnetosphere is lower than the Keplerian angular velocity at the magnetospheric radius, the infalling material is accreted, increasing the angular momentum of the NS. Thus, in Be HMXBs, the NS spin evolves towards an equilibrium spin period (Davidson & Ostriker 1973; Illarionov & Sunyaev 1975).

1.1.2 X-Ray Properties of HMXBs

The X-ray luminosity function (LF) of HMXBs has been studied down to 2–10 keV luminosity limits of $L_X \sim 10^{34}$ erg s^{-1} for Galactic HMXBs and $L_X \sim 10^{36}$ erg s^{-1} for extragalactic HMXBs (Lutovinov et al. 2013; Mineo et al. 2012; Voss & Ajello 2010; Grimm et al. 2002). The shape and slope of the HMXB LF appears to be consistent in different galaxies, while its normalization is correlated with the SFR of the galaxy and shows significant dispersion, hinting at its potential depedence on other galaxy properties such as metallicity (Mineo et al. 2012). The HMXB LF displays a break at $\sim 10^{37} - 10^{40}$ erg s^{-1} (Lutovinov et al. 2013; Mineo et al. 2012; the measured value of the break luminosity differs between studies depending on whether the sample of HMXBs is limited to persistent sources, and, if transient sources are included, how their average luminosities are calculated. The power-law

[4]The magnetospheric radius is the distance from the NS at which the magnetic field pressure is equal to the ram pressure of the infalling material.

slope of the LF is measured to be -1.4 to -1.6 at luminosities below the break and > 2 above the break (Lutovinov et al. 2013; Mineo et al. 2012.

In some external galaxies, X-ray binaries with $L_X > 10^{39}$ erg s^{-1} have been detected; given that the Eddington luminosity[5] of a NS with a typical mass of $1.4M_\odot$ is $L_X \sim 10^{38}$ erg s^{-1}, it was hypothesized that these sources, known as ultra-luminous X-ray sources (ULXs), are black hole systems. Many ULXs exhibit X-ray variability and spectral properties similar to those of Galactic BH binaries, and it is thought that most ULXs are X-ray binaries with stellar-mass compact objects accreting at super-Eddington rates, although some may host intermediate-mass BHs with masses of $\sim 10^2 - 10^3 M_\odot$ (e.g., King et al. 2001; Walton et al. 2013; Walton et al. 2015; Brightman et al. 2016). However, periodic pulsations detected in M82 X-2 revealed that some ULXs harbor neutron stars (Bachetti et al. 2014), and it has since been argued that such systems may make up a significant fraction ($\sim 10\%$) of ULXs (Fragos et al. 2015; King & Lasota 2016).

HMXBs display X-ray variability on a variety of timescales. On timescales of milliseconds to hours, they exhibit significant aperiodic variability resulting in red noise continuum components in their power spectra (Belloni & Hasinger 1990). Early models of the power-law red noise described it as shot noise associated with the superposition of short X-ray ourbursts (Terrell 1972), but these models failed to account for the breaks observed in the power spectra of some NS HMXBs as well as the variations of the noise properties with X-ray luminosity. Thus, a number of other hydrodynamic processes have been suggested to contribute to this aperiodic variability including: (1) stochastic perturbations in the accretion disk at frequencies characteristic of a given radius being advected by the accretion flow to the magnetospheric radius (Revnivtsev et al. 2009a), (2) magnetohydrodynamic turbulence in the accreting plasma (Hoshino & Takeshima 1993), (3) wind inhomogeneities and instabilities in the shock front due to the photo-ionization of the stellar wind by the NS emission (Blondin 1994; Manousakis & Walter 2015), and (4) Rayleigh-Taylor instabilities at the magnetospheric boundary when the accretion rate is low and the flow is subsonic (Shakura et al. 2013). The power spectra of HMXBs can also exhibit quasi-periodic oscillations and, in the case of a NS HMXBs, pulsations due to the accretion flow being channeled towards the magnetic poles of the NS (Belloni & Hasinger 1990).

On long timescales of ∼days to years, different classes of HMXBs exhibit different types of variability. As discussed in §1.1.1, many Be HMXBs exhibits periodic type I outbursts; some also display type II outbursts, during which the X-ray flux increases by a factor of $\sim 10^3 - 10^4$ for the duration of a large fraction of an orbital period or multiple orbital periods (Reig 2011). Type II outbursts are thought to result from the expansion of the Be star decretion disk and can result in the disappearance of the Be disk (Reig 2011). The X-ray luminosity of typical Sg HMXBs can vary by factors of $\sim 10 - 100$, variations which are attributed to wind inhomogeneities and hydrodynamic processes (Walter et al. 2015). Ten Sg HMXBs exhibit flares with X-ray luminosities higher than the quiescent state by factors of $\sim 10^3 - 10^5$ erg s^{-1} and durations of a few hours (Sguera et al. 2005; Negueruela

[5]The Eddington luminosity is the luminosity for which the force due to radiation pressure is equal to the gravitational force.

et al. 2006). These systems are referred to supergiant fast X-ray transients (SFXTs), and their extreme flaring behavior cannot be explained by the models for typical HMXBs. The strong variability of SFXTs may be explained by large density variations in clumpy winds (Negueruela et al. 2008) or by the presence of centrifugal and magnetic barriers to accretion (assuming the compact object are magnetized NS; Bozzo et al. 2008). The X-ray luminosity of Sg-BH HMXBs can vary by factors of $\lesssim 10$ on long timescales; these brightness variations are correlated with spectral variations (Esin et al. 1998). The high/soft state of BH HMXBs is dominated by thermal blackbody emission from the accretion disk and exhibits power-law emission (with photon index $\Gamma \sim 2-3$ due to Compton scattering of the blackbody emission by nonthermal electrons (Zdziarski 2000; Gilfanov 2010). In contrast, during the low/hard state, it is thought that the inner radius of the accretion disk recedes farther away from the black hole and the spectrum is characterized by the thermal Comptonized continuum from a corona of hot electrons, which exhibits a cutoff around $kT \approx 50-100$ keV (Zdziarski 2000; Gilfanov 2010). Since the only known Be-BH HMXB has a very low X-ray luminosity ($L_X \sim 10^{31}$ erg s^{-1}), its X-ray variability and spectrum has not been well-studied and so it is not known whether its X-ray properties resemble those of Sg-BH systems.

The spectra of NS HMXBs differ from those of BH HMXBs. Accreting neutron stars typically have power-law spectra with photon indices of $\Gamma \sim 0-2$ and exponential cutoffs with e-folding energies of $E_{\rm cut} \lesssim 20$ keV (Coburn et al. 2002). Their emission has been interpreted as arising from the thermal and bulk Comptonization[6] of seed photons by electrons in the accretion column above the NS magnetic poles; the seed photons are thought to originate from bremmstrahlung and cyclotron emission within the accretion column and the accretion shock as well as blackbody emission from the NS polar cap (Farinelli et al. 2016). Some NS HMXB spectra exhibit cyclotron absorption features as photons are scattered by electrons whose energies are quantized into Landau levels by the strong magnetic field of the NS (Coburn et al. 2002). These cyclotron lines provide a way of measuring the strength of the NS magnetic field, which has been found to be $B \sim 10^{12}$ G in NS HMXBs. A soft blackbody excess has been observed in some NS HMXBs (Reig et al. 2009). In disk-fed Sg systems, this excess has $kT_{\rm BB} \approx 0.1$ keV and $R_{\rm BB} \approx 1000$ km, and is thought to originate from the reprocessing of hard X-rays by the inner edge of the accretion disk (Hickox et al. 2004). In wind-fed Sg HMXBs, the excess has $kT_{\rm BB} \approx 0.2$ keV and $R_{\rm BB} \approx 100$ km, and may arise from a diffuse cloud of plasma around the NS associated with the photoionized stellar wind (Hickox et al. 2004; Masetti et al. 2006). In Be HMXBs, this blackbody excess has a higher temperature ($kT_{\rm BB} \approx 1$ keV) and a smaller emitting region ($R_{\rm BB} \approx 0.1$ km), likely originating from the NS hot spots at the polar caps (Mukherjee & Paul 2005; La Palombara & Mereghetti 2006).

Both NS and BH HMXBs can exhibit iron (Fe) fluorescent emission lines in their spectra[7].

[6]Compton up-scattering of photons in the accretion column is thought to result from both electrons with a thermal velocity distribution and electrons moving with the bulk accretion flow velocity.

[7]X-rays are energetic enough to eject inner shell electrons from elements such as iron, leaving the atom in an excited state. When an electron from an upper level falls down to the lower energy level in the inner shell, it produces fluorescent emission. If the electron falls down to the innermost shell, the emission is called Kα or Kβ emission depending on whether it starts from the L atomic level or an even higher level

In NS HMXBs, Fe Kα emission is observed with equivalent widths of $\sim$ 100 eV at 6.4 keV, indicating that is originates from neutral or low-ionization material (Coburn et al. 2002). This iron emission can be useful in studying the geometric structure of material around the NS (Manousakis & Walter 2011; Naik et al. 2011; Fürst et al. 2011). In BH HMXBs, the iron line can be relativistically broadened while the BH is in the soft state and it is thought to arise from the inner edge of the accretion disk (Remillard & McClintock 2006). The broadening of these lines can be modeled in order to estimate the spin of the BH (e.g., Tomsick et al. 2014b).

1.2 HMXBs in a Broader Astrophysical Context

1.2.1 HMXBs and the Evolution of High-Mass Stars

An accurate understanding of massive stellar evolution is crucial in building our knowledge of our Universe, but several aspects of massive stellar evolution remain poorly constrained, because the rarity and short lifetimes of massive stars make them difficult to study. The study of HMXB populations can address some of these open questions.

Stars with masses $\gtrsim$10 $M_\odot$ are relatively rare but of profound importance to our understanding of the Universe, because due to the steep scaling between a star's initial mass and its luminosity, a small number of massive stars can outshine the much larger population of low-mass stars in a galaxy. Thus, our knowledge of star-forming galaxies across the history of the Universe depends on our ability to accurately relate their ultraviolet (UV) emission, partly reprocessed by dust and gas, to the star-formation rate (SFR) and the initial mass function (IMF) of a galaxy's stellar population. Massive stars also significantly impact their galactic environments, chemically enriching the interstellar medium with heavy elements and providing feedback that contributes to the regulation of future star formation through their UV radiation, stellar winds, and supernova explosions.

Significant uncertainties remain in our understanding of massive stellar evolution, especially with regards to mass loss due to stellar winds or eruptions, and the effect that a close binary companion (which most OB stars possess) has on stellar evolution (Sana et al. 2012; Smith 2014). The mass loss rates of stellar winds at different stages of a massive star's evolution, the stellar envelope binding energy and the efficiency of orbital energy transfer to the envelope during the common envelope phase are poorly constrained. Since these uncertainties affect the predicted luminosities and burning lifetimes of stars, improving the mass-loss prescriptions for stellar evolutionary models is important for making ultraviolet, infrared, and Hα luminosities more reliable SFR indicators. Furthermore, while the metallicity[8] dependence of line-driven winds of main-sequence OB stars is fairly well understood (Vink et al. 2001), it is unknown how metallicity might affect the mass loss rates of evolved massive stars or the prevalence of mass exchange episodes in binaries (Smith 2014), which in turn will impact SFR estimates.

HMXBs provide the opportunity to learn both about the stellar winds of high-mass

[8]Metallicity is the relative abundance of elements heavier than helium.

stars and the effects of binary interaction on stellar evolution. Some Sg HMXBs show very high levels of X-ray absorption ($N_{\rm H} \sim 10^{23}$ cm^{-2}) local to the source, providing insight into the density and clumpiness of stellar winds (Negueruela et al. 2008; Walter et al. 2003). Furthermore, comparing the properties of observed HMXB populations (such as the distribution of their orbital periods, compact object masses, and luminosities) to those predicted by theoretical simulations can help constrain different phases of binary evolution. In population synthesis studies, the numbers and types of HMXBs produced from a given population of high-mass binaries depend on factors such as the stellar wind strength prescription, the physical treatment of the common envelope phase, and the speed distribution of natal kicks received by BHs and NSs when their progenitor explodes as a supernova (Fragos et al. 2013b). For example, the expected number of Be-BH sytems in the Galaxy varies by an order of magnitude depending on the value adopted for the efficiency of orbital energy transfer during the common envelope phase (Belczynski & Ziolkowski 2009; Grudzinska et al. 2015); the treatment of the common envelope phase in theoretical models also results in different predictions for the correlation between the X-ray luminosity of HMXBs and their spatial offset from nearby star clusters in which they were likely born (Zuo & Li 2014). Other studies predict that due to the weaker stellar winds of low-metallicity stars, a larger number of luminous HMXBs should be formed in low-metallicity environments (Dray 2006; Zampieri & Roberts 2009; Linden et al. 2010). Thus, comparing the properties of observed populations of HMXBs to the predictions of such models can constraints on the processes governing the evolution of high-mass stars.

With the advent of gravitational wave (GW) astronomy, a more thorough understanding of HMXB populations will be especially useful for interpreting the origins of the double compact binaries detected by observatories such as the Advanced Laser Interferometer Gravitatioval-Wave Observatory (LIGO) (LIGO Scientific Collaboration et al. 2015) and the Advanced European Gravitational Observatory-VIRGO (Accadia et al. 2015). The frequency range of GW emission observable by LIGO/VIRGO enables the detection of the final inspiral and merging of NS-NS, NS-BH, and BH-BH binaries. Some of these double compact systems may be dynamically formed in clusters (O'Leary et al. 2006; Rodriguez et al. 2015), but many are expected to be the descendants of HMXBs (Belczynski et al. 2011; Bulik et al. 2011; Belczynski et al. 2013; Postnov & Yungelson 2014). Thus, HMXBs provide a means of connecting the dots between main-sequence binary stars and these inspiraling compact objects.

Two GW signals have been detected to date; both are attributed to BH-BH mergers. The masses of the BHs associated with the first GW signal were measured to be 36^{+5}_{-4} and $29 \pm 4 M_{\odot}$ (Abbott et al. 2016c), while the BHs associated with the second signal have masses of 14^{+8}_{-4} and $7.5 \pm 2.3 M_{\odot}$ (Abbott et al. 2016b). The latter BH masses are similar to those of Galactic BHs in X-ray binaries (Özel et al. 2010), but the former are significantly higher. If the two $\sim 30 M_{\odot}$ BHs whose merger produced the first GW detection are descendants of an HMXB, then they likely formed in a low-metallicity galaxy (Abbott et al. 2016a; Belczynski et al. 2016) given that an enhanced number of ULXs are found in low-metallicity galaxies (Prestwich et al. 2013), and population synthesis models predict that HMXBs in

low-metallicity environments host more massive BHs (Zampieri & Roberts 2009; Linden et al. 2010). Other more exotic origins for the first GW signal have been suggested, including the collapse of a rapidly rotating massive stars (Loeb 2016) and the coalescence of primordial BHs (Sasaki et al. 2016). Further studies of HMXB populations in low-metallicity environments will help assess the feasibility that the first GW signal was produced by the descendant of a high-mass binary rather than one of these more exotic scenarios. As more double compact mergers are detected by GW observatories, our understanding of HMXB populations will be valuable in determining the implications of the detection rates of GW sources for stellar evolutionary models.

1.2.2 The Impact of HMXBs on Early Galaxies and the Epoch of Reionization

Studies of extragalactic X-ray binaries (XRB) in the local and low-redshift Universe have found that the X-ray luminosity of HMXBs is strongly correlated with a galaxy's star formation rate (SFR), while the X-ray luminosity of LMXBs is correlated with a galaxy's stellar mass (Grimm et al. 2003; Lehmer et al. 2010; Mineo et al. 2012). A weaker correlation, which may be subject to sample selection biases, has been measured between the HMXB L_X/SFR and the gas-phase metallicity[9] of a galaxy (Basu-Zych et al. 2013a; Brorby et al. 2016). In the nearby Universe, these correlations reveal how the formation and evolution of XRB populations depend on their galactic environments; the inverse effect, the impact that XRBs can have on their host galaxy, is negligible and limited to their local environments because they constitute such a small fraction of the stellar population.

However, in the early Universe, HMXBs may play an important role in the evolution of galaxies and the intergalactic medium (IGM). It has been suggested that HMXBs may be an important source of feedback in young dwarf galaxies ($M \lesssim 10^8 M_\odot$). If HMXBs "turn on" before the first energetic supernovae[10] inject significant energy into the interstellar medium (ISM), then feedback from HMXBs may help a galaxy to retain more of its gas which could eventually form additional stars (Justham & Schawinski 2012). The physical mechanism by which this occurs is as follows: (1) radiative feedback from HMXBs creates hot, photoionized pockets of gas, (2) when energetic SNe do explode, they preferentially expand through regions of hot, low-density gas and do not eject as much of the colder, denser gas. Justham & Schawinski (2012) argue that the interplay between the relative strength and timing of HMXB and SN feedback will result in large statistical variations of the gas retention fraction in different dwarf galaxies of similar mass.

The effect that HMXBs may have on the IGM in the early Universe may be of even greater consequence than their impact on young dwarf galaxies. Using population synthesis models and constraints on the star formation history and metallicity evolution of the universe,

[9]The gas-phase metallicity derived from strong emission lines originating in HII regions is a proxy for the metallicity of the young stellar population, including HMXBs.

[10]A SN will always precede the formation of an HMXB since it requires the creation of a compact object, but direct collapse SN that form BHs are not expected to produce powerful explosions.

Fragos et al. (2013a) predict that the X-ray luminosity per co-moving volume from XRBs will exceed the X-ray emissivity from AGN above $z \gtrsim 6-8$. Thus, during the Epoch of Reionization, when the neutral hydrogen gas in the IGM was being reionized by the first stars and galaxies, XRBs may have been the primary producers of X-ray emission. Hydrodynamic simulations which include radiative transfer of UV and X-ray photons indicate that while not having a significant net effect on star formation in a typical halo, HMXBs heat the IGM to temperatures of $\sim 10^3$ K over scales of hundreds of kiloparsecs and smooth out small scale structures, reducing the recombination rate and making it easier to keep the reionized gas ionized (Jeon et al. 2014). Futhermore, feedback from X-ray binaries may facilitate the escape of Lyman-α emission from galaxies in the early Universe (Prestwich et al. 2015). Measurements of the HI 21 cm power spectrum can constrain the amount of X-ray heating during the Epoch of Reionization (Pober et al. 2014; Ewall-Wice et al. 2016) and have already ruled out models that do not include any X-ray heating (Parsons et al. 2014; Pober et al. 2015). Improving constraints on the expected number, luminosity distribution, and spectral shape of HMXBs in low-metallicity, high-redshift galaxies will help to interpret measurements of the 21 cm power spectrum.

1.3 Other Galactic X-ray Populations

Although the three main studies presented in this dissertation share a common motivation to improve our undestanding of HMXB populations and evolution, the largest project, which is discussed in Chapter 2, also aims to study other Galactic X-ray populations. In particular, the goals of this project were to find low-luminosity HMXBs, and to identify the dominant low-luminosity X-ray populations in the Galactic disk and compare them to the X-ray sources in the Galactic Center. Therefore, this section provides short descriptions of different X-ray populations and their X-ray emission; additional details about these different types of sources are included in Chapter 2.

1.3.1 Accreting Binaries

Low-Mass X-ray Binaries

Low-mass X-ray binaries (LMXBs) consist of a NS or BH accreting material from a low-mass star that is overfilling its Roche lobe. LMXBs display X-ray luminosities of $10^{35} - 10^{39}$ erg s^{-1} and have orbital periods of $\lesssim 10$ hours (Lamb 1989; Gilfanov 2004). BH LMXBs exhibit similar spectral states to BH HMXBs (see §1.1.2). NS LMXBs can be divided into two subclasses, Z sources and atoll sources, based on the pattern they trace in X-ray color-color diagrams as they transition between different spectral states (Hasinger & van der Klis 1989; van der Klis 1989b). Z sources radiate at luminosities close to the Eddington luminosity ($\sim 10^{38}$ erg s^{-1}) and exhibit soft spectra regardless of their position in the color-color diagram. In contrast, atoll sources span a lower and larger luminosity range ($\sim 10^{35} - 10^{37}$ erg s^{-1}), exhibiting soft spectra at high luminosities and hard power-law tails

at low luminosities. The differences between Z and atoll sources are thought to be driven by differences in the mass accretion rate, while the causes of spectral state transitions are not well understood but likely associated with variations in the inner disk radius and the size and temperature of the corona (Lamb 1989; Lin et al. 2009).

Cataclysmic Variables

Cataclysmic variables (CVs) are short-period ($P_{\rm orb} \lesssim 20$ hours) binary systems in which a white dwarf (WD) accretes material via disk accretion from a low-mass main-sequence star overfilling its Roche lobe. CVs display a variety of spectral and timing properties and are divided into different subclasses based on the magnetic field strength of their WDs and the CV variability.

About 75% of CVs have weak magnetic fields ($B \lesssim 10^4$ G); in these nonmagnetic CVs, the accretion disk extends all the way to the WD surface (Cropper 1990). Thermonuclear eruptions have been observed from some nonmagnetic CVs, releasing as much as $\sim 10^{45}$ ergs of energy. Classical novae are CVs from which a single, luminous eruption has been observed, while recurrent novae are CVs which have exhibited multiple eruptions that are 10–100 times less powerful that classical novae and have recurrence times of 10–100 years (Robinson 1976). Most nonmagnetic CVs are either dwarf novae, which exhibit small outbursts during which the optical flux increases by a factor of $\lesssim 100$, or novalike CVs, which do not display significant outbursts (Robinson 1976; Verbunt et al. 1997). The X-ray emission from nonmagnetic CVs primarily originates in the boundary layer between the accretion disk and the WD surface, and some of the emission is then reflected off the WD surface (Connon Smith 2007). Nonmagnetic CVs have X-ray luminosities of $L_X = 10^{29} - 10^{32}$ erg s^{-1} and their spectra tend to be well described by thermal bremsstrahlung spectra with $kT \approx 1 - 15$ keV (Eracleous et al. 1991; Verbunt et al. 1997; Muno et al. 2004; Xu et al. 2016).

Polars are CVs with strong magnetic fields with $B \sim 10^7 - 10^8$ G. The magnetic field in polars is strong enough to prevent the formation of an accretion disk; material is channeled directly from the accretion stream onto the magnetic poles of the WD. The strong magnetic field also tends to synchronize the WD spin with the binary orbital period. Intermediate polars (IPs) are CVs with magnetic field strengths of $\sim 10^6 - 10^7$ G. In IPs, the accretion disk is truncated by the WD magnetosphere, which channels material towards the WD magnetic poles. In magnetic CVs, X-rays are produced, primarily by bremsstrahlung emission (and in polars, by cyclotron emission) in the accretion column, and can be Compton scattered to higher energies by electrons in the accretion column or reflected by the WD surface (Patterson 1994; Cropper 1990). Polars make up about 10–20% of CVs, have $L_X = 10^{30} - 10^{32}$ erg s^{-1}, and exhibit thermal spectra with $kT \approx 5 - 25$ keV (Cropper 1990; Muno et al. 2004; Xu et al. 2016). It is estimated that only 5–10% of CVs are IPs, which have the highest luminosities ($L_X = 10^{31} - 10^{33}$ erg s^{-1}) and hardest spectra ($kT \approx 10 - 50$ keV) of all CVs (Patterson 1994; Muno et al. 2004; Xu et al. 2016).

All CVs exhibit fluorescent iron emission lines in their X-ray spectra. The most prominent line transitions that are observed are Kα lines from neutral and weakly-ionized species

at 6.4 keV, from helium-like iron ions at 6.7 keV, and from hydrogen-like ions at 7.0 keV. Fluorescent emission occurs as photons are reflected by the WD surface, as well as in the accretion column (for magnetic CVs) or the accretion disk (in nonmagnetic CVs). The equivalent widths and line flux ratios of the iron lines detected in nonmagnetic CVs, polars, and IPs differ from each other, and thus can be useful in distinguishing these different types of CVs (Xu et al. 2016).

Symbiotic Binaries

Symbiotic binaries (SBs) typically consist of a white dwarf accreting from a red giant in a wide orbit with orbital periods of $\sim 100 - 1000$ days (Belczyński et al. 2000). Although SBs are sometimes considered a subclass of CVs, they are distinguished by the fact that accretion is powered by the red giant wind rather than Roche lobe overflow. Nonetheless, disk formation around the WDs in SBs is common, and, as a result, the X-ray properties of SBs are similar to those of CVs (Livio & Warner 1984; Wynn 2008). Most SBs have X-ray luminosities of $10^{31} - 10^{33}$ erg s^{-1}, although they have been observed to be as bright as 10^{34} erg s^{-1} (Masetti et al. 2002; Smith et al. 2008; Nespoli et al. 2010; Luna et al. 2013).

SBs are divided into subclasses based on their spectral properties. α-type sytems have the softest emission, with photon energies below 1 keV, which is thought to originate from a quasi-steady burning shell on the WD surface (Orio et al. 2007). β-type binaries are soft X-ray sources, with most photons having energies below 2.4 keV, whose emission is likely produced in collisions of the red giant wind with a wind coming off the WD (Muerset et al. 1997). The emission from hard X-ray SBs, known as δ-type systems, is modeled as optically thin thermal plasma with $kT \gtrsim 10$ keV; the likely origin of this hard X-ray emission is the boundary layer between the WD surface and the accretion disk (Luna et al. 2013). Finally, γ-type SBs, which exhibit hard Comptonized spectra with $\Gamma = 1 - 2$, are thought to host neutron stars accretors given the short spin periods detected in some of these systems (Lewin et al. 1971; Koyama et al. 1991; Masetti et al. 2007); γ-type SBs are sometimes called symbiotic X-ray binaries (SyXBs) because of they harbor NSs.

1.3.2 Stellar Sources and Isolated Compact Objects

Neutron Stars

Neutron stars can produce significant amounts of X-ray emission even if they are not part of an accreting binary. NSs are born as rapidly spinning pulsars ($P_{\rm spin} \sim 10-100$ milliseconds); isolated millisecond pulsars (MSPs) can produce X-ray luminosities of $10^{28} - 10^{31}$ erg s^{-1} as they spin down and emit magnetic dipole radiation (Possenti et al. 2002). If the MSPs are located in dense regions of the interstellar medium (ISM), then the interaction of the ISM and the particles accelerated in the NS magnetosphere can produce higher X-ray luminosities of $10^{31} - 10^{33}$ erg s^{-1} (Cheng et al. 2004). The X-ray spectra of MSPs in the 2–10 keV band are well described by power-law models with $\Gamma \approx 2$ (Possenti et al. 2002).

Young pulsars with very high spin-down luminosities can power a pulsar wind nebula (PWN; Gaensler & Slane 2006). Electrons and positrons that are accelerated by the pulsar emit synchrotron radiation that dominates the radio and X-ray emission from PWN. Young PWNe, which are often associated with supernova remnants (SNRs), have X-ray luminosities of $10^{32} - 10^{37}$ erg s^{-1} and typical photon indices of $\Gamma \approx 2$ (Gotthelf 2003). Since asymmetries in supernova explosions tend to impart velocity kicks of $\sim 100 - 1000$ km s^{-1} to the pulsars they produce, pulsars can travel outside of their associated SNRs in $\sim 10^4$ years (Lyne et al. 1982). As the pulsar travels supersonically through the ISM, it drives a bow shock, leading to the emission of non-thermal synchrotron radiation with a cometary morphology that can be observed in the X-ray and radio bands (Gaensler & Slane 2006).

Isolated NSs can also be detected at X-ray energies if they have very high magnetic fields of $10^{14} - 10^{15}$ G. Such NSs, known as magnetars, exhibit persistent X-ray emission of $L_X \sim 10^{34} - 10^{35}$ erg s^{-1}, as well as occasional outbursts that increase the X-ray flux by factors of 10–1000, powered by the decay of the magnetic field (Duncan & Thompson 1992; Thompson et al. 2002; Rea & Esposito 2011). Magnetars exhibit very soft spectra in the $2 - 10$ keV band ($\Gamma \approx 3 - 4$) and faint hard X-ray tails with $\Gamma \approx 0 - 1$ extending out to hundreds of keV (Olausen & Kaspi 2014).

Colliding wind binaries and high-mass stars

Colliding wind binaries (CWBs) are binaries consisting of two high-mass stars that produce X-ray emission through shocks in their stellar winds. Often at least one of the binary companions in an evolved star, such as a Wolf-Rayet or a supergiant star, since these evolved stars have much more powerful winds (Pollock 1987; (Smith 2014)). CWBs can exhibit X-ray emission with $L_X \sim 10^{33} - 10^{35}$ erg s^{-1} and thin thermal plasma spectra with $kT \approx 1 - 4$ keV (Pollock 1987; Portegies Zwart et al. 2002).

X-rays can also be produced within the wind of a single, isolated high-mass star, but the emission from an isolated star is weaker since the relative velocity of the shocked material is lower for a single star than for one in a binary (Portegies Zwart et al. 2002). The X-ray emission of isolated high-mass stars, including O-type stars, early B-type, and Wolf-Rayet stars, follow the correlation $L_X/L_{\rm bol} \approx 10^{-7}$ (Berghoefer et al. 1997; Sana et al. 2006). The X-ray emission from isolated high-mass stars is softer than that from CWBs, having $kT \approx 0.1 - 1$ keV (Sana et al. 2006).

X-ray active binaries and isolated low-mass stars

Low-mass stars of spectral type G, K, and M have dynamo-generated magnetic fields due to their rotation and large convective envelopes; late M-type stars are fully convective, but still have strong magnetic fields generated by turbulent convection. The magnetically heated coronae of low-mass stars produce soft X-rays with $kT < 1$ keV and low X-ray luminosities below 10^{29} erg s^{-1} (Krishnamurthi et al. 2001).

In X-ray active binaries (ABs), such as RS Canum Venaticorum (RS CVn), magnetic coronal activity is enhanced because the rotation of the two low-mass stars is higher than for

typical isolated stars; stars in ABs rotate faster because their rotation periods are tidally synchronized to the orbital period, which is $\lesssim 30$ days (Dempsey et al. 1993). The persistent X-ray emission of ABs typically is in the luminosity range $L_X = 10^{29} - 10^{31.5}$ erg s^{-1} and has a soft spectrum with $kT < 2$ keV (Dempsey et al. 1993). However, they can exhibit flares with peak luminosities of $\sim 10^{32}$ erg s^{-1} and $kT \approx 10$ keV (Franciosini et al. 2001).

1.4 X-ray Focusing Telescopes

While X-ray astronomy began with the rocket flight experiments of the 1960s, it was revolutionized by the development of telescopes that could focus X-rays. The first X-ray focusing satellite, *EINSTEIN* (Giacconi et al. 1979), was launched in 1978, and it had an angular resolution of a few arcseconds, facilitating the association of X-ray sources with multiwavelength counterparts, and a sensitivity several hundred times greater than previous satellites. X-ray wavelengths are so short that they cannot be reflected by conventional optics used for visible light. However, since the refractive index of most materials to X-rays is less than unity (the refractive index of vacuum), X-rays can undergo total external reflection when they have very low incidence angles (are almost parallel) with respect to the reflective surface. Taking advantage of this effect, Hans Wolter developed grazing incidence optics that could focus X-rays in 1952. Although Wolter developed this design for an X-ray microscope, it was adopted for X-ray telescopes by Giacconi & Rossi (1960). The Wolter-I design, shown in Figure 1.2, uses two sets of mirrors to focus X-rays; X-ray photons are first reflected off a mirror section shaped as a parabola and then reflected a second time off a section shaped as a hyperbola. The critical incidence angles, which are typically $< 1 - 2$ degrees, are very shallow and result in a small collecting area per mirror surface area; to compensate for this effect, many mirrors shells are nested within one another to increase the effective collecting area. The mirrors are typically coated with high density materials such as gold or iridium; the heavier the element used for the coating, the higher the critical incidence angle at a given photon energy is, which increases the collecting area.

The studies described in this dissertation make extensive use of data from three X-ray focusing telescopes, which are described in this section: the *Chandra X-ray Observatory* (*Chandra*), the *X-ray Multi-Mirror Mission* (*XMM-Newton*), and the *Nuclear Spectroscopic Telescope Array* (*NuSTAR*).

1.4.1 *Chandra*

The *Chandra X-ray Observatory*, one of NASA's Great Observatories, was launched on 1999 July 23 into a 64 hour eccentric orbit and is still operating at the time of this writing (Weisskopf et al. 2002). The *Chandra* telescope, shown in Figure 1.3, is made up of four sets of nested mirrors coated with iridium, providing an effective area of ≈ 300 cm^2 in the $0.1 - 10$ keV band (although the effective area drops off steeply below 0.5 keV and above 7 keV). *Chandra* has the best angular resolution of any X-ray telescope launched to date,

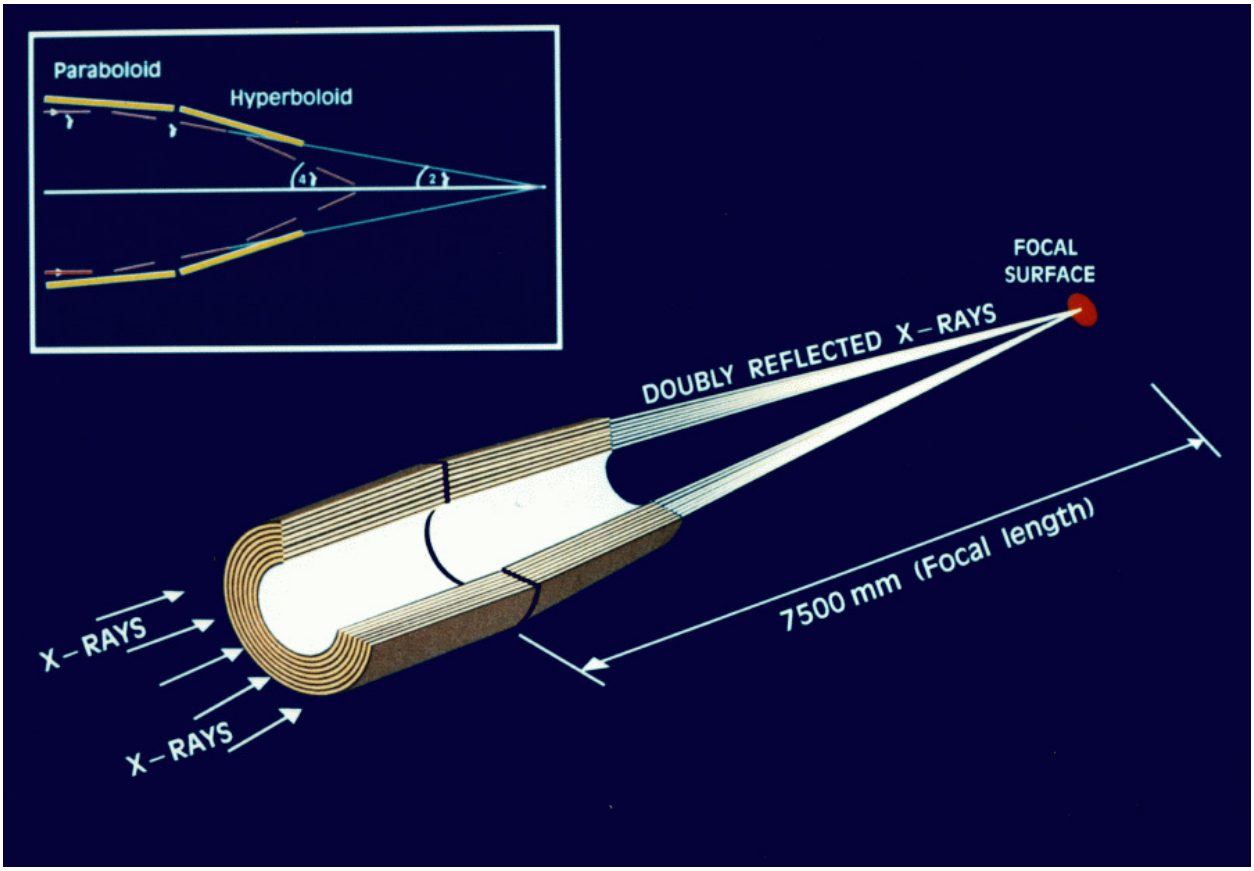

Figure 1.2: Wolter-I mirror design for focusing X-rays. X-rays are reflected twice at grazing incidence, first off a paraboloid mirror and then off a hyperboloid mirror. This particular design is for the *XMM-Newton* telescope. (Credit: ESA)

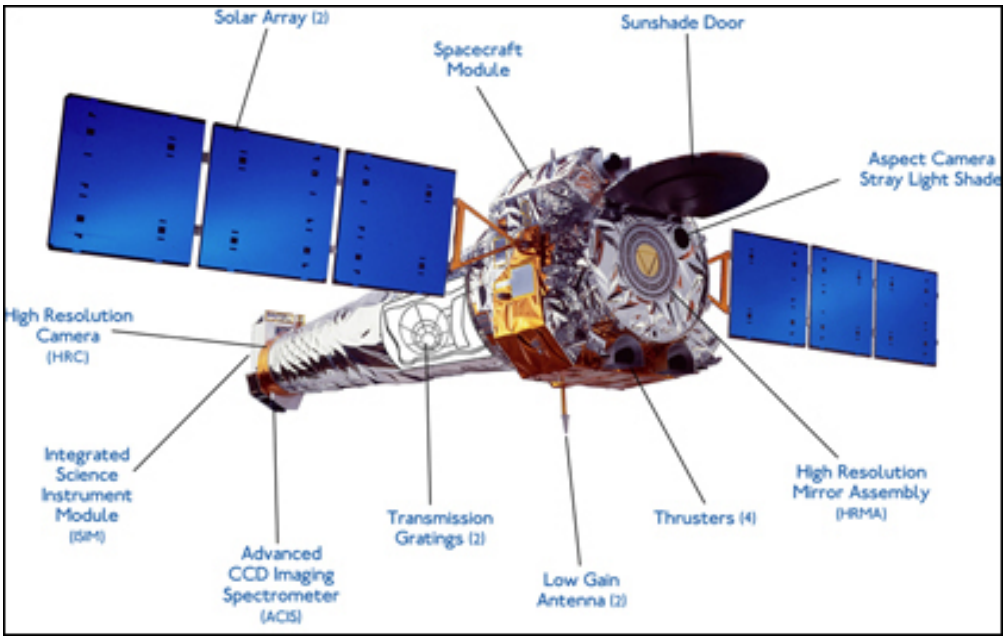

Figure 1.3: Schematic of the *Chandra X-ray Observatory* including the locations of the instruments. (Credit: NASA/CXC)

having a half-power diameter (HPD) of 1″ on-axis; however, its point spread function (PSF) significantly worsens at large off-axis angles from the telescope aim point, reaching an HPD of approximately 10″ at off-axis angles of 12′ for photon energies of 6 keV.

The *Chandra* data used in this dissertation is taken by the Advanced CCD Imagining Spectrometer (ACIS; Garmire et al. 2003). ACIS is equipped with eight charged-coupled devices (CCDs), up to six of which can be simultaneously collecting data for any given observation. Four CCDs are arranged in a 2×2 configuration providing a total field of view (FoV) of $17' \times 17'$, while the other four are arranged in a single row. The four CCDs in the square configuration are the ones most frequently employed for large surveys, including the Norma Arm Region *Chandra* survey discussed in this dissertation. Each ACIS CCD consists of 1024×1024 pixels, each of which subtends 0.″492 on the sky. ACIS provides moderate spectral resolution ($E/\Delta E \approx 20$); its time resolution in standard mode is $\Delta t = 3.2$ s and can be as high as ~ 6 ms in fast timing mode. For bright sources with count rates $\gtrsim 0.1$ counts s^{-1}, *Chandra*'s standard time resolution can result in pileup, which occurs when more than one photon hits the same pixel within a single read-out cycle; pileup affects the measured flux and spectrum of a source.

Chandra is also equipped with the High Resolution Camera (HRC; Murray et al. 2000), which provides better than arcsecond (HPD) imaging over a $30' \times 30'$ FoV. The energy resolution of HRC ($E/\Delta E \approx 1$) is lower than that of ACIS. *Chandra* also possesses two gratings for higher resolution spectroscopy, the High Energy Transmission Grating with $E/\Delta E \approx 1000$ and the Low Energy Transmission Grating with $E/\Delta E \approx 20$.

1.4.2 *XMM-Newton*

The ESA mission *XMM-Newton* was launched just a few months after *Chandra* on 1999 December 10 and placed in a 48 hour eccentric orbit (Jansen et al. 2001). *XMM-Newton* continues to operate as of this writing. There are three telescopes on board *XMM-Newton*; each of them consists of 58 nested mirrors with a gold coating. These telescopes provide an angular resolution of about 14″ HPD.

At the focus of each of the telescopes is a CCD-based European Photon Imaging Camera (EPIC). Two of these cameras use metal oxide semiconductor (MOS) CCD arrays (Turner et al. 2001), and one uses a pn semiconductor CCD (Strüder et al. 2001). The EPIC pn effective area is approximately 800 cm^{-2}, while the MOS cameras have an effective area of roughly 200 cm^{-2}; the energy range covered by all three cameras is $0.1 - 12$ keV, although the effective area drops off steeply below 0.5 keV and above 10 keV. Both the MOS and pn cameras have moderate spectral resolution ($E/\Delta E \approx 50$); the Reflection Grating Spectrometers (den Herder et al. 2001) provide high-resolution spectra ($E/\Delta E \approx 200 - 800$) in the 0.3-2.1 keV energy range and can be used with the MOS cameras.

The EPIC cameras can be operated in several different modes. Full frame mode, which collects data from the full CCD area, has a time resolution of 2.6 s and 73.4 ms for the EPIC MOS and pn cameras, respectively. The large window and small window modes trade off a smaller FoV for better time resolution. In timing mode, imaging is only carried out in a single dimension to permit high-speed readout; timing mode has a time resolution of 1.75 ms for MOS and 0.03 ms for EPIC pn.

1.4.3 *NuSTAR*

On 2012 June 13, the NASA Small Explorer mission *NuSTAR* was launched into a near-equatorial, low-Earth orbit (Harrison et al. 2013). *NUSTAR*, shown in Figure 1.4, is the first telescope to focus hard X-rays above 15 keV. This achievement was made possible by the development of depth-graded multilayer mirror coating. These multilayer coatings consist of about 200 thin coatings of two alternating materials of different densities. The high/low density material combinations used in the *NuSTAR* multilayers are platinum/silicon carbide and tungsten/silicon. Due to the high density contrast of the materials, the multilayer coating effectively works as a crystal lattice, producing constructive interference that enhances the reflectivity of the mirrors. The multilayer coatings used by *NuSTAR* allow the mirrors to reflect photons with energies as high as 79 keV; above this energy, platinum begins to absorb rather than reflect X-rays. The full *NuSTAR* energy band is $3 - -79$ keV.

NuSTAR has two telescopes, each with 133 nested mirrors, and two detector units (called focal plane modules), one at the focus each of the two co-aligned telescopes. Each focal plane module is comprised of four cadmium-zinc-telluride (CZT) detectors, which have a moderate energy resolution of $E/\Delta E \approx 15$. *NuSTAR*'s angular resolution is 58″ (HPD) and its times resolution is ~ 0.1 ms.

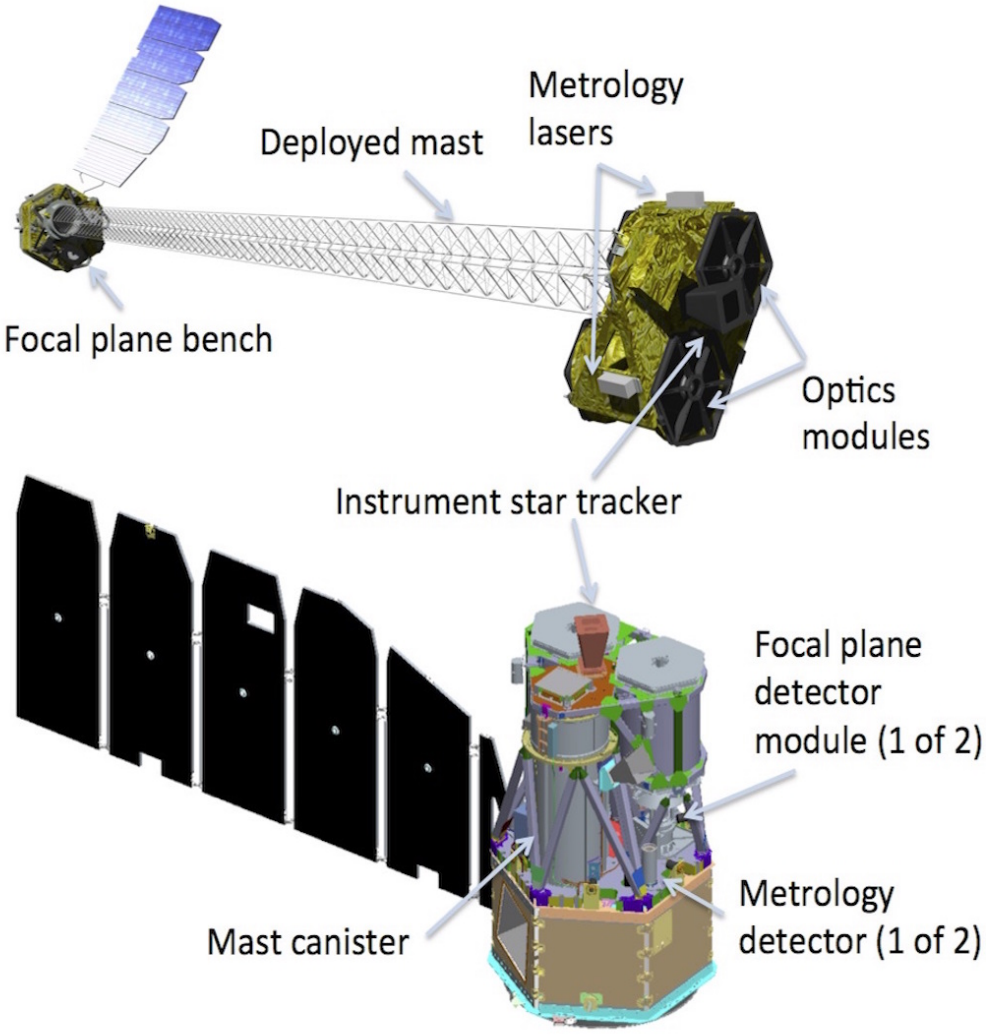

Figure 1.4: *Top*: Schematic of the *NuSTAR* spacecraft with the 10 meter mast extended. The deployable mast provides the long focal length required to focus X-rays. *Bottom*: Schematic arrangement of the *NuSTAR* focal plane bench. Each optics module focuses X-rays onto one of the two focal plane modules. (Credit: NASA/*NuSTAR* collaboration)

1.5 Open Questions Addressed by this Dissertation

Using data from X-ray focusing telescopes, this dissertation addresses open questions regarding HMXBs and Galactic X-ray sources. Chapter 2 describes *Chandra* and *NuSTAR* surveys of the Norma spiral arm of the Milky Way, the aim of which is to improve our understanding of low-luminosity X-ray sources and constrain the faint HMXB population. Chapter 3 presents preliminary results of a study that tests models of the metallicity dependence of HMXBs using deep extragalactic *Chandra* surveys. Chapter 4 discusses the relative fractions of NS and BH HMXBs and identification of the nature of the compact object in a non-pulsating HMXB based on detailed timing and spectral analysis using *XMM-Newton* and *NuSTAR* observations.

1.5.1 The faint: How many low-luminosity HMXBs exist in our Galaxy? What types of sources dominate the Galactic ridge hard X-ray emission?

How many low-luminosity HMXBs exist in our Galaxy and what constraints do their properties place on the evolution of high-mass stars?

As discussed in §1.1.2, the luminosity function (LF) of Galactic HMXBs has been measured down to luminositities of $\sim 10^{34}$ erg s^{-1} (Lutovinov et al. 2013). Although some outbursting Be HMXBs have been detected in quiescence at lower luminosities (e.g. Rutledge et al. 2007; Doroshenko et al. 2014; Reig et al. 2014; Elshamouty et al. 2016), it is unknown how large a population of HMXBs with persistently low luminosities exists in the Galaxy. Lutovinov et al. (2013) developed a simple model for the expected luminosity function of the persistent wind-accreting HMXB population which predicts that the HMXB LF should flatten below 10^{34} erg s^{-1} from a power-law slope of -1.4 to a slope of about -1.0. This model does not take into account that magnetic and centrifugal barriers to accretion could be important in NS HMXBs accreting at low rates (Bozzo et al. 2008), and thus the flattening of the HMXB LF could be even more pronounced than predicted by this simple model. Thus, constraining the faint end of the HMXB LF can inform our understanding of how accretion proceeds at low-accretion rates.

Identifying low-luminosity HMXBs could also lead to the discovery of additional Be-BH binaries, since the only known Be-BH binary, MWC 656, has an X-ray luminosity of $\sim 10^{31}$ erg s^{-1} (Munar-Adrover et al. 2014). As discussed in §1.2.1, the number and orbital periods of Be-BH binaries predicted to reside in the Galaxy is very sensitive to the treatment of the common envelope phase and the strength of BH natal kicks in population synthesis models (Grudzinska et al. 2015). Thus, constraining the number of Be-BH HMXBs and their period distribution could improve our understanding of these important aspects of stellar evolution. Since Be-BH binaries could be progenitors of BH-NS systems, based on the binary properties of MWC 656, Grudzinska et al. (2015) estimate that the LIGO/VIRGO detection rate of BH-NS mergers could be as high as 1 every 5 years. Finding additional Be-BH HMXBs

and measuring their orbital periods will help to refine these estimates as well.

Therefore, one of the goals of this dissertation research is to identify low-luminosity HMXB candidates, which, once their HMXB nature is confirmed, will help constrain the faint end of the HMXB LF and contribute to our understanding of accretion processes in HMXBs and the evolution of high-mass stellar binaries. In order to find HMXB candidates, we observed a region of the Galactic disk tangent to the Norma spiral arm that has the highest number of HII regions and OB associations (clusters of high-mass stars) with *Chandra* and *NuSTAR* because HMXBs are found in close proximity to regions of recent star formation. *Chandra*'s subarcsecond angular resolution was necessary to identify unique optical and infrared counterparts to the X-ray sources we detected, which we followed-up spectroscopically to determine whether they were high-mass or low-mass stars. *NuSTAR*'s sensitivity to hard X-rays was crucial for improving the X-ray spectral constraints of detected sources, facilitating the distinction of accreting HMXBs from colliding wind binaries.

What are the dominant low-luminosity hard X-ray populations in the Galactic disk and how do they compare to those in the Galactic Center?

The *Chandra* and *NuSTAR* surveys of the Norma region that we carried out to search for low-luminosity HMXBs are also ideally suited to the study of other low-luminosity Galactic X-ray sources. and their contribution to the Galactic ridge X-ray emission (GRXE). Since the discovery of the GRXE (Bowyer et al. 1968), several studies have been devoted to determining the source of this large-scale feature in the X-ray sky. Deep *Chandra* surveys have resolved over 80% of the GRXE into point sources in the 6–7 keV band, which corresponds to the energies of fluorescent iron line emission (Revnivtsev et al. 2009b), ruling out a diffuse origin for the bulk of the GRXE. The study of individual sources detected in these deep surveys and the comparison of the flux ratios and equivalent widths of the iron lines in the GRXE spectrum to those of nearby X-ray sources indicate that the soft (< 10 keV) X-ray component of the GRXE primarily arises from dwarf novae and active binaries (Xu et al. 2016). However, it is less clear what sources contribute to the GRXE at hard X-ray energies. It has been suggested that magnetic CVs, especially IPs, dominate the GRXE spectrum above 10 keV (Revnivtsev et al. 2006b); assuming that is the case, fitting the broadband GRXE spectrum with an IP spectral model suggests that the typical white dwarf mass in IPs is $\approx 0.6 M_{\odot}$ (Krivonos et al. 2007; Türler et al. 2010; Yuasa et al. 2012). However, with non-focusing hard X-ray telescopes, which have poor angular resolution of ∼tens of arcminutes, it was not possible to resolve the hard X-ray sources with $L_X \lesssim 10^{33}$ erg s^{-1} that contribute to the GRXE spectrum above 10 keV.

As the first mission to focus hard X-rays, *NuSTAR* is the first telescope that can resolve a significant fraction of the GRXE above 10 keV. Thus, a second goal of our *Chandra* and *NuSTAR* surveys of the Norma region is to classify the hard X-ray sources detected by *NuSTAR*, and to confirm whether IPs are the primary contributors to the GRXE at hard X-ray energies. Since similar surveys have been performed of a square degree region in the vicinity of the Galactic Center, an additional aim of this research is to compare the hard X-ray

populations in the Norma and Galactic Center regions; variations in the relative fractions of different types of X-ray sources in these two regions can inform our understanding of the star formation history of the Galaxy and how stellar evolution may be impacted by different galactic environments. For example, it has been suggested, both by simulations and observations, that the initial mass function in the vicinity of the Galactic Center may be more top-heavy, which would result in more massive compact objects (Morris 1993; Paumard et al. 2006).

1.5.2 The poor: Are HMXB populations in metal-poor environments more luminous?

Since more metal-poor stars have weaker stellar winds (Vink et al. 2001), a star's metallicity can significantly impact its evolution. Several population synthesis studies have been performed to assess the effect of metallicity on HMXBs; while these studies differ in some details, they all predict that HMXB populations in low-metallicity environments should be more X-ray luminous due to a larger number of BH HMXBs accreting via Roche lobe overflow being produced per star formation rate (Dray 2006; Linden et al. 2010; Fragos et al. 2013b). An inverse correlation between the gas-phase metallicity of star-forming galaxies and L_X/SFR has been observed in a sample of nearby galaxies, although the correlation is largely driven by the X-ray luminosities of blue compact dwarf galaxies (BCDs; Basu-Zych et al. 2013a; Brorby et al. 2016), which have very low-metallicity and are considered analogs of high-redshift galaxies. However, the measured correlation may be biased because upper limits on L_X/SFR for BCDs that are not X-ray detected are not taken into account, and the X-ray luminosities of about half of the galaxy sample may be dominated by stochastic variations; even if the measured correlation is accurate, it may be caused by a galaxy property other than metallicity such as the compactness of BCDs compared to other nearby star-forming galaxies. Another piece of evidence often cited in favor of the hypothesis that HMXB evolution is metallicity-depedent is the increase of L_X/SFR of star-forming galaxies with increasing redshift (Basu-Zych et al. 2013b; Lehmer et al. 2016), but this evidence is indirect.

Determining whether HMXB evolution is truly metallicity dependent is of particular relevance to understanding the Epoch of Reionization. As discussed in §1.2.2, HMXBs may contribute to the heating of the IGM and to feedback in early galaxies, especially if HMXB populations are more luminous in lower-metallicity environments. Chapter 3 of this dissertation investigates the metallicity dependence of HMXB evolution through a study of the X-ray emission of star-forming galaxies at $z \sim 2$ as a function of galaxy metallicity.

1.5.3 The steady: What is the nature of the compact objects in non-pulsating HMXBs?

As was mentioned in §1.1.1, only three of the ≈100 HMXBs in the Milky Way are known to host BHs. About 60% of the Milky Way HMXBs are known host NSs through the detection of X-ray pulsations (Bird et al. 2016). In the remaining Galactic HMXBs, the nature of

the compact object is unclear, and additional BH HMXBs may exist within this sample. Determining whether the compact objects in these HMXBs are NSs or BHs can be useful for constraining models of stellar evolution, since the ratio of NS to BH HMXBs predicted by population synthesis models depends on parameters such as the strength of the stellar winds, the common envelope phase, and the velocity distributions of natal kicks imparted to BHs and NSs (Dray 2006; Muno 2007; Belczynski & Ziolkowski 2009). The measured BH/NS ratio in HMXBs also impacts estimates of the expected numbers of different double compact object binaries which may merge and produce gravitational waves (Postnov & Yungelson 2014).

Thus, to further our knowledge of the compact objects in Galactic HMXBs, Chapter 4 of this dissertation dicusses a study performed with *XMM-Newton* and *NuSTAR* observations of the timing and spectral properties of IGR J18214-1318, an Sg HMXB whose compact object could not be identified based on previous studies.

Chapter 2

The Faint

2.1 Searching for low-luminosity HMXBs and identifying other faint Galactic X-ray populations

X-ray observations of the Galactic stellar population provide an important probe of several stages of stellar evolution. The brightest stellar X-ray sources are associated with compact stellar remants. Neutron stars (NS), black holes (BH), and white dwarfs (WD) that are accreting matter from a binary companion are bright X-ray emitters. Isolated neutron stars are also bright X-ray sources when they are young and hot, or if they accelerate particles in strong magnetic fields ($10^{12} \lesssim B \lesssim 10^{14}$ G). We can learn about earlier stages of stellar evolution from X-ray observations as well. Massive OB and Wolf-Rayet stars can produce X-rays through shocks in their stellar winds, and are sometimes more luminous than X-ray sources associated with compact stellar remnants. Low-mass main sequence stars can produce low levels of X-ray emission in their magnetic coronae, and young stellar objects can produce X-rays due to their strong magnetic fields.

Over the past decade, studies of X-ray source populations in several Galactic regions have been carried out using observations from the *Chandra X-ray Observatory*. These surveys have targeted the Galactic center (Wang et al. 2002; Muno et al. 2009), the Galactic bulge (Hong et al. 2009), the Orion region (Grosso et al. 2005), the Carina arm (Townsley et al. 2011), and a "typical" region of the Galactic plane without point sources brighter than 2×10^{-13} ergs cm^{-2} s^{-1} (Ebisawa et al. 2005). Although some young, X-ray emitting massive stars have been discovered in the Galactic center (Mauerhan et al. 2010), the Galactic center and bulge are dominated by old X-ray stellar populations. In contrast, the Orion region is a well-known star-forming region, and it has been argued that the Carina region is also a very young star-forming region since there is no evidence of a supernova explosion having occurred there yet (Smith & Brooks 2007).

We have conducted X-ray surveys of a square-degree region in the direction of the Norma spiral arm, which complement the aforementioned surveys since Norma's stellar population is likely more evolved than that of the Orion and Carina regions, but less evolved than

that of the Galactic center and bulge. The line-of-sight tangent to the Norma spiral arm contains the highest number of massive star-forming complexes in the Galaxy (Russeil 2003), demonstrating there is a significant population of young stars in this arm. Further evidence that this is a region of recent star formation is the presence of warm dust emission in *Spitzer* 8 μm images and several HII regions mapped by 1420 MHz continuum emission from the Southern Galactic Plane Survey (Georgelin et al. 1996). However, the supernova remnants discovered in this region (Green 2004; Combi et al. 2005; Funk et al. 2007) suggest that the Norma stellar population is older than the populations in the Orion and Carina regions observed with *Chandra*. Thus, the relative fractions of X-ray populations in the Norma arm may differ from those in other regions of the Galactic plane; in particular, the fraction of X-ray sources associated with evolved massive stars may be enhanced in Norma.

The Norma Arm region was observed by the *Chandra X-ray Observatory* in 2011 and with the *Nuclear Spectroscopic Telescope Array* (*NuSTAR*) between 2013 and 2015. The goals of these surveys were to identify the physical nature of low-luminosity ($L_X \lesssim 10^{34}$ erg s^{-1}) X-ray sources, to compare the Norma X-ray populations to those in other Galactic regions, and to search for low-luminosity high-mass X-ray binaries (HMXBs). As discussed in §1.5.1, improving the characterization of low-luminosity X-ray populations in different Galatic regions can shed light on the origin of the Galactic Ridge X-ray Emission (GRXE), as well as further our understanding of stellar evolution and how it may be influenced by different galactic environments. The discovery of new low-luminosity HMXBs can help inform our models of the binary evolution of high-mass stars and assess the prevalence of magnetic barriers to accretion in low accretion rate systems (see §1.5.1).

The *Chandra* observations of the Norma region allowed us to localize X-ray sources to ∼arcsecond precision, identify likely infrared and optical counterparts, determine the dominant X-ray populations based on their X-ray and infrared properties, and pinpoint candidate HMXBs and other sources of interest for near-IR spectroscopic follow-up. Through their sensitivity to hard X-rays (> 10 keV), the *NuSTAR* observations enabled more precise classification of the brighter Norma sources, revealing significant differences between the populations of cataclysmic variables (CVs) in the Norma region and the Galactic Center. Combined with our follow-up infrared spectroscopic campaigns, the *NuSTAR* survey also were important for narrowing our list of HMXB candidates. The Norma Arm Region *Chandra* and *NuSTAR* surveys are described in §2.2 and §2.3, respectively, and the HMXB candidates discovered by these surveys are discussed in §2.4.

2.2 The Norma Arm Region *Chandra* Survey (NARCS)

2.2.1 Introduction

The Norma Arm Region *Chandra* Survey (NARCS) is a large *Chandra* program which observed a $2^\circ \times 0.^\circ8$ region in the direction of the Norma spiral arm to a depth of 20 ks. The near side of the Norma arm is located at a distance of about 4 kpc while the far Norma arm

is at a distance of 10–11 kpc. Through *Chandra*'s superior angular resolution, which is 0.″5 on-axis, we were able to detect 1130 point-like sources at $\geq 3\sigma$ confidence in the Norma region and to identify reliable IR counterparts for 52% of them. The complete catalog of NARCS sources is provided in Appendix A. The NARCS observations are described in §2.2.2, while the source detection method is discussed in §2.2.3. In §2.2.4-2.2.6, we describe the photometric analysis (§2.2.4), X-ray variability studies (§2.2.5, and search for IR counterparts (§-2.2.6) that was performed for all sources. Since most of the sources were too faint for individual spectral modeling, we relied on quantile analysis to estimate their spectral properties §2.2.7, divided the sources into groups based on their quantile properties, and then fit the stacked spectra of these quantile groups (§2.2.8). Then we analyzed the photometric and spectral properties of each group in order to identify the dominant X-ray populations in this survey (§2.2.9). Our calculation of the NARCS number-flux distribution, including corrections for the Eddington bias, the incompleteness of our detection procedure, and the variations in sensitivity across the surveyed area, can be found in §2.2.10. Finally, the observed number-flux distribution is compared to predictions based on previous surveys of Galactic X-ray sources in §2.2.11.

2.2.2 Observations and Source Catalog

We performed *Chandra* ACIS-I observations in faint mode of a $2^\circ \times 0.^\circ 8$ region of the Norma spiral arm in June 2011. The primary goal of this survey was to discover faint High-Mass X-ray Binaries (HMXBs) that may have been missed in previous surveys performed with instruments with less sensitivity and angular resolution than *Chandra*. The Norma spiral arm was chosen as the target for this search because it hosts the largest number of known HMXBs of any line-of-sight through the Galaxy, likely due to its evolutionary state (Bodaghee et al. 2012c). Even though HMXBs are more common in the Norma arm than elsewhere, they are rare sources compared to other X-ray populations; thus, our ongoing efforts to identify new HMXBs will be discussed in future papers while here we will focus on studying the dominant classes of X-ray sources in this survey.

Our field was subdivided into 27 pointings; Table 2.1 reports their coordinates and exposure times and Figure 2.1 is a mosaic image of the survey. Our observing strategy was to cover a wide area with relatively uniform flux sensitivity and good spatial resolution; therefore, we chose field centers spaced by 12′, which provided roughly 70 arcmin^2 of overlap on the outskirts of adjacent observations such that the additional exposure time in these overlapping regions partly made up for the worsening point-spread function (PSF) at large off-axis angles. There are only four archival *Chandra* imaging observations of >20 ks which fall within the area of our survey region. We chose not to incorporate these data into our survey because they do not add much value compared to the modifications we would have to make to our analysis strategy, and because they might bias our study of faint X-ray populations in the Norma region since they only provide deeper coverage of a fourth of the surveyed area which may not be representative of the region as a whole.

The ACIS-I consists of four 1024 × 1024 pixel CCDs, covering a 17′ × 17′ field of view (Garmire et al. 2003). The on-axis spatial resolution of the ACIS-I is fully sampled by the

Table 2.1: *Chandra* Observations of the Norma Region

ObsID (1)	R.A. (deg) (2)	Dec. (deg) (3)	Roll (deg) (4)	Start Time (UT) (5)	Exposure (ks) (6)
12507	250.373201	-46.662951	342.217237	2011 Jun 6 10:15:53	18.8
12508	250.155011	-46.530604	342.217232	2011 Jun 6 15:57:13	18.5
12509	249.937805	-46.397816	342.217176	2011 Jun 6 21:22:23	19.4
12510	250.180190	-46.812896	342.217230	2011 Jun 9 12:29:02	19.9
12511	249.961646	-46.681456	333.217149	2011 Jun 17 11:15:19	19.3
12512	249.743370	-46.550407	317.716418	2011 Jun 27 04:52:55	20.5
12513	249.984947	-46.965904	317.716539	2011 Jun 27 11:00:21	20.2
12514	249.767582	-46.829470	342.217317	2011 Jun 10 16:07:39	19.8
12515	249.550110	-46.695978	342.217265	2011 Jun 10 22:04:48	19.5
12516	249.790838	-47.111874	342.217386	2011 Jun 11 03:46:38	19.5
12517	249.572205	-46.978413	342.217342	2011 Jun 11 09:28:28	19.5
12518	249.354673	-46.844540	342.217308	2011 Jun 11 15:10:18	19.5
12519	249.594334	-47.262081	333.217286	2011 Jun 13 04:25:13	19.3
12520	249.375577	-47.128273	333.217242	2011 Jun 13 10:13:08	19.0
12521	249.157932	-46.994022	333.217206	2011 Jun 13 15:46:38	19.0
12522	249.396933	-47.410725	333.217339	2011 Jun 13 21:20:08	19.0
12523	249.178061	-47.276529	333.217293	2011 Jun 14 02:53:38	19.0
12524	248.960334	-47.141940	333.217275	2011 Jun 14 08:27:08	19.5
12525	249.198427	-47.559064	333.217397	2011 Jun 14 14:08:58	19.5
12526	248.979417	-47.424468	333.217332	2011 Jun 14 19:50:48	19.0
12527	248.761625	-47.289491	333.217351	2011 Jun 15 19:36:46	19.3
12528	248.998831	-47.707016	333.217482	2011 Jun 16 01:24:35	19.0
12529	248.779750	-47.572056	333.217441	2011 Jun 16 06:58:05	19.0
12530	248.561776	-47.436667	333.217382	2011 Jun 16 12:31:35	19.3
12531	248.798050	-47.854617	333.217515	2011 Jun 16 18:09:14	19.5
12532	248.578823	-47.719259	333.217450	2011 Jun 16 23:51:04	19.5
12533	248.360823	-47.583518	333.217451	2011 Jun 17 05:32:54	19.5

Notes:
(1) Observation ID number.
(2) Right ascension (J2000.0) of observation pointing.
(3) Declination (J2000.0) of observation pointing.
(4) Roll angle of observation.
(5) Start time of observation.
(6) Exposure time of observation.

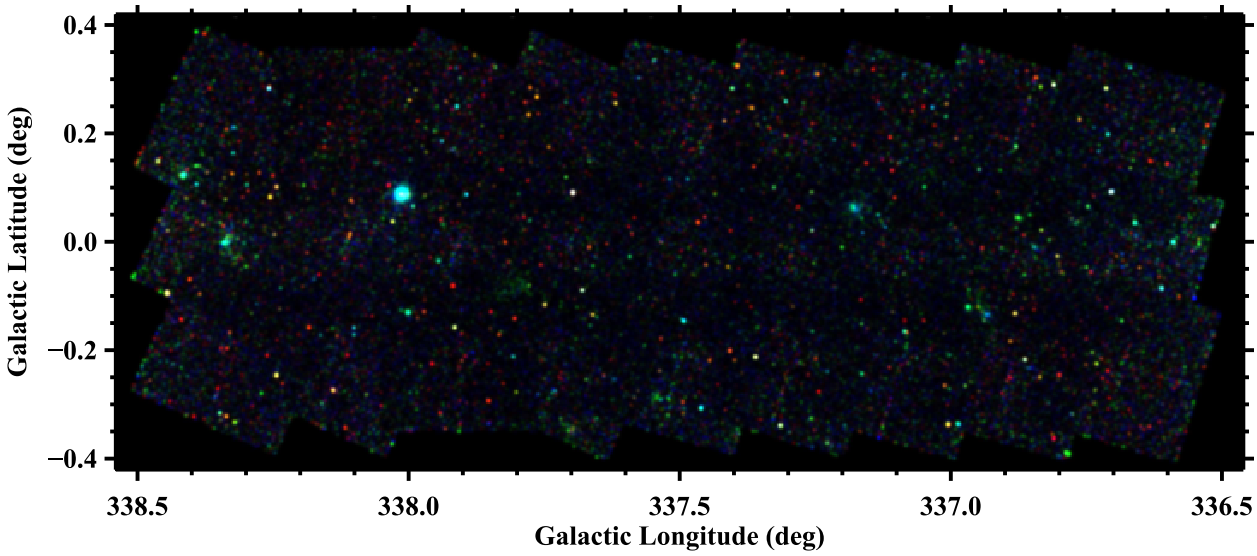

Figure 2.1: Three-color image of the Norma survey area. Red is 0.5-2 keV, green is 2-4.5 keV, and blue is 4.5-10 keV. Each energy band was smoothed using `aconvolve`. Some artifacts are present at the chip edges.

$0\farcs492 \times 0\farcs492$ CCD pixel but it increases greatly off-axis. The PSF increases in size and becomes more elliptical at large off-axis angles, such that at an off-axis angle of $10'$, the PSF has ellipticity ≈ 0.3 and semi-major axis $\approx 15'$ for an ECF of 90% for 4.5 keV photons (Allen et al. 2004). The CCDs are sensitive to incident photons with energies in the 0.3-10.0 keV range, and have a resolution of about 50-300 eV. The time resolution of the CCDs, which is determined by the read-out time, is 3.2 s.

We analyzed the data using standard tools from the CIAO package, version 4.4.[1] We used `chandra_repro` to reprocess the level 1 event lists provided by the *Chandra* X-Ray Center (CXC). This tool calls on `acis_process_events` to clean the cosmic ray background for very faint mode observations and also applies the sub-pixel event repositioning algorithm EDSER. Background flares accounted for <1% of the exposure time and were all relatively weak so, for simplicity, they were not removed.

2.2.3 Source Detection and Localization

We searched for X-ray sources in each observation separately using the wavelet detection algorithm `wavdetect`. For each observation, we generated images in three energy bands and four spatial resolutions. The three energy bands were the full 0.5-10 keV band (FB), the soft 0.5-2 keV band (SB), and the hard 2-10 keV band (HB); these three bands were chosen to make our source search sensitive to spectrally different sources. For each energy band, we made one image with the full resolution ($0.5''$), one binned by a factor 2 ($1''$), one binned by

[1] Available at http://cxc.harvard.edu/ciao4.4/

a factor of 4 (2″), and another binned by a factor of 8 (4″). Exposure maps for each of the three energy bands and four spatial resolutions were also generated applying the spectral weights for a power-law model with $\Gamma = 2.0$ and $N_{\rm H} = 5.0 \times 10^{22}$ cm^{-2}, a column density appropriate for sources in the far Norma arm at $10 - 12$ kpc distances;[2] the `wavdetect` exposure threshold was set to 0.1 to minimize spurious detections at detector locations with low exposure times. PSF maps of the 39.3% enclosed-count fraction (ECF)[3] at 4.5 keV (for the full and hard bands) and at 1.5 keV (for the soft band), computed using `mkpsfmap`, were also supplied to `wavdetect`. We used wavelet scales that increased by a factor of $\sqrt{2}$ from 1 to 16; this range of wavelet scales and four different spatial resolutions were chosen because the ACIS-I PSF varies significantly with offset from the aim point. We selected the Mexican Hat wavelet, and a sensitivity threshold equal to one over the number of pixels in the image, which corresponds to the chance of detecting approximately one spurious source per image assuming a spatially uniform background. Therefore, we expect `wavdetect` to identify 324 spurious sources (27 observations × 3 energy bands × 4 resolutions); we find 315 sources are detected at $< 3\sigma$, which is in rough agreement with the expected number of spurious sources, so the sample of sources detected at $\geq 3\sigma$ in at least one energy band is probably mostly free of spurious sources.

We combined the source lists from the four images with different spatial resolutions for each observation and energy band. Sources were identified as matches if the separation between them was smaller than the 50% encircled energy contour for the PSF of 4.5 keV photons at the detector position of the source plus the uncertainty in position due to the pixel size in the lower resolution image (e.g. when comparing sources in the full resolution image and the image binned by a factor of 2, this uncertainty is 2 pixels$\times\sqrt{2} \times 0\farcs492$/pixel$=1\farcs39$). When duplicate sources were identified, we only retained the position of the source detected in the highest resolution image.

Then we made background maps for each of the observations and energy bands by removing the counts of sources detected in that particular observation and energy band and filling these regions in with a number of counts determined from the average local background. The source regions we removed were defined as circles centered on the source position, with a radius ($r_{96\%}$) equal to the 96% enclosed count fraction (ECF) PSF for 4.5 keV photons (for the full and high energy bands) or for 1.5 keV (for the low energy band). In addition, we manually defined regions for the extended sources present in observations ObsID 12508, 12516, 12523, 12525, 12526, and 12528. The background regions were defined as annuli with an inner radius equal to the radius of the punched-out region, and an outer radius twice as large; if an annulus overlapped a punched-out region, that overlapping segment was removed from the annulus. The number of background counts to be randomly distributed within the punched-out region was calculated by multiplying the counts in the background region by the ratio of the region areas and the ratio of the region mean effective areas, as determined from the exposure maps. After the punched-out regions had been filled in with the appropriate number of background counts, the background maps were smoothed using

[2] See §2.2.8 for details on the calculation of $N_{\rm H}$ to a given distance.

[3] As recommended by Freeman et al. (2002a)

csmooth with Gaussian kernels of sizes ranging from 20 to 50 pixels. For the observations containing extended sources, first, a smoothed background map was made with both the extended and points sources removed. This map was passed to `csmooth` as a background map, and a smoothed background map was made with only the point sources removed.

We then employed `wavdetect` again to search for X-ray sources in each observation, but this time we used the smoothed background maps we made instead of defaulting to the background maps automatically generated by `wavdetect`. We found that when the background maps we made were used, a larger fraction of sources was detected in higher resolution images than with the automatically-generated maps. As before, for each observation, we combined the source lists from the four images with different spatial resolutions. Then we combined the source lists from the three energy bands. When two sources were identified as a match, only one source entry was retained; preference was given to sources detected in the full energy band and then the soft band, because the PSF size is smaller at low energies, allowing better source localization.

In order to refine the astrometry of our observations, we searched the VISTA Variables in the Via Lactea (VVV) Survey catalog (Minniti et al. 2010) for infrared counterparts to the X-ray sources we detected[4] For each *Chandra* observation, we made a list of VVV sources within $12'$ of the observation aim point with less than a 0.137% probability of being a noise fluctuation. We then determined the reliability of each IR counterpart based on the positional uncertainties of the X-ray and IR sources, the distance between the X-ray and IR source, and the density of IR sources following the treatment of Sutherland & Saunders (1992) but without making any assumptions about the probability distribution function in magnitude of the true IR counterparts.[5] The 1σ positional uncertainty of sources in the VVV catalog is typically $0\farcs07$. We determined the positional uncertainty of the *Chandra* sources using the parameterization of the statistical error as a function of offset angle and net counts[6] in Equation 5 of Hong et al. (2005). These statistical errors were combined in quadrature with a systematic error of $0\farcs7$ (95% error[7]) due to Chandra guide star alignment uncertainties. We used VVV matches with a reliability greater than 0.9 and `reproject_aspect` to derive a linear and rotational astrometric correction for each *Chandra* observation, reducing the systematic astrometric errors to $\leq 0\farcs54$. We applied the same corrections to the source positions in our source lists. We replaced the $0\farcs7$ systematic errors with the average residuals from the astrometric transformation derived from the VVV counterparts to the X-ray sources. Table 2.2 presents the refined astrometry for each observation.

[4]See http://www.eso.org/sci/observing/phase3/data_releases/vvv_dr1.html for the first data release used in this paper.

[5]Our calculation takes into account the probability that the NIR counterpart of an X-ray source is undetected in the VVV survey. In Sutherland & Saunders (1992) this null probability is the quantity (1-Q). Since we do not know Q a priori, we guess its value and then refine our guess iteratively until the Q value meets the criterion in Equation (7) of Sutherland & Saunders (1992). In this way, we find $Q = 0.85$.

[6]These are the net counts reported by `wavdetect`, not those determined by aperture photometry.

[7]See http:/cxc.harvard.edu/cal/ASPECT/celmon.

Table 2.2: Refined Astrometry of *Chandra* Observations

ObsID (1)	R.A. (deg) (2)	Dec. (deg) (3)	Roll (deg) (4)	Unc. (5)	# Counterparts (6)
12507	250.373197	-46.666299	342.207886	0.″38	14
12508	250.155064	-46.530768	342.256256	0.″16	6
12509	249.937691	-46.397888	342.258575	0.″42	26
12510	250.180484	-46.812861	342.220398	0.″32	21
12511	249.961539	-46.681483	333.150848	0.″39	7
12512	249.743528	-46.550463	317.725342	0.″38	14
12513	249.985150	-46.965931	317.737030	0.″35	24
12514	249.767578	-46.829508	342.200439	0.″39	9
12515	249.550029	-46.696055	342.115234	0.″35	22
12516	249.790920	-47.111803	342.203583	0.″35	10
12517	249.572277	-46.978334	342.136200	0.″54	5
12518	249.354557	-46.844589	342.191071	0.″35	23
12519	249.594337	-47.262048	333.187683	0.″36	19
12520	249.375668	-47.128341	333.142365	0.″35	3
12521	249.157996	-46.994096	333.227539	0.″32	24
12522	249.396838	-47.410790	333.249512	0.″34	18
12523	249.178005	-47.276545	333.162964	0.″31	6
12524	248.960241	-47.141987	333.209045	0.″34	24
12525	249.198264	-47.559033	333.258545	0.″29	15
12526	248.979187	-47.424375	333.234863	0.″28	5
12527	248.761554	-47.289507	333.188904	0.″37	19
12528	248.998873	-47.707003	333.211639	0.″39	19
12529	248.779969	-47.572088	333.210205	0.″30	9
12530	248.561714	-47.436723	333.186920	0.″39	15
12531	248.797988	-47.854470	333.221191	0.″31	17
12532	248.578674	-47.719259	333.231171	0.″34	9
12533	248.360765	-47.583555	333.165527	0.″32	18

Notes:
(1) Observation ID number.
(2) Right ascension (J2000.0) after astrometric correction.
(3) Declination (J2000.0) after astrometric correction.
(4) Roll angle after astrometric correction.
(5) Average systematic uncertainty between IR and X-ray positions after astrometric refinement.
(6) Number of VVV counterparts used to refine astrometry.

Table 2.3: Sample *Chandra* Catalog of Point and Extended Sources: Detection and Localization

No.	Source (CXOU J)	ObsID (125**)	R.A. (deg)	Dec. (deg)	Unc. (arcsec)	Offset (arcmin)	Sig. FB	Sig. SB	Sig. HB	Radius (arcsec)	PSF (arcsec)	Flags
(1)	(2)	(3)	(4)	(5)	(6)	(7)	(8)	(9)	(10)	(11)	(12)	(13)
1	163228.2-473755	33	248.117829	-47.632173	4.03	10.3	3.6	2.3	2.5	13.8	13.8	...
2	163241.5-474039	33	248.172944	-47.677522	1.79	9.5	9.0	10.4	2.5	11.9	11.9	...
3	163244.6-474133	33	248.186065	-47.692513	3.63	9.6	2.4	0.0	2.8	12.2	12.2	...
4	163248.7-473017	33	248.203151	-47.504857	1.41	7.9	8.4	1.2	8.5	9.2	9.2	...
5	163251.0-474135	33	248.212798	-47.693198	3.16	8.9	3.0	5.0	0.0	10.7	10.7	...
6	163253.0-474201	33	248.221111	-47.700286	2.26	9.0	5.2	1.8	4.8	10.9	10.9	...
7	163259.0-473819	33	248.246176	-47.638806	1.13	5.7	7.5	7.2	4.1	5.2	5.2	...
8	163259.4-472804	33	248.247582	-47.467941	3.39	8.3	2.3	3.4	0.4	10.1	10.1	...
9	163303.2-472547	33	248.263337	-47.429724	13.98	10.0	0.0	0.8	0.0	14.0	14.0	...
10	163306.2-473239	33	248.276159	-47.544291	1.55	4.2	3.3	0.7	3.1	3.5	3.5	...

Notes: Table 2.3 is published in its entirety in Appendix A.1 along with detailed column descriptions. A portion is shown here for guidance regarding its form and content.

Table 2.4: Sample *Chandra* Catalog of Point and Extended Sources: Photometry

No. (1)	C_{net} FB (2-4)	C_{net} SB (5-7)	C_{net} HB (8-10)	$f_{\rm ph}$FB(10^{-6} cm^{-2} s^{-1}) (11-13)	$f_{\rm ph}$SB(10^{-6} cm^{-2} s^{-1}) (14-16)	$f_{\rm ph}$HB(10^{-6} cm^{-2} s^{-1}) (17-19)	E_{50} (keV) (20-21)	E_{25} (keV) (22-23)	E_{75} (keV) (24-25)	f_X(10^{-14}erg cm^{-2} s^{-1}) (26-28)	Phot. Flag (29)	Quantile Group (30)
1	16^{+7}_{-6}	6^{+4}_{-3}	10^{+6}_{-5}	$3.76^{+1.57}_{-1.32}$	$0.76^{+0.55}_{-0.40}$	$2.47^{+1.39}_{-1.13}$	2.9±1.8	1.6±0.8	5.6±2.4	$1.75^{+1.31}_{-1.25}$	- - -	C
2	47^{+9}_{-8}	37^{+7}_{-6}	10^{+6}_{-5}	$10.55^{+1.99}_{-1.76}$	$4.68^{+0.93}_{-0.80}$	$2.28^{+1.31}_{-1.07}$	1.4±0.1	1.0±0.1	1.8±0.5	$2.35^{+0.49}_{-0.44}$	- - -	A
3	9^{+5}_{-4}	3	9^{+5}_{-4}	$3.48^{+2.15}_{-1.71}$	0.69	$3.88^{+2.14}_{-1.69}$	5.4±0.9	4.5±1.3	6.1±0.9	$3.03^{+1.93}_{-1.56}$	- S -	D
4	36^{+8}_{-7}	2^{+3}_{-2}	34^{+7}_{-6}	$7.95^{+1.69}_{-1.46}$	$0.28^{+0.40}_{-0.24}$	$7.60^{+1.66}_{-1.42}$	4.6±0.3	3.7±0.3	5.2±0.5	$5.90^{+1.33}_{-1.17}$	- - -	D
5	13^{+6}_{-5}	13^{+5}_{-4}	6	$2.85^{+1.36}_{-1.12}$	$1.70^{+0.65}_{-0.51}$	1.32	1.0±0.1	0.9±0.2	1.1±0.1	$0.44^{+0.21}_{-0.18}$	- - H	A
6	22^{+7}_{-6}	4^{+4}_{-2}	19^{+6}_{-5}	$6.00^{+1.82}_{-1.53}$	$0.59^{+0.55}_{-0.36}$	$5.07^{+1.71}_{-1.41}$	3.0±0.7	2.2±0.4	5.7±1.2	$2.90^{+1.10}_{-0.99}$	- - -	C
7	20^{+6}_{-5}	12^{+5}_{-3}	9^{+4}_{-3}	$4.70^{+1.35}_{-1.10}$	$1.53^{+0.60}_{-0.46}$	$2.08^{+1.04}_{-0.78}$	1.8±0.6	1.5±0.1	3.5±0.5	$1.37^{+0.57}_{-0.53}$	- - -	B
8	8^{+5}_{-4}	7^{+4}_{-3}	1^{+4}_{-1}	$1.82^{+1.17}_{-0.92}$	$0.85^{+0.51}_{-0.37}$	$0.33^{+0.93}_{-0.33}$	1.6±0.9	1.4±0.3	1.8±3.8	$0.47^{+0.40}_{-0.35}$	- - -	A
9	7	2^{+3}_{-2}	5	1.74	$0.27^{+0.48}_{-0.27}$	1.23	5.2±4.8	2.9±7.1	7.6±7.1	1.46	F - H	C
10	6^{+4}_{-3}	1^{+2}_{-1}	5^{+4}_{-2}	$1.11^{+0.74}_{-0.50}$	$0.08^{+0.26}_{-0.08}$	$0.98^{+0.72}_{-0.47}$	5.1±0.8	4.4±1.4	5.4±0.3	$0.91^{+0.62}_{-0.44}$	- - -	E

Notes: Table 2.4 is published in its entirety in Appendix A.2, along with detailed column descriptions. A portion is shown here for guidance regarding its form and content.

Table 2.5: Sample *Chandra* Catalog of Point and Extended Sources: Infrared Counterparts

No.	VVV Source Name	R.A. (deg)	Dec. (deg)	Δ_{X-IR} (arcsec)	p_{noise}	Reliability
(1)	(2)	(3)	(4)	(5)	(6)	(7)
1	515727792649	248.117752	-47.631649	1.89	3.07e-03	0.3216
2	515726841264	248.172806	-47.677017	1.84	5.29e-07	0.8660
3	515726837733	248.185730	-47.693638	4.13	5.29e-07	0.3508
4	515727238897	248.203003	-47.505127	1.05	1.71e-04	0.7804
5	515726847521	248.212341	-47.693485	1.52	1.71e-04	0.9482
6	515727540494	248.220947	-47.700108	0.76	1.71e-04	0.9142
7	515726868309	248.246140	-47.638630	0.64	5.29e-07	0.9777
8	515726918176	248.247345	-47.468082	0.78	9.52e-06	0.4607
9	515726930863	248.262817	-47.429794	1.29	5.29e-07	0.0657
10	515727577185	248.276459	-47.544682	1.59	2.81e-04	0.8825

Notes: Table 2.5 is published in its entirety Appendix A.3, along with detailed column descriptions. A portion is shown here for guidance regarding its form and content.

We detected a total of 1658 sources but since each of the 27 observations partially overlaps with at least three other survey observations, we checked for duplicate sources between the different observations in order to only have one entry per source in our final catalog (see Tables 2.3, 2.4, and 2.5 for a sample). A source was considered a true duplicate if the distance between the two sources was smaller than the quadrature sum of the positional uncertainties of the two sources. If the distance between two sources was larger than the quadrature sum of the positional uncertainties but smaller than the regular sum of the uncertainties, then the sources were flagged for manual inspection. Some sources that met the true duplicate criterion but were unusual in some respect (e.g. one source was flagged as extended while the other was not) were also flagged by the algorithm for manual inspection. Whether or not the sources flagged for manual inspection were determined to be duplicates, they were flagged with "id" for "inspected duplicate" in the catalog.[8]. In total, 38 sets of sources were flagged for manual inspection and we determined 28 of them were true duplicates. The catalog entries for duplicates were combined so that exposure times and net counts were summed, source positions were weight-averaged, and the ObsIDs, offsets from the aim point, source region radii, 90% PSF sizes, and flags of the duplicate sources were all listed. If a source was determined to be variable on long timescales (see §2.2.5), its derived photometric properties were averaged, but if it was determined to be constant, they were weight-averaged. After combining the entries of duplicate sources, our catalog contains 1415 sources.

[8]Flags for each source are provided in column 13 of Table 2.3. Descriptions of all flags are provided in Appendix A.1.

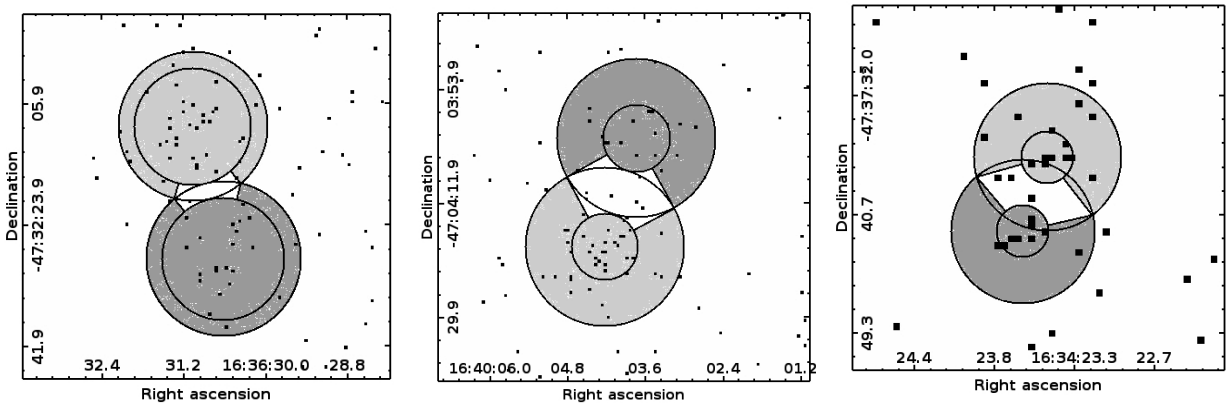

(a) Flag "m1" case. (b) Flag "m2" case. (c) Flag "m3" case.

Figure 2.2: Examples of modified overlapping regions.

2.2.4 Aperture photometry

We used `dmextract` to compute photometric quantities for each of the X-ray sources in our catalog. In most cases, we defined an aperture region for each source as a circle with radius ($r_{90\%}$) equal to the 90% ECF PSF for 4.5 keV photons. Given the relatively low source counts for the vast majority of sources, this radius is well-optimized to obtain the highest S/N ratio. However, if the semi-major axis of the source region provided by `wavdetect` was more than twice as large as $r_{90\%}$ in all images in which the source was detected, then the semi-major axis was used as the radius of the aperture region and the source was flagged with "e" for "extended", to denote that it may be an extended source. In some cases, these "e" source regions surrounded another source region; these sources were additionally flagged with an "s" for "surrounding". We nonetheless included these sources in our analysis of point-like sources, but they only constitute 3% of sources detected at $\geq 3\sigma$. We also modified the aperture regions of overlapping sources; following the method of Hong et al. (2005), we defined a source region as the sum of a circular core and a pie sector of an annular shell that excludes the common sector with the neighbor's source region. The core size was determined empirically to maximize the source photons included and to minimize contamination from neighbors, as described in Table 2.6, which also lists the flags associated with each type of source region modification from the standard one. As was implemented in Hong et al. (2005), if the source region overlapped with more than one neighbor, the core size was determined by the nearest neighbor and the pie sector excluded all common sectors with the neighbors' aperture regions. Figure 2.2 shows some examples of these modified overlapping source regions. We manually modified 12 aperture regions of sources with multiple nearby neighbors. Finally, we manually created source and background regions for the extended sources in observations ObsID 12508, 12516, 12523, 12525, 12526, and 12528 that were not detected by `wavdetect` and flagged these sources with a "c" for "created".

The background region for each source was defined as an annulus with an inner radius equal to $r_{96\%}$ and an outer radius equal to $2r_{96\%}$. In the few instances when a source flagged as "e" had a source radius larger than $r_{96\%}$, then the inner radius of the annulus was set equal to the source radius, and the outer radius was twice as large as this inner radius. As we did when making the background maps, we generated images with punched-out $r_{96\%}$ source regions, which were again defined as circles with radii equal to $r_{96\%}$. When extracting photometric information from the background regions, we used these punched-out images so that contamination from neighboring sources was avoided. When calculating the background region area, we corrected the annular area for any segments that were excluded due to overlap with punched-out source regions.

Having defined source and background regions, we used `dmextract` to calculate the source core, source shell, and background region counts ($C_{\rm core}$, $C_{\rm pie}$, and $C_{\rm bkg}$) in the full, hard, and soft energy bands, their areas ($A_{\rm core}$, $A_{\rm pie}$, and $A_{\rm bkg}$), and their mean effective areas ($E_{\rm core}$, $E_{\rm pie}$, and $E_{\rm bkg}$) by including exposure maps in the call to `dmextract`. We calculated the 1σ Gaussian errors in the measured counts (both in the source and background regions) using the recommended approximations for upper and lower limits in Gehrels (1986). For sources with apertures consisting of a circular core and a pie sector of an annular shell, the total source region counts, area, and effective area were calculated in the following manner, assuming azimuthal symmetry of the PSF:

$$C_{\rm src} = C_{\rm core} + \frac{A_{\rm ann}}{A_{\rm pie}} C_{\rm pie} \tag{2.1}$$

$$A_{\rm src} = A_{\rm core} + A_{\rm ann} \tag{2.2}$$

$$E_{\rm src} = E_{\rm core} + \frac{A_{\rm ann}}{A_{\rm pie}} E_{\rm pie} \tag{2.3}$$

where $A_{\rm ann} = \pi(r^2_{\rm outer} - r^2_{\rm inner})$ is the total area of the annular shell. For all other sources, the source region simply consists of the circular core region, and thus $C_{\rm src} = C_{\rm core}$, $A_{\rm src} = A_{\rm core}$, and $E_{\rm src} = E_{\rm core}$. The total observed source region counts include contributions from the source and from the background. The background counts within the source region were estimated and subtracted as shown below to estimate the true source counts:

$$C_{\rm net} = C_{\rm src} - f C_{\rm bkg}, \qquad f = \frac{A_{\rm src} E_{\rm src}}{A_{\rm bkg} E_{\rm bkg}}. \tag{2.4}$$

If the estimated background counts were equal to or greater than the source region counts, then we calculated the 90% upper confidence limit to the net source counts based on the method described in Kraft et al. (1991). The photon flux for each energy band was calculated by dividing the net source counts by the mean source region effective area and the exposure time. Since the mean effective area was determined from the exposure maps, these photon fluxes will not be accurate for all sources because in making the exposure maps we assumed a source spectral model with $\Gamma = 2.0$ and $N_{\rm H} = 5.0 \times 10^{22}$ cm^{-2}. To determine the extent to which we may be under or overestimating the fluxes of sources with different spectral

properties, we made exposure maps for one observation using different spectral models spanning the range of Γ and $N_{\rm H}$ covered by our sources. We find that the mean effective areas vary by $\lesssim 20\%$ in the full band and $\lesssim 5\%$ in the soft and hard bands, making our derived photon fluxes uncertain by the same percentages.

We also computed the probability that the sources in our catalog could be noise fluctuations of the local background using the following formula derived in Appendix A of Weisskopf et al. (2007):

$$P(\geq C_{\rm src}|C_{\rm bkg}; C_{\rm net}=0) = \sum_{c=C_{\rm src}}^{C_{\rm bkg}+C_{\rm src}} \frac{(C_{\rm bkg}+C_{\rm src})!}{c!(C_{\rm bkg}+C_{\rm src}-c)!}\left(\frac{f}{1+f}\right)^{c}\left(1-\frac{f}{1+f}\right)^{C_{\rm bkg}+C_{\rm src}-c} \quad (2.5)$$

We determine the significance of a source based on this probability and the Gaussian cumulative distribution function. For sources detected in multiple observations, these probability values from individual observations were multiplied together, and the source significance was determined from this combined probability. The photometric values used in our data analysis are included in our catalog, a sample of which can be seen in Table 2.4. Although in our catalog we include all detected sources, in our analysis we only use sources detected at $\geq 3\sigma$ in the full, soft, or hard energy band and refer to these sources as the full sample. Figure 2.3 shows the histogram distribution of the total 0.5-10 keV counts detected for these sources; as can be seen, most of these sources have fewer than 100 counts, which is roughly the number of photons required to determine their spectral and variability properties accurately enough

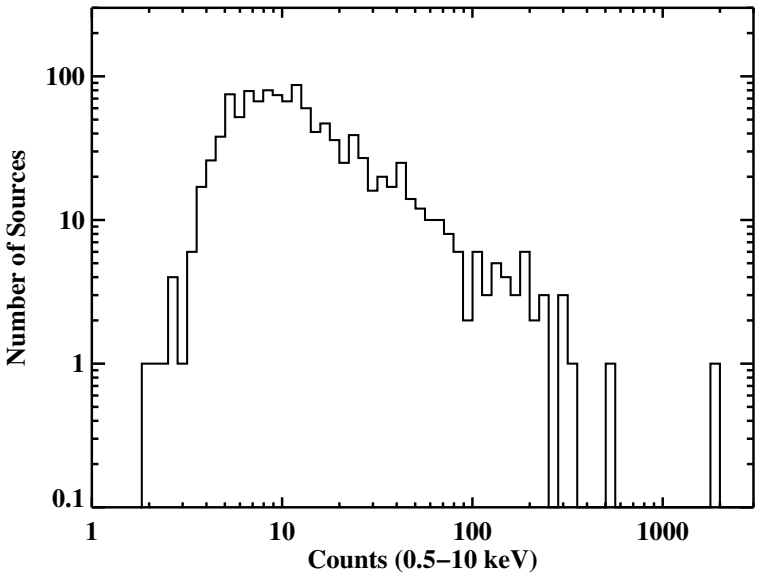

Figure 2.3: Histogram of 0.5-10 keV net counts for $\geq 3\sigma$ sources. The brightest source with 14,720 counts is not shown.

Table 2.6: Aperture Region Definitions

Source Region Overlap	Condition	Core Radius r_c	Refined Source Region	Background Region	Flag
No....	$\Delta \geq r_{90\%} + r'_{90\%}$	$r_{90\%}$	$r \leq r_c = r_{90\%}$	$r_{96\%} < r < 2r_{96\%}$ and $r'' > r''_{96\%}$ for all neighbors	...
Yes...	$\Delta \geq 1.5r'_{90\%}$, $\Delta < r_{90\%} + r'_{90\%}$	$\Delta - r'_{90\%}$	$r \leq r_c$ and pie sector with $r_c < r \leq r_{90\%}$	Same as above	m1
Yes...	$\Delta < 1.5r'_{90\%}$, $\Delta \geq r_{68\%} + r'_{90\%}$	$\Delta - r'_{90\%}$	Same as above	Same as above	m2
Yes...	$\Delta < r_{68\%} + r'_{90\%}$	$\Delta/3$	Same as above	Same as above	m3

Notes: Parameter Δ is the distance between the source and its nearest neighbor, and $r'_{90\%}$ is the 90% PSF radius of the nearest neighbor. r refers to the distance from the source and r'' refers to the distance from neighbors. The PSF radii are calculated for 4.5 keV photons. For sources flagged as potentially extended ("e"), these criteria remain the same, except that instead of using $r_{90\%}$ and $r_{96\%}$, the radii listed in the catalog are used.

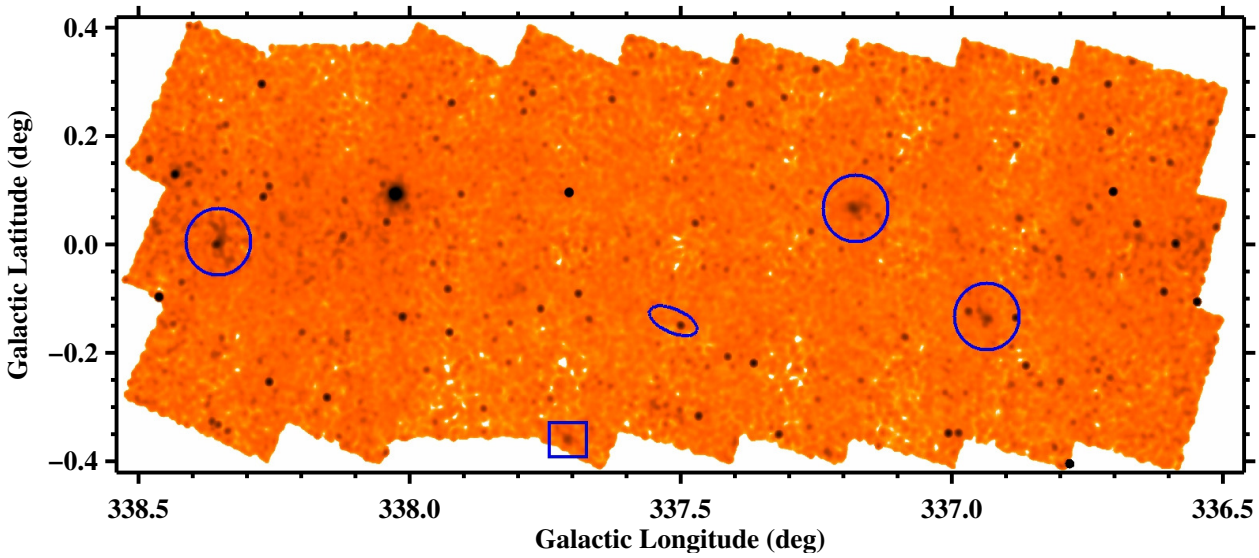

Figure 2.4: Mosaic image of the 0.5-10 keV band showing locations of extended sources identified by eye. Circles indicate confirmed SNRs, while the square indicates a candidate SNR, and the ellipse indicates a PWN candidate.

to determine the nature of the X-ray source. Our catalog contains 1130 point-like sources detected at $\geq 3\sigma$ in at least one of the three energy bands and 5 extended sources which we identified by eye and are shown in Figure 2.4. Three of these extended sources are confirmed supernova remnants (G337.2+0.1, G337.8-0.1, and HESS J1640-465), another is a possible SNR based on its morphology (CXOU J163942.3-471257), and one has a jet-like morphology and is probably a pulsar wind nebula (CXOU J163802.6-471345). New results about these extended sources are discussed in Jakobsen (2013) and Jakobsen et al. (2014).

2.2.5 X-ray Variability

X-ray sources can be variable on timescales from milliseconds to years, so we tried to characterize the variability of the sources in our catalog to help classify them. We determined whether a source was variable on short timescales (seconds to hour) by comparing the arrival times of events with a constant event rate using the K-S test. Sources that have $\geq$99.73% chance of not being constant are flagged with “vs" (short variability), while those that have $\geq$95% chance of not being constant are flagged with “vp" (probable short variability). The K-S test is more reliable for sources with more counts; we only consider the K-S test to be reliable for sources with at least 40 counts. Of the 80 sources with more than 40 counts (in a single observation), 27 (16) show short-timescale variability with $\geq$95% (99.73%) confidence.

We also checked whether sources detected in multiple observations demonstrated long-term variability (hours-days) by determining whether the source photon flux in two observations differed by more than 3σ in the full, soft, or hard energy band; these sources were flagged

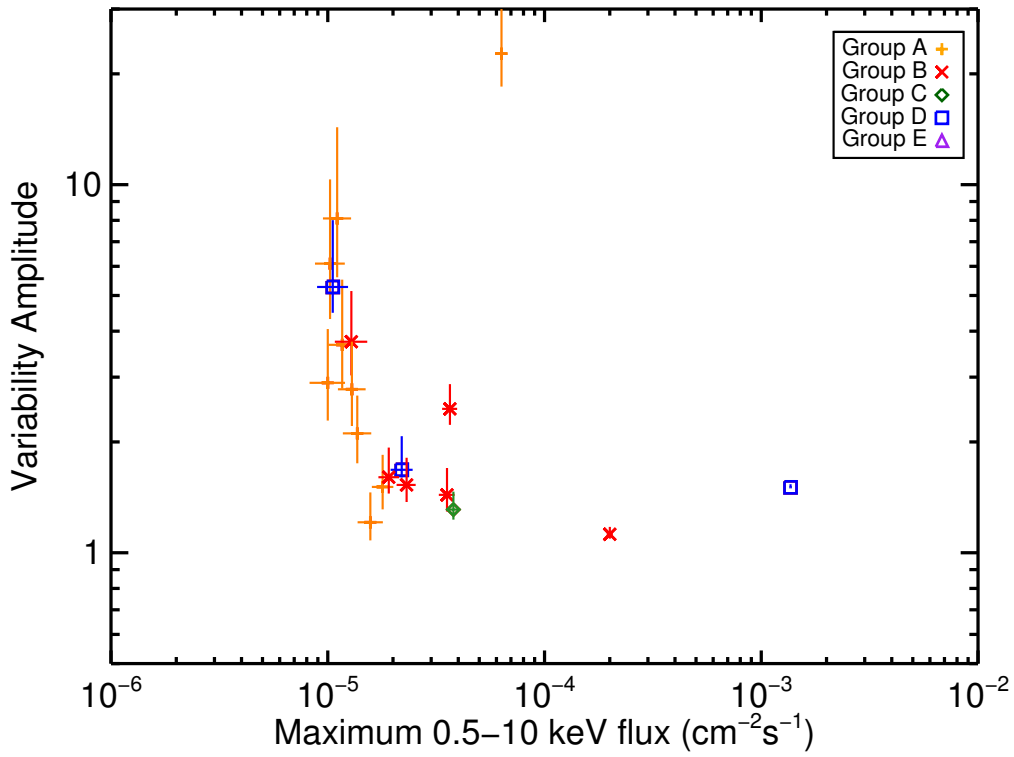

Figure 2.5: Variability amplitudes in the 0.5-10 keV band (maximum photon flux divided by the minimum photon flux) versus maximum photon flux for sources that are detected in multiple observations and found to vary between observations at $\geq 3\sigma$ confidence. Different symbols represent different quantile groups.

with "vl" (long variability). In cases in which a source's flux is measured in one observation but only an upper limit can be obtained in another, we consider the source to be variable on long timescales if the measured flux and upper limit are inconsistent at $> 3\sigma$ confidence. We found 220 sets of sources detected in two or more observations with a combined significance $\geq 3\sigma$, 19 of which show long-term variability. We calculated the variability amplitude of each source displaying long-term variability, which we defined as the ratio of the maximum photon flux to the minimum photon flux in the 0.5-10 keV band. As shown in Figure 2.5, we do not detect significant long-term variability in sources with maximum (average) photon fluxes $\lesssim 10^{-5}$ cm^{-2} s^{-1} ($\lesssim 5.5 \times 10^{-6}$ cm^{-2} s^{-1}) due to the large error bars of the measured source fluxes as they approach the survey sensitivity ($\sim 2 \times 10^{-6}$ cm^{-2} s^{-1}). There are 53 sets of sources detected in multiple observations that exceed these flux limits, thus the fraction of sources that are variable on long timescales is 36%. Of the 758 sources with $\geq 3\sigma$ confidence located in regions where multiple observations overlap, 373 are not detected in multiple observations. This is not surprising because the fluxes of all but seven of these 373 sources are lower than the flux to which 100% of our survey area is sensitive (see §2.2.10).

Finally, we searched for a coherent signal with period 6.8 s $< P <$ 10 ks in sources

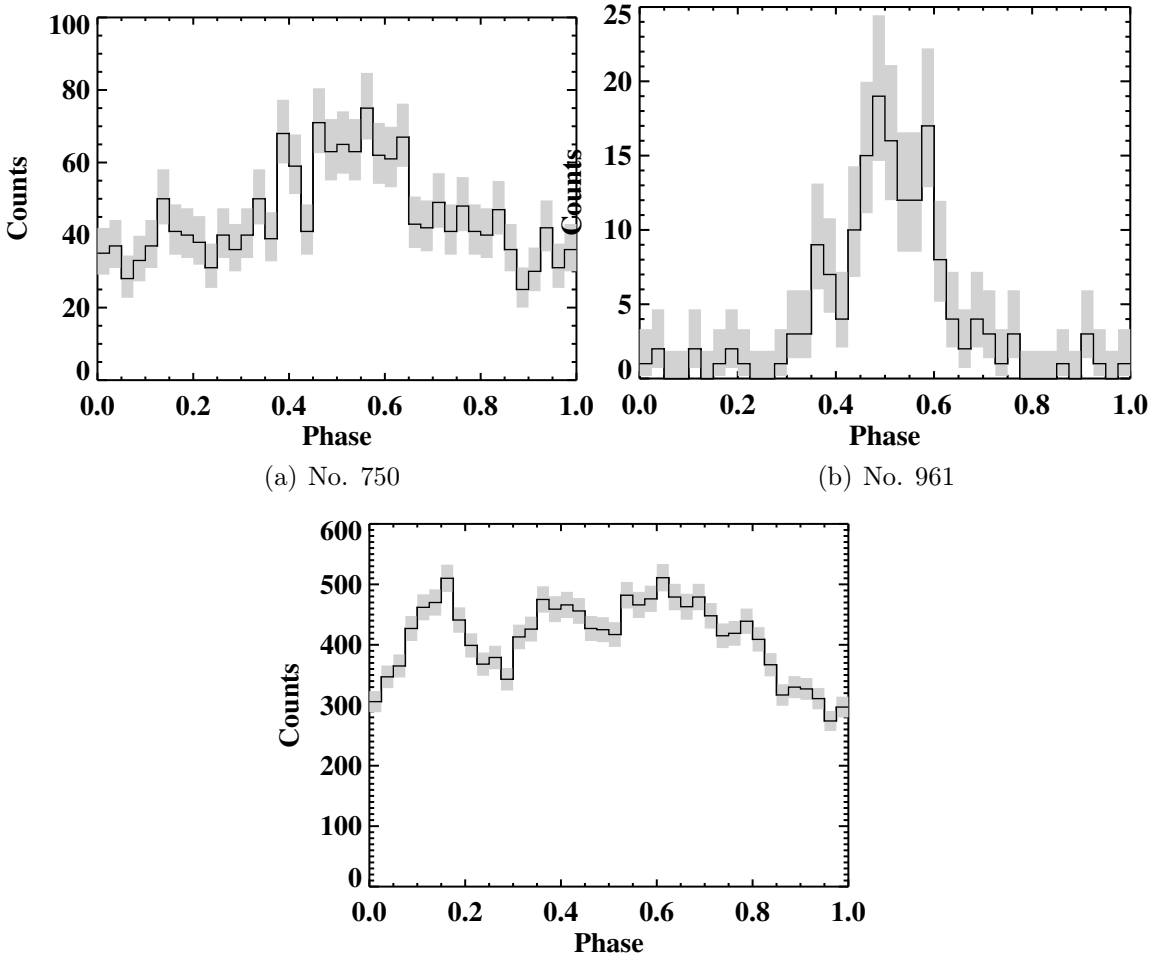

(a) No. 750

(b) No. 961

(c) No. 999

Figure 2.6: Phase-folded lightcurves of periodic sources labeled with source catalog number. Periods are presented in Table 2.7. Gray bars show 1σ errors.

with more than 50 counts in at least one observation using the Z_n^2-test (Buccheri et al. 1983), which depends on the sum of the Fourier powers of the first n harmonics. Since it is not feasible to try an infinite number of n values, Buccheri et al. (1983) suggested using $n = 2$ as a general test; we decided to use both $n = 2$ and $n = 1$ since the latter is equivalent to the traditional Rayleigh test. For each source, photon arrival times were corrected to the Solar System barycenter using the JPL DE405 ephemeris and our catalog coordinates, and for sources detected in multiple observations, photon arrival times from different observations were combined. We found three sources with significant Z_2^2 values; these sources have significant Z_1^2 values as well. Table 2.7 provides the periods and Z_2^2 values of these sources; the uncertainties in the periods were calculated using the method described in Ransom et al. (2002). In Figure 2.6 we present the phase-folded lightcurve of each periodic

Table 2.7: Periodic Variability of *Chandra* Sources

No.	Source (CXOU J)	C_{net} FB	Period (s)	Z_2^2	Variability Flags
(1)	(2)	(3)	(4)	(5)	(6)
750	163750.8-465545	1790±40	7150±50	95	vs, vl
961	163855.1-470145	160±10	5660±20	213	vp, vl
999	163905.6-464212	14720±120	906±1	368	vs, vl

Notes:
(1) Catalog source number.
(2) *Chandra* source name.
(3) Net source counts in the full 0.5-10 keV band.
(4) Most probable period determined by the Z_2^2-test.
(5) Result of Z_2^2-test.
(6)"vl" - variability on long timescales (hours-days), "vp" - variability on short timescales (sec-hour) at $\geq 95\%$ confidence, "vs" - variability on short timescales at $\geq 99.73\%$ confidence

source. Source 999 is a previously discovered HMXB; the period we measure is consistent with the period found by Bodaghee et al. (2006). The other two sources are most likely magnetic cataclysmic variables (CVs), as discussed in §2.2.9.

2.2.6 Infrared Counterparts

We searched for infrared counterparts to our X-ray sources in the VVV catalog. First, we created a list of non-duplicate VVV sources lying within our surveyed area; we considered an entry in the VVV catalog to be duplicate if the angular difference between the source positions was less than the 3σ positional uncertainty of the sources (approximately $0\farcs21$). Then, we determined the reliability of each counterpart as described in §2.2.3, and consider a match good if its reliability is $\geq 90\%$ and the noise probability of the VVV source is $\leq 0.31\%$. The latter constraint excludes low-significance detections and very bright sources, which saturate the array and have less accurate positions and magnitudes. Table 2.5 provides information about the closest VVV source to each *Chandra* source and its reliability as a counterpart.

We have found reliable counterparts for 52% of X-ray sources detected at $\geq 3\sigma$. X-ray sources without reliable counterparts may have IR counterparts below the sensitivity limits of the VVV survey, have large positional uncertainties, and/or be in a particularly crowded region in which multiple IR sources are equally likely counterparts. Figure 2.7 shows the $(J-H)$ vs. H magnitude of the reliable counterparts (the K_s magnitudes have not yet been made publicly available). In this color-magnitude diagram, the distribution of reliable counterparts does not match that of all the VVV sources located within our field-of-view, indicating that the majority of these counterparts are not random associations.

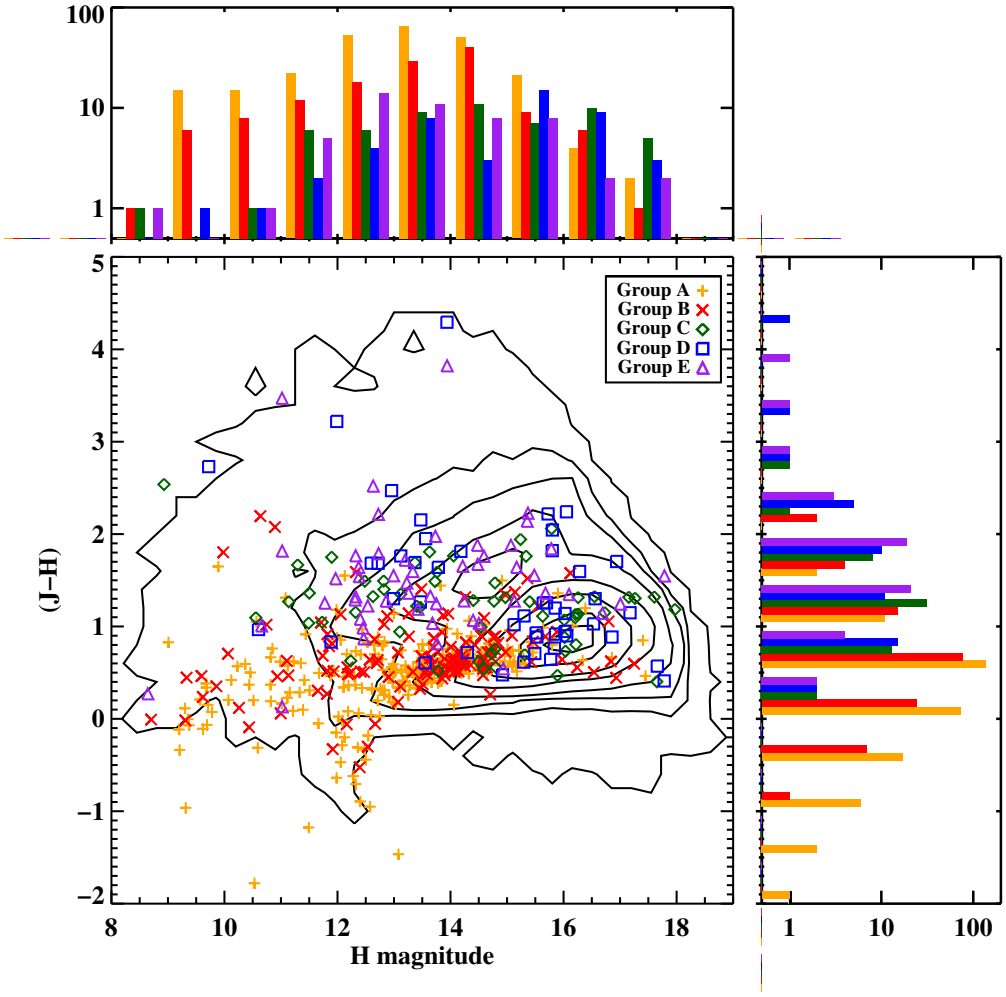

Figure 2.7: Near-IR color-magnitude diagram showing the distribution of all VVV sources in our surveyed area (black contours) and the reliable counterparts to X-ray sources in our survey (symbols). The black contours, from outside inwards, encircle 99%, 95%, 90%, 80%, 60%, 40%, 20%, and 10% of the VVV sources. For the counterparts represented with symbols, the median 1σ error is 0.005 magnitudes for the H magnitude and 0.007 magnitudes for the $(J-H)$ color.

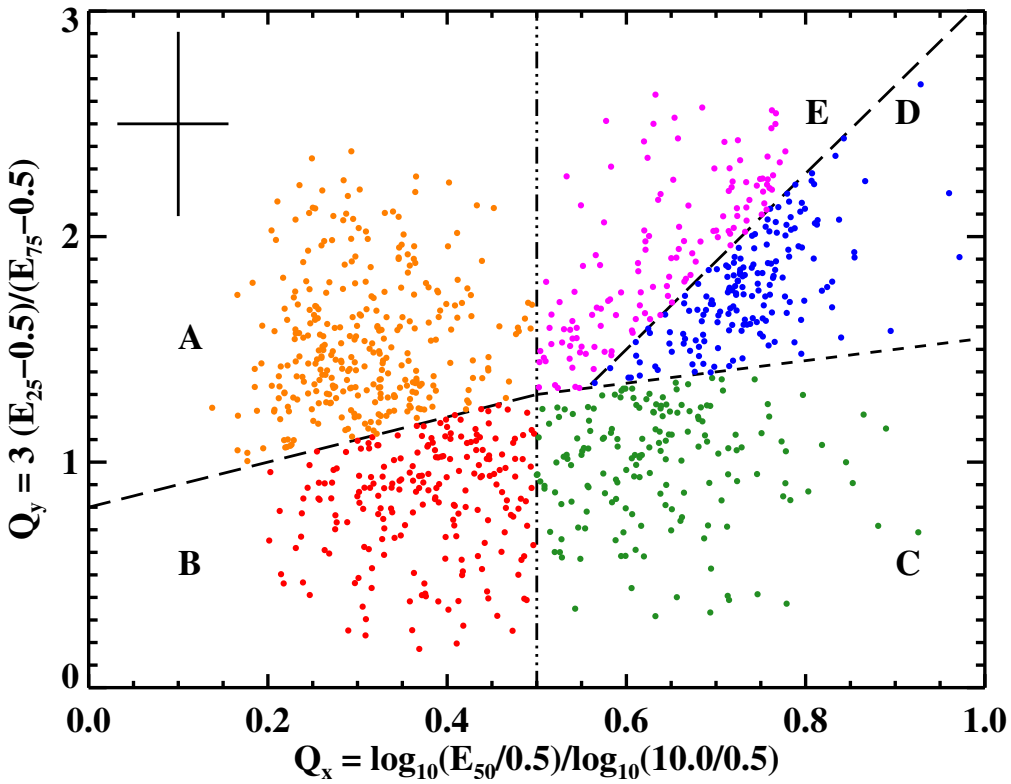

Figure 2.8: Quantile diagram for sources detected at $\geq 3\sigma$ in the 0.5-10 keV band. Sources were split into five spectral groups defined by the black lines. Short dashes at $N_{\rm H} \approx 2 \times 10^{22}$ cm^{-2} roughly divide nearby ($\lesssim 6$ kpc) and distant ($\gtrsim 6$ kpc) sources. Long dashes roughly separate thermal and nonthermal sources. The dash-dotted line at $Q_x = 0.5$ subdivides sources detected in the soft energy band from those detected in the hard energy band. Median 1σ errors are shown in the upper left.

2.2.7 Quantile Analysis

Robust identifications of X-ray sources typically require multiwavelength information, but the X-ray data itself can provide clues to the nature of a source. First, we tried to classify the sources using a hardness ratio and a soft and hard X-ray color. However, we found that this method was ineffective for distinguishing between sources with intrinsically hard spectra and very absorbed sources. This distinction is important since the HII regions near which we expect to find younger populations of X-ray sources, the primary target of this survey, are at a distance of ∼11 kpc and thus the X-ray emission from such sources would be attenuated by large amounts of intervening gas.

Therefore, we instead employed quantile analysis to classify the X-ray sources. Quantile analysis, first introduced by Hong et al. (2004), uses the median energy and other quantile energies of a source as proxies for its spectral hardness and spectral shape. Its main advantage is that it does not require subdivision of the full energy range into different bands, making it free of the selection effects inherent in the hardness ratio and colors methods and yielding

meaningful results even for low-count sources. The fundamental quantities required in quantile analysis are E_x, the energy below which $x\%$ of the source counts reside. We made event files for each source and background region and passed them to `quantile.pro`, an IDL program developed by J. Hong.[9]. The other input to this code is the ratio of source and background areas and effective areas:

$$\text{ratio} = \frac{(A_{\text{core}} + A_{\text{pie}})(E_{\text{core}} + E_{\text{pie}})}{A_{\text{bkg}} E_{\text{bkg}}} \tag{2.6}$$

With this code, we computed E_{25}, E_{50}, and E_{75}, which are included in our catalog and can be seen in Table 2.4. These parameters were then combined into two quantities, $Q_x = \log(E_{50}/E_{min})/\log(E_{max}/E_{min})$ and $Q_y = 3(E_{25} - E_{min})/(E_{75} - E_{min})$, where E_{min} and E_{max} are 0.5 and 10 keV, respectively. Q_x measures the hardness of the spectrum, while Q_y indicates how broad or narrow the spectrum is. Figure 2.8 shows diagrams of Q_x and Q_y for all sources in our catalog detected at $\geq 3\sigma$ in the full energy band. To faciliate interpretation of this diagram, we have overlaid grids for a power-law model and a thermal bremsstrahlung model, both attenuated by interstellar absorption (see Figures 2.9 and 2.10).

2.2.8 Spectral Analysis

One of the goals of our survey is to understand the nature of the X-ray sources in our field. Analyzing the X-ray spectrum of a source can provide important clues about its physical nature, but most of our sources have too few counts to permit meaningful spectral analysis. Therefore, to identify the dominant populations of X-ray sources in our survey, we divided them into spectral groups based on their quantile properties (see §2.2.7) and analyzed the stacked spectrum of each quantile group. Our goals in making group divisions were to combine enough sources together to reduce the errors caused by poor statistics in spectral fitting, but also to maintain the maximum spectral diversity in our sample.

As can be seen in Figure 2.8, the sources are loosely confined to a U-shaped region in the Q_x-Q_y diagram, with overdensities towards the upper right and middle left. However, apart from these slight overdensities, the sources do not split up into visibly discernible groups, so we decided to split up the sources into groups with physically-motivated dividing lines roughly following the $N_{\text{H}} \approx 2 \times 10^{22}$ cm^{-2} and $\Gamma \approx 3$ grid lines, as shown in Figure 2.9. The dividing N_{H} line corresponds to the average N_{H} out to a distance of ~ 6 kpc in our survey region, as determined from the sum of N_{HI} estimated from the Leiden/Argentine/Bonn (LAB) Survey (Kalberla et al. 2005) and N_{H_2} estimated from the MWA CO survey (Bronfman et al. 1989);[10] this line roughly divides sources in the foreground and in the Scutum-Crux and near

[9]Available at http://hea-www.harvard.edu/ChaMPlane/quantile

[10]To estimate N_{HI} (N_{H_2}) to a distance of 6 kpc, we calculated the line-of-sight velocity of an object at this distance in circular motion around the Galaxy, integrated the brightness temperature measured in the LAB (MWA) survey from 0 km/s to this velocity, and multiplied the total brightness by $N_{\text{HI}}/I_{\text{H}} = 1.8 \times 10^{18}$ cm^{-2} K^{-1} km^{-1} s ($N_{\text{H}_2}/I_{\text{CO}} = 2 \times 10^{20}$ cm^{-2} K^{-1} km^{-1} s derived in Dame et al. (2001)). The sum of N_{HI} and N_{H_2} will actually be a lower limit of N_{H} since this calculation assumes the emission lines are optically thin.

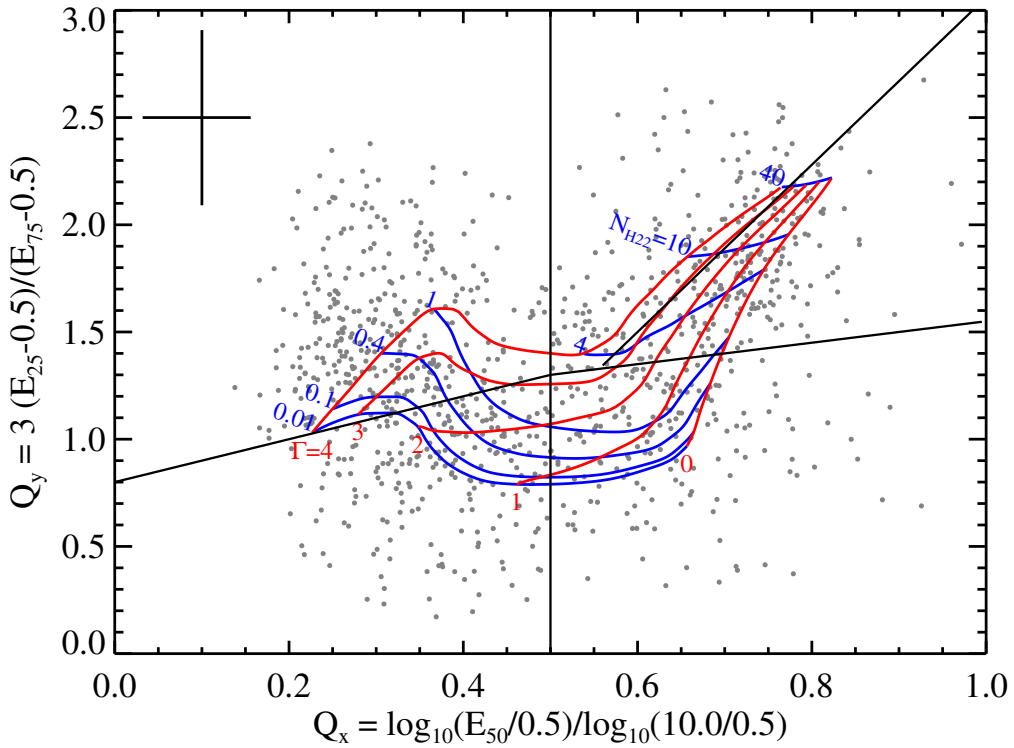

Figure 2.9: Quantile diagram or sources detected at $\geq 3\sigma$ in the 0.5-10 keV band. A grid of power-law spectra attenuated by interstellar absorption is overlaid. Red (primarily vertical) lines represent values of the photon index $\Gamma = 0, 1, 2, 3$, and 4 from right to left. Blue (primarily horizontal) lines represent values of the hydrogen column density $N_{\rm H} = 10^{20}, 10^{21}, 10^{21.6}, 10^{22}, 10^{22.6}, 10^{23}$, and $10^{23.6}$ cm^{-2} from bottom to top. Black solid lines separate the five spectral groups defined in §2.2.8.

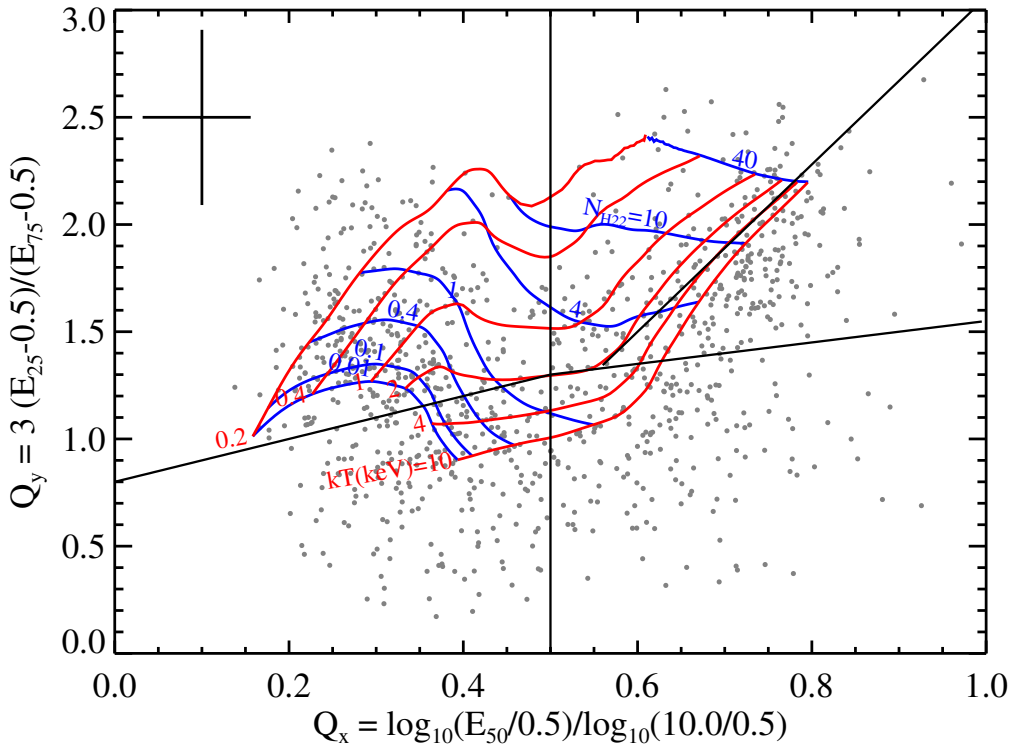

Figure 2.10: Quantile diagram or sources detected at $\geq 3\sigma$ in the 0.5-10 keV band. A grid of thin thermal plasma spectra attenuated by interstellar absorption is overlaid. Red (primarily vertical) lines represent values of the bremsstrahlung temperature $kT = 0.2, 0.4, 1, 2, 4$, and 10 keV from left to right. Blue (primarily horizontal) lines represent values of the hydrogen column density $N_{\rm H} = 10^{20}, 10^{21}, 10^{21.6}, 10^{22}, 10^{22.6}, 10^{23}$, and $10^{23.6}$ cm^{-2} from bottom to top. Black solid lines are the same as in Figure 2.9.

Norma spiral arms from sources in the far Norma arm. The dividing Γ line instead splits thermal and nonthermal sources. We further subdivided sources along $Q_x = 0.5$, because, as shown in Figure 2.11, this Q_x value roughly separates sources detected in the soft band from sources detected in the hard band. The equations of the dividing lines, in counterclockwise order from the top left of the diagram, are:

$$\begin{aligned} Q_y &= Q_x + 0.8 \\ Q_x &= 0.5 \\ Q_y &= 0.5Q_x + 1.05 \\ Q_y &= 3.9Q_x - 0.84 \end{aligned} \tag{2.7}$$

Varying the quantile divisions by $\sim$0.1 dex leads to no significant change in the best-fitting spectral parameters of the stacked spectum of each quantile group (§2.2.9), and the maximum likelihood slopes of the number-flux distributions of the sources in each quantile group remain consistent at the 2σ level or better (§2.2.11). Thus, our results are robust to $\sim$0.1 dex variations in the quantile group definitions.

For each source, we used `specextract` to extract source and background spectra and build associated ARFs and RMFs. Then the spectra of sources within each quantile group were combined with `combine_spectra`. Sources with more than 500 net counts were excluded from the stacked spectra to prevent individual sources from excessively influencing the combined spectrum. The spectra of these three individual sources are shown in Figure 2.12 and their best-fit spectral parameters are provided in Table 2.8. Sources 78 and 999 fall in quantile group D while source 750 falls in quantile group B, and they are best fit by absorbed power-laws.

Each of the stacked spectra was fit with an interstellar absorption model (`tbabs`, Wilms et al. 2000, with cross-section from Verner et al. 1996a) convolved with a power-law model (`pegpwrlw`) and an optically thin thermal plasma model (`vapec`, Smith et al. 2001, with abundances frozen to values from Güdel et al. 2007 relative to Anders & Grevesse 1989, scaled to Wilms et al. 2000). If an Fe line was visible between 6 and 7 keV, we added a Gaussian component to the power-law model. If neither the power-law nor thermal model produced a fit with reduced χ^2 less than 1.2, then a second component was added to the model; both power-law and thermal second components were tried in all such cases and the best fit was determined by the minimum reduced χ^2. For each quantile group, we made and fit a stacked spectrum first only using sources detected at $\geq 3\sigma$ confidence in the 0.5-10 keV band and then only using sources detected at $\geq 3\sigma$ confidence in the 2-10 keV band. The stacked spectra and their best fits are shown in Figure 2.13 and Table 2.9.

Following the example of Ebisawa et al. (2005), we studied how the spectral parameters of sources with or without IR counterparts differ. We split up the sources detected at $\geq 3\sigma$ in the full band in each quantile group into two groups, based on whether or not they have a VVV counterpart with $\geq 90\%$ reliability. A stacked spectrum for each of these subgroups was made and fit with the best-fitting model for its parent quantile group. For the case of a power-law model (with or without a Gaussian component), the power-law index, column

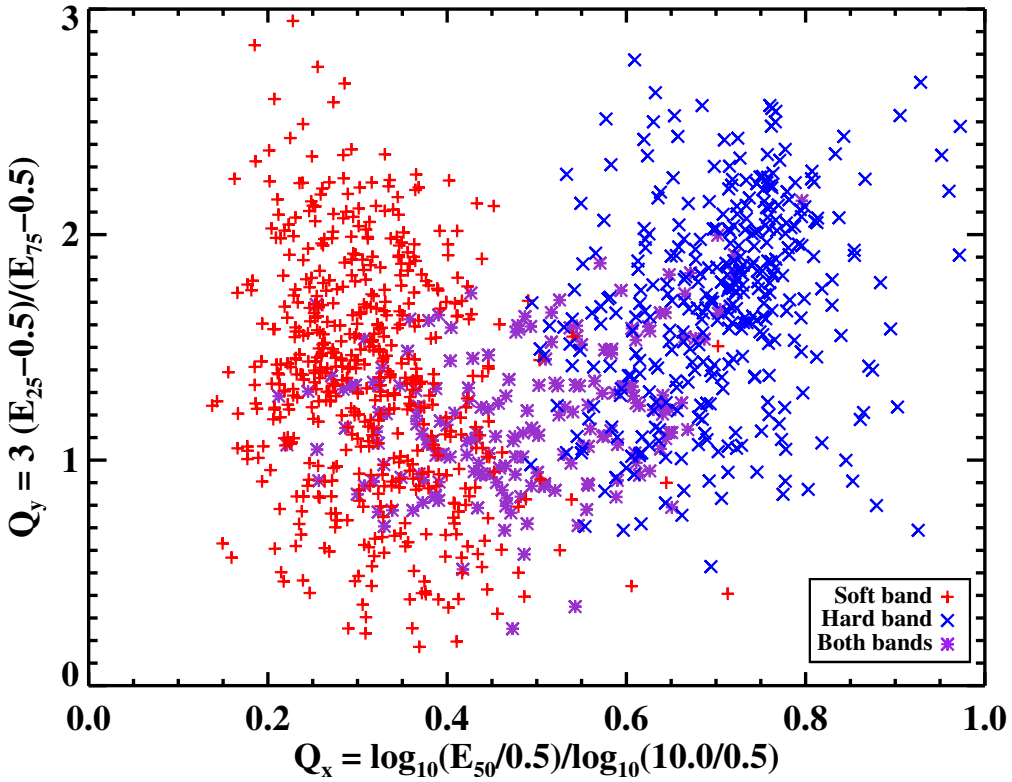

Figure 2.11: Quantile diagram showing soft sources in red crosses (detected at $\geq 3\sigma$ in SB but not HB), hard sources in blue X's (detected at $\geq 3\sigma$ in HB but not SB), and bright sources in purple asterisks (detected at $\geq 3\sigma$ in both SB and HB).

density, and the normalization of the power-law and Gaussian components were left free, while for two-temperature thermal models, only the normalizations of the two components were allowed to vary. In addition, since the strength of the Fe emission line for group E sources with and without IR counterparts appeared different, we decided to measure the equivalent width of the Fe line in the group E stacked spectra by fitting the 5-9 keV band of these stacked spectra with a power-law plus Gaussian line model. The results of this spectral analysis are shown in Table 2.10. Finally, we also studied how the spectral parameters of a given quantile group vary with source brightness. The sources within each quantile group were organized by photon flux and combined into subgroups containing 800-1000 total source counts. The analysis of the stacked spectra for these subgroups was done in the same way as for the subgroups based on the presence/absence of IR counterparts. All the brightness trends that we found can be explained by changes in the relative fraction of sources with and without IR counterparts as a function of flux. Thus, we only discuss the dependence of the spectral fitting results on the presence/absence of an IR counterpart.

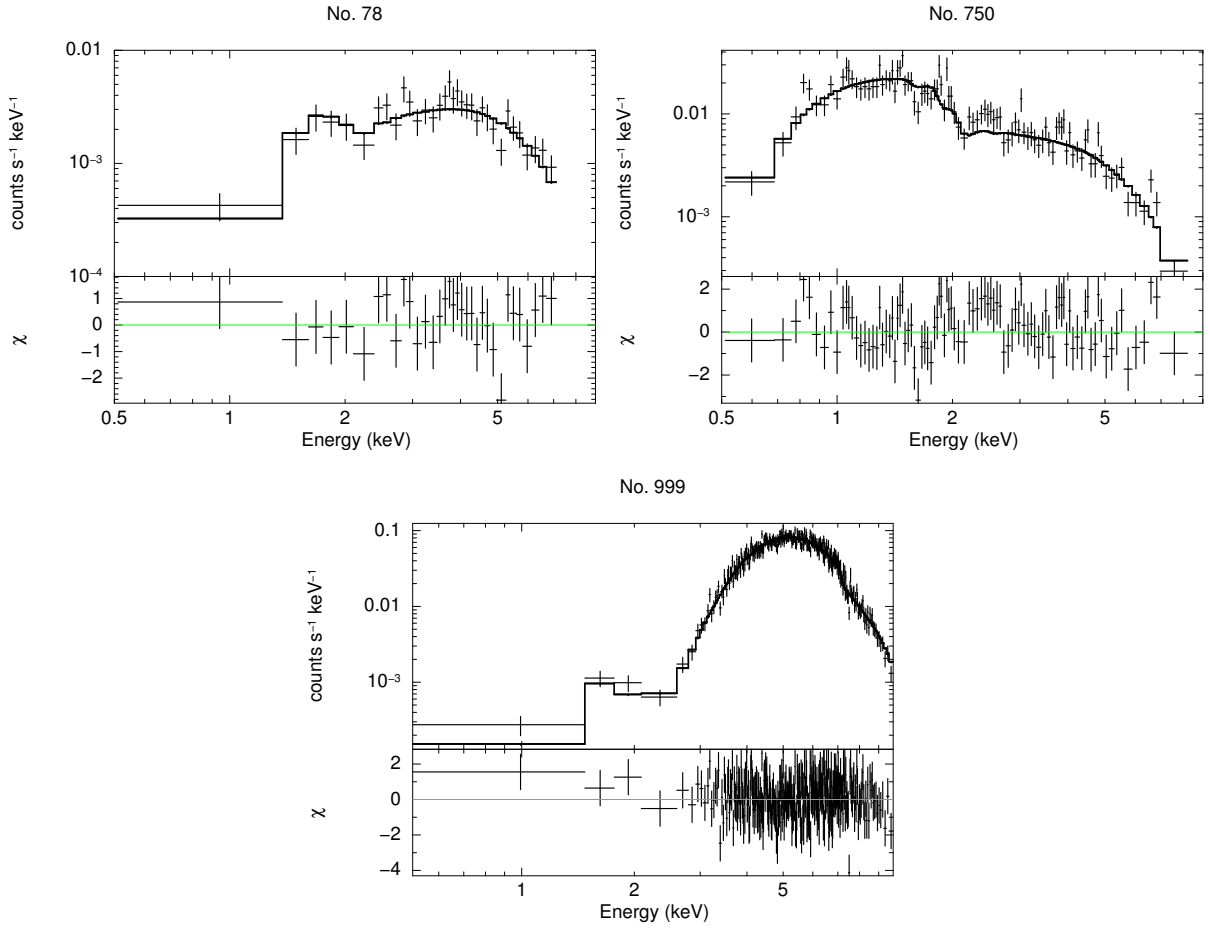

Figure 2.12: X-ray spectra of sources with more than 500 net counts in the 0.5-10 keV band. Title labels provide source catalog number. Grouped data and the best-fit model convolved with the instrumental response are shown in the upper panels. Lower panels show the data residuals. Table 2.8 provides the best-fit parameters.

Table 2.8: Spectral Fit Results for Individual Bright Sources

No.	Source CXOU J	C_{net} FB	$N_{\rm H}$ (10^{22}cm^{-2})	Γ	f_X FB (10^{-13}erg cm^{-2}s^{-1})	χ^2/dof	Galactic $N_{\rm H}$ (10^{22}cm^{-2})	Unabsorbed f_X FB (10^{-13}erg cm^{-2}s^{-1})
(1)	(2)	(3)	(4)	(5)	(6)	(7)	(8)	(9)
78	163355.1-473804	530±20	$2.4^{+1.1}_{-0.9}$	0.5±0.4	$8.8^{+0.8}_{-0.9}$	31/31	7.0	$10.0^{+0.9}_{-1.0}$
750	163750.8-465545	1790±40	$0.12^{+0.09}_{-0.08}$	1.2±0.1	9.9±0.4	124/95	9.4	10.3±0.5
999	163905.4-464212	14720±120	49±2	0.9±0.1	268^{+5}_{-4}	347/314	8.1	301^{+6}_{-5}

Notes: Quoted errors are 1σ unless specified in notes.
(1) Catalog source number.
(2) *Chandra* source name.
(3) Net source counts in the full 0.5-10 keV band.
(4) Hydrogen column density from spectral fit with 90% uncertainties.
(5) Power-law photon index from spectral fit with 90% uncertainties.
(6) 0.5-10 keV flux determined from spectral model.
(7) Chi-square of best-fit model over degrees of freedom.
(8) Estimated line-of-sight $N_{\rm H}$ through the Galaxy based on N(H) from the LAB survey and $N(H_2)$ from the MWA CO survey (see §2.2.8).
(9) 0.5-10 keV flux corrected for line-of-sight $N_{\rm H}$.

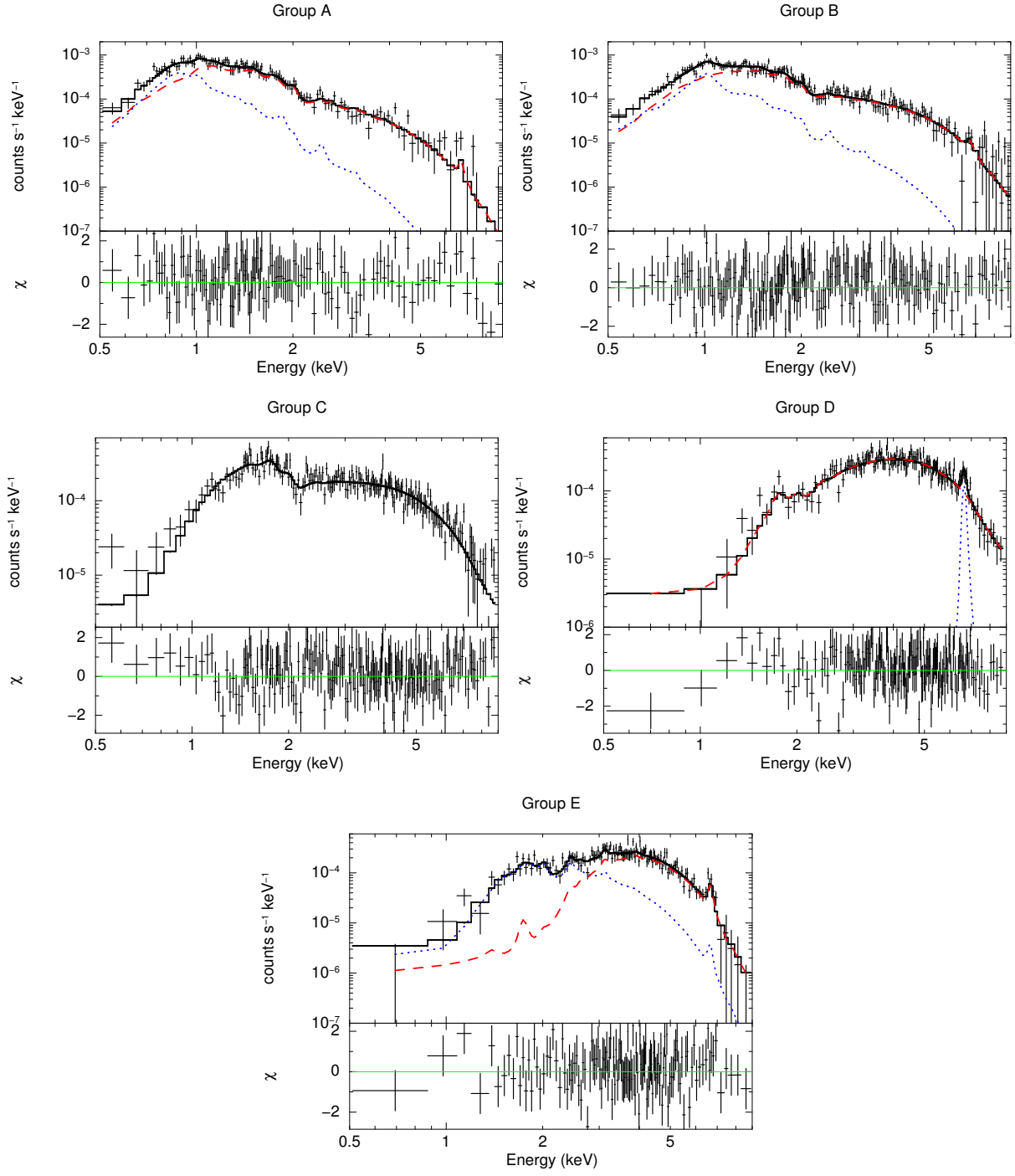

Figure 2.13: Stacked spectra and the best-fit models for each quantile group. Best-fit parameters can be found in Table 2.9.

Table 2.9: Spectral Fit Results for Stacked Sources

Power-law fit parameters									
Quantile Group (1)	Energy Band (2)	# Sources (3)	$N_{\rm H}$ (10^{22}cm^{-2}) (4)	Γ (5)	Line E (keV) (6)	Eq. Width (eV) (7)	f_X 2-10 keV (10^{-14}erg cm^{-2}s^{-1}) (8)	χ^2_ν/dof (9)	ϵ^{-1} (10^{-9}erg/ph.) (10)
C	full	170	$1.4^{+0.3}_{-0.2}$	1.1±0.1	–	–	$2.94^{+0.08}_{-0.13}$	1.02/180	8.66
	hard	137	1.8±0.3	1.2±0.1	–	–	$3.2^{+0.10}_{-0.2}$	0.99/158	8.60
D	full	162	7±1	0.7±0.2	$6.65^{+0.04}_{-0.05}$	300^{+60}_{-50}	$7.1^{+0.1}_{-0.4}$	1.06/153	11.47
	hard	167	$6.6^{+0.9}_{-0.8}$	0.6±0.2	6.60±0.04	300^{+50}_{-40}	$6.83^{+0.09}_{-0.31}$	1.16/186	11.13
Thermal fit parameters									
Quantile Group (1)	Energy Band (2)	# Sources (3)	$N_{\rm H}$ (10^{22}cm^{-2}) (4)	kT_1 (keV) (11)	$N_{\rm H}$ (10^{22}cm^{-2}) (4)	kT_2 (keV) (11)	$f_{X,low}/f_{X,high}$ (12)	χ^2_ν/dof (9)	ϵ^{-1} (10^{-9}erg/ph.) (10)
A	full	312	<0.43	$2.4^{+1.5}_{-0.4}$	<0.58	$0.75^{+0.05}_{-0.12}$	$0.04^{+0.05}_{-0.01}$	0.95/124	2.60
	hard	41	0.7±0.4	$2.4^{+0.6}_{-0.4}$	0.3±0.2	0.39±0.06	0.0092±0.0006	1.01/106	5.78
B	full	213	$0.3^{+0.4}_{-0.1}$	7±3	<0.14	$1.2^{+0.1}_{-0.2}$	0.04±0.02	1.08/186	3.83
	hard	71	5^{+9}_{-3}	4^{+3}_{-2}	0.29±0.08	$2.1^{+0.9}_{-0.3}$	0.74±0.05	1.09/134	7.33
E	full	130	25^{+7}_{-5}	$1.8^{+0.5}_{-0.3}$	5.4±0.9	$1.4^{+0.8}_{-0.4}$	$0.25^{+0.10}_{-0.07}$	1.01/125	16.5
	hard	127	24^{+7}_{-6}	$1.8^{+0.5}_{-0.3}$	6±1	$1.2^{+0.9}_{-0.4}$	0.20±0.01	0.99/122	9.51

Notes: All quoted errors are 90% unless otherwise indicated.
(1) Quantile groups defined in §2.2.7.
(2) Stacked spectrum contains all sources that are detected at $\geq 3\sigma$ in given energy band with fewer than 500 counts.
(3) Number of sources in stacked spectrum.
(4) Hydrogen column density associated with model component in next column.
(5) Power-law photon index.
(6) Energy of Gaussian line component.
(7) Equivalent width of Gaussian line component (1σ errors).
(8) 2-10 keV absorbed flux (1σ errors).
(9) Chi-square of best-fit model over degrees of freedom.
(10) Photon flux to unabsorbed energy flux conversion factor.
(11) Temperature of thin thermal plasma component.
(12) Flux ratio in 2-10 keV band of low kT component over high kT component (1σ errors).

Table 2.10: Spectral Comparison of Sources with and without IR Counterparts

Power-law stacked spectra							
Quantile Group	With/Without IR Counterparts	# Sources	$N_{\rm H}$ (10^{22}cm^{-2})	Γ	Line Eq. Width (eV)	f_X 2-10 keV (10^{-14} erg cm^{-2} s^{-1})	χ^2_ν/dof
(1)	(2)	(3)	(4)	(5)	(6)	(7)	(8)
C	IR	62	1.6±0.3	1.3±0.2	–	2.8±0.2	0.93/72
	No IR	108	1.4±0.4	0.9±0.2	–	3.0±0.2	1.08/120
D	IR	50	6^{+2}_{-1}	$0.8^{+0.4}_{-0.3}$	330^{+150}_{-100}	$5.1^{+0.1}_{-0.7}$	0.89/55
	No IR	112	7±1	0.6±0.3	270^{+80}_{-50}	$8.6^{+0.2}_{-0.6}$	1.12/115

Thermal stacked spectra								
Quantile Group	With/Without IR Counterparts	# Sources	f_X 2-10 keV (10^{-14} erg cm^{-2} s^{-1})	$f_{X,low}/f_{X,high}$	χ^2_ν/dof	Γ	Line Eq. Width (eV)	χ^2_ν/dof
(1)	(2)	(3)	(7)	(9)	(8)	(10)	(11)	(12)
A	IR	245	0.49±0.02	0.034±0.004	0.99/97	–	–	–
	No IR	67	0.26±0.02	0.036±0.006	1.71/49	–	–	–
B	IR	137	1.37±0.03	0.034±0.003	1.22/157	–	–	–
	No IR	76	0.55±0.04	0.07±0.01	1.33/57	–	–	–
E	IR	62	2.50±0.10	0.29±0.02	1.08/73	5±2	1700^{+1000}_{-100}	0.20/11
	No IR	68	2.14±0.09	0.21±0.02	1.06/64	2^{+2}_{-1}	<316	1.25/11

Notes: All quoted uncertainties are 90% unless stated otherwise.
(1) Quantile groups defined in §2.2.7.
(2) Stacked spectrum of sources with or without IR counterparts.
(3) Number of sources in stacked spectrum.
(4) Hydrogen column density associated with model component in next column.
(5) Power-law photon index.
(6) Equivalent width of Gaussian line component at energy 6.65 keV, line center determined from stacked spectrum of all FB, group D sources (1σ errors).
(7) 2-10 keV absorbed flux (1σ errors).
(8) Reduced chi-square of best-fit model over degrees of freedom.
(9) Flux ratio in 2-10 keV band of low kT component over high kT component (1σ errors).
(10) Power-law photon index of 5-9 keV band when fitting with power-law plus Gaussian line model.
(11) Equivalent width of Gaussian line component at 6.65 keV, line center determined from stacked spectrum of all FB group E sources (1σ errors).
(12) Reduced chi-square of best-fit model for 5-9 keV band over degrees of freedom.

2.2.9 Discussion of NARCS X-ray Populations

Although it is difficult to determine the nature of individual sources in our survey, it is possible to make reasonable inferences about the classes of X-ray sources that dominate each quantile group defined in §2.2.7. The stacked spectra, variability, and IR counterparts of the sources in each group provide important clues to the nature of the sources. In order to facilitate our understanding of the reliable counterparts, we estimated the J and H magnitudes of main sequence and supergiant high-mass (O,B) and low-mass (G,K,M) stars at distances of 100 pc, 1 kpc, 4 kpc, 10 kpc, 12 kpc with corresponding $N_{\rm H}$ values[11] of 0.0, 0.3, 1.0, 3.0, and 5.0×10^{22} cm^{-2}. These J and H magnitude estimates were based on the absolute V magnitudes from Wegner (2007), the intrinsic colors from Ducati et al. (2001), the $N_{\rm H} - A(V)$ relationship derived by Güver & Özel (2009), and the $A(\lambda)/A(V)$ relations from Cardelli et al. (1989). Unless explicitly stated otherwise, we refer readers to Muno et al. (2004) and references therein for an overview of the spectral and timing properties of Galactic X-ray sources.

Group A

The group A stacked spectrum is best fit by a two-temperature thermal plasma model. The column density associated with each temperature component is low ($\lesssim 10^{21}$ cm^{-2}), suggesting most sources in this group are foreground sources, located at a distance $\lesssim$1 kpc. Both components have low temperatures ($kT \lesssim 2$ keV), and the sources in this group have 0.5-10 keV luminosities[12] between $L_X = 10^{27} - 10^{31}$ ergs s^{-1}, assuming they are located at a distance between 100 pc and 1 kpc. The very soft component ($kT = 0.75$ keV) most likely originates from the magnetic coronae of low-mass stars, which are the faintest sources of X-ray emission. X-ray active low-mass stars typically have $kT < 1$ keV and $L_X < 10^{29}$ ergs s^{-1}. The higher kT component is more consistent with X-ray emission from coronally active binaries (ABs) such as RS CVn systems. These binaries usually have $kT \approx 0.1 - 2$ keV and $L_X = 10^{29} - 10^{32}$ ergs s^{-1}. Other types of sources which could contribute to the group A X-ray emission are symbiotic binaries and massive stars. Symbiotic binaries, which consist of a mass-losing cool supergiant and white dwarf companion, are often considered a subtype of CVs and tend to have $kT = 0.3 - 1.3$ keV and $L_X = 10^{30} - 10^{33}$ ergs s^{-1} (Muerset et al. 1997). X-rays can be produced in the shocks in the winds of high-mass stars, either in isolation or in a colliding-wind binary, and typically have $kT = 0.1 - 6$ keV; in fact, three group A sources (#622, 469, and 298) are coincident with previously identified O and B stars, HD149452, HD149358, and ALS 3666, respectively. Based on the optical band spectral and photometric information available on these sources, we estimate they are located at a distance of approximately 1-4 kpc, farther than the majority of sources in this group appear to be based on the column density of the group A stacked spectrum.

Group A contains an enhanced fraction of variable sources compared to other quantile

[11] For each distance listed, the corresponding $N_{\rm H}$ value was calculated as described in §2.2.8.

[12] In the remainder of this section, L_X refers to 0.5-10 keV luminosity.

groups. Ten of 26 (38%) group A sources with $\geq$ 40 counts show variability on $\sim$hour timescales (see §2.2.5) at $\geq$ 95% confidence. Of the 17 group A sources detected in multiple observations with average 0.5–10 keV fluxes $\geq 5.5 \times 10^{-6}$ cm^{-2} s^{-1}, 9 (53%) are found to be variable between observations, a higher percentage than is found for sources in the full sample detected in multiple observations. The significant variability seen in this group of sources is consistent with the flaring behavior of low-mass active stars and interacting binaries. As can be seen in Figure 2.5, the fluxes of some group A sources vary by large factors (> 5) in between observations; hour-long flares with amplitudes as large as a factor of 10 have been observed in RS CVns and could be the origin of these large variability amplitudes.

In the VVV catalog, we found reliable infrared counterparts to 67% of the group A sources. The only significant difference between the X-ray properties of group A sources with and without IR counterparts is that those without counterparts tend to have lower X-ray fluxes; thus sources without IR counterparts may be intrinsically dimmer in both the X-ray and NIR bands or they may located at larger distances. As can be seen in Figure 2.7, these counterparts have blue $(J - H)$ colors, in agreement with our inference that group A sources are mostly foreground sources. In this color-magnitude diagram, there is a tight cluster of counterparts with H magnitudes between 13 and 15, and a looser cluster of counterparts with H magnitudes between 8 and 13. The former is consistent with the colors and magnitudes of low-mass main sequence stars at a distance of $\approx$ 1 kpc, while the latter is likely a mixture of low-mass main sequence stars at $\approx$ 100 pc and cool giants at $\approx$ 1 kpc; the small number of counterparts with negative $(J - H)$ are more likely to be high mass stars at $\approx$ 1 kpc. The fact that the majority of counterparts are most likely to be low-mass stars, either on the main sequence or in a giant/supergiant phase, is consistent with the suggestion that the dominant X-ray populations in group A are X-ray active low-mass stars and interacting binaries.

Group B

Similar to group A, the group B stacked spectrum is also best-fit by a two-temperature thermal model with low hydrogen column densities. However, the temperature of the hotter component is significantly higher ($kT \approx 7$ keV) for the B sources than for the A sources. The origin of the low-temperature component may be low-mass X-ray active stars, ABs, and symbiotic binaries, the dominant sources in group A, while the high-temperature component is more typical of CVs. The majority of CVs are close binary systems with a white dwarf accreting matter from a low-mass main-sequence stellar companion, although some have been found to have giant donors (Kuulkers et al. 2006). CVs are typically subdivided into three main categories based on the magnetic field strength of the WD they host. The majority of CVs have weak magnetic fields ($B \lesssim 10^4$ G) which do not significantly affect the accretion flow from the Roche lobe-filling donor and are called nonmagnetic CVs. About 20% of CVs are polars, exhibiting strong magnetic fields ($B \gtrsim 10^{6.5}$ G) which prevent the formation of an accretion disk; about 5% are intermediate polars (IPs), having intermediate strength magnetic fields which channel material from the inner accretion disk onto the magnetic poles. Nonmagnetic CVs and polars have $\Gamma \approx 1 - 2$ or $kT \approx 1 - 25$ keV and $L_X = 10^{29} - 10^{32}$ erg

s^{-1}. IPs tend to be more luminous ($L_X = 10^{31} - 10^{33}$ erg s^{-1}) and display harder emission ($\Gamma < 1$) than other CVs. Assuming that the group B sources lie at a distance between 100 pc and 1 kpc based on their low $N_{\rm H}$, they span the luminosity range $10^{27.4} - 10^{31.5}$ ergs s^{-1}, consistent with the luminosities of low-mass stars at the faint end and with the luminosities of active binaries and CVs at the bright end.

Further evidence that a CV population exists in group B is provided by one of the brightest sources in our survey, source 750, which is coincident with ASCA source AX J1637.8-4656 (Sugizaki et al. 2001) This source has $\Gamma = 1.15$ (see Table 2.8), and, assuming a distance of 1 kpc from its low $N_{\rm H}$, $L_X \approx 8 \times 10^{31}$ ergs s^{-1}. In addition to having a luminosity and photon index consistent with that of a CV, this source is variable on both short and long timescales. As can be seen in Table 2.7, this source was determined to be periodic by the Z_n^2 test (Buccheri et al. 1983), with a best period of roughly 7100 s. Periodic X-ray emission has been observed from magnetic CVs and is believed to be associated with the spin period of the white dwarf, which can range from 10^2 to 10^4 seconds (Scaringi et al. 2010). Finally, the near-IR spectrum obtained of the IR counterpart of this source exhibits strong emission lines suggestive of an accretion disk (Rahoui et al. 2014). Thus source 750 is likely a CV with an intermediate strength magnetic field that is not fully disrupting the accretion disk.

As mentioned in §2.2.5, source 961, another group B source, is also likely to be a magnetic CV. Its ≈5700 second period is consistent with the spin and orbital periods of CVs. As can be seen in Figure 2.6(b), its pulse profile shows large brightness variations from approximately zero to twenty counts; such variations could either result from pulsations due to emission from accretion spots at the WD magnetic poles as the WD rotates or from eclipsing of the WD by its companion. Its location in the quantile diagram indicates it has $\Gamma \approx 1.5$, which is more typical of polars and nonmagnetic CVs than IPs. Although it is likely a nearby source based on its low $N_{\rm H}$ (estimated to be $\sim 10^{21}$ cm^{-2} from its quantile parameters), it has no stellar IR counterpart in the VVV survey; we do find an infrared counterpart to this source in the VVV survey, but it is morphologically classified as a galaxy, and therefore it cannot be the true counterpart since the X-ray spectrum of the *Chandra* source shows very little absorption. Since the source is likely located $\lesssim 1$ kpc, the stellar IR counterpart must be very faint to avoid detection, thus making it unlikely that this source has a significant accretion disk which indicates that, of all CV types, this source is most likely a polar. Thus, there is evidence that both sources 750 and 961 are magnetic CVs, and their location in the quantile diagram supports the hypothesis that group B may contain a significant CV population.

Group B has a comparable percentage of variable sources to group A. Eight of the 17 (47%) group B sources with ≥40 counts are variable on short timescales, and 6 of the 14 (43%) group B sources detected in multiple observations with average 0.5–10 keV fluxes $\geq 5.5 \times 10^{-6}$ cm^{-2} s^{-1} are variable on long timescales. Group B sources are thus comparable in variability to group A sources, which is consistent with both groups containing large numbers of X-ray active stars and ABs.

We found reliable IR counterparts for 61% of group B sources, which largely overlap in the color-magnitude diagram with the group A counterparts, indicating that they have similar stellar types and are located at similar distances. This similarity is not surprising

since the X-ray properties of the group B sources indicate that they are dominated by the same X-ray populations as group A plus a population of CVs, which tend to have near-IR properties similar to low-mass main sequence or evolved stars (Hoard et al. 2002). As can be seen in Table 2.10, group B sources without IR counterparts have a lower average flux and a more significant contribution from the low kT component compared to group B sources with IR counterparts. These trends suggest that X-ray active low-mass stars make up a relatively larger fraction of group B sources without counterparts than of B sources with counterparts.

Group C

The group C stacked spectrum is best-fit by an absorbed power-law with $\Gamma \approx 1.1$ and $N_{\rm H} = 1.4 \times 10^{22}$ cm^{-2}, which suggests that these sources are located at a distance of 3–5 kpc, in the Scutum-Crux and near Norma spiral arms. The luminosities spanned by group C sources are $L_X = 10^{31} - 10^{32.7}$ ergs s^{-1}, assuming a distance of 4 kpc. Possible classes of X-ray sources present in this group are magnetic and nonmagnetic CVs, hard-spectrum symbiotic binaries, low-mass X-ray binaries (LMXBs), and HMXBs. IPs and HMXBs tend to have $\Gamma < 1$ while nonmagnetic CVs, polars, symbiotic binaries, and LMXBs tend to have $\Gamma > 1$. CVs are the most numerous accreting sources, so they are most likely the dominant population.

Group C sources show the lowest levels of variability of any group. Only 2 of 12 (17%) sources with ≥ 40 counts exhibit short-timescale variability and only one of 7 (14%) sources detected in multiple observations with average 0.5–10 keV fluxes $\geq 5.5 \times 10^{-6}$ cm^{-2} s^{-1} are variable on long timescales. These results are consistent with magnetic CVs and LMXBs dominating group C, since although they show periodic variations and occasional outburts, they generally have stable emission.

Reliable IR counterparts were found for 35% of group C sources. They have redder $(J-H)$ colors than the counterparts of group A and B sources, confirming that they are more distant than the group A or B counterparts. Their H magnitudes are consistent with high-mass stars and evolved low-mass stars located at $\sim$4 kpc. Considering the extinction resulting from the $N_{\rm H}$ measured for these sources and their likely distances, most main-sequence, low-mass counterparts of group C sources would be undetectable in the VVV survey. The stacked spectrum of group C sources with IR counterparts has a softer power-law index ($\Gamma \approx 1.3$) than the sources lacking IR counterparts ($\Gamma \approx 0.9$). Thus, the majority of group C sources with counterparts may be symbiotic binaries and CVs with subgiant and giant companions, while those without counterparts may primarily be CVs with main-sequence companions, especially IPs given the lower photon index of these sources. The presence of some type II AGN among the group C sources lacking IR counterparts could also help explain their lower photon index, but, as discussed in §2.2.9, very few AGN are likely to be found in group C.

Group D

The group D stacked spectrum has a very hard photon index ($\Gamma \approx 0.7$), a prominent Fe line, and a high $N_{\rm H}$ indicating that these sources typically lie on the far side of the Galaxy,

near, in, or beyond the far Norma arm. The Fe emission is well-modeled by a Gaussian centered at 6.65 keV with an equivalent width of approximately 300 eV; this emission likely results from the blending of lines at 6.4 keV and 6.7 keV, arising from low-ionization Fe and He-like Fe respectively. The presence of this strong, non-redshifted Fe line suggests that many of the sources in this group must be Galactic; otherwise, if this group were dominated by AGN, their spread in redshift would result in a smearing out of the Fe line.

Two classes of X-ray sources that are frequently observed having spectra with $\Gamma < 1$ are IPs and HMXBs. Fe line emission has been observed from both of these types of sources. Although the luminosity range spanned by group D ($L_X = 10^{32} - 10^{33.7}$ ergs s^{-1} assuming $d = 10$ kpc) extends to higher luminosities than are typically observed for IPs, roughly 80% of group D sources have $L_X \lesssim 10^{33}$ ergs s^{-1} for $d = 10$ kpc, a reasonable luminosity range for IPs. Thus, IPs could be the dominant population among faint group D sources. In contrast, HMXBs can have X-ray luminosities as high as $L_X \sim 10^{34}$ ergs s^{-1} during quiescence and $L_X \sim 10^{38}$ ergs s^{-1} during outburst. In fact, one of the group D sources, source 999, is a previously discovered HMXB (Sugizaki et al. 2001; Bird et al. 2004; Bodaghee et al. 2006) and has $\Gamma \approx 0.9$ and $L_X \approx 10^{35.3}$ ergs s^{-1}.

Five of 14 (36%) group D sources exhibit short-timescale variability, and 3 of 11 (27%) group D sources detected in multiple observations with average 0.5–10 keV fluxes $\geq 5.5 \times 10^{-6}$ cm^{-2} s^{-1} display long-timescale variability. These modest levels of variability are consistent with, although not necessarily proof of, group D being dominated by a population of IPs, which tend to have fairly stable emission.

Only 30% of group D sources have reliable IR counterparts. The $(J - H)$ color and H magnitudes of these counterparts are consistent with being high-mass and evolved low-mass stars at distances between 8–12 kpc. The low fraction of detected counterparts is more easily explained by a dominant population of IPs rather than HMXBs, since a large fraction of the low-mass companions of the white dwarfs in IPs would have J and H magnitudes greater than the VVV sensitivity limit when located at distances of 8–12 kpc. However, while most massive stellar counterparts of HMXBs in group D should be above the VVV sensitivity limit, they can occasionally be so obscured by circumbinary gas and dust that they are much fainter than otherwise expected (Bodaghee et al. 2012b); in fact, our counterpart-matching algorithm does not find the faint massive counterpart of HMXB IGR J16393-4643 (Bodaghee et al. 2012a) in the VVV catalog.

The X-ray spectral differences between group D sources with and without IR counterparts are not statistically significant. Nonetheless, if the lower photon index and lower Fe equivalent width of the sources without IR counterparts is a real trend, it could be explained if the sources without counterparts are primarily IPs and type II AGN (see §2.2.9), while those with counterparts include some hard-spectrum symbiotic binaries (Luna et al. 2013), whose spectra are a bit softer and whose red giant companions should be detectable by the VVV survey.

Group E

The group E stacked spectrum is best-fit by a two-temperature thermal model, making it significantly different from the group D power-law spectrum, even though some of the same classes of X-ray sources must be present in both groups D and E since they are not sharply separated in the quantile diagram. Both temperature components have $kT = 1 - 2$ keV but very different hydrogen column densities, the lower of which is similar to that of group D, and the higher of which is $N_{\rm H} \approx 2.4 \times 10^{23}$ cm^{-2}. This $N_{\rm H}$ value is roughly 3 times higher than the maximum $N_{\rm H}$ value measured through the Galaxy along a line of sight within our surveyed area, indicating that some E sources are obscured by large amounts of local absorption and/or may be imbedded in the molecular clouds of the far Norma arm. Assuming the same typical distance of 10 kpc as we did for group D, these sources span the luminosity range $L_X = 10^{32} - 10^{33.7}$ ergs s^{-1}. A significant fraction of these sources may be associated with the shocks produced in the winds of high-mass stars; these sources typically have $kT = 0.1 - 6$ keV, $L_X \sim 10^{33} - 10^{35}$ ergs s^{-1}, and their emission can be significantly absorbed by circumstellar material. The photometric and spectral properties of group E are also consistent with symbiotic binaries. In addition, a small number of magnetars could be present in this group. In fact, one of the group E sources is a previously discovered magnetar, SGR 1627-41, and data from this survey was used in an in-depth study of this magnetar by An et al. (2012).

Only two of the nine (22%) group E sources with ≥40 counts exhibits variability on short timescales. None of the group E sources detected in multiple observations are found to vary significantly, but only 4 of them are bright enough ($f_{\rm ph} \geq 5.5 \times 10^{-6}$ cm^{-2} s^{-1}) for long-term variability to have been detected. Thus, the variabilty of group E sources is not well constrained, but appears more comparable to that of groups C and D than groups A or B. Such moderate variability is consistent with populations of high-mass stars and symbiotic binaries (Luna & Sokoloski 2007; Corbet et al. 2008; Mauerhan et al. 2010), although it does not constitute proof of such a physical origin for group E sources.

Although group E sources are roughly located at the same distance as group D sources based on the $N_{\rm H}$ measured in their stacked spectra, a higher fraction of group E sources (47%) have reliable IR counterparts. At distances of ≈10 kpc, only high-mass stars and cool giants have J and H magnitudes above the sensitivity limit of the VVV survey. The higher percentage of IR counterparts is consistent with group E having a larger fraction of high-mass stellar X-ray sources and symbiotic binaries than group D, since the high-mass and giant counterparts of these sources are brighter than the primarily main-sequence low-mass counterparts of IPs. A significant fraction of group E sources without IR counterparts are also likely to be type I AGN, as discussed in the following section.

AGN Contribution

In addition to the Galactic classes of sources described in the previous sections, we expect a significant population of AGN to be present in our catalog. Using the AGN count-distribution from the COSMOS survey (Cappelluti et al. 2009) and taking into account the sensitivity

variations across the survey area (see §2.2.10) and the incompleteness of our detection method (see §2.2.10), we estimate that roughly 150 AGN could be present in our catalog. X-ray emission from AGN is attenuated by the integrated column density through the whole galaxy and typically has $\Gamma \approx 1.7$ (Molina et al. 2009) for type I AGN or $\Gamma \lesssim 1$ for type II AGN with a reflection component. Thus, AGN are most likely to be found in groups D and E based on the regions of quantile space they occupy. Due to the spread in $N_{\rm H}$ values across our field of view and the large median error bars on Q_x and Q_y, some group C sources may also be AGN.

We expect to find most of the AGN in our sample among the sources without NIR counterparts. Only 2% of AGN in the Chandra COSMOS Survey (Civano et al. 2012) with $f_X > 1 \times 10^{-15}$ erg cm^{-2} s^{-1} have H magnitudes ≤ 18 –the sensitivity limit of the VVV survey–and we would expect an even smaller percentage of the AGN in NARCS to be detected in the VVV survey due to the higher extinction in the Galactic plane compared to the COSMOS field; the integrated $N_{\rm H}$ through the galaxy in the NARCS region varies between $3 - 8 \times 10^{22}$cm^{-2}, which corresponds to extinction values of $A(J) \approx 4 - 10$ mag and $A(H) \approx 3 - 7$ mag.

Based on the spectral properties of group E sources without IR counterparts, it seems likely that many of them are AGN. Their stacked spectrum shows a more prominent high-column density component compared to the spectrum of group E sources with counterparts; this enhancement could be due to a large number of AGN, which suffer from extinction by their local environment and host galaxy as well as the Milky Way ISM. In addition, fitting the 5-9 keV stacked spectra of group E sources with and without counterparts with a power law plus Fe line model shows that the sources lacking IR counterparts have a harder spectrum with $\Gamma \approx 2$ and a lower Fe line equivalent width. This photon index is typical of type I AGN and the lower Fe equivalent width is expected for a group of extragalactic sources whose Fe line would be smeared out due to their redshift distribution. Thus, a large number of type I AGN among the group E sources lacking IR counterparts can explain the difference between the stacked spectra of group E sources with and without IR counterparts.

There is weaker evidence for the presence of AGN among the group C and group D sources lacking IR counterparts. The stacked spectrum of group D sources without counterparts is harder ($\Gamma \approx 0.6$) and has a lower Fe line equivalent width that the spectrum of sources with counterparts; however, while these trends are consistent with the presence of type II AGN with a reflection component among the sources lacking counterparts, these differences are not statistically significant. Thus, these trends may be real and indicative of an AGN population, or they may be statistical fluctuations, in which case the group D sources lacking counterparts are probably just faint and/or distant versions of the group D sources with counterparts. The stacked spectrum of group C sources without counterparts is harder ($\Gamma \approx 0.9$) than that of the sources with counterparts; this difference could be driven by a population of type II AGN among the sources lacking counterparts. However, it is unlikely that many AGN would be found in group C, since the average column density of sources in this group is $N_{\rm H} \approx 10^{22}$ cm^{-2}, which is low for an AGN whose light would be shining through the entire Galaxy. Thus, it appears more likely that the differences between the group C sources with and without counterparts are due to different populations of Galactic sources (as discussed in

§2.2.9), although a small AGN contribution cannot be ruled out.

In order for our survey to contain the expected number of AGN, the majority of group E sources lacking IR counterparts and 30%-50% of group C and D sources without counterparts must be AGN. Given that there is good evidence for the former and that the latter cannot be ruled out, it is possible that about 150 AGN are present in our catalog, as expected from other surveys.

2.2.10 Computing the Number-Flux Distribution

Having determined the X-ray populations which likely dominate each of the quantile groups, we sought to compare the populations in our survey to predictions based on surveys of other regions of the Galaxy. A useful tool in comparing the populations of different surveys is the number count distribution. In addition, for a particular population of sources located at similar distances, the number-flux distribution is closely related to the luminosity function of the sources and thus can also shed light on the physics which determines the brightness of these sources.

At faint fluxes, this calculation is complicated by the nonuniform sensitivity across the *Chandra* image, the incompleteness of the source-detection algorithm, and the Eddington bias, which is caused by fluctuations in the source and/or background making a faint source appear brighter. To help correct for these effects, we used a method similar to that developed by Georgakakis et al. (2008a) and adapted by Lehmer et al. (2012), which uses a Bayesian approach with maximum-likelihood optimizations. We decided to compute the number count distribution in the 2–10 keV band, because (1) most foreground, thermal sources are not detected in this band, allowing us to concentrate on the populations in the spiral arms, (2) photons in this energy band are less likely to be absorbed by dust along the line-of-sight, resulting in more robust conversion factors between the net counts of a source and its unabsorbed energy flux, and (3) it will enable comparisons to published number count distributions from previous surveys of Galactic X-ray populations, which are primarily in the 2–10 or 2–8 keV band. In the remainder of this section, whenever we refer to catalog sources, we only mean sources detected at $\geq 3\sigma$ in the 2–10 keV band.

Sensitivity Curves

Near the flux limit of a survey, a source of a given flux can only be detected over a limited fraction of the total solid angle covered by the survey due to the inhomogeneous background and nonuniform PSF across the *Chandra* image. In order to account for this varying sensitivity in our number count distribution, we calculate the effective solid angle as a function of source flux, which we refer to as the sensitivity curve. This sensitivity curve depends on the significance threshold we choose to select our sources. In computing the number count distribution of sources in our survey, we select point-like sources that have been detected by `wavdetect` in any energy band as described in §2.2.3 and have $P(\geq C_{\rm src}) \leq 0.00137 = P_{\rm thresh}$ in the 2–10 keV band as determined by Equation 2.5, which is the probability

required for a 3σ detection. This selection procedure will not include all real sources with $P(\geq C_{\rm src}) \leq P_{\rm thresh}$ because of `wavdetect`'s complex source detection criteria (see Freeman et al. 2002a). Correcting for this detection incompleteness is discussed in §2.2.10.

To compute the sensitivity curve, we follow the method described in Georgakakis et al. 2008a, which should allow us to extrapolate the number-flux distribution to fluxes roughly an order-of-magnitude fainter than the formal survey flux limit–the flux to which $\gtrsim$90% of the image is sensitive. First, we determine the minimum number of counts, $C_{\rm lim}$, required for a detection, such that $P(\geq C_{\rm lim}) = P_{\rm thresh}$, at each location in the image. We use the background maps (see §2.2.3) to determine the mean expected background counts, $\langle C_{\rm bkg} \rangle$, within circular regions with radii equal to the local 90% ECF radius. The cumulative probability that the observed counts will exceed $C_{\rm lim}$ within a particular region is

$$P(\geq C_{\rm lim}) = \gamma(C_{\rm lim}, \langle C_{\rm bkg} \rangle) \tag{2.8}$$

where $\gamma(a, x)$ is the lower incomplete gamma function, defined as

$$\gamma(a, x) = \frac{1}{\Gamma(a)} \int_0^x e^{-t} t^{a-1} dt \tag{2.9}$$

Equation 2.8 is a simplication of Equation 2.5 for situations in which the mean background within an aperture region is well determined. Setting $P(\geq C_{\rm lim}) = P_{\rm thresh} = 0.00137$, we invert Equation 2.8 numerically to find $C_{\rm lim}$ for a region with mean expected background $\langle C_{\rm bkg} \rangle$. For each observation, we perform this procedure for different regions, which combined cover the full image area, thus obtaining a 2D image of $C_{\rm lim}$ known as a sensitivity map.

Then we can compute the probability of detecting a source of a given flux f_X and spectral shape within each region of the sensitivity map. The total observed counts in the region are the sum of the source and background contributions, which can be expressed as:

$$C_{\rm src} = C_{\rm net} + \langle C_{\rm bkg} \rangle = f_X t_{\rm exp} E_{\rm src} \eta \epsilon + \langle C_{\rm bkg} \rangle \tag{2.10}$$

where $t_{\rm exp}, E_{\rm src}, \eta$, and ϵ are the exposure time, mean effective area, ECF, and unabsorbed energy flux to observed photon flux conversion factor, respectively. ϵ includes a correction factor for extinction along the line-of-sight due to the amount of $N_{\rm H}$ determined by the spectral fits of each quantile group, but not exceeding $5.5{\times}10^{22}$ cm^{-2}, the average $N_{\rm H}$ integrated through the entire Galaxy in our surveyed area; we assume that larger values of $N_{\rm H}$ are likely due to both interstellar and intrinsic absorption, and we do not wish to correct for absorption that may be intrinsic or very local to the source. The energy flux to photon flux conversion factor depends on the source spectrum, and we used the same ϵ for all sources in the same quantile group; the conversion factors are listed in Table 2.9. For a region with particular values of $\langle C_{\rm bkg} \rangle$ and $C_{\rm lim}$, the probability of detecting a source of flux f_X is given by

$$P_{f_X}(\geq C_{\rm lim}) = \gamma(C_{\rm lim}, C_{\rm src}). \tag{2.11}$$

We calculate the sensitivity curve for each observation by summing the $P_{f_X}(\geq C_{\rm lim})$ distributions of individual regions, each weighted by the solid angle (in degrees) of each region.

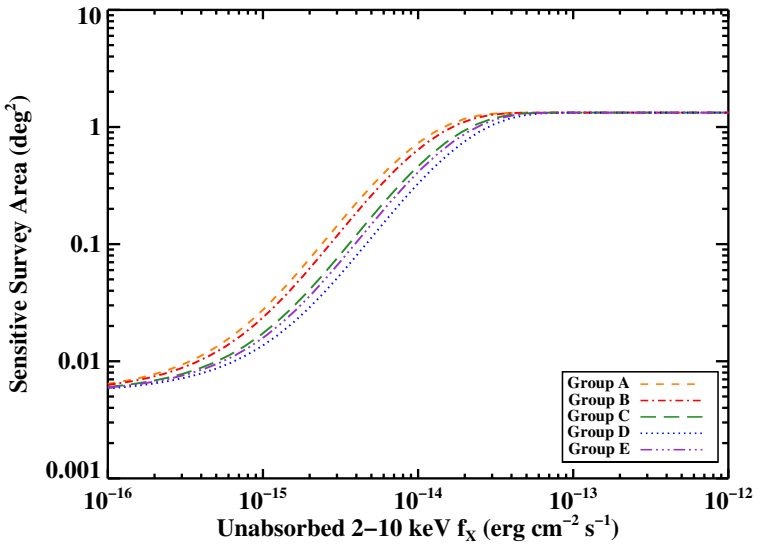

Figure 2.14: Angular area of our survey that is sensitive to a given source flux.

Then we added together the sensitivity curves of all the individual observations, and divided the combined sensitivity curve by a factor of 1.54 so that the maximum value of the sensitivity curve was equal to the total survey area (1.3268 deg^2); this division was necessary because the observations partially overlap. This combined sensitivity curve, $A(f_X, \epsilon)$ (shown in Figure 2.14), is an approximation which overweights the overlapping regions, which generally have worse sensitivity since they are at large off-axis angles. We estimate errors in the sensitivity curve to be 0.1 dex, which are satisfactory for our purposes. We choose to only compute number counts to a flux limit of 1×10^{-15} erg cm^{-2} s^{-1}, to which 1–3% of the total solid angle is sensitive; below this flux, too few sources are detected by `wavdetect` to make reliable predictions. Note that the sensitivity curve as a function of source counts is the same for all spectral groups, but since different spectral groups have different count-to-flux conversions, they have different sensitivity curves as a function of flux.

Recovery Fraction Correction

The sensitivity curve will only successfully correct for the incompleteness of our catalog if all sources are detected above a specific selection probability. However, due to the complex criteria of `wavdetect`, some faint sources that would meet the probability criterion are not detected. Employing an approach similar to that of Lehmer et al. (2012) to compute and correct for detection incompleteness, we generated 200 mock images in the full, soft, and hard energy bands of ObsID 12519, which we took to be representative of all observations since they have very similar exposure and background maps. To make each set of mock observations, we added 60 sources to the full, soft, and hard unsmoothed background images (see §2.2.3), since this was the average number of sources detected in an individual observation. Each source was assigned a random position on the sky and a random number of total counts between

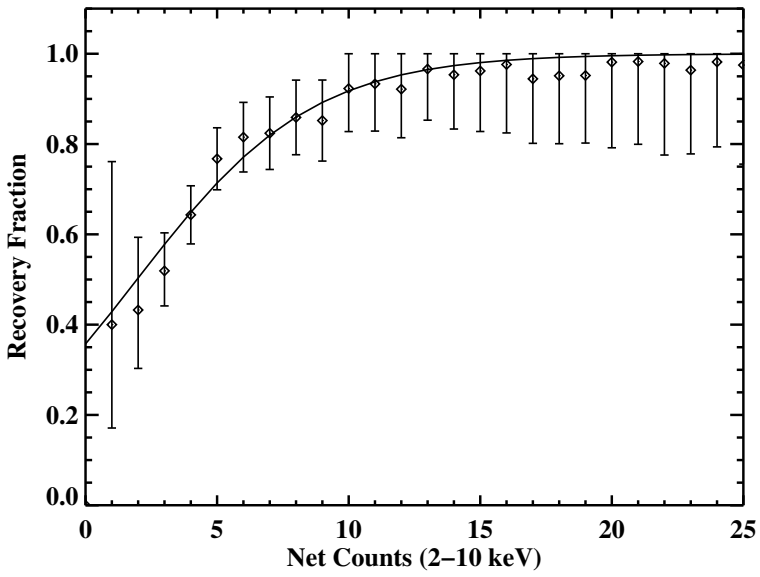

Figure 2.15: Fraction of simulated sources that are detected at $\geq 3\sigma$ in the 2-10 keV band and are also detected by our detection procedure as a function of net 2-10 keV counts. The solid line shows our best-fit model for this recovery fraction, which we use in §2.2.10 to correct for incompleteness in our number-count computation.

3 and 50, taken from a power-law count distribution with an index of -1.6 (a compromise between approximating the count distribution we measure and having a statistically significant sample of sources within each count bin). The total counts were then randomly divided between the soft and hard band. We approximated the PSF at the location of each source as an azimuthally-symmetric Rayleigh distribution in the radial direction, the normalization parameters of which were determined from the size of the PSF for 4.5 keV photons (for the full and high energy band mock images) or 1.5 keV (for the low energy band mock images) and a range of ECFs. The counts for each source were then distributed according to this approximation of the local PSF.

We determined the photometric properties of the 60 sources in each set of mock observations as described in §2.2.4. We also produced a sourcelist including photometric properties for each set of mock observations using our standard pipeline beginning with the second round of `wavdetect` using the background and exposure maps for ObsID 12519. Then we calculated, as a function of the input source counts in a particular energy band, what fraction of input sources that satisfy our 3σ threshold in that energy band were detected by `wavdetect`. This recovery fraction is shown in Figure 2.15 for the 2–10 keV band, and it is well-fit by the analytic form $F_{\rm rec}(C) = 1/(1+\exp[-\delta\{C-\xi\}])$, where C are the input source counts in a given band, and δ and ξ are fitting constants that vary with energy band. For the 2–10 keV band, $\delta = 0.30\pm0.07$ and $\xi = 1.96\pm0.79$.

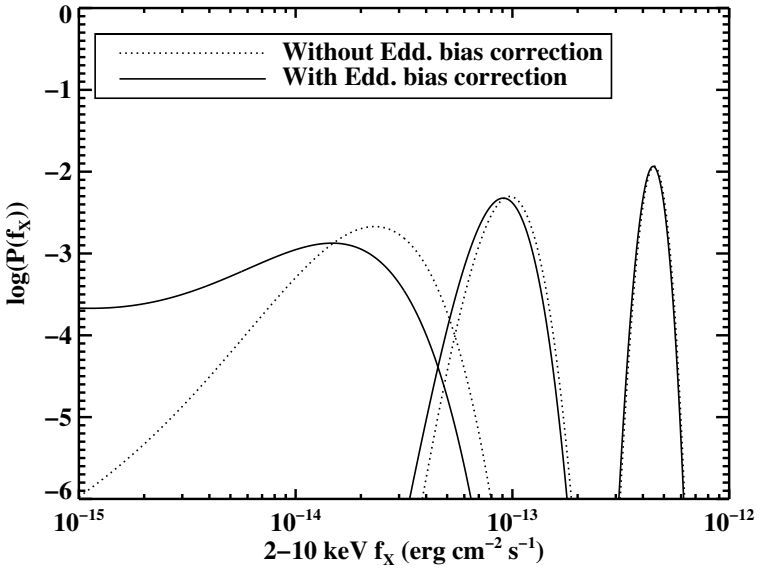

Figure 2.16: Example flux probability density distributions, before and after implementing the Eddington bias correction based on the best-fit power-law index β reported in Table 2.11. From left to right, these sources are detected at confidence levels of 3.2σ, 8.5σ, and 29.8σ, respectively, in the 2–10 keV band.

Flux Probability Distributions

In addition to correcting for incompleteness in our catalog, we take into account the fact that the observed counts in a given source aperture can be attributed to a source with a range of possible fluxes, rather than assigning a single flux value to each source. For $C_{\rm src}$ total counts in the source aperture and $C_{\rm bkg}$ counts in the background aperture, the probability distribution of source counts, $C_{\rm net}$ within the source aperture is given by (derived from Weisskopf et al. (2007) with $\psi_T \to 1$ and $\psi_R \to 0$)

$$P(C_{\rm net}|C_{\rm src},C_{\rm bkg}) = \frac{1}{Z}\sum_{i=0}^{C_{\rm src}} \frac{(C_{\rm src}+C_{\rm bkg}-i)!}{C_{\rm bkg}!(C_{\rm src}-i)!}\omega_B^{C_{\rm bkg}}\omega_S^{C_{\rm src}-i}\frac{C_{\rm net}^i e^{-C_{\rm net}}}{i!} \tag{2.12}$$

where the partition function, Z, is

$$Z = \sum_{i=0}^{C_{\rm src}} \frac{(C_{\rm bkg}+i)!}{C_{\rm bkg}!i!}\omega_B^{C_{\rm bkg}}\omega_S^i \tag{2.13}$$

and ω_B or ω_S is the probability that a background event occurs in the background or source aperture, respectively:

$$\omega_B = \frac{A_{\rm bkg}E_{\rm bkg}}{A_{\rm bkg}E_{\rm bkg}+A_{\rm src}E_{\rm src}}, \qquad \omega_S = \frac{A_{\rm src}E_{\rm src}}{A_{\rm bkg}E_{\rm bkg}+A_{\rm src}E_{\rm src}}. \tag{2.14}$$

$P(C_{\rm net})$ is normalized and converted into $P(f_X)$, using the relationship included in Equation 2.10. Finally, assuming that the differential counts of sources within each quantile group obey a power law of the form $dN/df_X \propto f_X^{\beta}$, we corrected for the Eddington bias by multiplying each source flux distribution, $P(f_X)$, by f_X^{β}. Examples of the resulting flux distributions are shown in Figure 2.16.

Cumulative Number-Flux Computation

The number count distribution is equal to the sum of the flux probability distributions of individual sources, divided by the sensitivity curve calculated in §2.2.10 and the recovery fraction function determined in §2.2.10:

$$N(>f_X) = \int_{f_X}^{\infty} \left[\sum_{i=1}^{N_{\rm src}} \frac{P_i(f_X)}{A(f_X,\epsilon_i)F_{{\rm rec},i}} \right] df_X \tag{2.15}$$

However, the number count distribution depends on the power-law index β through $P(f_X)$. We estimate β using a maximum likelihood (ML) method with power-law differential number-flux Bayesian priors. The probability of source i being present in our catalog is

$$p_i = \frac{\int P_i(f_X) df_X}{\int dN/df_X|_{\epsilon_i} A(f_X,\epsilon_i) F_{{\rm rec},i} df_X} \tag{2.16}$$

Therefore, the total likelihood of obtaining the sources in our catalog is $\prod_i p_i$. We find the best-fit power-law index for each quantile group by maximizing the total likelihood for each quantile group model separately. The normalization, K, of each group model was found by computing the differential number counts in 20 flux bins,

$$\frac{dN}{df_X} = \left(\int_{f_{X,\rm min}}^{f_{X,\rm max}} \left[\sum_{i=1}^{N_{\rm src}} \frac{P_i(f_X)}{A(f_X,\epsilon_i)F_{{\rm rec},i}} \right] df_X \right) / \left(f_{X,\rm max} - f_{X,\rm min}\right) \tag{2.17}$$

calculating 20 corresponding normalizations, and then weight-averaging these normalization values. We calculate the statistical errors of the number counts using the bootstrap method; we resample our list of catalog sources, determine new best-fit β and K parameters, and recompute the number count distribution.

2.2.11 The Number-Flux (log$N$-log$S$) Distribution

Figure 2.17 compares the number-flux distribution calculated using the methodology described in §2.2.10 with the "simple" distribution constructed using a single flux value for each detected source and without corrections for the Eddington bias, sensitivity curve, or recovery fraction. As can be seen in the figure, we can compute the number-flux distribution down to a flux limit roughly an order-of-magnitude below the nominal flux limit of the survey, the point at which the "simple" distribution turns over ($f_X \approx 2 \times 10^{-14}$ erg cm^{-2} s^{-1}) The

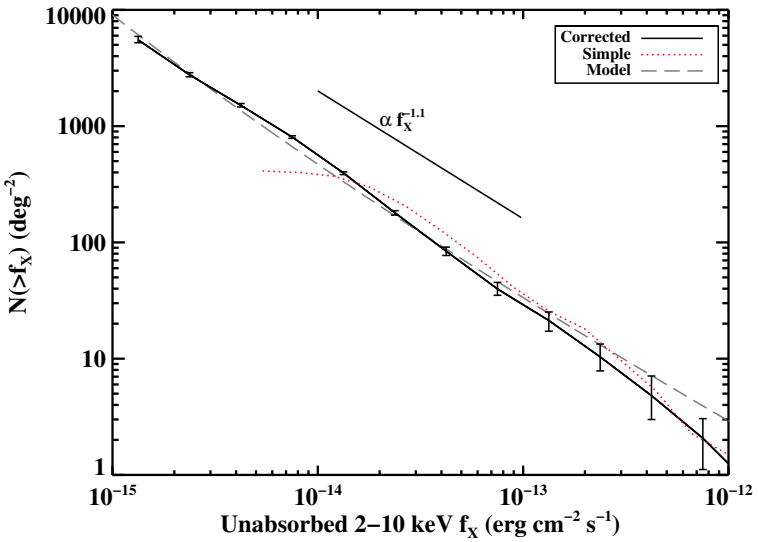

Figure 2.17: Cumulative number-flux distribution for all sources detected at $\geq 3\sigma$ in the 2-10 keV band. The red dotted line is calculated by assigning a single flux value to each detected source and not correcting for any systematic errors. The bars represent 1σ uncertainties. The gray dashed line represents the sum of the maximum-likelihood models for each quantile group computed as described in §2.2.10. The black solid line is the result of using a flux probability distribution for each source and correcting for the Eddington bias, the variations in sensitivity across the surveyed area, and the incompleteness of our detection procedure. A line with a power-law index equal to -1.1 is shown as a visual aid.

power-law parameters describing the differential count distribution for each quantile group in the 2-10 keV band that are found to have maximum likelihood are provided in Table 2.11, and the differential and cumulative count distributions are shown in Figure 2.18. The combined cumulative distribution for all groups has a power-law index of roughly -1.1. This index is similar to those found for the cumulative distributions of sources in other surveys, which vary from -1.0 to -1.5 (Muno et al. 2009; Hong et al. 2009; Ebisawa et al. 2005). The group D sources dominate in the 2-10 keV band down to a flux limit of $\approx 5 \times 10^{-14}$ erg cm^{-2} s^{-1}, below which group C and E sources dominate. We modified the quantile groups divisions by $\sim$0.1 dex and re-calculated the number-flux distributions; the power-law indices of the differential count distributions of the modified quantile groups vary by $< 2\sigma$, and the log$N$-log$S$ distributions also remain consistent at the 2σ level or better.

Groups B, C, and E have differential count distributions with power-law indices that are consistent with each other at $\lesssim 1\sigma$ confidence, with $\beta \approx -2.4$. The similarity between the group B and C slopes was expected since the majority of hard sources in these groups are likely to be a mixture of different types of CVs. However, it is somewhat surprising that the group E slope is so similar to those of groups B and C since we expect group E to contain a significant fraction of high-mass stars and AGN in addition to white dwarf binary systems. Perhaps group E does not contain quite as many high-mass stellar X-ray sources as

Table 2.11: Maximum Likelihood Parameters for dN/df_X Distributions in 2-10 keV Band

Quantile Group (1)	β (2)	K_{norm} (10^{14} deg^{-2} (erg cm^{-2} s^{-1})$^{-1}$) (3)
A	-3.1±0.3	20^{+4}_{-8}
B	-2.5±0.1	52^{+8}_{-11}
C	$-2.37^{+0.05}_{-0.08}$	150^{+10}_{-20}
D	-1.97±0.05	200^{+10}_{-30}
E	-2.31±0.05	140^{+20}_{-50}

Notes: All quoted errors are 1σ statistical.
(1) Quantile groups defined in §2.2.7.
(2) Power-law index of dN/df_X distribution.
(3) Normalization of dN/df_X distribution.

we expect based on the spectral properties of this group, or perhaps the flux distribution of X-ray sources associated with high-mass stars is similar to that CVs.

The group A power-law index is significantly steeper than $\beta \approx -2.4$, which may be because this group is made up of very different X-ray populations, such as low-mass X-ray active stars, coronally active binaries, and high-mass stars. However, this very steep power-law index may be a result of poor statistics, since only a small number of group A sources detected in the 2-10 keV band. In addition, since only about 5 group A sources have fluxes higher than fluxes at which the sensitivity curve and recovery fraction corrections become important, its differential count distribution parameters will be more severely impacted than any other group by any systematic imperfections in these corrections. However, even if the maximum likelihood results for this group are not reliable, the results for all other groups are independent and since group A only contributes $\lesssim$10% of sources at all fluxes, it also has little impact on the combined group distribution.

The other power-law index that significantly differs from those of groups B, C, and E is that of group D, which is significantly flatter. It is not too surprising that the group D slope is different since this group appears to be dominated by a single class of CVs, intermediate polars, rather than a mixture of magnetic and nonmagnetic CVs. As can be seen in Figure 2.18, only the group D differential-count distribution deviates at $> 3\sigma$ confidence from a simple power-law model at fluxes $< 10^{-13}$ erg cm^{-2} s^{-1}; while other group distributions deviate significantly from a simple power-law model above this flux, there are simply not enough bright sources in each group to constitute a statistically significant sample. The group D distribution deviates from the simple power-law model at fluxes $\lesssim 10^{-14}$ erg cm^{-2} s^{-1} by as much as 8σ at the faintest fluxes. The turnover in the group D distribution remains significant even when we modify the quantile divisions by ∼0.1 dex. Although our sensitivity curve, recovery fraction, and Eddington bias corrections may still not perfectly correct for all these systematic errors, it is unlikely that this group D deviation is simply due to a systematic error since it is the only group displaying this turnover at faint fluxes.

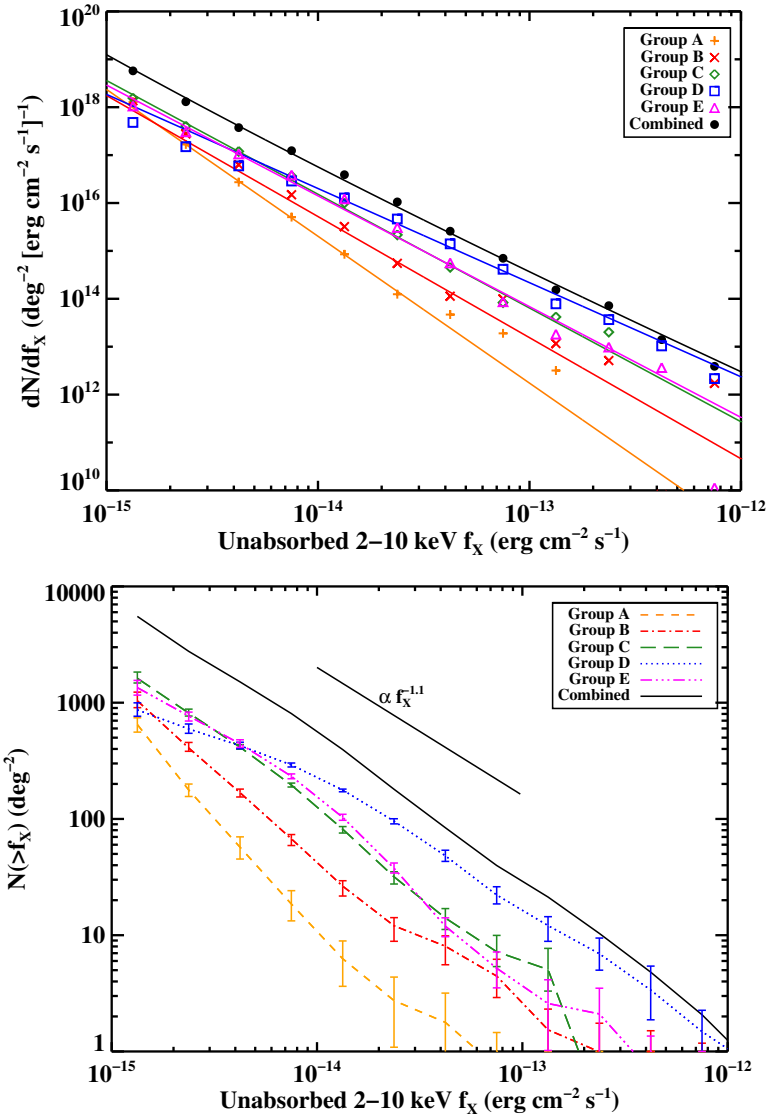

Figure 2.18: Upper panel shows the differential number counts versus 2-10 keV flux calculated as described in §2.2.10. The solid lines represent the maximum-likelihood simple power-law models while the points represent the corrected data with 1σ errors. Lower panel shows the cumulative number counts versus 2-10 keV flux. Lines represent the corrected data with 1σ errors. Both dN/dS and log$N$-log$S$ are shown for the five quantile groups and for all groups combined.

Thus, the turnover at faint fluxes in the group D number-count distribution is likely indicative of a real break in the power-law distribution. Such a break could result if the sources in group D have a break in their luminosity function, a minimum luminosity, or a high enough luminosity to be seen through the entire galaxy. As discussed in §2.2.9, 30-50% of group D sources without IR counterparts may be AGN, which have a number-count distribution that is shallower at fluxes $< 10^{-14}$ erg cm^{-2} s^{-1} (Cappelluti et al. 2009), and therefore, the break in the AGN distribution could at least partly explain the break in the group D distribution. However, if the turnover in the group D distribution is primarily due to AGN, it is surprising that a significant turnover is not also seen in the group E distribution, since there is stronger evidence for AGN being present in group E than group D. Since group D appears to be dominated by IPs, this break in the number-count distribution could be an indication of a break in the luminosity function of IPs, although we emphasize that this is a possibility but it cannot be confirmed with this data alone. A break in the IP luminosity function could be due to the propeller effect, a centrifugal barrier to accretion at low mass accretion rates that results when the magnetosphere of a compact object has a higher angular velocity than the accretion flow at the Alfven radius (Illarionov & Sunyaev 1975). The propeller effect has been invoked to explain the turnover of the HMXB luminosity function at the faint end (Shtykovskiy & Gilfanov 2005), the variability of supergiant fast X-ray transients (SFXTs, Bozzo et al. 2008), and the state transitions in some LMXBs (Zhang et al. 1998). Although this effect has primarily been used to explain the behavior of low-luminosity accreting neutron stars, similar physical mechanisms may be important in accreting white dwarf systems, even in CVs with weak magnetic fields (Matthews et al. 2006). We only present this interpretation of the break in the group D number-count distribution as a speculative hypothesis; a theoretical study of the propeller effect in IPs is beyond the scope of this paper, and multiwavelength follow-up of group D sources that will help to confirm whether they indeed are primarily IPs is ongoing.

2.2.12 Comparison to Expectations Based on Previous Surveys

Having calculated the number-count distribution of the NARCS X-ray sources, we want to compare it to the expected distribution based on other Galactic surveys since any significant discrepancies would indicate that the X-ray populations in this region might be unusual in some way. Thus, we estimated the expected contributions of ABs, CVs, LMXBs, HMXBs, and AGN to the observed number-count distribution.

In the hard X-ray band, CVs are the most numerous Galactic X-ray sources and they are thought to be the main contributors to the observed Galactic Ridge X-Ray Emission, the large-scale background emission of the Galaxy. CVs are low-luminosity sources ($L_X \lesssim 10^{33}$ erg s^{-1}) and trace the old stellar population of the Milky Way. Another significant population of low-luminosity sources that follow the stellar mass distribution are ABs. Thus, to calculate the expected flux distribution of ABs and CVs in NARCS, both their luminosity functions and a model of the Galactic stellar mass distribution are required. Sazonov et al. (2006) measured the combined luminosity function of ABs and CVs in the local vicinity of the Sun

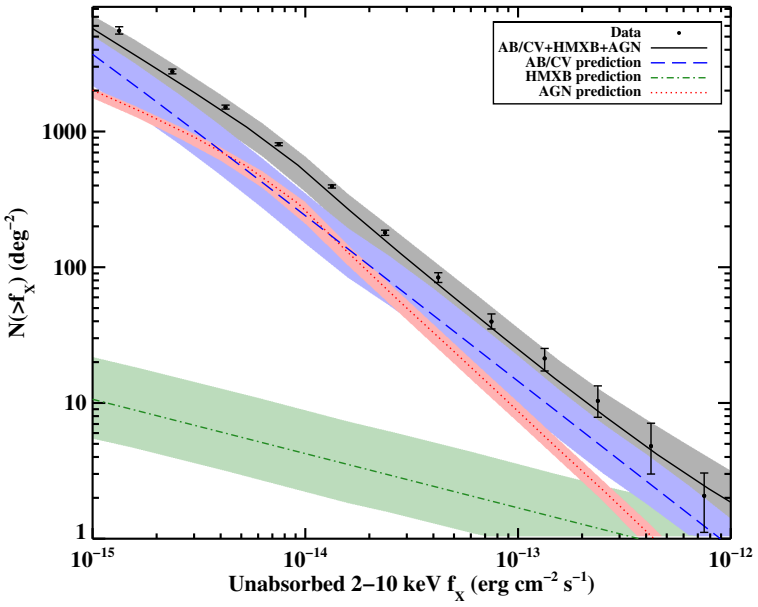

Figure 2.19: The observed number-flux distribution compared to the combined estimates of the expected AB/CV, HMXB, and AGN flux distributions based on the luminosity functions of these populations from other surveys. Estimated uncertainties for the predictions are shown as shaded regions. The AB/CV line shown is the average distribution of the ones we calculated by varying the parameters of the Galatic stellar mass model.

over the luminosity range $L_X = 10^{27} - 10^{34}$ erg s^{-1}. Since the local AB/CV cumulative emissivity per unit stellar mass was found to be consistent with that measured elsewhere in the Galaxy (Revnivtsev et al. 2006b; Revnivtsev & Sazonov 2007; Krivonos et al. 2007; Revnivtsev et al. 2008), we used the AB/CV luminosity function per unit stellar mass from Sazonov et al. (2006) to estimate the AB/CV flux distribution in NARCS. We utilize a stellar mass model similar to that used by Sazonov et al. (2006), which is an exponential disk with a central hole:

$$\rho \propto \exp\left[-\left(\frac{R_{\rm m}}{R}\right)^3 - \frac{R}{R_{\rm scale}} - \frac{z}{z_{\rm scale}}\right] \tag{2.18}$$

where R is the radial distance from the Galactic center, z is the height above the plane, $R_{\rm m}$ is the radius of the hole in the Galactic disk, $R_{\rm scale}$ is the disk scale length, and $z_{\rm scale}$ is the scale height of CVs. We assume $R_{\rm m} = 3$ kpc (Binney et al. 1997; Freudenreich 1998), but adopt a range of values for parameters that are not well constrained: 2.5-3.5 kpc for $R_{\rm scale}$ (Binney et al. 1997; Freudenreich 1998; Hammersley et al. 1999) and 80-220 pc for $z_{\rm scale}$ (Revnivtsev et al. 2008). For our stellar mass model we futher adopt a disk-to-bulge mass ratio of 2:1 and a range of values for the Galactic bulge mass of $1.3 \pm 0.5 \times 10^{10} M_\odot$ (Dwek et al. 1995). Using this model, the projected stellar mass contained in NARCS is roughly $1.4 \times 10^8 M_\odot$.

To compute the number of ABs/CVs expected above a given flux, $f_{\rm lim}$, in our survey,

we first consider a small volume element dV within the surveyed volume, and integrate the luminosity function per stellar mass from $L_{\rm lim} = f_{\rm lim} \times 4\pi d^2$, where d is the distance to dV, to $L_{\rm max}$. Multiplying by the stellar mass contained in dV as determined from our stellar mass model distribution then gives the number of ABs/CVs with $f_X > f_{\rm lim}$ in dV. Integrating the number per volume over all distances d and all lines of sight through our survey, and then simply repeating this procedure for the range $10^{-15} < f_{\rm lim} < 10^{-11}$, we obtain the expected log$N$-log$S$ for ABs/CVs. We repeat this calculation many times, choosing values randomly for each of the uncertain stellar mass model parameters.

Table 2.12: Normalizations and Indices of log(N)-log(S) Distributions

Population (1)	Normalization (2)	Power-law Index (3)
Observed	630	$-1.14, f_X < 10^{-14}$ erg cm^{-2} s^{-1} $-1.24, f_X > 10^{-14}$ erg cm^{-2} s^{-1}
AB/CV predicted	250±100	-1.21
HMXB predicted	4^{+4}_{-2}	-0.40
AGN predicted	260^{+40}_{-50}	$-0.90, f_X < 10^{-14}$ erg cm^{-2} s^{-1} $-1.46, f_X > 10^{-14}$ erg cm^{-2} s^{-1}

Notes:
(1) Population of sources, observed or predicted.
(2) Number of sources with $f_X > 10^{-14}$ erg cm^{-2} s^{-1}.
(3) Power-law index of distribution.

LMXBs are more luminous and far rarer than CVs, but they too scale with the old stellar mass. Thus, to estimate the number of LXMBs expected in NARCS, we take the LMXB luminosity function from Sazonov et al. (2006) and apply the same method as for ABs/CVs, except that we use a scale height of $z_{scale} = 410$ pc (Grimm et al. 2002). We find that $\lesssim 1$ LMXB is expected in our survey region.

Unlike CVs and LMXBs, the number of HMXBs is not correlated with the old stellar mass, and thus our estimate of the HMXBs in NARCS is independent of the Galactic stellar mass model. Our predictions for the HMXB contribution to the number-count distribution is based on the luminosity function from Lutovinov et al. (2013), which is derived from the number of Galactic HMXBs observed by *International Gamma-Ray Astrophysics Laboratory* (*INTEGRAL*, Winkler et al. (2003)). Since the *INTEGRAL* luminosity function was calculated in the 17-60 keV band, we converted it to the 2-10 keV band by assuming a typical spectral model for accreting pulsars that includes a power-law with a high-energy cutoff (White et al. 1983):

$$f(E) \propto E^{-\Gamma} \times \begin{cases} 1, & (E \leq E_{\rm cut}) \\ e^{-(E-E_{\rm cut})/E_{\rm fold}}, & (E > E_{\rm cut}) \end{cases} \quad (2.19)$$

Using $\Gamma = 1$, $E_{\rm cut} = 20$ keV, $E_{\rm fold} = 10$ keV, and intrinsic $N_{\rm H} = 5{\times}10^{22}$ cm^{-2} (Filippova et al. 2005), the conversion factor $f_{2-10{\rm keV}}/f_{17-60{\rm keV}} \simeq 0.5$. Since out HMXB prediction is

based on a survey of the HMXB population throughout the whole Galaxy, it does not take into account that, as discussed in §2.2.1, the Norma region appears to have an enhanced number of HMXBs due to its star formation activity. Therefore, we may be underestimating the number of HMXBs in this region, but probably by no more than a factor of two based on the comparison of predictions and observations presented in Lutovinov et al. (2013) for the brightest HMXBs in the whole Norma arm.

One population of sources whose contribution is difficult to predict are isolated high-mass stars and colliding wind binaries (CWBs) because they are not evenly distributed throughout the Galaxy and their X-ray luminosity functions have yet to be determined. However, we do expect high-mass stellar X-ray sources to be present in our survey due to the presence of massive-star forming complexes and HII regions along this line-of-sight, and we have already identified a small number of these sources. As discussed in §2.2.9, three group A sources with known massive counterparts are likely isolated high-mass stars. In addition, Rahoui et al. (2014) find that five of 20 NARCS counterparts for which they obtained infrared spectra are high-mass stars; their X-ray properties favor the interpretation that three of these sources (#239, 1168, and 1326) are quiescent HMXBs and two (#1278 and 1279) are CWBs. Ongoing spectroscopic follow-up of IR counterparts and improved constraints on the X-ray properties of NARCS sources with *NuSTAR* observations will help to determine their total number and their flux distribution. Given the rarity of high-mass stars even in regions of recent star formation like the Norma arm, we do not expect these sources to constitute a large fraction of the NARCS population; however, identifying even a small sample ($\sim$10) of such sources would be a significant contribution to the number of known high-mass X-ray sources (e.g. Mauerhan et al. 2010; Gagné et al. 2011) and our understanding of their X-ray properties.

Figure 2.19 shows our estimates for the expected flux distributions of ABs/CVs and HMXBs in our survey region (there are too few expected LMXBs to be shown), while Table 2.12 provides their power-law indices and normalizations. The observed AGN distribution from the COSMOS survey (Cappelluti et al. 2009) is also included, attenuated by the average column density from the outer Norma arm to the outer edge of the Galaxy ($N_{\rm H} \approx 3 \times 10^{22}$ cm^{-2}). Uncertainties in the predicted AGN distribution are determined by considering $N_{\rm H}$ values from zero to 8×10^{22} cm^{-2}, the maximum measured along any line-of-sight in our surveyed area.

As can be seen, the sum of the predicted distributions of ABs/CVs, AGN, and HMXBs matches the calculated flux distribution of hard sources in NARCS. The fact that the slope of the expected distribution matches the observed one so well, including some of the kinks in the slope, suggests that ABs, CVs, and AGN are the dominant populations in our survey and that their relative numbers are similar to the proportions predicted from other observations.

2.2.13 Conclusions

We constructed a catalog of 1130 $\geq 3\sigma$ point-like sources and five extended sources detected in a *Chandra* survey of a $2^\circ \times 8^\circ$ region in the direction of the Norma spiral arm. These sources span the luminosity range $L_X = 10^{27} - 10^{35}$ erg s^{-1}. The systematic positional

errors were reduced by matching X-ray sources to infrared VVV counterparts, so that the median positional error for sources in our catalog is 1.″26 (95% statistical plus systematic uncertainty). The median number of counts for sources in our survey is 11, making most of them too faint to enable accurate determination of their spectral properties. Therefore, to help classify the sources, we split them into five spectral groups based on their quantile properties. The stacked spectra, photometric variability, and IR counterparts of the sources within each spectral group allowed us to identify the classes of X-ray sources that populate the foreground, the Scutum-Crux and near Norma arm, and the far Norma arm. Foreground sources, which make up roughly 50% of catalogued sources, are a heterogeneous group, probably containing X-ray active low-mass stars, interacting binaries, symbiotic binaries, and CVs. The X-ray populations of the Scutum-Crux and near Norma arms are most likely dominated by a mixture of magnetic and nonmagnetic CVs. The far Norma arm hard X-ray population is likely dominated by IPs, while the softer X-ray population probably includes high-mass stars (both isolated and in colliding wind binaries) and symbiotic binaries.

We also calculated the number-flux distribution for sources in our survey down to a flux limit of 10^{-15} erg cm^{-2} s^{-1}, correcting for the Eddington bias, the variations in sensitivity across the surveyed area, and the incompleteness of our detection procedure. The observed distribution matches predictions based on AB, CV, AGN, and HMXB luminosity functions very well, lending further support to our conclusions that CVs are the dominant population in NARCS. Furthermore, the fact that the observed number-flux distribution shows the same changes in slope as the predicted distribution, suggests that roughly a third of the NARCS sources detected in the hard energy band probably are AGN as predicted; we see some evidence for the presence of AGN in the stacked spectrum of group C, D, and E sources lacking NIR counterparts. However, it is unclear whether AGN can fully account for the flattening at faint fluxes that is seen in the number-flux distribution of group D sources; additional X-ray observations to better constrain the spectrum and variability of NARCS sources can help to disentangle the relative fractions of AGN and IPs in this group and determine which population is responsible for the break in the $\log N$-$\log S$ distribution.

Our analysis of NARCS sources was primarily statistical in nature, but multiwavelength data has permitted the classification and deepened understanding of individual sources. Our follow-up campaigns were focused on but not limited to group D X-ray sources, since any HMXBs in this survey are most likely to belong to this group. Near-IR spectroscopic follow-up of counterparts to 42 X-ray sources has been completed (Rahoui et al. 2014; Corral-Santana et al, in prep) and helped us to determine which of these X-ray sources have high-mass versus low-mass counterparts. By constraining the hard X-ray emission and variability of NARCS sources, the *NuSTAR* survey of the Norma region has also provided important clues to identify the physical nature of 28 of the brightest NARCS sources. In §2.3-§2.4, we describe how the combination of this multiwavelength data enables us to distinguish different populations of X-ray sources and to identify the most likely HMXB candidates.

2.3 The *NuSTAR* Norma Arm Region Survey

2.3.1 Introduction

Hard X-ray observations of the Galaxy can be used to identify compact stellar remnants – white dwarfs, neutron stars, and black holes – and probe stellar evolution in different environments. While a number of sensitive surveys of Galactic regions (e.g. Muno et al. 2009; Townsley et al. 2011; Fornasini et al. 2014) have been performed by the *Chandra X-ray Observatory*, its soft X-ray band (0.5–10 keV) is often insufficient for differentiating between different types of compact objects. The *Nuclear Spectroscopic Telescope Array* (*NuSTAR*; Harrison et al. 2013), with its unprecedented sensitivity and angular resolution at hard X-ray energies above 10 keV, provides a unique opportunity to study the X-ray populations in the Galaxy. During the first two years of its science mission, *NuSTAR* performed surveys of the Galactic Center and the Norma spiral arm in order to compare the X-ray populations in these regions of the Galaxy, which differ with regard to their star formation history and stellar density. The *NuSTAR* sources found among the old, high-density Galactic Center stellar population are described in Hong et al. (2016), and, in this chapter, we present the results from the *NuSTAR* Norma Arm survey.

As discussed in §2.2, in 2011, the Norma Arm Region *Chandra* Survey (NARCS) observed a $2^\circ \times 0.^\circ 8$ region in the direction of the Norma spiral arm (Fornasini et al. 2014, hereafter F14). The Norma region was targeted because its stellar populations are younger than those in the Galactic Center but older than those in the young Carina and Orion star-forming regions observed by *Chandra* (F14 and references therein). An additional goal of this survey was to identify low-luminosity high-mass X-ray binaries (HMXBs) falling below the sensitivity limits of previous surveys in order to constrain the faint end of the HMXB luminosity function; the evolutionary state of the Norma arm and the large number of OB associations along this line-of-sight (Bodaghee et al. 2012c) make it an ideal place to search for HMXBs.

About 300 of the 1130 *Chandra* sources detected at $\geq 3\sigma$ confidence in the Norma region were found to be spectrally hard in the 0.5–10 keV band, with median energies >3 keV. The majority of these sources are expected to be magnetic cataclysmic variables (CVs) and active galactic nuclei (AGN), although some could also be HMXBs, low-mass X-ray binaries (LMXBs), or colliding wind binaries (CWBs). Distinguishing between these types of sources is not possible based on *Chandra* data alone, especially since most of the Norma X-ray sources have low photon statistics.

Since *Chandra*'s resolution enables the identification of unique optical/infrared counterparts, spectral identification of the counterparts has helped shed light on the physical nature of some of the Norma X-ray sources (Rahoui et al. 2014). However, not even this information is necessarily sufficient; for example, HMXBs and CWBs both have massive stellar counterparts in the optical/infrared and it can be difficult to differentiate them spectrally in the *Chandra* band with < 100 photon counts, as is the case for most NARCS sources. *NuSTAR* observations, due to their superior sensitivity above 10 keV and in the energy range of the iron Kα and Kβ lines, provide critical information to differentiate hard X-ray

sources. For example, CWBs can be distinguished from HMXBs because they have thermal spectra that fall off steeply above 10 keV and strong 6.7 keV Fe emission (Mikles et al. 2006 and references therein), and magnetic CVs can be distinguished from non-magnetic CVs by their harder spectra, lower equivalent widths of the 6.7 keV line, and higher line ratios of 7.0/6.7 keV Fe emission (e.g. Xu et al. 2016).

The first set of observations of the *NuSTAR* Norma Arm survey were carried out in February 2013 and improved the identification of three NARCS sources (Bodaghee et al. 2014, hereafter B14), discovered one transient (Tomsick et al. 2014a, hereafter T14), and permitted the study of the disk wind of the LMXB 4U 1630-472 (King et al. 2014). In this section, we present a catalog of all point sources detected in the *NuSTAR* Norma Arm survey. The *NuSTAR* observations and basic data processing are described in § 2.3.2. Descriptions of our analysis, including our source detection technique, aperture photometry, and spectral analysis are found in § 2.3.4–2.3.10. In § 2.3.11-2.3.14, we discuss the physical nature of *NuSTAR* sources, present their number-flux distribution, and compare the Norma X-ray populations to those seen in the Galactic Center region.

2.3.2 Observations

NuSTAR

NuSTAR observations of the Norma arm region began in February 2013, and were completed in June 2015. During this period, *NuSTAR* performed 61 observations in the Norma region, shown in Figure 2.20; every pointing consists of data from two co-aligned focal plane modules (FPM), A and B, each of which has a field-of-view (FOV) of $13' \times 13'$.

The *NuSTAR* observations were planned to minimize contamination from stray light and ghost rays. Stray light is the result of zero-bounce photons reaching the detector from bright sources within a few degrees of the FOV, while ghost rays are single-bounce photons from bright sources within about 1° of the FOV. The pattern of stray light contamination is well-understood and can be carefully predicted[13], while the patterns of ghost rays are more challenging to model (Koglin et al. 2011; Harrison et al. 2013; Wik et al. 2014; Mori et al. 2015; Madsen et al. 2015).

Therefore, rather than observing the whole region surveyed by *Chandra*, we performed simulations of stray light contamination and focused our observations on three areas of the sky that would be least affected by stray light. Even in these "cleaner" areas, at least one of the focal plane modules was often affected by stray light, so exposure times for more contaminated observations were lengthened to compensate for the fact that we would not be able to combine data from both modules. Seven additional pointings were specifically made at the locations of some of the brightest NARCS sources found to be hard in the *Chandra* band and for which optical or infrared spectra have been obtained (Rahoui et al. 2014, Corral-Santana et al., in prep). Unfortunately, despite this adopted strategy, the first

[13]Stray light constraints for new observations can be checked with the stray light simulation tool at http://www.srl.caltech.edu/NuSTAR_Public/NuSTAROperationSite/CheckConstraint.php

mini-survey of the Norma region was highly contaminated by ghost rays because a black hole binary in the region, 4U 1630-472, serendipitously went into outburst while the *NuSTAR* observations were taking place (B14). Having learned about the spatial extent of ghost ray contamination, later observations in proximity of 4U 1630-472 were timed to occur only when it was in quiescence.

Finally, in addition to the observations dedicated to the Norma survey either as part of the baseline *NuSTAR* science program or the *NuSTAR* legacy program, a series of observations were made to regularly monitor the pulsar associated with HESS J1640-465 (Gotthelf et al. 2014, hereafter G14), a very luminous TeV source which resides within the Norma survey area. When combining all such observations taken prior to March 2015, they yield a total exposure of 1 Ms over a 100 arcmin^2 field, which we call the "deep HESS field". While the detailed analysis of the pulsar's braking index is discussed in Archibald et al. (2016), here we present the other *NuSTAR* sources detected in the deep HESS field.

Table 2.13 lists all the *NuSTAR* observations included in our analysis. Although the sources in the first mini-survey (King et al. 2014; B14; T14), HESS J1640-465 (G14), and IGR J16393-4643 (Bodaghee et al. 2016, hereafter B16) have been analyzed separately and in more detail by others, we include these sources in our analysis to measure the photometric properties of all sources in a consistent way, allowing us to calculate the number-flux (log$N$-log$S$) distribution of *NuSTAR* Norma Region (NNR) sources.

Chandra

In this study, we make extensive use of information from the Norma Arm Region *Chandra* Survey (NARCS) catalog as well as the soft (< 10 keV) X-ray spectra of some of the NARCS sources. The analysis of these *Chandra* observations and the details of the spectral extraction are provided in F14. We also use two other archival *Chandra* observations that cover part of the area surveyed by *NuSTAR*: ObsID 7591 provides an additional epoch for a transient source (NuSTAR J164116-4632.2, discussed in § 2.3.8), and ObsID 11008 provides spatially resolved observations of NARCS sources 1278 and 1279 (Rahoui et al. 2014), which are blended in the NARCS and *NuSTAR* Norma observations. For reference, we provide information about all these relevant archival *Chandra* observations in Table 2.14.

Furthermore, in this study we make use of *Chandra* observations which were triggered to follow-up four transient sources discovered by *NuSTAR*. These *Chandra* observations were used to constrain their soft X-ray spectra and better localize their positions so as to be able to search for optical and infrared counterparts. The follow-up observations of one of these transients, NuSTAR J163433-4738.7, are discussed in T14, and the others are presented in § 2.3.8 and listed in Table 2.15.

2.3.3 *NuSTAR* Data Processing and Mosaicking

The raw data of each observation was processed using CALDB v20150612 and the standard *NuSTAR* pipeline v1.3.1 provided under HEASOFT v6.15.1 to produce event files and

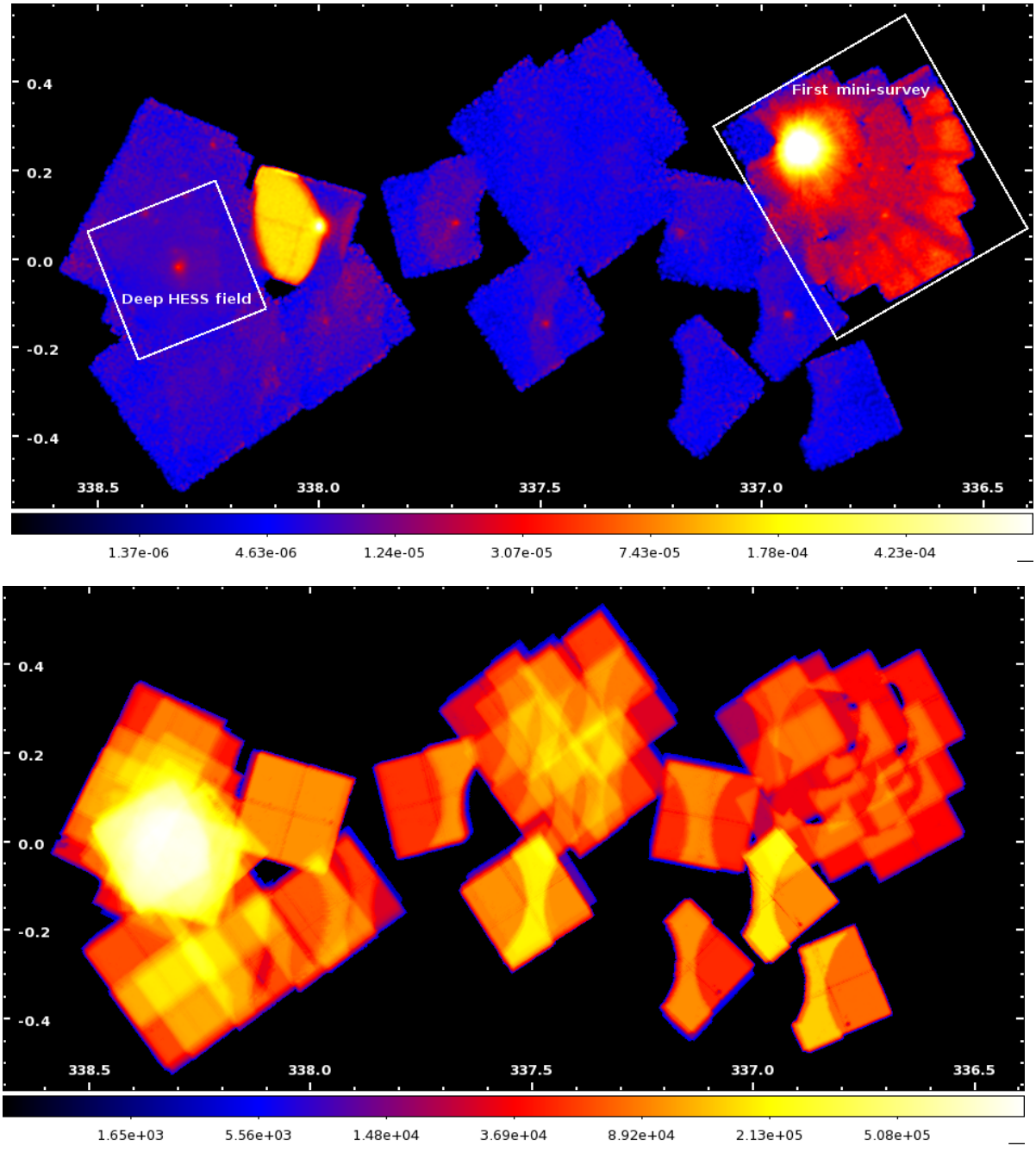

Figure 2.20: The top panel shows the smoothed 3–40 keV count rate mosaic (units of counts per second) and the bottom shows the 3–40 keV exposure map without vignetting correction (units of seconds). The mosaics have been cleaned of most contamination from ghost rays and stray light; some residual ghost ray contamination can be seen in the first mini survey (upper right of the mosaic) while one wedge of stray light around $(\ell, b) = (338°, 0.08°)$, which is due to GX 340+0, is not removed since a bright source, IGR J16393-4643, is embedded in it.

Table 2.13: *NuSTAR* Observations of the Norma Arm Region

ObsID	Pointing (J2000)			Start Time	Exposure	SL Removal	SL	Other
	R.A. (°)	Dec. (°)	PA (°)	(UT)	(ks)	(FPM)	Source	Contamination
(1)	(2)	(3)	(4)	(5)	(6)	(7)	(8)	(9)
Wide Shallow Survey								
First mini-survey								
40014001001	248.4829	-47.7204	160.1494	2013-02-24 01:46	18.4			Ghost rays from 4Ub in AB
40014002001	248.3623	-47.6444	160.1471	2013-02-24 11:31	19.5			Ghost rays from 4Ub in AB
40014003001	248.2407	-47.5669	160.1266	2013-02-21 20:31	20.8			Ghost rays from 4Ub in AB
40014004001	248.5977	-47.6374	160.1231	2013-02-22 07:46	19.5			Ghost rays from 4Ub in AB
40014005001	248.4775	-47.5622	160.1304	2013-02-22 17:31	21.3			Ghost rays from 4Ub in AB
40014006001	248.3529	-47.4868	160.1393	2013-02-23 04:46	18.9			Ghost rays from 4Ub in AB
40014007001	248.7099	-47.5554	160.1350	2013-02-23 14:31	22.7			Ghost rays from 4Ub in AB
40014008002	248.5845	-47.4826	160.1196	2013-02-20 23:32	16.6			Ghost rays from 4Ub in AB
40014009001	248.4670	-47.4038	160.1198	2013-02-21 10:46	14.7			Ghost rays from 4Ub in AB
Later observations								
40014011002	250.0712	-46.4909	280.7063	2013-06-20 00:06	21.5	AB	4Ua	
40014012001	250.0006	-46.4546	280.7266	2013-06-20 14:21	19.7	AB	4Ua	
40014013001	249.9200	-46.4004	281.4251	2013-06-21 03:16	20.5	A	4Ua	
40014014001	250.2358	-46.3989	285.7049	2013-06-21 17:46	16.4			1.5′ streak in AB
40014015001	250.0770	-46.3706	285.7091	2013-06-22 08:21	19.2			
40014016001	250.2620	-46.5441	285.6937	2013-06-23 21:21	19.6	AB	4Ua	
40014017001	250.1762	-46.5238	285.6774	2013-06-23 11:51	24.2	AB	4Ua	
40014018001	249.9326	-46.3469	286.8740	2013-06-24 00:51	23.8			
40014019001	250.1520	-46.3873	286.8743	2013-06-24 15:21	25.6			
40014021002	249.1106	-47.1553	168.0928	2014-03-09 21:56	29.1	AB	GX, 4Ua	
40014022001	249.0348	-46.9577	168.0985	2014-03-10 15:31	28.4	AB	GX, 4Ua	
40014023001	249.2029	-47.1072	168.1000	2014-03-11 07:41	28.8	AB	GX, 4Ua	
40014024001	248.8388	-46.9903	168.1169	2014-03-11 23:46	28.1	AB	GX, 4Ua	
40014025001	248.8796	-47.0734	168.1144	2014-03-12 17:36	29.1	AB	GX, 4Ua	
40014026001	249.1206	-46.9073	168.0941	2014-03-13 11:26	30.2	AB	GX, 4Ua	
40014027001	249.1610	-47.0090	168.1171	2014-03-14 03:31	30.2	AB	GX, 4Ua	

NuSTAR Observations (continued)

ObsID	Pointing (J2000)			Start Time	Exposure	SL Removal	SL	Other
	R.A. (°)	Dec. (°)	PA (°)	(UT)	(ks)	(FPM)	Source	Contamination
40014028002	249.0277	-47.1640	168.1544	2014-03-18 12:36	29.6	AB	GX, 4Ua	
40014029001	249.9367	-46.8984	168.2590	2014-03-19 04:41	29.2	AB	GX, 4Ua	
40014030001	250.2174	-46.7179	168.3050	2014-03-19 20:46	27.3	B	4Ua	
40014031001	250.5222	-46.7773	168.3521	2014-03-20 13:01	30.0	B	4Ua	
40014032001	250.4317	-46.7896	168.4181	2014-03-21 05:01	30.9	B	4Ua	
40014033002	250.4849	-46.6649	168.2038	2014-03-24 10:41	31.5	B	4Ua	
40014034001	250.2701	-46.8265	168.1849	2014-03-25 02:46	31.2	AB	GX, 4Ua	
40014035001	250.0454	-46.8714	168.1523	2014-03-25 18:56	39.2	AB	GX, 4Ua	
30001008002	249.8301	-46.6567	295.0558	2014-06-26 02:21	50.4			
30001012002	248.6712	-47.6364	171.9830	2013-03-23 08:31	16.3	A	GX	Ghost rays from 4Ub in AB
30001016002	248.5333	-47.3795	164.6452	2014-03-06 22:56	21.3	AB	GX, 4Ua	
30001017002	248.8967	-47.3836	210.3881	2014-05-12 21:31	49.0	AB	GX, 4Ua	
30001033002	249.4897	-46.9015	145.8254	2015-01-28 05:16	51.8	AB	GX, 4Ua	
30160001002	249.3137	-47.5723	267.7851	2015-06-11 14:46	49.4	AB	GX, 4Ua	
30160002002	248.9436	-47.5918	261.9558	2015-06-07 23:46	97.1	AB	GX, 4Ua	
30160003002	249.0412	-47.8404	244.4634	2015-05-31 11:11	76.7	AB	GX, 4Ua	
40001022002	249.5341	-47.2183	164.5577	2014-03-07 11:51	100.6	AB	GX, 4Ua	
Deep HESS Field								
30002021002	250.1049	-46.5763	353.7407	2013-09-29 6:56	62.8	AB	GX, 4Ua	SL of unknown origin in A
30002021003	250.1324	-46.5412	353.7551	2013-09-30 16:31	20.8	A	4Ua	SL of unknown origin in A
30002021005	250.2036	-46.5095	161.2653	2014-02-38 23:16	99.5	AB	4Ua	
30002021007	250.2027	-46.5145	161.2702	2014-03-06 01:51	35.9	AB	4Ua	
30002021009	250.2175	-46.5088	166.7254	2014-03-14 21:21	32.5	AB	4Ua	
30002021011	250.2296	-46.5012	179.7925	2014-04-11 13:11	22.5	AB	4Ua	
30002021013	250.1923	-46.5268	227.3736	2014-05-25 01:56	21.6			
30002021015	250.1802	-46.5601	289.9801	2014-06-23 12:51	29.2	A	4Ua	
30002021017	250.1814	-46.5644	295.1336	2014-06-25 13:31	22.0			
30002021019	250.1913	-46.5447	295.1661	2014-06-28 01:20	19.5			
30002021021	250.1762	-46.5687	295.1179	2014-06-30 01:41	19.8			

NuSTAR Observations (continued)

ObsID	Pointing (J2000)			Start Time	Exposure	SL Removal	SL	Other
	R.A. (°)	Dec. (°)	PA (°)	(UT)	(ks)	(FPM)	Source	Contamination
30002021023	250.1892	-46.5586	311.5738	2014-07-11 02:21	22.1			
30002021025	250.1569	-46.5398	330.9082	2014-08-10 05:36	21.9	A	IGR, 4Ua	6′ streak in B
30002021027	250.1477	-46.5524	344.3607	2014-09-11 10:56	20.0	AB	GX, 4Ua	
30002021029	250.1247	-46.5392	356.5397	2014-10-11 01:01	22.1	AB	4Ua	
30002021031	250.1400	-46.5260	15.7729	2014-11-05 07:56	4.3	AB	4Ua	
30002021033	250.2058	-46.4950	129.7677	2015-01-08 04:46	4.2			
30002021034	250.2115	-46.4858	129.7237	2015-01-12 18:16	16.7			
30002031036	250.2188	-46.5018	154.4146	2015-02-16 02:41	31.8	AB	4Ua, 4Ub	

Notes: (4) Position angle (east of North).
(7) Focal plane module(s) from which stray light background photons from sources in column 8 were removed.
(8) Stray light background sources: GX = GX 340+0, 4Ua = 4U 1624-49, 4Ub = 1630-472, IGR = IGR J16318-4848. Although additional stray light from IGR J16320-4751 was present in some of the first mini-survey observations, and stray light from 4U 1624-49 and GX 340+0 was present in observation 30001008002, this stray light background was not removed since real sources could be seen in the raw data residing in the stray light-contaminated regions. The contamination in observations 30002021002A, 30002021003A, 30002021036B, and 30001012002 was so extensive that these observations were not included in our analysis.

exposure maps for both focal plane modules. We made exposure maps with and without vignetting corrections to be used in different parts of our analysis.

Next, we cleaned the event files of stray light contamination by filtering out X-ray events in stray light affected regions. Table 2.1 indicates whether stray light removal occurred in either FPMA or FPMB as well as the source responsible for the stray light. In one exceptional case, we did not remove stray light seen in FPMA and FPMB of observation 30001008002, since a bright source, IGR J16393-4643, is located within the stray light regions caused by GX 340+0 and 4U 1624-49. We also excised the most significant ghost rays from observations from the first mini-survey, defining the ghost ray pattern regions in the same way as B14. One observation, 30001012002, was performed to follow-up NuSTAR J163433-4738.7, a transient source discovered in the first mini-survey; this observation helped to characterize the outburst duration of this transient (T14), but it was so extensively contaminated by ghost rays that it was not included in our analysis. Finally, a few observations show additional contamination features such as sharp streaks, listed in Table 2.1, which were also removed.

To improve the astrometric accuracy of the *NuSTAR* observations, we calculated the shifts between the positions of bright *NuSTAR* sources and their *Chandra* counterparts in NARCS observations which were astrometrically registered using infrared counterparts in the VISTA Variables in the Via Lactea (VVV; Minniti et al. 2010) survey (Fornasini et al. 2014). The positions of bright sources, which could be easily identified in raw images, were determined using the IDL `gcntrd` tool, which makes use of the DAOPHOT "FIND" centroid algorithm. This source localization was done independently for each FPM of each observation and was used to apply translational shifts to event files and exposure maps. In performing astrometric corrections, we limited ourselves to using sources with > 100 net counts in each individual observation and FPM and located on-axis. For on-axis sources with this number of counts, we expect the statistical error on the centroid to be $< 6''$ based on simulations (Brian Grefenstette, personal communication, May 7, 2014). NARCS 999 is very bright, with $> 10,000$ net counts, and therefore the statistical uncertainties of the astrometric corrections derived from this source are $< 2''$ at 90% confidence; the other sources used for astrometric corrections have $100 - 300$ net counts, and their associated statistical uncertainties are expected to be $5 - 6''$ at 90% confidence. Table 2.16 lists the applied boresight shifts and the bright sources used for astrometric correction. We were only able to apply these astrometric corrections to 23 out of 60 observations (43 out of 117 modules) due to the dearth of bright X-ray sources in our survey. Our inability to astrometrically correct all the observations does not significantly impact the results of our photometric and spectral analysis since the radii of the source regions we use are significantly larger than the expected shifts. The boresight shifts range from $1''$ to $14''$; 20% of the shifts are larger than $8''$, which is more than expected based on *NuSTAR*'s nominal accuracy of $\pm 8''$ at 90% confidence (Harrison et al. 2013), but is not unexpected given that the statistical errors on the source positions may be as high as $6''$. Checking each shifted and un-shifted image by eye and comparing the locations of *NuSTAR* sources with their *Chandra* counterparts in shifted and un-shifted mosaic images, we confirm that these boresight shifts constitute an improvement over the original *NuSTAR* positions.

We re-projected the event files of each observation onto a common tangent point and

Table 2.14: Archival *Chandra* observations used in this study

Chandra ObsID (1)	Pointing (J2000) R.A. (°) (2)	Dec. (°) (3)	Start Time (UT) (4)	Exposure (ks) (5)	References (6)
7591	250.187126	-46.520108	2007-05-11 11:01	28.8	Lemiere et al. 2009
11008	250.134287	-46.393394	2010-06-19 22:10	39.6	Rahoui et al. 2014
Norma Arm Region Chandra Survey (NARCS)					Fornasini et al. 2014
12507	250.373201	-46.662951	2011-06-06 10:15	18.8	
12508	250.155011	-46.530604	2011-06-06 15:57	18.5	
12509	249.937805	-46.397816	2011-06-06 21:22	19.4	
12510	250.180190	-46.812896	2011-06-09 12:29	19.9	
12511	249.961646	-46.681456	2011-06-17 11:15	19.3	
12512	249.743370	-46.550407	2011-06-27 04:52	20.5	
12513	249.984947	-46.965904	2011-06-27 11:00	20.2	
12514	249.767582	-46.829470	2011-06-10 16:07	19.8	
12515	249.550110	-46.695978	2011-06-10 22:04	19.5	
12516	249.790838	-47.111874	2011-06-11 03:46	19.5	
12517	249.572205	-46.978413	2011-06-11 09:28	19.5	
12518	249.354673	-46.844540	2011-06-11 15:10	19.5	
12519	249.594334	-47.262081	2011-06-13 04:25	19.3	
12520	249.375577	-47.128273	2011-06-13 10:13	19.0	
12521	249.157932	-46.994022	2011-06-13 15:46	19.0	
12522	249.396933	-47.410725	2011-06-13 21:20	19.0	
12523	249.178061	-47.276529	2011-06-14 02:53	19.0	
12524	248.960334	-47.141940	2011-06-14 08:27	19.5	
12525	249.198427	-47.559064	2011-06-14 14:08	19.5	
12526	248.979417	-47.424468	2011-06-14 19:50	19.0	
12527	248.761625	-47.289491	2011-06-15 19:36	19.3	
12528	248.998831	-47.707016	2011-06-16 01:24	19.0	
12529	248.779750	-47.572056	2011-06-16 06:58	19.0	
12530	248.561776	-47.436667	2011-06-16 12:31	19.3	
12531	248.798050	-47.854617	2011-06-16 18:09	19.5	
12532	248.578823	-47.719259	2011-06-16 23:51	19.5	
12533	248.360823	-47.583518	2011-06-17 05:32	19.5	

Notes:
(6) References in which archival observations were previously presented and analyzed.

Table 2.15: *Chandra* follow-up observations of *NuSTAR* transients

Chandra ObsID (1)	Src No. (2)	Pointing (J2000) R.A. (°) (3)	Dec. (°) (4)	Start Time (UT) (5)	Exposure (ks) (6)	Delay between obs (days) (7)
16170	19	250.315079	-46.540562	2014-03-17 05:44	4.9	3
16171	20	250.591644	-46.716049	2014-10-20 06:31	4.9	210
17242	25	248.999542	-47.807671	2015-07-04 10:26	9.8	34

Notes:
(2) NNR source that triggered the *Chandra* observation.
(7) Time elapsed between *NuSTAR* observation where source is detected and *Chandra* follow-up observation. These times vary significantly because some of these sources were obvious in the raw images while others required mosaicking and careful photometric analysis to determine that they were significant detections.

merged all the observations and both FPM together to maximize photon statistics. We then generated mosaic images on the common sky grid in the 3–78, 3–10, 3–40, 10–20, 10–40, 20–40, and 40–78 keV bands. To create mosaic exposure maps, we combined the individual exposure maps by adding exposure values at the location of each sky pixel in the mosaic image; we made exposure maps both without vignetting corrections and with vignetting corrections evaluated at 8, 10, and 20 keV. We used the exposure maps without vignetting corrections when we calculated the source significance and net counts, since these calculations require comparing the exposure depth in the source and background region apertures and the background is dominated by non-focused emission. Instead, when calculating sensitivity curves (§ 2.3.12), we used exposure maps with vignetting corrections since the source emission is focused by the telescope mirrors. When calculating the source fluxes, vignetting corrections are taken into account through the ancillary response file (ARF). An exposure-corrected *NuSTAR* mosaic image in the 3–40 keV band and exposure map without vignetting correction are shown in Figure 2.1. As can be seen, the typical exposure depth of the Norma survey is 30–100 ks while the exposure of the deep field is 1 Ms.

Table 2.16: Boresight Corrections

ObsID (1)	Total shift (″) (2)	R.A. Shift (″) (3)	Dec. Shift (″) (4)	Reference Source (NARCS ID) (5)
30001008002A	5.5	-6.5	3.25	999
30001008002B	6.9	-0.1	6.7	999
30001033002A	5.6	-1.9	-5.4	750
30001033002B	3.2	-2.1	-2.8	750
30002021002B	4.2	6.0	0.0	1321
30002021003B	10.8	13.7	-5.2	1321
30002021005A	4.5	5.0	-2.9	1321

Boresight Corrections (continued)

ObsID	Total shift (″)	R.A. Shift (″)	Dec. Shift (″)	Reference Source (NARCS ID)
30002021005B	3.7	-5.3	0.5	1321
30002021007A	4.2	3.1	-3.6	1321
30002021007B	3.7	-5.4	-0.8	1321
30002021009A	1.7	-0.3	-1.7	1321
30002021009B	4.4	-6.1	1.2	1321
30002021011A	4.3	-4.4	3.1	1321
30002021011B	4.7	-6.9	0.3	1321
30002021013A	7.9	8.2	5.5	1321
30002021013B	6.1	1.8	6.0	1321
30002021015A	4.5	3.7	3.7	1321
30002021015B	6.0	0.6	5.9	1321
30002021017A	2.2	2.1	1.6	1321
30002021017B	2.9	4.1	0.6	1321
30002021019A	7.1	10.0	-1.6	1321
30002021019B	10.0	11.2	6.4	1321
30002021021A	1.8	-0.6	-1.8	1321
30002021021B	7.2	9.4	3.2	1321
30002021023A	1.2	1.8	0.1	1321
30002021023B	7.9	-6.2	-6.6	1321
30002021025A	7.7	11.2	0.0	1321
30002021025B	9.3	13.3	1.0	1321
30002021027A	0.6	0.9	0.1	1321
30002021027B	8.7	11.7	-3.2	1321
30002021029A	10.2	12.1	-5.9	1321
30002021029B	5.9	5.9	-4.3	1321
30002021031A	9.3	10.9	5.5	1321
30002021031B	7.2	0.8	7.2	1321
30002021033A	7.2	1.3	-7.1	1321
30002021033B	14.4	-20.6	-2.6	1321
30002021034A	10.5	-8.7	-8.7	1321
30002021034B	9.8	10.8	6.3	1321
30002021036A	5.7	-8.4	-0.1	1321
40001022002A	4.9	-5.9	-2.9	786
40001022002B	6.4	-9.5	0.3	786
40014017001A	9.0	6.9	-7.7	1321
40014017001B	7.7	6.6	6.2	1321

Boresight Corrections (continued)

ObsID	Total shift (″)	R.A. Shift (″)	Dec. Shift (″)	Reference Source (NARCS ID)

Notes:
The 90% confidence statistical uncertainties of the astrometric corrections are estimated to be $< 2''$ for NARCS 999 and $5 - 6''$ for all other NARCS sources.
(2) Angular distance between original pointing and boresight corrected pointing.
(5) NARCS ID of source used to determine astrometric correction.

2.3.4 Source Detection

Generating trial maps

To identify sources in the *NuSTAR* Norma survey, we employed a technique that was specifically developed for the *NuSTAR* surveys. This technique, which we refer to as the "trial map" technique, is described in detail by Hong et al. (2016), so we only provide a brief explanation here. The *NuSTAR* Galactic Center region survey (Hong et al. 2016), and the *NuSTAR* extragalactic surveys (Civano et al. 2015; Mullaney et al. 2015; Lansbury et al., submitted) all use this technique as the basis for their detection method. As a result of *NuSTAR*'s point spread function (PSF) being larger and its background being higher and more complex compared to other focusing X-ray telescopes such as *Chandra* and *XMM-Newton*, the utility of typical detection algorithms, such as `wavdetect` (Freeman et al. 2002b), is limited when applied to *NuSTAR* data. One way of dealing with this problem is to add an additional level of screening to the results of conventional algorithms, calculating the significance of detections by independent means and setting a significance detection threshold. The trial map technique is more direct, skipping over the initial step of using a detection algorithm such as `wavdetect`.

To make a trial map, for each sky pixel, we calculate the probability of acquiring more than the total observed counts within a source region due to a random background fluctuation. For each pixel, the source and background regions are defined as a circle and an annulus, respectively, centered on that pixel. The mean background counts expected within the source region are estimated from the counts in the background region scaled by the ratio of the areas and exposure values of the source and background regions. Using background regions that are symmetric around the central pixel helps to account for spatial variations of the background. In making trial maps, we plot the inverse of the random chance probability, which is the number of random trials required to produce the observed counts simply by

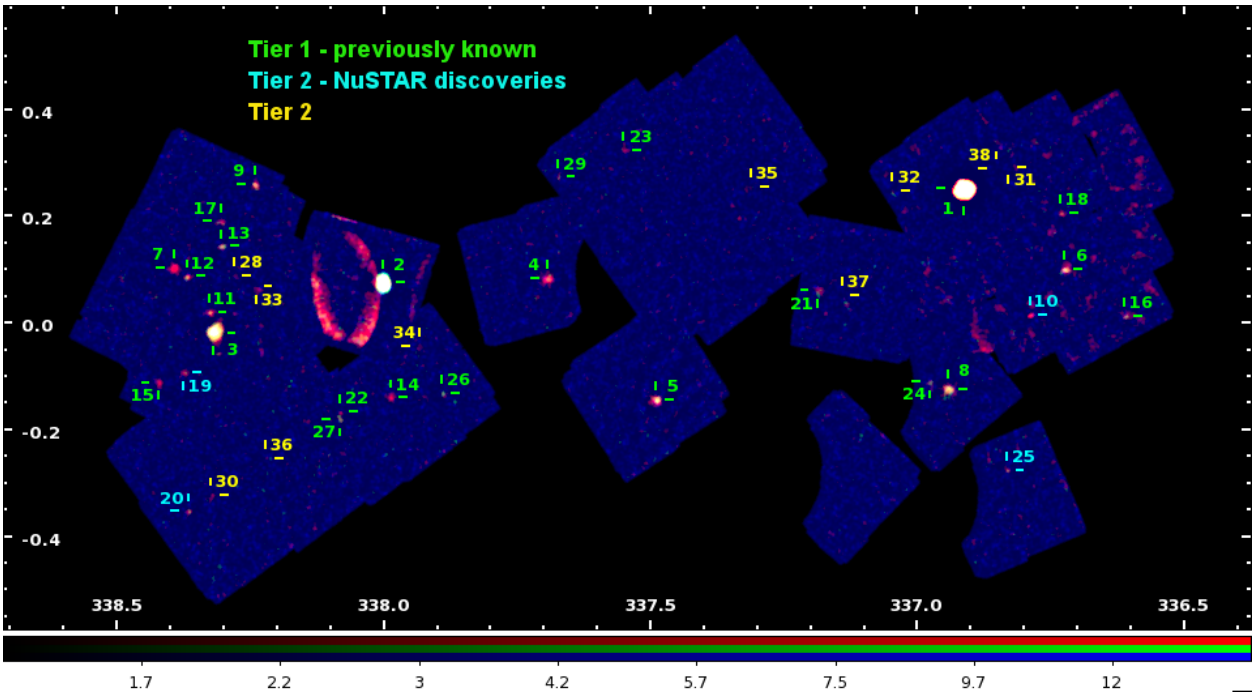

Figure 2.21: Composite trial map showing the 3–10 keV band in red, 10–20 keV band in green, and 20–40 keV band in blue. The colors are scaled by the logarithmic trial map values. Tier 1 sources are labeled in green, if they were observed by NARCS or were previously well-studied, or cyan, if they were discovered by the *NuSTAR* Norma survey. Tier 2 sources are labeled in yellow. The streaks in the vicinity of NNR 2 are due to stray light which has not been removed because NNR 2 is partially embedded in it. The small streaks seen in the area covered by the first mini-survey are due to ghost rays from NNR 1.

random background fluctuations, such that brighter sources with higher significance have higher values in the maps.

We generated trial maps using three different source region sizes with radii of 9.″5, 12″, and 17″ (corresponding to 15, 22, and 30% enclosures of the PSF, respectively) and six different energy bands (3–78, 3–10, 10–40, 40–78, 10–20, 20–40 keV). The source region sizes we used are slightly larger than those used in the analysis of the *NuSTAR* Galactic Center survey since the smaller sizes are especially suited for picking out relatively bright sources in areas of diffuse emission, but in the Norma region there is no evident diffuse emission apart from stray light and ghost rays. The inner and outer radii of the background regions are 51″ (corresponding to 70% of the PSF) and 85″ (equal to 5/3 of the inner radius), respectively, in all cases . Figure 2.21 shows trial maps made using the 22% PSF enclosure and the 3–10, 10–20, and 20–40 keV bands; the three energy bands are combined into a three-color image so that spectral differences between sources can be seen.

2.3.5 Detection Thresholds and Source Selection

When considering how to set detection thresholds for our trial maps, we excluded the observations from the first mini-survey and observation 30001008002 since they have significantly higher levels of stray light and ghost ray contamination than the rest of the survey; in the remainder of this paper, we will refer to this subset of observations as the "clean" sample. Figure 2.22 shows the fractional distributions of the values from the "clean" trial maps using source region sizes of 22% PSF enclosures. As can be seen, the distribution for the 40–78 keV band is very close to that expected for a Poissonian distribution of random background fluctuations, and in fact no sources are clearly visible in the "clean" trial maps.

Following the procedure described in Hong et al. (2016) to establish detection thresholds, we began by cross-correlating each trial map with the NARCS source catalog. Figure 2.23 shows the maximum trial map value within 10″ of the locations of NARCS sources detected at $> 3\sigma$ in the 2–10 keV band as a function of *Chandra* photon flux. Above *Chandra* fluxes of 6×10^{-6} cm^{-2} s^{-1}, more than 1/3 of NARCS sources have trial map values which are significantly higher than the bulk of NARCS sources clustered between trial map values of $10^{0.3}$ to 10^{3}. For *Chandra* fluxes lower than 2×10^{-6} cm^{-2} s^{-1}, the distribution of trial map values are uncorrelated with source flux, having a linear Pearson correlation coefficient $|p| < 0.04$ for all trial maps.

For a source to be considered for the final catalog, we require that it exceed the detection threshold in at least two trial maps. If all 18 trial maps were independent of each other, the expected number of false sources ($N_{\rm F}$) would be equal to $N_{\rm can}C(18,2)p^{16}(1-p)^2$, where $N_{\rm can}$ is the number of NARCS sources included in a *NuSTAR* counterpart search, $C(i,j)$ is a binomial coefficient, and p is the fraction of false sources to be rejected in each map (Hong et al. 2016). However, the trial maps are not completely independent given that their energy ranges overlap. Thus, to at least partly account for the fact that some of the trial maps are correlated, we set a stringent limit on the expected number of false sources, setting $N_{\rm F}$=0.5. Since the long-term variability of NARCS sources is unknown, we search for *NuSTAR* detections among all NARCS sources. Thus, in the "clean" map regions, $N_{\rm can}$=579; limiting $N_{\rm F}$ to 0.5 requires a rejection percentage $p = 99.76\%$. Making a cumulative distribution function of the trial map values of uncorrelated NARCS sources lying in the gray area of Figure 2.23, we determine the corresponding trial value threshold for each trial map; the detection thresholds range from $10^{5.2}$ in the 20–40 keV band with 15% PSF enclosures to $10^{10.3}$ in the 3–10 keV band for 30% PSF enclosures.

Having established detection thresholds for each trial map, we first searched for any *Chandra* sources detected by *NuSTAR*. We cross-correlated all NARCS sources detected at $> 3\sigma$ in the 2–10 keV *Chandra* band with the trial maps of the full set of observations, including those with significant background contamination. We considered all NARCS sources that exceed the detection threshold in at least two trial maps as tier 1 candidate sources. All sources with 2–10 keV *Chandra* flux $> 6 \times 10^{-6}$ cm^{-2} s^{-1} that are not tier 1 sources are considered tier 2 candidate sources, regardless of their trial map values. Although for tier 2 sources, we do not expect to be able to retrieve significant spectral information, we can at

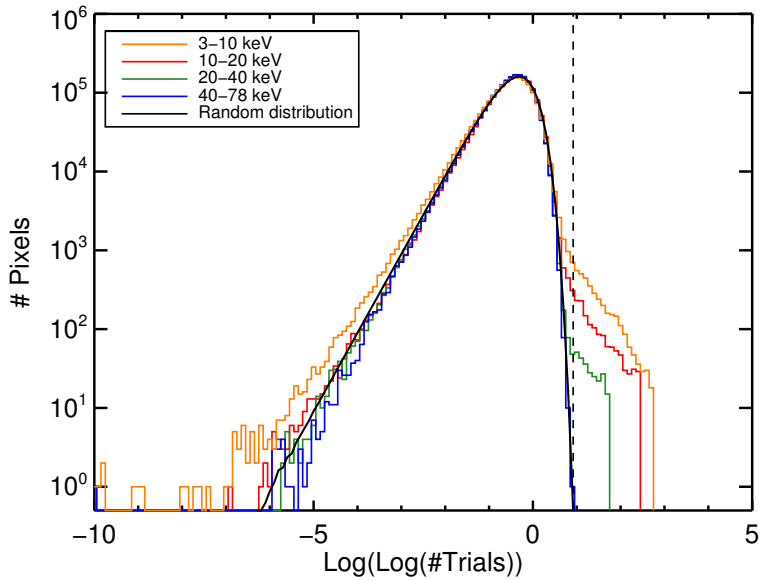

Figure 2.22: Distribution of trial map values in different energy bands for 22% PSF enclosures. The x-axis is shown in a double logarithmic scale. The 40–78 keV distribution closely matches the random distribution expected due to Poissonian fluctuations of the background; this is consistent with the fact that among the "clean" observations included in creating this plot, only one source is detected in the 40–78 keV band. The vertical dashed line shows the detection threshold set for the 3–10 keV band trial map. The excess of high trial map values relative to the 40–78 keV band distribution is due to the presence of sources, stray light, and ghost rays; the excess of low trial map values result from the vicinity of bright sources, which effectively increase the local background.

least check for significant variability between the *Chandra* and *NuSTAR* observations and place upper limits on the flux above 10 keV. We also performed a blind search for *NuSTAR* sources that were not detected in NARCS; we consider any pixels that exceed the detection threshold in at least three trial maps as additional tier 1 candidate sources.

We then examine all tier 1 and tier 2 candidate sources by eye, looking at them in each trial map, image mosaic, as well as individual observations to check that they are not associated with artifacts due to stray light, ghost rays, or the edges of different observations. In twelve cases, multiple NARCS sources are associated with a single *NuSTAR* detection due to *NuSTAR*'s much larger PSF; however, in all these cases, one NARCS source is more clearly centered on the *NuSTAR* position and is also significantly brighter, demonstrating the more likely association. In addition, since tier 2 candidate sources do not exceed the trial map detection thresholds, in order for them to be included in our final catalog, we require that their aperture photometry have a signal-to-noise ratio (S/N)$> 3\sigma$ in at least one of the 3–10, 3–40, or 10–20 keV energy bands (see § 2.3.6 for details). In total, after these different screenings, 28 out of 41 tier 1 candidates and 10 of 21 tier 2 candidates are included in our final source list, shown in Table 2.17.

To determine the best position of tier 1 *NuSTAR* sources, we applied the DAOPHOT

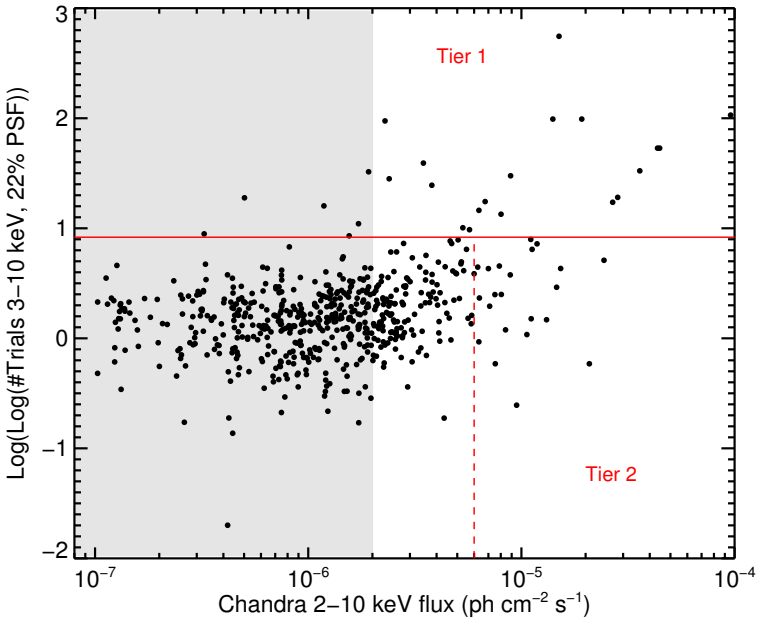

Figure 2.23: Trial map value in the 3–10 keV band using 22% PSF enclosures versus *Chandra* 2–10 keV photon flux for NARCS sources in the surveyed *NuSTAR* area. Fluxes of sources in the gray region are uncorrelated with the trial map values and used to set the detection threshold, which is shown by the red horizontal line. Sources above the horizontal line in at least two trial maps are tier 1 sources, while bright sources below that line but to the right of the vertical dashed line are tier 2 candidates.

"FIND" algorithm in the proximity of each source in the 3–10 keV trial map with 22% PSF enclosure; we found that using the centroid algorithm on the trial maps rather than the mosaic images yielded better results, allowing the algorithm to converge for all tier 1 sources with lower statistical errors. When applying the centroid algorithm, we used the 3–10 keV, 22% PSF trial map since all the tier 1 sources are clearly discernible in this map. The tier 2 sources are not bright enough for the centroid algorithm to yield reliable results, so we simply adopt the *Chandra* positions for these sources. The offsets between tier 1 sources and their *Chandra* counterparts vary from 0.″9 to 14″, excluding two extended sources (NNR 8 and 21) whose *Chandra* positions were determined subjectively by eye and whose *NuSTAR* positions were slightly adjusted so that their aperture regions would reside on a single detector. There are four sources with offsets significantly larger than 8″, constituting 16% of the sample, which is a bit larger than the 10% expected based on *NuSTAR*'s nominal astrometric accuracy, but understandable considering that both the *Chandra* and *NuSTAR* positions have associated statistical and systematic uncertainties and that most of the NNR sources are much fainter than those used to determine *NuSTAR*'s nominal accuracy. Looking carefully at the four sources with the largest offsets, the similarity between their fluxes and/or spectral properties in the 2–10 keV band between *Chandra* and *NuSTAR* suggests that they are true counterparts despite the large positional offsets. Table 2.17 provides information about the detection of all

Table 2.17: *NuSTAR* Source List

Src No. (1)	R.A. (J2000 °) (2)	Dec. (J2000 °) (3)	Unc. (″) (4)	Source Name (5)	NARCS ID (6)	Offset (″) (7)	Exp. (ks) (8)	No. Trials (10^X) (9)	Band (keV) (10)	EEF (%) (11)	No. Det. (12)	Tier (13)
1	248.506998	-47.392280	8	4U 1630-472	–	–	63	1596934.6	3-78	30	18	1
2	249.773296	-46.704057	2⋆	IGR J16393-4643	999	2.3	101	15406.9	3-78	30	18	1
3	250.181262	-46.527207	2⋆	CXOU J164043.5-463135	1321[a]	2.3	1039	1180.9	3-78	30	17	1
4	249.462661	-46.929877	2⋆	CXOU J163750.8-465545	750	3.2	96	141.2	3-10	30	10	1
5	249.511239	-47.232651	2⋆	CXOU J163802.6-471358	786	0.9	200	132.6	3-10	30	14	1
6	248.481220	-47.634188	8	CXOU J163355.1-473804	78	4.3	43	92.3	3-78	30	13	1
7	250.121368	-46.392912	8	CXOU J164029.5-462329	1278/9[b]	6.6	215	77.6	3-10	30	6	1
8	248.946823	-47.623795	–	CXOU J163547.0-473739	365[c]	14.0*	94	64.9	3-78	30	12	1
9	249.805954	-46.402649	8	CXOU J163912.9-462357	1024	13.2	87	45.4	3-10	30	12	1
10	248.640661	-47.643862	8	NuSTAR J163433-4738.7	–	–	45†	40.6	3-10	30	6	1
11	250.146690	-46.499055	9	CXOU J164035.5-462951	1301	6.6	1123	34.9	3-10	30	10	1
12	250.114312	-46.422583	9	CXOU J164027.8-462513	1276	8.5	654	31.1	3-10	30	10	1
13	249.991123	-46.432861	9	CXOU J163957.8-462549	1181	8.4	208	28.4	3-78	30	12	1
14	249.994262	-46.858396	10	CXOU J163957.2-465126	1180	14.1	69	28.0	3-10	30	6	1
15	250.382330	-46.514530	9	CXOU J164130.8-463048	1379	9.7	39	27.7	3-10	30	6	1
16	248.463884	-47.776170	11	CXOU J163350.9-474638	72	5.7	37	21.8	3-78	30	11	1
17	249.942056	-46.402268	10	CXOU J163946.1-462359	1137	8.3	161	19.4	3-10	30	6	1
18	248.374250	-47.556869	9	CXOU J163329.5-473332	38	8.5	37	18.4	3-78	30	6	1
19	250.317553	-46.537330	10	NuSTAR J164116-4632.2	–	13.2	424†	15.7	3-10	30	5	1
20	250.592695	-46.715336	10	NuSTAR J164222-4642.9	–	3.6	123	14.9	3-10	30	8	1
21	248.987518	-47.320057	–	CXOU J163555.4-471907	402/4[d]	16.9*	47	14.8	3-10	30	3	1
22	250.115636	-46.805970	10	CXOU J164027.6-464814	1273	7.0	66	13.4	3-10	20	4	1
23	249.061868	-46.873598	13	CXOU J163614.2-465222	454	6.7	86	12.8	3-10	30	6	1
24	248.964993	-47.589350	13	CXOU J163551.8-473523	391	2.8	187	12.8	3-78	30	4	1
25	249.002044	-47.807801	11	NuSTAR J163600-4748.4	–	6.1	77	11.8	3-78	30	5	1
26	249.891094	-46.925434	12	CXOU J163933.2-465530	1090	6.7	58	10.8	3-78	30	9	1
27	250.130394	-46.814203	15	CXOU J164031.0-464845	1291	6.1	121	9.9	10-20	30	3	1
28	250.010117	-46.533497	–	CXOU J164002.4-463200	1203	–	212	8.7	3-10	30	0	2
29	249.238168	-46.816093	13	CXOU J163657.1-464903	585	5.6	26	8.5	3-10	20	2	1

NuSTAR Source List (continued)

Src No.	R.A. (J2000 °)	Dec.	Unc. (″)	Source Name	NARCS ID	Offset (″)	Exp. (ks)	No. Trials (10^X)	Band (keV)	EEF (%)	No. Det.	Tier
30	250.519111	-46.728140	–	CXOU J164204.5-464341	1408	–	177	7.2	3-10	30	0	2
31	248.378422	-47.426572	–	CXOU J163330.8-472535	40	–	11	6.0	3-78	30	0	2
32	248.644724	-47.296690	–	CXOU J163434.7-471748	139	–	20	5.6	10-20	30	0	2
33	250.028717	-46.487190	–	CXOU J164006.8-462913	1216	–	434	5.3	3-10	30	0	2
34	249.835116	-46.835169	–	CXOU J163920.4-465006	1039	–	29	5.1	3-10	30	0	2
35	248.901036	-47.096680	–	CXOU J163536.2-470548	325	–	115	4.6	10-20	20	0	2
36	250.345276	-46.758179	–	CXOU J164122.8-464529	1374	–	178	4.4	3-10	30	0	2
37	248.951799	-47.358978	–	CXOU J163548.4-472132	373	–	89	3.6	40-78	15	0	2
38	248.406225	-47.411937	–	CXOU J163337.4-472442	52	–	21	2.3	3-10	30	0	2

Notes:

(1) *NuSTAR* Norma Region (NNR) source ID.

(2-3) Right ascension and declination of source determined from centroid algorithm for tier 1 sources and adopting *Chandra* positions from Fornasini et al. (2014) for tier 2 sources.

(4) 90% confidence positional uncertainty, including statistical and systematic uncertainties summed in quadrature. In most cases, the 90% confidence systematic uncertainty is 8″; however for sources that were used to derive astrometric corrections (⋆), the 90% systematic uncertainty is taken to be the maximum estimate based on simulations (2″ for NARCS 999 and 6″ for all sources marked with a ⋆). Uncertainties for tier 2 sources are not provided since the positions of these sources are simply set to the *Chandra* positions.

(5) NARCS source name or other commonly used name for source. For *NuSTAR* discoveries, a *NuSTAR* name is provided.

(6) NARCS catalog ID number.

(7) Angular distance between the source positions in *NuSTAR* and *Chandra* observations. For tier 2 sources, no offset is shown since the *Chandra*-determined position in adopted for the *NuSTAR* analysis.

(8) Total *NuSTAR* exposure, including both modules (FPMA and FPMB) and all observations used in measuring photometric properties of the source (see § 2.3.6 for details).

(9) The maximum value from the trial maps at the location of the source; this value is the number of random trials required to produce the observed counts from a random background fluctuation. For extended sources, this is the maximum trial map value within 30″ of the listed source location.

(10) The energy band of the trial map in which the maximum trial value for the source is measured.

(11) The PSF enclosed energy fraction of the trial map in which the maximum trial value for the source is measured.

NuSTAR Source List (continued)

Src No.	R.A. (J2000 °)	Dec.	Unc. (″)	Source Name	NARCS ID	Offset (″)	Exp. (ks)	No. Trials (10^X)	Band (keV)	EEF (%)	No. Det.	Tier

(12) The total number of trial maps in which the source exceeds the detection threshold. There are 18 trial maps in total, using six different energy bands and three different PSF enclosure fractions.
(13) Tier 1 sources are those detected in at least two trial maps. Tier 2 sources are NARCS sources with 2–10 keV fluxes $> 6 \times 10^{-6}$ ph cm^{-2} s^{-1} which do not meet the NuSTAR detection threshold requirements but have S/N$>$ 3 in the 3–10, 10–20, or 3–40 keV bands (S/N values can be found in Table 2.18).
(a) Point source embedded in extended emission. We treat it as a point source and leave the detailed analysis of the extended emission to Gotthelf et al. (2014). (b) Blend of two *Chandra* sources, which are also blended in NARCS but resolved in *Chandra* ObsID 11008 (Rahoui et al. 2014). (c) Extended source. (d) In *Chandra*, point source 402 is resolved within extended emission (404), but in *NuSTAR* the two are not distinguishable so we treat it as extended source.
(*) These large offsets are due to the fact that the positions for these extended sources were determined by eye in NARCS. The *NuSTAR* position of NNR 21 is also adjusted slightly so that the source region falls primarily on a single detector.
(†) For these transients sources, the exposure times listed only include observations in which the source was detected at $> 2\sigma$ level.

NuSTAR Norma region (NNR) sources. The tier 1 sources include five sources not detected in NARCS; one of them is the well-known LMXB 4U 1630-472 (Kuulkers et al. 1997) while the others are new transient sources discussed in § 2.3.8.

2.3.6 Aperture Photometry

Defining source and background regions

For photometry and spectral extraction, we used circular source regions and, whenever possible, annular background regions centered on the source positions provided in Table 2.17. At energies below 20 keV, the *NuSTAR* background is not uniform as it is dominated by non-focused emission, which exhibits spatial variations due to shadowing of the focal plane (Harrison et al. 2013). Using aperture regions that are symmetric about the source position helps to compensate for this non-uniformity. We performed our photometric analysis with two different source extraction regions with 30″ and 40″ radii (corresponding to roughly 50% and 60% PSF enclosures, respectively), to assess possible systematic errors associated with aperture selection. The default background regions are annuli with 60″ inner radii and 90″ outer radii. For NNR 8 and 21, which appear extended and are not fully contained within the default source regions, we adopted radii of 45″ and 60″ for the small and large circular source regions, respectively, and annular background regions with 80″ inner radii and 110″ outer radii.

For about 1/3 of sources, it was necessary to modify the background aperture regions. In order to prevent contamination to the background from other sources, it is preferable for background regions not to extend within 60″ of any tier 1 source. In addition, above 20 keV, as the relative contribution of the internal background becomes more significant, the background is fairly uniform across any given detector but differs between detectors (Harrison et al. 2013; Wik et al. 2014), so it is advantageous for the background region to be located on the same detector as the source region. Furthermore, when a source is located close to the edge of the field of view, using an annular background region may not sample a statistically large enough number of background counts. Finally, although we removed the most significant patches of stray light and ghost ray contamination from *NuSTAR* observations, non-uniform low-level contamination remains. Thus, we modified the background region in situations where the default background region comes within 60″ of any tier 1 source, the low-level contamination from stray light or ghost rays appears to differ significantly between the source and default background regions, or $> 50\%$ of the annular background region falls outside the observation area or on a detector different from the one where the source is located. In these cases, we adopted a circle with a 70″ radius for the background region and placed it in as ideal a location as possible following these criteria:

i. Keeping the region as close to the source as possible to minimize variations due to vignetting effects and other background inhomogeneities, but at least 60″ away from the source and any tier 1 sources.

ii. Maximizing the fraction of the background region area that falls on the same detector

as the source region.

iii. Placing the background region at a location that exhibits a similar level of low-level stray light or ghost ray contamination as the source region.

For a given source, background aperture regions were defined for each observation and FPM individually since stray light and ghost ray contamination as well as the fraction of the default annular background that lies on a given detector varies depending on the observation and the module. Furthermore, if a source fell close to the edge of an observation, such that >50% of the area of a 40″ radius source region was outside the observation area, that observation was not used to extract photometric or spectral information for the source. Thus, the exposure value at the location of a source in the mosaicked exposure map may be higher than the effective exposure for the source based only on observations used for photometric analysis; the latter effective exposure is the value reported in Table 2.17. Table 2.18 provides the results of our aperture photometry and includes flags that indicate which sources required modified background regions.

The only exceptions to this method of defining background regions are NNR 22 and 27. These sources are only separated by 47″ and thus contaminate each other's default background regions although they do not suffer from any additional background problems. Therefore, since annular background regions are preferable for minimizing vignetting effect, we simply redefined their background regions as an annulus with an 80″ inner radius and 110″ outer radius centered in between the two sources. Due to their proximity, the photometric and spectral properties of these sources as derived from 40″ radius circular apertures are less reliable than those from the 30″ radius apertures.

Net counts and source significance

Having defined aperture regions, we extracted the source and background counts for each source in each observation. We then calculated the expected number of background counts ($\langle c_{\rm bkg}\rangle$) in each source region by multiplying the counts in the background region by the ratio $(A_{\rm src}E_{\rm src})/(A_{\rm bkg}E_{\rm bkg})$, where $A_{\rm src}$ and $A_{\rm bkg}$ are the areas, in units of pixels, and $E_{\rm src}$ and $E_{\rm bkg}$ are the exposures (without vignetting corrections) of the source and background regions, respectively. Then for each source, we summed the source counts ($C_{\rm src}$), total background counts ($C_{\rm bkg}$), background counts expected in the source region ($\langle C_{\rm bkg}\rangle$), and exposures across all observations and modules in 7 different energy bands: 3–78, 3–40, 40–78, 3–10, 10–40, 10–20, and 20–40 keV. The 1σ errors in the total counts were calculated using the recommended approximations for upper and lower limits in Gehrels (1986). Then, the net source counts ($C_{\rm net}$) were calculated by subtracting the total expected background counts in the source region from the total source counts.

In each energy band, we then calculated the signal-to-noise ratio (S/N) of the photometric measurements from the probability that the source could be generated by a noise fluctuation

of the local background using the following equation from Weisskopf et al. (2007):

$$P(\geq C_{\rm src}|C_{\rm bkg}; C_{\rm net}=0) = \sum_{c=C_{\rm src}}^{C_{\rm bkg}+C_{\rm src}} \frac{(C_{\rm bkg}+C_{\rm src})!}{c!(C_{\rm bkg}+C_{\rm src}-c)!}\left(\frac{f}{1+f}\right)^{c}\left(1-\frac{f}{1+f}\right)^{C_{\rm bkg}+C_{\rm src}-c} \quad (2.20)$$

where $f = \langle C_{\rm bkg}\rangle / C_{\rm bkg}$. Using this probability, we define the S/N as the equivalent Gaussian significance in units of the standard deviation (e.g., $P = 0.0013$ corresponds to S/N$= 3\sigma$). These S/N measurements are used to select which tier 2 sources to include in our catalog, but not to set detection thresholds for tier 1 sources, which are determined by the trial maps. Only five sources have photometric measurements with S/N$\geq 3\sigma$ above 20 keV. Therefore, we focus the remainder of our analysis on the 3–40, 3–10, and 10–20 keV energy bands. Of the tier 2 source candidates, we only included those with S/N$\geq 3\sigma$ in at least one of these three energy bands, using either of the two source aperture regions, in our final source list. Table 2.18 provides the significance of each source in our final catalog in these three energy bands, the net counts in the 3–40 keV band, and additional photometric properties described in the following sections.

Photon and energy fluxes

In § 2.3.10, we describe how we derived fluxes from spectral modeling, but for all sources we also derived fluxes in a model-independent way since the spectral fitting of faint sources is prone to significant uncertainty. or each source and background region in each observation and module, we used `nuproducts` to extract a list of photon counts as a function of energy and generate both an ARF and a response matrix file (RMF); the ARFs are scaled by the PSF energy fraction enclosed by the aperture region. We first calculated the source photon flux within each observation and module in the 3–10 and 10–20 keV bands by dividing the counts in each channel by the corresponding ARF, summing all these values within the given energy band, and then dividing by the source region exposure; the estimated background contribution, scaled from the photon flux measured in the background region, was subtracted. These photon flux measurements assume a quantum efficiency of 1, which is a decent approximation for the *NuSTAR* CdZnTe detectors, which have a quantum efficiency of 0.98 over the vast majority of the *NuSTAR* energy range (Bhalerao 2012). If the significance of a source in a particular observation was $< 1\sigma$, then we calculated a 90% confidence upper limit to its photon flux by converting the probability distribution of true source counts (from Equation A21 in Weisskopf et al. 2007) to a photon flux distribution using the source region effective area.

For the five transient sources which were detected by *NuSTAR* but not by NARCS, we looked at lightcurves of their 3–10 keV photon fluxes to check whether they are detected at $> 2\sigma$ confidence in individual *NuSTAR* observations. We found that NNR 1 is only detected in ObsIDs 40014008002 and 40014009001, NNR 10 is only detected in ObsID 40014007001 (which is consistent with T14), and NNR 19 is only detected in ObsIDs 30002021005, 30002021007,

Table 2.18: Photometry of *NuSTAR* Norma Region Sources

Src No. (1)	S/N 3–40 keV (2)	S/N 3–10 keV (3)	S/N 10–20 keV (4)	Net Counts 3–40 keV (5)	Ph. Flux (10^{-6} cm^{-2} s^{-1}) 3–10 keV (6)	Ph. Flux (10^{-6} cm^{-2} s^{-1}) 10–20 keV (7)	En. Flux (10^{-14} erg cm^{-2} s^{-1}) 3–10 keV (8)	En. Flux (10^{-14} erg cm^{-2} s^{-1}) 10–20 keV (9)	Hardness Ratio (10)	E_{50} (keV) (11)	QR (12)	Var. Flag *NuST* (13)	Var. Flag *Chan* (14)	Aper. Flag (15)
1	134534.5 130019.1	142889.4 138317.1	15742.0 15422.4	3214900±18000 4079200±2000	598180±340 603320±300	19112±55 19060±49	473890±270 477130±240	38210±110 38119±100	-0.9246 ±0.0008	5.3245 ±0.0006	1.0334 ±0.0004	l	–	pcm
2	616.4 581.4	350.0 331.0	648.6 614.8	37360±200 46720±240	1634±14 1623±13	1710±14 1694±13	1748±14 1737±13	3954±32 3914±29	-0.112 ±0.006	9.83 ±0.03	1.077 ±+0.006	sp*	slp	pcm
3	144.2 153.3	128.5 140.4	84.4 87.4	9590±120 13550±150	50.1±0.8 57.9±0.8	21.5±0.5 23.3±0.5	46.4±0.7 53.3±0.7	48.7±1.2 52.7±1.2	-0.41±0.01	8.0±0.1	0.90±+0.02	sp*		pcm
4	21.3 20.3	24.6 23.3	6.5 5.9	556±32 723±40	49.1±2.7 50.8±2.7	7.6±1.3 7.8±1.4	40.3±2.2 41.8±2.2	18.8±3.2 19.7±3.4	-0.72±0.06	6.4±0.1	0.92±+0.10	l	slp	pcm
5	23.0 21.4	22.9 21.3	9.6 9.1	842±42 1087±55	23.6±1.3 24.0±1.4	6.4±0.8 6.9±0.9	21.6±1.2 22.0±1.2	13.7±2.0 14.7±2.2	-0.55±0.06	7.8±0.3	0.93±+0.06			p
6	14.3 13.4	12.8 11.7	6.9 7.3	359±29 464±38	77.8±7.7 76.0±8.0	18.0±3.2 21.2±3.3	67.7±6.2 67.6±6.5	40.0±7.1 46.4±7.5	-0.63±0.09	6.5±0.2	0.91±+0.14			pc
7	17.5 17.0	20.6 19.6	1.7 3.0	621±40 835±53	37.4±2.2 38.1±2.2	1.1±0.8 2.3±1.0	29.6±1.7 30.6±1.8	$1.7^{+2.0}_{-1.7}$ 4.4±2.2	-0.92±0.08	5.5±0.2	0.90±+0.06			pc
8	24.9 21.9	22.3 20.0	14.4 12.5	884±41 1083±52	40.5±2.3 44.9±2.5	17.0±1.4 17.6±1.6	37.6±2.0 40.7±2.2	37.4±3.3 38.3±3.7	-0.41±0.05	8.0±0.2	0.90±+0.06			e
9	13.4 11.9	13.3 12.5	7.1 5.8	303±26 371±34	33.9±3.2 37.1±3.4	14.1±2.5 12.9±2.5	32.1±3.0 33.4±3.0	30.8±5.6 28.5±5.9	-0.47±0.09	7.5±0.4	1.02±+0.11			p
10	9.7 6.5	10.6 6.9	1.7 1.6	240±27 220±35	84.0±9.1 56.2±9.1	$4.0^{+3.1}_{-2.8}$ 3.8±3.1	67.3±7.1 46.5±7.1	$8.0^{+7.0}_{-6.3}$ 6.9±6.9	$-0.89^{+0.14}_{-0.11}$	5.6±0.3	0.83±+0.11	l	–	p
11	17.1 17.1	18.8 19.0	6.8 6.6	1310±81 1830±110	9.8±0.6 10.9±0.6	1.9±0.3 2.1±0.4	8.3±0.5 9.4±0.5	4.1±0.8 4.6±0.8	-0.64±0.07	6.4±0.1	0.92±+0.08	l		pcm
12	12.6 12.2	13.9 13.7	5.0 5.0	687±58 929±79	11.1±0.9 12.1±1.0	2.2±0.5 2.5±0.6	9.7±0.8 10.5±0.8	4.5±1.2 5.3±1.4	-0.65±0.09	6.6±0.2	1.06±+0.15			pcm
13	10.5 9.3	8.6 7.4	6.6 6.1	339±35 418±47	10.1±1.5 9.5±1.6	5.8±1.0 5.9±1.0	9.7±1.3 9.2±1.3	13.4±2.4 13.5±2.5	-0.34±0.11	8.9±0.7	0.95±+0.11			p
14	7.7 6.5	9.9 9.3	0.9 0.3	159±23 187±30	20.9±2.5 21.6±2.5	<3.6 <3.2	17.2±2.1 17.7±2.1	<8.8 <7.8	>-1	5.7±0.4	1.11±+0.19			p
15	6.0 6.0	7.8 7.5	0.6 0.3	89±16 125±22	28.6±4.4 31.2±4.6	<3.9 <3.9	23.5±3.6 24.7±3.7	<8.5 <9.0	>-1	5.6±0.6	0.87±+0.13	s		p
16	9.6 9.4	8.5 8.5	4.2 3.4	287±32 393±44	60.8±8.9 65.7±9.6	$10.2^{+3.0}_{-2.8}$ 8.6±2.8	54.9±7.1 60.2±7.7	$22.5^{+6.7}_{-6.1}$ 18.7±6.3	-0.71±0.14	6.4±0.3	0.85±+0.10			p
17	7.8 7.5	8.1 7.3	3.0 3.9	215±30 292±40	9.0±1.5 9.2±1.7	2.5±1.0 3.8±1.1	9.2±1.3 9.3±1.4	5.0±2.3 8.3±2.6	-0.62±0.15	7.3±0.5	1.13±+0.22			p
18	6.3 5.4	6.6 5.8	1.9 1.5	134±23 159±30	47.7±8.0 47.8±8.5	$3.7^{+3.1}_{-2.7}$ $3.3^{+3.3}_{-3.1}$	38.1±6.2 37.5±6.6	$5.8^{+6.6}_{-5.8}$ $5.6^{+7.4}_{-5.6}$	$-0.78^{+0.21}_{-0.20}$	5.9±0.7	0.54±+0.09		s	pc
19	10.3 9.0	11.7 10.5	2.7 2.0	399±41 487±56	11.0±1.1 11.1±1.2	1.6±0.6 1.3±0.7	9.5±0.9 9.4±1.0	3.7±1.5 3.1±1.6	-0.77±0.12	6.6±0.2	1.09±+0.18	l	–	p
20	5.9 6.4	6.7 7.1	3.3 3.5	126±23 191±31	10.0±1.9 11.8±2.0	$4.5^{+1.5}_{-1.3}$ 5.0±1.4	9.4±1.6 11.1±1.7	$11.7^{+3.6}_{-3.3}$ 12.4±3.3	-0.53±0.17	6.8±0.6	1.27±+0.39	l	–	p
21	13.4 12.3	13.5 12.7	6.1 5.5	312±26 408±35	46.4±4.1 52.3±4.5	12.1±2.4 13.4±2.7	39.9±3.5 45.4±3.8	26.0±5.4 29.9±6.3	-0.58±0.09	6.7±0.3	0.79±+0.11			e
22	6.0 5.9	7.4 7.6	1.4 1.4	96±18 132±23	17.5±2.7 20.0±2.9	$2.1^{+2.2}_{-2.0}$ 2.3±2.2	15.0±2.3 17.3±2.4	$4.3^{+5.2}_{-4.3}$ $4.3^{+5.1}_{-4.3}$	$-0.75^{+0.22}_{-0.21}$	6.9±0.5	1.30±+0.43			p

Photometry of *NuSTAR* Norma Region Sources (continued)

Src No.	S/N 3–40 keV	S/N 3–10 keV	S/N 10–20 keV	Net Counts 3–40 keV	Ph. Flux (10^{-6} cm^{-2} s^{-1}) 3–10 keV	Ph. Flux (10^{-6} cm^{-2} s^{-1}) 10–20 keV	En. Flux (10^{-14} erg cm^{-2} s^{-1}) 3–10 keV	En. Flux (10^{-14} erg cm^{-2} s^{-1}) 10–20 keV	Hardness Ratio	E_{50} (keV)	QR	Var. Flag *NuST*	Var. Flag *Chan*	Aper. Flag
23	6.0	5.9	2.7	108±20	8.4±1.8	$2.6^{+1.2}_{-1.1}$	7.6±1.5	$6.0^{+2.8}_{-2.5}$	-0.55±0.20	7.4±0.9	0.91±+0.30			p
	4.8	4.9	2.2	122±26	7.5±1.9	2.1±1.1	7.1±1.6	4.4±2.6						
24	6.7	5.0	4.0	198±31	6.8±1.2	2.3±0.6	5.3±1.0	4.7±1.5	-0.37±0.18	9.0±2.1	0.35±+0.10			pcm
	5.4	3.5	3.0	222±42	5.9±1.3	1.9±0.7	4.6±1.0	3.7±1.6						
25	6.0	5.8	1.4	98±18	6.4±1.5	$1.4^{+0.9}_{-0.8}$	6.4±1.3	$3.8^{+2.4}_{-2.1}$	$-0.74^{+0.25}_{-0.24}$	8.1±0.9	0.60±+0.25	l	–	p
	6.2	5.5	2.0	144±24	6.8±1.6	$1.8^{+1.0}_{-0.9}$	6.7±1.3	$4.6^{+2.4}_{-2.2}$						
26	6.0	5.7	4.3	107±19	11.5±2.2	6.6±1.7	9.5±1.8	16.6±4.1	-0.25±0.16	8.3±0.9	0.55±+0.16			pcm
	6.1	6.1	4.1	152±26	13.2±2.3	6.4±1.7	11.5±2.0	14.8±4.1						
27	7.3	6.0	5.3	179±26	11.0±2.1	8.5±1.8	10.0±1.8	20.3±4.3	-0.20±0.14	8.3±1.1	0.75±+0.18	l		p
	7.4	6.5	5.0	252±35	13.9±2.3	9.1±1.9	12.4±2.0	22.5±4.6						
28	5.5	6.0	2.3	169±32	9.1±1.7	2.3±1.1	8.1±1.4	5.0±2.7	-0.60±0.20	7.5±0.8	0.94±+0.30	l		pcm
	4.7	5.5	3.0	201±43	9.0±1.8	3.5±1.3	8.2±1.5	7.5±3.0						
29	3.5	2.7	2.7	32^{+11}_{-10}	$15.3^{+7.0}_{-5.9}$	$11.6^{+6.1}_{-4.9}$	$11.9^{+5.7}_{-4.9}$	$28.7^{+15.3}_{-12.2}$	$-0.17^{+0.36}_{-0.30}$	10.3±4.1	0.42±+0.26	l		p
	3.0	2.1	2.2	37±13	$11.5^{+6.6}_{-5.8}$	$10.4^{+5.9}_{-4.9}$	$9.4^{+5.6}_{-4.9}$	$25.7^{+14.8}_{-12.2}$						
30	4.7	6.1	0.9	128±28	6.6±1.3	<2.4	6.1±1.1	<15.9	>-1	6.3±0.6	0.93±+0.41			pcm
	3.9	5.8	0.8	147±39	7.9±1.5	<2.5	6.6±1.2	<6.2						
31	4.6	3.9	1.5	29^{+9}_{-8}	$37.7^{+15.8}_{-13.3}$	$10.4^{+10.2}_{-7.5}$	$35.3^{+13.7}_{-11.6}$	$23.7^{+23.5}_{-17.2}$	$-0.61^{+0.42}_{-0.34}$	7.0±2.3	0.67±+0.44			pc
	4.5	3.7	1.7	38^{+11}_{-10}	$29.9^{+13.9}_{-12.2}$	$12.3^{+9.7}_{-7.7}$	$33.1^{+12.6}_{-11.0}$	$28.1^{+22.4}_{-17.6}$						
32	2.5	1.9	1.9	18^{+9}_{-8}	$9.0^{+6.4}_{-5.3}$	$8.5^{+6.2}_{-4.9}$	$8.4^{+5.6}_{-4.6}$	$19.1^{+14.6}_{-11.5}$	$-0.11^{+0.49}_{-0.39}$	10.1±3.8	$0.68^{+0.56}_{-0.68}$			p
	3.0	1.6	2.3	32^{+12}_{-11}	$10.0^{+6.8}_{-5.8}$	$11.7^{+6.5}_{-5.4}$	$8.1^{+5.7}_{-4.8}$	$26.4^{+15.3}_{-12.6}$						
33	2.5	3.4	0.5	113±45	3.2±1.3	<1.6	3.2±1.0	<17.4	>-1	6.6±0.4	1.62±+0.57		l	p
	2.0	2.8	0.0	125±63	2.9±1.4	<1.3	3.0±1.1	<3.1						
34	3.1	3.3	1.5	46±15	14.6±4.7	$5.1^{+4.2}_{-3.7}$	12.6±4.1	$11.1^{+10.0}_{-8.9}$	$-0.49^{+0.34}_{-0.33}$	6.2±1.4	0.83±+0.38			p
	2.4	3.2	0.5	49±21	17.4±5.2	<7.9	13.9±4.5	<18.7						
35	4.1	3.6	3.3	85±22	5.4±1.6	$3.4^{+1.2}_{-1.1}$	4.4±1.3	$8.3^{+2.8}_{-2.5}$	-0.25±0.23	7.4±1.0	0.82±+0.37	l		p
	3.6	4.2	1.5	104±30	6.6±1.8	1.6±1.1	5.7±1.5	3.8±2.5						
36	3.5	1.7	3.2	101±29	3.3±1.5	3.5±1.2	2.1±1.2	8.4±2.9	0.17±0.31	11.8±3.3	$0.48^{+0.42}_{-0.48}$	l	sl	p
	4.2	2.4	3.5	168±41	4.7±1.7	4.4±1.3	3.1±1.4	10.6±3.2						
37	2.2	2.2	1.0	40±18	3.4±1.6	$1.2^{+1.1}_{-1.0}$	2.7±1.3	$3.2^{+2.7}_{-2.4}$	$-0.56^{+0.51}_{-0.44}$	6.5±2.0	$0.32^{+0.50}_{-0.32}$			p
	3.4	3.2	1.4	84±25	6.7±1.9	$1.8^{+1.2}_{-1.1}$	5.0±1.6	$4.8^{+2.9}_{-2.7}$						
38	2.8	3.7	0.5	23^{+10}_{-9}	$11.4^{+4.3}_{-3.8}$	<4.4	$10.7^{+3.7}_{-3.2}$	<11.5	>-1	7.1±1.6	$0.61^{+0.60}_{-0.61}$			pc
	3.2	3.3	1.6	37±12	$11.4^{+4.3}_{-3.9}$	$3.6^{+2.6}_{-2.2}$	$10.0^{+3.6}_{-3.2}$	$8.9^{+6.2}_{-5.1}$						

Notes: (2)-(9) The signal-to-noise ratios, net counts, photon flux, and energy flux of the source in the specified energy bands. Values in the top (bottom) row for each entry are based on using source aperture regions with small (large) radius. All other table column values are based on using small aperture regions.
(10) The hardness ratio is defined as (H-S)/(H+S), where H represents the net counts in the 10–20 keV band and S represents the net counts in the 3–10 keV band.
(11)-(12) Median energy in the 3–40 keV band, and the y-value of the quantile plot, defined as $3(E_{25}\text{-}3\text{ keV})/(E_{75}\text{-}3\text{ keV})$.
(13) Flags indicating source variability: 's' - short timescale (< few hours) variability, 'l' - long timescale (weeks-years) variability, 'p' - periodic modulations detected. See 2.3.7 for details.
(14) Variability flags from Fornasini et al. (2014): 's' - short timescale (< few hours) variability; within a single observation, KS test probability that the source is constant is < 0.3%, 'l' - long timescale (days-weeks) variability; the 0.5–10, 0.5–2, or 2–10 keV photon flux varies by $> 3\sigma$ between NARCS observations, 'p' - periodic modulations detected by Z_n^2 test, '–' - source not detected in NARCS.
(15) 'p' - point source region aperture; circle with 30″/40″ radius, 'e' - extended source aperture; circle with 45″/60″ radius, 'c' - background region is a circle with 70″ radius offset from the source rather than an annulus centered on the source, 'm' - stray light and background spatial variations require background regions to be modified for each observation.
(*) Periodic variability for NNR 2 detected by Bodaghee et al. (2016), and for NNR 3 by Gotthelf et al. (2014).

30002021009, 30002021011, and 30002021013. Excluding the observations in which the transient sources are not detected, we re-evaluated their 3–40 keV net counts and source significance as described in § 2.3.6, and continued to exclude these observations for these sources when determining their other average photometric and spectral properties. Thus, the photometric and spectral properties derived for NNR 1, 10, 19, and 25 should be considered as their average properties during high flux states.

For each source, we then computed average 3–10 and 10–20 keV photon fluxes by combining the count lists and ARFs from different observations and modules. These measurements are presented in Table 2.18. We also calculate the average 3–10 and 10–20 keV energy flux for each source using the same model-independent method but with the additional step of multiplying the source counts in each channel by the channel energy. Fluxes derived using the two different source region sizes are in 1σ agreement with one another, except for three sources which are located in regions of diffuse emission or ghost rays and thus do not appear as exactly point-like. Comparing the model-independent fluxes with those we derived from spectral modeling (see § 2.3.10) for tier 1 sources, we find they are in good agreement when using the smaller aperture regions, but show a significant number of discrepancies at $> 2\sigma$ confidence when using the larger aperture regions. In the larger aperture regions, while the net number of source counts is higher, so is the background/source count ratio, which is why in most cases the source significance derived from the larger aperture regions is slightly lower; as a result, accurate background subtraction is more important when using the larger aperture regions and it is not surprising that our crude subtraction method, which assumes a spectrally flat background, for the model-independent fluxes leads to discrepancies with the spectral fluxes.

2.3.7 X-ray Variability

NuSTAR's high time resolution allows us to characterize the timing properties of detected sources over a range of timescales. *NuSTAR*'s time resolution is good to ~ 2 ms rms, after being corrected for thermal drift of the on-board clock, and the absolute accuracy is known to be better than < 3 ms (Mori et al. 2014; Madsen et al. 2015). For our timing studies, all photon arrival times were converted to barycentric dynamical time (TDB) using the *NuSTAR* coordinates of each point source.

To characterize the source variability on $\sim$ hourly timescales we used the Kolmogorov-Smirnov (KS) statistic to compare the temporal distributions of X-ray events extracted from source and background apertures in the $3 - 20$ keV energy band. The background light curve acts as a model for the count rate variations expected in the source region due to the background. The maximal difference between the two cumulative normalized light curves gives the probability that they are drawn from the same distribution, i.e. that the light curve in the source region is consistent with that expected from the background plus a source with constant flux. Any source with a KS statistic lower than 0.05% in any observation is flagged as short-term variable by an "s" in Table 2.18. For each source, we ran the KS test independently for each of the observations in which it was covered. Since the KS test

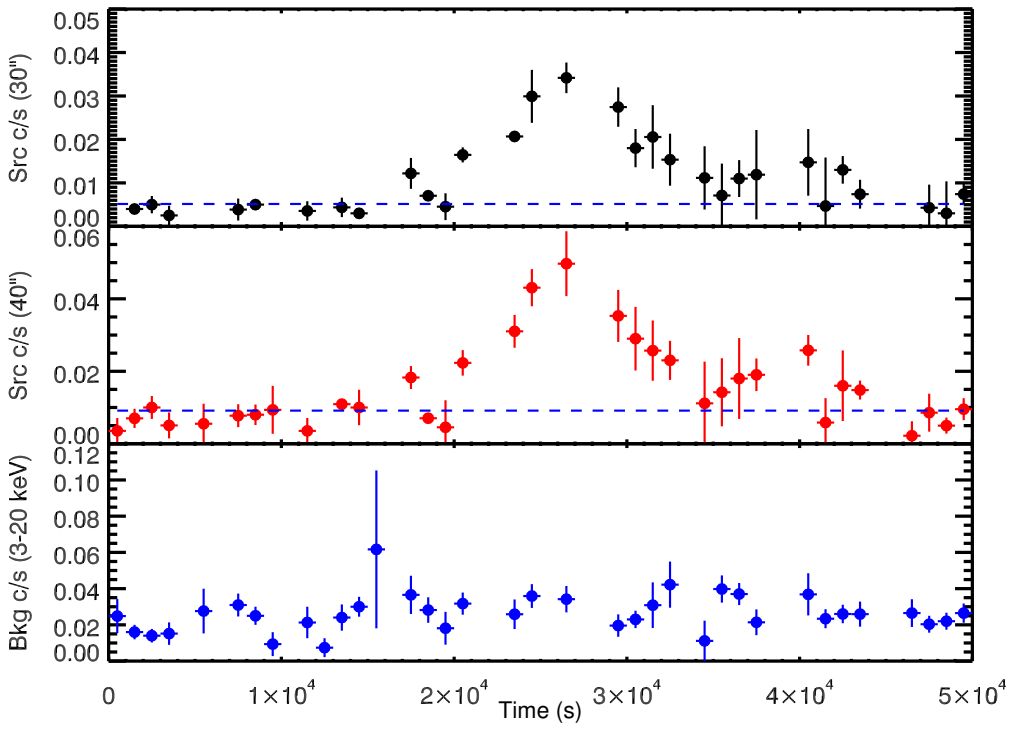

Figure 2.24: Light curve of NNR 15 in the *NuSTAR* 3–20 keV band from ObsID 40014016001, FPMA and FPMB combined. The light curve displays evident short-term variability. The blue dashed lines in the top two panels show the mean background count rate scaled by the source region area.

is applied 160 times in total, the adopted threshold corresponds to $\lesssim 1$ spurious detection. We identify two sources as variable using the KS test. An examination of the lightcuves of these sources, NNR 2 (presented in B16) and NNR 15 (Figure 5), shows clear variability on ∼hourly timescales.

We checked for variability of the NNR sources on week to year timescales by comparing the flux detected between repeated *NuSTAR* observations. Sources were flagged as long-term variable with an "l" in Table 2.18 if their $3-10$ keV photon flux differed by $> 3\sigma$ based on their flux measured uncertainties; given the number of flux comparisons performed, this 3σ threshold should result in $\lesssim 1$ spurious detection. NNR 1, 10, 11, 19, and 28 were found to be variable using this criterion. In addition, we compared *Chandra* and *NuSTAR* fluxes to check for variability on year timescales. For all sources with sufficient photon statistics, we compared the joint spectral fits to *Chandra* and *NuSTAR* data (see § 2.3.10 for details), and identified sources with normalizations that differed at the $> 90\%$ confidence level. Since we performed these joint fits for 24 sources, we would expect as many as two spurious detections of variability, but we made the criterion more stringent by requiring that for a source to be considered variable between the *Chandra* and *NuSTAR* observations, its *Chandra* and *NuSTAR* normalizations must be inconsistent regardless of which of three different spectral

Table 2.19: X-ray Variability of *NuSTAR* Sources

Source No. (1)	*NuSTAR* Var. Flag (2)	Max. 3–10 keV Flux (10^{-6} ph cm^{-2} s^{-1}) (3)	Var. Amplitude 3–10 keV (4)	Criteria for Long-term Var. Detection (5)
1	l	641200±700	> 427500	T, N
2	sp	10100±700	> 34	–
4	l	71^{+2}_{-5}	$1.5^{+0.1}_{-0.2}$	CS
10	l	84±9	> 56	T, N
11	l	26±4	> 18	N, CS
15	s	220±40	> 6	–
19	l	11±1	> 7	T, N
20	l	10±2	> 2	CS
25	l	6±1	> 4	T
27	l	11±2	$2.2^{+1.6}_{-0.9}$	CS
28	l	40±7	6.5±1.3	N
29	l	15^{+7}_{-6}	11^{+8}_{-6}	CQ
35	l	13±2	2.5±0.6	CQ
36	l	9^{+2}_{-1}	2.8±1.4	CQ

Notes:
(2) *NuSTAR* variability flag: 's' - short timescale (< few hours) variability, long timescale (weeks-years) variability, 'p' - periodic modulations detected. See 2.3.7 for details.
(3) Maximum 3–10 keV photon flux either from *Chandra* photometry or *NuSTAR* photometry (based on 30″-radius aperture regions).
(4) Ratio of maximum to minimum 3–10 keV photon fluxes.
(5) Criteria by which long-term variability was determined for sources flagged with "l": T - transient source detected by *NuSTAR* but falling below the survey sensitivity of NARCS, N - photon flux varies by $> 3\sigma$ between different *NuSTAR* observations, CS - cross-normalization between *Chandra* and *NuSTAR* spectra is inconsistent at $> 90\%$ confidence, CQ - *Chandra* 2–10 keV and *NuSTAR* 3–10 keV photon fluxes are inconsistent at $> 90\%$ confidence when adopting a range of spectral models consistent with the quantile values of the source

models is adopted. This more selective criterion is only met by NNR 4, 11, and 27. For fainter sources (NNR 28-38), we considered a range of spectral models that would be consistent with their quantile values, and assessed whether their 2–10 keV *Chandra* flux was incompatible with their average 3–10 keV *NuSTAR* flux at $> 90\%$ confidence, regardless of the spectral model assumed. NNR 29, 35, and 36 are found to be variable by this criterion. In Table 2.19, we provide maximum photon fluxes and the ratio of maximum and minimum fluxes for all *NuSTAR* sources that demonstrate X-ray variability; the transient sources, NNR 1, 10, 19, 20, and 25, which are detected by *NuSTAR* but not detected in NARCS, are flagged as long-term variable and included in this table as well.

We searched for a periodic signal from those *NuSTAR* sources with sufficient counts to detect a coherent timing signal, determined as follows. The ability to detect pulsations depends strongly on the source and background counts and number of search trials. For a sinusoidal signal, the aperture counts (source plus background) necessary to detect a signal of pulsed fraction f_p is $N = 2S/f_p^2$, where S is the power associated with the single trial false detection probability of a test signal $\wp = e^{-S/2}$; S is distributed as χ^2 with two degrees of freedom (van der Klis 1989a). In practice, for a blind search, we need to take into account the number of frequencies tested $N_{trials} = T_{span}/f_{Nyq}$, when T_{span} is the data span and $f_{Nyq} = 250$ Hz, the effective *NuSTAR* Nyquist frequency. In computing N we must allow for the reduced sensitivity of the search due to background contamination in the source aperture (N_b); the minimum detectable pulse fraction $f_p(\mathrm{min})$ is then increased by $(N_s + N_b)/N_s$.

We computed the detectability in individual observations for each source in our sample and considered those suitable for a pulsar search, with $f_p(\mathrm{min}) > 50\%$ at the 3σ level. For the three brightest sources in the Norma survey, their timing properties are already presented elsewhere: i) the quasi-periodic oscillations of the black hole binary 4U 1630- 472 (NNR 1) were extensively studied using the *Rossi X-ray Timing Explorer* (Tomsick & Kaaret 2000; Dieters et al. 2000; Seifina et al. 2014), ii) the high mass X-ray binary pulsar HMXB IGR J16393-4643 (NNR 2) with a period of 904 seconds, whose spin-up rate was determined from recent *NuSTAR* observations (B16), and iii) the *NuSTAR*-discovered 206 ms pulsar PSR J1640−4631 (NNR 3) associated with the TeV source HESS J1640−465 (G14;Archibald et al. 2016).

For NNR 4, 5, 8, and 21, we extracted event lists in the $3 - 20$ keV band from $r = 40''$ radius apertures and searched for periodic signals between 4 ms and 100 seconds. For each source, we evaluated the power at each frequency (oversampling by a factor of two) using the unbinned Z_n^2 test statistic (Buccheri et al. 1983) summed over $n = 1, 2, 3, 5$ harmonics, to be sensitive to both broad and narrow pulse profiles. We repeated our search for an additional combination of energy ranges $3 < E < 25$ keV, $3 < E < 10$ keV, $10 < E < 25$ keV, $10 < E < 40$ keV, and aperture size $r < 20''$ and $r < 30''$. For all these searches, no significant signals were detected. For NNR 5 and 8, we can constrain the pulsed fraction of X-ray emission to be $< 45\%$ and $< 48\%$, respectively, at the 3σ confidence. We also performed periodic searches for longer periods, with special attention to NNR 4 for which *Chandra* detected a 7150 second period, but we were unable to pick out any signals that could clearly be attributed to the *NuSTAR* sources due to the artifacts introduced by *NuSTAR*'s orbital

Table 2.20: Properties of *Chandra* counterparts to *NuSTAR* discoveries

Source No.	R.A.	Dec.	Unc.	Significance	Net counts	E_{50}	QR
	J2000 (°)		(″)	0.5–10 keV	0.5–10 keV	(keV)	
(1)	(2)	(3)	(4)	(5)	(6)	(7)	(8)
19	250.315033	-46.540543	0.68	15	245^{+17}_{-16}	2.9±0.2	0.92±0.06
20	250.591644	-46.716049	0.87	2.9	3^{+3}_{-2}	−*	–
25	248.999542	-47.807671	0.71	6	33^{+7}_{-6}	2.3±0.4	0.9±0.3

Notes:
(4) 90% statistical and systematic positional uncertainties summed in quadrature.
(*) The *Chandra* counterpart of NNR 20 has too few counts to perform quantile analysis. The energies of the three photons attributed to this source are 4.2, 5.7, and 7.0 keV; since the *Chandra* effective area is higher at softer energies, the fact that no photons are detected with energies < 4 keV suggests that this source is subject to high levels of absorption.

occultations to the Fourier power spectrum.

2.3.8 *Chandra* Follow-up of *NuSTAR* Discoveries

As discussed in § 2.3.2, we triggered *Chandra* follow-up observations for the four sources discovered by *NuSTAR*, NNR 10, 19, 20, and 25. NNR 10, 19, and 25 were not detected by NARCS despite its much higher sensitivity compared to the *NuSTAR* Norma survey, indicating these are transient sources. NNR 20 falls outside the area surveyed by *Chandra*, but our follow-up *Chandra* observations show that its flux is also highly variable.

The analysis of the *Chandra* follow-up of NNR 10 is presented in T14, while the analysis of the other three observations, which are listed in Table 2.15, is described here. The archival *Chandra* observation 7591 (see Table 2.14, which provides additional coverage of NNR 19) was also subjected to the same analysis. The *Chandra* observations were processed using CIAO version 4.7 adopting standard procedures. Then we used `wavdetect` to determine the positions of *Chandra* sources in the vicinity of the *NuSTAR* sources. The statistical uncertainties of the *Chandra* positions were calculated using the parametrization in Equation 5 of Hong et al. (2005); the 90% statistical uncertainty was then combined with *Chandra*'s 0.″64 systematic uncertainty[14] in quadrature. Since NNR 19 was also detected in an archival *Chandra* observation, we averaged the positions determined from ObsIDs 7591 and 16170. The *Chandra* positions and uncertainties are reported in Table 2.20. The *Chandra* follow-up observations of NNR 9, 20, and 25 are shown in Figure 2.25, where green circles indicate the *NuSTAR* source positions and magenta circles show the locations of the nearest *Chandra* sources.

The closest *Chandra* source to NNR 19 is located at a distance of 13.″2, which is outside of the 90% confidence *NuSTAR* error circle. However, as noted in Table 2.17, a few of the

[14]See http:/cxc.harvard.edu/cal/ASPECT/celmon.

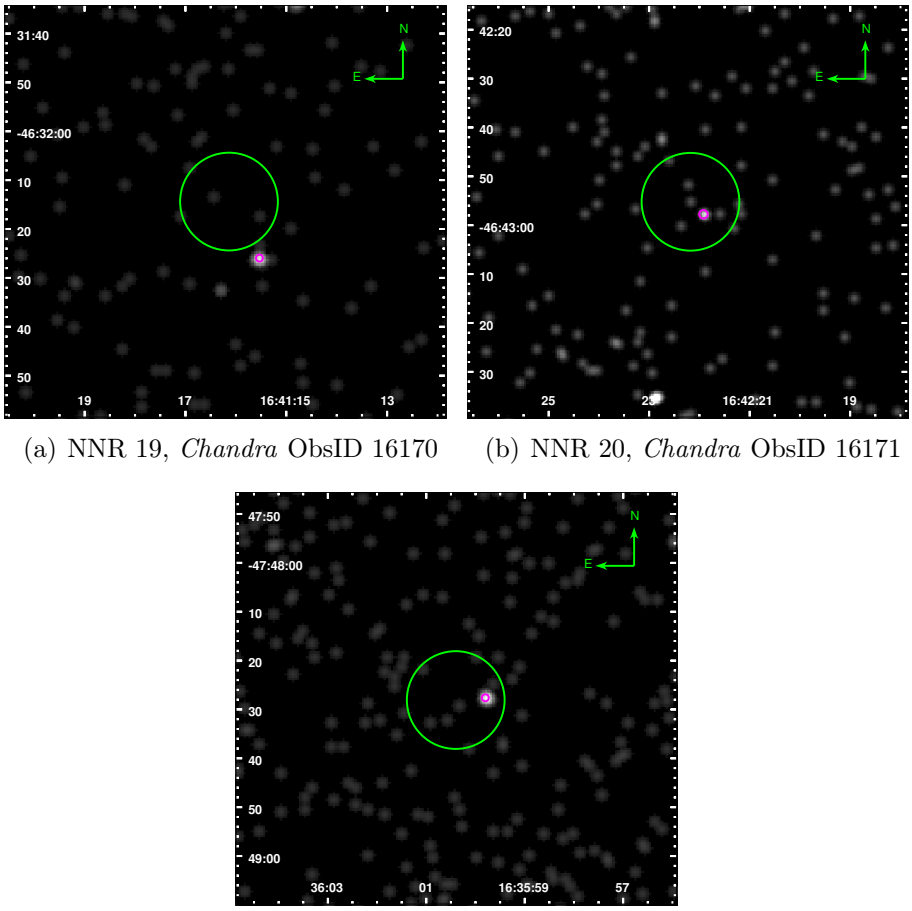

(a) NNR 19, *Chandra* ObsID 16170 (b) NNR 20, *Chandra* ObsID 16171

(c) NNR 25, *Chandra* ObsID 17242

Figure 2.25: *Chandra* follow-up observations of *NuSTAR* transients in the 0.5–10 keV band (see Table 2.15). *NuSTAR* source positions are shown with 90% confidence error circles in green, and the locations of the nearest *Chandra* sources are indicated with 90% confidence error circles in magenta. The *NuSTAR* and *Chandra* positional uncertainties are provided in Tables 2.17 and 2.20, and are approximately $10''$ and $0\farcs7$, respectively, for all three sources.

NARCS counterparts have similarly large offsets, suggesting that in some cases the systematic *NuSTAR* positional uncertainties may be underestimated. The fact that only three days elapsed between the *NuSTAR* and *Chandra* observations of NNR 19 strengthens the case that these sources are indeed associated. Furthermore, this *Chandra* source was detected in 2007 in *Chandra* ObsID 7591, but undetected in 2011 in ObsID 12508; the fact that this *Chandra* source is a transient boosts the probability that it is the counterpart of NNR 19.

The only *Chandra* source in the vicinity of NNR 20 lies within the *NuSTAR* error circle but is only detected at 2.9σ confidence. NNR 20 was not covered by previous *Chandra* observations, including NARCS, so before our follow-up observation (ObsID 16171), we did not know whether this source was a transient or not; based on its *NuSTAR* 3–10 keV flux, we would have expected to detect at least 10 counts from its *Chandra* counterpart if it was persistent. Thus, even if it is not definite that the weak *Chandra* detection is truly the counterpart of NNR 20, the lack of any brighter *Chandra* sources proves NNR 20 is a variable source.

Follow-up observations of NNR 25 were performed 34 days after the *NuSTAR* observations, and a *Chandra* source is clearly detected within the *NuSTAR* error circle. This *Chandra* source was not detected during the 2011 NARCS observations; its transient nature boosts the probability that it is the true counterpart of the transient NNR 25. As was done by F14 for all the NARCS sources, we searched for infrared counterparts to the *NuSTAR*-discovered sources in the VVV survey. We did not find any infrared counterparts to NNR 19, 20, or 25 within the 95% uncertainty of the *Chandra*-derived positions.

In order to extract photometric and spectral information for each *Chandra* counterpart, we defined source aperture regions as circles with $2\farcs5$ radii and background regions as annuli with $15''$ inner radii and $44''$ outer radii. As the counterpart of NNR 19 was at a larger angular offset from the *Chandra* aimpoint in ObsID 7591, and the *Chandra* PSF increases in size with angular offset, the circular source region used for this observation had a $5''$ radius. For each source in each *Chandra* observation, we calculate the net 0.5–10 keV counts, detection significance, and quantile values (see § 2.3.9), which are provided in Table 2.20.

2.3.9 Hardness Ratios and Quantile Analysis

Since spectral fitting can be unreliable or impractical for faint sources, we use hardness ratios and quantile values (Hong et al. 2004) to probe and compare the spectral properties of *NuSTAR* sources. In order to reduce the level of background contamination and prevent the hardness ratios and quantile values from being skewed towards the values of the *NuSTAR* background, we opted to use the aperture regions with smaller radii to derive these spectral parameters. The hardness ratio for each source is calculated as $(H - S)/(H + S)$, where H is the counts in the hard (10–20 keV) band and S is the counts in the soft (3–10 keV) band. The *NuSTAR* hardness ratios are listed in Table 2.18.

While hardness ratios are the most widely used proxy for spectral hardness of faint X-ray sources, they are subject to selection effects associated with having to choose two particular energy bands and they do not yield meaningful information for sources which have zero net

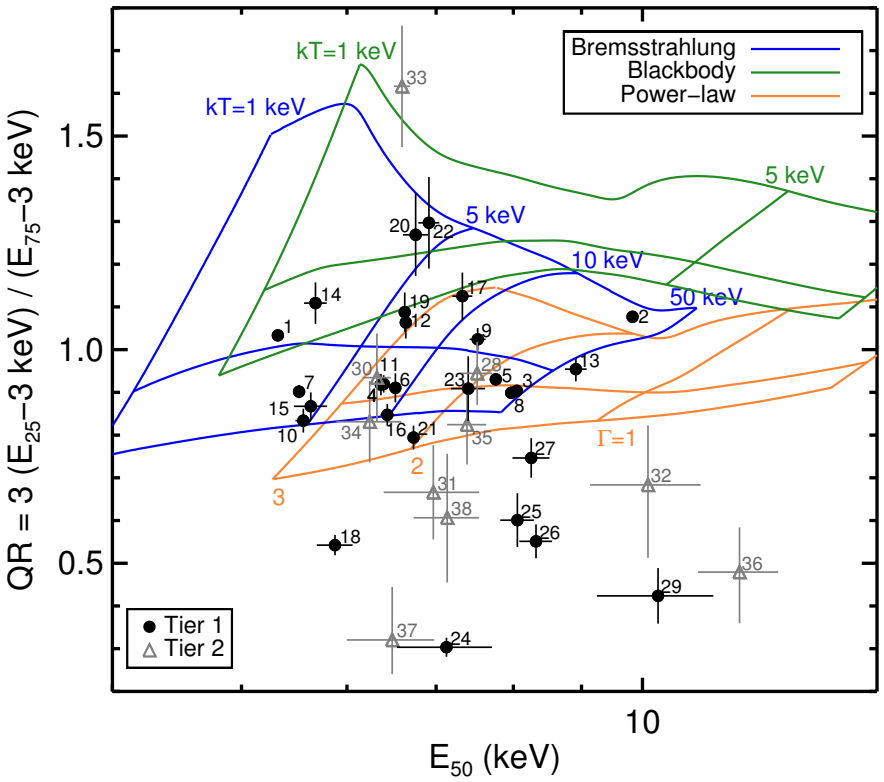

(a) *NuSTAR* quantile diagram. To make it easier to view all the sources, the quantile error bars have been reduced to 25% of the actual 1σ errors. The *NuSTAR* 3–40 keV background has $E_{50} = 10$–15 keV and $QR = 0.4$–0.6, which is why several tier 2 sources, which are most affected by the background, are found near that position in the diagram. Grids representing absorbed bremsstrahlung, blackbody, and power-law models are shown in blue, green, and orange, respectively. Roughly vertical grid lines represent different values of the temperature (kT) or photon index (Γ). Primarily horizontal grid lines represent $N_{\rm H} = 10^{22}, 10^{23}, 5 \times 10^{23}$ cm^{-2} from bottom to top.

Figure 2.26: Quantile diagrams showing the quantile ratio on the y-axis and the median energy on the x-axis (or median energy "normalized" by the *Chandra* 0.5–10 keV band for the lower panel). Quantile values of tier 1 sources are shown in black and those of tier 2 sources are shown in gray. Comparing the positions of sources in the quantile diagrams to the spectral model gridlines provides a rough measurement of their spectral parameters. The *Chandra* quantiles are very sensitive to the amount of absorption suffered by a source, while the *NuSTAR* quantiles are more capable of differentiating sources with different spectral slopes.

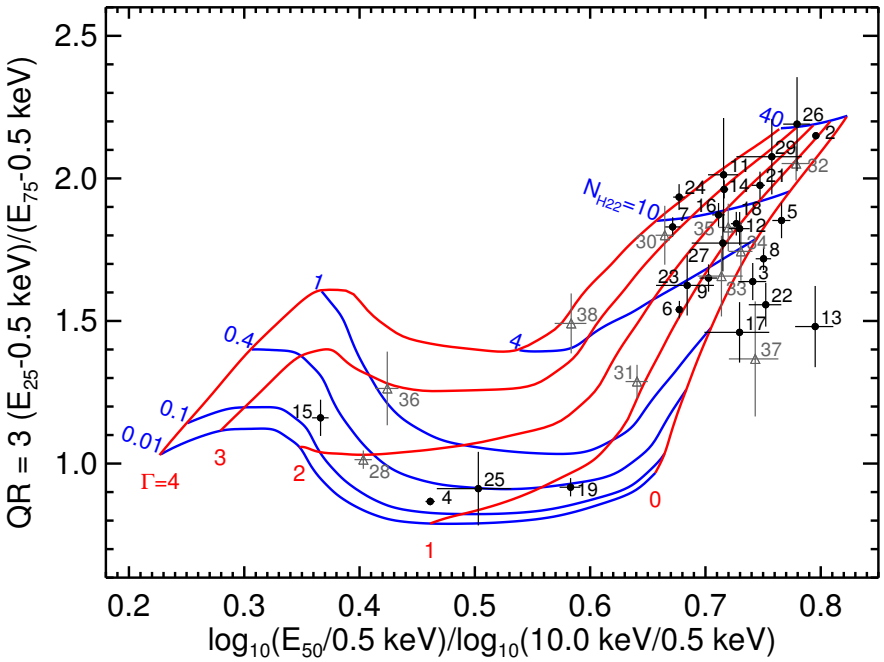

(b) *Chandra* quantile diagram. The error bars have been reduced to 50% of the actual 1σ errors. A grid of a power-law spectral model attenuated by interstellar absorption is overlaid. Red (primarily vertical) lines represent values of the photon index $\Gamma = 0, 1, 2, 3$, and 4 from right to left. Blue (primarily horizontal) lines represent values of the hydrogen column density $N_{\rm H} = 10^{20}, 10^{21}, 10^{21.6}, 10^{22}, 10^{22.6}, 10^{23}$, and $10^{23.6}$ cm^{-2} from bottom to top.

Figure 2.26: This figure is continued from the previous page.

counts in one of the two energy bands. Therefore, we also calculated quantile values for each source in the 3–40 keV band; these values are the median energy E_{50}, E_{25} and E_{75}, the energies below which 25% and 75% of the source counts reside, respectively. The latter energies were combined into a single quantile ratio (QR) which is a measure of how broad or peaked the spectrum is and is defined as $QR = 3(E_{25} - E_{\rm min})/(E_{75} - E_{\rm min})$, where $E_{\rm min}$ is the lower bound of the energy band, 3 keV for *NuSTAR* and 0.5 keV for *Chandra*. The *NuSTAR* median energy and QR value of each source is provided in Table 2.18 and shown in Figure 2.26(a). The gridlines in this figure indicate where a source with a particular blackbody, bremsstrahlung, or power-law spectrum would fall in the *NuSTAR* quantile space; gridlines which are roughly vertical represent different temperatures (kT) or photon indices (Γ) while roughly horizontal gridlines represent different values of the absorbing column density along the line-of-sight to the source ($N_{\rm H}$).

Figure 2.26(b) shows the quantile values of the *Chandra* counterparts of the *NuSTAR* sources in the 0.5–10 keV band. Most of these values are taken from the NARCS catalog (F14). The quantile values for *Chandra* counterparts of NNR 19 and 25 were derived using the aperture regions described in § 2.3.8; the values for NNR 19 derived from ObsIDs 7591 and 16170 were combined in a weighted average. The *Chandra* counterpart of NNR 20 only has 3 counts, which are too few for quantile analysis; however, all three photons have energies > 4 keV, indicating that this source is subject to significant absorption since *Chandra*'s effective area peaks below 2 keV. Finally, we did not adopt the NARCS catalog quantile values for extended sources, because they were derived using aperture regions whose position and extent were determined by eye and which removed embedded point sources not distinguishable with *NuSTAR*. Instead, we recalculated the quantiles for extended sources using circular aperture regions with 45″-radii centered on the *NuSTAR*-determined positions of NNR 8 and 21; these *Chandra* quantiles are weighted averages of values derived from ObsIDs 12528 and 12529[15] for the counterpart of NNR 8 and ObsIDs 12523 and 12526 for the counterpart of NNR 21.

As can be seen in Figure 2.26, the *Chandra* quantiles can easily differentiate between foreground sources and those subject to high levels of absorption due to gas along the line-of-sight. The integrated column density of neutral and molecular hydrogen due to the interstellar medium along the line-of-sight in the Norma region varies from $4 - 9 \times 10^{22}$ cm^{-2}, as derived from the sum of $N_{\rm HI}$ measured by the Leiden/Argentine/Bonn survey (Kalberla et al. 2005) and $N_{\rm H_2}$ estimated from the MWA CO survey (Bronfman et al. 1989) using the $N_{\rm H_2}/I_{\rm CO}$ factor from Dame et al. (2001); since these surveys have 0.5° resolution, the interstellar $N_{\rm HI+H_2}$ values we derive are averages over 0.25 deg^2 regions, so it is possible that the interstellar absorption is actually higher or lower along particular lines-of-sight due to the clumpy nature of molecular clouds. Thus, the sources whose X-ray spectra show column densities in excess of these values may be located behind dense molecular clouds or suffer from

[15]The *Chandra* counterpart of NNR 8 is also observed in ObsID 12525. However, in this observation, a nearby transient point source which falls within the aperture region is visible. Comparing the 3–10 keV photon fluxes of NNR 8 in *Chandra* and *NuSTAR*, it does not appear that this nearby transient was present during the *NuSTAR* observation, and therefore we decided not to include ObsID 12525 in our *Chandra* analysis.

additional absorption due to gas or dust local to the X-ray source. The *NuSTAR* quantiles are not particularly sensitive to $N_{\rm H}$, but instead are able to separate sources with intrinsically soft and hard spectra, regardless of their level of absorption. Thus, the combination of quantile values in the *Chandra* and *NuSTAR* bands allows us to learn a fair amount about the spectral properties of sources which are too faint for spectral fitting and provide a check on spectral fitting results which can depend on the choice of binning for low photon statistics.

2.3.10 Spectral Analysis

For all tier 1 sources with >100 net counts in the 40″ radius aperture in the 3–40 keV band, we perform spectral analysis using XSPEC version 12.8.2 (Arnaud 1996), jointly fitting the *NuSTAR* and *Chandra* data when it is available. All spectral parameters were tied together for these joint fits, except for a cross-normalization factor between the *Chandra* and *NuSTAR* observations which was left as a free parameter to account for source variability and differences in instrumental calibrations (measured to be consistent to 10% precision, Madsen et al. 2015). We also included a cross-normalization constant between *NuSTAR* FPMA and FPMB in our models; for most sources, due to limited photon statistics, the errors on this normalization constant are large and the constant is consistent with 1.0 to better than 90% confidence. Thus, for the *NuSTAR* sources detected with lowest significance (i.e., with trial map values $< 10^{15}$), we fixed the FPMA/B normalization constant to 1. To maximize the number of counts per spectral bin, we used the larger aperture source regions to extract information for spectral fitting; however, for NNR 22 and 27, which are only separated by 47″, we extracted spectral information from 30″ source regions to limit the blending of the two sources. The spectra of the *Chandra* counterparts were extracted as described in F14 for NARCS sources and § 2.3.8 for the counterparts of *NuSTAR* discoveries; however, for the extended counterparts of NNR 8 and 21, we defined aperture regions as 60″-radius circles centered on the *NuSTAR*-derived position in order to match the *NuSTAR* extraction region.

The *Chandra* and *NuSTAR* spectra were grouped into bins of $> 2-10\sigma$ confidence, depending on the net counts of each source. For the three brightest sources which have been carefully analyzed in other papers, we adopt simplified versions of the best-fitting models found in King et al. (2014), B16, and G14, in order to easily measure their observed and unabsorbed fluxes in the 3–10 and 10–20 keV bands which we use to calculate the $\log N$-$\log S$ distribution of our survey (§ 2.3.13). For other tier 1 sources, we fit absorbed power-law, bremsstrahlung, and collisionally-ionized models; we employed the `tbabs` absorption model with solar abundances from Wilms et al. (2000) and photoionization cross-sections from Verner et al. (1996b). When Fe line emission was clearly visible between 6.4 and 7.1 keV, we also included a Gaussian line in the spectral models. Due to *NuSTAR*'s 0.4 keV resolution at 6–7 keV enegies, multiple Fe lines would appear blended in our spectra, especially given the low photon statistics. Thus, measurements of the Fe line parameters should be interpreted as the average energy of the Fe line complex and the combined equivalent width of the Fe lines. If Fe line emission was not evident, the source spectrum was first fit without a Gaussian component. Then, having determined which of the three spectral models best fit the spectrum,

a Gaussian component was added in order to place constraints on the strength of Fe line emission that may not be visible due to poor photon statistics. The central energy of this Gaussian component was constrained to be between 6.3 and 7.1 keV and its width was fixed to zero; we tested the effect of fixing the width to values as high as 0.1 keV, but the impact on the results was negligible. Then the 90% upper limit on the line normalization was used to calculate the 90% upper limit on the Fe line equivalent width. In addition, when significant residuals remained at soft energies, we introduced a partial covering model (`pcfabs`) to test if it provides a significant improvement of the chi-squared statistic. Including this component substantially improved χ^2 for NNR 4 and 6, but for NNR 6 the $N_{\rm H}$ of the partial absorber could not be well constrained and the covering fraction was found to be consistent with 1.0 to 90% confidence. Thus, since the spectral quality of NNR 6 was not good enough to constrain the additional `pcfabs` component, we did not include it in our final model fit for NNR 6.

The results of our spectral analysis can be found in Table 2.21, and the spectra and fit residuals are shown in Figure 2.27 and the appendix. As can be seen, spectra with < 300 *NuSTAR* counts cannot place strong constraints on the spectral parameters. However, we nonetheless include these results to be able to compare non-parametric fluxes with spectrally derived fluxes, and as a reference to aid the design of future *NuSTAR* surveys.

We used the model fit with the best reduced chi-square statistic to determine observed energy fluxes for each source in the 2–10, 3–10, and 10–20 keV bands and conversion factors from photon fluxes to unabsorbed energy fluxes, which are listed in Table 2.22. These conversion factors are used to calculate the log$N$-log$S$ distribution for unabsorbed fluxes (see § 2.3.13). The faintest tier 1 source, NNR 29, does not have enough counts to permit spectral fitting; based on its quantile values, it has $N_{\rm H} \approx 10^{23}$ cm^{-2} and $\Gamma \approx 1.8$. Fixing the parameters of an absorbed power-law model to these values while allowing the *Chandra* and *NuSTAR* normalizations to vary independently, we fit the unbinned spectra of NNR 29 using the C-statistic (Cash 1979) and find a goodness of fit lower than 28%. The observed and unabsorbed fluxes of NNR 29 measured from these fits are included in Table 2.22.

To ensure that these results were not significantly dependent on the binning that was chosen, we compared the best-fitting parameters with those derived by fitting unbinned spectra using the C-statistic and the locations of sources in the quantile diagrams; no significant discrepancies were found except for sources with strong Fe lines, which is to be expected since the quantile grids do not account for the presence of Fe lines. However, for NNR 17, our analysis yields a harder spectrum than is found by B14. This source lies in the ghost ray pattern of 4U 1630-472, making background subtraction particularly challenging. The background region we selected contains higher ghost ray contamination than the background chosen by B14; we consider our selection more appropriate given that this source resides in a region of high ghost ray contamination. Since the spectrum of 4U 1630-472 is dominated by a blackbody component with $kT \approx 1.4$ keV, the fact that B14 measured a softer spectrum for NNR 17 than we do, with $\Gamma = 3.7 \pm 0.5$ rather than $2.0^{+1.0}_{-0.8}$, suggests that the background contribution from ghost rays may have been underestimated by B14. The photon index we measure is also more consistent with the hard photon index indicated by the *Chandra* quantiles (see Figure 2.26(b)).

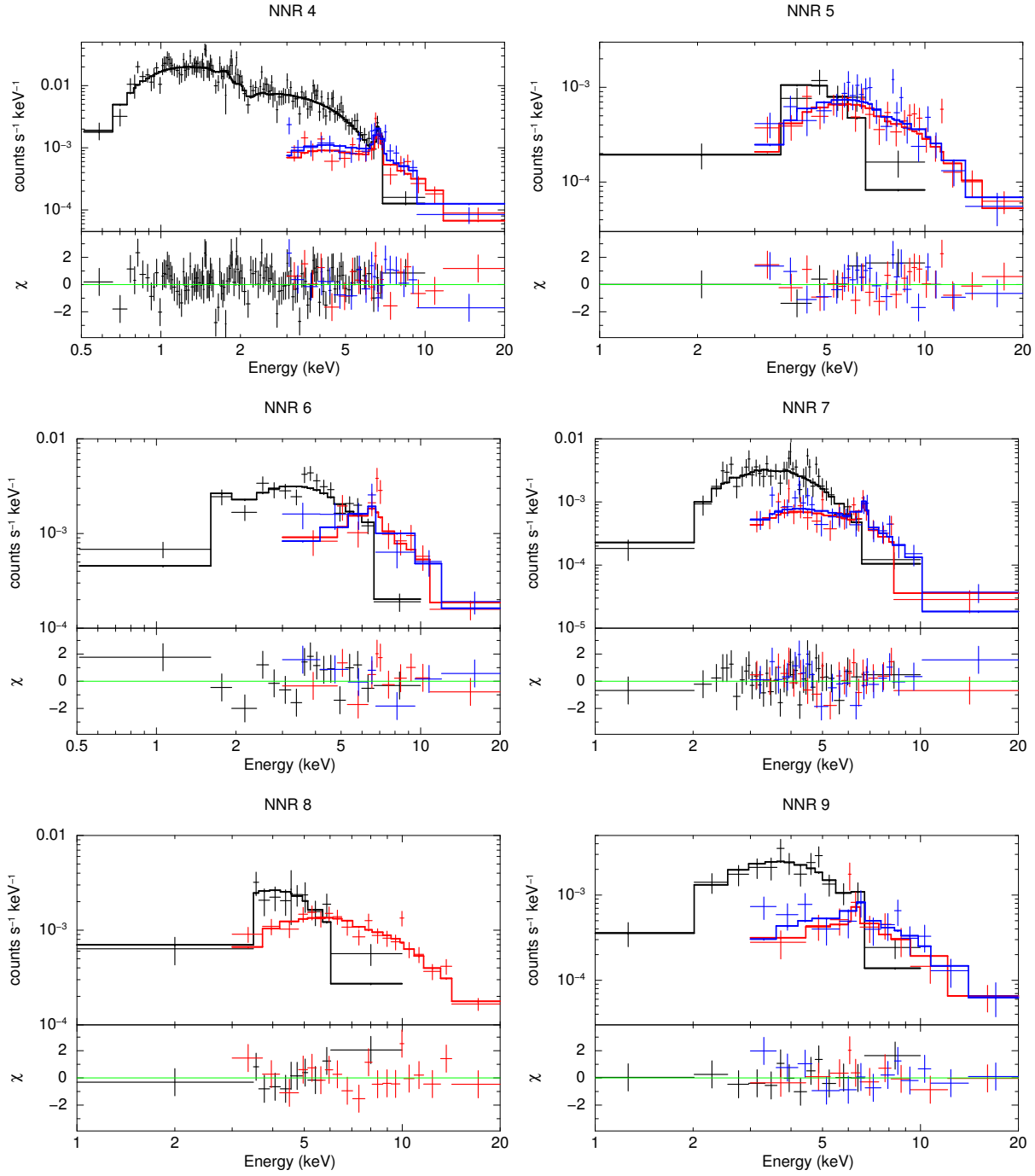

Figure 2.27: Example *Chandra* and *NuSTAR* spectra with residuals of best-fitting model. *Chandra* data is shown in black, *NuSTAR* FPMA data is shown in red, and FPMB data is shown in blue. Additional spectra are shown in Appendix B. Spectral analysis results can be found in Table 2.21.

Table 2.21: Spectral Fitting Results for *NuSTAR* Sources

Src No. (1)	Model `tbabs*X` (2)	N/C norm (3)	FPMA/B norm (4)	$N_{\rm H}$ (10^{22}cm^{-2}) (5)	Γ (6)	$E_{\rm cut}$ (keV) (7)	Power-law norm (8)	kT_{BB} (keV) (9)	Bbody norm (10)	χ^2_ν/dof (11)	Bin (σ) (12)	Comments (13)
1	`PL+diskbb`	–	$0.978^{+0.01}_{-0.02}$	12.47±0.08	2.15±0.03	–	0.22±0.02	$1.425^{+0.002}_{-0.003}$	192±2	2.68/806	10	See King et al. (2014) for fit including disk reflection and wind absorption.
2	`cutoffpl +bbodyrad`	$0.67^{+0.02}_{-0.01}$	$1.02^{+0.03}_{-0.02}$	46.0±1.5	$-2.5^{+0.4}_{-0.5}$	$4.05^{+0.33}_{-0.06}$	$1.3^{+1.5}_{-0.1}\times10^{-5}$	$1.56^{+0.06}_{-0.08}$	$0.75^{+0.12}_{-0.08}$	1.14/1096	5,5	See Bodaghee et al. (2016) for fit including cyclotron absorption line.

Src No.	Model `tbabs*X`	N/C norm	FPMA/B norm	$N_{\rm H}$ (10^{22}cm^{-2})	Γ or kT (keV) (14)	Norm (10^{-5}) (15)	Line En. (keV) (16)	Line Eq. (keV) (17)	Line norm (10^{-6}) (18)	χ^2_ν/dof	Bin (σ)	Comments
3	`PL`	$3.4^{+1.0}_{-0.7}$	$1.04^{+0.04}_{-0.03}$	12±2	1.71±0.06	$6.7^{+1.0}_{-0.6}$				1.02/263	3,5	*Chandra* only includes point source while *NuSTAR* includes extended emission. See Gotthelf et al. (2014) for detailed analysis.
4	`PCA*(PL+G)`	$0.59^{+0.10}_{-0.09}$	$0.92^{+0.15}_{-0.13}$	$0.35^{+0.11}_{-0.10}$	2.34±0.22	56^{+26}_{-17}	$6.65^{+0.10}_{-0.06}$	$0.9^{+0.2}_{-0.1}$	$6.2^{+2.4}_{-1.9}$	1.19/154	3,3	`pcfabs` reduces χ^2_ν by ≈0.2. For `PL`, $N_{\rm H,cvr}=6^{+2}_{-1}\times10^{22}$ cm^{-2}, cvrf= $0.77^{+0.06}_{-0.08}$. For `BR` and `AP`, $N_{\rm H,cvr}=5\pm2\times10^{22}$ cm^{-2}, cvrf= 0.5 ± 0.1.
	`PCA*(BR+G)`	$0.57^{+0.09}_{-0.08}$	$0.90^{+0.15}_{-0.12}$	0.14±0.08	$7.9^{+2.4}_{-1.7}$	24^{+4}_{-3}	$6.65^{+0.09}_{-0.06}$	0.8±0.2	$5.6^{+2.1}_{-1.8}$	1.20/154	3,3	
	`PCA*(AP+G)`	$0.56^{+0.04}_{-0.08}$	$0.90^{+0.16}_{-0.12}$	$0.13^{+0.09}_{-0.08}$	$7.4^{+2.1}_{-1.5}$	68^{+11}_{-9}	$6.56^{+0.12}_{-0.17}$	0.2±0.1	$2.1^{+2.2}_{-1.6}$	1.19/154	3,3	
5	`PL`	$1.3^{+0.5}_{-0.3}$	$0.9^{+0.3}_{-0.2}$	27^{+10}_{-8}	2.3±0.3	28^{+40}_{-16}	6.3-7.1	< 0.36	< 1.3	1.07/47	3,3	
	`BR`	$1.3^{+0.5}_{-0.3}$	$0.9^{+0.3}_{-0.2}$	21^{+8}_{-6}	10^{+5}_{-3}	9^{+5}_{-3}				1.07/47	3,3	
	`AP`	$1.2^{+0.5}_{-0.3}$	$0.9^{+0.3}_{-0.2}$	17^{+6}_{-5}	13^{+5}_{-3}	21^{+8}_{-7}				1.15/47	3,3	
6	`PL+G`	1.0±0.2	$0.9^{+0.3}_{-0.2}$	5±1	1.5±0.3	13^{+7}_{-4}	$6.5^{+0.3}_{-1.7}$	1.5±0.5	11^{+62}_{-5}	1.79/27	5,3	
	`BR+G`	$1.0^{+0.3}_{-0.2}$	0.98±0.25	$4.3^{+0.9}_{-1.5}$	> 15	18^{+3}_{-2}	$6.5^{+0.4}_{-0.3}$	1.3±0.4	10^{+7}_{-5}	1.72/27	5,3	
	`AP+G`	1.0±0.2	$1.0^{+0.3}_{-0.2}$	$4.3^{+0.9}_{-0.7}$	> 15	51^{+9}_{-6}	6.4±0.4	1.2±0.5	9^{+6}_{-5}	1.69/27	5,3	
7	`PL+G`	1.0±0.2	$0.8^{+0.2}_{-0.1}$	15^{+3}_{-2}	$3.4^{+0.4}_{-0.3}$	220^{+80}_{-90}	6.76±0.12	0.65±0.20	$2.1^{+1.1}_{-0.9}$	0.92/75	2.5,2.5	`apec` abundance = 0.5±0.3. NARCS 1278 flux is 30% of total (Rahoui et al. 2014).
	`BR+G`	1.0±0.2	$0.9^{+0.2}_{-0.1}$	11^{+2}_{-1}	$3.4^{+0.7}_{-0.6}$	32^{+6}_{-7}	6.76±0.12	0.5±0.2	$1.8^{+1.1}_{-0.9}$	0.93/75	2.5,2.5	
	`AP`	1.0±0.2	$0.9^{+0.2}_{-0.1}$	11±2	$3.2^{+0.8}_{-0.5}$	100^{+30}_{-25}				0.89/77	2.5,2.5	
8	`PL`	1.0±0.2	–	14^{+7}_{-5}	1.8±0.2	18^{+15}_{-8}	6.3-7.1	< 0.26	<1.9	1.01/27	3,5	Only FPMA used.
	`BR`	1.0±0.2	–	12^{+5}_{-4}	25^{+22}_{-9}	15^{+5}_{-4}				1.03/27	3,5	
	`AP`	1.0±0.2	–	10^{+4}_{-3}	> 21	44^{+11}_{-10}				1.14/27	3,5	
9	`PL+G`	$0.9^{+0.3}_{-0.2}$	$0.9^{+0.3}_{-0.2}$	7^{+3}_{-2}	1.5±0.3	9^{+7}_{-4}	6.5±1.2	0.6±0.4	3^{+25}_{-2}	0.84/29	3,2.5	
	`BR+G`	$0.9^{+0.3}_{-0.2}$	$0.9^{+0.3}_{-0.2}$	7^{+2}_{-1}	> 15	11^{+6}_{-3}	$6.4^{+0.7}_{-0.3}$	0.5±0.3	3^{+8}_{-2}	0.83/29	3,2.5	
	`AP+G`	$0.8^{+0.3}_{-0.2}$	0.9±0.2	7^{+2}_{-1}	> 15	33^{+8}_{-6}	$6.4^{+0.5}_{-0.4}$	0.4±0.2	$2.2^{+2.7}_{-1.7}$	0.82/29	3,2.5	
10	`PL`	–	$0.9^{+0.6}_{-0.3}$	28	$4.1^{+0.9}_{-0.8}$	1800^{+6400}_{-1400}	6.3-7.1	< 0.61	< 4.2	1.09/10	2	$N_{\rm H}$ set to values from Tomsick et al. (2014)
	`BR`	–	$0.9^{+0.6}_{-0.3}$	17	3^{+2}_{-1}	70^{+100}_{-40}				1.14/10	2	
	`AP`	–	$0.9^{+0.6}_{-0.4}$	17	$1.9^{+5.0}_{-0.7}$	330^{+800}_{-290}				1.77/10	2	
11	`PL`	5^{+7}_{-2}	$1.3^{+0.9}_{-0.8}$	11^{+11}_{-9}	2.3±0.4	$2.4^{+6.1}_{-2.0}$				1.32/42	3,3	
	`BR`	6^{+21}_{-3}	$1.3^{+1.1}_{-1.0}$	< 14	10^{+6}_{-3}	$0.7^{+0.9}_{-0.6}$	6.3-7.1	< 0.35	< 0.1	1.27/42	3,3	
	`AP`	17^{+15}_{-12}	$1.4^{+3.4}_{-0.6}$	< 5	14^{+5}_{-3}	$0.6^{+1.6}_{-0.3}$				1.33/42	3,3	

Spectral Fitting Results for *NuSTAR* Sources (continued)

Src No.	Model `tbabs*X`	N/C norm	FPMA/B norm	$N_{\rm H}$ (10^{22}cm^{-2})	Γ or kT (keV)	Norm (10^{-5})	Line En. (keV)	Line Eq. (keV)	Line norm (10^{-6})	χ^2_ν/dof	Bin (σ)	Comments
12	PL+G	$1.1^{+0.5}_{-0.3}$	$1.0^{+0.4}_{-0.3}$	20^{+9}_{-6}	2.4±0.5	14^{+26}_{-9}	$6.78^{+0.14}_{-0.12}$	1.2±0.4	$1.7^{+1.2}_{-0.8}$	1.14/33	2.5,2.5	
	BR+G	$1.0^{+0.5}_{-0.3}$	$1.0^{+0.4}_{-0.3}$	16^{+7}_{-5}	9^{+8}_{-3}	5±2	$6.77^{+0.13}_{-0.12}$	$1.2^{+0.5}_{-0.3}$	$1.6^{+1.2}_{-0.8}$	1.17/33	2.5,2.5	
	AP	$1.1^{+0.5}_{-0.3}$	$1.0^{+0.4}_{-0.3}$	19^{+7}_{-5}	6^{+3}_{-1}	17^{+8}_{-6}				1.21/36	2.5,2.5	
13	PL	$1.5^{+1.1}_{-0.6}$	$1.0^{+0.7}_{-0.4}$	9^{+17}_{-6}	1.0±0.5	$0.7^{+1.8}_{-0.5}$	6.3−7.1	< 2.7	< 3.4	1.22/23	2,2	
	BR	$1.6^{+1.1}_{-0.6}$	$1.0^{+0.7}_{-0.4}$	11^{+11}_{-6}	> 31	$2.9^{+2.2}_{-0.4}$				1.25/23	2,2	
	AP	1.6±0.7	$1.0^{+0.7}_{-0.4}$	13^{+24}_{-7}	> 21	7^{+1}_{-3}				1.28/23	2,2	
14	PL+G	$0.7^{+0.2}_{-0.1}$	–	29^{+9}_{-7}	$4.1^{+1.2}_{-0.9}$	760^{+5700}_{-610}	$6.59^{+0.08}_{-0.06}$	1.8±0.5	6^{+3}_{-2}	1.07/28	3,2.5	Only FPMB used.
	BR+G	$0.7^{+0.2}_{-0.1}$	–	22^{+7}_{-5}	$2.4^{+1.4}_{-0.9}$	60^{+130}_{-30}	$6.59^{+0.10}_{-0.06}$	$1.7^{+0.6}_{-0.4}$	5^{+3}_{-2}	1.08/28	3,2.5	
	AP	0.8±0.2	–	25^{+7}_{-5}	$2.1^{+0.9}_{-0.5}$	190^{+240}_{-90}				1.11/31	3,2.5	
15	PL	$1.9^{+1.4}_{-0.8}$	$0.7^{+0.4}_{-0.3}$	< 0.4	2.6±0.4	13^{+6}_{-4}	6.3-7.1	< 1.7	< 2.1	0.75/20	3,2	
	BR	$1.8^{+1.1}_{-0.8}$	$0.6^{+0.3}_{-0.2}$	< 0.08	$2.9^{+1.0}_{-0.7}$	11±2				0.90/20	3,2	
	AP	$1.8^{+1.1}_{-0.8}$	$0.6^{+0.3}_{-0.2}$	< 0.10	$2.9^{+0.8}_{-0.7}$	28^{+9}_{-7}				0.82/19	3,2	
16	PL	$1.6^{+0.7}_{-0.5}$	$0.7^{+0.3}_{-0.2}$	19^{+6}_{-5}	$2.9^{+0.6}_{-0.5}$	130^{+240}_{-80}				1.05/24	3,2.5	Harder spectrum than found by Bodaghee et al. (2014) due to different background regions.
	BR	$1.6^{+0.6}_{-0.5}$	$0.7^{+0.3}_{-0.2}$	14^{+4}_{-3}	5^{+3}_{-1}	25^{+14}_{-8}	6.3-7.1	< 0.8	< 4.8	0.95/24	3,2.5	
	AP	$1.2^{+0.5}_{-0.4}$	0.7±0.2	13±3	6^{+4}_{-2}	58^{+27}_{-15}				1.06/24	3,2.5	
17	PL	$1.1^{+1.2}_{-0.5}$	$0.8^{+0.6}_{-0.4}$	21^{+32}_{-16}	$2.0^{+1.0}_{-0.8}$	6^{+65}_{-5}	6.3-7.1	< 1.0	< 1.3	0.94/13	2,2	
	BR	$1.1^{+1.3}_{-0.5}$	$0.8^{+0.6}_{-0.4}$	16^{+24}_{-12}	> 6	3^{+6}_{-2}				0.95/13	2,2	
	AP	$1.1^{+1.3}_{-0.5}$	$0.8^{+0.6}_{-0.4}$	14^{+17}_{-10}	> 8	9^{+9}_{-5}				0.94/13	2,2	
18	PL	$1.1^{+0.6}_{-0.5}$	$0.8^{+0.7}_{-0.4}$	19^{+9}_{-6}	$2.6^{+1.0}_{-0.8}$	50^{+260}_{-40}				1.87/13	3,2	
	BR	$1.1^{+0.6}_{-0.4}$	$0.8^{+0.7}_{-0.4}$	16^{+7}_{-4}	6^{+11}_{-3}	16^{+19}_{-6}	6.3-7.1	< 0.9	< 3	1.81/13	3,2	
	AP	$1.0^{+0.5}_{-0.4}$	$0.8^{+0.8}_{-0.4}$	13^{+7}_{-3}	9^{+24}_{-6}	33^{+51}_{-8}				1.97/13	3,2	
19	PL	1.0±0.3	$1.2^{+0.6}_{-0.4}$	$1.7^{+0.8}_{-0.6}$	$1.7^{+0.3}_{-0.4}$	4±2				1.66/25	3,3	N/C=$0.8^{+0.3}_{-0.2}$ for *Chandra* Obs 7591.
	BR	$1.0^{+0.4}_{-0.2}$	$1.1^{+0.6}_{-0.3}$	$1.4^{+0.5}_{-0.4}$	13^{+18}_{-5}	$4.0^{+0.8}_{-0.6}$				1.44/25	3,3	
	AP	1.0±0.3	$1.1^{+0.6}_{-0.3}$	$1.4^{+0.5}_{-0.4}$	11^{+18}_{-4}	12±2	6.3-7.1	< 1.3	< 2.4	1.44/25	3,3	
20	PL	1	1	70^{+130}_{-50}	$2.6^{+2.1}_{-1.4}$	52^{+15000}_{-50}	6.3-7.1	< 0.6	< 6.4	1.26/11	2,2	If the cross-normalization constant between *Chandra* and *NuSTAR* is left as a free parameter, $N/C > 2$ at 90% confidence.
	BR	1	1	60^{+90}_{-40}	> 3	8^{+80}_{-5}				1.31/11	2,2	
	AP	1	1	50^{+50}_{-30}	> 6	18^{+27}_{-8}				1.30/11	2,2	
21	PL	0.9±0.2	–	26^{+9}_{-7}	$2.6^{+0.5}_{-0.4}$	120^{+200}_{-70}	6.3-7.1	< 0.5	< 4.6	1.01/47	3,3	Only FPMB used. Point source (NARCS 402) flux is 20±5% of total.
	BR	0.9±0.2	–	20^{+7}_{-5}	8^{+5}_{-2}	31^{+15}_{-9}				1.04/47	3,3	
	AP	0.8±0.2	–	17^{+5}_{-4}	10^{+7}_{-3}	71^{+22}_{-16}				1.13/47	3,3	
22	PL	$1.7^{+1.5}_{-0.8}$	1	13^{+12}_{-7}	$2.0^{+1.3}_{-1.2}$	$5.1^{+41}_{-4.4}$				1.92/10	2,2	
	BR	$1.6^{+1.4}_{-0.8}$	1	11^{+10}_{-5}	> 4	3^{+6}_{-1}				1.91/10	2,2	
	AP	$1.8^{+1.3}_{-0.7}$	1	13^{+13}_{-5}	5^{+23}_{-3}	12^{+24}_{-6}	6.3-7.1	< 3.8	< 4.4	1.67/10	2,2	
23	PL	$1.7^{+2.1}_{-0.9}$	1	7^{+65}_{-5}	$1.8^{+2.0}_{-0.8}$	$1.6^{+340}_{-1.3}$				0.83/6	2,2	
	BR	$1.7^{+2.0}_{-0.9}$	1	6^{+49}_{-4}	> 4	$1.5^{+14.5}_{-0.9}$				0.75/6	2,2	
	AP	$1.7^{+2.0}_{-0.9}$	1	7^{+29}_{-5}	> 5	$4.6^{+13}_{-2.6}$	6.3-7.1	< 3.9	< 2.9	0.64/6	2,2	

Spectral Fitting Results for *NuSTAR* Sources (continued)

Src No.	Model `tbabs*X`	N/C norm	FPMA/B norm	$N_{\rm H}$ (10^{22}cm^{-2})	Γ or kT (keV)	Norm (10^{-5})	Line En. (keV)	Line Eq. (keV)	Line norm (10^{-6})	χ^2_ν/dof	Bin (σ)	Comments
24	PL	0.7±0.3	1	28^{+12}_{-8}	$5.0^{+2.2}_{-1.4}$	1180^{+41220}_{-1070}	6.3-7.1	< 16	< 6.2	1.25/23	2,2	
	BR	0.7±0.3	1	20^{+8}_{-6}	$1.7^{+1.3}_{-0.7}$	50^{+290}_{-30}				1.33/23	2,2	
	AP	0.7±0.3	1	24^{+7}_{-6}	$1.4^{+0.8}_{-0.4}$	160^{+500}_{-110}				1.32/23	2,2	
25	PL	$1.3^{+1.3}_{-0.6}$	–	$3.1^{+3.8}_{-2.8}$	1.8±0.7	$1.9^{+4.2}_{-1.5}$				1.14/8	2,2	Only FPMA used.
	BR	$1.3^{+1.7}_{-0.6}$	–	$2.3^{+3.0}_{-2.2}$	> 6	$1.7^{+1.1}_{-1.0}$				1.05/8	2,2	
	AP	$1.3^{+1.7}_{-0.6}$	–	$2.3^{+2.9}_{-2.1}$	> 6	5±3	6.3-7.1	< 2.1	< 1.8	1.02/8	2,2	
26	PL	$1.3^{+2.8}_{-0.7}$	1	30^{+35}_{-23}	$1.5^{+1.0}_{-0.9}$	$2.8^{+30}_{-2.5}$	6.3-7.1	< 1.2	< 1.9	1.57/10	2,2	
	BR	$1.3^{+2.6}_{-0.6}$	1	28^{+31}_{-21}	> 9	$3.5^{+5.5}_{-2.5}$				1.58/10	2,2	
	AP	$1.3^{+2.5}_{-0.6}$	1	28^{+28}_{-19}	> 13	11^{+12}_{-8}				1.59/10	2,2	
27	PL	$4.4^{+5.9}_{-3.5}$	1	< 23	$0.9^{+0.8}_{-0.4}$	$0.18^{+2.68}_{-0.09}$	6.3-7.1	< 1.1	< 0.5	0.85/8	2,2	
	BR	$6.3^{+6.2}_{-5.2}$	1	< 27	> 23	$0.7^{+6.0}_{-0.3}$				0.95/8	2,2	
	AP	$7.4^{+10.2}_{-2.7}$	1	< 34	> 20	$1.4^{+13.8}_{-0.7}$				1.08/8	2,2	

Notes: Errors provided are 90% confidence intervals, except for errors on the line equivalent widths which are 1σ confidence intervals.
(2) For sources NNR 1-3, which have been analyzed in more detail in other papers, we present the results of simplified models, used to derive the fluxes and conversion factors in Table 2.22. For all other sources, we present fits using power-law (`PL`), bremsstrahlung (`BR`), and collisionally-ionized apec models (`AP`). Some models include a Gaussian line (`G`) or partial covering absorption (`PCA`). The best-fitting model for each source is written in bold text.
(3) Multiplicative `constant` included in all spectral models. The constant is set to 1.0 for *Chandra* and, if enough spectral bins are available, it is allowed to vary independently for *NuSTAR* FPMA and FPMB. N/C provides the ratio of the *NuSTAR* FPMA constant relative to *Chandra*.
(4) Ratio of the FPMA to FPMB fitting constants, providing the cross-calibration of the two *NuSTAR* modules. For sources with insufficient photon statistics, this ratio is set to 1.0.
(11) Reduced χ^2 statistic and degrees of freedom for the best-fitting model.
(12) Minimum significance of bins for *Chandra*, *NuSTAR* spectra.
(16-18) The central energy, equivalent width, and normalization of a Gaussian model accounting for iron line emission. In cases where an iron line is clearly visible in the spectrum, a Gaussian line (`G`) is included in the model; otherwise, we provide the results of the best-fit models without a Gaussian line and an upper limit to the Fe line equivalent width derived by adding a Gaussian component as described in § 2.3.10.

Table 2.22: Spectrally Derived Fluxes of *NuSTAR* Sources

	Ph. Flux (10^{-6}cm^{-2}s^{-1})			Abs. Flux (10^{-14}erg cm^{-2}s^{-1})			Ph. flux to unabs. flux (10^{-9}erg/ph)		
Src No.	*Chandra* 2-10 keV	*NuSTAR* 3-10 keV	*NuSTAR* 10-20 keV	*Chandra* 2-10 keV	*NuSTAR* 3-10 keV	*NuSTAR* 10-20 keV	*Chandra* 2-10 keV	*NuSTAR* 3-10 keV	*NuSTAR* 10-20 keV
(1)	(2)	(3)	(4)	(5)	(6)	(7)	(8)	(9)	(10)
1	–	614000±300	19950^{+30}_{-50}	–	490300^{+200}_{-300}	39590^{+60}_{-100}	–	12.2	20.9
2	2200^{+200}_{-500}	1500^{+100}_{-300}	1700^{+500}_{-700}	2500^{+300}_{-600}	1700^{+200}_{-300}	4000^{+1000}_{-2000}	27.0	24.7	26.3
3	$19^{+0.2}_{-0.3}$	$56.0^{+0.3}_{-1.9}$	$22.8^{+0.1}_{-0.8}$	16±2	$52.1^{+0.2}_{-1.8}$	$51.3^{+0.3}_{-1.9}$	14.4	12.6	23.4
4	101^{+3}_{-7}	43^{+1}_{-4}	$7.0^{+0.4}_{-0.7}$	71^{+2}_{-6}	36^{+1}_{-3}	$15.3^{+0.8}_{-1.6}$	9.3	9.7	22.3
5	16^{+2}_{-4}	$21.8^{+0.4}_{-3.6}$	$7.1^{+0.2}_{-1.4}$	15^{+1}_{-4}	$20.6^{+0.3}_{-3.4}$	$15.7^{+0.3}_{-3.0}$	26.5	19.0	24.1
6	82^{+3}_{-7}	68^{+4}_{-9}	21^{+2}_{-5}	68^{+3}_{-7}	63^{+3}_{-8}	47^{+4}_{-11}	9.9	10.2	22.7
7	42^{+1}_{-3}	36^{+1}_{-3}	$1.7^{+0.2}_{-0.4}$	32^{+1}_{-3}	$29.1^{+0.9}_{-2.5}$	$3.3^{+0.4}_{-0.8}$	14.3	11.7	20.7
8	43^{+3}_{-7}	$40.3^{+0.6}_{-6.4}$	$16.6^{+0.3}_{-2.6}$	39^{+3}_{-6}	$37.8^{+0.5}_{-5.8}$	$37.5^{+0.8}_{-6.0}$	15.7	13.4	23.5
9	43±3	33^{+2}_{-3}	$12.5^{+0.9}_{-1.1}$	37±3	31±2	28±2	11.2	10.9	22.9
10	–	55^{+3}_{-24}	$3.6^{+0.3}_{-2.1}$	–	44^{+2}_{-19}	$7.5^{+0.7}_{-4.4}$	–	23.2	23.0
11	$2.6^{+0.6}_{-1.1}$	$10.3^{+0.2}_{-4.1}$	$2.15^{+0.03}_{-0.98}$	$2.0^{+0.6}_{-0.9}$	$9.0^{+0.2}_{-3.5}$	$4.65^{+0.06}_{-2.13}$	9.8	10.0	22.0
12	$10.4^{+0.8}_{-3.9}$	$10.4^{+0.2}_{-3.1}$	$2.35^{+0.03}_{-0.8}$	9^{+2}_{-3}	$9.7^{+0.1}_{-2.8}$	$5.18^{+0.06}_{-1.70}$	20.7	15.6	23.5
13	$6.4^{+0.9}_{-2.8}$	$8.4^{+0.2}_{-3.4}$	$5.8^{+0.1}_{-2.4}$	6^{+1}_{-3}	$8.27^{+0.09}_{-3.38}$	$13.5^{+0.2}_{-5.5}$	12.5	11.9	23.7
14	$28.3^{+0.9}_{-4.1}$	20^{+1}_{-4}	$1.1^{+0.2}_{-0.4}$	$23.5^{+0.9}_{-3.7}$	$16.9^{+0.9}_{-3.4}$	$2.4^{+0.4}_{-0.8}$	48.5	22.5	23.1
15	25±4	30^{+3}_{-5}	$3.6^{+0.5}_{-0.9}$	14^{+3}_{-2}	23^{+3}_{-4}	8^{+1}_{-2}	5.9	7.8	21.7
16	41^{+2}_{-7}	69^{+4}_{-13}	$9.1^{+0.9}_{-2.2}$	34^{+2}_{-6}	60^{+3}_{-11}	19^{+2}_{-5}	16.0	13.1	21.8
17	8^{+2}_{-3}	$9.5^{+0.5}_{-2.8}$	$3.6^{+0.2}_{-1.1}$	7^{+2}_{-3}	$9.0^{+0.4}_{-2.6}$	$8.2^{+0.5}_{-2.6}$	20.3	15.9	23.8
18	26^{+1}_{-11}	31^{+3}_{-12}	$5.1^{+0.6}_{-2.5}$	22^{+1}_{-10}	28^{+2}_{-11}	11^{+1}_{-5}	17.0	13.9	22.2
19	15^{+3}_{-4}	$10.1^{+0.4}_{-1.8}$	$1.9^{+0.3}_{-0.9}$	11^{+2}_{-3}	$8.8^{+0.4}_{-1.7}$	$4.2^{+0.7}_{-2.0}$	7.8	9.0	21.8
20	$7.3^{+0.2}_{-5.5}$	$7.3^{+0.1}_{-5.2}$	$4.4^{+0.2}_{-2.5}$	$7.8^{+0.2}_{-5.8}$	$7.79^{+0.09}_{-5.52}$	$9.7^{+0.6}_{-5.6}$	80.5	52.4	28.3
21	49^{+1}_{-15}	$43.4^{+0.9}_{-12.2}$	$11.5^{+0.4}_{-4.2}$	$43.9^{+0.8}_{-14.1}$	$40.0^{+0.6}_{-11.3}$	25^{+1}_{-9}	27.9	19.1	23.9
22	$8.4^{+0.5}_{-4.9}$	$13.4^{+0.1}_{-9.2}$	$1.7^{+0.3}_{1.6}$	$7.1^{+0.4}_{-4.6}$	$12.0^{+0.1}_{-8.3}$	$3.6^{+0.8}_{-3.3}$	14.9	12.7	21.8
23	6^{+1}_{-4}	$7.9^{+0.1}_{-4.9}$	$1.9^{+0.2}_{-1.8}$	5^{+1}_{-3}	$7.1^{+0.1}_{-4.7}$	$4.3^{+0.6}_{-4.0}$	11.1	10.7	22.3
24	$9.8^{+0.2}_{-3.0}$	$6.3^{+0.7}_{-2.4}$	$0.16^{+0.03}_{-0.09}$	$6.9^{+0.2}_{-2.3}$	$4.7^{+0.5}_{-1.8}$	$0.32^{+0.06}_{-0.18}$	78.9	25.8	22.5
25	8^{+1}_{-5}	$7.6^{+0.1}_{-3.7}$	$1.8^{+0.2}_{-1.6}$	6^{+1}_{-4}	$6.7^{+0.2}_{-3.3}$	$4.0^{+0.6}_{-3.5}$	8.4	9.4	22.1

Spectrally Derived Fluxes of *NuSTAR* Sources (continued)

	Ph. Flux (10^{-6}cm^{-2}s^{-1})			Abs. Flux (10^{-14}erg cm^{-2}s^{-1})			Ph. flux to unabs. flux (10^{-9}erg/ph)		
Src No.	*Chandra* 2-10 keV	*NuSTAR* 3-10 keV	*NuSTAR* 10-20 keV	*Chandra* 2-10 keV	*NuSTAR* 3-10 keV	*NuSTAR* 10-20 keV	*Chandra* 2-10 keV	*NuSTAR* 3-10 keV	*NuSTAR* 10-20 keV
26	$6.1^{+0.7}_{-3.0}$	$7.8^{+0.2}_{-4.2}$	$5.4^{+0.1}_{-3.1}$	$6.3^{+0.8}_{-3.1}$	$8.0^{+0.1}_{-4.2}$	$12.4^{+0.2}_{-7.1}$	23.9	19.7	25.0
27	$3.0^{+0.2}_{-2.0}$	$10.1^{+0.6}_{-5.7}$	$6.2^{+0.3}_{-4.2}$	$2.4^{+0.2}_{-1.6}$	$9.5^{+0.4}_{-5.2}$	$14.3^{+0.7}_{-9.6}$	8.1	9.4	23.2
29*	2.1±0.7	$24.9^{+0.1}_{-4.6}$	$8.79^{+0.06}_{-2.07}$	1.8±0.6	$22.6^{+0.1}_{-4.1}$	$19.8^{+0.1}_{-4.7}$	13.1	11.8	23.2

Notes: These fluxes and conversion factors are determined from spectral fitting. The *NuSTAR* fluxes represent the average of the FPMA and FPMB fluxes. Errors provided are 1σ confidence intervals.

(*) Due to the poor photon statistics of NNR 29, it was not possible to perform spectral fitting in the same way as for the other sources. Adopting an absorbed power-law model for this source with $\Gamma = 1.8$ and $N_{\rm H} = 10^{23}$ cm^{-2}, we determined the *Chandra* and *NuSTAR* fluxes using the C-statistic (see § 2.3.10 for more details).

2.3.11 Classification of *NuSTAR* Sources

The X-ray spectral and timing properties of the *NuSTAR* sources, as well as information about their optical and infrared counterparts, can help identify their physical nature. The three brightest sources in the *NuSTAR* Norma survey are well-studied and classified; 4U 1630-472 (NNR 1) is a black hole LMXB (e.g. Barret et al. 1996; Klein-Wolt et al. 2004), IGR J16393-4643 (NNR 2) is a neutron star HMXB (Bodaghee et al. 2006; B16), and HESS J1640-465 (NNR 3) is a pulsar and associated pulsar wind nebula (G14;Archibald et al. 2016). Here we present the most likely classifications of the fainter *NuSTAR* sources and their hard X-ray properties.

Colliding wind binaries

Two of the *NuSTAR* sources in the Norma region are likely colliding wind binaries (CWBs), NNR 7 and 14.

NNR 7 actually consists of two *Chandra* sources blended together due to *NuSTAR*'s PSF. In *Chandra* ObsID 11008, where these two sources are resolved, they exhibit very similar spectral properties ($N_{\rm H}$ and kT values are consistent at $<1\sigma$ level), but the 0.5–10 keV flux of NARCS 1279 is 2 times higher than the flux of NARCS 1278. These sources are blended in *Chandra* ObsIDs 12508 and 12509 because they are far off-axis, and the combined flux of the two sources is a factor of 3 higher in these later observations. Spectroscopic follow-up of the near-IR counterparts of both of these *Chandra* sources revealed they are Wolf-Rayet stars of spectral type WN8 (Rahoui et al. 2014). These stars belong to the young massive cluster Mercer 81 (Mercer et al. 2005) located at a distance of 11±2 kpc (Davies et al. 2012). The *Chandra* spectra of these sources were better fit by thermal plasma models than power-law models, suggesting that these sources were more likely to be CWBs than HMXBs with compact objects accreting from the powerful Wolf-Rayet stellar winds.

The *NuSTAR* data provides even stronger support for the CWB hypothesis for NNR 7. Joint fitting of the *Chandra* (from NARCS) and *NuSTAR* spectra of these blended sources reveal that they fall off steeply above 1 keV and show prominent Fe line emission, primarily due to Fe XXV based on its 6.76±0.1 keV line energy (House 1969). The spectra are best fit by an `apec` thermal model with $kT = 3.2^{+0.8}_{-0.5}$ keV and a metal abundance of 0.5±0.3 solar, or a steep power-law model with $\Gamma = 3.4^{+0.4}_{-0.3}$ and Fe line emission with 650 ± 20 eV equivalent width. These spectral properties rule out the possibility that NNR 7 could be an accreting HMXB, since accreting HMXBs have harder power-law spectra and Fe I Kα emission at 6.4 keV, typically with equivalent widths < 100 eV (Torrejón et al. 2010). Elshamouty et al. (2016) found that, in quiescence, one neutron star HMXB, V0332+53 exhibits a soft spectrum ($\Gamma \approx 4$ or $kT_{\rm BB} \approx 0.4$ keV) without prominent Fe lines; if this spectrum is typical of quiescent HMXBs, then we can also rule out the possibility that NNR 7 is a quiescent HMXB given its hard spectrum and prominent Fe emission. The unabsorbed 0.5–10 keV flux of NNR 7 based on the combined NARCS and *NuSTAR* spectrum[16] is $1.20^{+0.04}_{-0.12} \times 10^{-12}$ erg cm^{-2} s^{-1}.

[16]The unabsorbed 0.5–10 keV flux reported here for NARCS 1278 and 1279 combined is higher than that

Adopting the 0.5–10 keV flux ratio for NARCS 1278 and 1279 and the bolometric luminosities of their Wolf-Rayet counterparts calculated by Rahoui et al. (2014), we find that their respective X-ray luminosities are 5×10^{33} erg s^{-1} and 1.2×10^{34} erg s^{-1}, and they have $L_X/L_{\rm bol} = 1.3 \times 10^{-6}$ and 8×10^{-7}, respectively.

Isolated high-mass stars are known to be X-ray emitters, but their spectra typically have $kT \sim 0.5$ keV and their 0.5–10 keV luminosities follow the scaling relation $L_X/L_{\rm bol} \approx 10^{-7}$ (e.g. Berghoefer et al. 1997; Sana et al. 2006). The harder X-ray emission and higher $L_X/L_{\rm bol}$ exhibited by NNR 7 have been observed from the wind-wind shocks in CWBs (Zhekov & Skinner 2000; Portegies Zwart et al. 2002) and the magnetically channeled shocks of high-mass stars with ∼kG fields (Gagné et al. 2005; Petit et al. 2013). For NNR 7, a CWB nature is more likely given the strength of the Fe line at 6.7 keV; magnetic high-mass stars tend to exhibit weak Fe XXV line emission (Schulz et al. 2000; Schulz et al. 2003), while the Fe XXV lines in CWB spectra can have equivalent widths as large as $\sim 1-2$ keV (Viotti et al. 2004; Mikles et al. 2006). The X-ray spectrum of NNR 7 exhibits substantial absorption corresponding to $N_{\rm H} = 1.1 \pm 0.2 \times 10^{23}$ cm^{-2}, which is in excess of the integrated interstellar absorption along the line-of-sight ($N_{\rm HI+H_2} = 7.8 \times 10^{22}$ cm^{-2}). The excess absorption measured in the X-ray spectrum of NNR 7 could either be due to inhomogeneities in the ISM or local absorption, which is observed in some CWBs, such as η Carinae (Hamaguchi et al. 2007). Finally, X-ray variability is more common in CWBs than isolated high-mass stars (Corcoran 1996). The X-ray flux variations displayed by CWBs are primarily associated with the orbital period of the binary and can be as large as a factor of ≈ 20 (Pittard et al. 1998; Corcoran 2005). Thus, the X-ray variability exhibited by NNR 7 provides further evidence of its CWB origin.

NNR 14 shares many similarities with NNR 7 and is also likely to be a CWB. The near-IR spectrum of the counterpart of NNR 14 shows emission lines typical of a Wolf-Rayet star of spectral type WN7 in the K-band, but the H-band spectrum lacks the emission lines expected for this spectral type. Overall, the near-IR spectrum may be consistent with an O3I star (Corral-Santana et al., in prep). Its X-ray spectrum is well fit by an `apec` thermal model with $kT = 2.1^{+0.9}_{-0.5}$ keV or a power-law with $\Gamma = 4.1^{+1.2}_{-0.9}$ and Fe line emission centered at $6.59^{+0.08}_{-0.06}$ keV (consistent with Fe XXV 6.7 keV emission) with a very high equivalent width of 1.8 ± 0.5 keV, making it very similar to the CWB candidate CXO J174536.1-285638 (Mikles et al. 2006). Furthermore, NNR 14 exhibits a very high X-ray absorbing column ($N_{\rm H} = 2.9^{+0.9}_{-0.7} \times 10^{23}$ cm^{-2}) that is well in excess of the integrated interstellar column density along the line-of-sight ($N_{\rm HI+H_2} = 8 \times 10^{22}$ cm^{-2}); this amount of absorption local to the X-ray source is larger than for NNR 7 but still within the range observed in CWBs (Hamaguchi et al. 2007). NNR 14 is coincident with G338.0-0.1, an HII region most likely located at a distance of 14.1 kpc (Wilson et al. 1970; Kuchar & Clark 1997; Jones & Dickey 2012). It would not be surprising for NNR 14 and G338.0-0.1 to be physically associated since HII regions are photoionized by high-mass stars and the extreme $N_{\rm H}$ along the line-of-sight to NNR 14 indicates it is likely located in the far Norma arm or beyond. Thus, adopting a distance of 14 kpc for NNR 14, its unabsorbed 3–10 keV luminosity is 10^{34} erg s^{-1}, which is

reported in Rahoui et al. (2014) because we account for the absorption due to the X-ray derived $N_{\rm H}$ while in Rahoui et al. (2014) only absorption attributed to the ISM is removed.

within the typical range for CWBs.

Supernova remnants and pulsar wind nebulae

In addition to HESS J1640-465, there are three other extended sources in the *NuSTAR* Norma survey, NNR 5, 8, and 21.

Jakobsen et al. (2014) identified the *Chandra* counterpart of NNR 5 as a pulsar wind nebula (PWN) candidate due to its bow-shock, cometary morphology and hard power-law spectrum. Although an AGN or LMXB origin cannot be ruled out, these possibilities were disfavored due to the lack of significant X-ray variability, both on short-term timescales during the *NuSTAR* observation and on long-term timescales between the *Chandra* and *NuSTAR* observations, separated by three years. Our search for pulsations in the *NuSTAR* data did not yield a detection that would have secured a PWN origin, but our search was only sensitive to high pulsed fractions $> 45\%$. A joint spectral fit to the *NuSTAR* and *Chandra* data, covering the point source and extended emission in both data sets, yielded a higher $N_{\rm H}$ value and steeper photon index than measured by Jakobsen et al. (2014). Our best fit photon index of $\Gamma = 2.3 \pm 0.3$ for a power-law model is possible for a pulsar/PWN ($\Gamma \sim 1-2$; Kargaltsev & Pavlov 2008), which is consistent with the earlier results, derived using *Chandra* and *XMM-Newton* data. However, the $N_{\rm H}$ value we measure ($2.7^{+1.0}_{-0.8} \times 10^{23}$ cm^{-2}) is higher than the integrated interstellar absorption along the line-of-sight ($N_{\rm H} = 8 \times 10^{22}$ cm^{-2}), indicating that NNR 5 is likely on the far side of the Galaxy and may be associated with the star-forming complexes located at ~ 10 kpc; this source may be subject to additional local absorption or lie within or behind molecular clouds.

The source NNR 8 is a region of extended emission with a centrally peaked morphology coincident with the CTB 33 supernova remnant (SNR) and HII complex located at a distance of $\sim$11 kpc and visible at radio wavelengths (Sarma et al. 1997). While NNR 8 may be associated with this complex, it notably does not overlap nearby SNR G337.0-0.1, as shown in Figure 2.28. This hard X-ray diffuse emission was discovered in an *XMM-Newton* field containing the soft gamma-ray repeater (SGR) 1627-41 (here NNR 24) and is attributed by Esposito et al. (2009) to either a galaxy cluster or a PWN. The joint *Chandra* and *NuSTAR* spectrum of NNR 8 is well-fit by an absorbed power-law model with a typical pulsar/PWN index of $\Gamma = 1.8 \pm 0.2$. In contrast, an absorbed bremsstrahlung model yields a temperature of $kT = 25^{+22}_{-9}$ keV in the 0.5–20 keV band, which is higher than expected for most galaxy clusters (Maughan et al. 2012). No pulsations were detected from NNR 8, but our search was only sensitive to periodic signals with very high pulsed fractions ($> 48\%$), leaving open the possibility of a pulsar embedded in diffuse PWN emission.

Assuming NNR 8 is a PWN, we can estimate the spin down energy loss of the pulsar from correlations based on the PWN X-ray luminosity and photon index. Since the high $N_{\rm H}$ ($1.4^{+0.7}_{-0.5} \times 10^{23}$ cm^{-2}) measured from the X-ray spectrum of NNR 8 indicates that it lies on the far side of the Galaxy and it is reasonable to expect a PWN to be in the vicinity of star-forming regions, we adopt the 11 kpc distance of the far Norma arm and CTB 33 for NNR 8 and calculate its unabsorbed 2–10 keV luminosity to be 1.0×10^{34} erg s^{-1}. Using

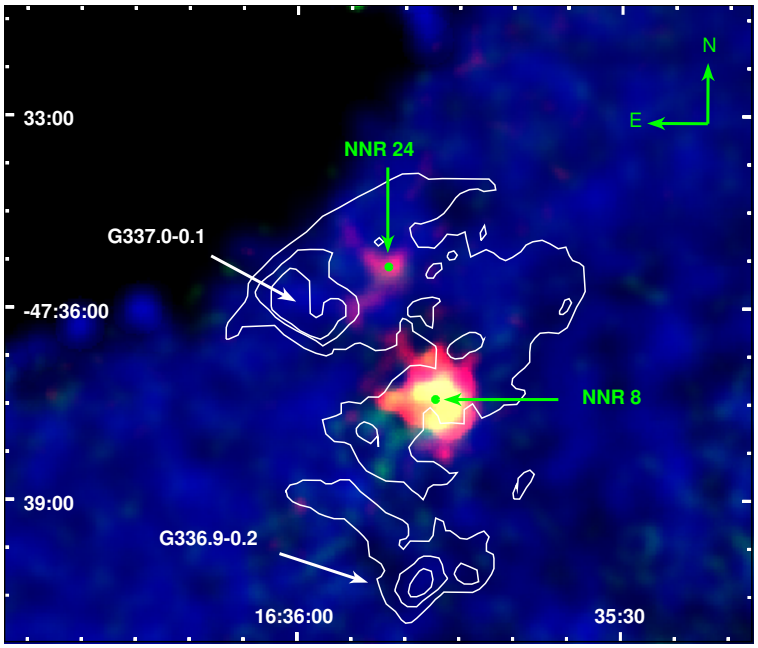

Figure 2.28: *NuSTAR* image of the region around NNR 8. The 3–10 keV band is shown in red, 10–20 keV in green, and 20–40 keV in blue. White contours show the radio continuum emission of the CTB 33 complex from Sarma et al. (1997). Green points denote the positions of *NuSTAR* sources. G337.0-0.1 is a confirmed supernova remnant while G336.9-0.2 is an HII region. It has been suggested that the magnetar, NNR 24, is associated with this SNR (Brogan et al. 2000). However, the extended emission of NNR 8 is clearly not coincident with G337.0-0.1 and its origin may be an unassociated PWN.

the correlation between 2–10 keV luminosity and spin down energy loss from Possenti et al. (2002), we estimate the pulsar $\dot{E} \approx 7 \times 10^{36}$ erg s^{-1}. The pulsar spin-down luminosity can also be estimated from the PWN photon index using correlations derived by Gotthelf (2003); the photon index of NNR 8 yields $\dot{E} \approx 1.4 \times 10^{37}$ erg s^{-1}, which is consistent with the value determined from the correlation of L_X and $\dot{E}$ given the statistical uncertainties of the X-ray luminosity and photon index of NNR 8. The fact that these estimates of $\dot{E}$ are consistent provides additional support in favor of a PWN origin for this source.

The extended emission of NNR 21 is associated with SNR G337.2+0.1, located at a distance of ~ 14 kpc. Using *Chandra* observations, Jakobsen (2013) found that the radial profile of the SNR exhibits a central compact source, suggesting a pulsar powering a PWN, as well as excess emission at a radius of $\approx 1\farcm8$, attributable to the SNR shell. The dearth of *NuSTAR* photons from the central point source does not allow for a significant detection of a pulsar signal, so we cannot confirm the PWN origin of NNR 21. *XMM-Newton* observations of this SNR revealed that it has a non-thermal spectrum which steepens further from the central core (Combi et al. 2006, hereafter C06), as is seen in many plerionic SNRs (e.g. IC 443, 3C 58, G21.5-0.9; Bocchino & Bykov 2001 and references therein). Spectral fitting of the

NuSTAR and *Chandra* data results in a higher column density ($N_{\rm H} = 2.6^{+0.9}_{-0.7} \times 10^{23}$ cm^{-2}) and steeper photon index ($\Gamma = 2.6^{+0.5}_{-0.4}$) than measured by C06 for the pulsar/PWN (central source and extended emission combined). The *Chandra/NuSTAR*-derived photon index, while consistent at the 90% confidence level with the *XMM* measured value ($\Gamma = 1.82 \pm 0.45$), is steeper than expected for a pulsar/PWN. We find that the unabsorbed 2–10 keV luminosity of NNR 21 is 3×10^{34} erg s^{-1}, and thus the $L_X - \dot{E}$ correlation from Possenti et al. (2002) yields a spin-down luminosity estimate of $\dot{E} \approx 1.5 \times 10^{37}$ erg s^{-1}. The spin-down luminosity that is estimated using the $\Gamma - \dot{E}$ correlation from Gotthelf (2003) is in good agreement if it is based on the *XMM*-derived $\Gamma = 1.8$ ($\dot{E} \approx 1.4 \times 10^{37}$ erg s^{-1}), but it is at odds if the *Chandra/NuSTAR*-derived Γ is adopted ($\dot{E} > 1.7 \times 10^{38}$ erg s^{-1}).[17]

Comparing our power-law fits of NNR 21 with the results of C06, the *Chandra/NuSTAR*-derived $N_{\rm H}$ is statistically higher than the $N_{\rm H} = 1.15 \pm 0.27 \times 10^{23}$ cm^{-2} measured by C06 for the whole PWN, but it is consistent at better than 90% confidence with the value C06 measure for the outer region of the PWN ($N_{\rm H} = 1.62 \pm 0.56 \times 10^{23}$ cm^{-2}), which excludes the central 12″-radius region; this central region has a much lower column density of $5.9 \pm 1.5 \times 10^{22}$ cm^{-2}. Even if we compare the results of our `apec` model fits with C06, the *Chandra/NuSTAR*-derived $N_{\rm H}$ is more consistent with the $N_{\rm H}$ value that C06 measure for the outer region rather than the whole PWN. One possible explanation for these spatial and temporal $N_{\rm H}$ variations is that the outer region of the PWN is interacting with a molecular cloud. This scenario would naturally explain the higher $N_{\rm H}$ measured in the outer region of the PWN compared to the central region by C06, and the increase in the average $N_{\rm H}$ measured for the whole PWN between the 2004 *XMM* observation and the 2011 *Chandra* observation could be attributed to a larger fraction of the PWN interacting with the dense interstellar medium as the PWN expands. Additional X-ray observations to obtain spatially resolved spectroscopy of NNR 21 are required to better understand the origin of the spectral variations exhibited by this SNR.

Magnetars

A known magnetar and a magnetar candidate are present in the *NuSTAR* Norma survey. NNR 24 is a known soft gamma-ray repeater, SGR 1627-41, which was discovered by the Burst and Transient Source Experiment (BATSE) when the source went into outburst in 1998 June (Woods et al. 1999). It has been suggested that this SGR is associated with the young SNR G337.0-0.1 in the CTB 33 complex (Hurley et al. 1999), shown in Figure 2.28. SGR 1627-41 last went into outburst in 2008 (Esposito et al. 2008) and it was found to have returned to quiescence by 2011 in NARCS observations (An et al. 2012). The cross-normalization constant from fitting the *NuSTAR* and *Chandra* spectra is consistent with 1.0 at 90% confidence, indicating that the magnetar persists in quiescence and has not significantly decreased in flux since 2011. We measure a photon index of $5.0^{+2.2}_{-1.4}$ which is steeper but still consistent with that measured by An et al. (2012) at 90% confidence. Assuming a distance of 11 kpc,

[17] The $\Gamma - \dot{E}$ correlation is only valid for $\Gamma < 2.36$, so we can only provide a lower bound on $\dot{E}$ for the *Chandra/NuSTAR*-derived $\Gamma = 2.6^{+0.5}_{-0.4}$.

based on the association with the CTB 33 complex, we find that NNR 24 has unabsorbed luminosities of 2.3×10^{33} erg s^{-1} in the 3–10 keV band and 5.2×10^{31} erg s^{-1} in the 10–20 keV band.

NNR 10, a transient source, may also be a magnetar. The long-term variability and spectral analysis of this source is described in detail in T14, and our spectral analysis yields consistent results. The flux of NNR 10 varies by more than a factor of 20 over a three-week period, with the peak of activity lasting between 11 hours and 1.5 days and having a soft spectrum with $\Gamma = 4.1^{+0.9}_{-0.8}$ or $kT = 3^{+2}_{-1}$ keV for a bremsstrahlung model. The high $N_{\rm H}$ measured from the X-ray spectrum of NNR 10 suggests that this source is located at $\gtrsim 10$ kpc and thus has a peak $L_X \gtrsim 10^{34}$ erg s^{-1} in the 2–10 keV band. As argued by T14, NNR 10 is most likely either a shorter than average outburst from a magnetar or an unusually bright flare from a chromospherically active binary.

Black hole binary candidate

Among the remaining *NuSTAR* Norma sources not discussed in § 2.3.11- 2.3.11, NNR 15 stands out as the only source showing clear short-timescale variability in the *NuSTAR* band and also having the lowest median energy. As can be seen in Figure 2.24, NNR 15 displays flaring behavior in the 3–20 keV band; during one flare lasting about 15 ks, the source flux increases by a factor of >6, and during a smaller flare lasting about 7 ks, the flux increases by a factor of >2. This source also shows variability on year-long timescales since the 3–10 keV flux measured in 2013 *NuSTAR* observations is a factor of 2 higher than the *Chandra* flux measured from 2011 observations. The *NuSTAR* and *Chandra* spectra are well-fit by an absorbed power-law model with very low $N_{\rm H}$, indicating that the source must reside within a few kiloparsecs, and $\Gamma = 2.6 \pm 0.4$ (or $kT = 2.9^{+1.0}_{-0.7}$ keV for a bremsstrahlung model). No Fe line is visible in the spectrum, but due to the limited photon statistics, we can only constrain the equivalent width of a potential Fe line feature to be < 1.7 keV, a loose constraint that does not help to distinguish between different types of X-ray sources. Assuming a distance of 2 kpc, NNR 15 has an average unabsorbed 3–20 keV luminosity of 1.5×10^{32} erg s^{-1}. Its optical/infrared counterpart has been identified as a mid-GIII star (Rahoui et al. 2014).

Based on these properties, we identify NNR 15 as a black hole LMXB candidate in quiescence, although an active binary (AB) or CV origin cannot be entirely ruled out. In quiescence, ABs typically have $L_X = 10^{29} - 10^{31.5}$ erg s^{-1} and $kT < 2$ keV (Dempsey et al. 1993) but they can exhibit flares with peak luminosities of $\sim 10^{32}$ erg s^{-1} and $kT \approx 10$ keV (Franciosini et al. 2001). However, AB flares tend to have very short rise times and long decay times (Pandey & Singh 2012), whereas the flares seen in NNR 15 appear to have more symmetric profiles. CVs have $L_X = 10^{29-33}$ erg s^{-1} and $kT = 1 - 25$ keV (e.g. Eracleous et al. 1991; Muno et al. 2004), with magnetic CVs being more luminous and spectrally harder than non-magnetic CVs (Barlow et al. 2006; Landi et al. 2009), so their properties are consistent with NNR 15. However, the flaring exhibited by NNR 15 is not typically seen in CVs. Non-magnetic CVs have outbursts that last several days and have recurrence times of weeks to months; intermediate polars (IPs) have outbursts of similar duration but

which are very rare (Hellier et al. 1997; Szkody et al. 2002), and polars exhibit flares with ∼hour-long durations but they tend to be very soft ($kT < 1$ keV; Choi et al. 1999; Still & Mukai 2001; Traulsen et al. 2010). The properties of NNR 15 are reminiscent of the quiescent state of V404 Cyg, a well-known LMXB hosting a black hole (BH; Makino et al. 1989; Casares et al. 1992; Shahbaz et al. 1996). Recent *NuSTAR* observations of V404 Cyg in quiescence show that, in the 3–25 keV band, its power-law spectrum has $\Gamma = 2.35 \pm 0.2$ and it exhibits flux variations of up to a factor of 10 over periods of a few hours (Rana et al. 2016). Given the similarities between the X-ray spectra and light curves of NNR 15 and V404 Cyg, NNR 15 is most likely a BH LMXB, although it may be a CV or an AB. To order-of-magnitude accuracy, it is estimated that ~ 1000 quiescent BH LMXBs reside in the Galaxy (Tanaka 1996); the primary source of uncertainty in this estimate is our limited knowledge of the typical recurrence timescale of BH transients. Making the simplifying assumption that quiescent BH binaries trace the stellar mass distribution of Galaxy and using the estimate of the stellar mass enclosed in the Norma survey area by F14, we would expect ~ 4 BH LMXBs to reside in the survey area. Thus, it is at least plausible that one BH binary would be detected in the *NuSTAR* Norma survey.

Cataclysmic variables and active galactic nuclei

Based on NARCS results, we expect that the majority of *NuSTAR* Norma sources should be a mixture of CVs and AGN. CVs typically have thermal spectra with $kT \approx 1 - 30$ keV although IPs can display even higher temperatures ($kT \approx 30 - 50$ keV; Landi et al. 2009), while AGN exhibit power-law spectra with $\Gamma \approx 1.5 - 2$ (Tozzi et al. 2006; Sazonov et al. 2008). The remaining 17 tier 1 sources (NNR 4, 6, 9, 11–13, 16–20, 22, 23, 25–27, and 29) have bremsstrahlung temperatures and photon indices consistent with being either CVs or AGN. With the *NuSTAR*, *Chandra*, and infrared data available for these sources, there are three primary ways to distinguish CVs and AGN:

i. If the absorbing column density inferred from X-ray spectral fitting or *Chandra* quantiles is significantly lower than the integrated interstellar $N_{\rm H}$ along the line-of-sight to the source, it is a Galactic source.

ii. If the source does not have a point-like infrared counterpart with $> 98\%$ reliability in the VVV survey, it may be an AGN or a Galactic source with a K or M main-sequence companion, which would fall below the VVV sensitivity limits ($Ks < 18$ mag) if located at $\gtrsim 2$ kpc. Since the energy bands used by the *Wide-Field Infrared Survey Explorer* (WISE; Wright et al. 2010) can be more useful than the J, H, or K bands for identifying AGN (Stern et al. 2012; Mateos et al. 2012), we also searched for counterparts to the *NuSTAR* sources in the AllWISE catalog (Cutri & et al. 2013). The BH binary candidate NNR 15 and four tier 2 sources (NNR 28, 30, 31, and 38) have *WISE* matches located within the 95% positional uncertainty of their *Chandra* counterparts. The counterparts of NNR 15, 28, and 30 have been idenfitied as low-mass stars through spectroscopic follow-up (Rahoui et al. 2014), and the other *WISE* counterparts have $W1 - W2 < 0.1$, far below the typical value of $W1 - W2 \geq 0.8$ for X-ray luminous AGN (Stern et al.

2012); furthermore, the near-IR spectra of the counterparts of NNR 31 and 38 indicate they are Galactic sources (Corral-Santana et al., in prep). Thus, none of the NNR sources with *WISE* counterparts are AGN, but we cannot rule out the possibility that some AGN are undetected by *WISE*. For instance, in the *NuSTAR* serendipitous survey, which has comparable sensitivity limits to the *NuSTAR* Norma survey, about 25% of *NuSTAR* sources at Galactic latitudes $|b| > 10°$, which are likely to be AGN, do not have a WISE counterpart (Lansbury et al. 2016).

iii. If the source exhibits strong unshifted Fe emission, it is more likely to be a CV than an AGN. Both magnetic and non-magnetic CVs often exhibit Fe emission; in some sources, individual Fe lines at 6.4, 6.7, and 6.97 keV with equivalent widths of 100–200 eV can be seen, while in others, a broad component centered around 6.7 keV with an equivalent width of up to a few keV is seen, likely resulting from the blending of multiple Fe lines due to low energy resolution (e.g. Mukai & Shiokawa 1993; Ezuka & Ishida 1999; Baskill et al. 2005; Bernardini et al. 2012; Xu et al. 2016). Both type I and type II AGN often exhibit red-shifted Fe emission, with the neutral Fe line typically being strongest, except in some highly ionized AGN where the He-like and H-like Fe lines can rival the neutral Fe line in strength; Fe line emission from AGN typically has equivalent widths < 100 eV, but they can be higher in Compton-thick AGN (Page et al. 2004; Iwasawa et al. 2012; Ricci et al. 2014). The Fe lines in X-ray binaries also tend to have equivalent widths $\lesssim 100$ eV, so the strength of Fe line emission can also help discriminate between CVs and LMXBs (Hirano et al. 1987; Nagase 1989).

Seven of the tier 1 sources (NNR 4, 6, 9, 12, 18, 19, 25) fulfill at least one of the three criteria listed above and are most likely CVs. NNR 4 meets all three criteria and there is strong evidence that it is an IP, a CV in which the white dwarf (WD) magnetic field is strong enough ($B \approx 10^6 - 10^7$ G) to truncate the accretion disk and channel the accreting material onto the magnetic poles. The X-ray spectrum of NNR 4 shows low absorption ($N_{\rm H} < 4 \times 10^{21}$ cm^{-2}), indicating it is a Galactic source residing at a distance of $\lesssim 2$ kpc. The joint fitting of the *Chandra* and *NuSTAR* spectra provides evidence for partial-covering absorption, which is frequently observed in IPs as some of the X-rays produced in the accretion column pass through the accretion curtain on their way to the observer (de Martino et al. 2004; Bernardini et al. 2012). The near-IR counterpart of NNR 4 is variable and displays emission lines often produced in the accretion streams of IPs (Rahoui et al. 2014). Furthermore, this source also exhibits Fe line emission centered at $6.65^{+0.10}_{-0.06}$ keV line with high equivalent width ($0.9^{+0.2}_{-0.1}$ keV), and a 7150 second period detected by *Chandra*, both of which are typical for IPs (Scaringi et al. 2010). NNR 4 exhibits flux variations on month-year timescales, which is more typical for non-magnetic CVs and polars than IPs (Ramsay et al. 2004), but the flux only varies by a factor < 2, so the case for this source being an IP remains strong. Assuming a distance of 2 kpc, the unabsorbed 3–10 keV luminosity of NNR 4 is $2 - 4 \times 10^{32}$ erg s^{-1}, which is within the luminosity range of IPs (Muno et al. 2004 and references therein).

Sources NNR 6, 9, and 12 all have strong Fe emission centered between 6.4 and 6.8 keV and equivalent widths of 1.3 ± 0.4, 0.4 ± 0.2, and 1.2 ± 0.4 keV, respectively, strongly

indicating that these sources are CVs since both AGN and X-ray binaries tend to have much weaker Fe emission and the Fe emission from AGN is likely to be redshifted. These large equivalent widths are likely due to multiple Fe lines being blended due *NuSTAR*'s low energy resolution. Both NNR 6 and 9 are best-fit by thermal models with high plasma temperatures ($kT > 15$ keV), which are more typical of magnetic rather than non-magnetic CVs (Landi et al. 2009; Xu et al. 2016). The lack of flux variations for NNR 6 and 9 suggest they are most likely IPs. In addition, NNR 6 has a low-mass (late GIII) stellar counterpart (Rahoui et al. 2014), lending further support to a CV origin for this source. The nature of NNR 12 is less certain, because its softer spectrum ($kT = 6^{+3}_{-1}$ keV for an `apec` model) is typical for both non-magnetic and magnetic CVs. NNR 21 is likely located at a distance > 10 kpc given its high $N_{\rm H}$, so its 3–10 keV luminosity is likely $\gtrsim 2 \times 10^{33}$ erg s^{-1}; this high luminosity coupled with the lack of flux variability suggests this source is also probably an IP.

Another likely IP candidate is NNR 13. This source displays one of the hardest spectra of all the *NuSTAR* Norma sources, having $kT > 21$ keV or $\Gamma = 1.0 \pm 0.5$. Its very hard spectrum and constant flux over long timescales is typical of IPs.

The nature of NNR 18 is discussed in B14; our spectral analysis yields consistent results, finding a high $N_{\rm H}$ of $1.9^{+0.9}_{-0.6} \times 10^{23}$ cm^{-2} and $\Gamma = 2.6^{+1.0}_{-0.8}$. Assuming a distance of > 10 kpc based on the high $N_{\rm H}$ value, NNR 18 has an unabsorbed 3–10 keV luminosity $\gtrsim 5 \times 10^{33}$ erg s^{-1}. NNR 18 has an early MIII counterpart and exhibited mild X-ray variability on short timescales in *Chandra* observations. As discussed by B14, these properties are consistent with an IP or an LMXB. Another possibility is that this source is a hard-spectrum symbiotic binary (SB) hosting a WD or a symbiotic X-ray binary (SyXB) hosting a NS (Luna et al. 2013); the compact objects in SBs and SyXBs accrete material from the wind of a red giant companion, which is typically of spectral type M or K (Morihana et al. 2016). Hard-spectrum SBs and SyXBs display X-ray luminosities between 10^{32} and 10^{34} erg s^{-1} (Masetti et al. 2002; Smith et al. 2008; Nespoli et al. 2010), and variability on short and long timescales (Luna & Sokoloski 2007; Corbet et al. 2008). An IP origin is favored for NNR 18 based on its low levels of variability, while its estimated luminosity and the M giant spectral type of its counterpart favors an SB or SyXB origin.

NNR 19 and 25 show low absorption in their X-ray spectra, indicating they are Galactic sources and probably located at a distance of a few kpc. Both sources are transients which were not detected in NARCS, but they are detected in follow-up *Chandra* observations taken 3 and 34 days after the *NuSTAR* observations, respectively. The flux of NNR 25 increased by a factor of ≥ 4 in the couple of years between the NARCS and *NuSTAR* observations and remained high for at least 34 days. NNR 19 was detected at a consistent flux level in multiple *NuSTAR* observations that span ≈100 days. About 250 days before it is first detected by *NuSTAR*, the 90% confidence upper limit for its 3–10 keV photon flux is 2×10^{-6} cm^{-2} s^{-1} (a factor 4 below its peak flux), and about 40 days after it is detected by *NuSTAR*, its flux falls below 4×10^{-6} cm^{-2} s^{-1}. Thus, we find that the flux of NNR 19 increased by a factor of ≥ 4 and remained high for a period between 100 and 400 days. In addition, NNR 19 was detected in the archival *Chandra* ObsID 7591, demonstrating that this transient experienced an outburst in 2007, during which its flux was a factor of ≥ 7

higher than the upper limit measured by NARCS in 2011. The spectra of NNR 19 and 25 have $kT = 11^{+18}_{-4}$ keV ($\Gamma = 1.7^{+0.3}_{-0.4}$) and $kT > 6$ keV ($\Gamma = 1.8 \pm 0.7$), respectively. The temporal and spectral properties of NNR 19 and 25 most closely resemble those of polars, CVs with magnetic fields so strong ($B > 10^7$ G) that the white dwarf magnetosphere inhibits the formation of an accretion disk. Thus, compared to other CVs, polar X-ray emission is very sensitive to changes in the mass transfer rate, and they exhibit flux variations of factors ≥ 4 as they transition between low and high accretion states on ∼month-year timescales (Ramsay et al. 2004; Worpel et al. 2016), very similar to the behavior of NNR 19 and 25. No IR counterparts in the VVV survey are found for NNR 19 or 25 within the 90% positional uncertainty determined from *Chandra*. While the variability and spectra of NNR 19 and 25 would also be consistent with hard-spectrum SBs or SyXBs, the lack of a counterpart with $Ks < 18$ mag rules out the possibility that these sources have red giant companions, which should be visible out to $\gtrsim 10$ kpc. In contrast, it is possible for main-sequence K or M-type stars located at distances of a few kiloparsecs to fall below the VVV survey sensitivity.

The nine remaining tier 1 sources (NNR 11, 16, 17, 20, 22, 23, 26, 27, 29) are well-fit either by thermal models with $kT = 4 - 30$ keV or power-law models with $\Gamma \approx 2$, consistent with the spectra of CVs, SBs, SyXBs, LMXBs, or AGN; the uncertainties in the spectral parameters for many of these sources are quite large since they are among the faintest in our survey. All of these sources have high absorption, that is equal to or in excess of the ISM column density through the Galaxy, and they lack IR counterparts, so it is difficult to determine whether they are Galactic or extragalactic. The lack of counterparts does rule out the possibility that these sources are SBs or SyXBs since their red giant companions should be visible through most of the galaxy given the sensitivity of the VVV survey ($Ks < 18$ mag). Based on the log$N$-log$S$ distribution of AGN measured in the COSMOS survey (Cappelluti et al. 2009) and accounting for Galactic absorption, conversion from the 2–10 keV to the 3–10 keV band, and the sensitivity curve of the *NuSTAR* Norma survey (see § 2.3.12), we estimate that about five AGN are present in this survey. Therefore, roughly half of the remaining tier 1 sources may be AGN. The other half are probably CVs since quiescent LMXBs are expected to be relatively rare (Tanaka 1996). Additional *NuSTAR* or *XMM* observations are required to distinguish between the possible CV or AGN origin of these nine sources by measuring the strength of Fe line emission and better constraining their spectral hardness. The 3–10 keV fluxes of NNR 11, 20, and 29 vary by factors of > 5 between the NARCS and *NuSTAR* observations. Such long-term variability is common for AGN, polars, and non-magnetic CVs (Orio et al. 2001; Markowitz & Edelson 2004; Ramsay et al. 2004; Baskill et al. 2005), so it does not help us discriminate betwen Galactic and extragalactic sources but it at least excludes an IP origin for these three sources.

The ten tier 2 sources included in our catalog do not have enough *NuSTAR* counts to meaningfully constrain their spectral properties, but their distribution in the *Chandra* quantile diagram is very similar to the distribution of the 17 tier 1 sources described in this subsection; two are foreground sources while the rest are heavily absorbed and have $\Gamma < 2$. Seven of these tier 2 sources (NNR 28, 30, 31, 34, 35, 36, and 38) have reliable IR counterparts, three of which (NNR 28, 30, and 36) have been spectrally identified as low-mass stars (Rahoui

et al. 2014). These seven sources are likely to be a mixture of CVs, SBs, and SyXBs like the majority of identified tier 1 sources. Sources NNR 28 and 36 display such low absorption that they are likely located within a few kpc and thus have 3–10 keV luminosities $\lesssim 3\times10^{31}$ erg s^{-1}, so they could also be active binaries given their low luminosity (Strassmeier et al. 1993). An AGN origin cannot be ruled out for NNR 34 and 35, which have VVV counterparts but are not detected by *WISE*. NNR 32, 33, and 37 lack IR counterparts and are heavily absorbed, and could be AGN or Galactic sources. Based on the log$N$-log$S$ derived for AGN and CVs in the Norma region by F14, a 1:2 ratio of AGN to CVs/ABs is expected in the 2–10 keV flux range of these tier 2 sources ($4\times10^{-14} < f_X < 1\times10^{-13}$ erg cm^{-2} s^{-1}). Such a ratio is plausible among tier 2 sources given the current constraints we can place on their physical nature. However, it is odd that none of the sources which may be AGN are detected by *WISE* with $W1-W2 \geq 0.8$, since the majority of AGN discovered in the *NuSTAR* serendipitous survey have these properties (Lansbury et al. 2016). The fact that our AGN candidates either lack IR counterparts or have only VVV, but not *WISE*, counterparts indicates that, if they truly are AGN, they are likely to have low-luminosities ($L_X \lesssim 10^{43}$ erg s^{-1}).

Table 2.23: Classification of *NuSTAR* Norma Region Sources

Source No.	Classification
	Confirmed
1	BH LMXB
2	NS HMXB
3	pulsar/PWN
	Candidate
4	CV (IP)
5	bow shock PWN
6	CV (IP)
7	CWB
8	young PWN
9	CV (IP)
10	magnetar or AB
11	CV (polar or non-magnetic) or AGN
12	CV (IP)
13	CV (IP)
14	CWB
15	BH LMXB
16	CV or AGN
17	CV or AGN
18	CV (IP), SB, SyXB
19	CV (polar)
20	CV (polar or non-magnetic) or AGN
21	PWN/SNR

Classification of *NuSTAR* Norma Region Sources (continued)

Source No.	Classification
22	CV or AGN
23	CV or AGN
25	CV (polar)
26	CV or AGN
27	CV or AGN
29	CV (polar or non-magnetic) or AGN
	Tentative
28	Galactic
30	Galactic
31	Galactic
32	Galactic or AGN
33	Galactic or AGN
34	Galactic or AGN
35	Galactic or AGN
36	Galactic
37	Galactic or AGN
38	Galactic

Notes: Classifications of NNR sources are discussed in § 2.3.11. The classifications of NNR 1, 2, and 3 are robust, while all other classifications for tier 1 sources should be considered candidate identifications (see § 2.3.11 for details). For candidate CVs, we provide in parenthesis the most likely CV type when possible. For tier 2 sources we provide only tentative classifications of these sources as Galactic or extragalactic AGN.

2.3.12 Survey Sensitivity

To compute the sky coverage for the *NuSTAR* Norma survey, we used the same method employed for NARCS, which is taken from Georgakakis et al. (2008b). For a given detection probability threshold, $P_{\rm thresh}$, we determined the minimum number of total counts required for a detection ($C_{\rm lim}$) at each position in the image, such that $P(\geq C_{\rm lim}) = P_{\rm thresh}$. To this end, we made background maps in the 3–10 keV and 10–20 keV bands by removing the counts within 60″ (90″) radius circular regions centered on the point (extended) source positions listed in Table 2.17, and then filling in these regions by randomly distributing the expected background counts determined from the local background. Using these background maps, we calculated the mean expected background counts ($\langle C_{\rm bkg}\rangle$) in circular regions centered on each pixel with radii equal to the 15, 22, and 30% PSF enclosures, which are the cell sizes we used for source detection (see § 2.3.4). The probability that the observed counts will exceed

$C_{\rm lim}$ within a particular region is

$$P(\geq C_{\rm lim}) = \gamma(C_{\rm lim}, \langle C_{\rm bkg}\rangle) \tag{2.21}$$

where $\gamma(a, x)$ is the lower incomplete gamma function, defined as

$$\gamma(a, x) = \frac{1}{\Gamma(a)} \int_0^x e^{-t} t^{a-1} dt \tag{2.22}$$

Calculating $C_{\rm lim}$ requires setting $P(\geq C_{\rm lim}) = P_{\rm thresh}$, and inverting Equation 2.21 numerically.

Then we computed the probability of detecting a source of a given flux f_X at each pixel, given by

$$P_{f_X}(\geq C_{\rm lim}) = \gamma(C_{\rm lim}, C_{\rm src}) \tag{2.23}$$

and $C_{\rm src} = f_X t_{\rm exp} A_{\rm src} \epsilon + \langle C_{\rm bkg}\rangle$, where $t_{\rm exp}$, $A_{\rm src}$, and ϵ are the exposure time, mean effective area, and unabsorbed energy flux to observed photon flux conversion factor, respectively. For ϵ, we used the mean of the ratios of photon fluxes to energy fluxes measured for tier 1 sources for a given energy band. To estimate the effective area at each pixel location, we made vignetting-corrected exposure maps, and by comparing the ratio of the vignetting-corrected exposure over the the uncorrected exposures to the effective areas of tier 1 sources, we derived a linear relation to convert the exposure ratio at a given source location to the source-spectrum average effective area. These relations were derived using vignetting corrections evaluated at 8 keV for the 3–10 keV band and at 10 keV for the 10–20 keV band; they were also calibrated for the three different cell sizes. Different ϵ values and effective area to exposure ratio relations are derived based on non-parametric and modeling-derived fluxes. Finally, the sky coverage is given by the sum of probabilities in Equation 2.23 over all pixels multiplied by the solid angle per pixel. We repeated this calculation for a range of fluxes to produce a sensitivity curve for each of the three detection cell sizes in both the 3–10 keV and 10–20 keV bands.

Figure 2.29 shows the sky coverage for different energy bands and cell sizes. We used the sensitivity curves for the 22% PSF enclosures to calculate the log$N$-log$S$ distribution and sensitivity limits of our survey, because the largest number of tier 1 sources are detected in the 22% PSF trial maps and its sky coverage represents a rough average of the different curves. The deep field of the *NuSTAR* Norma survey has an area of about 0.04 deg^2 and sensitivity limits of 4×10^{-14} erg cm^{-2} s^{-1} (5×10^{-14} erg cm^{-2} s^{-1}) in the observed (unabsorbed) 3–10 keV band and 4×10^{-14} erg cm^{-2} s^{-1} in the 10–20 keV band. The shallow survey has an area of $\sim$1 deg^2 with sensitivity limits of 1×10^{-13} erg cm^{-2} s^{-1} (1.5×10^{-13} erg cm^{-2} s^{-1}) in the observed (unabsorbed) 3–10 keV band and 1.5×10^{-13} erg cm^{-2} s^{-1} in the 10–20 keV band.

2.3.13 The log$N$-log$S$ Distribution

Since many of the *NuSTAR* Norma sources have fluxes approaching our sensitivity limits, when calculating the number-count distribution for our survey, it is important to consider the effect of Poisson fluctuations of the source and background counts on the measured source

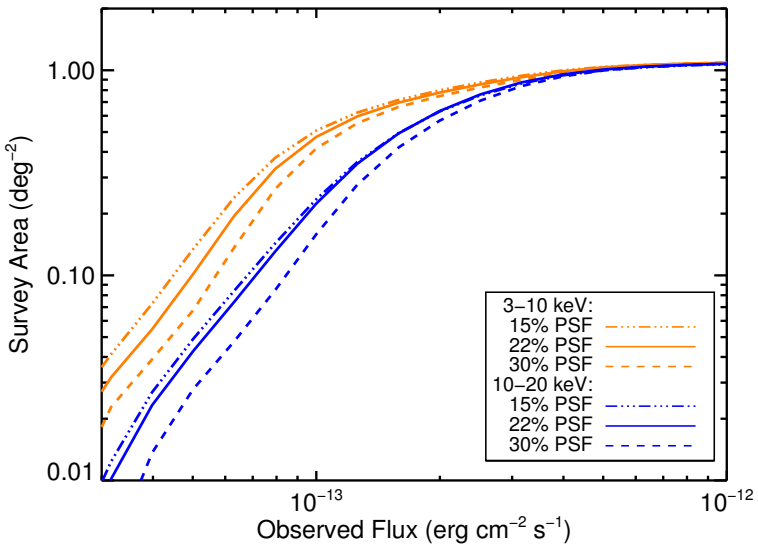

Figure 2.29: Sky coverage of the *NuSTAR* Norma Region survey for different energy bands and PSF enclosure fractions.

flux. Thus, rather than assigning a single flux value to each source, we determine its flux probability distribution by computing the source count distribution from Equation A21 in Weisskopf et al. (2007) and converting counts to energy fluxes. The number count distribution is then equal to the sum of the flux probability distributions of individual sources, divided by the sensitivity curve calculated in § 2.3.12.

We compute log$N$-log$S$ distributions in the 3–10 keV and 10–20 keV bands, both for observed and unabsorbed fluxes; in order to check for systematic errors, we perform these calculations using both the modeling-derived and non-parametric fluxes. When constructing the distribution in a given energy band, we only included the sources that exceed the detection threshold in that particular energy band. In addition, in order to compare the *NuSTAR* number-count distribution with that derived from NARCS, we excluded extended sources, and for sources that are blended in *NuSTAR* observations but resolved with *Chandra*, we estimate the *NuSTAR* fluxes of individual sources by assuming the ratio of fluxes (see comments in Table 2.21) of the two sources is the same in *NuSTAR* as it is in the *Chandra* 2–10 keV band. Thus, NNR 8 is excluded from the sample of sources used in the number-count distribution, the fluxes of the point sources at the center of the extended sources, NNR 3 and 21, are estimated to be 30% and 20% of the total respectively, and the fraction of NNR 7's flux attributed to NARCS 1278 and 1279 is 30% and 70%, respectively.

Figure 2.30 shows the resulting log$N$-log$S$ distributions for the *NuSTAR* Norma region. In these panels, magenta and green lines show the log$N$-log$S$ distribution measured by NARCS converted from the unabsorbed 2–10 keV band to the *NuSTAR* bands assuming different spectral models, thermal models with $kT = 10$, 20, and 50 keV and power-law models with $\Gamma = 1$, 2, and 3; when converting to observed energy fluxes, a typical $N_{\rm H}$ value of 10^{23} cm^{-2}

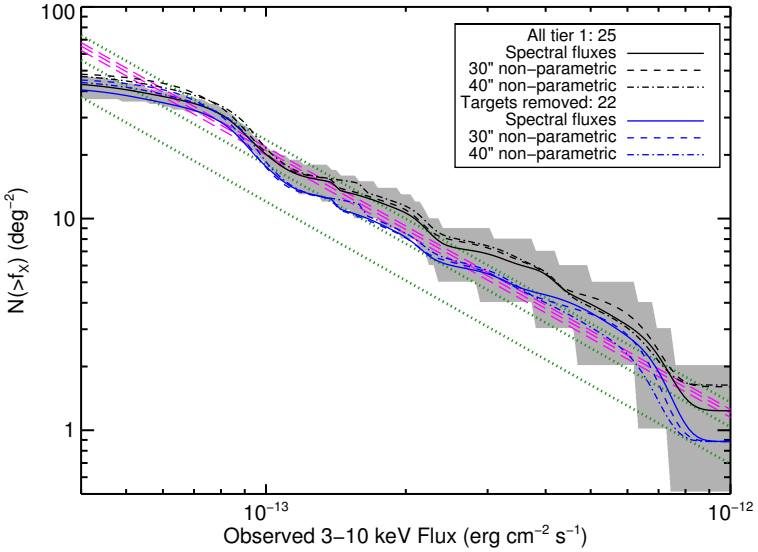

(a) The log$N$-log$S$ distribution in the 3–10 keV band, calculated using observed fluxes derived from spectral fitting, as well as non-parametric fluxes calculated from aperture photometry using $30''$ and $40''$ radius regions.

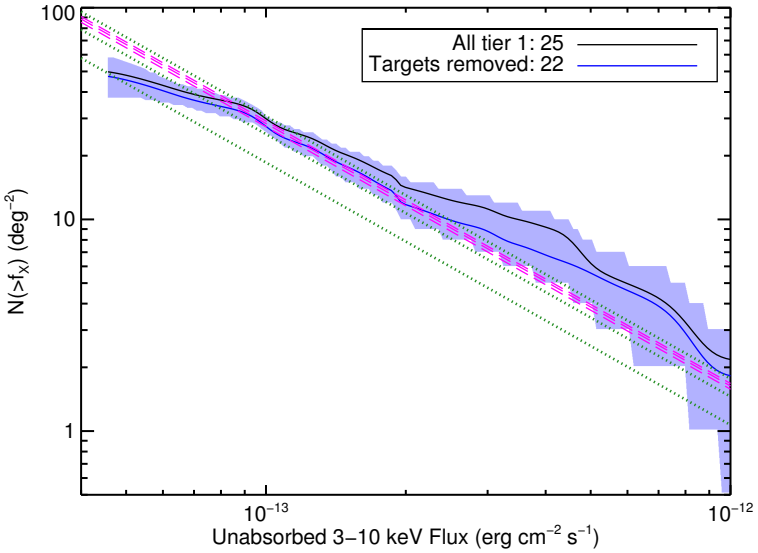

(b) The log$N$-log$S$ distribution in the 3–10 keV band calculated using unabsorbed fluxes derived from spectral fitting. The blue band shows the 1σ errors on the distribution shown in blue.

Figure 2.30: *All*: The log$N$-log$S$ distributions shown in black include all tier 1 sources exceeding the detection threshold in a given energy band; the gray band shows the 1σ errors on the log$N$-log$S$ distribution. The log$N$-log$S$ distributions shown in blue exclude NNR 2, 4, and 5, which were specifically targeted by *NuSTAR*. The green dotted (magenta dashed) lines show the NARCS log$N$-log$S$ converted from unabsorbed 2–10 keV into the given bands assuming power-law spectral models with $\Gamma = 3$, 2, and 1 (thermal models with kT=10, 20 and 50 keV). When converting the NARCS distribution into the observed 3–10 or 10–20 keV bands, a column density of $N_{\rm H} = 10^{23}$ cm^{-2} is used, the mean of measured $N_{\rm H}$ values for the *NuSTAR* sources; varying $N_{\rm H}$ between $0.7 - 2.0 \times 10^{23}$ cm^{-2} does not significantly change the conversion factor.

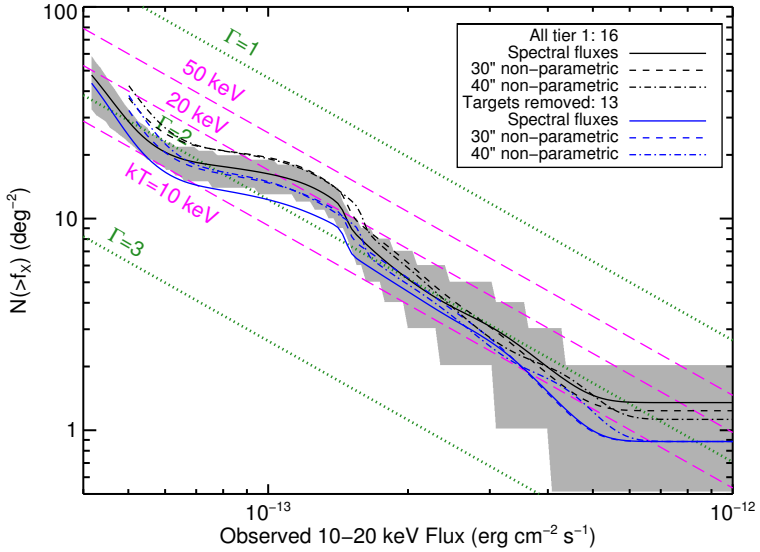

(c) The log$N$-log$S$ distribution in the 10–20 keV band, calculated using observed fluxes derived from spectral fitting, as well as non-parametric fluxes calculated from aperture photometry using 30″ and 40″ radius regions.

Figure 2.30: This figure is continued from the previous page.

is used. The log$N$-log$S$ distributions shown in black include all tier 1 sources that exceed the detection threshold in a given energy band, while the blue distributions exclude the sources that were specifically targeted by *NuSTAR* and detected (NNR 2, 4, and 5), which could unnaturally inflate the log$N$-log$S$ distribution. As shown in the top panel, there is little difference between the NARCS distributions converted using different spectral models into the observed 3–10 keV band, which is not surprising given its large amount of overlap with the *Chandra* 2–10 keV band. Regardless of how the source energy fluxes are calculated, the *NuSTAR* distribution is consistent with the NARCS distribution at 1σ confidence, exhibiting a similar slope of $\alpha \approx -1.24$. The *NuSTAR* distribution only deviates significantly from the NARCS distribution at low fluxes. This discrepancy may be due to the Eddington bias or variance in the spatial density of sources, given that the sources with the lowest fluxes are only detected in the deep HESS field, which is only 100 arcmin^2 in size.

The middle panel of Figure 2.30 shows the log$N$-log$S$ distribution calculated using the unabsorbed 3–10 keV fluxes from spectral fitting. Although this distribution is still largely consistent with the NARCS distribution at 1σ confidence when the sources specifically targeted by *NuSTAR* are removed (shown in blue), the *NuSTAR* distribution is slightly higher than the *Chandra* distribution above $> 3 \times 10^{-13}$ erg cm^{-2} s^{-1}. The fact that this excess is only seen using unabsorbed 3–10 keV fluxes but not the observed 3–10 keV fluxes suggests that, for some sources, we measure $N_{\rm H}$ values that are too high and thus overcorrect for absorption.

The bottom panel of Figure 2.30 shows the log$N$-log$S$ distributions calculated using modeling-derived and non-parametric fluxes in the observed 10–20 keV band. Since there is very little difference between the observed and unabsorbed 10–20 keV fluxes, the log$N$-log$S$ distribution in the unabsorbed 10–20 keV band is not shown. Although the 10–20 keV *NuSTAR* distributions deviate from a simple power-law due to the small number of sources (16) detected in this hard X-ray band, overall the slope is still consistent with the NARCS slope. The normalizations of the different NARCS distributions extrapolated into the 10–20 keV band are distinct depending on the spectral model assumed; for the *NuSTAR* and NARCS normalizations to be consistent, the average spectrum of Norma sources must either have $kT = 10 - 20$ keV or $\Gamma = 2$. This average spectrum is indeed consistent with the individual spectral fits of most of the *NuSTAR* sources and their locations in the *NuSTAR* quantile space.

2.3.14 Comparison of the *NuSTAR* Populations in the Norma Region and the Galactic Center

Comparing the log$N$-log$S$ distributions of sources in the Norma region and the $1^\circ \times 0.6^\circ$ Galactic Center (GC) region surveyed by *NuSTAR*, the number density of *NuSTAR* sources is ≈ 2 times higher in the GC (Hong et al. 2016), which is to be expected since the stellar density in the vicinity of the GC is higher than the stellar density along the line-of-sight of the Norma region. The power-law slope of the number-count distribution is also steeper in the GC ($\alpha \approx -1.4$; Hong et al. 2016), which is consistent with the trend that is seen for *Chandra* sources in the GC and the field in the 0.5–8 keV band (Muno et al. 2009). In order for the normalizations of the GC *NuSTAR* and *Chandra* number-count distributions to be consistent, the typical spectrum of GC sources must either have $kT = 20 - 50$ keV or $\Gamma \approx 1.5$, which is harder than the typical spectrum of Norma sources.

Hong et al. (2016) argue that $40-60\%$ of *NuSTAR* GC sources are magnetic CVs, primarily IPs, given their very hard X-ray spectra ($\Gamma \lesssim 1.5$) and the presence of strong Fe emission. All but two of the Norma CV candidates have softer spectra ($\Gamma > 1.5$, $kT \lesssim 20$ eV). The spectral differences between the *NuSTAR* populations in the Norma and GC regions are mirrored in the differences between the Galactic Ridge X-ray emission (GRXE; Revnivtsev et al. 2006b; Revnivtsev et al. 2006a; Revnivtsev et al. 2009b) and the central hard X-ray emission (CHXE) discovered by *NuSTAR* in the GC (Perez et al. 2015). The lower temperatures of the Norma CV candidates are consistent with the thermal spectra of the GRXE, whose hot component has a temperature of $kT \approx 15$ keV (Türler et al. 2010; Yuasa et al. 2012), while the high temperatures of GC CVs resemble the $kT > 25$ keV emission observed in the inner few parsecs of the Galaxy (Perez et al. 2015; Hong et al. 2016).

However, it is unclear why the X-ray populations in the GC and the disk are different. Under the assumption that most of the sources contributing to the CHXE and GRXE are IPs, the differences in their typical X-ray temperatures have been attributed to differences in their WD masses, with WDs in the GC CVs having masses $\gtrsim 0.8 M_\odot$ (Perez et al. 2015; Hong et al. 2016) and those in the disk CVs having masses $\approx 0.6 M_\odot$ (Krivonos et al. 2007;

Türler et al. 2010; Yuasa et al. 2012). However, the mean WD mass among all CVs has been measured to be $0.83 \pm 0.23 M_{\odot}$ (Zorotovic et al. 2011), and the X-ray inferred masses of confirmed field IPs are consistent with this higher value of $\approx 0.8 M_{\odot}$ (Hailey et al. 2016). The discrepancy between the measured WD masses for field CVs and the lower masses inferred from the temperature of the GRXE suggests that it may be incorrect to assume that the GRXE is dominated by IPs (Hailey et al. 2016). Thus, it may be similarly incorrect to attribute the temperature differences between the *NuSTAR* CV candidates in the GC and Norma regions to differences in their WD masses.

In fact, as discussed in § 2.3.11, a significant fraction of the Norma CV candidates may not be IPs but rather a mixture of polars, non-magnetic CVs, hard-spectrum SBs, and SyXBs. These types of sources have softer spectra than IPs, and thus the difference in the average temperatures of Norma and GC sources may be explained by variations in the relative fractions of different types of CVs and symbiotic binaries. It is unclear what physical processes would drive variations in the relative fractions of different types of compact object binaries in these two Galactic regions, but investigating these issues further will first require confirmining the true nature of the CV candidates.

The clearest ways of distinguishing different types of CVs and SBs is by measuring the relative flux ratios of their Fe emission lines (Xu et al. 2016) or measuring both their spin and orbital periods (Scaringi et al. 2010), but since most of the Norma CV candidates are quite faint, it will be difficult to obtain X-ray spectra or light curves with enough photons to make such measurements with current telescopes. Monitoring the long-term X-ray and infrared variability of the CV candidates, and determining the spectral types of their counterparts more accurately to estimate distances and luminosities will help to identify the nature of these sources.

2.3.15 Conclusions

We have detected 28 hard X-ray sources in a square-degree region in the direction of the Norma spiral arm surveyed by *NuSTAR*, which are designated as tier 1 sources. Twenty-three of these sources were previously detected in observations of the Norma Arm Region *Chandra* survey, one was a well-studied black hole transient (4U 1630-472), and four were newly discovered transients that we followed up and localized with *Chandra*. Out of 28 sources, 16 of them are detected above 10 keV. In addition, we found ten NARCS sources with 2–10 keV fluxes $> 6 \times 10^{-6}$ cm^{-2} s^{-1} that did not exceed our formal detection threshold for *NuSTAR* but which displayed significant X-ray emission (S/N$>$ 3) in at least one of three energy bands, which are designated as tier 2 sources. We have provided photometric information for these sources in our catalog but do not include them in our calculation of the log$N$-log$S$ distribution since they do not meet our detection thresholds.

The log$N$-log$S$ distribution of *NuSTAR* sources in the 3–10 keV band is consistent with the distribution of 2–1 keV *Chandra* sources in the Norma region. The *NuSTAR* log$N$-log$S$ distribution in the 10–20 keV band is consistent with the 2–10 keV *Chandra* distribution if the average spectrum of the *NuSTAR* sources can be described by a power-law model with

$\Gamma = 2$ or a single temperature `apec` model with a plasma temperature between 10 and 20 keV. The broadband (3–40 keV) energy quantiles of the *NuSTAR* sources show that the majority of sources have photon indices of $\Gamma = 2 - 3$ for a power-law model or $kT = 5 - 30$ keV for a bremsstrahlung model, which are consistent with the spectral parameters required for good agreement between the 10–20 keV and 2–10 keV log$N$-log$S$ distributions.

We fit the joint *Chandra* and *NuSTAR* spectra of all sources with > 100 counts in the 3–40 keV band, but find that > 300 *NuSTAR* counts are required to provide meaningful constraints on spectral model parameters. We find good agreement between the spectral parameters from our fits and the location of sources in the quantile diagrams.

Four of the sources detected in the *NuSTAR* Norma Arm Region survey are previously well-studied sources: NNR 1 is the black hole LMXB 4U 1630-472, NNR 2 is the supergiant HMXB IGR J16393-4643, NNR 3 is the PWN and luminous TeV source HESS J1640-465, and NNR 24 is the magnetar SGR J1627-41. Based on the X-ray variability, spectral fits, and infrared counterpart information for each source, we determined the most likely nature of the fainter sources in our survey, which are summarized in Table 2.23. Sources NNR 5, 8, and 21 are PWN candidates, NNR 7 and 14 are likely colliding wind binaries, NNR 10 is a possible magnetar, and NNR 15 is a quiescent black hole LMXB candidate. The other sources are primarily CV candidates, a mixture of IPs, polars, non-magnetic CVs, and symbiotic binaries. We estimate that five background AGN are present among the tier 1 *NuSTAR* sources.

Compared to the *NuSTAR* sources that are detected in the Galactic Center region, the sources in the Norma region have softer spectra on average. Even restricting the comparison to the CV candidates in these two regions, the Norma CVs exhibit lower plasma temperatures than those in the GC. The $kT \approx 15$ keV temperatures of Norma CV candidates resemble the hot component of the GRXE spectrum.

If most of the Norma CV candidates are IPs, then their plasma temperatures indicate the white dwarfs in these systems have masses of $\approx 0.6 M_{\odot}$, which are lower than the WD masses of $\gtrsim 0.8 M_{\odot}$ estimated for the GC IPs. However, we argue that it is more likely that the fraction of IPs relative to polars, non-magnetic CVs, and symbiotic binaries is lower among Norma CV candidates than in the GC region. Since IPs have the hardest X-ray spectra of all these types of sources, a lower fraction of IPs in the Norma region would result in lower plasma temperatures for the average source.

In order to understand the nature of the hard X-ray sources in the Norma region and why they differ from the hard X-ray sources in the GC region, it is necessary to continue monitoring the X-ray variability of the Norma CV candidates, better characterize the variability and spectral types of their infrared counterparts, and obtain higher quality spectra, especially at Fe line energies, for the brighter sources. Follow-up multiwavelength observations of the candidate PWN, CWBs, and quiescent black hole binary would be useful in furthering our understanding of compact stellar remnants and the evolution of massive stars.

2.4 HMXB Candidates Discovered in the Norma Arm Region Surveys

As discussed in §2.1, one of the goals of the *Chandra* and *NuSTAR* Norma surveys was to search for low-luminosity HMXBs in order to further our understanding of the HMXB luminosity function and the evolution of high-mass stars. The primary criteria used to identify candidates HMXBs are the presence of a high-mass stellar counterpart, the X-ray spectral properties typical of accreting HMXBs, and X-ray luminosities higher than typical values for isolated massive stars.

Accurately distinguishing an optical/IR counterpart as a high-mass star requires optical or near-IR spectroscopy. As discussed in Rahoui et al. (2014), it would require too much observing time to obtain optical or infrared spectra for all the ~ 500 optical/IR counterparts of the NARCS sources. therefore, we prioritized X-ray sources to follow-up based on six criteria: (1) X-ray brightness high enough to place meaningful constraints on source's X-ray spectrum, (2) a hard X-ray spectrum with $\Gamma < 2$ in the 0.5-10 keV band, which is typical of accreting HMXBs, (3) X-ray variability, which is common in HMXBs, (4) a high column density ($N_{\rm H} > 10^{22}$ cm^{-2}) to focus on sources at distances of the Scutum arm or beyond where most of the known star-forming regions and OB associations are located, which are correlated with the locations of HMXBs (Bodaghee et al. 2012c), (5) a counterpart with $J-K$ color > 1.5, indicating that it is also subject to significant absorption, and (6) the reliability of the near-IR counterpart. We obtained near-IR spectra for the 20 most highly prioritized NARCS sources using the Ohio State Infrared Imager/Spectrometer (OSIRIS) mounted on the 4m SOAR telescope at CTIO (Rahoui et al. 2014), and obtained near-IR spectra for 22 additional NARCS counterparts using the MMT and Magellan Infrared Spectrograph (MMIRS) on Magellan's 6.5m Clay telescope (Corral-Santana & et al. in prep).

We have identified six high-mass stars among the 42 near-IR counterparts we observed. Three of these are supergiant stars, including two Wolf-Rayet stars, and are discussed in §2.3.11; the *NuSTAR* spectra of these sources indicate they are most likely colliding wind binaries rather than HMXBs since they exhibit strong 6.7 keV emission and fall off steeply above 10 keV (having $\Gamma > 3$). The remaining three sources are HMXB candidates whose properties are described in §2.4.1.

2.4.1 Properties of HMXB Candidates

We have discovered three HMXB candidates in the Norma region: CXOU J163515.1-472304, J163955.2-463145, and J164045.5-464607 (NARCS 239, 1168, and 1326, respectively).

Two of these sources, NARCS 239 and 1326 exhibit emission lines in their near-IR spectra and IR excess consistent with Be III/V or supergiant B[e] stars (Rahoui et al. 2014); in the former, the IR excess is attributed to bremsstrahlung emission from an ionized decretion disk (Rivinius et al. 2013), while in the latter it is attributed to a combination of bremsstrahlung and thermal dust emission from a complex circumstellar environment (Zickgraf et al. 1985). NARCS 239 and 1326 also have very similar quantile values and lie in a region of the quantile

diagram (see §2.2.7) that indicates they are highly absorbed ($N_{\rm H} > 4 \times 10^{22}$ cm^{-2}) and have $\Gamma \lesssim 2$ in the *Chandra* energy band. Since the similarity of their quantile values suggests they have similar spectral properties, we jointly fit the *Chandra* spectra of these two sources, maintaining only their flux normalizations as independent free parameters. Adopting an absorbed power-law model, we measured the spectral parameters for these sources to be $N_{\rm H} = 1.2^{+1.7}_{-0.6} \times 10^{23}$ cm^{-2} and $\Gamma = 2.4^{+3.0}_{-1.3}$. The unabsorbed 2–10 keV fluxes of NARCS 239 and 1326 were found to be $8.5^{+1.8}_{-1.2} \times 10^{-14}$ erg cm^{-2} s^{-1} and $7.3^{+1.8}_{-1.5} \times 10^{-14}$ erg cm^{-2} s^{-1}, respectively. The high $N_{\rm H}$ and A_V measured for these two sources suggest they lie at a distance of $\gtrsim$ 10 kpc (Rahoui et al. 2014). Adopting a 10 kpc distance, the 2–10 keV luminosities of NARCS 239 and 1326 are $L_X \sim 10^{33}$ erg s^{-1}.

The X-ray luminosities of NARCS 239 and 1326 are $>$ 2 orders of magnitude higher than typical isolated Be stars (Cohen et al. 1997). Thus, if the IR counterparts of these sources are Be stars, NARCS 239 and 1326 are likely either Be HMXBs or γ-Cas analogs. γ-Cas analogs are rare Be stars that exhibit brighter ($L_X \sim 10^{32} - 10^{33}$ erg s^{-1}) and harder ($kT \approx 10 - 20$ keV)[18] X-ray emission than most Be stars (Lopes de Oliveira 2007); it has been suggested that this hard X-ray emission may either be due to accretion onto a white dwarf companion or from the interaction of the Be star's equatorial magnetic field with its circumstellar disk. Recent work indicates that γ-Cas analogs may be the fastest rotating Be stars and favors the latter hypothesis (Motch et al. 2015). Another possibility is that these two sources are sgB[e] stars in colliding wind binaries. A couple of sgB[e] CWBs have been discovered, and they have $L_X \sim 10^{33}$ erg s^{-1} like NARCS 239 and 1326 (Clark et al. 2013b; Clark et al. 2013a). However, CWBs, including the known sgB[e] CWBS, have softer spectra than NARCS 239 and 1326, typically having thermal spectra with $kT \approx 2 - 3$ keV (Clark et al. 2013b). Thus, NARCS 239 and 1326 are most likely to be low-luminosity accreting Be HMXBs or γ-Cas analogs.

The third HMXB candidate, NARCS 1168, has a B8-A3IV/V counterpart and is estimated to lie at a distance of 3.5 kpc based on its stellar blackbody temperature (Rahoui et al. 2014). Fitting the X-ray spectrum of NARCS 1168 with an absorbed power-law model, we measure its spectral parameters to be $N_{\rm H} = 3^{+3}_{-2} \times 10^{21}$ cm^{-2} and $\Gamma = 1.8 \pm 0.4$. Its average unabsorbed 2–10 keV flux is $7 \pm 0.7 \times 10^{14}$ erg cm^{-2} s^{-1} and varies by a factor of 2 in between *Chandra* observations on ∼month timescales. Its X-ray luminosity is $1.0 \pm 0.1 \times 10^{32}$ erg s^{-1}, and its X-ray-to-bolometric luminosity is $L_X/L_{\rm bol} \approx 10^{-4}$. This X-ray luminosity is at least an order of magnitude higher than isolated B8-A3 stars (Berghoefer et al. 1997). Its X-ray luminosity, X-ray variability, and hard photon index make NARCS 1168 a strong HMXB candidate.

None of the three HMXB candidates were detected in the *NuSTAR* Norma survey. The upper limits derived on the 3–10 keV fluxes from the *NuSTAR* data are consistent with the fluxes measured in the *Chandra* observations. The lack of strong *NuSTAR* detections for these sources does not allow us to improve our measurements of their spectral parameters, which could have shed light on whether they truly are HMXBs, and if so, whether they harbor black holes or neutron stars.

[18] In the *Chandra* 0.5–10 keV band and with the low photon statistics of these HMXB candidates, a thermal spectrum with $kT \approx 10$ keV is indistinguishable from a power-law spectrum with $\Gamma \approx 2$.

2.4.2 Prospects for Constraining the HMXB Luminosity Function

As discussed in §1.5.1, one of the motivations for searching for low-luminosity HMXBs is to place constraints on the faint end of the HMXB luminosity function (LF). Although the nature of the HMXB candidates still needs to be confirmed in order to place firm constraints on the HMXB LF, in the meantime, we can assess the potential constraints they could place on the HXMB LF.

In order to assess these potential constraints, it is important to determine the completeness of our HXMB candidate sample. Our detection method and the NARCS sky coverage are complete to X-ray sources of similar brightness to the three HMXB candidates (see Figures 2.14-2.15). Seventy *Chandra* sources with fluxes greater than or equal to the fluxes of the HMXB candidates were detected in quantile regions B, C, D, and E, where accreting HMXBs could reside (see §2.2.7). Twenty-one of these sources belong to the sample of near-IR counterparts we followed-up spectroscopically. Sixteen of these sources have reliable near-IR counterparts which we have not yet followed-up. The high-mass donor stars in HMXBs are bright enough that they should be detectable in the near-IR through the whole Galaxy, so if any additional HMXB candidates are present in this survey, they would likely be among the subsample of X-ray sources with reliable IR counterparts. Since the near-IR counterparts we already followed-up are those which we deemed most likely to potentially be HMXBs, we would not expect to find as large a fraction of HMXB candidates among the sources that have not yet been followed-up. Thus, to place an upper limit on the number of unidentified HMXB candidates that exist in NARCS, we assume that the fraction of high-mass stars among near-IR counterparts that have not yet been followed-up is the same as for those that have been followed-up. Under this assumption, we estimate that up to two additional HMXB candidates with X-ray fluxes greater than or equal to those of the three candidates we have identified could be present in the Norma region.

Due to large uncertainties in the current distance estimates to some of our HMXB candidates, rather than attempting to place constraints on the HMXB LF directly, we instead assess the constraints that can be placed on the HMXB log$N$-log$S$ distribution. Lutovinov et al. (2013) (hereafter L13) measure the HMXB LF down to a 17–60 keV luminosity limit of 10^{34} erg s^{-1} using persistent HMXBs detected by *INTEGRAL*. The power-law slope of the HMXB LF between 10^{34} and 10^{36} erg s^{-1} is measured to be -1.4 ± 0.2; L13 develop a toy model for the wind-accreting NS HXMBs that fits the measured LF well and predicts that the power-law slope of the LF flattens below 10^{34} erg s^{-1}. For both the measured and toy model LF, L13 calculate the average surface density of HMXBs in the Galactic Plane as a function of 17–60 keV flux, shown in the black lines in Figure 2.31; the upper solid line represents the expected surface density distribution assuming that there is no break in the power-law slope at $\sim 10^{34}$ erg s^{-1}, while the lower dash-dotted line assumes that below 10^{34} erg s^{-1}, the power-law index flattens to -1.0 as predicted by the toy model. To compare the constraints from the NARCS HMXB candidates to the predicted distributions, we convert the X-ray fluxes from the 2–10 keV to the 17–60 keV band by using a range of F_{2-10}/F_{17-60} ratios of 0.3–0.8 based on typical NS HMXB spectra (Filippova et al. 2005).

The estimate of the HMXB surface density determined from the presence of IGR J16393-4643, a confirmed HMXB, in NARCS is shown in green in Figure 2.31. The blue point, which is consistent with the constraint set by IGR J16393-4643, shows the surface density of HMXBs in a wider survey of the Norma arm ($300^\circ < \ell < 345^\circ$) evaluated at the lower flux limit reached by the *INTEGRAL* Galactic Plane survey. The solid purple line indicates the constraint that would be placed on the faint end of the log$N$-log$S$ HMXB distribution if all three of the Norma HMXB candidates are confirmed to be HMXBs; the yellow polygon represents 1σ uncertainties associated with this measurement. The dashed purple lines indicate the possible extremes of the HMXB distribution measured using NARCS sources; the lower line represents the case in which none of the HMXB candidates are truly HMXBs while the upper line represents the case where two additional HMXB candidates are discovered in the NARCS sample and all five candidates are confirmed to be HMXBs.

Given the large statistical uncertainty associated with our potential measurement, it will not be possible in most cases to determine whether the NARCS HMXB distribution is more consistent with a LF with or without a break at $\sim 10^{34}$ erg s^{-1}. However, if none of the HMXB candidates turn out to be true HMXBs, it would suggest that the HMXB LF flattens even more below 10^{34} erg s^{-1} than predicted by L13. A lack of faint HMXBs in the Norma region would be especially surprising given that the L13 predictions in Figure 2.31 are for an average sightline through the Galaxy but the Norma region is expected to have an enhanced number of HMXBs due to its large number of star-forming regions and OB associations. A change in power-law slope of the HMXB LF more extreme than predicted by L13 would suggest that in low accretion rate HMXBs, accretion onto the compact object is somehow inhibited. At low accretion rates, the magnetospheric radius of the NS in a HMXB can become larger than the corotation radius, causing accretion to stall or be greatly reduced (Illarionov & Sunyaev 1975; Bozzo et al. 2008). In this propeller regime, not only can the X-ray emission of an HMXB be significantly lowered but it may also be spectrally softer than in the normal accretion regime. While some NS HMXBs continue to exhibit hard power-law spectra while in quiescence (e.g. Doroshenko et al. 2014, Rutledge et al. 2007), others only display blackbody spectra with $kT \sim 1$ keV which is thought to originate from the hot polar caps of the NS (e.g. Reig et al. 2014; Elshamouty et al. 2016). Quiescent HMXBs with soft spectra would be unlikely to be detected by our Norma surveys, since they are likely to be associated with star-forming regions, most of which are located at distances $> 3-4$ kpc, and HMXBs at such distances would be subject to significant interstellar absorption. Therefore, these surveys can only place constraints on the surface density of HMXBs that continue accreting even at low-luminosities, but not on the total number of binaries that host a high-mass star and a NS or BH.

Confirming the nature of the NARCS HMXB candidates could provide insight into the physics of accretion in low-luminosity HMXBs. In pursuit of this goal, we are continuining our efforts to follow-up these sources and determine their true physical nature. Future X-ray observations with *XMM-Newton* could help confirm whether NARCS 239 and 1326 are Be HMXBs or γ-Cas analogs, since the latter have much stronger Fe emission than HMXBs and *XMM-Newton* has very high effective area between 6 and 7 keV. We are also pursuing

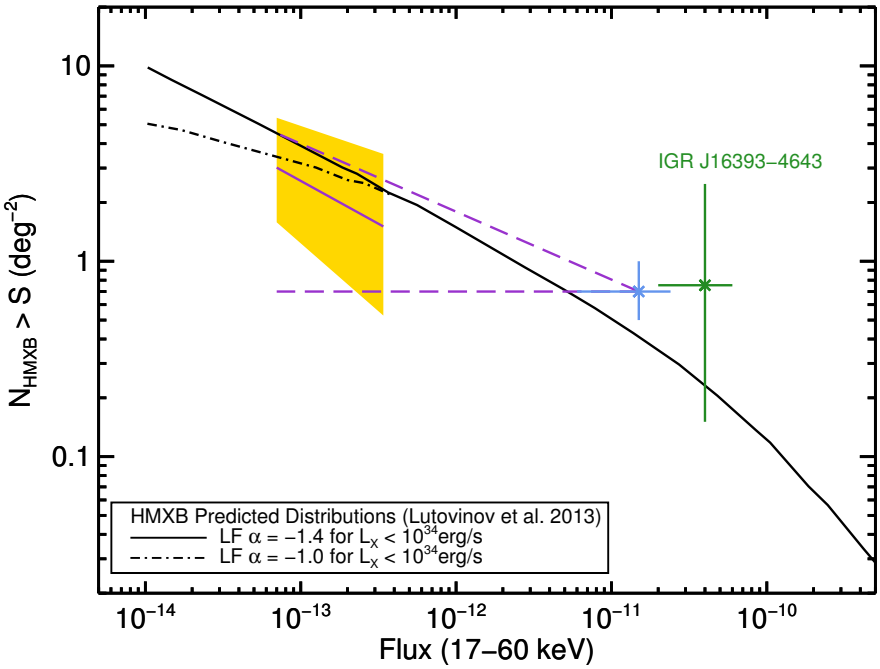

Figure 2.31: Predicted log$N$-log$S$ distributions of HMXBs from Lutovinov et al. (2013) are shown in black. The upper solid black curve assumes that the slope of the HMXB luminosity function does not change below 10^{34} erg s^{-1}, while the lower dash-dotted black curve assumes that the faint end of the HMXB LF flattens below 10^{34} erg s^{-1} to $\alpha = -1.0$. The green point represents the constraint on the HMXB flux distribution in the Norma region based on IGR J16393-4643. The blue point represents the minimum flux constraint derived from the HXMBs detected by the *INTEGRAL* Galactic Plane survey at Galactic latitudes $300° < \ell < 345°$, a wider section of the Norma arm than was covered by our *Chandra* and *NuSTAR* surveys. The solid purple line displays our measurement of the faint end of the HMXB flux distribution in the Norma region, assuming that the three HMXB candidates we discovered are all HMXBs and constitute a complete sample in the Norma region; the yellow polygon represents the 1σ uncertainty associated with this measurement. The dashed purple lines represent the possible extreme values of the HMXB flux distribution in the Norma region; the lower dashed line assumes that none of our HMXB candidates are true HMXBs, while the upper dashed line assumes that all three candidates are HMXBs and that as many as two additional HMXBs with similar X-ray fluxes have been missed by our current surveys.

additional spectroscopic near-IR observations of these HMXB candidates to more accurately determine their spectral types, which can improve estimates of the source distances, and to measure radial velocity (RV) curves for these systems; detecting Doppler shifts in these systems would confirm their binary nature, and RV measurements would allow us to constrain the mass of the compact object.

If any of the HMXB candidates contain a black hole, that would be especially interesting since only one Be-BH binary has been discovered to date (Casares et al. 2014) and was found to have very low X-ray luminosity ($L_X \sim 10^{31}$ erg s^{-1}; Munar-Adrover et al. 2014). The discovery of additional B/Be-BH binaries could help constrain some uncertain aspects of the binary evolution of high-mass stars such as the common envelope phase, the different physical treatments of which results in theoretical estimates of the total number of B/Be-BH systems that vary by more than an order of magnitude (Grudzinska et al. 2015). As possible progenitors of BH-NS binaries that may merge and produce gravitational waves detectable by advanced LIGO/VIRGO, the discovery of additional Be-BH systems and the determination of their orbital parameters could also help constrain predictions of the BH-NS merger rate. If some of the HMXB candidates are determined to be γ-Cas analogs, they could place constraints on the surface density of γ-Cas analogs in the Galaxy. Constraining the prevalence of the γ-Cas phenomenon among Be stars can help to distinguish between models that attribute the rapid rotation of Be stars to spin-up during main-sequence evolution (Granada et al. 2013) or mass transfer from a binary companion that is then ejected when it explodes as a supernova (de Mink et al. 2013); the former model cannot easily produce critically rotating Be stars, which is thought to be the most likely origin of the γ-Cas phenomenon (Motch et al. 2015). Finally, it is clear from Figure 2.31 that the Norma survey may not be sufficient to determine whether the HMXB LF does or does not flatten below 10^{34} erg s^{-1}. Finding additional faint HMXBs in archival *Chandra* observations of the Galactic plane would help to reduce the statistical uncertainties on the HMXB surface density and to account for potential variations in the spatial distribution of HMXBs.

2.5 Summary and Future Work

The *Chandra* and *NuSTAR* surveys of the Norma Arm region have shed light on the nature of the faint X-ray populations in the Galactic disk and allowed us to identify three low-luminosity HMXB candidates for further study. The *Chandra* survey reached a sensitivity limits of 10^{-14} erg cm^{-2} s^{-1} in the 2–10 keV band, detecting 1130 point sources. About half of the *Chandra* sources have soft thermal spectra and exhibit low X-ray absorption indicating they are primarily isolated X-ray active stars and active binaries located at a distance of $\lesssim 2$ kpc. The other half of the *Chandra* sources exhibit harder X-ray spectra, and the majority of them were identified as CVs based on their stacked *Chandra* spectra.

Along with the spectroscopic follow-up of the near-IR counterparts of some of the *Chandra* sources, *NuSTAR* observations of the Norma region have facilitated the individual classification of 28 of the brightest hard *Chandra* sources, including two colliding wind binaries, three

pulsar wind nebulae, a candidate black hole binary. We confirmed that a plurality of *NuSTAR* sources are most likely to be CVs. The CV candidates in the Norma region have plasma temperatures of ≈10–20 keV, consistent with the spectrum of the Galactic Ridge X-ray emission but lower than those of CVs near the Galactic Center. This temperature difference may indicate that the Norma region has a lower fraction of intermediate polars relative to other types of CVs and symbiotic binaries when compared to the Galactic Center. The *NuSTAR* log$N$-log$S$ distribution in the 10–20 keV band is consistent with the log$N$-log$S$ distribution measured by *Chandra* in the 2–10 keV band if the average source spectrum is assumed to be a thermal model with $kT \approx 15$ keV, as observed for the CV candidates.

Determining the underlying physical reasons for the difference in the observed CV populations in the Norma and Galactic Center regions will require more accurate classifications of these X-ray sources. Monitoring of the long-term X-ray variability of the CV candidates and *XMM-Newton* observations, which are better suited to detect and measure the strength of Fe lines, are the best current tools for ascertaining the fraction of IPs among the CV candidate in the Norma and Galactic Center regions.

Through the combination of *Chandra*, *NuSTAR*, and near-IR data for X-ray sources in the Norma region, we have identified three HMXB candidates with X-ray luminosities of $10^{32} - 10^{33}$ erg s^{-1}. All three HMXB candidates have main-sequence Be/B counterparts. The X-ray luminosities of these HMXB candidates are lower than the typical quiescent state luminosities of known HMXBs ($L_X \sim 10^{34}$ erg s^{-1}), but 1–2 orders of magnitude higher than the typical luminosities of isolated Be/B stars.

Determining how many of these candidates truly are HMXBs would help us understand how common it is for accretion in low-luminosity systems to be inhibited by physical mechanisms such as the propeller effect. If any of the HMXB candidates are found to harbor BHs, they would be useful in constraining theoretical models of the binary evolution of high-mass stars, and if any are determined to be γ-Cas analogs, their study could contribute to our understanding of the Be phenomenon. *XMM-Newton* observations to constrain the Fe line emission of the HMXB candidates, and radial velocity studies of their near-IR counterparts are crucial to confirm the HMXB nature of these sources. The discovery of additional HMXB candidates in archival *Chandra* observations of the Galactic plane will enhance the impact of these results by reducing the statistical uncertainties associated with all these measurements.

Chapter 3

The Poor

3.1 Investigating the metallicity dependence of HMXB populations

It has been well-established that the integrated X-ray luminosity of a population of HMXBs is linearly correlated with a galaxy's star formation rate (SFR; Ranalli et al. 2003; Grimm et al. 2003; Persic et al. 2004; Gilfanov et al. 2004; Lehmer et al. 2010; Mineo et al. 2012), which is not surprising given the fact that HMXBs form just ≈4-40 Myr after a starburst and remain X-ray active only for $\sim$ 10 Myr (Iben et al. 1995; Bodaghee et al. 2012c; Antoniou & Zezas 2016). However, there is a lot of scatter ($\sim$ 0.4 dex) in the $L_{X,\mathrm{HMXB}}$-SFR correlation measured by these studies. Mineo et al. (2012) show that possible contamination from LMXBs or active galactic nuclei (AGN), dust attenuation, and survey sensitivity variations cannot explain the observed scatter, and suggest that metallicity (Z) is the primary quantity source of scatter. Additional possible sources of scatter include HMXB variability and the fact that the ultraviolet (UV) and infrared (IR) SFR indicators typically used in these studies are sensitive to star formation on timescales which are longer ($\sim 10^8$ years; Conroy 2013) than the lifetimes of HMXBs.

Over the past decade, several binary population synthesis studies have investigated the effects of metallicity on HMXB evolution. Since the winds of main-sequence high-mass stars are line-driven, higher-metallicity stars experience higher mass loss rates due to the large number of metal atomic lines in the UV band. As a result, it is expected that in lower-metallicity binaries, the more massive star (i.e, the compact object progenitor) loses less mass prior to exploding as a supernova and is more likely to produce a BH than a NS (Belczynski et al. 2004; Dray 2006; Fragos et al. 2013b). Another effect of the weaker winds of lower-metallicity stars is that less angular momentum is lost from the binary, resulting in a larger fraction of HMXBs in which accretion occurs via Roche lobe overflow (Linden et al. 2010). Thus, lower-metallicity HMXB populations are expected to contain larger fractions of Roche lobe overflow BH HMXBs, which can drive higher accretion rates than NS HMXBs. There is a general consensus that larger populations of luminous HMXBs exist in

lower metallicity environments, although the strength of this trend varies between studies. Estimates of the increase in X-ray luminosity per SFR between $Z_\odot$ and $0.1Z_\odot$ vary from a factor of 2 to 10 (Linden et al. 2010; Fragos et al. 2013b).

There is increasing observational evidence that a larger number of HMXBs, especially ultra-luminous X-ray sources (ULXs, $L_X \gtrsim 10^{39}$ erg s^{-1}), per unit SFR exist is nearby low-metallicity galaxies (Mapelli et al. 2011; Kaaret et al. 2011; Prestwich et al. 2013; Basu-Zych et al. 2013a; Brorby et al. 2014; Douna et al. 2015). This enhanced number of bright HMXBs cannot be accounted for by stochasticity and suggests that at very low metallicities (12+log(O/H) < 8.0), the HMXB production rate is approximately 10 times higher than in solar metallicity galaxies (Brorby et al. 2014; Douna et al. 2015). Using a compilation of measurements for 49 galaxies from the literature, Brorby et al. (2016) parametrize the L_X/SFR-Z correlation as:

$$\log\left(\frac{L_X}{\text{erg s}^{-1}}\frac{M_\odot \text{ yr}^{-1}}{\text{SFR}}\right) = b \times (12 + \log(\text{O/H}) - 8.69) + c \tag{3.1}$$

where the solar gas phase metallicity is taken to be 12+log(O/H)=8.69, and the best-fitting parameters are $b = -0.59 \pm 0.13$ and $c = 39.49 \pm 0.09$. However, the correlation is largely driven by the blue compact dwarf galaxies (BCDs) in the sample that are X-ray detected, and the parametrization is likely biased since it does not take into account the upper limits on L_X/SFR for 20 BCDs that are not X-ray detected. Thus, the L_X/SFR-Z correlation may not be as strong as measured by Brorby et al. (2016). Furthermore, even if the L_X/SFR-Z trend is as strong as is claimed, it may be driven by factors other than metallicity. BCDs have star-forming regions that are more spatially concentrated and form denser star clusters than other nearby star-forming galaxies (Elmegreen et al. 1996; Hunter & Elmegreen 2004); it is therefore possible that the crowded star-forming clouds in BCDs have higher gas surface densities, which simulations predict should result in a more top-heavy stellar initial mass function (IMF; Krumholz et al. 2010). Thus, the enhanced number of HMXBs per SFR in BCDs could result from a top-heavy IMF rather than metallicity-dependent HMXB evolution. Similarly, the increase of L_X/SFR of star-forming galaxies with increasing redshift up to $z \sim 3$ (Basu-Zych et al. 2013b; Lehmer et al. 2016), which is typically attributed to the lower metallicities of high-redshift galaxies, may instead reflect differences in the star formation process in high-redshift galaxies.

Therefore, additional investigations are required to confirm whether more luminous HMXBs are formed in low-metallicity environments. This chapter presents the preliminary results of a study which seeks to measure the L_X/SFR-Z correlation using data from the *Chandra* extragalactic surveys and a star-forming sample of galaxies at $z \sim 2$ from the MOSFIRE Deep Evolution Field (MOSDEF; Kriek et al. 2015) survey. At this redshift, most star-forming galaxies are too X-ray faint to be detected even in the deepest X-ray surveys, so we stack the X-ray data from groups of galaxies with similar metallicity to obtain significant detections and measure their average X-ray luminosities. §3.2 describes the data sets used in this study, §3.3 explains our X-ray stacking method, and §3.4 discusses our preliminary results and planned improvements to the current study. In addition to teaching us about the

metallicity evolution of high-mass stars, this study could also have significant implications for estimates of the contribution of HMXBs to the heating of the intergalactic medium during the Epoch of Reionization at $z \gtrsim 8$ (Power et al. 2009; Parsons et al. 2014; Pober et al. 2015), as discussed in §1.2.2. Throughout this chapter, we assume a cosmology with $\Omega_m = 0.3$, $\Omega_\Lambda = 0.7$, and $h = 0.7$.

3.2 Data

3.2.1 The MOSDEF Survey

Our galaxy sample for this study is taken from the MOSDEF survey (Kriek et al. 2015). This four-year survey has obtained moderate-resolution (R = 3000–3650) rest-frame optical spectra for about 1500 H-band selected galaxies in the AEGIS, COSMOS, GOODS-N, and GOODS-S fields, where extensive multi-wavelength coverage is available (Grogin et al. 2011; Koekemoer et al. 2011). Targets were selected in three redshift intervals ($1.37 \leq z \leq 1.70$, $2.09 \leq z \leq 2.61$, and $2.95 \leq z \leq 3.80$), which were chosen with the criterion of maximizing coverage of strong rest-frame optical emission lines falling within atmospheric transmission windows. The redshifts used for target selection were determined by simultaneously fitting the broadband photometry and grism spectra obtained by the 3D-HST survey (Brammer et al. 2012; Momcheva et al. 2016), as well as some previous spectroscopic campaigns (Reddy et al. 2006; Barger et al. 2008; Coil et al. 2011; Cooper et al. 2012; Newman et al. 2013; van de Sande et al. 2013). The magnitude limits used to select galaxies in each of these redshift intervals are $H = 24.0$, $H = 24.5$, and $H = 25.0$ for the lower, middle, and higher redshift intervals, respectively; these magnitude limits roughly correspond to a lower mass limit of $\sim 10^9 M_\odot$ in each redshift interval. For this preliminary study, we use MOSDEF data taken during the first three years of the survey, which includes about 1000 galaxies.

MOSDEF Data Reduction and Galaxy Measurements

The MOSDEF survey observations were peformed with the MOSFIRE multi-object near-IR spectrograph (McLean et al. 2012) on the 10-meter Keck I telescope. The MOSFIRE spectra were reduced using a custom automated pipeline which divides the multi-object science frames into individual two-dimensional slits, performs flatfielding, subtracts sky contamination, cleans cosmic rays, rectifies the frames, combines all individual exposures for a given source, and calibrates the flux (see Kriek et al. (2015) for details). The reduced 2D spectra were calibrated using telluric standards by comparing the spectrum of a slit star with the photometry from the 3D-HST catalogs (Skelton et al. 2014). An additional slit-loss correction was applied to account for the fact that galaxies are resolved using the galaxy profiles from *Hubble Space Telescope* (*HST*) F160W imaging (Kriek et al. 2015); the uncertainties in flux calibration performed using this procedure were determined to be $\approx 16\%$ with a bias of $< 18\%$. Two-dimensional error spectra were calculated which include the

effects of Poisson counts from the source and sky as well as read noise. Then one-dimensional science and error spectra were optimally extracted based on the algorithm of Horne (1986).

Emission-line fluxes were measured by fitting Gaussian line profiles to the one-dimensional spectra. Flux uncertainties were estimated by performing 1,000 Monte Carlo realizations of the spectrum of each object perturbed by its error spectrum and refitting the line profiles; the average line fluxes and dispersions were measured from the resulting line flux distributions. Spectroscopic redshifts were measured using the centroids of the highest signal-to-noise ratio (S/N) emission lines, typically Hα or [OIII] λ5007.

Stellar masses were estimated by modeling the available photometric data (Skelton et al. 2014) for each galaxy with the spectral energy distribution (SED) fitting program FAST (Kriek et al. 2009), adopting the MOSDEF-derived redshift for each galaxy. For the SED fitting, we used the stellar population synthesis models of Conroy et al. (2009), assumed a Chabrier (2003) IMF, adopted the Calzetti et al. (2000) dust attenuation curve, and parametrized star-formation histories using delayed exponentially declining models of the form SFR(t) $\propto te^{-t/\tau}$, where t is the time since the onset of star formation and tau is the characteristic star formation timescale. For each galaxy, the best-fitting model was found through χ^2 minimization, with the free parameters being the stellar population age, characteristic star formation timescale, metallicity, and dust extinction; stellar masses and SFRs are derived from the best-fitting model parameters. For each stellar population parameter, confidence intervals were calculated from the distributions from 500 Monte Carlo simulations which perturbed the input SED and refit it.

SFRs were also derived from dust-corrected Hα luminosities. The dust corrections were calculated using the Balmer decrement (Hα/Hβ), correcting the Hα and Hβ fluxes for Balmer absorption and adopting the Calzetti et al. (2000) dust-attenuation curve (Reddy et al. 2015). The dust-corrected Hα luminosities were converted into SFRs using the calibration of Kennicutt (1998) converted to a Chabrier (2003) IMF. An Hα-derived SFR is only calculated if both Hα and Hβ are detected with S/N$\geq$ 3.

The gas-phase metallicity of each galaxy is derived from the fluxes of emission lines originating in HII regions, and is thus a proxy for the metallicity of the young stellar population including HMXBs. The N2 (log([NII]λ6584/Hα)) and O3N2 (log(([OIII]λ5007/Hβ)/([NII]λ6584/Hα))) indicators were used to estimate the gas-phase oxygen abundances. If one of the emission lines used in a given line flux ratio was not detected with S/N$\geq$ 3, then a 3σ upper limit on the line flux was computed and used to calculate an upper or lower limit for the metallicitiy indicator. For both the N2 and O3N2 indicators, we used the calibrations of Pettini & Pagel (2004), which are based on a sample of HII regions with direct electron temperature measurements. These calibrations are

$$12 + \log(\mathrm{O/H}) = 8.90 + 0.57 \times \mathrm{N2} \tag{3.2}$$

$$12 + \log(\mathrm{O/H}) = 8.73 - 0.32 \times \mathrm{O3N2} \tag{3.3}$$

where 12+log(O/H) is the oxygen abundance. For reference, the solar oxygen abundance is measured to be 12+log(O/H)$\approx$ 1.69 (Allende Prieto et al. 2001; Asplund et al. 2004). Pettini

& Pagel (2004) find that 68% of the log(O/H) measured by the direct electron temperature method lie within ±0.18 (±0.14) of the value determined by the N2 (O3N2) calibrator.

3.2.2 *Chandra* Extragalactic Surveys

During the course of its first 17 years in space, the *Chandra X-ray Observatory* performed several deep surveys of extragalactic CANDELS fields. For this study, we make use of the *Chandra* ACIS imaging in the GOODS-N, GOODS-S, and EGS fields, since they have the deepest X-ray exposures. The exposure depths reached by the data used from these fields is 4 Ms in GOODS-S[1], 2 Ms in GOODS-N, and 800 ks in EGS (Rosati et al. 2002; Giacconi et al. 2002; Alexander et al. 2003; Luo et al. 2008; Laird et al. 2009; Xue et al. 2011; Nandra et al. 2015). The flux limits (over $> 50\%$ of the survey area) in the 0.5–2 keV band reached by these surveys are 7×10^{-17}, 1.2×10^{-16}, and 2×10^{-16} erg cm^{-2} s^{-1}, respectively, which correspond to 2–10 keV rest-frame X-ray luminosities of 2×10^{42}, 4×10^{42}, 7×10^{42} erg s^{-1} at $z \sim 2$ assuming a power-law spectrum with $\Gamma = 1.8$.

Data Processing

The *Chandra* data from all three fields were analyzed using a consistent procedure described in detail in Laird et al. (2009), Nandra et al. (2015), and Aird et al. (2015). The data was processed using the CIAO analysis software v4.1.2. Each observation was cleaned and calibrated using standard CIAO algorithms, and periods of high background were rejected. Then, the astrometry of individual observations was improved using the Canada-France-Hawaii Telescope Legacy survey (CFHTLS) *i*-band catalog. For each observation, the *Chandra* wavelet source detection algorithm `wavdetect` was run on the 0.5–7 keV band image with a detection threshold of 10^{-6}. The positions of `wavdetect` sources were then compared to sources from the CFHTLS *i*-band catalog using the CIAO tool `reproject_aspect`, which applied a positional shift to each *Chandra* observation that minimized the offsets between *Chandra* positions and CFHTLS counterparts.

For each individual observation, event files, images, exposure maps, and PSF maps of the 90% encircled energy fraction (EEF) as calculated by the MARX simulator were created in the 0.5–7, 0.5–2, 2–7, and 4–7 keV bands. The exposure maps provide the exposure multiplied by the effective collecting area at each pixel location; they were weighted for a $\Gamma = 1.4$ power-law spectrum since AGN and X-ray binaries exhibit power-law spectra with $\Gamma \approx 1 - 2$ in the *Chandra* band[2]. Then, for each field, the event files, images, exposure maps, and PSF maps were merged together using the CIAO tool `merge_all`. These mosaic files for each field were used in our X-ray stacking analysis (see §3.3).

[1]The total exposure depth of in the *Chandra* Deep Field South to date is 7 Ms, but we have not yet included the most recent 3 Ms of observations in our preliminary study.

[2]Adopting a different value of Γ in the range from 1.0 to 2.0 would change the exposure map values by $< 10\%$.

Source Catalogs

An important part of our X-ray stacking analysis is the removal of detected sources from our background maps. Source catalogs for the *Chandra* Deep Field South (CDFS), *Chandra* Deep Field North (CDFN), and AEGIS-X Deep (AEGIS-XD) surveys are provided by Xue et al. (2011), Alexander et al. (2003), and Nandra et al. (2015), respectively. In this preliminary study, we make use of these published catalogs, but since they use different false probability thresholds with the `wavdetect` tool and perform the searches in different energy bands, in the future we will make a catalog using a commom detection threshold and the same energy bands across all the fields.

We also make use of the MOSDEF X-ray catalog from Coil et al. (2015). This catalog matches *Chandra* sources detected by `wavdetect` with a false probability threshold $< 4 \times 10^{-6}$ in at least one of four energies bands (0.5–7, 0.5–2, 2–7, and 4–7 keV) to likely counterparts in the 3D-HST catalog used for MOSDEF target selection. For X-ray sources observed by MOSDEF, this catalog provides 2–10 keV rest-frame X-ray luminosities assuming a power-law spectrum with $\Gamma = 1.9$ subject only to Galactic absorption ($N_{\rm H} \sim 10^{20}$ cm^{-2}). For all galaxies in the MOSDEF sample that are not associated with an X-ray detection, Coil et al. (2015) estimate 95% confidence upper limits on the X-ray luminosity.

3.2.3 Galaxy Sample Selection

Since our goal is to study HMXB emission from star-forming galaxies, we applied several selection criteria to the MOSDEF galaxy sample in order to minimize contamination from other X-ray sources. First, we excluded from our sample any MOSDEF galaxy that was identified as an AGN using the three criteria described in Coil et al. (2015). We excluded galaxies that were individually detected in the *Chandra* extragalactic surveys since their high X-ray luminosities ($L_X > 10^{42}$ erg s^{-1}) indicate they host AGN; the MOSDEF galaxies that are X-ray detected have 2–10 keV rest-frame X-ray luminosities of 10^{43} to 10^{45} erg s^{-1}. Since *Spitzer* IRAC data is available for MOSDEF galaxies (Skelton et al. 2014), we also excluded from our sample any galaxies that meet the Donley et al. (2012) criteria for IR AGN; these IR criteria select AGN with heavy obscuration ($N_{\rm H} > 10^{24}$ cm^{-2}), which may not be detected in the rest-frame X-ray 2–10 keV band. We also used line flux ratios to exclude optically-identified AGN from our sample. Optical diagnostics such as the "BPT diagram" (Baldwin et al. 1981; Veilleux & Osterbrock 1987) can be used to identify AGN via their enhanced ratios of nebular emission lines [OIII]λ5008 to Hβ and [NII]λ6584 to Hα; these optical diagnostics can identify AGN even if the direct line-of-sight to the accretion disk is obscured. We remove from our sample any galaxy with log([NIIλ6584/Hα)> -0.3 and any galaxy with [OIII/Hβ and [NII]/Hα values or lower limits that place it above the Kauffmann et al. (2003) line in the BPT diagram. Some of the galaxies above the Kauffmann et al. (2003) may be starbursts, but we choose to be conservative in our sample selection to limit AGN contamination as much as possible.

While the X-ray luminosity of HMXB populations is correlated with the SFR, the X-ray

luminosity of LMXBs scales with the stellar mass of the galaxy (Gilfanov 2004). Thus, to maximize the contributions of HMXBs relative to LMXBs to the total X-ray luminositiy, we only include galaxies with high specific SFR (sSFR$> 10^{-10}$ yr^{-1}), which is defined as the ratio of SFR to stellar mass (M_*). The sSFR limit we adopt is based on studies of local galaxies, which find that the sSFR at which a galaxy's X-ray luminosity transitions from being LMXB-dominated to HMXB-dominated is $\sim 10^{-10}$ yr^{-1} (Lehmer et al. 2010). We think this sSFR limit is reasonable for $z \sim 2$ galaxies as well, since while it is expected that between $z = 0$ and $z \approx 2$, the X-ray luminosity of LMXBs per M_* increases by about an order-of-magnitude (Fragos et al. 2013b), simulations indicate galaxies may grow in mass by an order-of-magnitude during the same time (Moster et al. 2013).

We also exclude from our galaxy sample any galaxies with SFR$< 1 M_\odot$ yr^{-1}. At lower SFRs, the number of HMXBs that are produced is so small that the HMXB luminosity function is not well sampled and stochastic variations dominate the integrated X-ray luminosity (Grimm et al. 2003). At low SFR, the typical galaxy luminosity produced by HMXBs is lower than the mean X-ray luminosity (averaged over a population of galaxies), and the scatter of HMXB luminosities in low-SFR galaxies is much larger than in high-SFR galaxies (Justham & Schawinski 2012).

We only included galaxies from the GOODS-S, GOODS-N, and EGS fields, since the *Chandra* data in these fields is much deeper than in COSMOS or UDS. Furthermore, only galaxies in the two lowest redshift intervals ($1.37 \leq z \leq 1.70$ and $2.09 \leq z \leq 2.61$) are used because the galaxy sample at $z \sim 3$ is too small to produce significant detections through X-ray stacking analysis.

Finally, we restricted our sample to galaxies with Hα-derived SFRs, since they are more reliable than SED-derived SFRs and sensitive to star formation on shorter timescales, more similar to those of HMXBs (Conroy 2013). In the MOSDEF observations gathered before mid-2015, there are 158 (154) galaxies which meet these criteria and for which MOSDEF metallcity measurements or upper/lower limits derived with the N2 (O3N2) indicator are available. We primarily use the sample with O3N2 metallicity measurements, since comparisons of metallicity indicators between $z = 0 - 2$ suggest that the O3N2 indicator is not significantly biased at high-redshift (Liu et al. 2008; Steidel et al. 2014), while the N2 indicator tends to overestimate oxygen abundance in high-redshift galaxies (Liu et al. 2008; Newman et al. 2014). The O_{32} and R_{23} indicators appear to be the most robust as a function of redshift (Shapley et al. 2015), but they require the [OII]$\lambda\lambda$3726,3729 line, which is only detected in a smaller subsample of galaxies.

The redshift distribution for the sample of MOSDEF galaxies meeting our selection criteria is shown in Figure 3.1. A quarter of the sample is made up of galaxies with $z \sim 1.5$, while the majority of the sample has $z \sim 2.3$. Figures 3.2 and 3.3 display the distributions of metallicities, SFRs, and stellar masses of our galaxy sample. As can be seen in the histogram distributions, the $z \sim 1.5$ and $z \sim 2.3$ galaxy samples cover similar ranges in SFR and stellar mass, but the mean metallicity of the $z \sim 1.5$ galaxies is lower than that of the $z \sim 2.3$ galaxies, which is not surprising due to the metallicity evolution of the Universe. The correlation between galaxy mass and metallicity, which has been well-studied locally and

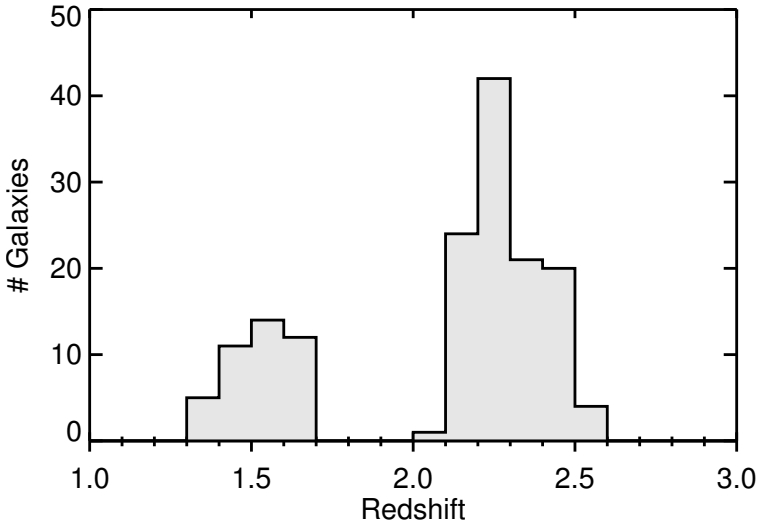

Figure 3.1: Redshift distribution of the sample of MOSDEF galaxies used in our *Chandra* stacking analysis. This distribution includes all galaxies meeting our selection criteria and for which we have either a metallicity measurement or an upper/lower limit on metallicity based on the O3N2 indicator.

confirmed at redshifts up to $z \sim 3.5$ (e.g. Tremonti et al. 2004; Kewley & Ellison 2008; Erb et al. 2006; Maiolino et al. 2008), can be seen in Figure 3.2; Sanders et al. (2015) studied this correlation with the MOSDEF sample specifically and found that, unlike at low redshifts, the mass-metallicity relation at $z \sim 2$ is independent of SFR. In line with this result from Sanders et al. (2015), we do not find a significant correlation between metallicity and SFR in our sample of MOSDEF galaxies (see Figure 3.3).

3.3 X-ray Stacking Analysis

The typical X-ray luminosities of normal (non-AGN) star-forming galaxies with SFRs$\sim 1-100 M_{\odot}$ yr^{-1} are $L_X \sim 10^{39.5} - 10^{41.5}$ erg s^{-1} in the rest-frame 2–10 keV band. Since these luminosities fall below the sensitivity limits of the *Chandra* extragalactic surveys, studying the X-ray emission of these galaxies requires stacking the X-ray data. We developed an X-ray stacking technique that is similar to that used by Rangel et al. (2013) and Mezcua et al. (2016). In order to achieve the highest sensitivity, we performed the stacking in the 0.5–2 keV band because *Chandra* has the highest effective area and best angular resolution at soft X-ray energies. Thus, any time we refer to images or exposure maps

First, in order to prevent contamination from detected sources to our stacks, we removed counts lying within two times the 90% EEF PSF radius of the position of any detected sources in the CDFS, CDFN, and AEGIS-XD source catalogs (Alexander et al. 2003; Xue et al. 2011; Nandra et al. 2015), regardless of what energy band the source was detected in. To keep track of the areas of the mosaics from which counts were removed, we created a mask with pixel values of zero in regions where counts were removed and values of one everywhere else.

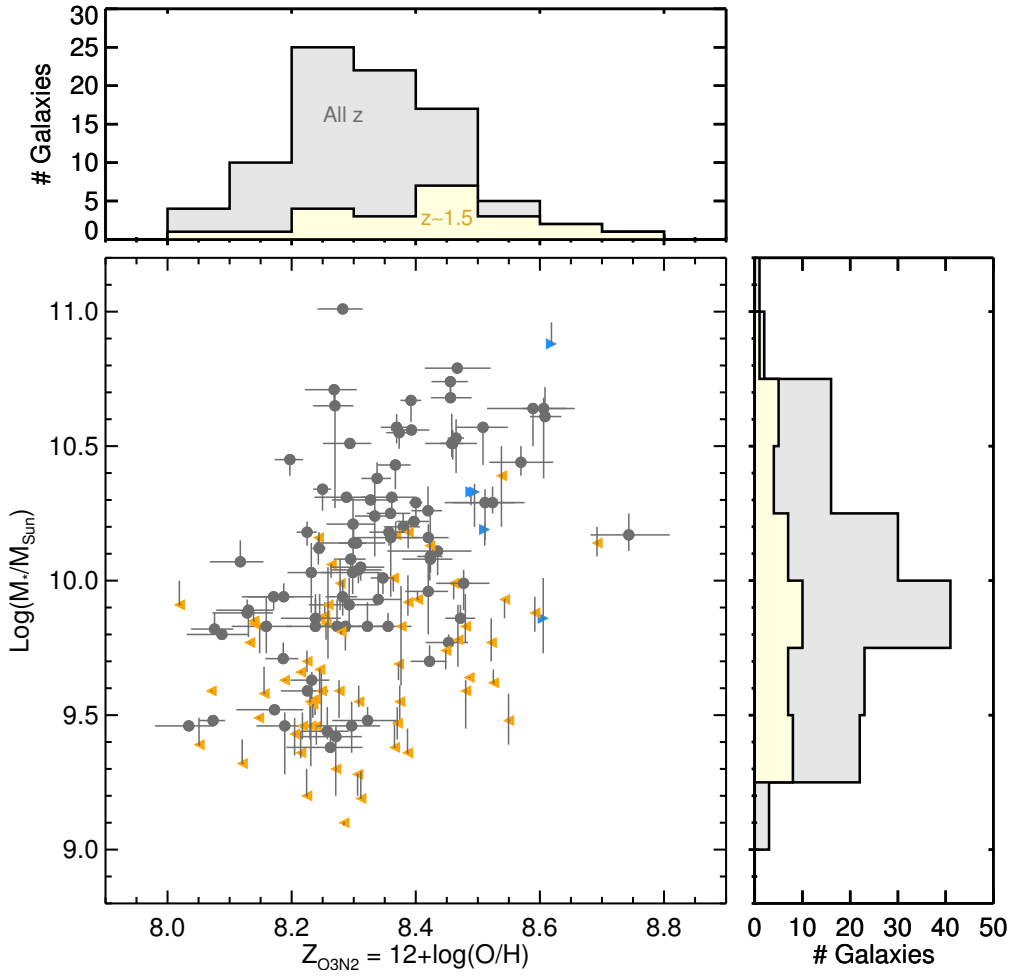

Figure 3.2: The main plot shows the stellar mass versus oxygen abundance derived from the O3N2 indicator for individual galaxies. Metallicity measurements (which require S/N> 3 detections of [OIII], [NII], Hα, and Hβ) are shown in gray points, 3σ upper limits are shown as orange triangles, and 3σ lower limits are shown as blue triangles. The top panel shows the distribution of metallicity measurements (not including upper/lower limits) for $z \sim 1.5$ galaxies in yellow and for the full redshift sample in gray. The right panel shows the distribution of stellar masses. Gray error bars represent the 1σ confidence intervals.

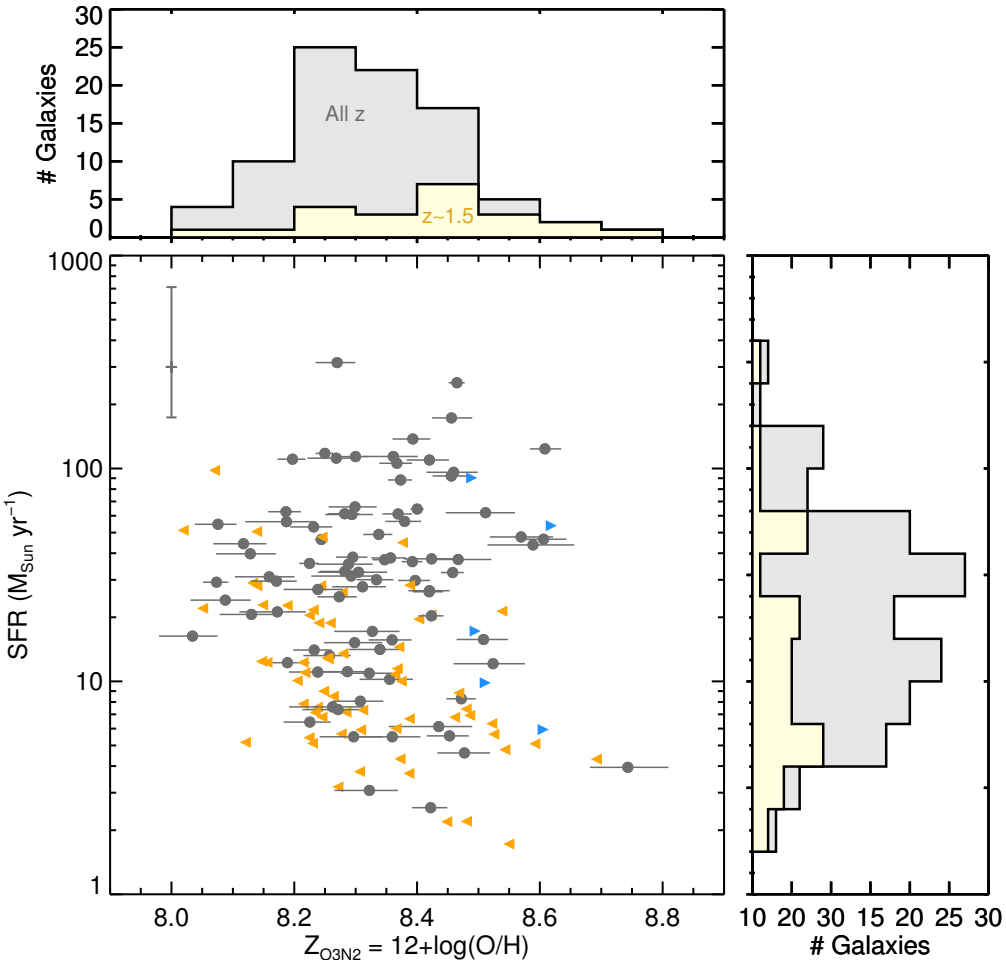

Figure 3.3: This figure is organized in the same way as Figure 3.2, except that it shows the star formation rates rather than the stellar masses of our MOSDEF galaxy sample.

For each of the galaxies in our MOSDEF sample, we created source and background aperture regions. Each source aperture was defined as a circular region centered on the galaxy position from the 3D-HST catalog with a radius equal to the 90% EEF PSF radius. Each background aperture was defined as an annulus with an inner radius equal to 10″ and an outer radius equal to 30″.

Then we made some final refinements to our galaxy sample. To further reduce contamination to our stacks, we excluded any galaxies that were located within a distance less than three times the 90% EEF radius from any detected X-ray sources. We also excluded a small number of galaxies located so far off-axis in the *Chandra* observations that their 90% EEF radius was larger than 6″, since such large aperture regions would introduce a lot of additional background to the stacks. Finally, we removed four galaxies from our sample whose *Chandra* apertures overlapped with one another and one galaxy located in an area of diffuse X-ray emission.

We extracted the counts ($C_{\rm src}$, $C_{\rm bkg}$), exposure times ($t_{\rm src}$, $t_{\rm bkg}$), and mean effective areas ($A_{\rm src}$, $A_{\rm bkg}$) in both the source and background regions for each galaxy using the CIAO tool `dmextract`. The background region counts were extracted from a background map we made by removing the counts within the source aperture regions from the mosaic images; in corresponding fashion, we also punched out the source aperture regions from the mask we created, setting the mask value to zero in regions from which counts were removed. We then used the background mask to calculate what fraction of each aperture area may be "lost" to the regions we punched out from the mosaics.

For each source, we calculated the net background-subtracted counts and a conversion factor to translate the net counts into the rest-frame X-ray luminosity. The net source counts are given by:

$$C_{\rm net} = C_{\rm src} - C_{\rm bkg} \times \frac{t_{\rm src} A_{\rm src} P_{\rm src}}{t_{\rm bkg} A_{\rm bkg} P_{\rm bkg}} \tag{3.4}$$

where $P_{\rm src}$ and $P_{\rm bkg}$ are the source and background aperture areas, respectively, in units of pixels^2 and corrected for any fraction of the aperture that overlaps with any of the regions punched-out from the mosaic images. For an individual source, converting the net counts in the 0.5–2 keV band into the rest-frame 2–10 keV X-ray luminosity requires the following components: the exposure time, effective area, the EEF, the mean energy per photon ($E_{\rm avg}$), the luminosity distance ($D_{\rm L}$, and the k-correction ($k_{\rm corr}$), which is the multiplicative factor required to convert the luminosity in the observed band to the chosen rest-frame. The mean photon energy and the k-correction depend on the source spectrum, which we assume to be a power-law with $\Gamma = 1.7$, a typical 2–10 keV spectrum for HMXBs in nearby galaxies (Ptak et al. 1999). Galactic absorption along the line-of-sight to the *Chandra* extragalactic fields is negligible, and for the rest-frame 2–10 keV band emission to be significantly absorbed, the column density within the host galaxy would have to be $\gtrsim 5 \times 10^{22}$ cm^{-2}. It has been suggested that a simple power-law spectrum may not be appropriate for HMXB populations in low-metallicity galaxies, since the HMXB luminosity of nearby, low-Z dwarf galaxies is dominated by ULXs, which exhibit exponentially cutoff power-law spectra with $\Gamma \approx 1 - 1.5$ and $E_{\rm cut} \approx 2 - 6$ keV (Kaaret 2014). However, when converting fluxes from the 0.5–2 keV

band to the rest-frame 2–10 keV band for $z < 4$, the k-correction for these different spectral models differs by $\lesssim 15\%$. Therefore, we adopt a $\Gamma = 1.7$ power-law model for simplicity. The k-correction is calculated as follows:

$$k_{\rm corr} = \frac{E_{\rm rest,2}^{(2-\Gamma)} - E_{\rm rest,1}^{(2-\Gamma)}}{E_{\rm obs,2}^{(2-\Gamma)} - E_{\rm obs,1}^{(2-\Gamma)}}(1+z)^{(\Gamma-2)} \tag{3.5}$$

where $E_{\rm obs,1} = 0.5$ keV, $E_{\rm obs,2} = 2.0$ keV, $E_{\rm rest,1} = 2.0$ keV, and $E_{\rm rest,2} = 10.0$ keV. For each source, we calculate a conversion factor to convert the observed photon flux to the rest-frame X-ray luminosity, defined as:

$$f_{\rm conv} = 4\pi D_{\rm L}^2 E_{\rm avg} k_{\rm corr}/{\rm EEF} \tag{3.6}$$

For a given galaxy stack, the net counts and the expected number of background counts of individual source apertures were summed. We also computed the product of exposure time and effective area ($w_{\rm exp} = t_{\rm src} A_{\rm src}$) for individual galaxies, and then added these products together. To calculate the average X-ray luminosity of the galaxy stack, the total net counts were divided by the sum of $w_{\rm exp}$ and multiplied by a weighted average of the luminosity conversion factors, $f_{\rm conv}$. The weights applied to $f_{\rm conv}$ are $w_{\rm exp}$, because the combination of exposure time and effective area determines the relative sensitivity (S/N) of observations of different sourcesl. Since our goal is to study the relationship between L_X/SFR and metallicity, for each galaxy stack, we also calculate the weighted average SFR, applying the same weights ($w_{\rm exp}$) used to calculate the X-ray luminosity of each stack.

Since we need to combine galaxies from different redshifts and from surveys with different exposure depths in our stacks to obtain enough sensitivity, we tested whether our stacking procedure can accurately measure average X-ray luminosities even when combining galaxies between $z \sim 1.3$ and $z \sim 2.6$ and exposure depths ranging from 800 ks to 4 Ms. For this test, we applied our stacking procedure to groups of detected X-ray sources in the CDFS, CDFN, and AEGIS-XD surveys with a similar redshift distribution to our MOSDEF galaxy sample. We calculated the average X-ray luminosity of stacks of these sources using our stacking method and compared them to exposure-weighted averages of their individual X-ray luminosities in *Chandra* catalogs. We found that the average X-ray luminosities derived using our stacking procedure were consistent with the averages of individual measurements at the 3% level.

We considered two sources of error on each stacked signal. The first is Poisson noise associated with the background, which we used to establish the significance of the signal in each stack. We calculated the Poisson probability that a random fluctuation of the total background counts could result in a number of counts within the combined source aperture greater than or equal to the total stacked counts (source plus background). If this probability is $\leq 0.0036\%$, the significance is $\geq 2.7\sigma$ and the stacked signal is considered to be a detection; otherwise, only an upper limit on the average X-ray luminosity of the galaxies in the stack was calculated. These upper limits and the uncertainties associated with the measured X-ray luminosities are calculated using a bootstrapping method, which measures

how the contribution of individual sources affects the average stacked signal. To determine the bootstrapping errors, we randomly resampled the galaxies in each stacking bin 1000 times and repeated our stacking analysis with these samples. The number of galaxies in a given stack is conserved during the resampling, leading some values to be duplicated while others are eliminated in a particular iteration. From the resulting distribution of stacked X-ray luminosities, we measure 1σ confidence intervals for stacked signals exceeding our detection threshold and 2σ upper limits for stacked signals which do not exceed the threshold.

3.4 Preliminary Results

We divided the MOSDEF galaxies into different metallicity bins and stacked their X-ray data to measured the average X-ray luminosity per SFR of galaxies in each bin. We tried two different binning schemes with the O3N2-derived oxygen abundances, dividing the galaxies into two metallicity bins with $\approx 3.8\sigma$ significance or splitting them into three metallicity bins with $\approx 3.1\sigma$ significance. We also stacked the galaxies in two metallicity bins based on the N2 indicator to test whether any trends we saw were independent of the metallicity-indicator use.

The resulting L_X/SFR measurements are shown in Figure 3.4. The green lines in this figure display the L_X-SFR correlation measured using nearby samples of galaxies; Mineo et al. (2012) measure a linear relationship between L_X and SFR for HMXB-dominated galaxies while Lehmer et al. (2010) find that the X-ray emission from both LMXB and HMXB dominated galaxies can be accounted for by a linear depedence on M_* in addition to a linear dependence on SFR. These studies did not investigate whether the HMXB luminosity varies with metallicity, but they did find significant scatter of 0.3-0.4 dex in the L_X-SFR correlation and suggested that metallicity-dependent HMXB evolution (Dray 2006; Linden et al. 2010) could be one of the underlying causes of the scatter. As can be seen in Figure 3.4, the L_X/SFR values of the MOSDEF galaxies lie $\gtrsim 2\sigma$ above the $z = 0$ relations, which is consistent with other studies that have found that galaxies at redshifts $\gtrsim 1$ have higher values of L_X/SFR compared to star-forming galaxies in the local Universe (Basu-Zych et al. 2013b; Lehmer et al. 2016).

Regardless of the metallicity bins used, the L_X/SFR values of the MOSDEF stacks are not statistically correlated with metallicity. In Figure 3.4, the purple dashed line shows the L_X/SFR$-Z$ relationship predicted by population synthesis models for HMXBs (Fragos et al. 2013a), while the purple dotted line shows the L_X/SFR-Z correlation measured by Brorby et al. (2016) using samples of normal star forming galaxies, Lyman-break analogs, and blue compact dwarf galaxies (BCDs). Although the MOSDEF stacks are consistent with a constant L_X/SFR, due to the large uncertainties of these L_X/SFR measurements, we cannot definitively rule out that the predicted correlation does not exist. With the exception of the middle metallicity bin of the three-bin O3N2-indicator stacks, the L_X/SFR values of the stacks are consistent at $< 1.2\sigma$ confidence with the L_X/SFR-Z relations from Fragos et al. (2013a) and Brorby et al. (2016).

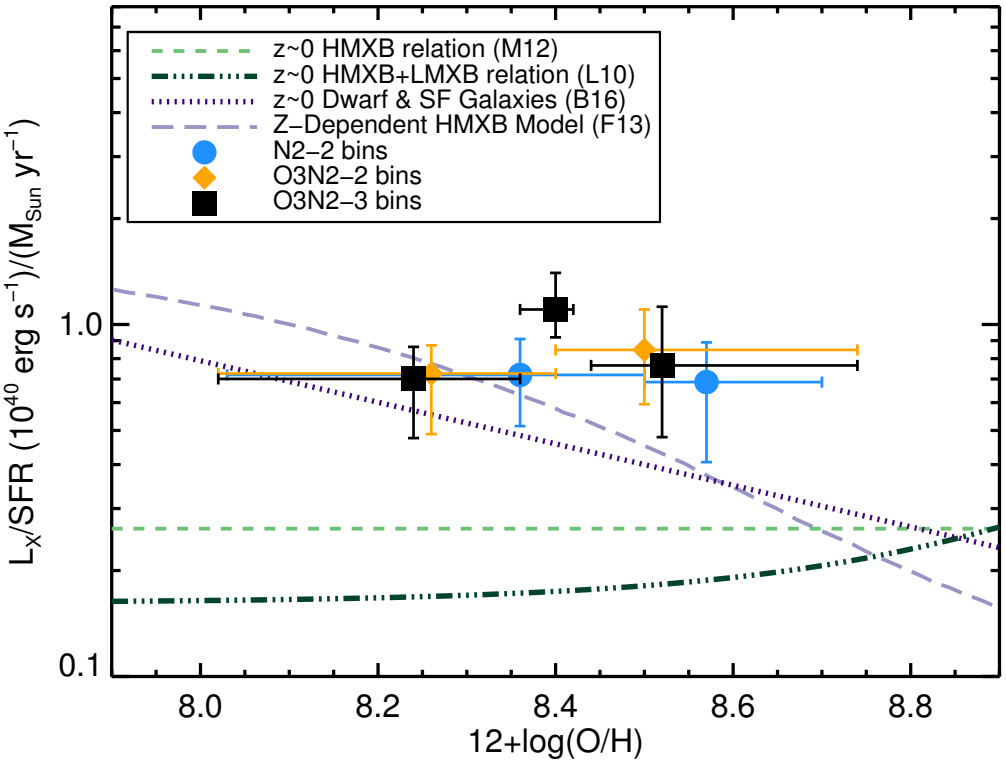

Figure 3.4: The weighted average rest-frame 2–10 keV X-ray luminosity per SFR for stacks of $z \sim 2$ star-forming galaxies as a function of metallicity. Black (orange) points split up the sample into three (two) metallicity bins based on the O3N2 indicator, while blue points split up the sample into two metallicity bins based on the N2 indicator. There are systematic offsets between the oxygen abundances derived using the N2 and O3N2 indicators, just as is the case at low redshift. Vertical error bars show 1σ confidence interval of L_X/SFR, while horizontal error bars represent the range of metallicity of the galaxies in a given stack. The two green lines show measured L_X/SFR relations using samples of nearby galaxies. The dashed green line shows the linear L_X-SFR relation measured by Mineo et al. (2012), and the dash-dotted line displays a model for a galaxy's X-ray luminosity from Lehmer et al. (2010) which includes a linear depedence on both SFR due to HMXBs and M_* due to LMXBs; in order to compare the latter model to the MOSDEF stacks, Lehmer et al. (2010)'s relation was converted into a function of Z for this plot using the SFR$-M_*$ correlation from Shivaei et al. (2015) and the $M_* - Z$ correlation from Steidel et al. (2014). The dotted purple line is the measured L_X/SFR$-Z$ correlation from Brorby et al. (2016) based on nearby normal star-forming and dwarf galaxies. The dashed purple line is the predicted L_X/SFR$-Z$ relation for HMXBs based on population synthesis models by Fragos et al. (2013a). All the L_X-SFR relations shown have been calibrated for the O3N2 metalllicity indicator.

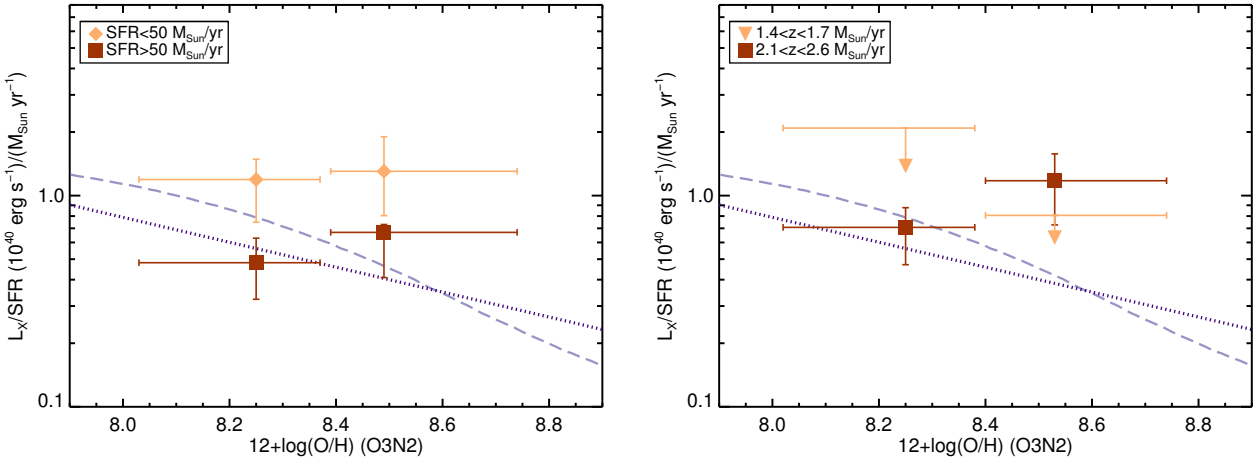

Figure 3.5: *Left*: The weighted average L_X/SFR versus metallicity for stacks of MOSDEF galaxies divided into high and low SFR groups. The light (dark) orange points show L_X/SFR for galaxies with SFR$< 50 M_\odot$ yr^{-1} (SFR$> 50 M_\odot$ yr^{-1}), along with 1σ uncertainties. *Right*: The weighted average L_X/SFR versus metallicity for stacks of MOSDEF galaxies divided into two redshift intervals. The light orange points are 2σ upper limits on L_X/SFR for $z \sim 1.5$ galaxies. The dark orange points represent L_X/SFR for $z \sim 2.3$ galaxies, along with 1σ uncertainties. In both panels, horizontal error bars show the metallicity range spanned by the galaxies in a given stack. The purple lines are the same as in Figure 3.4.

We investigate whether any systematic effects may be flattening the appearance of the L_X/SFR$-Z$ relation in our MOSDEF stacks. First, we consider the impact of the SFR on the measurements of L_X/SFR versus Z. We split up the MOSDEF galaxy sample into two SFR bins and two metallicity bins. As shown in Figure 3.5, galaxies with lower SFR have higher L_X/SFR; this trend has been observed in other studies, and is attributed to a larger fraction of a galaxy's X-ray luminosity being produced by LMXBs as the SFR, and therefore the contribution of HMXBs, decreases (e.g., Lehmer et al. 2010; Basu-Zych et al. 2013b). In Figure 3.4, the higher-metallicity bins contain galaxies with higher average SFRs. Thus, taking into account the observed trend between L_X/SFR and SFR, we conclude that the L_X/SFR values of higher-metallicity bins in Figure 3.4 may be biased towards lower values than they should be. Thus, potential bias due to the SFR distribution of galaxies in each metallicity bin cannot explain why the predicted negative correlation between L_X/SFR and Z is not observed.

We also consider the effects of redshift evolution on the observed L_X/SFR$-Z$ relation. Figure 3.5 shows L_X/SFR for MOSDEF galaxies that have been split into two redshift intervals and two metallicity bins. There are not enough galaxies in the lower redshift ($1.37 \leq z \leq 1.61$) interval to obtain significant stacked X-ray detections so we calculate upper limits for these lower-redshift stacks. The upper limit we can place on the lower-Z bin is not particularly meaningful, but the limit we can place on the higher-Z (12+log(O/H)> 8.4)

bin is lower than the L_X/SFR value of the higher-redshift ($2.09 \leq z \leq 2.61$) galaxies in the higher-Z bin, indicating that L_X/SFR does increase between $z \sim 1.5$ and $z \sim 2.3$. Since a larger fraction of the galaxies in the higher-metallicity stacks in Figure 3.4 are at $z \sim 1.5$, when we combine galaxies from different redshift intervals in our stacks, the L_X/SFR values of the higher-metallicity bins are more impacted relative to the lower-metallicity bins. When we measure L_X/SFR versus Z for the $z \sim 2.3$ galaxies by themselves, the higher-metallicity bin lies $\approx 2.0\sigma$ above the predicted L_X/SFR$-Z$ relation, and the data is more consitent with either no correlation or a positive correlation of L_X/SFR with Z rather than a negative correlation, as shown in Figure 3.5.

While the X-ray luminosity of HMXBs is predicted to be inversely correlated with metallicity, the X-ray luminosity of AGN could be positively correlated with metallicity. Studies of AGN and their host galaxies in the redshift range $0.2 < z < 2.5$ discovered that the AGN occupation fraction (the fraction of galaxies hosting an AGN) increases with stellar mass (Bongiorno et al. 2012; Aird et al. 2012; Jones et al. 2014). A galaxy at the upper end of the mass range ($\log(M_*/M_\odot)$=11) of the MOSDEF sample is approximately 6–10 times more likely to host an AGN than a galaxy at the lower end of the mass range ($\log(M_*/M_\odot)$=9.3). Therefore, given the positive correlation between stellar mass and metallicity (e.g. Sanders et al. 2015), galaxies with higher metallicities are more likely to host an AGN. If, despite our efforts to remove AGN from our galaxy sample, some AGN contamination is still present, we would expect to see a stronger positive correlation between L_X/SFR and mass than between L_X/SFR and metallicity. We therefore divided the MOSDEF galaxy sample in three mass bins; the L_X/SFR of these stacks is shown in Figure 3.6, and they do not exhibit any correlation with stellar mass. Although this result does not definitively rule out the possibility that low-luminosity AGN could be contaminating our galaxy sample, it does suggest that the level of such contamination is low. Interestingly, the highest-mass bin has a large upper error bar on L_X/SFR, suggesting that there may be one or more sources with signifcantly higher L_X/SFR than the rest of the sources in this bin. As part of the improvements we intend to make to these preliminary results, we will identify the sources responsible for the large upper error bar of this bin and examine their location in the BPT diagram, their IRAC colors, and their individual X-ray significance to assess whether they may be AGN.

Having examined the systematics that could impact our results, there are two important caveats to keep in mind when interpreting the lack of correlation that we observe between the X-ray luminosity per SFR and the metallicity of star-forming galaxies at $z \sim 2$: (i) our preliminary results cannot rule out the possibility that AGN contamination among the higher-metallicity galaxies is artificially inflating their measured L_X/SFR, and (ii) since we can only measure the global metallicity of each galaxy, the metallicity we measure may not always correspond to the metallicity of its HMXB population, which will introduce scatter into any L_X/SFR$-Z$ dependence that may exist. Thus, we cannot definitively conclude that there is no correlation between the X-ray luminosity per SFR and the metallicity of HMXBs at $z \sim 2$.

However, if our results are not significantly biased by AGN contamination or discrepancies between the metalliciites of HMXBs and their host galaxies, they challenge the increasingly

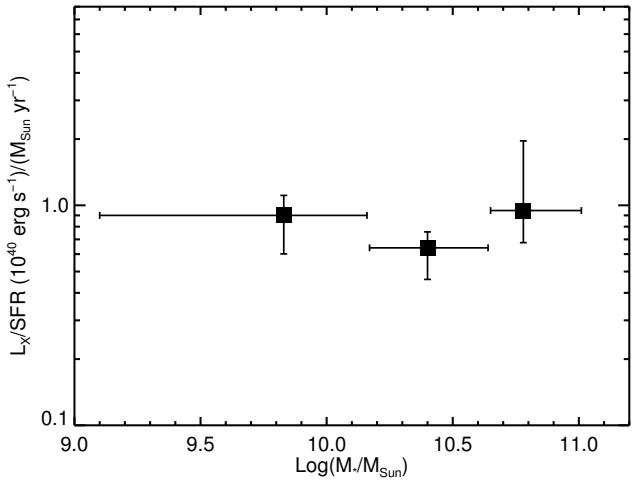

Figure 3.6: The weighted average L_X/SFR versus stellar mass. Vertical error bars show 1σ confidence interval of L_X/SFR. Horizontal error bars show the metallicity range spanned by the galaxies in a given stack.

accepted hypothesis that the metallicity dependence of HMXB evolution is the underlying cause of the observed increase in the L_X/SFR of star-forming galaxies with redshift. It is possible that the enhanced number of bright HMXBs observed in very low-metallicity BCDs (12+log(O/H)$<$ 8.0) is driven by a variable other than the metallicity dependence of stellar winds, such as the compactness and density of star-formation regions, which may impact the stellar IMF (Krumholz et al. 2010). Similar conditions in star forming clouds in high-redshift galaxies might then explain the increase of L_X/SFR with redshift. It is also possible that metallicity does play a role, but is not the only factor involved, in producing the higher HMXB luminosities per SFR in BCDs and high-redshift galaxies.

Apart from our results, there are other reasons to be skeptical of the predictions of population synthesis models with regards to the metallicity dependence of HMXBs. Over the past decade, two key developments have revealed inadequacies in our stellar evolutionary models. First, observations of wind clumping indicate that mass-loss rates for line-driven winds had been previously overestimated by factors of $\sim 3-10$ (e.g., Bouret et al. 2005, Fullerton et al. 2006) while the mass lost during the short-lived, eruptive episodes of Luminous Blue Variables (LBVs) had probably been underestimated (Smith & Owocki 2006). The physical mechanism responsible for LBV eruptions is poorly understood and may not be metallicity-dependent, in which case the total fraction of mass lost by a high-mass star during its lifetime may not be a strong function of metallicity (Smith 2014), as current models predict (Belczynski et al. 2010). Second, studies of the high binary fraction among massive stars suggest that the vast majority of them have orbital periods that are short enough for mass exchange to occur (Sana et al. 2012), and therefore most massive stars cannot be treated as isolated systems. Even if population synthesis models that study HMXB production have included the effects of binary evolution (such as mass transfer and the common envelope

phase) into their simulations, the stellar evolutionary tracks they adopt for high-mass stars have been calibrated by comparing the observed massive stellar population with evolutionary models that do not typically include binary interactions (Smith 2014). Thus, it is possible that the metallicity dependence of HMXBs is overestimated by current population synthesis models.

There are several improvements we can make to these preliminary results and establish with greater confidence whether there is a correlation between L_X/SFR and metallicity in star-forming galaxies at $z \sim 2$. The most valuable improvement we will make is to increase our galaxy sample by roughly 50%, making use of the data from full MOSDEF survey. With this larger sample, we will be able to split up the galaxies into more metallicity bins and simultaneously probe multiple parameters, such as SFR, M_*, and redshift. With a larger sample, we may also be able to use the O_{32} and R_{23} metallicity indicators, which are more consistent across different redshifts, improving the accuracy of comparisons between $z \sim 0$ local relations and our stacked measurements. Using all the observations that are currently available for the *Chandra* Deep Field South, which provide a total exposure depth of 7 Ms, will also help to maximize the number of bins we can use in our stacking analysis. In addition, we can also make several improvements to our background subtraction and stacking analysis. We can apply a consistent detection method to all *Chandra* fields rather than relying on the published catalogs which use different detection thresholds. In order to check for systematics in our analysis, we will compare the distribution of net counts within from the apertures of our galaxy sample to the net counts from randomly distributed apertures, and then apply our stacking analysis to the randomly distributed apertures to check for false detections. Furthermore, we will also update the Hα-derived SFRs using the attenuation curve derived from the MOSDEF galaxy sample by Reddy et al. (2015), which can alter the derived SFRs by $\approx 20\%$. Finally, we will perform a new fit for the local L_X/SFR$-Z$ relation based on the galaxy sample from Brorby et al. (2016) including the upper limits of galaxies which are not detected; this will allow us to better assess the significance of the local relation and of the difference between our results and the local relation.

3.5 Summary

We studied the X-ray emission of a sample of ≈ 150 star-forming galaxies in the CANDELS fields with spectroscopically confirmed redshifts in the range $1.37 \leq z \leq 2.61$ in order to investigate the metallicity dependence of HMXBs. Population synthesis models predict that HMXB populations produced in low-metallicity environments should be more X-ray luminous (Dray 2006; Linden et al. 2010; Fragos et al. 2013b), and studies of local galaxies have discovered an enhanced number of bright HMXBs in very low-metallicity blue compact dwarf galaxies (Kaaret 2014; Douna et al. 2015; Brorby et al. 2016). The X-ray luminosity per SFR of star-forming galaxies is observed to increase with redshift, a trend which which is attributed to the metallicity dependence of HMXBs, even though this correlation has not been measured directly (Basu-Zych et al. 2013b; Lehmer et al. 2016). The goal of this study

was to measure the L_X/SFR-Z relation in high-redshift galaxies and to test whether the metallicity dependence of HMXBs can account for the observed increase in L_X/SFR as a function of redshift.

The sample of galaxies used in this study was selected from the MOSDEF survey. AGN were identified by their X-ray luminosity, IRAC colors, or location in the BPT diagram and removed from the sample. From the emission lines in the near-IR MOSSFIRE spectrum of each galaxy, we calculated the galaxy redshift, Hα-derived star formation rate, and metallicity based on the O3N2 oxygen abundance indicator. Stellar masses were derived from the multiwavelength photometric data sets available in the CANDELS fields.

The X-ray binary emission from individual star-forming galaxies at $z \sim 2$ is too faint to be detected, even in the deep *Chandra* extragalactic fields. Therefore, we developed code to stack the X-ray data at the positions of galaxies from the three deepest *Chandra* fields, the 4 Ms *Chandra* Deep Field South, the 2 Ms *Chandra* Deep Field North, and the *Chandra* AEGIS-X Deep survey. All detected sources included in the published catalogs of these *Chandra* surveys were removed from our mosaic images prior to stacking the individually undetected star-forming galaxies. For a given X-ray stack, the net X-ray counts of all individual galaxies were summed together, and an exposure-weighted average conversion factor was calculated to convert 0.5–2 keV photon counts into the rest-frame 2–10 keV luminosity.

Dividing the galaxy sample into three metallicity bins, we calculated the average X-ray luminosity per SFR for galaxies in each bin. Our preliminary results show that the L_X/SFR of $z \sim 2$ star-forming galaxies is a factor of $2-3$ higher than the value measured in local galaxies, as has been found by previous studies. However, we do not find any significant correlation between L_X/SFR and Z. Splitting the galaxies into different SFR bins, we find that galaxies with lower SFRs have higher L_X/SFR, a trend discovered by other studies. Measuring the L_X/SFR of galaxies in different redshift intervals ($1.37 \leq z \leq 1.70$ and $2.09 \leq z \leq 2.61$) also does not yield a significant correlation between L_X/SFR and Z, and the highest metallicity bin for galaxies at $z \sim 2.3$ has a value of L_X/SFR that is $\approx 2\sigma$ higher than the predictions of population synthesis models.

Although we take an aggressive approach to removing AGN from our galaxy sample, it is possible that low-luminosity AGN could be contaminating our sample at high stellar masses because the AGN occupancy fraction increases with mass. Due to the mass-metallicity correlation (e.g., Sanders et al. 2015), such AGN contamination could inflate the value of L_X/SFR in high-metallicity bins. We stack the galaxies in mass bins to look for a positive correlation between M_* and L_X/SFR that would provide evidence of AGN contamination, but we do not find evidence of such a correlation. Thus, there is no significant indication of AGN contamination, but neither can we definitively rule it out.

Nonetheless, our results suggest that we should exercise caution regarding the claim that the metallicity dependence of HMXB evolution is the underlying cause of the observed increase in the L_X/SFR of star-forming galaxies with redshift. Other factors may contribute to the enhanced X-ray luminosity of HMXBs at high-redshift and in local blue compact dwarfs, such as the compactness of star forming regions resulting in a top-heavy IMF. We will improve our preliminary measurement of the L_X/SFR$-Z$ relation at $z \sim 2$ by expanding our

galaxy sample once the data from the complete MOSDEF survey is analyzed. Future work could explore HMXB luminosity as a function of the concentration and clumpiness of galaxies through the use of Gini coefficients (Conselice 2003; Lotz et al. 2004) or the luminosity of high-density tracers of molecular clouds.

Chapter 4

The Steady

4.1 Investigating the nature of the compact object in a non-pulsating HMXB

High-mass X-ray binaries (HMXBs) inform our understanding of the evolution of massive stars, which is still subject to significant uncertainties (Smith 2014). Studying the accreting neutron stars (NS) and black holes (BH) in these systems offers a special tool to probe the strength and clumping of the stellar winds of their massive companions. Moreover, comparing the properties of HMXB populations to predictions of population synthesis models (i.e. distributions of their orbital periods, compact object masses, and donor spectral types) helps constrain theoretical models of stellar mass loss, mass transfer episodes in massive binaries, and the natal kicks received by compact objects during supernova explosions (e.g., Negueruela et al. 2008; Linden et al. 2010; Fragos et al. 2013b; Grudzinska et al. 2015). Since HMXBs are the likely progenitors of many of the double compact binaries which may merge and produce gravitational waves (Postnov & Yungelson 2014), such as the BH-BH mergers recently detected by LIGO (Abbott et al. 2016c; Abbott et al. 2016b), studies of HMXB populations naturally complement the new field of gravitational wave astronomy and will be useful in determining the implications of gravitational wave sources for stellar evolutionary models. Constraining the ratio of NS to BH HMXBs and whether this ratio varies with binary properties (e.g., donor spectral type and metallicity) can shed light on the net mass loss experienced by a high-mass star due to its stellar wind, binary interactions, and supernova explosion (Dray 2006; Muno 2007; Belczynski & Ziolkowski 2009) as well as improve our estimates of the relative fractions of different double compact binaries expected to descend from HMXBs (Postnov & Yungelson 2014).

HMXBs hosting black holes exhibit different spectral properties than those hosting neutron stars. NS HMXBs typically have hard power-law spectra with exponential cutoffs with e-folding energies typically $\lesssim 20$ keV (Coburn et al. 2002), whereas BH HMXBs exhibit power-law cutoffs around 50–100 keV in their hard states and $\Gamma \sim 2$ power-law tails extending to MeV energies in their soft states (Grove et al. 1998; Zdziarski 2000). Thus, the presence of

an exponential cutoff below 20 keV in the X-ray spectrum of an HMXB is a strong indication that it harbors a neutron star; however, only the detection of X-ray pulsations or cyclotron line features constitute definitive proof of the presence of a neutron star. Most X-ray pulsars in HMXBs have spin periods between ~ 0.1 and $\sim 10^3$ seconds (Corbet 1986; Chaty 2013), although a couple of longer-period pulsars have been discovered (Reig et al. 2009; Corbet et al. 1999). In addition to NS X-ray pulsations, the X-ray lightcurves of some HMXBs can exhibit orbital or superorbital modulations with typical periods of a few hours to a few hundred days (Corbet et al. 2006; Corbet & Krimm 2013). The cyclotron lines that have been observed in some HMXB spectra have energies between 10 and 80 keV, corresponding to magnetic field strengths of a few 10^{12} G (Coburn et al. 2002; Pottschmidt et al. 2005; Caballero et al. 2007; Doroshenko et al. 2010; Caballero & Wilms 2012; Tsygankov et al. 2012; Fürst et al. 2014; Tendulkar et al. 2014; Yamamoto et al. 2014; Bellm et al. 2014). An HMXB with an unbroken power-law spectrum extending beyond 50 keV which does not show X-ray pulsations can be considered a black hole candidate, but confirming the BH nature of the compact object requires a dynamical mass measurement in excess of 2–3 $M_\odot$, the maximum theoretically expected NS mass (Lattimer 2012), although such measurements can be challenging to obtain.

Since its launch in 2002, the *International Gamma-Ray Astrophysics Laboratory (INTEGRAL)* has discovered a large number of sources that were given "IGR" source names, including 40 new HMXBs in the 4th IBIS/ISGRI catalog (Bird et al. 2016). X-ray pulsations have only been detected from about a quarter of the IGR HMXBs, and the nature of the compact object in the remaining systems is undetermined since many of them are relatively recent discoveries and have not yet been well-studied. Identifying the nature of compact objects in IGR HMXBs is of special interest since they are demographically different from the population of HMXBs discovered prior to *INTEGRAL*, consisting of roughly equal numbers of HMXBs with Be and supergiant (Sg) stellar companions, whereas Be HMXBs dominate the pre-*INTEGRAL* population (Walter et al. 2015). Many of the IGR Sg HMXBs have unusual properties, exhibiting high levels of obscuration ($N_{\rm H} \sim 10^{23} - 10^{24}$ cm^{-2}) local to the source (Walter et al. 2006; Chaty et al. 2008) or extreme flaring behavior characterized by hard X-ray flux variations of several orders of magnitude on timescales of a few hours (Negueruela et al. 2006; Sguera et al. 2006). The discovery of these Sg HMXBs was made possible by the greater sensitivity and higher cadence of the *INTEGRAL* Galactic Plane survey compared to previous hard X-ray missions.

A few of the flaring IGR Sg HMXBs, known as supergiant fast X-ray transients (SFXTs), are known to host neutron stars based on the detection of X-ray pulsations (Romano et al. 2014) or cyclotron lines (Bhalerao et al. 2015), and several of the models proposed to explain SFXT behavior depend on the presence of a NS magnetosphere (the propeller effect, Grebenev & Sunyaev 2007; magnetic gating, Bozzo et al. 2008; quasi-spherical settling accretion of hot plasma shells, Shakura et al. 2014), suggesting that all SFXTs may host neutron stars. However, the nature of compact objects in many IGR HMXBs which are not SFXTs remains unknown, and as several Sg HMXBs are known to harbor BHs (e.g., Cyg X-1, M33 X-7, LMC X-1, LMC X-3) compared to only one known Be-BH binary (Casares et al. 2014), IGR Sg

HMXBs consistute a particularly promising group to search for BHs.

IGR J18214-1318 is one of the Sg HMXBs lacking a clear compact object identification. This source was first reported in the second IBIS/ISGRI catalog (Bird et al. 2006) and detected consistently by *INTEGRAL* with a flux of 1–2 mCrab in the 20-40 keV band (Krivonos et al. 2012; Bird et al. 2016). The source was localized with arcsecond precision to R.A. = $18^{\rm h}21^{\rm m}19.76^{\rm s}$, decl. = $-13°18'38.9''$ through a *Chandra* observation (Tomsick et al. 2008). The localization of this source permitted its association with an optical counterpart which is a high-mass star of most likely spectral-type O9 I (Butler et al. 2009), thus securing the identification of IGR J18214-1318 as a Sg HMXB. Its *Chandra* spectrum is well-fit by an absorbed power-law with $N_{\rm H} = 1.2 \pm 0.3 \times 10^{23}$ cm^{-2} and $\Gamma = 0.7^{+0.6}_{-0.5}$. Later *Swift* observations of this source measured a similar photon index ($\Gamma = 0.4 \pm 0.2$) but a much lower absorbing column density of $N_{\rm H} = 3.5^{+0.8}_{-0.5} \times 10^{22}$ cm^{-2}, which is consistent with the Galactic $N_{\rm H}$ integrated along the line-sight (3.1×10^{22} cm^{-2})[1]. Although the *Chandra* data suffered from photon pile-up, since the photon indices derived by *Chandra* and *Swift* are so similar, it is unlikely that the large difference in the derived $N_{\rm H}$ values is simply a result of the photon pile-up in *Chandra*. Thus, the large variability of $N_{\rm H}$ is likely real and associated with material local to the source; similar $N_{\rm H}$ variations have been seen in other Sg HMXBs (e.g, IGR J19140+0951; Prat et al. 2008). The hard power-law index measured in the soft X-ray band suggests that the compact object in IGR J18214-1318 is more likely to be a neutron star than a black hole, but it does not constitute strong or definitive evidence.

Therefore, we observed IGR J18214-1318 with the *Nuclear Spectroscopic Telescope Array (NuSTAR)* and *XMM-Newton* (§4.2) to better constrain the nature of the compact object in this HMXB. *NuSTAR* and *XMM-Newton* are ideally suited for this study, because their instruments have the fast temporal resolution required to search for X-ray pulsations and their combined broadband X-ray spectral coverage from 0.3-79 keV permits the measurement of cyclotron lines and hard X-ray cutoffs which may be present in the HMXB power-law spectrum. Spectral analysis of this data, resulting in the detection of a high-energy cutoff, is described in §4.4, and timing analysis ruling out the existence of a pulse period $\lesssim 1$ hour is presented in §4.3. In §4.5, we discuss IGR J18214-1318 in the context of other non-pulsating and long pulse period HMXBs.

4.2 *XMM-Newton* and *NuSTAR* Observations of IGR J18214-1318

NuSTAR and *XMM-Newton* observed IGR J18214-1318 on 2014 September 18. Observation details are provided in Table 4.1. The duration of the *NuSTAR* observation is about twice as long as that of *XMM-Newton* because Earth occultations reduce the effective exposure of *NuSTAR*. The exposure times of the two *NuSTAR* focal plane modules (FPM)

[1]The Galactic $N_{\rm H}$ along the line-of-sight to IGR J18214-1318 is calculated as the sum of the HI contribution measured from the Leiden/Argentine/Bonn (LAB) survey of HI (Kalberla et al. 2005) and the H_2 contribution estimated from the MWA CO survey (Bronfman et al. 1989).

Table 4.1: Observations of IGR J18214-1318

Telescope	Observation ID	Start Time (UTC)	Duration (ks)	Instrument/ Detector	Exposure (ks)
(1)	(2)	(3)	(4)	(5)	(6)
NuSTAR	3000114002	2014-09-18 01:16:07	49.8	FPMA	26.0
				FPMB	25.8
XMM-Newton	0741470201	2014-09-18 02:34:26	26.9	EPIC pn	18.5
				MOS1	25.9
				MOS2	25.8

Notes: (6) Exposure does not include dead time.

and the two *XMM* Metal Oxide Semi-conductor (MOS) CCD arrays of the European Photon Imaging Camera (EPIC) are roughly equal (26 ks), while the exposure time of the EPIC pn CCD is significantly lower (18.5 ks) due to its higher dead-time fraction.

4.2.1 *NuSTAR*

NuSTAR is the first hard X-ray focusing telescope in space, providing 58″ half-power diameter angular resolution (Harrison et al. 2013). The *NuSTAR* FPMs cover the 3-79 keV band with moderate energy resolution (0.4 keV energy at 6 keV) and operate with 0. ms temporal resolution (Harrison et al. 2013). We processed the data from the two *NuSTAR* instruments, FPMA and FPMB, with the NuSTARDAS pipeline software v1.4.1, the 20150612 version of the *NuSTAR* Calibration Database (CALDB), and High Energy Astrophysics Software (HEASOFT) version 6.16.

Cleaned event lists were produced with the routine `nupipeline`. We used `nuproducts` to extract spectra, including response matrix files (RMFs) and ancillary response files (ARFs), and light curves, applying barycenter and deadtime corrections. In order to choose the aperture region sizes, we measured the surface brightness of the profile of the source by measuring the average count rate per pixel in concentric annuli centered on the source. We found that the profile substantially flattens at a distance of 150″ from the source, so to guarantee a clean background measurement, we defined the background region as an annulus centered on the source with an inner radius of 200″ and an outer radius of 250″. Within 60″ of the source, the count rate per pixel is at least 10 times higher than in the background region, so we defined the source aperture region as a circle with a 60″ radius (corresponding to the PSF encircled energy fraction of 75%) to limit background contamination while still ensuring good photon statistics (∼30,000 counts in FPMA and FPMB combined). Figure 4.1 displays the *NuSTAR* FPMA observation with the source and background regions. We checked the lightcurves from the background regions for significant count rate variations, but did not find any significant background variability in the 3–79, 3–12, or 12–30 keV bands. The 3–30 keV dead-time corrected source count rate is 1.2 counts s^{-1} for FPMA and FPMB

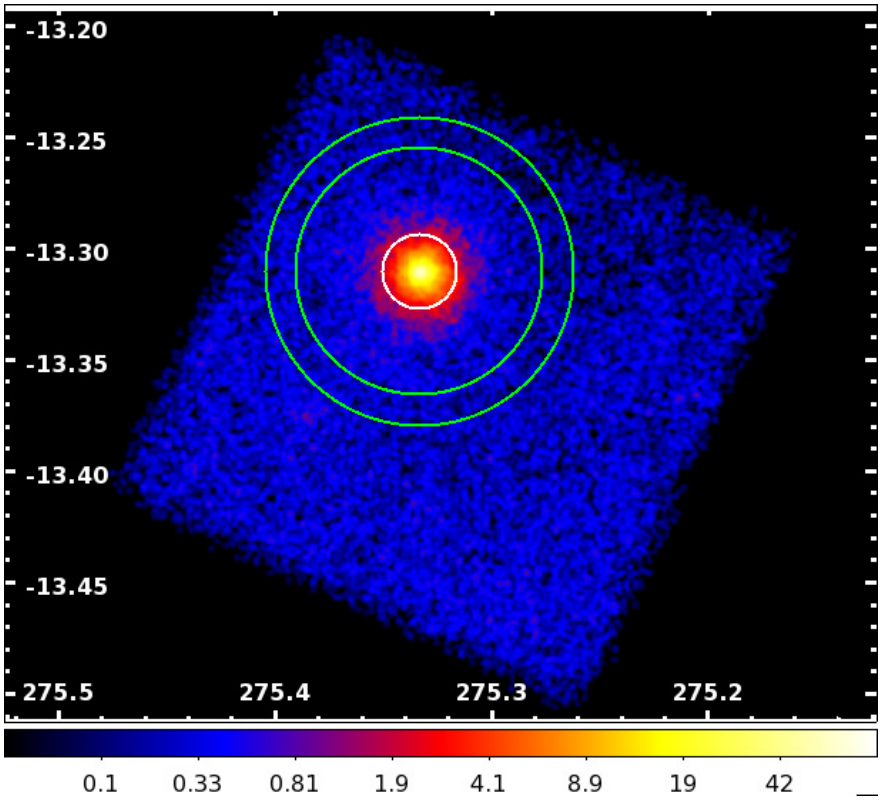

Figure 4.1: The *NuSTAR* FPMA observation in the 3–79 keV band smoothed by a Gaussian kernel with a 3 pixel radius. The colorbar displays the counts per pixel on a logarithmic scale. The source region is represented by a white circle, and the background region is represented by a green annulus.

combined.

4.2.2 *XMM-Newton*

We made use of data from the EPIC pn and MOS instruments on *XMM-Newton*, which provides 15″ HPD angular resolution at soft X-ray energies. Observations were performed in small window mode with a medium filter. The EPIC pn instrument covers the 0.3–12 keV band with energy resolution of 150 eV at 6 keV and, in the small window mode, it has 5.7 ms time resolution (Strüder et al. 2001). The MOS cameras provide similar energy resolution in the 0.3–10 keV band but have poorer timing resolution of 0.3 s in small window mode (Turner et al. 2001).

We processed the *XMM-Newton* data with Science Analysis Software (SAS) v13.5.0, making images, spectra, and light curves for EPIC pn, MOS1, and MOS2. To look for contamination from proton flares, we made EPIC pn and MOS light curves in the 10–12 keV bandpass, but we did not find any significant flares. For all three instruments, we made new event lists using the standard filtering criteria[2], and we converted the photon arrival times to the solar system barycenter.

We used `xmmselect` to extract the data products, using the images primarily to create the source and background extraction regions. The source extraction region is a circle with a 40″ radius centered on the source position. For EPIC pn, the background region is a rectangle with an area of 1.4 square arcminutes that is located approximately 2′ from the source. For the MOS detectors, rectangular background regions are also used, but they are farther away from the source because they had to be located on one of the outer MOS CCDs due to the CCD configuration of the small window mode. The 0.3–12 keV live-time corrected count rate is 1.3 counts s^{-1} with EPIC pn and 0.8 counts s^{-1} for the two MOS cameras combined. We checked the observations for pile-up and found that it was not an issue.

4.3 Timing Analysis

IGR J18214-1318 exhibits a high level of variability in its X-ray lightcurve, as can be seen in Figure 4.2. This strong aperiodic variability is common in HMXBs (Belloni & Hasinger 1990), and in order to determine whether this HMXB hosts a neutron star, we searched for periodic pulsations in this noisy lightcurve through analysis of its power spectrum. We performed this pulsation search using both *NuSTAR* and *XMM-Newton* EPIC pn data, since the EPIC pn camera has the highest temporal resolution and effective area of the *XMM* instruments. Although *NuSTAR*'s temporal resolution is better than *XMM*'s, the Earth occultations *NuSTAR* experiences during its orbit create large gaps in its lightcurves, which in turn introduce additional noise in the power spectrum at low frequencies. Furthermore, since pulsars in Sg HMXBs tend to have periods $\gtrsim$1 second (Corbet 1986; Skinner et al. 1982), the 5.7 ms resolution of *XMM-Newton* should be sufficient for detecting possible pulsations

[2]See http://xmm.esac.esa.int/sas/current/documentation/threads/

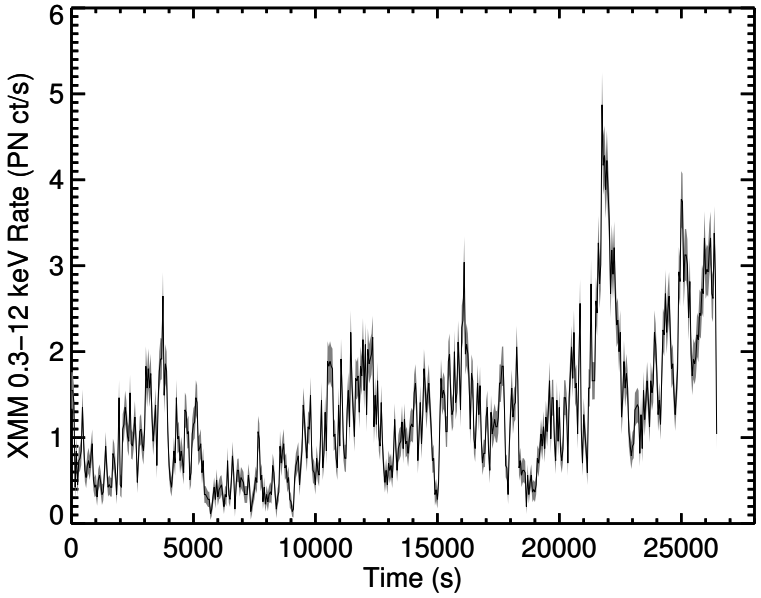

Figure 4.2: Dead-time corrected lightcurve from *XMM-Newton* EPIC pn instrument binned by 50 seconds. 1σ errors shown in gray.

in IGR J18214-1318. We first describe our analysis of the *XMM* EPIC pn power spectrum, and then compare the results to those obtained using *NuSTAR* data.

We corrected the arrival time of each event detected by the *XMM-Newton* EPIC pn instrument to the solar system barycenter, and used this corrected event list to make a light curve in the 0.3–12 keV band with the maximum possible time resolution of 5.6718 ms. We then used the XRONOS tool `powspec` to produce a Leahy-normalized power spectrum (Leahy et al. 1983) of this light curve, shown in Figure 4.3. The power spectrum spans frequencies from $3.7{\times}10^{-5}$ Hz (based on the 27 ks duration of the observation) to 88.1 Hz (the Nyquist frequency). In a Leahy-normalized power spectrum, Poissonian noise results in power being distributed as a χ^2 probability distribution with 2 degrees of freedom (dof); we used this distribution and the number of trials (which is equal to the number of frequency bins) to calculate the 90% confidence detection threshold for this power spectrum as 35.1, shown by the dashed lines in Figure 4.3. This detection threshold is only exceeded at frequencies $< 5.06 \times 10^{-3}$ Hz, but significant red noise at low frequencies suggests we should be cautious in ascribing this excess power to periodic pulsations. Thus, in order to account for the red noise present at frequencies <0.1 Hz, we analyzed the power spectrum above and below 0.1 Hz separately.

Above 0.1 Hz, the maximum Leahy power ($P_{\rm max}$) measured is 30.9, which is below the 90% confidence threshold but can be used to calculate an upper limit on the strength of a periodic signal. As derived by van der Klis (1989a), the 90% confidence upper limit of the Leahy power ($P_{\rm UL}$) is given by $P_{\rm UL} = P_{\rm max} - P_{\rm exceed}$, where $P_{\rm exceed}$ is the power level exceeded by 90% of the frequency bins. In our case, $P_{\rm exceed}$ is 0.2, which implies that $P_{\rm UL}$

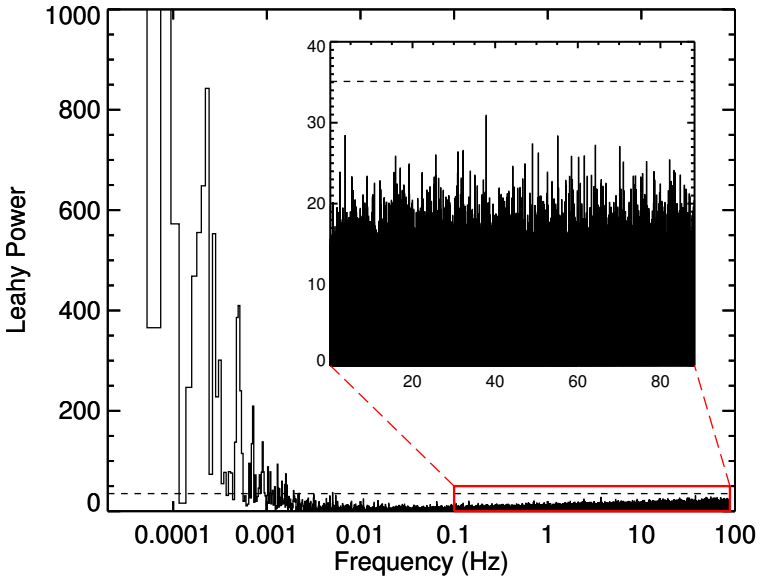

Figure 4.3: Leahy-normalized power spectrum based on *XMM-Newton* EPIC pn lightcurve in the 0.3–12 keV band. Short-dashed black line shows 90% confidence detection threshold of 35.1, which is exceeded below 5.06×10^{-3} Hz due to red noise from source's aperiodic variability. The inset image shows a zoom-in of the portion of the power spectrum above 0.1 Hz (with a linear frequency scale) so that the highest power peaks in the high-frequency part of the power spectrum can be seen.

is 30.7. This upper limit on the Leahy power can be converted into an upper limit on the source fractional rms variability for a periodic signal using the following formula:

$$\mathrm{rms} = \sqrt{\frac{P_{\mathrm{UL}} - 2}{CR} \left(\frac{S+B}{S} \right)^2 \Delta\nu} \tag{4.1}$$

where CR is the mean (source plus background) count rate, S represents the net source counts, B represents the estimated background counts in the source region, and $\Delta\nu$ is the width of the frequency bin. Thus, the 90% upper limit on the rms noise level for a periodic signal between 0.1 and 88 Hz is $< 2.2\%$.

In order to search for periodic signals at low frequencies, we first characterized the red noise below 0.1 Hz. We produced a 0.3–12 keV light curve with 5 second resolution, and used it to make a rms-normalized power density spectrum (PDS) with a Nyquist frequency of 0.1 Hz and a minimum frequency of 9.8×10^{-5} Hz, since we averaged together PDS made from three time intervals of ~ 10 ks. The rebinned PDS from which the Poisson noise level of 2.0 has been subtracted is shown in Figure 4.4. The PDS is dominated by red noise below 0.02 Hz, so we fit the PDS below this frequency with a power-law model ($P = A(\nu/1\mathrm{Hz})^{-\alpha}$) using Whittle statistics (Whittle 1953; Whittle 1957). The best-fit parameters are $\alpha = 1.40^{+0.02}_{-0.20}$ and $A = 0.0018^{+0.006}_{-0.0001}$, where the quoted errors correspond to the 90% confidence intervals. The integrated source fractional rms for frequencies between 10^{-3} to 0.1 Hz is $24 \pm 1\%$. The

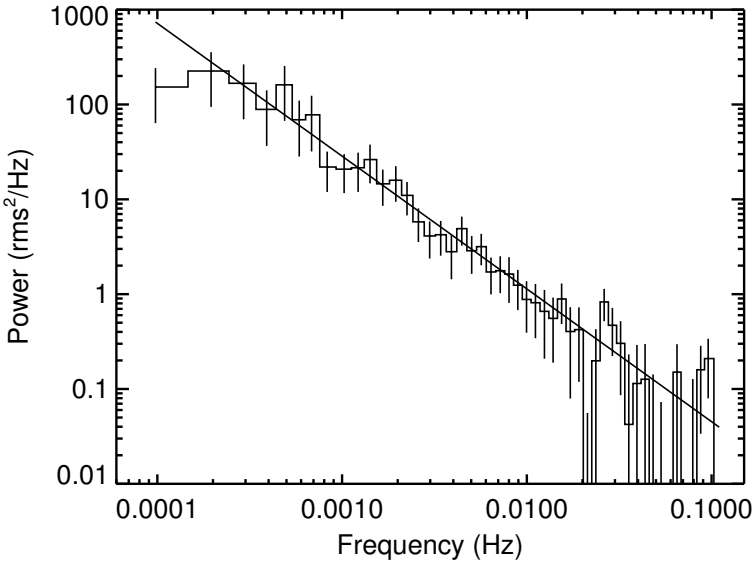

Figure 4.4: The rms-normalized power density spectrum with 1σ error bars based on the *XMM-Newton* 0.3–12 keV lightcurve. The Poisson noise level of 2.0 has been subtracted from the PDS. The black line shows the best power-law fit to the red noise dominated PDS below 0.02 Hz with $\alpha = 1.40^{+0.02}_{-0.20}$.

rms PDS slope and integrated fractional rms measured using 3–12 keV *XMM* lightcurves are consistent with the values measured from the 0.3–12 keV data to better than 1σ confidence. Fitting a power-law model plus a constant to the Leahy-normalized power spectrum from 9.8×10^{-5} to 88 Hz results also results in a consistent power-law slope. We also tried fitting a broken power-law model to the rms-normalized and the Leahy-normalized power spectra, but in both cases, the best-fitting break frequency was poorly constrained and exceeded the maximum frequency of the power spectrum. Thus, we do not find a significant break in the power spectrum between 0.0003 and 88 Hz.

In order to properly subtract the red noise component from the Leahy-normalized power spectrum in the 0.00003–0.1 Hz range, we follow the procedure described in van der Klis (1989a). The Leahy power spectrum was multiplied by a factor of 2 and then divided by the (appropriately re-normalized) best-fit power-law model; we checked that the resulting power spectrum, shown in Figure 4.5, follows a χ^2 distribution with 2 dof, a requirement for applying the method described in van der Klis (1989a) to power spectra with red noise. Taking into account the number of trials, we calculated the 90% confidence detection threshold to be 21.2. As can be seen in Figure 4.5, no frequency bin exceeds this power level. Given that $P_{\rm max}$ in this low-frequency range is 17.0 and $P_{\rm exceed}$ is 0.2, $P_{\rm UL}$ is 16.8, which corresponds to an upper limit on the source fractional rms of 1.7%. We verified that varying the red noise slope and normalization within their 90% confidence intervals does not significantly affect these results.

In some binaries, a periodic signal may be difficult to detect because it may be spread out in frequency space due to orbital motion. However, HMXBs tend to have orbital periods of a

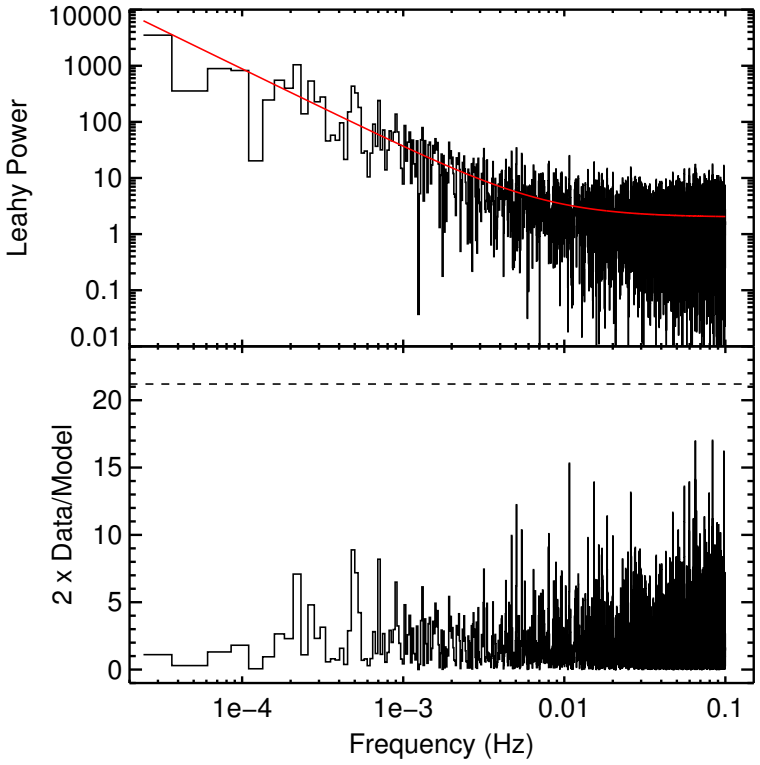

Figure 4.5: Upper panel shows low-frequency part of the Leahy-normalized power spectrum based on the *XMM-Newton* 0.3–12 keV lightcurve. The red solid line shows the appropriately re-normalized power-law model derived by fitting the PDS. The lower panel shows the Leahy power spectrum divided by the model and multiplied by 2. The dashed line shows the 90% confidence detection threshold for frequencies below 0.1 Hz, which is equal to 21.2.

few to hundreds of days, and thus our observations of IGR J18214-1318 are short enough that orbital modulations of the pulsation frequency should not be significant. Thus, given the stringent upper limits on the fractional rms for periodic signals in the 0.00003–88 Hz frequency range, pulsations with periods $\lesssim$1 hour are strongly ruled out.

We performed the same timing analysis with *NuSTAR* data in the 3–12 and 12–30 keV bands. All *NuSTAR* photon arrival times were converted to barycentric dynamical time (TDB). After being corrected for thermal drift of the on-board clock, the *NuSTAR* time resolution is $\sim$ 2 ms rms, and its absolute accuracy is known to be better than 3 ms (Mori et al. 2014). Thus, we used the *NuSTAR* data to search for spin periods as short as $\sim$1 ms by binning the lightcurves by 1/2048 seconds (488 μs). We produced Leahy-normalized power spectra from FPMA and FPMB lightcurves using both the XRONOS tool `powspec` and the power spectrum tools developed by M. Bachetti [3], but we did not find any significant peaks in the power spectrum below 1024 Hz. Above 0.1 Hz, the 90% confidence upper limit on the

[3]Tools can be found at https://bitbucket.org/mbachett/maltpynt and are described in Bachetti et al. (2015).

source fractional rms is 3.4% in the 3–12 keV band and 6.4% in the 12–30 keV band.

We produced a rms-normalized, noise-subtracted PDS and fit the red noise dominated continuum in the 6×10^{-5} to 0.02 Hz frequency range with a power-law model. Jointly fitting the PDS produced from FPMA and FPMB data yields $\alpha = 1.32^{+0.06}_{-0.10}$ in the 3–12 keV band and $\alpha = 1.46^{+0.07}_{-0.12}$ in the 12–30 keV band. These measured power-law slopes are consistent with the values derived from *XMM-Newton*. Using the PDS power-law fits to "normalize" the red noise continuum in the Leahy power spectrum below 0.1 Hz, we checked that the resulting power spectrum follows a χ^2 distribution with 2 dof, and then calculated that the 90% confidence upper limit on the source fractional rms is 2.7% in the 3–12 keV band and 6.0% in the 12–30 keV band. The integrated source fractional rms between 10^{-3} to 0.1 Hz is 31±2% and 23±8% in the 3–12 and 12–30 keV bands, respectively. Thus, the *NuSTAR* 3–12 keV integrated fractional rms is higher at 3σ confidence than that measured in the *XMM-Newton* 3–12 keV band; this difference may be partly attributed to the *XMM-Newton* and *NuSTAR* observations not being fully coincident in time and the additional artificial noise injected into the *NuSTAR* power spectrum by the lightcurve gaps due to Earth occultations. Due to the large errors bars of the integrated fractional rms measured in the *NuSTAR* 12–30 keV band, this value is consistent at 1σ confidence with both the integrated rms measured by *XMM-Newton* and the *NuSTAR* 3–12 keV band.

Overall, the results from our *XMM-Newton* and *NuSTAR* timing analysis are in agreement, ruling out the presence of pulsations with periods shorter than about an hour. The integrated source fractional rms values measured between 10^{-3} and 0.1 Hz by both telescopes are within the typical range of 10-30% seen in HMXBs (Belloni & Hasinger 1990). For most accreting X-ray pulsars, the red noise power-law index is $\alpha = 1.4 - 2.0$ at frequencies higher than the pulsation frequency and $\alpha = 0 - 1.0$ at lower frequencies (Hoshino & Takeshima 1993). Thus, the red noise power-law slope of IGR J18214-1318 is similar to the slopes observed above the pulsation frequency in X-ray pulsars. This fact, combined with the lack of a frequency break in the red noise continnum, suggests, but does not prove, that the pulsation frequency in IGR J18214-1318 may be lower than the range probed by our data.

4.4 Spectral Analysis

We extracted spectra, ARFs, and RMFs from the *XMM-Newton* EPIC pn, MOS1/2, and *NuSTAR* FPMA/B instruments as described in §4.2. The spectra were rebinned with the requirement that the source significance in each bin be ≥ 10, except for the highest energy bin which was required to have a significance ≥ 3. We used the XSPEC version 12.8.2 software to jointly fit the five spectra, allowing for different calibration constants for each instrument. The cross-calibration constants for the MOS1 and MOS2 instruments were consistent in all the fits, differing by less than 1σ from each other, so we linked the MOS1/2 constants together, removing one free parameter from the models.

We first fit the data using an absorbed power-law model (`tbabs*powerlaw`), adopting the abundances from Wilms et al. (2000) and photoionization cross-sections from Verner et al.

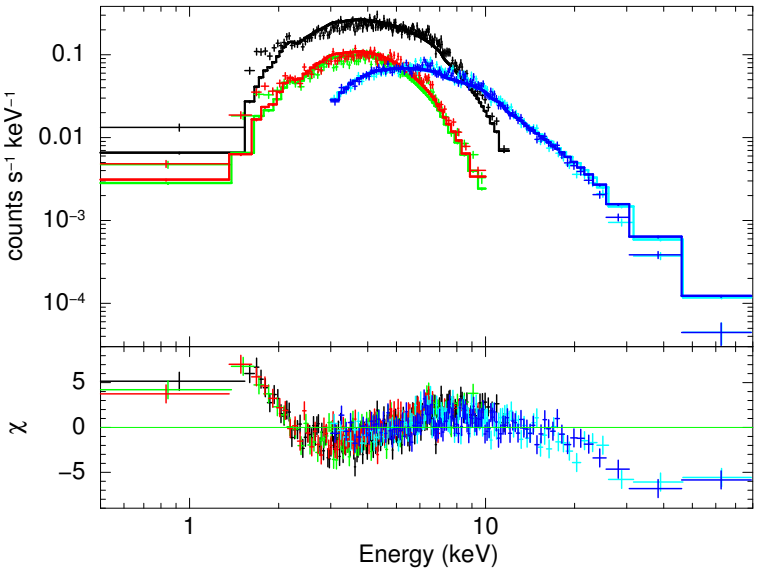

Figure 4.6: Spectrum of IGR J18214-1318, with *XMM-Newton* EPIC pn data shown in black, MOS1 in green, MOS2 in red, *NuSTAR* FPMA in light blue, and FPMB in dark blue. Data points are shown with 1σ error bars. Fit shown is for a simple absorbed power-law model. The residuals in the lower panel show there is an excess below 2 keV and a flux deficit above 10 keV.

(1996b). This simple model, which was sufficient for describing previously available soft X-ray data with lower photon statistics (Tomsick et al. 2008; Rodriguez et al. 2009), yields a poor fit ($\chi^2_\nu = 3.3$ for 585 dof). As can be seen in the residuals in Figure 4.6, this simple power-law fit underestimates the flux below 2 keV and overestimates it above 20 keV. Accounting for the flux above 20 keV requires introducing an exponential cutoff to the power-law spectrum, while the soft excess can be accounted for either by adding a blackbody component (Model 1) or a partial covering absorber (Model 2), which provide equally good fits. Adding only one of these components (`highecut`, `bbody`, or `pcfabs`) to the absorbed powerlaw model is insufficient, leaving large residuals either below 2 keV or above 20 keV.

The spectral fits and residuals resulting from our best-fitting models are shown in Figure 4.7. These models also include a Gaussian line to fit the Fe Kα line emission at 6.40±0.02 keV which is clearly visible in Figure 4.8. The energy of this line indicates it must originate in cool, low-ionization material located in the supergiant wind (Torrejón et al. 2010). The spectral parameters of the best-fitting models are listed in Table 4.2. As can be seen, the reduced χ^2 values of the spectral fits are good enough that no additional components are required, and no prominent features remain in the residuals.

However, in order to statistically test for the presence of cyclotron lines, we added a cyclotron absorption component (`cyclabs`) to our models and performed new spectral fits. Since the cyclotron line width was very poorly constrained when left as a free parameter, we set its upper limit to 10 keV, since cyclotron line widths of accreting X-ray pulsars typically fall in the 1–10 keV range (Coburn et al. 2002). We also set the optical depth of the second

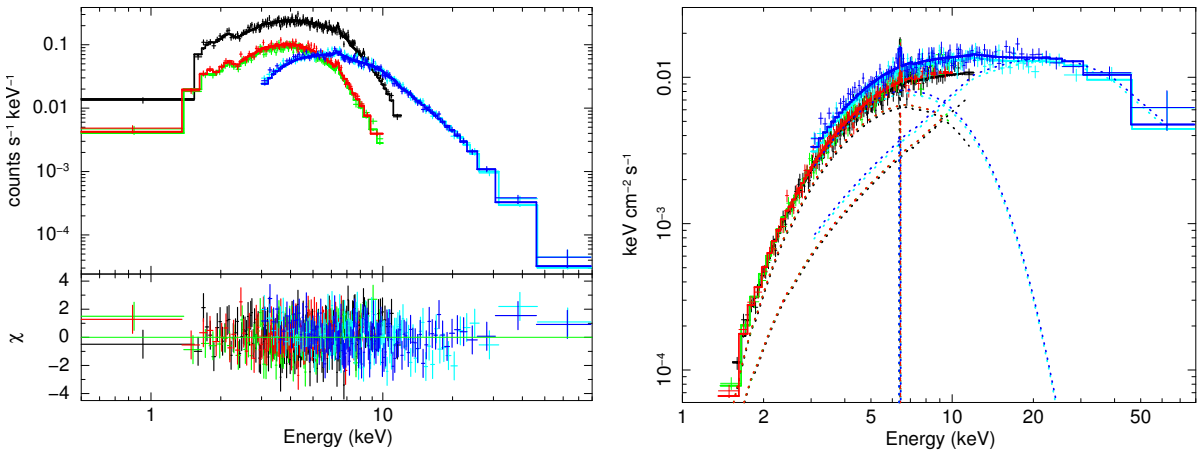

Figure 4.7: *Left*: The model fit shown is for an absorbed power-law with a high-energy cutoff, a partial covering absorber, and a Gaussian Fe line. *Right:* The spectral energy density is shown with a model including blackbody and cutoff power-law components subject to the same absorption. A Gaussian line to account for Fe Kα emission is also included. The different model components are shown with dashed lines. Colors of data points shown are as described in Figure 4.6.

harmonic to zero since it could not be constrained. The spectral parameters of all the other Model 1 and 2 components were allowed to vary in order to find the best-fitting model which includes `cyclabs` as a multiplicative component. The best-fitting cyclotron line parameters derived by adding `cyclabs` to Model 1 are an optical depth $\tau_{\rm cyc} = 0.25^{+0.21}_{-0.18}$ and line energy $E_{\rm cyc} = 27^{+4}_{-6}$ keV; the inclusion of `cyclabs` only reduced the chi-squared value of the fit by 5 and left χ^2_ν unchanged. The cyclotron parameters derived by adding `cyclabs` to Model 2 are $\tau_{\rm cyc} = 0.16 \pm 0.06$ and $E_{\rm cyc} = 11^{+4}_{-7}$ keV, which differs from the cyclotron energy found for Model 1; adding the `cyclabs` component to Model 2 improved the chi-squared value by 19.2 and reduced χ^2_ν to 1.07 from 1.10, a marginal improvement on the quality of the fit.

In order to determine the significance of this improvement to the chi-squared value for Model 2, we generated 1000 simulated datasets, including both the *NuSTAR* and *XMM* data and followed the procedure applied in Bellm et al. (2014), Bhalerao et al. (2015), and Bodaghee et al. (2016). Each simulated dataset was fit by the null model (Model 2 without `cyclabs`) and the test model with a `cyclabs` feature, and the difference in chi-squared values ($\Delta\chi^2$) between the two model fits was calculated. The maximum value of $\Delta\chi^2$ from these simulations was 19.3, slightly higher than the observed value. Based on the distribution of $\Delta\chi^2$ from our simulations, we estimate there is roughly a 0.001% chance of measuring the observed value of $\Delta\chi^2 = 19.2$ by chance, and that therefore the significance of the cyclotron line in IGR J18214-1318 is about 3.3σ. Given the fact that this detection is marginal and dependent on adopting Model 2 rather than Model 1 for the soft excess, it does not constitute substantive evidence for the presence of a cyclotron absorption feature.

Nonetheless, the absence of such features does not disprove the possibility that IGR J18214-1318 harbors a neutron star. The fact that the e-folding energy of the exponential

Table 4.2: Parameters of Best-fit Spectral Models

	Model 1 `tbabs*(bbody+ powerlaw*highecut +gaussian)`	Model 2 `tbabs*pcfabs* (powerlaw*highecut +gaussian)`
$N_{\rm H}$ (10^{22} cm^{-2})	$4.2^{+0.3}_{-0.2}$	4.3±0.6
$kT_{\rm BB}/N_{\rm H,partial}$	$1.74^{+0.04}_{-0.05}$ keV	$9.8^{+1.5}_{-1.1} \times 10^{22}$ cm^{-2}
BB norm./Cov. frac.	$1.7\pm0.2 \times 10^{-4}$	$0.77^{+0.05}_{-0.06}$
Γ	$0.4^{+0.3}_{-0.4}$	$1.48^{+0.08}_{-0.07}$
PL norm.	$1.6^{+1.7}_{-1.1} \times 10^{-4}$	$3.9^{+0.7}_{-0.5} \times 10^{-3}$
$E_{\rm cut}$ (keV)	$12.0^{+1.0}_{-1.3}$	$7.4^{+0.6}_{-0.5}$
$E_{\rm fold}$ (keV)	$14.0^{+3.2}_{-1.5}$	$23.0^{+3.3}_{-2.4}$
$E_{\rm line}$ (keV)	$6.40^{+0.03}_{-0.02}$	6.40±0.02
$\sigma_{\rm line}$ (eV)	< 85	< 102
EW$_{\rm line}$ (eV)	53^{+16}_{-21}	57^{+16}_{-14}
$C_{\rm MOS1,2}$	1.04±0.02	1.04±0.02
$C_{\rm FPMA}$	1.25±0.02	1.24±0.02
$C_{\rm FPMB}$	1.32±0.03	1.31±0.03
χ^2_ν/dof	1.10/578	1.10/578

Notes: Errors provided are 90% confidence. Cross-normalizations between instruments are calculated relative to *XMM-Newton* EPIC pn instrument. Abbreviations: BB-blackbody, PL-power-law. The BB normalization is the source luminosity in units of 10^{39} erg s^{-1} assuming a distance of 10 kpc. The PL normalization is the photon flux at 1 keV.

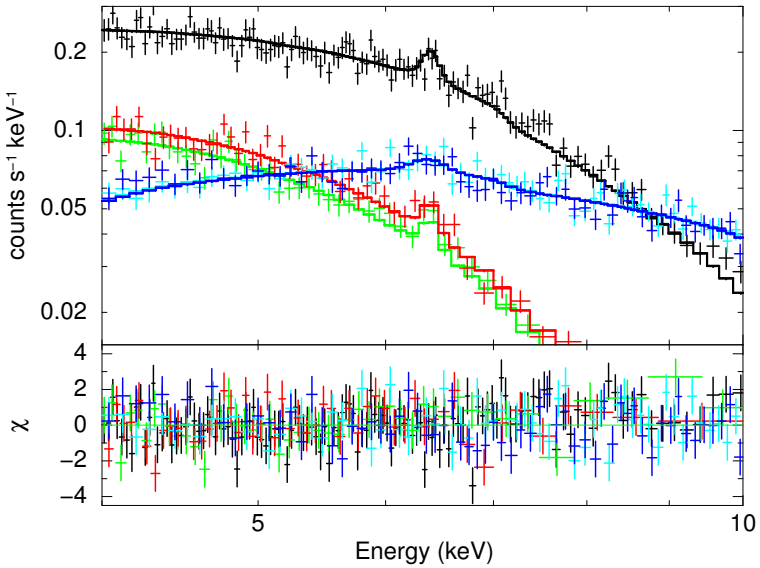

Figure 4.8: Zoom-in of spectrum from 4-10 keV band clearly shows presence of Fe line around 6.4 keV. Colors of data points shown are as described in Figure 4.6.

cutoff is < 25 keV, regardless of which of the two best models is adopted, strongly suggests that IGR J18214-1318 is a NS HMXB. Furthermore, the photon index below the cutoff is harder when adopting the blackbody rather than the partial-covering model, but in both cases is within the range observed in NS HMXBs, which tend to exhibit harder photon indices than BH HMXBs (Coburn et al. 2002).

For Model 1, the blackbody component accounting for the soft excess has a temperature of 1.7 keV, which is higher than the $kT \approx 0.1$ keV thermal component exhibited by BH HMXBs in the hard state (Di Salvo et al. 2001; McClintock & Remillard 2006; Makishima et al. 2008); BH HMXBs can exhibit blackbody temperatures as high as 2 keV in the soft state, but the power-law component of IGR J18214-1318 is much stronger than that of a BH in the soft state (McClintock & Remillard 2006). Assuming that IGR J18214-1318 lies at a distance of 9-10 kpc, as favored by the properties of its near-IR counterpart (Butler et al. 2009), the radius of the blackbody emitting region is 0.3 km, which is consistent with the size of NS hot spots. However, while the blackbody interpretation thus provides some additional evidence in favor of the NS hypothesis, the soft excess seen in the spectrum can be equally well-fit by a partial covering model. Using this model, we measure that the whole system lies behind a column density of 4×10^{22} cm^{-2}, which is just in excess of the Galactic interstellar column density integrated along the line-of-sight, and that about 77% of the X-ray emission is obscured by an additional column density of $\sim 10^{23}$ cm^{-2}. This partial-covering absorber can be attributed to dense clumps in the supergiant wind, and thus does not provide any additional insight about the compact object in this HMXB.

The mean 3–12 keV flux is $1.70^{+0.02}_{-0.05} \times 10^{-11}$ erg cm^{-2} s^{-1} in the *XMM-Newton* EPIC pn obsevations and $2.18^{+0.03}_{-0.10} \times 10^{-11}$ erg cm^{-2} s^{-1} in the *NuSTAR* observations (FPMA

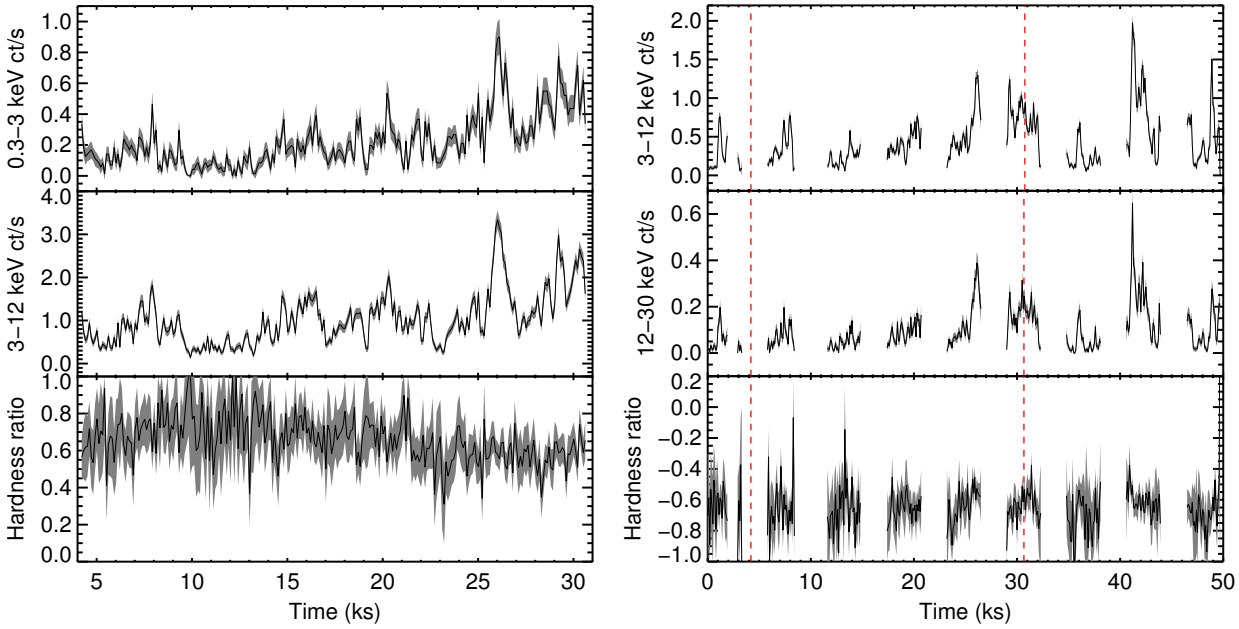

Figure 4.9: *Left: XMM-Newton* EPIC pn lightcuves in the 0.3–3 and 3–12 keV bands binned by 100 seconds. The hardness ratio in the lower panel is defined as $(H - S)/(H + S)$, where H is the count rate in the 3–12 keV band and S is the count rate in the 0.3–3 keV band. Time on the x-axis is measured from the beginning of the *NuSTAR* observations. *Right: NuSTAR* lightcurves, FPMA and FPMB combined, binned by 100 seconds. The hardness ratio is calculated with 3–12 keV as the soft band and 12–30 keV as the hard band. The gaps in the lightcurves are due to Earth occultations. The red dashed lines indicate the beginning and end of the *XMM-Newton* observations.

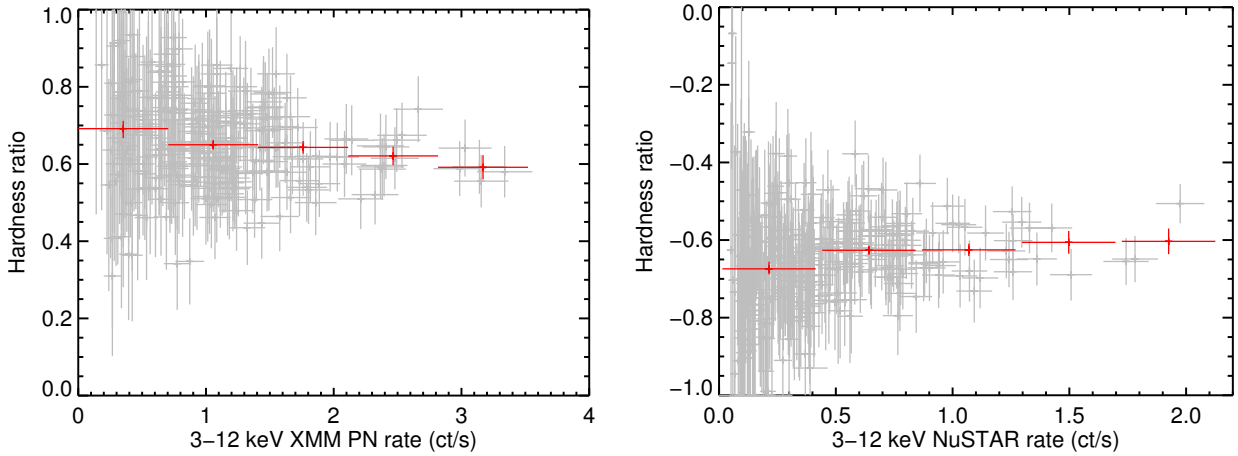

Figure 4.10: The left panel *XMM-Newton* hardness ratio versus 3–12 keV count rate, while right panel shows the same for *NuSTAR* data. Gray points show data from 100 second lightcurve bins. Red points show the average hardness ratio in five count rate bins.

and FPMB averaged). At a distance of 9–10 kpc, these fluxes correspond to unabsorbed luminosities of $\approx 1 - 2 \times 10^{35}$ erg/s. Through simultaneous *NuSTAR* and *XMM-Newton* observations of PKS 2155-304 and 3C 273, Madsen et al. (2015) found that the flux cross-calibrations of the *XMM-Newton* and *NuSTAR* instruments are accurate to better than 7%; in our spectral fits, the *NuSTAR* fluxes (see Table 4.2) are higher than the *XMM-Newton* fluxes by about 30% primarily because the *NuSTAR* observations cover a longer duration of time and the source undergoes some large flares after the *XMM-Newton* observations end, as shown in Figure 4.9. The average X-ray flux during these observations is a factor of 3 lower than the average flux during the 2008 and 2009 observations (Tomsick et al. 2008; Rodriguez et al. 2009), and the lightcurves in Figure 4.9 show that on hour-long timescales the flux can vary by more than a factor of 20.

Since IGR J18214-1318 exhibits strong variability, we checked whether its spectrum varies substantially with the source flux. As shown in Figure 4.9, the hardness ratios in both the *XMM-Newton* and *NuSTAR* bands, which are proxies for spectral shape, remain pretty constant throughout the observations but the errors on the hardness ratio calculated within each 100-second section of the observations are large. To better establish the significance of any potential correlation between the source flux and spectral properties, we split up the 100-second lightcurve fragments into five count rate bins and evaluated the mean hardness ratio in each bin. As can be seen in Figure 4.10, in the *XMM-Newton* band, the mean hardness ratio decreases slightly with increasing count rate, whereas in the *NuSTAR* band, the mean hardness ratio appears to increase slightly with count rate. If real, such trends could indicate that as the source flux increases, both $N_{\rm H}$ and Γ decrease, which is seen in other Sg HMXBs (e.g., IGR J16207−5129 and 4U 2206+54; Tomsick et al. 2009; Wang 2013), but the significance of these trends is $< 2\sigma$ and, even if present, such spectral variations are

likely small given that the hardness ratio changes by < 0.1. Therefore, we do not expect any strong spectral variations with brightness, lending confidence to the spectral parameters derived from our joint fitting of the *XMM-Newton* and *NuSTAR* spectra of IGR J18214-1318 even though the mean count rates differed in these observations.

4.5 Discussion

4.5.1 The physical origin of the soft excess

As discussed in §4.4, the soft excess below 2 keV seen in the spectrum of IGR J18214-1318 can be accounted for either by introducing a blackbody component with properties typical of NS hot spots or a partial-covering absorber associated with the clumpy supergiant wind. In both models, the column density obscuring the whole binary system is measured to be $N_{\rm H} \approx 4 \times 10^{22}$ cm^{-2}, which can largely be ascribed to the interstellar medium and is consistent with the low column density measured by Rodriguez et al. (2009). The high column density measured by Tomsick et al. (2008), well in excess of the ISM value, is comparable to the $N_{\rm H}$ of the partial-covering absorber. Thus, the partial-covering model can naturally explain the observed variations in $N_{\rm H}$ as the result of changes in the density of clumps in the supergiant wind or how deeply embedded the compact object is in the stellar wind at different orbital phases.

However, these observed spectral variations are more difficult to explain using the blackbody model for the soft excess. Since spectra from the 2008 and 2009 soft X-ray observations of IGR J18214-1318 were fit with simple aborbed power-law models due to their low photon statistics, it is possible that variations in the strength of the blackbody emission could be incorrectly interpreted as $N_{\rm H}$ variations. If this blackbody emission is indeed associated with hot spots at the NS polar caps, then it should be pulsed due to the NS spin. Based on our timing analysis, such pulsations would have periods longer than an hour, and thus it is possible that, given their short 5-6 ks exposures, during one of the 2008/2009 observations the hot spot was visible while during the other the hot spot was primarily hidden. We made fake 0.3–10 keV spectra with blackbody components of different strengths and fit them with simple absorbed power-law models to determine the effect that the blackbody emission alone can have on the measured $N_{\rm H}$, but found that it can only account for about 25% of the measured variations, which span the range of 3–12$\times 10^{22}$ cm^{-2}). Thus, even in the case that the soft excess is modeled by blackbody emission, significant obscuration ($N_{\rm H} \sim 10^{23}$ cm^{-2}) from the stellar wind is required to explain some of the observed $N_{\rm H}$ measurements, making IGR J18214-1318 part of the class of highly obscured HMXBs discovered by *INTEGRAL* (Walter et al. 2006).

In addition to the fact that the partial-covering absorber model provides a more natural explanation for the observed $N_{\rm H}$ variations, some unusual properties of the blackbody model make the partial-covering model the preferred interpretation for the soft excess. Although the temperature ($kT \sim 1.7$ keV) and size ($R_{\rm BB} \approx 0.3$ km) of the blackbody emission region are

typical for NS hot spots, emission from these hot spots is typically only seen in NS HMXBs with Be or main-sequence donors and $L_X \lesssim 10^{35}$ erg/s (Reig et al. 2009). Furthermore, the flux of the blackbody component of IGR J18214-1318 is 65% of the total 0.3–10 keV flux, which is much higher than the $\sim 30\%$ hot spot blackbody flux fraction typically seen in other HMXBs (Mukherjee & Paul 2005; La Palombara & Mereghetti 2006; La Palombara & Mereghetti 2007; La Palombara et al. 2009). Sg HMXBs can also exhibit soft excess emission, but it tends to have lower temperature ($kT \sim 0.2$ keV) and originate from larger areas ($R_{\rm BB} \sim 100$ km) (Reig et al. 2009). Such emission likely arises from a cloud of diffuse photoionized plasma around the compact object associated with the supergiant wind; the photoionized plasma only absorbs photons at $\gtrsim 2$ keV and produces significant emission at $\lesssim 1$ keV, resulting in a soft excess (Hickox et al. 2004, Szostek & Zdziarski 2008). However, the soft excess of IGR J18214-1318 exhibits a higher blackbody temperature and smaller radius than is typically seen in Sg HMXBs with photoionized winds (Reig et al. 2009). As a result, we believe that the introduction of a partial-covering absorber is the most natural way of accounting for the soft excess, even if the blackbody model cannot be definitively dismissed.

4.5.2 The compact object in IGR J18214-1318

Since neither pulsations nor cyclotron lines are detected in the *XMM-Newton* and *NuSTAR* data of IGR J18214-1318, we cannot definitively identify the compact object in this HMXB. Although we cannot rule out that this system hosts a black hole, the exponential cutoff to its power-law spectrum with e-folding energy < 25 keV argues in favor of a neutron star since BH HMXBs exhibit power-law spectra out to $\gtrsim 100$ keV (Zdziarski 2000). Fitting the *NuSTAR* spectrum above 20 keV with a power-law model, we find that $\Gamma = 2.5 \pm 0.2$. This soft photon index above the cutoff energy is typical for "normal" accreting pulsars, whereas anomalous X-ray pulsars (AXPs), which are thought to be magnetars, have $\Gamma = 1 - 2$ above 20 keV (Reig et al. 2012). The persistence of the hard X-ray emission from IGR J18214-1318 also disfavors a magnetar origin for this source, since most magnetars (all soft gamma-ray repeaters (SGRs) and many AXPs) exhibit bursting behavior (Olausen & Kaspi 2014 and references therein). Thus, the compact object in IGR J18214-1318 is most likely an accreting neutron star with a typical magnetic field strength ($10^{12} - 10^{13}$ G). The lack of detected pulsations with periods $\lesssim 1$ hour can be explained by the geometry of the system (e.g., the nearly-perfect alignment of the magnetic and rotational axes of the neutron star, the NS beam being narrow and not pointing towards Earth, or the NS beam being broad enough so as to wash out spin modulations) or a spin period $> 1 - 2$ hours, longer than is typically seen in NS HMXBs.

4.5.3 Comparison to other HMXBs

IGR J18214-1318 belongs to a small but growing number of HMXBs that may host neutron stars but do not exhibit pulsations with periods $\lesssim 10^3$ seconds. For two of these HMXBs,

4U 2206+54 and 2S 0114+650, long pulsation periods of 1.5 and 2.7 hours respectively have been measured (Reig et al. 2009; Corbet et al. 1999), which implies that they both host slowly spinning neutron stars. The 3-50 keV spectra of these sources are quite similar and resemble the spectrum of IGR J18214-1318, with photon indices of ≈1 and exponential cutoffs with $E_{\rm cut} \approx 6$ keV and $E_{\rm fold} \approx 12 - 15$ keV (Farrell et al. 2008; Reig et al. 2009). Neither source exhibits clear cyclotron absorption features, although low-significance detections of such features have been claimed by some authors (Bonning & Falanga 2005; Torrejón et al. 2004). 4U 2206+54 displays a soft excess below 2 keV, which is well-fit by a blackbody with $kT \approx 1.6$ keV and $R_{\rm BB} \approx 0.4$ km attributed to hot spots at the polar caps of the neutron star (Reig et al. 2012); as discussed in §4.5.1, the possibility that the soft excess in IGR J18214-1318 originates from NS hot spots is disfavored in part because it is unusual to see hot spot emission from Sg HMXBs, but the donor star in 4U 2206+54 is an O9.5 V star with an unusually slow stellar wind velocity of ∼350 km/s (Ribó et al. 2006) which resembles the donor stars in Be HMXBs where hot spot blackbody emission is frequently seen. In contrast, the donor star in 2S 0114+650 is a B1 Ia supergiant (Reig et al. 1996), making it a closer analogue to IGR J18214-1318 than 4U 2206+54. Li & van den Heuvel (1999) proposed that the slow spin of the neutron star in 2S 0114+650 indicates that it was born as a magnetar with $B \gtrsim 10^{14}$ G, was slowed down efficiently by the propeller effect before its magnetic field significantly decayed to its current expected value of $\sim 10^{12}$ G. In the case of 4U 2206+54, magneto-rotational models which can account for the neutron star's spin and spin-down rate require magnetic fields strengths between 5×10^{13} and 3×10^{15} G (Ikhsanov & Beskrovnaya 2010); thus, it is possible that 4U 2206+54 currently contains a magnetar and would evolve into a system like 2S 0114+650.

Neutron stars with long spin periods have also been discovered in some symbiotic X-ray binaries (SyXBs). The two SyXBs with the longest spin periods, IGR J16358-4726 and 4U 1954+319, have spin periods of ∼1.6 hr and ∼5.3 hr, respectively (Kouveliotou et al. 2003; Patel et al. 2004; Corbet et al. 2006; Marcu et al. 2011). Both of these sources have spectra which are very similar to those of long spin-period HMXBs and IGR J18214-1318 (Patel et al. 2007; Enoto et al. 2014), but they have giant M-type stellar companions rather than high-mass donors. While SyXBs with slowly spinning NSs share many properties in common with long-period HMXBs and IGR J18214-1318, their late-type stellar counterparts indicate a distinct evolutionary origin. Although it has been suggested that the long spin-period SyXBs may host magnetars or magnetar descendants just like long spin-period HMXBs (Patel et al. 2007; Enoto et al. 2014), models which assume quasi-spherical wind accretion for SyXBs rather than disk accretion do not require magnetar-strength fields to explain their timing properties (Lü et al. 2012).

We know of five HMXBs other than IGR J18214-1318 from which pulsations have not yet been detected despite sensitive searches for periods $\lesssim 10^3$ seconds and for which the nature of the compact object remains uncertain. All but one of these non-pulsating[4] HMXBs have supergiant donor stars; the source with a main-sequence OB companion is IGR J08262-3736

[4]Here we use the term "non-pulsating" to mean having no detected pulsation with a period lower than 1000 seconds.

(Masetti et al. 2010). This HMXB also differs from all the other non-pulsating or long-pulsation HMXBs in that its X-ray luminosity of 3×10^{34} erg/s is significantly lower than that of the others ($L_X \sim 10^{35} - 10^{36}$ erg/s), and its power-law spectrum with $\Gamma \approx 1.8$ does not show a cutoff below 70 keV (Bozzo et al. 2012). Like IGR J18214-1318, the spectrum of IGR J08262-3736 exhibits a soft excess which can be accounted for either by a partial absorber or a blackbody component potentially arising from NS hot spots (Bozzo et al. 2012); since we cannot discriminate between these two possibilities, the soft excess should not be interpreted as evidence for the presence of a neutron star. Rather, the lack of an exponential cutoff in the spectrum of IGR J08262-3736 makes it the most plausible BH candidate of all the non-pulsating HMXBs, and differentiates it from all the other HMXBs discussed in this section, including 4U 2206+54 which also hosts a main-sequence donor star.

The four currently known non-pulsating HMXBs with supergiant donors, IGR J16207-5129, IGR J16318-4848, IGR J19140+0951, and 4U 1700-377, all exhibit exponential cutoffs with e-folding energies < 25 keV, suggesting they all likely harbor neutron stars. IGR J16207-5129 is the non-pulsating HMXB that most resembles IGR J18214-1318. It has a very similar X-ray spectrum, with $\Gamma \approx 1.0$, an exponetial cutoff with e-folding energy ≈ 20 keV (Bodaghee et al. 2010), and a soft excess which Tomsick et al. (2009) argue most likely results from partial obscuration by the stellar wind with $N_{\rm H} \approx 10^{23}$ cm^{-2}. This source has a B1 Ia donor star (Nespoli et al. 2008) and its 0.5-10 keV X-ray luminosity is $2 - 3 \times 10^{35}$ erg/s, similar to IGR J18214-1318. The power density spectrum of IGR J16207-5129 has been carefully studied, and, like the PDS of IGR J18214-1318, it shows significant red noise below 0.01 Hz which is well-fit by a simple power-law; however, the slope of the red noise in IGR J16207-5129 is steeper, having power-law index $\alpha = 1.76 \pm 0.05$ (Tomsick et al. 2009), which is typical value for frequencies above the pulsation frequency, suggesting but not proving that the neutron star in this HMXB may have a period longer than the ~ 2 hour limit probed by the data.

Another non-pulsating Sg HMXB that is similar to IGR J18214-1318 is IGR J19140+0951, which has a B0.5 Ia donor star (Hannikainen et al. 2007). Its average X-ray luminosity is approximately 3×10^{35} erg/s (Prat et al. 2008), similar to both IGR J18214-1318 and IGR J16207-5129. The spectrum of this source varies strongly with orbital phase ($P_{\rm orb} = 15.55$ days); Γ varies between 1 and 2, the e-folding energy of the exponential cutoff fluctuates between 6 and 10 keV, and $N_{\rm H}$ varies from $< 10^{22}$ and 2×10^{23} cm^{-2} (Prat et al. 2008). These large variations in $N_{\rm H}$ are similar to those observed in IGR J18214-1318, although for that source we do not know whether the variations are related to orbital phase. One spectral component that is seen in IGR J19140+0951 but not IGR J18214-1318 is a soft excess modeled by a $kT = 0.3$ keV blackbody, which is attributed to a shock formed between the ionized gas around the neutron star and the stellar wind (Prat et al. 2008). However, this soft excess is only seen at particular points of its 13.6 day orbit, which may be the reason it has not been seen in the limited observations of IGR J18214-1318.

IGR J16318-4848 is the HMXB with the highest measured local column density ($N_{\rm H} \sim 10^{24}$ cm^{-2}; Walter et al. 2003), which is due to its sgB[e] donor star (Filliatre & Chaty 2004). The relatively slow 400 km/s wind of this donor star helps maintain a high mass accretion rate onto the compact object, resulting in a slightly higher X-ray luminosity ($L_X \sim 10^{36}$ erg/s)

than in other Sg HMXBs (Barragán et al. 2009). Aside from its extreme obscuration and unusually strong Fe line emission, the spectral properties of IGR J16318-4848 are similar to those of IGR J18214-1318 and other Sg HMXBs; it exhibits a power-law spectrum with $\Gamma \approx 0.7$ and an e-folding cutoff energy of 20 keV (Barragán et al. 2009). However, due to the influence of its extremely dense stellar wind, the spectral similarity of IGR J16318-4848 does not necessarily imply that the radiative processes occurring in this system are the same as those in other non-pulsating Sg HMXBs.

The final non-pulsating HMXB is 4U 1700-377, which has a very similar X-ray spectrum to the other Sg HMXBs, but also has many unique properties. This source has $\Gamma \approx 1.0$, $E_{\rm fold} \approx 24$ keV, $E_{\rm cut} \approx 6$ keV, and a soft excess that may either result from a blackbody component with $kT \approx 0.2$ keV, as seen in IGR J19140+0951, or line emission (Reynolds et al. 1999; van der Meer et al. 2005). The donor star in this HMXB is an O6.5 Iaf star (Heap & Corcoran 1992), and it displays the highest levels of variability of any of the non-pulsating Sg HMXBs; its flux, even at hard X-ray energies, varies by factors >100, and the pattern of spectral variations as a function of luminosity are further evidence that 4U 1700-377 likely hosts a neutron star (Seifina et al. 2016). However, the mass of the compact object in this system has been measured to be 2.44 ± 0.27 $M_{\odot}$ (Clark et al. 2002), placing it among the most massive neutron stars observed (Ozel & Freire 2016).

In summary, in addition to IGR J18214-1318, there are five currently known HMXBs lacking pulsations with periods $\lesssim 10^3$ seconds, four of which have exponential cutoff energies < 25 keV, suggesting they most likely harbor neutron stars. Like IGR J18214-1318, all four of these HMXBs have supergiant donor stars and resemble the Sg HMXB 2S 0114+650, which hosts a neutron star with a 2.7 hour pulsation period thought to have been born as a magnetar. Population synthesis models predict that 8-9% of all neutron stars are born as magnetars, and that only $\sim 2\%$ of neutron stars in binaries are magnetars; these models predict that an even a smaller percentage of magnetars would be part of an X-ray binary because many of them are produced from the secondary rather than the primary (Popov & Prokhorov 2006). About 100 HMXBs have been discovered in the Galaxy, and only about 60 of them are known to host pulsars (Bird et al. 2016), so with the discovery of 2S 0114+650 and 4U 2206+54, both of which may host magnetars (or former magnetars), the observed number of magnetar HMXBs already agrees with theoretical expectations. Thus, if future observations reveal that several of the "non-pulsating" HMXBs actually host long-period pulsars, it could imply that either current models of magnetar origins or models of the spin evolution of neutron stars in binaries need to be revised.

4.6 Summary

Timing analysis of the *XMM-Newton* and *NuSTAR* observations of IGR J18214-1318 shows that this HMXB has strong levels of aperiodic variability but no pulsations with periods shorter than an hour. Joint fitting of the *XMM-Newton* and *NuSTAR* spectra reveals the presence of an exponential cutoff with e-folding energy < 25 keV. Thus, although we

cannot definitively identify the nature of the compact object in this system, the spectral cutoff energy is a strong indication that it is a neutron star. A soft excess is also detected in the spectrum of IGR J18214-1318, which we argue most likely results from partial covering absorption from the supergiant wind; the column density associated with the stellar wind is $\sim 10^{23}$ cm^{-2}, making this source a candidate member of the group of highly obscured Sg HMXBs discovered by *INTEGRAL*.

This study demonstrates the usefulness of the combination of *XMM-Newton* and *NuSTAR* observations to identify the likely nature of compact objects in HMXBs. Similar observations of other HMXBs will help place better constrains on the BH/NS ratio in HMXB populations. We know of four other HMXBs which, like IGR J18214-1318, have supergiant donor stars, cutoff energies $\lesssim 20$ keV suggesting they harbor neutron stars, but no detected pulsations despite sensitive timing observations. These sources also resemble 2S 0114+950, a Sg HMXB with 2.7 hour pulsations thought to host a former magnetar. Determining how many of the non-pulsating HMXBs in fact harbor long-period pulsars could shed light on the origins of magnetars and their possible connection to long-period pulsars in HMXBs.

Chapter 5

Conclusions and Future Outlook

5.1

High-mass X-ray binaries were among the first X-ray sources discovered outside our solar system by the rocket flight X-ray experiments in the 1960s, but many open questions persist about the factors that impact their formation and evolution, and the physics of accretion in the extreme gravity and magnetic fields of the compact objects they host. A more complete knowledge of the properties of HMXB populations, (such as the relative fractions of different HMXB classes, the diversity of temporal and spectral behavior, and their luminosity function) and how these properties differ depending on the galactic environment, can inform our understanding of massive stellar evolution, accretion processes in binaries, and the physical properties of compact objects. This dissertation contributes to three questions regarding HMXB populations:

i. How many low-luminosity HMXBs exist in our Galaxy and what are their properties?

ii. Are HMXB populations in low-metallicity environments more luminous?

iii. What is the nature of the compact objects in non-pulsating HMXBs?

5.2 Low-luminosity Galactic X-ray populations

In order to address the first question, *Chandra* and *NuSTAR* observed a square degree region in the direction of the Norma spiral arm. *Chandra* detected about 1100 point sources in this region, and *NuSTAR* measured the hard X-ray emission for the brightest ≈ 30 sources. Since at most ~ 10 of these sources were expected to be HMXBs, these surveys also provided the opportunity to study other faint X-ray populations in the Galaxy. Combined with companion *Chandra* and *NuSTAR* surveys of a square-degree region of the Galactic Center, the Norma region surveys also sought to address the following questions:

iv. What are the dominant populations of hard X-ray sources in the Galactic disk and how do they compare to those in the vicinity of the Galactic Center?

Through analysis of the spectra, X-ray variability, and the infrared counterparts of *Chandra* and *NuSTAR* sources, we determined that the dominant population of hard X-ray sources in the Norma region are CVs with plasma temperatures of $kT \approx 10 - 20$ keV, which is consistent with the hard X-ray component of the Galactic Ridge X-ray Emission. Although the majority of hard X-ray sources in the vicinity of the Galactic Center are also CVs, they have temperatures of $kT \approx 20 - 50$ keV. It is possible that the majority of CVs in both Galactic regions are primarily intermediate polars, in which case, their temperature differences correspond to differences in the mass of their white dwarfs. However, based on their variability properties, we think it is more likely that the Norma CV candidates have lower average temperatures because a larger fraction of them are non-magnetic CVs, polars, and symbiotic binaries rather than intermediate polars. It is unclear what evolutionary processes may cause the differences between the CV populations of the Norma region and the Galactic Center, but more accurate classifications of these CV candidates would help to develop new hypotheses. Monitoring the long-term variability of the CV candidates and measuring the equivalent widths and line flux ratios of their iron emission lines would aid this classification.

Through near-IR spectroscopic follow-up of hard X-ray sources detected in the *Chandra* and *NuSTAR* surveys of the Norma region, we identified three HMXB candidates. All three HMXB candidates have main-sequence Be/B counterparts. Their X-ray luminosities of $10^{32} - 10^{33}$ erg s^{-1} are lower than the typical quiescent state luminosities of known HMXBs, but 1–2 orders of magnitude higher than the typical luminosities of isolated Be/B stars. Future spectroscopic observations of the infrared counterparts of these candidates will be able to confirm whether they are indeed binaries through the detection of Doppler shifts; if they are binaries, measuring their radial velocity curves will determine their orbital period and constrain the mass of the compact object in these systems. If these sources are HMXBs, their low X-ray luminosities could be due to: (*i*) very wide orbits, which could teach us about the maximum initial period distribution of HMXBs and the strength of natal kicks from supernovae, (*ii*) the inhibition of accretion by the magnetosphere of neutron star accretors, or (*iii*) black holes accreting material inefficiently from the stellar wind, which would be especially interesting since only one Be-BH binary has been discovered to date and finding additional Be-BHs would help constrain models of massive stellar evolution. If none of these sources are HMXBs, it would suggest that the luminosity function of HMXBs flattens considerably at $L_X < 10^{34}$ erg s^{-1}, possibly as a result of centrifugal inhibition of accretion by the NS magnetosphere at low accretion rates.

5.3 The metallicity dependence of HMXBs

It is increasingly assumed that the enhanced number of bright HMXBs observed in low-metallicity blue compact dwarf galaxies and the increase of L_X/SFR of star-forming galaxies are the result of metallicity-dependent HMXB evolution. To investigate this hypothesis, we studied the X-ray emission of star-forming galaxies at $z \sim 2$ from the MOSDEF survey.

Using a sample of galaxies in the GOODS-N, GOODS-S, and EGS fields, where *Chandra* extragalactic surveys have achieved the deepest exposures, we grouped the galaxies into different metallicity bins and stacked the X-ray data to measure the average X-ray luminosity per SFR of galaxies in each bin. In agreement with previous studies, we find that the average L_X/SFR of star-forming galaxies at $z \sim 2$ is elevated compared to local $z = 0$ galaxies and that L_X/SFR decreases with increasing SFR. However, in contrast to the expectations of population synthesis models, our preliminary results do not find a significant correlation between the L_X/SFR and the galaxy metallicity in the metallicity range $8.0 < 12 + \log(\mathrm{O/H}) < 8.8$. Although we cannot rule out the possibility that contamination from low-luminosity AGN is biasing our results, the lack of correlation nonetheless suggests that we should not de facto assume that the redshift evolution of L_X/SFR of star-forming galaxies is driven by the metallicity dependence of HMXB evolution and that it may be worthwhile to investigate other possible origins for this trend. Our results will be improved by using the full MOSDEF galaxy sample now that the survey has been completed and by more thoroughly checking our background subtraction method and stacking analysis for possible systematic biases.

5.4 Compact objects in non-pulsating HMXBs

The detection of X-ray pulsations from an HMXB is strong proof of the presence of a neutron star in the system. However, X-ray pulsations may not always be detected from a NS HMXB depending on the geometry of the orbit and the angle between the rotational and magnetic axis of the NS. Thus, the nature of the compact object in a non-pulsating HMXB is unclear without more detailed study. In order to make progress towards a more complete characterization of the Galactic HMXB population, we performed a detailed study of the timing and spectral properties of IGR J18214-1318, a Sg HMXB from which no pulsations have been detected. Using observations from *XMM-Newton* and *NuSTAR*, we ruled out the presence of pulsations with periods shorter than an hour and measured an exponetial cutoff in the power-law spectrum of this source. The e-folding energy of this cutoff, which is below 25 keV, indicates that this HMXB hosts a NS accretor. IGR J18214-1318 shares many similiarities with four Sg HMXBs which exhibit spectral cutoff energies $\lesssim 20$ keV but no detected pulsations with periods $\lesssim 1$ hour, and it also resembles 2S 0114+950, a Sg HMXB with a long pulsation period of 2.7 hours. Long-period pulsars may be born as magnetars, and therefore determining whether any of the non-pulsating HMXBs actually host long-period pulsars could inform our understanding of magnetar formation. As exemplified by this study, future *XMM-Newton* and *NuSTAR* observations of other HMXBs which lack pulsations but have not been studied in detail would be powerful tools for identifying the likely nature of their compact objects.

5.5 Future outlook

Over the next decade, there will be great synergy between studies of HMXBs and the new frontiers of gravitational wave astronomy and the Epoch of Reionization. HMXBs are possible progenitors of NS/NS, NS/BH, and BH/BH binaries which may merge and produce gravitational waves detectable by Advanced LIGO/VIRGO. Advanced LIGO detected two gravitational wave signals produced by BH/BH mergers during its first observing run in 2015, and by 2018, $\sim$ 30 more BH/BH mergers are expected to be detected (The LIGO Scientific Collaboration et al. 2016). Increasing our knowledge of the properties of the HMXB populations, especially the ratio of HMXBs hosting BHs versus NSs, the HMXB orbital period distribution, and how these properties may vary with redshift and in different galactic environments, will improve estimates of the expected merger rates from HMXB descendants, helping to determine the evolutionary origins of the merging double compact binaries and to assess the implications of the gravitaional wave merger rates for stellar evolutionary models.

Measurements of the HI 21 cm power spectrum are beginning to place constraints on the level of X-ray heating of the intergalactic medium (IGM) during the Epoch of the Reionization. The next generation of 21 cm experiments will be capable of constraining parameters such as the spectral shape of the sources of X-ray heating to $\lesssim 10\%$ accuracy (Ewall-Wice et al. 2016). Further investigations of how the number, X-ray luminosity, and X-ray spectral shape of HMXBs depends on metallicity and other environmental variables will improve models of the contribution of HMXBs to the heating of the IGM in the early Universe, and constraints from the 21 cm power spectrum on these models will in turn inform our understanding of the evolution of the first generations of stars.

Direct X-ray detections of the first HMXBs and AGN which helped to heat and reionize the IGM will be possible with the next generation of X-ray observatories, *Athena* and *X-ray Surveyor*[1]. These future missions will not only enable the study of HMXBs out to high redshifts, but also provide enough sensitivity to study the individual spectra of a much larger fraction of Galactic X-ray sources, resulting in more accurate measurements of the relative numbers of different X-ray populations based on the classification of individual sources rather than the modeling of stacked spectra.

[1] *Athena* has been selected as a large-scale mission by ESA to be launched in 2028, whereas *X-ray Surveyor* is in the mission concept study phase and, if selected by NASA, would likely be launched in the early 2030s.

Bibliography

Abbott, B. P., Abbott, R., Abbott, T. D., et al. 2016a, ApJ, 818, L22

—. 2016b, Physical Review Letters, 116, 241103

—. 2016c, Physical Review Letters, 116, 061102

Accadia, T., Acernese, F., Agathos, M., et al. 2015, in Particle Physics at the Year of Centenary of Bruno Pontecorvo - PROCEEDINGS OF THE SIXTEENTH LOMONOSOV CONFERENCE ON ELEMENTARY PARTICLE PHYSICS. Edited by STUDENIKIN ALEXANDER I. Published by World Scientific Publishing Co. Pte. Ltd., 2015. ISBN #9789814663618, pp. 261-270, ed. S. V. Salikhov, 261

Aird, J., Coil, A. L., Georgakakis, A., et al. 2015, MNRAS, 451, 1892

Aird, J., Coil, A. L., Moustakas, J., et al. 2012, ApJ, 746, 90

Alexander, D. M., Bauer, F. E., Brandt, W. N., et al. 2003, AJ, 126, 539

Allen, C., Jerius, D. H., & Gaetz, T. J. 2004, in Society of Photo-Optical Instrumentation Engineers (SPIE) Conference Series, Vol. 5165, Society of Photo-Optical Instrumentation Engineers (SPIE) Conference Series, ed. K. A. Flanagan & O. H. W. Siegmund, 423

Allende Prieto, C., Lambert, D. L., & Asplund, M. 2001, ApJ, 556, L63

An, H., Kaspi, V. M., Tomsick, J. A., et al. 2012, ApJ, 757, 68

Anders, E., & Grevesse, N. 1989, Geochim. Cosmochim. Acta, 53, 197

Antoniou, V., & Zezas, A. 2016, MNRAS, 459, 528

Archibald, R. F., Gotthelf, E. V., Ferdman, R. D., et al. 2016, ApJ, 819, L16

Arnaud, K. A. 1996, in Astronomical Society of the Pacific Conference Series, Vol. 101, Astronomical Data Analysis Software and Systems V, ed. G. H. Jacoby & J. Barnes, 17

Asplund, M., Grevesse, N., Sauval, A. J., Allende Prieto, C., & Kiselman, D. 2004, A&A, 417, 751

Bachetti, M., Harrison, F. A., Walton, D. J., et al. 2014, Nature, 514, 202

Bachetti, M., Harrison, F. A., Cook, R., et al. 2015, ApJ, 800, 109

Bahcall, J. N. 1978, ARA&A, 16, 241

Baldwin, J. A., Phillips, M. M., & Terlevich, R. 1981, PASP, 93, 5

Barger, A. J., Cowie, L. L., & Wang, W.-H. 2008, ApJ, 689, 687

Barlow, E. J., Knigge, C., Bird, A. J., et al. 2006, MNRAS, 372, 224

Barragán, L., Wilms, J., Pottschmidt, K., et al. 2009, A&A, 508, 1275

Barret, D., McClintock, J. E., & Grindlay, J. E. 1996, ApJ, 473, 963

Baskill, D. S., Wheatley, P. J., & Osborne, J. P. 2005, MNRAS, 357, 626

Basu-Zych, A. R., Lehmer, B. D., Hornschemeier, A. E., et al. 2013a, ApJ, 774, 152
—. 2013b, ApJ, 762, 45
Belczynski, K., Bulik, T., & Bailyn, C. 2011, ApJ, 742, L2
Belczynski, K., Bulik, T., Fryer, C. L., et al. 2010, ApJ, 714, 1217
Belczynski, K., Bulik, T., Mandel, I., et al. 2013, ApJ, 764, 96
Belczynski, K., Holz, D. E., Bulik, T., & O'Shaughnessy, R. 2016, Nature, 534, 512
Belczynski, K., Kalogera, V., Zezas, A., & Fabbiano, G. 2004, ApJ, 601, L147
Belczyński, K., Mikołajewska, J., Munari, U., Ivison, R. J., & Friedjung, M. 2000, A&AS, 146, 407
Belczynski, K., & Ziolkowski, J. 2009, ApJ, 707, 870
Bellm, E. C., Fürst, F., Pottschmidt, K., et al. 2014, ApJ, 792, 108
Belloni, T., & Hasinger, G. 1990, A&A, 230, 103
Berghoefer, T. W., Schmitt, J. H. M. M., Danner, R., & Cassinelli, J. P. 1997, A&A, 322, 167
Bernardini, F., de Martino, D., Falanga, M., et al. 2012, A&A, 542, A22
Bhalerao, V. 2012, PhD thesis, Caltech <EMAIL>varun@astro.caltech.edu</EMAIL>
Bhalerao, V., Romano, P., Tomsick, J., et al. 2015, MNRAS, 447, 2274
Binney, J., Gerhard, O., & Spergel, D. 1997, MNRAS, 288, 365
Bird, A. J., Barlow, E. J., Bassani, L., et al. 2004, ApJ, 607, L33
—. 2006, ApJ, 636, 765
Bird, A. J., Bazzano, A., Malizia, A., et al. 2016, ApJS, 223, 15
Blondin, J. M. 1994, ApJ, 435, 756
Bocchino, F., & Bykov, A. M. 2001, A&A, 376, 248
Bodaghee, A., Rahoui, F., Tomsick, J. A., & Rodriguez, J. 2012a, ApJ, 751, 113
Bodaghee, A., Tomsick, J. A., & Rodriguez, J. 2012b, ApJ, 753, 3
Bodaghee, A., Tomsick, J. A., Rodriguez, J., et al. 2010, ApJ, 719, 451
Bodaghee, A., Tomsick, J. A., Rodriguez, J., & James, J. B. 2012c, ApJ, 744, 108
Bodaghee, A., Walter, R., Zurita Heras, J. A., et al. 2006, A&A, 447, 1027
Bodaghee, A., Tomsick, J. A., Krivonos, R., et al. 2014, ApJ, 791, 68
Bodaghee, A., Tomsick, J. A., Fornasini, F. M., et al. 2016, ApJ, 823, 146
Bolton, C. T. 1975, ApJ, 200, 269
Bongiorno, A., Merloni, A., Brusa, M., et al. 2012, MNRAS, 427, 3103
Bonning, E. W., & Falanga, M. 2005, A&A, 436, L31
Bouret, J.-C., Lanz, T., & Hillier, D. J. 2005, A&A, 438, 301
Bowyer, C. S., Field, G. B., & Mack, J. E. 1968, Nature, 217, 32
Bowyer, S., Byram, E. T., Chubb, T. A., & Friedman, H. 1965, Science, 147, 394
Bozzo, E., Falanga, M., & Stella, L. 2008, ApJ, 683, 1031
Bozzo, E., Pavan, L., Ferrigno, C., et al. 2012, A&A, 544, A118
Brammer, G. B., van Dokkum, P. G., Franx, M., et al. 2012, ApJS, 200, 13
Brightman, M., Harrison, F. A., Barret, D., et al. 2016, ArXiv e-prints, arXiv:1607.03903 [astro-ph.HE]
Brogan, C. L., Frail, D. A., Goss, W. M., & Troland, T. H. 2000, ApJ, 537, 875
Bronfman, L., Alvarez, H., Cohen, R. S., & Thaddeus, P. 1989, ApJS, 71, 481

Brorby, M., Kaaret, P., & Prestwich, A. 2014, MNRAS, 441, 2346
Brorby, M., Kaaret, P., Prestwich, A., & Mirabel, I. F. 2016, MNRAS, 457, 4081
Buccheri, R., Bennett, K., Bignami, G. F., et al. 1983, A&A, 128, 245
Bulik, T., Belczynski, K., & Prestwich, A. 2011, ApJ, 730, 140
Butler, S. C., Tomsick, J. A., Chaty, S., et al. 2009, ApJ, 698, 502
Caballero, I., & Wilms, J. 2012, Mem. Soc. Astron. Italiana, 83, 230
Caballero, I., Kretschmar, P., Santangelo, A., et al. 2007, A&A, 465, L21
Calzetti, D., Armus, L., Bohlin, R. C., et al. 2000, ApJ, 533, 682
Cappelluti, N., Brusa, M., Hasinger, G., et al. 2009, A&A, 497, 635
Cardelli, J. A., Clayton, G. C., & Mathis, J. S. 1989, ApJ, 345, 245
Casares, J., Charles, P. A., & Naylor, T. 1992, Nature, 355, 614
Casares, J., Negueruela, I., Ribó, M., et al. 2014, Nature, 505, 378
Cash, W. 1979, ApJ, 228, 939
Chabrier, G. 2003, PASP, 115, 763
Chaty, S. 2011, in Astronomical Society of the Pacific Conference Series, Vol. 447, Evolution of Compact Binaries, ed. L. Schmidtobreick, M. R. Schreiber, & C. Tappert, 29
Chaty, S. 2013, Advances in Space Research, 52, 2132
Chaty, S., Rahoui, F., Foellmi, C., et al. 2008, A&A, 484, 783
Cheng, K. S., Taam, R. E., & Wang, W. 2004, ApJ, 617, 480
Choi, C.-S., Dotani, T., & Agrawal, P. C. 1999, ApJ, 525, 399
Civano, F., Elvis, M., Brusa, M., et al. 2012, ApJS, 201, 30
Civano, F., Hickox, R. C., Puccetti, S., et al. 2015, ApJ, 808, 185
Clark, J. S., Bartlett, E. S., Coe, M. J., et al. 2013a, A&A, 560, A10
Clark, J. S., Goodwin, S. P., Crowther, P. A., et al. 2002, A&A, 392, 909
Clark, J. S., Ritchie, B. W., & Negueruela, I. 2013b, A&A, 560, A11
Coburn, W., Heindl, W. A., Rothschild, R. E., et al. 2002, ApJ, 580, 394
Cohen, D. H., Cassinelli, J. P., & MacFarlane, J. J. 1997, ApJ, 487, 867
Coil, A. L., Blanton, M. R., Burles, S. M., et al. 2011, ApJ, 741, 8
Coil, A. L., Aird, J., Reddy, N., et al. 2015, ApJ, 801, 35
Combi, J. A., Albacete Colombo, J. F., Romero, G. E., & Benaglia, P. 2006, ApJ, 653, L41
Combi, J. A., Benaglia, P., Romero, G. E., & Sugizaki, M. 2005, A&A, 431, L9
Connon Smith, R. 2007, ArXiv Astrophysics e-prints, astro-ph/0701654
Conroy, C. 2013, ARA&A, 51, 393
Conroy, C., Gunn, J. E., & White, M. 2009, ApJ, 699, 486
Conselice, C. J. 2003, ApJS, 147, 1
Cooper, M. C., Griffith, R. L., Newman, J. A., et al. 2012, MNRAS, 419, 3018
Corbet, R., Barbier, L., Barthelmy, S., et al. 2006, The Astronomer's Telegram, 797
Corbet, R. H. D. 1984, A&A, 141, 91
—. 1986, MNRAS, 220, 1047
Corbet, R. H. D., Finley, J. P., & Peele, A. G. 1999, ApJ, 511, 876
Corbet, R. H. D., & Krimm, H. A. 2013, ApJ, 778, 45
Corbet, R. H. D., Sokoloski, J. L., Mukai, K., Markwardt, C. B., & Tueller, J. 2008, ApJ,

675, 1424
Corcoran, M. F. 1996, in Revista Mexicana de Astronomia y Astrofisica Conference Series, Vol. 5, Revista Mexicana de Astronomia y Astrofisica Conference Series, ed. V. Niemela, N. Morrell, P. Pismis, & S. Torres-Peimbert, 54
Corcoran, M. F. 2005, AJ, 129, 2018
Corral-Santana, J., & et al. in prep, in preparation
Cowley, A. P., Crampton, D., Hutchings, J. B., Remillard, R., & Penfold, J. E. 1983, ApJ, 272, 118
Cropper, M. 1990, Space Sci. Rev., 54, 195
Cutri, R. M., & et al. 2013, VizieR Online Data Catalog, 2328
Dame, T. M., Hartmann, D., & Thaddeus, P. 2001, ApJ, 547, 792
Davidson, K., & Ostriker, J. P. 1973, ApJ, 179, 585
Davies, B., de La Fuente, D., Najarro, F., et al. 2012, MNRAS, 419, 1860
de Martino, D., Matt, G., Belloni, T., et al. 2004, Nuclear Physics B Proceedings Supplements, 132, 693
Dempsey, R. C., Linsky, J. L., Fleming, T. A., & Schmitt, J. H. M. M. 1993, ApJS, 86, 599
den Herder, J. W., Brinkman, A. C., Kahn, S. M., et al. 2001, A&A, 365, L7
Di Salvo, T., Done, C., Życki, P. T., Burderi, L., & Robba, N. R. 2001, ApJ, 547, 1024
Dieters, S. W., Belloni, T., Kuulkers, E., et al. 2000, ApJ, 538, 307
Donley, J. L., Koekemoer, A. M., Brusa, M., et al. 2012, ApJ, 748, 142
Doroshenko, V., Santangelo, A., Doroshenko, R., et al. 2014, A&A, 561, A96
Doroshenko, V., Suchy, S., Santangelo, A., et al. 2010, A&A, 515, L1
Douna, V. M., Pellizza, L. J., Mirabel, I. F., & Pedrosa, S. E. 2015, A&A, 579, A44
Dray, L. M. 2006, MNRAS, 370, 2079
Ducati, J. R., Bevilacqua, C. M., Rembold, S. B., & Ribeiro, D. 2001, ApJ, 558, 309
Duncan, R. C., & Thompson, C. 1992, ApJ, 392, L9
Dwek, E., Arendt, R. G., Hauser, M. G., et al. 1995, ApJ, 445, 716
Ebisawa, K., Tsujimoto, M., Paizis, A., et al. 2005, ApJ, 635, 214
Elmegreen, B. G., Elmegreen, D. M., Salzer, J. J., & Mann, H. 1996, ApJ, 467, 579
Elshamouty, K., Heinke, C., & Chouinard, R. 2016, ArXiv e-prints, arXiv:1604.07808 [astro-ph.HE]
Enoto, T., Sasano, M., Yamada, S., et al. 2014, ApJ, 786, 127
Eracleous, M., Halpern, J., & Patterson, J. 1991, ApJ, 382, 290
Erb, D. K., Shapley, A. E., Pettini, M., et al. 2006, ApJ, 644, 813
Esin, A. A., Narayan, R., Cui, W., Grove, J. E., & Zhang, S.-N. 1998, ApJ, 505, 854
Esposito, P., Israel, G. L., Zane, S., et al. 2008, MNRAS, 390, L34
Esposito, P., Tiengo, A., Mereghetti, S., et al. 2009, ApJ, 690, L105
Ewall-Wice, A., Hewitt, J., Mesinger, A., et al. 2016, MNRAS, 458, 2710
Ezuka, H., & Ishida, M. 1999, ApJS, 120, 277
Farinelli, R., Ferrigno, C., Bozzo, E., & Becker, P. A. 2016, A&A, 591, A29
Farrell, S. A., Sood, R. K., O'Neill, P. M., & Dieters, S. 2008, MNRAS, 389, 608
Filippova, E. V., Tsygankov, S. S., Lutovinov, A. A., & Sunyaev, R. A. 2005, Astronomy

Letters, 31, 729
Filliatre, P., & Chaty, S. 2004, ApJ, 616, 469
Fornasini, F. M., Tomsick, J. A., Bodaghee, A., et al. 2014, ApJ, 796, 105
Fragos, T., Lehmer, B. D., Naoz, S., Zezas, A., & Basu-Zych, A. 2013a, ApJ, 776, L31
Fragos, T., Linden, T., Kalogera, V., & Sklias, P. 2015, ApJ, 802, L5
Fragos, T., Lehmer, B., Tremmel, M., et al. 2013b, ApJ, 764, 41
Franciosini, E., Pallavicini, R., & Tagliaferri, G. 2001, A&A, 375, 196
Freeman, P. E., Kashyap, V., Rosner, R., & Lamb, D. Q. 2002a, ApJS, 138, 185
—. 2002b, ApJS, 138, 185
Freudenreich, H. T. 1998, ApJ, 492, 495
Fullerton, A. W., Massa, D. L., & Prinja, R. K. 2006, ApJ, 637, 1025
Funk, S., Hinton, J. A., Pühlhofer, G., et al. 2007, ApJ, 662, 517
Fürst, F., Suchy, S., Kreykenbohm, I., et al. 2011, A&A, 535, A9
Fürst, F., Pottschmidt, K., Wilms, J., et al. 2014, ApJ, 780, 133
Gaensler, B. M., & Slane, P. O. 2006, ARA&A, 44, 17
Gagné, M., Oksala, M. E., Cohen, D. H., et al. 2005, ApJ, 628, 986
Gagné, M., Fehon, G., Savoy, M. R., et al. 2011, ApJS, 194, 5
Garmire, G. P., Bautz, M. W., Ford, P. G., Nousek, J. A., & Ricker, Jr., G. R. 2003, in Society of Photo-Optical Instrumentation Engineers (SPIE) Conference Series, Vol. 4851, Society of Photo-Optical Instrumentation Engineers (SPIE) Conference Series, ed. J. E. Truemper & H. D. Tananbaum, 28
Gehrels, N. 1986, ApJ, 303, 336
Georgakakis, A., Nandra, K., Laird, E. S., Aird, J., & Trichas, M. 2008a, MNRAS, 388, 1205
—. 2008b, MNRAS, 388, 1205
Georgelin, Y. M., Russeil, D., Marcelin, M., et al. 1996, A&AS, 120, 41
Giacconi, R., Gursky, H., Paolini, F. R., & Rossi, B. B. 1962, Physical Review Letters, 9, 439
Giacconi, R., & Rossi, B. 1960, J. Geophys. Res., 65, 773
Giacconi, R., Branduardi, G., Briel, U., et al. 1979, ApJ, 230, 540
Giacconi, R., Zirm, A., Wang, J., et al. 2002, ApJS, 139, 369
Gilfanov, M. 2004, MNRAS, 349, 146
Gilfanov, M. 2010, in Lecture Notes in Physics, Berlin Springer Verlag, Vol. 794, Lecture Notes in Physics, Berlin Springer Verlag, ed. T. Belloni, 17
Gilfanov, M., Grimm, H.-J., & Sunyaev, R. 2004, MNRAS, 347, L57
Gotthelf, E. V. 2003, ApJ, 591, 361
Gotthelf, E. V., Tomsick, J. A., Halpern, J. P., et al. 2014, ApJ, 788, 155
Granada, A., Ekström, S., Georgy, C., et al. 2013, A&A, 553, A25
Grebenev, S. A., & Sunyaev, R. A. 2007, Astronomy Letters, 33, 149
Green, D. A. 2004, Bulletin of the Astronomical Society of India, 32, 335
Grimm, H.-J., Gilfanov, M., & Sunyaev, R. 2002, A&A, 391, 923
—. 2003, MNRAS, 339, 793
Grogin, N. A., Kocevski, D. D., Faber, S. M., et al. 2011, ApJS, 197, 35
Grosso, N., Feigelson, E. D., Getman, K. V., et al. 2005, ApJS, 160, 530

Grove, J. E., Johnson, W. N., Kroeger, R. A., et al. 1998, ApJ, 500, 899
Grudzinska, M., Belczynski, K., Casares, J., et al. 2015, MNRAS, 452, 2773
Güdel, M., Briggs, K. R., Arzner, K., et al. 2007, A&A, 468, 353
Güver, T., & Özel, F. 2009, MNRAS, 400, 2050
Haberl, F., & Sturm, R. 2016, A&A, 586, A81
Hailey, C. J., Mori, K., Perez, K., et al. 2016, ApJ, 826, 160
Hamaguchi, K., Corcoran, M. F., Gull, T., et al. 2007, ApJ, 663, 522
Hammersley, P. L., Cohen, M., Garzón, F., Mahoney, T., & López-Corredoira, M. 1999, MNRAS, 308, 333
Hannikainen, D. C., Rawlings, M. G., Muhli, P., et al. 2007, MNRAS, 380, 665
Harrison, F. A., Craig, W. W., Christensen, F. E., et al. 2013, ApJ, 770, 103
Hasinger, G., & van der Klis, M. 1989, A&A, 225, 79
Heap, S. R., & Corcoran, M. F. 1992, ApJ, 387, 340
Hellier, C., Mukai, K., & Beardmore, A. P. 1997, MNRAS, 292, 397
Hickox, R. C., Narayan, R., & Kallman, T. R. 2004, ApJ, 614, 881
Hirano, T., Hayakawa, S., Nagase, F., Masai, K., & Mitsuda, K. 1987, PASJ, 39, 619
Hoard, D. W., Wachter, S., Clark, L. L., & Bowers, T. P. 2002, ApJ, 565, 511
Hong, J., Schlegel, E. M., & Grindlay, J. E. 2004, ApJ, 614, 508
Hong, J., van den Berg, M., Schlegel, E. M., et al. 2005, ApJ, 635, 907
Hong, J., Mori, K., Hailey, C. J., et al. 2016, ApJ, 825, 132
Hong, J. S., van den Berg, M., Grindlay, J. E., & Laycock, S. 2009, ApJ, 706, 223
Horne, K. 1986, PASP, 98, 609
Hoshino, M., & Takeshima, T. 1993, ApJ, 411, L79
House, L. L. 1969, ApJS, 18, 21
Hunter, D. A., & Elmegreen, B. G. 2004, AJ, 128, 2170
Hurley, K., Kouveliotou, C., Woods, P., et al. 1999, ApJ, 519, L143
Hutchings, J. B., Crampton, D., & Cowley, A. P. 1983, ApJ, 275, L43
Iben, Jr., I., Tutukov, A. V., & Yungelson, L. R. 1995, ApJS, 100, 217
Ikhsanov, N. R., & Beskrovnaya, N. G. 2010, Astrophysics, 53, 237
Illarionov, A. F., & Sunyaev, R. A. 1975, A&A, 39, 185
Ivanova, N., Justham, S., Chen, X., et al. 2013, A&A Rev., 21, 59
Iwasawa, K., Mainieri, V., Brusa, M., et al. 2012, A&A, 537, A86
Jakobsen, S. J. 2013, Master's thesis, Niels Bohr Institute, Copenhagen University
Jakobsen, S. J., Tomsick, J. A., Watson, D., Gotthelf, E. V., & Kaspi, V. M. 2014, ApJ, 787, 129
Jansen, F., Lumb, D., Altieri, B., et al. 2001, A&A, 365, L1
Jeon, M., Pawlik, A. H., Bromm, V., & Milosavljević, M. 2014, MNRAS, 440, 3778
Jones, C., & Dickey, J. M. 2012, ApJ, 753, 62
Jones, T. M., Kriek, M., van Dokkum, P. G., et al. 2014, ApJ, 783, 25
Justham, S., & Schawinski, K. 2012, MNRAS, 423, 1641
Kaaret, P. 2014, MNRAS, 440, L26
Kaaret, P., Schmitt, J., & Gorski, M. 2011, ApJ, 741, 10

Kalberla, P. M. W., Burton, W. B., Hartmann, D., et al. 2005, A&A, 440, 775
Kargaltsev, O., & Pavlov, G. G. 2008, in American Institute of Physics Conference Series, Vol. 983, 40 Years of Pulsars: Millisecond Pulsars, Magnetars and More, ed. C. Bassa, Z. Wang, A. Cumming, & V. M. Kaspi, 171
Kauffmann, G., Heckman, T. M., Tremonti, C., et al. 2003, MNRAS, 346, 1055
Kennicutt, Jr., R. C. 1998, ARA&A, 36, 189
Kewley, L. J., & Ellison, S. L. 2008, ApJ, 681, 1183
King, A., & Lasota, J.-P. 2016, MNRAS, 458, L10
King, A. L., Walton, D. J., Miller, J. M., et al. 2014, ApJ, 784, L2
King, A. R., Davies, M. B., Ward, M. J., Fabbiano, G., & Elvis, M. 2001, ApJ, 552, L109
Klein-Wolt, M., Homan, J., & van der Klis, M. 2004, Nuclear Physics B Proceedings Supplements, 132, 381
Klus, H., Ho, W. C. G., Coe, M. J., Corbet, R. H. D., & Townsend, L. J. 2014, MNRAS, 437, 3863
Koekemoer, A. M., Faber, S. M., Ferguson, H. C., et al. 2011, ApJS, 197, 36
Koglin, J. E., An, H., Barrière, N., et al. 2011, in Proc. SPIE, Vol. 8147, Society of Photo-Optical Instrumentation Engineers (SPIE) Conference Series, 81470J
Kouveliotou, C., Patel, S., Tennant, A., et al. 2003, IAU Circ., 8109
Koyama, K., Kunieda, H., Takeuchi, Y., & Tawara, Y. 1991, ApJ, 370, L77
Kraft, R. P., Burrows, D. N., & Nousek, J. A. 1991, ApJ, 374, 344
Kriek, M., van Dokkum, P. G., Labbé, I., et al. 2009, ApJ, 700, 221
Kriek, M., Shapley, A. E., Reddy, N. A., et al. 2015, ApJS, 218, 15
Krishnamurthi, A., Reynolds, C. S., Linsky, J. L., Martín, E., & Gagné, M. 2001, AJ, 121, 337
Krivonos, R., Revnivtsev, M., Churazov, E., et al. 2007, A&A, 463, 957
Krivonos, R., Tsygankov, S., Lutovinov, A., et al. 2012, A&A, 545, A27
Krumholz, M. R., Cunningham, A. J., Klein, R. I., & McKee, C. F. 2010, ApJ, 713, 1120
Kuchar, T. A., & Clark, F. O. 1997, ApJ, 488, 224
Kuulkers, E., Norton, A., Schwope, A., & Warner, B. 2006, in Compact stellar X-ray sources, ed. W. H. G. Lewin & M. van der Klis ((Cambridge University Press), 421
Kuulkers, E., Parmar, A. N., Kitamoto, S., Cominsky, L. R., & Sood, R. K. 1997, MNRAS, 291, 81
La Palombara, N., & Mereghetti, S. 2006, A&A, 455, 283
—. 2007, A&A, 474, 137
La Palombara, N., Sidoli, L., Esposito, P., Tiengo, A., & Mereghetti, S. 2009, A&A, 505, 947
Laird, E. S., Nandra, K., Georgakakis, A., et al. 2009, ApJS, 180, 102
Lamb, F. K. 1989, in ESA Special Publication, Vol. 296, Two Topics in X-Ray Astronomy, Volume 1: X Ray Binaries. Volume 2: AGN and the X Ray Background, ed. J. Hunt & B. Battrick
Landi, R., Bassani, L., Dean, A. J., et al. 2009, MNRAS, 392, 630
Lansbury, G. B., Stern, D., Aird, J., et al. 2016, submitted to ApJ
Lattimer, J. M. 2012, Annual Review of Nuclear and Particle Science, 62, 485

Leahy, D. A., Darbro, W., Elsner, R. F., et al. 1983, ApJ, 266, 160
Lehmer, B. D., Alexander, D. M., Bauer, F. E., et al. 2010, ApJ, 724, 559
Lehmer, B. D., Xue, Y. Q., Brandt, W. N., et al. 2012, ApJ, 752, 46
Lehmer, B. D., Basu-Zych, A. R., Mineo, S., et al. 2016, ApJ, 825, 7
Lewin, W. H. G., Ricker, G. R., & McClintock, J. E. 1971, ApJ, 169, L17
Li, X.-D., & van den Heuvel, E. P. J. 1999, ApJ, 513, L45
LIGO Scientific Collaboration, Aasi, J., Abbott, B. P., et al. 2015, Classical and Quantum Gravity, 32, 074001
Lin, D., Remillard, R. A., & Homan, J. 2009, ApJ, 696, 1257
Linden, T., Kalogera, V., Sepinsky, J. F., et al. 2010, ApJ, 725, 1984
Liu, Q. Z., van Paradijs, J., & van den Heuvel, E. P. J. 2006, A&A, 455, 1165
Liu, X., Shapley, A. E., Coil, A. L., Brinchmann, J., & Ma, C.-P. 2008, ApJ, 678, 758
Livio, M., & Warner, B. 1984, The Observatory, 104, 152
Loeb, A. 2016, ApJ, 819, L21
Lopes de Oliveira, R. 2007, PhD thesis, Instituto de Astronomia, Geofísica e Ciências Atmosféricas, Universidade de São Paulo, R. do Matão 1226, 05508-090 São Paulo, Brazil Observatoire Astronomique, UMR 7550 CNRS, Université Louis Pasteur, 11 rue de l'Université, 67000 Strasbourg, France <EMAIL>rlopes@astro.iag.usp.br;</EMAIL>
Lotz, J. M., Primack, J., & Madau, P. 2004, AJ, 128, 163
Lü, G.-L., Zhu, C.-H., Postnov, K. A., et al. 2012, MNRAS, 424, 2265
Luna, G. J. M., & Sokoloski, J. L. 2007, ApJ, 671, 741
Luna, G. J. M., Sokoloski, J. L., Mukai, K., & Nelson, T. 2013, A&A, 559, A6
Luo, B., Bauer, F. E., Brandt, W. N., et al. 2008, ApJS, 179, 19
Lutovinov, A. A., Revnivtsev, M. G., Tsygankov, S. S., & Krivonos, R. A. 2013, MNRAS, 431, 327
Lyne, A. G., Anderson, B., & Salter, M. J. 1982, MNRAS, 201, 503
Madsen, K. K., Harrison, F. A., Markwardt, C. B., et al. 2015, ApJS, 220, 8
Maiolino, R., Nagao, T., Grazian, A., et al. 2008, A&A, 488, 463
Makino, F., Wagner, R. M., Starrfield, S., et al. 1989, IAU Circ., 4786
Makishima, K., Takahashi, H., Yamada, S., et al. 2008, PASJ, 60, 585
Manousakis, A., & Walter, R. 2011, A&A, 526, A62
—. 2015, A&A, 575, A58
Mapelli, M., Ripamonti, E., Zampieri, L., & Colpi, M. 2011, Astronomische Nachrichten, 332, 414
Marcu, D. M., Fürst, F., Pottschmidt, K., et al. 2011, ApJ, 742, L11
Markowitz, A., & Edelson, R. 2004, ApJ, 617, 939
Masetti, N., Orlandini, M., dal Fiume, D., et al. 2006, A&A, 445, 653
Masetti, N., Dal Fiume, D., Cusumano, G., et al. 2002, A&A, 382, 104
Masetti, N., Landi, R., Pretorius, M. L., et al. 2007, A&A, 470, 331
Masetti, N., Parisi, P., Palazzi, E., et al. 2010, A&A, 519, A96
Mateos, S., Alonso-Herrero, A., Carrera, F. J., et al. 2012, MNRAS, 426, 3271
Matthews, O. M., Wheatley, P. J., Wynn, G. A., & Truss, M. R. 2006, MNRAS, 372, 1593

Mauerhan, J. C., Muno, M. P., Morris, M. R., Stolovy, S. R., & Cotera, A. 2010, ApJ, 710, 706
Maughan, B. J., Giles, P. A., Randall, S. W., Jones, C., & Forman, W. R. 2012, MNRAS, 421, 1583
McClintock, J. E., & Remillard, R. A. 2006, Black hole binaries, ed. W. H. G. Lewin & M. van der Klis, 157
McLean, I. S., Steidel, C. C., Epps, H. W., et al. 2012, in Proc. SPIE, Vol. 8446, Ground-based and Airborne Instrumentation for Astronomy IV, 84460J
Mercer, E. P., Clemens, D. P., Meade, M. R., et al. 2005, ApJ, 635, 560
Mezcua, M., Civano, F., Fabbiano, G., Miyaji, T., & Marchesi, S. 2016, ApJ, 817, 20
Mikles, V. J., Eikenberry, S. S., Muno, M. P., Bandyopadhyay, R. M., & Patel, S. 2006, ApJ, 651, 408
Mineo, S., Gilfanov, M., & Sunyaev, R. 2012, MNRAS, 419, 2095
Minniti, D., Lucas, P. W., Emerson, J. P., et al. 2010, New Astronomy, 15, 433
Molina, M., Bassani, L., Malizia, A., et al. 2009, MNRAS, 399, 1293
Momcheva, I. G., Brammer, G. B., van Dokkum, P. G., et al. 2016, ApJS, 225, 27
Mori, K., Gotthelf, E. V., Dufour, F., et al. 2014, ApJ, 793, 88
Mori, K., Hailey, C. J., Krivonos, R., et al. 2015, ApJ, 814, 94
Morihana, K., Tsujimoto, M., Dubath, P., et al. 2016, PASJ, arXiv:1604.06779 [astro-ph.HE]
Morris, M. 1993, ApJ, 408, 496
Moster, B. P., Naab, T., & White, S. D. M. 2013, MNRAS, 428, 3121
Motch, C., Lopes de Oliveira, R., & Smith, M. A. 2015, ApJ, 806, 177
Muerset, U., Wolff, B., & Jordan, S. 1997, A&A, 319, 201
Mukai, K., & Shiokawa, K. 1993, ApJ, 418, 863
Mukherjee, U., & Paul, B. 2005, A&A, 431, 667
Mullaney, J. R., Del-Moro, A., Aird, J., et al. 2015, ApJ, 808, 184
Munar-Adrover, P., Paredes, J. M., Ribó, M., et al. 2014, ApJ, 786, L11
Muno, M. P. 2007, in American Institute of Physics Conference Series, Vol. 924, The Multicolored Landscape of Compact Objects and Their Explosive Origins, ed. T. di Salvo, G. L. Israel, L. Piersant, L. Burderi, G. Matt, A. Tornambe, & M. T. Menna, 166
Muno, M. P., Arabadjis, J. S., Baganoff, F. K., et al. 2004, ApJ, 613, 1179
Muno, M. P., Bauer, F. E., Baganoff, F. K., et al. 2009, ApJS, 181, 110
Murray, S. S., Austin, G. K., Chappell, J. H., et al. 2000, in Proc. SPIE, Vol. 4012, X-Ray Optics, Instruments, and Missions III, ed. J. E. Truemper & B. Aschenbach, 68
Nagase, F. 1989, PASJ, 41, 1
Naik, S., Paul, B., & Ali, Z. 2011, ApJ, 737, 79
Nandra, K., Laird, E. S., Aird, J. A., et al. 2015, ApJS, 220, 10
Negueruela, I., Smith, D. M., Reig, P., Chaty, S., & Torrejón, J. M. 2006, in ESA Special Publication, Vol. 604, The X-ray Universe 2005, ed. A. Wilson, 165
Negueruela, I., Torrejón, J. M., Reig, P., Ribó, M., & Smith, D. M. 2008, in American Institute of Physics Conference Series, Vol. 1010, A Population Explosion: The Nature & Evolution of X-ray Binaries in Diverse Environments, ed. R. M. Bandyopadhyay, S. Wachter,

D. Gelino, & C. R. Gelino, 252
Nespoli, E., Fabregat, J., & Mennickent, R. E. 2008, A&A, 486, 911
—. 2010, A&A, 516, A94
Newman, J. A., Cooper, M. C., Davis, M., et al. 2013, ApJS, 208, 5
Newman, S. F., Buschkamp, P., Genzel, R., et al. 2014, ApJ, 781, 21
Olausen, S. A., & Kaspi, V. M. 2014, ApJS, 212, 6
O'Leary, R. M., Rasio, F. A., Fregeau, J. M., Ivanova, N., & O'Shaughnessy, R. 2006, ApJ, 637, 937
Orio, M., Covington, J., & Ögelman, H. 2001, A&A, 373, 542
Orio, M., Zezas, A., Munari, U., Siviero, A., & Tepedelenlioglu, E. 2007, ApJ, 661, 1105
Orosz, J. A., McClintock, J. E., Aufdenberg, J. P., et al. 2011, ApJ, 742, 84
Ozel, F., & Freire, P. 2016, ArXiv e-prints, arXiv:1603.02698 [astro-ph.HE]
Özel, F., Psaltis, D., Narayan, R., & McClintock, J. E. 2010, ApJ, 725, 1918
Page, K. L., O'Brien, P. T., Reeves, J. N., & Turner, M. J. L. 2004, MNRAS, 347, 316
Pandey, J. C., & Singh, K. P. 2012, MNRAS, 419, 1219
Parsons, A. R., Liu, A., Aguirre, J. E., et al. 2014, ApJ, 788, 106
Patel, S. K., Kouveliotou, C., Tennant, A., et al. 2004, ApJ, 602, L45
Patel, S. K., Zurita, J., Del Santo, M., et al. 2007, ApJ, 657, 994
Patterson, J. 1994, PASP, 106, 209
Paumard, T., Genzel, R., Martins, F., et al. 2006, ApJ, 643, 1011
Perez, K., Hailey, C. J., Bauer, F. E., et al. 2015, Nature, 520, 646
Persic, M., Rephaeli, Y., Braito, V., et al. 2004, A&A, 419, 849
Petit, V., Owocki, S. P., Wade, G. A., et al. 2013, MNRAS, 429, 398
Pettini, M., & Pagel, B. E. J. 2004, MNRAS, 348, L59
Pittard, J. M., Stevens, I. R., Corcoran, M. F., & Ishibashi, K. 1998, MNRAS, 299, L5
Pober, J. C., Liu, A., Dillon, J. S., et al. 2014, ApJ, 782, 66
Pober, J. C., Ali, Z. S., Parsons, A. R., et al. 2015, ApJ, 809, 62
Pollock, A. M. T. 1987, ApJ, 320, 283
Popov, S. B., & Prokhorov, M. E. 2006, MNRAS, 367, 732
Portegies Zwart, S. F., Pooley, D., & Lewin, W. H. G. 2002, ApJ, 574, 762
Possenti, A., Cerutti, R., Colpi, M., & Mereghetti, S. 2002, A&A, 387, 993
Postnov, K. A., & Yungelson, L. R. 2014, Living Reviews in Relativity, 17, arXiv:1403.4754 [astro-ph.HE]
Pottschmidt, K., Kreykenbohm, I., Wilms, J., et al. 2005, ApJ, 634, L97
Power, C., Wynn, G. A., Combet, C., & Wilkinson, M. I. 2009, MNRAS, 395, 1146
Prat, L., Rodriguez, J., Hannikainen, D. C., & Shaw, S. E. 2008, MNRAS, 389, 301
Prestwich, A. H., Jackson, F., Kaaret, P., et al. 2015, ApJ, 812, 166
Prestwich, A. H., Tsantaki, M., Zezas, A., et al. 2013, ApJ, 769, 92
Ptak, A., Serlemitsos, P., Yaqoob, T., & Mushotzky, R. 1999, ApJS, 120, 179
Rahoui, F., Tomsick, J. A., Fornasini, F. M., Bodaghee, A., & Bauer, F. E. 2014, A&A, 568, A54
Ramsay, G., Cropper, M., Wu, K., et al. 2004, MNRAS, 350, 1373

Rana, V., Loh, A., Corbel, S., et al. 2016, ApJ, 821, 103
Ranalli, P., Comastri, A., & Setti, G. 2003, A&A, 399, 39
Rangel, C., Nandra, K., Laird, E. S., & Orange, P. 2013, MNRAS, 428, 3089
Ransom, S. M., Eikenberry, S. S., & Middleditch, J. 2002, AJ, 124, 1788
Rea, N., & Esposito, P. 2011, Astrophysics and Space Science Proceedings, 21, 247
Reddy, N. A., Steidel, C. C., Erb, D. K., Shapley, A. E., & Pettini, M. 2006, ApJ, 653, 1004
Reddy, N. A., Kriek, M., Shapley, A. E., et al. 2015, ApJ, 806, 259
Reig, P. 2011, Ap&SS, 332, 1
Reig, P., Chakrabarty, D., Coe, M. J., et al. 1996, A&A, 311, 879
Reig, P., Doroshenko, V., & Zezas, A. 2014, MNRAS, 445, 1314
Reig, P., Torrejón, J. M., & Blay, P. 2012, MNRAS, 425, 595
Reig, P., Torrejón, J. M., Negueruela, I., et al. 2009, A&A, 494, 1073
Remillard, R. A., & McClintock, J. E. 2006, ARA&A, 44, 49
Revnivtsev, M., Churazov, E., Postnov, K., & Tsygankov, S. 2009a, A&A, 507, 1211
Revnivtsev, M., Molkov, S., & Sazonov, S. 2006a, MNRAS, 373, L11
Revnivtsev, M., & Sazonov, S. 2007, A&A, 471, 159
Revnivtsev, M., Sazonov, S., Churazov, E., et al. 2009b, Nature, 458, 1142
Revnivtsev, M., Sazonov, S., Gilfanov, M., Churazov, E., & Sunyaev, R. 2006b, A&A, 452, 169
Revnivtsev, M., Sazonov, S., Krivonos, R., Ritter, H., & Sunyaev, R. 2008, A&A, 489, 1121
Reynolds, A. P., Owens, A., Kaper, L., Parmar, A. N., & Segreto, A. 1999, A&A, 349, 873
Ribó, M., Negueruela, I., Blay, P., Torrejón, J. M., & Reig, P. 2006, A&A, 449, 687
Ricci, C., Ueda, Y., Paltani, S., et al. 2014, MNRAS, 441, 3622
Rivinius, T., Carciofi, A. C., & Martayan, C. 2013, A&A Rev., 21, 69
Robinson, E. L. 1976, ARA&A, 14, 119
Rodriguez, C. L., Morscher, M., Pattabiraman, B., et al. 2015, Physical Review Letters, 115, 051101
Rodriguez, J., Tomsick, J. A., & Chaty, S. 2009, A&A, 494, 417
Romano, P., Krimm, H. A., Palmer, D. M., et al. 2014, A&A, 562, A2
Rosati, P., Tozzi, P., Giacconi, R., et al. 2002, ApJ, 566, 667
Russeil, D. 2003, A&A, 397, 133
Rutledge, R. E., Bildsten, L., Brown, E. F., et al. 2007, ApJ, 658, 514
Sana, H., Rauw, G., Nazé, Y., Gosset, E., & Vreux, J.-M. 2006, MNRAS, 372, 661
Sana, H., de Mink, S. E., de Koter, A., et al. 2012, Science, 337, 444
Sanders, R. L., Shapley, A. E., Kriek, M., et al. 2015, ApJ, 799, 138
Sarma, A. P., Goss, W. M., Green, A. J., & Frail, D. A. 1997, ApJ, 483, 335
Sasaki, M., Suyama, T., Tanaka, T., & Yokoyama, S. 2016, Physical Review Letters, 117, 061101
Sazonov, S., Krivonos, R., Revnivtsev, M., Churazov, E., & Sunyaev, R. 2008, A&A, 482, 517
Sazonov, S., Revnivtsev, M., Gilfanov, M., Churazov, E., & Sunyaev, R. 2006, A&A, 450, 117
Scaringi, S., Bird, A. J., Norton, A. J., et al. 2010, MNRAS, 401, 2207
Schulz, N. S., Canizares, C., Huenemoerder, D., & Tibbets, K. 2003, ApJ, 595, 365

Schulz, N. S., Canizares, C. R., Huenemoerder, D., & Lee, J. C. 2000, ApJ, 545, L135
Seifina, E., Titarchuk, L., & Shaposhnikov, N. 2014, ApJ, 789, 57
—. 2016, ApJ, 821, 23
Sguera, V., Barlow, E. J., Bird, A. J., et al. 2005, A&A, 444, 221
Sguera, V., Bazzano, A., Bird, A. J., et al. 2006, ApJ, 646, 452
Shahbaz, T., Bandyopadhyay, R., Charles, P. A., & Naylor, T. 1996, MNRAS, 282, 977
Shakura, N., Postnov, K., Sidoli, L., & Paizis, A. 2014, MNRAS, 442, 2325
Shakura, N. I., Postnov, K. A., Kochetkova, A. Y., & Hjalmarsdotter, L. 2013, Physics Uspekhi, 56, 321
Shapley, A. E., Reddy, N. A., Kriek, M., et al. 2015, ApJ, 801, 88
Shivaei, I., Reddy, N. A., Shapley, A. E., et al. 2015, ApJ, 815, 98
Shtykovskiy, P., & Gilfanov, M. 2005, A&A, 431, 597
Skelton, R. E., Whitaker, K. E., Momcheva, I. G., et al. 2014, ApJS, 214, 24
Skinner, G. K., Bedford, D. K., Elsner, R. F., et al. 1982, Nature, 297, 568
Smith, N. 2014, ARA&A, 52, 487
Smith, N., & Brooks, K. J. 2007, MNRAS, 379, 1279
Smith, N., & Owocki, S. P. 2006, ApJ, 645, L45
Smith, R. K., Brickhouse, N. S., Liedahl, D. A., & Raymond, J. C. 2001, ApJ, 556, L91
Smith, R. K., Mushotzky, R., Mukai, K., et al. 2008, PASJ, 60, S43
Steidel, C. C., Rudie, G. C., Strom, A. L., et al. 2014, ApJ, 795, 165
Stern, D., Assef, R. J., Benford, D. J., et al. 2012, ApJ, 753, 30
Still, M., & Mukai, K. 2001, ApJ, 562, L71
Strassmeier, K. G., Hall, D. S., Fekel, F. C., & Scheck, M. 1993, A&AS, 100, 173
Strüder, L., Briel, U., Dennerl, K., et al. 2001, A&A, 365, L18
Sugizaki, M., Mitsuda, K., Kaneda, H., et al. 2001, ApJS, 134, 77
Sutherland, W., & Saunders, W. 1992, MNRAS, 259, 413
Szkody, P., Nishikida, K., Erb, D., et al. 2002, AJ, 123, 413
Szostek, A., & Zdziarski, A. A. 2008, MNRAS, 386, 593
Tanaka, Y. 1996, in Roentgenstrahlung from the Universe, ed. H. U. Zimmermann, J. Trümper, & H. Yorke, 85
Tendulkar, S. P., Fürst, F., Pottschmidt, K., et al. 2014, ApJ, 795, 154
Terrell, Jr., N. J. 1972, ApJ, 174, L35
The LIGO Scientific Collaboration, the Virgo Collaboration, Abbott, B. P., et al. 2016, ArXiv e-prints, arXiv:1606.04856 [gr-qc]
Thompson, C., Lyutikov, M., & Kulkarni, S. R. 2002, ApJ, 574, 332
Tomsick, J. A., Chaty, S., Rodriguez, J., Walter, R., & Kaaret, P. 2008, ApJ, 685, 1143
Tomsick, J. A., Chaty, S., Rodriguez, J., et al. 2009, ApJ, 694, 344
Tomsick, J. A., & Kaaret, P. 2000, ApJ, 537, 448
Tomsick, J. A., Gotthelf, E. V., Rahoui, F., et al. 2014a, ApJ, 785, 4
Tomsick, J. A., Nowak, M. A., Parker, M., et al. 2014b, ApJ, 780, 78
Torrejón, J. M., Kreykenbohm, I., Orr, A., Titarchuk, L., & Negueruela, I. 2004, A&A, 423, 301

Torrejón, J. M., Schulz, N. S., Nowak, M. A., & Kallman, T. R. 2010, ApJ, 715, 947
Townsley, L. K., Broos, P. S., Corcoran, M. F., et al. 2011, ApJS, 194, 1
Tozzi, P., Gilli, R., Mainieri, V., et al. 2006, A&A, 451, 457
Traulsen, I., Reinsch, K., Schwarz, R., et al. 2010, A&A, 516, A76
Tremonti, C. A., Heckman, T. M., Kauffmann, G., et al. 2004, ApJ, 613, 898
Tsygankov, S. S., Krivonos, R. A., & Lutovinov, A. A. 2012, MNRAS, 421, 2407
Türler, M., Chernyakova, M., Courvoisier, T. J.-L., et al. 2010, A&A, 512, A49
Turner, M. J. L., Abbey, A., Arnaud, M., et al. 2001, A&A, 365, L27
van de Sande, J., Kriek, M., Franx, M., et al. 2013, ApJ, 771, 85
van der Klis, M. 1989a, in NATO Advanced Science Institutes (ASI) Series C, Vol. 262, NATO Advanced Science Institutes (ASI) Series C, ed. H. Ögelman & E. P. J. van den Heuvel, 27
van der Klis, M. 1989b, in ESA Special Publication, Vol. 296, Two Topics in X-Ray Astronomy, Volume 1: X Ray Binaries. Volume 2: AGN and the X Ray Background, ed. J. Hunt & B. Battrick
van der Meer, A., Kaper, L., di Salvo, T., et al. 2005, A&A, 432, 999
Veilleux, S., & Osterbrock, D. E. 1987, ApJS, 63, 295
Verbunt, F., Bunk, W. H., Ritter, H., & Pfeffermann, E. 1997, A&A, 327, 602
Verner, D. A., Ferland, G. J., Korista, K. T., & Yakovlev, D. G. 1996a, ApJ, 465, 487
—. 1996b, ApJ, 465, 487
Vink, J. S., de Koter, A., & Lamers, H. J. G. L. M. 2001, A&A, 369, 574
Viotti, R. F., Antonelli, L. A., Rossi, C., & Rebecchi, S. 2004, A&A, 420, 527
Voss, R., & Ajello, M. 2010, ApJ, 721, 1843
Walter, R., Lutovinov, A. A., Bozzo, E., & Tsygankov, S. S. 2015, A&A Rev., 23, 2
Walter, R., Rodriguez, J., Foschini, L., et al. 2003, A&A, 411, L427
Walter, R., Zurita Heras, J., Bassani, L., et al. 2006, A&A, 453, 133
Walton, D. J., Fuerst, F., Harrison, F., et al. 2013, ApJ, 779, 148
Walton, D. J., Middleton, M. J., Rana, V., et al. 2015, ApJ, 806, 65
Wang, Q. D., Gotthelf, E. V., & Lang, C. C. 2002, Nature, 415, 148
Wang, W. 2013, MNRAS, 432, 954
Waters, L. B. F. M., & van Kerkwijk, M. H. 1989, A&A, 223, 196
Wegner, W. 2007, MNRAS, 374, 1549
Weisskopf, M. C., Brinkman, B., Canizares, C., et al. 2002, PASP, 114, 1
Weisskopf, M. C., Wu, K., Trimble, V., et al. 2007, ApJ, 657, 1026
White, N. E., Swank, J. H., & Holt, S. S. 1983, ApJ, 270, 711
Whittle, P. 1953, Ark. Mat., 2, 423
—. 1957, J R. Statistical Soc. B, 19, 38
Wik, D. R., Hornstrup, A., Molendi, S., et al. 2014, ApJ, 792, 48
Wilms, J., Allen, A., & McCray, R. 2000, ApJ, 542, 914
Wilson, T. L., Mezger, P. G., Gardner, F. F., & Milne, D. K. 1970, A&A, 6, 364
Winkler, C., Courvoisier, T. J.-L., Di Cocco, G., et al. 2003, A&A, 411, L1
Woods, P. M., Kouveliotou, C., van Paradijs, J., et al. 1999, ApJ, 519, L139

Worpel, H., Schwope, A. D., Granzer, T., et al. 2016, ArXiv e-prints, arXiv:1605.00927 [astro-ph.HE]
Wright, E. L., Eisenhardt, P. R. M., Mainzer, A. K., et al. 2010, AJ, 140, 1868
Wynn, G. 2008, in Astronomical Society of the Pacific Conference Series, Vol. 401, RS Ophiuchi (2006) and the Recurrent Nova Phenomenon, ed. A. Evans, M. F. Bode, T. J. O'Brien, & M. J. Darnley, 73
Xu, X.-j., Wang, Q. D., & Li, X.-D. 2016, ApJ, 818, 136
Xue, Y. Q., Luo, B., Brandt, W. N., et al. 2011, ApJS, 195, 10
Yamamoto, T., Mihara, T., Sugizaki, M., et al. 2014, PASJ, 66, 59
Yuasa, T., Makishima, K., & Nakazawa, K. 2012, ApJ, 753, 129
Zampieri, L., & Roberts, T. P. 2009, MNRAS, 400, 677
Zdziarski, A. A. 2000, in IAU Symposium, Vol. 195, Highly Energetic Physical Processes and Mechanisms for Emission from Astrophysical Plasmas, ed. P. C. H. Martens, S. Tsuruta, & M. A. Weber, 153
Zdziarski, A. A., Segreto, A., & Pooley, G. G. 2016, MNRAS, 456, 775
Zhang, S. N., Yu, W., & Zhang, W. 1998, ApJ, 494, L71
Zhekov, S. A., & Skinner, S. L. 2000, ApJ, 538, 808
Zickgraf, F.-J., Wolf, B., Stahl, O., Leitherer, C., & Klare, G. 1985, A&A, 143, 421
Zorotovic, M., Schreiber, M. R., & Gänsicke, B. T. 2011, A&A, 536, A42
Zuo, Z.-Y., & Li, X.-D. 2014, MNRAS, 442, 1980

Appendix A

NARCS Catalog Tables

Below are detailed descriptions of the information provided in the Norma Arm Region *Chandra* Survey catalog, followed by the complete catalog tables. In these tables, when a value is presented along with its errors, the first column listed in the column range contains the value. In the case of symmetric errors, the second column contains the error. In the case of asymmetric errors, the second column contains the upper error and the third column contains the lower error.

A.1 Detection and Localization Table

(1) NARCS catalog source number.
(2) *Chandra* source name.
(3) Observation(s) in which `wavdetect` detects the source. The format of ObsID numbers is 125XX, where the last two digits are those provided in the catalog. See §2.2.3 for details about `wavdetect` usage.
(4–5) Right ascension and declination (J2000.0) of the source. If the source is detected in multiple observations, the position reported is the weighted average of its positions in different observations.
(6) Positional uncertainty of the source. For a source detected in a given observation, this uncertainty is equal to the quadrature sum of the 95% statistical uncertainty based on Equation 5 of Hong et al. (2005) and the average systematic uncertainty of positions in that observation after astrometric refinement (see Column 5 in Table 2.2). For sources detected in multiple observations, the uncertainties associated with the source position in different obsevations were combined to provide the uncertainty of the weighted average of the source positions.
(7) Offset angular separation of the source from the center of the observation aim point. For sources detected in multiple observations, a semicolon-separated list of the offset angle of the source from each observation aim point is provided; the order of offsets matches the order of ObsIDs reported in Column 3.

(8–10) Significance of source in the full 0.5-10 keV band, the soft 0.5-2 keV band, and the hard 2-10 keV band. It is calculated by finding the probability that the source is a noise fluctuation using Equation 2.5 and using the Gaussian cumulative distribution function to determine the corresponding source significance. If the source is detected in multiple observations, the reported significance is the sum in quadrature of the source significance in individual observations.
(11) Radius of the aperture source region. For most sources, the aperture source region is defined as a circle with radius equal to the 90% ECF for 4.5 keV photons (see Column 12). For potentially extended sources, flagged with "e" (see Column 13), the radius is instead equal to the semi-major axis of the aperture region defined by `wavdetect`. In cases where two or more sources have overlapping circular regions, the regions are redefined as a circular core plus an annular pie sector following the guidelines in Table 2.6; in such cases, the radius provided in the catalog represents the outer radius of the pie sector. For sources detected in multiple observations, a semicolon-separated list of the aperture region radius used in different observations is provided; the order of radii matches the order of ObsIDs reported in Column 3.
(12) PSF radius for 90% ECF for 4.5 keV photons at the detector location of the source. The PSF radius varies with detector position, generally increasing with increasing offset angle from the observation aim point. For sources detected in multiple observations, a semicolon-separated list of the PSF radius at the source detector position in different observations is provided; the order of PSF radii matches the order of ObsIDs reported in Column 3.
(13) An alphabetical list of the possible flags:
"b" - "blended": Blended source that is unblended in another observation.
"c" - "created": Source noticed by eye but not detected by `wavdetect`. The source aperture region was created manually based on the visible position and extent of the source. The positional uncertainties calculated for such sources underestimate the true uncertainties, since the source is found by eye and not by `wavdetect`.
"e" - "extended": Possibly extended source. The semi-major axis of the smallest aperture region defined by `wavdetect` for such sources is larger than twice the PSF radius reported in Column (12). These sources are typically detected in images that have been binned by 4×4 or 8×8 pixels.
"id" - "inspected duplicate": Possible duplicate source flagged for manual inspection. A "duplicate" source refers to a single source detected in multiple overlapping observations; sources were considered to be duplicates of one another if the distance between them was smaller than the quadrature sum of their positional uncertainties. Sources were flagged for manual inspection if: a) they were separated by a distance greater than the quadrature sum of their positional uncertainties but smaller than the simple sum of their positional uncertainties, or b) they were separated by a distance smaller than the quadrature sum of their positional uncertainties but differed in a substantial way (e.g. one is flagged as possibly extended while another is not, one is found to have two duplicates by the distance criterion but these two duplicates of the first source are not found to be duplicates of one another by the distance criterion). Generally, if sources flagged with "id" showed consistent photon

fluxes and quantile parameters, they were determined to be true duplicates.
“m1", “m2", or “m3" - “modified": In cases where the circular source aperture region overlaps with the aperture region of another source, the source region is modified to reduce overlapping. See Table 2.6 for details.
“nb" - “near bright": Source near a very bright source which may be a spurious detection.
“nd" - “not detected": Source is located where at least two observations overlap but it is only detected in one observation.
“s" - “surrounding": A possibly extended source that completely surrounds one or more point sources. The aperture regions of the surrounded sources are excluded from the aperture region of the source flagged with “s".
“vl" - “variable long": Source determined to be variable on long (hours-days) timescales. The photon flux in at least one energy band (full, soft, or hard) varies by $\geq 3\sigma$ between different observations.
“vp" - “variable probable": Source is probably variable on short (second-hour) timescales. The K-S test finds the source lightcurve within a single observation to be inconsistent with a constant lightcurve at $\geq 95\%$ confidence.
“vs" - “variable short": Source is variable on short (second-hour) timescales. The K-S test finds the source lightcurve within a single observation to be inconsistent with a constant lightcurve at $\geq 3\sigma$ confidence.

For sources detected in multiple observations, a semicolon-separated list of the flags relevant for the source region in each observation is provided; the order of flags matches the order of ObsIDs reported in Column 3.

Table A.1: *Chandra* Catalog of Point and Extended Sources: Detection and Localization

No.	Source (CXOU J)	ObsID (125**)	R.A. (deg)	Dec. (deg)	Unc. (arcsec)	Offset (arcmin)	Sig. FB	Sig. SB	Sig. HB	Radius (arcsec)	PSF (arcsec)	Flags
(1)	(2)	(3)	(4)	(5)	(6)	(7)	(8)	(9)	(10)	(11)	(12)	(13)
1	163228.2-473755	33	248.117829	-47.632173	4.03	10.3	3.6	2.3	2.5	13.8	13.8	...
2	163241.5-474039	33	248.172944	-47.677522	1.79	9.5	9.0	10.4	2.5	11.9	11.9	...
3	163244.6-474133	33	248.186065	-47.692513	3.63	9.6	2.4	0.0	2.8	12.2	12.2	...
4	163248.7-473017	33	248.203151	-47.504857	1.41	7.9	8.4	1.2	8.5	9.2	9.2	...
5	163251.0-474135	33	248.212798	-47.693198	3.16	8.9	3.0	5.0	0.0	10.7	10.7	...
6	163253.0-474201	33	248.221111	-47.700286	2.26	9.0	5.2	1.8	4.8	10.9	10.9	...
7	163259.0-473819	33	248.246176	-47.638806	1.13	5.7	7.5	7.2	4.1	5.2	5.2	...
8	163259.4-472804	33	248.247582	-47.467941	3.39	8.3	2.3	3.4	0.4	10.1	10.1	...
9	163303.2-472547	33	248.263337	-47.429724	13.98	10.0	0.0	0.8	0.0	14.0	14.0	...
10	163306.2-473239	33	248.276159	-47.544291	1.55	4.2	3.3	0.7	3.1	3.5	3.5	...
11	163308.1-474316	33	248.284072	-47.721337	3.92	8.8	2.5	1.4	1.9	10.5	10.5	...
12	163309.3-472957	33,30	248.288757	-47.499290	0.65	5.8;11.7	25.6	16.9	19.4	5.7;17.6	5.7;17.6	vs;...
13	163312.4-473322	33	248.301795	-47.556327	0.79	2.9	5.6	2.4	5.0	2.4	2.4	...
14	163313.9-473817	33	248.308169	-47.638068	0.80	3.9	2.4	1.4	1.8	10.2	3.3	e
15	163315.2-473215	33	248.313374	-47.537728	1.09	3.4	3.7	2.3	2.8	2.8	2.8	...
16	163315.5-473938	33	248.314750	-47.660642	1.50	5.0	4.4	0.0	4.6	4.2	4.2	...
17	163315.6-473727	33	248.315323	-47.624352	0.99	3.1	5.4	0.0	5.7	2.5	2.5	...
18	163315.7-474642	32	248.315681	-47.778491	13.44	11.2	0.0	0.0	0.0	16.4	16.4	...
19	163316.8-473632	33	248.320023	-47.609018	0.62	2.2	7.3	7.1	3.6	2.3	2.3	...
20	163316.9-473121	33,30	248.320450	-47.522675	0.86	4.0;11.0	7.8	8.3	2.0	3.4;15.7	3.4;15.7	...;vp
21	163317.1-474023	33	248.321563	-47.673061	0.77	5.6	15.9	18.4	1.6	5.1	5.1	...
22	163318.1-473444	33	248.325455	-47.579086	0.68	1.5	4.2	0.0	4.5	2.1	2.1	...
23	163319.5-473711	33	248.331526	-47.619894	1.01	2.5	4.9	0.0	5.1	2.4	2.4	...
24	163322.2-473624	33	248.342527	-47.606780	0.73	1.6	3.6	4.7	0.0	2.2	2.2	...
25	163322.6-473904	33	248.344210	-47.651117	1.21	4.1	4.2	6.1	0.0	3.4	3.4	...
26	163322.6-472659	30	248.344535	-47.449869	8.54	8.8	0.7	2.4	0.0	10.8	10.8	vp,nd
27	163323.0-472755	30	248.346189	-47.465502	8.73	8.9	2.5	3.2	0.7	10.9	10.9	nd
28	163323.2-473830	33	248.346712	-47.641881	0.90	3.5	5.5	4.1	3.8	3.0	3.0	...
29	163323.5-473848	33	248.348197	-47.646885	0.61	3.8	15.8	17.4	3.0	3.2	3.2	...
30	163323.8-472610	33	248.349562	-47.436341	4.69	8.8	1.7	1.4	1.1	11.4	11.4	nd
31	163325.0-473726	33	248.354177	-47.624065	0.74	2.4	5.0	5.7	1.4	2.4	2.4	...
32	163325.0-473138	33	248.354420	-47.527468	1.01	3.4	4.2	0.9	4.0	2.8	2.8	nd
33	163325.6-474838	32	248.356710	-47.810764	2.17	10.5	9.9	4.5	8.3	14.4	14.4	...
34	163326.1-473203	30	248.358832	-47.534286	4.83	10.1	2.6	2.1	1.6	13.3	13.3	...
35	163328.4-473902	33	248.368607	-47.650776	1.00	4.0	1.5	2.2	0.4	10.0	3.4	e
36	163328.5-473302	33	248.368761	-47.550832	0.80	2.0	4.3	0.0	4.5	2.1	2.1	...
37	163329.3-473026	33	248.372126	-47.507292	1.34	4.6	3.9	1.6	3.4	4.0	4.0	nd
38	163329.5-473332	33	248.373255	-47.559121	0.47	1.6	32.6	2.8	32.8	2.0	2.0	vs
39	163330.7-473726	33	248.378097	-47.624007	0.67	2.5	8.1	3.4	7.2	2.4	2.4	...
40	163330.8-472535	30	248.378422	-47.426572	0.84	7.5	23.4	10.9	20.7	8.0	8.0	...
41	163332.7-474204	33	248.386480	-47.701167	3.02	7.1	3.9	4.4	0.3	7.3	7.3	nd
42	163332.8-473152	30	248.386793	-47.531170	2.92	9.1	3.6	0.0	5.0	11.1	11.1	nd

Chandra Catalog: Detection and Localization (continued)

No.	Source (CXOU J)	ObsID (125**)	R.A. (deg)	Dec. (deg)	Unc. (arcsec)	Offset (arcmin)	Sig. FB	Sig. SB	Sig. HB	Radius (arcsec)	PSF (arcsec)	Flags
43	163332.8-473157	33	248.387054	-47.532697	0.69	3.2	8.6	0.0	9.0	2.7	2.7	nd
44	163335.1-472338	30	248.396347	-47.394103	5.64	7.2	2.5	2.8	1.0	7.7	7.7	m3
45	163335.6-472336	30	248.398348	-47.393364	4.67	7.1	4.3	4.3	2.1	7.6	7.6	m3
46	163335.6-473748	33	248.398416	-47.630193	0.65	3.2	10.5	4.9	9.2	2.7	2.7	...
47	163335.6-473011	30	248.398434	-47.503189	1.10	7.7	14.9	13.1	8.3	8.4	8.4	vs,nd
48	163335.9-474547	33	248.399978	-47.763324	3.50	10.9	4.2	3.4	1.7	15.3	15.3	...
49	163336.1-472224	30	248.400658	-47.373404	2.08	7.6	5.5	6.8	1.5	8.3	8.3	...
50	163336.7-473546	33	248.402928	-47.596240	0.78	1.9	4.1	1.4	3.8	2.2	2.2	...
51	163336.8-473107	33	248.403655	-47.518875	1.63	4.3	1.7	2.0	0.7	10.5	3.7	e,vp,nd
52	163337.4-472442	30	248.406225	-47.411937	1.04	6.5	11.6	5.5	10.2	6.5	6.5	...
53	163338.0-474827	32	248.408375	-47.807728	2.64	8.7	4.5	4.5	1.6	10.3	10.3	...
54	163338.6-473337	33	248.411209	-47.560326	0.63	2.5	7.7	3.4	6.8	2.3	2.3	...
55	163338.8-474718	32	248.411805	-47.788410	4.69	7.9	2.3	3.5	0.2	8.8	8.8	...
56	163338.8-474342	33	248.411952	-47.728370	10.70	8.9	1.9	1.4	1.3	10.7	10.7	nd
57	163340.1-474848	32	248.417261	-47.813455	2.24	8.6	5.6	1.4	4.7	10.2	10.2	vp
58	163341.0-472139	30	248.420843	-47.360872	2.50	7.3	4.2	0.0	4.5	7.9	7.9	...
59	163341.8-473402	33	248.424209	-47.567346	0.61	2.7	10.8	0.0	11.2	2.4	2.4	vs
60	163341.8-472422	30	248.424566	-47.406211	3.35	5.9	2.8	0.0	3.2	5.6	5.6	...
61	163341.9-472331	30	248.424658	-47.392126	2.30	6.2	2.8	0.0	3.5	6.1	6.1	...
62	163342.1-474525	32	248.425739	-47.756945	2.08	6.6	4.3	1.5	3.9	6.6	6.6	nd
63	163343.4-473435	33	248.431246	-47.576428	1.22	2.9	4.0	4.3	1.4	2.5	2.5	...
64	163343.9-473318	33	248.432959	-47.555140	1.20	3.4	3.7	4.8	0.1	2.9	2.9	nd
65	163344.8-473327	33	248.437025	-47.557691	1.01	3.5	3.7	4.8	0.2	2.9	2.9	nd
66	163345.3-474620	33	248.438830	-47.772349	17.55	11.8	2.3	0.3	0.1	17.5	17.5	m1
67	163345.9-474243	32	248.441496	-47.712078	1.20	5.6	2.2	0.0	2.6	5.1	5.1	nd
68	163346.6-474849	32	248.444337	-47.813698	1.85	7.8	5.4	5.4	2.7	8.6	8.6	...
69	163347.7-472257	30	248.448864	-47.382552	1.73	5.6	3.9	4.8	0.6	5.3	5.3	vp
70	163347.7-474536	32	248.449088	-47.760149	2.48	5.8	3.0	4.0	1.1	14.5	5.4	e,vs,nd
71	163348.5-474624	33	248.452249	-47.773433	18.14	12.0	2.5	0.2	2.3	18.1	18.1	m1
72	163350.9-474638	32	248.462212	-47.777293	0.63	5.8	29.0	1.5	29.8	5.5	5.5	...
73	163352.0-471815	30	248.467082	-47.304243	2.84	8.8	4.5	7.3	0.0	11.3	11.3	...
74	163352.3-471541	30	248.468020	-47.261394	8.78	11.2	1.3	0.0	1.5	17.3	17.3	...
75	163354.2-473655	33	248.475956	-47.615332	2.02	5.0	4.0	3.9	1.9	4.3	4.3	nd
76	163354.8-473700	32	248.478369	-47.616792	2.02	7.4	3.1	0.0	3.8	8.1	8.1	nd
77	163354.8-473403	33,32	248.478409	-47.567680	1.62	4.9;9.9	3.7	6.0	0.0	4.2;13.7	4.2;13.7	...;vp
78	163355.1-473804	32,33	248.479614	-47.634697	0.44	6.5;5.7	50.5	19.4	48.8	6.7;5.3	6.7;5.3	...;...
79	163355.7-472636	30	248.482210	-47.443440	0.82	3.3	2.1	0.9	1.8	15.2	2.7	e
80	163357.9-474251	32	248.491266	-47.714409	0.95	3.5	5.0	2.4	4.2	3.0	3.0	nd
81	163358.9-474214	33,32	248.495621	-47.704166	0.54	9.1;3.5	25.6	3.5	25.7	11.1;2.9	11.1;2.9	...;...
82	163358.9-472702	30	248.495681	-47.450716	0.88	2.8	4.7	6.8	0.0	2.4	2.4	...
83	163359.2-471646	30	248.497039	-47.279545	3.85	9.8	3.3	0.0	2.8	13.4	13.4	...
84	163402.1-473244	33	248.508766	-47.545663	2.44	6.4	4.1	0.0	4.3	6.5	6.5	nd
85	163402.1-472926	33	248.508776	-47.490734	3.43	8.2	2.6	0.2	2.7	9.8	9.8	...
86	163403.6-474505	32	248.515144	-47.751655	0.86	3.2	6.4	0.0	6.6	2.7	2.7	...

Chandra Catalog: Detection and Localization (continued)

No.	Source (CXOU J)	ObsID (125**)	R.A. (deg)	Dec. (deg)	Unc. (arcsec)	Offset (arcmin)	Sig. FB	Sig. SB	Sig. HB	Radius (arcsec)	PSF (arcsec)	Flags
87	163404.7-474318	32	248.519873	-47.721741	0.68	2.4	2.9	0.0	3.1	7.9	2.3	e
88	163404.8-473702	32,33,29	248.520218	-47.617321	1.48	6.6;6.8;10.8	6.8	7.9	2.9	6.9;6.9;15.4	6.9;6.9;15.4	...;...;...
89	163405.8-473054	30	248.524188	-47.515047	2.17	4.9	3.9	4.4	1.4	4.1	4.1	nd
90	163406.6-474500	32	248.527601	-47.750135	0.85	2.8	4.4	5.8	0.2	2.4	2.4	...
91	163407.5-475440	31	248.531593	-47.911312	16.47	11.2	0.0	0.0	2.0	16.5	16.5	...
92	163408.8-474400	32	248.536707	-47.733427	0.65	1.9	3.0	0.0	3.6	5.8	2.2	e
93	163410.2-474207	32	248.542662	-47.701981	0.72	1.8	3.9	0.0	4.2	2.1	2.1	...
94	163412.4-473719	29,33,32	248.552002	-47.622143	0.81	9.7;8.1;5.9	13.3	5.7	12.1	25.8;9.2;5.9	12.6;9.2;5.9	e,id;id;id
95	163413.3-474810	32	248.555428	-47.803024	1.24	5.1	5.5	7.0	0.3	4.4	4.4	...
96	163413.4-475113	32	248.556098	-47.853776	2.82	8.1	3.3	5.8	0.0	9.1	9.1	...
97	163415.7-471610	27	248.565728	-47.269673	2.98	8.1	3.4	0.9	3.3	9.3	9.3	...
98	163416.2-472715	30	248.567672	-47.454311	0.54	1.1	15.7	5.1	14.8	2.1	2.1	...
99	163416.7-472600	30	248.569595	-47.433510	1.00	0.4	6.1	6.9	1.2	2.0	2.0	...
100	163416.9-471817	27	248.570808	-47.304847	2.39	7.8	4.4	4.9	1.7	8.7	8.7	nd
101	163417.6-474913	32	248.573562	-47.820424	0.69	6.1	23.1	3.5	23.2	5.8	5.8	...
102	163417.8-471404	27	248.574498	-47.234531	6.34	8.3	2.4	1.2	1.9	9.9	9.9	...
103	163417.9-474557	32	248.574736	-47.765969	0.59	2.8	12.4	10.8	6.6	2.5	2.5	...
104	163418.1-473207	30	248.575820	-47.535330	2.81	5.9	2.8	4.6	0.0	5.6	5.6	nd
105	163418.3-472221	27	248.576275	-47.372604	3.68	9.0	4.2	2.9	2.0	11.0	11.0	nd
106	163419.9-472029	30	248.582997	-47.341440	3.72	5.8	1.9	4.4	0.0	5.6	5.6	nd
107	163420.6-472830	30	248.586042	-47.475114	0.87	2.5	4.4	0.0	4.6	2.4	2.4	...
108	163420.6-474201	32	248.586152	-47.700417	0.67	1.2	1.6	0.2	1.5	6.3	2.0	e
109	163421.4-474943	32	248.589483	-47.828881	3.73	6.6	1.6	3.5	0.0	6.5	6.5	...
110	163421.6-472713	30	248.590085	-47.453853	0.73	1.5	4.4	0.0	4.6	2.2	2.2	...
111	163421.7-472327	30	248.590825	-47.390917	0.83	3.0	5.7	5.1	3.1	2.5	2.5	nd
112	163422.3-474446	32	248.592956	-47.746248	0.71	1.7	4.6	2.6	3.7	2.2	2.2	...
113	163422.6-474318	32	248.594485	-47.721830	0.53	0.7	8.3	8.5	3.2	2.0	2.0	...
114	163422.7-471804	27	248.594927	-47.301223	2.45	6.8	3.2	0.2	3.3	7.0	7.0	...
115	163423.1-473621	30	248.596271	-47.606070	4.41	10.3	3.1	1.8	2.4	13.5	13.5	vp,nd
116	163423.4-473736	32	248.597555	-47.626878	1.55	5.6	5.3	4.7	3.1	5.4	5.4	m3,nd
117	163423.5-473742	32	248.598293	-47.628375	1.85	5.5	2.7	0.1	2.3	5.2	5.2	m3,nd
118	163425.4-473658	32,30	248.606247	-47.616154	1.47	6.3;10.9	7.1	4.5	5.9	6.5;15.3	6.5;15.3	...;...
119	163425.7-473743	29,32	248.607224	-47.628857	1.64	7.8;5.5	6.2	1.4	6.0	8.5;5.3	8.5;5.3	...;...
120	163426.3-473308	30	248.609978	-47.552246	4.48	7.2	0.6	2.4	0.0	7.4	7.4	nd
121	163426.6-471839	30	248.610909	-47.310947	3.30	7.8	3.4	3.4	1.6	9.1	9.1	nd
122	163426.7-472508	30	248.611515	-47.419009	0.88	2.3	3.7	2.6	2.6	2.3	2.3	...
123	163426.8-473346	29	248.612038	-47.562791	2.72	6.8	2.8	3.4	0.9	7.0	7.0	vp,nd
124	163426.9-474320	32	248.612215	-47.722327	0.77	1.4	4.5	4.4	1.8	2.1	2.1	...
125	163427.0-471837	27	248.612514	-47.310412	1.06	6.2	10.0	8.8	5.7	6.0	6.0	nd
126	163429.0-473215	29	248.621017	-47.537775	2.01	6.7	4.1	2.3	3.2	7.0	7.0	vp,nd
127	163430.6-471559	27	248.627812	-47.266529	1.12	5.6	7.2	0.2	7.4	5.2	5.2	...
128	163431.1-474740	32	248.629961	-47.794595	1.92	5.0	2.9	4.4	0.0	4.2	4.2	nd
129	163431.6-472254	30	248.631837	-47.381884	1.59	4.4	2.9	0.8	2.6	3.8	3.8	nd
130	163432.1-471305	27	248.633806	-47.218285	1.40	6.7	7.6	1.4	7.6	7.0	7.0	...

Chandra Catalog: Detection and Localization (continued)

No.	Source (CXOU J)	ObsID (125**)	R.A. (deg)	Dec. (deg)	Unc. (arcsec)	Offset (arcmin)	Sig. FB	Sig. SB	Sig. HB	Radius (arcsec)	PSF (arcsec)	Flags
131	163433.1-473312	29	248.638043	-47.553348	1.64	5.8	4.7	0.2	4.9	5.6	5.6	nd
132	163433.1-471931	27,30	248.638138	-47.325485	0.98	5.5;7.4	9.9	2.1	9.8	4.9;8.2	4.9;8.2	...;...
133	163433.5-472137	30,27	248.639984	-47.360321	2.03	5.6;6.5	3.8	5.7	0.0	5.3;6.4	5.3;6.4	...;...
134	163433.5-474346	32	248.639987	-47.729688	0.66	2.6	7.3	4.9	5.4	2.4	2.4	...
135	163433.8-475420	32	248.641237	-47.905598	5.65	11.5	2.0	0.3	2.0	16.8	16.8	nd
136	163434.1-472746	30,29	248.642136	-47.462875	1.07	3.6;8.6	4.7	1.4	4.4	3.1;10.6	3.1;10.6	...;...
137	163434.4-471317	27	248.643631	-47.221662	2.39	6.3	3.7	0.0	4.2	6.3	6.3	vp
138	163434.6-473224	30	248.644415	-47.540095	5.13	7.1	1.7	3.6	0.0	7.2	7.2	...
139	163434.7-471748	27	248.644724	-47.296690	0.75	4.8	13.1	0.0	13.7	4.0	4.0	...
140	163434.8-473552	32	248.645089	-47.597883	4.35	7.8	1.4	1.0	1.0	20.2	9.0	e,nd
141	163436.0-471832	27	248.650295	-47.308897	1.61	4.7	3.9	3.9	2.0	3.9	3.9	...
142	163436.4-474957	32	248.651682	-47.832557	2.27	7.4	4.2	0.6	4.5	7.7	7.7	vp
143	163437.2-472608	30	248.655262	-47.435561	1.14	3.8	3.0	0.9	2.7	7.5	3.2	e,nd
144	163438.4-470929	27	248.660211	-47.158329	2.83	8.9	4.8	1.7	4.4	11.4	11.4	...
145	163438.4-471701	27	248.660403	-47.283706	0.78	4.1	9.8	11.6	0.0	3.5	3.5	vp
146	163438.9-472157	30,27	248.662231	-47.365891	0.91	5.9;6.1	10.7	10.4	5.5	5.8;5.8	5.8;5.8	...;vp
147	163439.3-474953	31	248.663908	-47.831490	1.23	5.6	6.1	4.7	4.0	5.1	5.1	vp,nd
148	163439.3-472325	30	248.664049	-47.390472	2.44	5.0	1.8	1.4	1.1	4.4	4.4	nd
149	163440.4-471449	27	248.668508	-47.246996	1.02	4.6	2.5	0.7	2.3	14.0	3.9	e
150	163441.0-474349	32	248.670971	-47.730510	1.39	3.8	3.3	3.7	1.0	3.2	3.2	nd
151	163441.1-474145	29,32	248.671570	-47.695892	0.68	8.6;4.0	12.1	5.0	11.1	10.1;3.4	10.1;3.4	...;...
152	163441.4-474229	32	248.672521	-47.708161	0.67	3.8	11.8	13.0	2.7	3.3	3.3	vp
153	163441.8-473323	30,29	248.674484	-47.556644	0.91	8.5;4.4	8.4	1.6	8.4	10.0;3.7	10.0;3.7	...;...
154	163441.9-471955	27	248.674611	-47.332054	1.25	4.4	3.9	0.0	4.2	3.7	3.7	nd
155	163442.3-471916	27	248.676398	-47.321312	0.98	4.0	5.9	7.8	0.0	3.3	3.3	...
156	163442.6-474613	31	248.677875	-47.770489	2.45	7.0	2.5	0.0	2.9	7.5	7.5	vp,nd
157	163442.8-473134	29	248.678707	-47.526265	2.62	4.9	3.3	3.4	1.4	4.2	4.2	nd
158	163443.0-472603	29,30	248.679367	-47.434250	0.81	9.2;4.8	12.0	7.0	9.8	12.1;4.1	12.1;4.1	...;...
159	163443.3-471017	27	248.680660	-47.171444	1.46	7.8	8.6	9.7	2.2	9.1	9.1	vp
160	163443.8-473528	30,29	248.682541	-47.591179	0.64	10.5;4.1	14.5	9.4	11.2	14.1;3.4	14.1;3.4	...;...
161	163444.0-475653	31	248.683693	-47.948216	2.31	7.3	4.0	1.1	3.8	7.5	7.5	...
162	163444.1-473645	29	248.684160	-47.612747	1.33	4.6	4.3	4.0	2.1	3.8	3.8	nd
163	163444.4-474341	32	248.685311	-47.728176	1.16	4.3	3.6	1.8	3.0	3.7	3.7	nd
164	163444.9-473649	32,29	248.687210	-47.613873	0.90	7.7;4.5	7.9	0.0	8.2	8.8;3.8	8.8;3.8	...;...
165	163445.2-471218	27	248.688481	-47.205240	1.66	5.9	4.0	4.5	1.3	5.7	5.7	vs
166	163445.3-471627	27	248.688862	-47.274297	0.77	3.1	8.0	8.6	1.9	2.5	2.5	...
167	163445.4-472912	29,30	248.689529	-47.486683	1.09	6.3;6.0	8.6	10.1	3.6	6.4;5.7	6.4;5.7	...;...
168	163445.5-474125	32	248.689629	-47.690396	1.32	4.8	4.5	1.4	4.2	4.2	4.2	nd
169	163446.5-474921	31	248.693777	-47.822550	1.46	4.6	4.3	5.8	0.0	3.9	3.9	nd
170	163447.0-475031	32	248.696196	-47.842115	2.41	8.8	4.9	2.4	3.3	10.4	10.4	vs,nd
171	163447.2-472732	29	248.697027	-47.459048	6.08	7.6	2.8	0.4	2.8	8.5	8.5	nd
172	163447.8-473243	29	248.699522	-47.545481	1.20	3.6	6.1	0.8	6.5	10.0	3.0	e,s,id,nd
173	163447.8-473243	29	248.699522	-47.545481	1.20	3.6	3.3	2.1	3.0	3.0	3.0	id,m3,nd
174	163448.0-473246	29,30	248.700073	-47.546196	1.67	3.6;8.7	6.3	3.0	5.7	3.0;10.3	3.0;10.3	id,m3;id,m2

Chandra Catalog: Detection and Localization (continued)

No.	Source (CXOU J)	ObsID (125**)	R.A. (deg)	Dec. (deg)	Unc. (arcsec)	Offset (arcmin)	Sig. FB	Sig. SB	Sig. HB	Radius (arcsec)	PSF (arcsec)	Flags
175	163448.3-472119	30,27	248.701340	-47.355438	1.63	7.5;4.6	4.4	6.1	0.0	8.2;3.9	8.2;3.9	...;...
176	163448.5-473230	29,30	248.702225	-47.541721	0.83	3.6;8.6	8.3	6.5	5.7	3.0;10.0	3.0;10.0	id;id,m3
177	163448.8-473839	29	248.703698	-47.644425	0.69	5.3	18.8	14.4	12.3	4.7	4.7	vs,nd
178	163449.4-471944	27	248.705882	-47.328937	1.02	3.3	3.2	1.2	2.9	6.7	2.7	e
179	163450.0-474054	31	248.708623	-47.681912	14.21	11.0	1.8	2.0	0.9	16.6	16.6	nd
180	163450.3-471133	27	248.709848	-47.192699	1.80	6.2	4.1	3.5	2.5	6.3	6.3	nd
181	163450.3-474450	31	248.709999	-47.747339	5.78	7.4	2.9	4.0	0.9	8.1	8.1	nd
182	163450.4-472040	27	248.710232	-47.344661	1.19	3.9	4.1	6.2	0.0	3.3	3.3	nd
183	163450.5-474832	31,32	248.710632	-47.809032	0.71	4.5;7.6	12.4	4.6	11.3	3.8;8.1	3.8;8.1	...;...
184	163450.7-472047	27	248.711328	-47.346405	0.95	4.0	6.1	6.3	2.4	3.3	3.3	vp,nd
185	163450.7-473918	32	248.711634	-47.655077	1.61	6.6	4.6	3.2	3.2	6.9	6.9	nd
186	163450.7-474510	31	248.711665	-47.752955	2.27	7.0	4.0	4.7	1.2	7.6	7.6	...
187	163450.8-473712	32	248.711762	-47.620191	3.79	8.0	2.3	0.8	2.0	9.5	9.5	...
188	163450.9-474621	32,31	248.712219	-47.772636	1.33	6.3;6.0	5.9	8.4	0.0	6.1;5.9	6.1;5.9	...;...
189	163451.2-472320	30	248.713455	-47.388937	2.67	6.8	4.8	4.8	2.1	7.1	7.1	nd
190	163451.2-472818	30	248.713601	-47.471845	2.16	6.5	3.6	2.9	2.3	6.5	6.5	nd
191	163452.3-475207	31	248.718237	-47.868731	0.92	3.3	4.7	0.0	5.1	2.8	2.8	...
192	163452.9-475723	31	248.720758	-47.956473	6.69	6.9	0.2	0.0	0.6	6.9	6.9	...
193	163453.2-471240	27	248.721905	-47.211229	1.93	5.0	3.0	4.4	0.0	4.3	4.3	nd
194	163453.8-473318	29	248.724227	-47.555141	0.65	2.5	6.8	0.0	7.3	2.3	2.3	vp
195	163453.9-474009	29,32	248.724655	-47.669289	1.32	6.2;6.6	6.8	7.8	2.7	6.0;6.9	6.0;6.9	...;m1
196	163453.9-473425	29	248.724726	-47.573822	0.60	2.2	8.4	10.4	0.6	2.3	2.3	...
197	163454.1-471927	27	248.725808	-47.324234	0.70	2.5	6.8	3.4	5.8	2.4	2.4	...
198	163454.6-473609	29	248.727798	-47.602767	0.71	2.8	7.0	0.0	7.2	2.4	2.4	...
199	163454.8-474125	32,31	248.728363	-47.690353	1.97	6.3;10.3	3.7	4.8	0.0	6.3;14.6	6.3;14.6	...;...
200	163454.9-474003	32	248.729126	-47.667518	2.90	6.8	2.8	1.6	2.1	7.2	7.2	m3,nd
201	163455.4-474008	32,29	248.731110	-47.669125	1.84	6.8;6.1	5.3	4.0	3.9	7.2;5.8	7.2;5.8	m3;...
202	163455.8-473003	29	248.732527	-47.500928	1.71	4.7	3.2	4.8	0.0	4.1	4.1	nd
203	163455.9-471300	24,27	248.733185	-47.216732	0.94	10.3;4.5	7.5	8.4	0.4	13.9;3.9	13.9;3.9	m3;...
204	163456.1-475214	31	248.733804	-47.870668	0.89	2.8	4.1	3.7	2.3	2.4	2.4	...
205	163456.1-471909	27	248.733899	-47.319360	0.71	2.1	5.5	1.5	5.2	2.3	2.3	vs
206	163456.2-471223	24	248.734575	-47.206492	7.94	10.0	3.3	3.7	0.0	13.0	13.0	nd
207	163456.4-475738	31	248.735054	-47.960678	6.86	6.8	0.0	1.2	0.0	6.9	6.9	...
208	163456.6-471317	27,24	248.735992	-47.221573	0.77	4.2;10.3	9.7	0.0	10.2	3.6;13.8	3.6;13.8	...;m3
209	163457.3-471041	27	248.738826	-47.178080	5.59	6.7	2.6	4.0	0.0	7.2	7.2	nd
210	163457.7-472651	29	248.740759	-47.447638	5.44	7.6	1.8	2.4	0.5	8.7	8.7	nd
211	163457.8-471353	27	248.741118	-47.231419	0.89	3.6	6.2	6.1	2.6	3.0	3.0	nd
212	163458.0-473937	29	248.741791	-47.660290	1.76	5.5	4.9	4.2	3.0	4.9	4.9	nd
213	163459.8-473555	29	248.749259	-47.598617	0.74	2.0	4.3	0.0	4.5	2.2	2.2	...
214	163500.6-474356	29	248.752669	-47.732240	10.58	9.7	0.5	0.0	1.2	12.2	12.2	nd
215	163500.9-471947	27	248.754074	-47.329736	0.68	2.4	7.0	0.0	7.3	2.4	2.4	vp
216	163502.1-473757	29	248.759166	-47.632671	1.14	3.7	4.4	4.5	1.8	3.1	3.1	...
217	163503.5-474347	32	248.764734	-47.729759	3.28	7.5	2.5	3.1	0.5	8.2	8.2	nd
218	163503.6-471847	27	248.765164	-47.313282	0.74	1.4	4.0	4.1	1.8	2.2	2.2	...

Chandra Catalog: Detection and Localization (continued)

No.	Source (CXOU J)	ObsID (125**)	R.A. (deg)	Dec. (deg)	Unc. (arcsec)	Offset (arcmin)	Sig. FB	Sig. SB	Sig. HB	Radius (arcsec)	PSF (arcsec)	Flags
219	163504.0-475020	31	248.766731	-47.839006	0.73	1.6	4.4	0.0	4.7	2.1	2.1	...
220	163504.2-475132	31	248.767763	-47.859065	0.62	1.2	6.4	4.7	4.2	2.1	2.1	...
221	163504.3-480037	31	248.768263	-48.010496	10.11	9.4	2.3	2.1	1.4	11.7	11.7	...
222	163504.7-472422	26,27	248.769653	-47.406353	1.64	8.6;7.0	6.6	2.0	6.2	10.4;7.1	10.4;7.1	...;...
223	163505.5-471802	27	248.772978	-47.300809	0.65	0.8	4.5	1.5	4.1	2.1	2.1	vp
224	163506.3-475125	31	248.776270	-47.857024	0.71	0.9	3.6	4.6	0.0	2.1	2.1	...
225	163506.6-473236	29	248.777717	-47.543476	0.62	1.7	6.1	3.7	4.7	2.1	2.1	...
226	163507.2-471641	27	248.780381	-47.278114	0.52	1.0	16.8	18.4	2.7	2.0	2.0	...
227	163508.5-474519	28,31	248.785828	-47.755383	2.19	9.1;6.0	5.9	5.4	2.9	11.3;6.0	11.3;6.0	...;...
228	163509.6-473215	29	248.790216	-47.537651	0.81	2.1	0.7	3.1	0.0	6.8	2.1	e
229	163509.7-470616	24	248.790699	-47.104449	1.05	7.3	13.3	14.9	3.4	7.8	7.8	vp
230	163509.7-471933	27	248.790740	-47.326103	0.92	2.5	4.6	2.7	3.5	2.4	2.4	...
231	163510.3-471509	24	248.792937	-47.252514	10.54	9.5	2.8	2.4	1.9	12.0	12.0	...
232	163511.1-473547	29	248.796570	-47.596643	0.73	1.6	5.0	5.5	0.7	2.2	2.2	...
233	163511.9-472741	29	248.799762	-47.461410	1.67	6.7	1.4	1.4	0.7	16.1	7.1	e,nd
234	163512.1-473726	29	248.800540	-47.623991	0.85	3.2	6.2	3.2	5.1	2.7	2.7	...
235	163513.0-475625	31	248.804238	-47.940436	2.35	5.2	2.9	3.8	0.4	4.4	4.4	...
236	163513.7-474310	32	248.807296	-47.719579	6.12	9.2	2.1	0.1	2.2	11.8	11.8	nd
237	163514.5-473809	29	248.810689	-47.635919	1.33	4.0	3.9	4.5	1.0	3.4	3.4	...
238	163514.6-474702	31,28	248.810913	-47.784023	0.91	4.3;8.9	7.6	9.8	0.0	3.7;10.8	3.7;10.8	...;...
239	163515.1-472304	30,27,26	248.813293	-47.384453	0.89	10.7;6.1;7.1	12.0	0.0	12.7	15.4;5.8;7.6	15.4;5.8;7.6	...;...;...
240	163515.7-471914	27	248.815453	-47.320581	0.84	2.9	6.3	4.1	4.7	2.5	2.5	...
241	163515.9-471536	24	248.816471	-47.260079	9.45	9.2	0.5	2.5	0.0	11.3	11.3	nd
242	163517.2-471822	27	248.821811	-47.306236	0.67	2.6	2.4	2.1	1.3	13.1	2.4	e
243	163517.2-470426	24	248.822071	-47.073891	2.80	7.0	3.2	4.7	0.1	7.4	7.4	...
244	163517.3-474941	31	248.822173	-47.828062	0.74	1.9	0.4	1.1	0.0	15.3	2.1	e,s
245	163517.4-474940	31	248.822852	-47.827788	1.05	1.9	3.0	2.8	1.5	5.6	2.1	e
246	163517.8-471837	27	248.824264	-47.310353	0.77	2.8	6.3	1.0	6.4	2.5	2.5	...
247	163517.8-471342	27	248.824436	-47.228559	2.87	4.5	2.7	0.0	3.2	3.9	3.9	nd
248	163518.2-473208	29,26	248.825974	-47.535801	0.58	2.9;9.1	12.3	13.4	4.0	2.4;11.2	2.4;11.2	...;...
249	163518.3-474833	31,28	248.826324	-47.809277	0.62	3.0;9.3	11.2	4.0	10.5	2.5;11.5	2.5;11.5	...;...
250	163518.6-473945	29	248.827879	-47.662609	2.37	5.8	2.0	4.2	0.0	5.3	5.3	nd
251	163518.9-472724	26	248.828803	-47.456813	2.44	6.4	2.4	3.3	0.0	17.1	6.3	e,nd
252	163519.1-472231	26	248.829743	-47.375530	2.36	6.7	3.4	0.0	3.7	7.0	7.0	nd
253	163519.4-475139	31	248.831026	-47.861111	0.62	1.4	2.5	0.0	2.7	5.4	2.1	e
254	163519.7-471006	27	248.832140	-47.168354	8.25	7.8	0.7	2.4	0.0	9.1	9.1	...
255	163520.0-475109	31	248.833344	-47.852588	0.49	1.4	16.4	18.0	1.7	2.1	2.1	...
256	163520.1-471245	27	248.834038	-47.212543	1.65	5.5	4.7	1.1	4.6	5.2	5.2	vp,nd
257	163520.2-472625	27	248.834182	-47.440401	3.99	9.5	3.9	6.4	0.0	11.9	11.9	nd
258	163520.3-475152	31	248.834658	-47.864518	0.59	1.6	5.9	5.4	3.0	2.2	2.2	...
259	163520.4-472756	29	248.835396	-47.465612	2.51	6.8	3.8	1.1	3.6	7.2	7.2	nd
260	163520.5-472831	29,26	248.835434	-47.475475	1.48	6.2;6.6	5.6	6.5	2.2	6.3;6.6	6.3;6.6	...;...
261	163520.6-474147	29	248.835879	-47.696495	3.76	7.8	2.5	2.8	1.1	8.4	8.4	vs,nd
262	163520.6-474028	29,28	248.835907	-47.674667	2.18	6.6;6.9	3.9	5.7	0.0	6.5;7.2	6.5;7.2	...;...

Chandra Catalog: Detection and Localization (continued)

No.	Source (CXOU J)	ObsID (125**)	R.A. (deg)	Dec. (deg)	Unc. (arcsec)	Offset (arcmin)	Sig. FB	Sig. SB	Sig. HB	Radius (arcsec)	PSF (arcsec)	Flags
263	163520.6-472515	26	248.836005	-47.421007	2.07	5.8	4.3	1.3	4.0	5.5	5.5	nd
264	163520.8-473058	29	248.836910	-47.516156	1.58	4.1	3.7	3.6	1.8	8.0	3.5	e
265	163520.8-474326	31	248.837040	-47.724069	6.25	8.0	1.7	2.5	0.1	9.5	9.5	nd
266	163521.1-471744	27	248.838037	-47.295590	0.80	3.1	6.8	7.6	1.4	2.6	2.6	...
267	163521.4-475903	31	248.839542	-47.984336	4.43	8.0	2.5	3.7	0.2	8.7	8.7	...
268	163521.7-474940	31	248.840750	-47.827837	0.55	2.4	13.4	9.4	9.6	2.3	2.3	...
269	163521.8-471918	27,26	248.840836	-47.321758	0.65	3.8;8.3	14.0	15.8	3.3	3.2;10.1	3.2;10.1	...;...
270	163521.9-471337	24	248.841369	-47.227051	2.74	7.0	3.5	5.3	0.0	7.2	7.2	nd
271	163522.6-470209	24	248.844251	-47.035949	5.42	7.9	0.8	3.0	0.0	9.2	9.2	...
272	163522.6-473916	28	248.844429	-47.654563	2.92	7.0	4.3	4.5	2.0	7.4	7.4	nd
273	163523.2-472819	26	248.846763	-47.472132	1.51	6.1	5.1	3.5	3.7	5.8	5.8	nd
274	163523.8-474046	28,29	248.849213	-47.679508	1.50	6.3;7.0	6.6	8.2	1.4	6.2;7.1	6.2;7.1	...;...
275	163523.9-470624	24	248.849977	-47.106826	1.68	5.0	3.5	0.6	3.4	4.3	4.3	...
276	163524.1-472839	27	248.850442	-47.477674	17.79	11.9	1.5	0.3	1.4	17.8	17.8	nd
277	163524.2-472554	27	248.851187	-47.431727	7.67	9.3	0.0	2.9	0.0	11.4	11.4	nd
278	163524.4-470324	24	248.851988	-47.056787	1.17	6.8	9.1	10.7	1.9	7.1	7.1	...
279	163524.5-471117	27	248.852486	-47.188300	2.46	7.1	0.3	0.0	0.5	7.8	7.8	m3,nd
280	163524.6-471110	27	248.852885	-47.186386	7.93	7.2	2.7	0.0	3.2	7.9	7.9	m3,nd
281	163524.6-471455	27	248.852892	-47.248836	1.47	4.4	4.3	0.0	4.7	3.8	3.8	nd
282	163524.8-480231	31	248.853694	-48.041948	16.70	11.5	3.0	2.0	2.2	16.7	16.7	...
283	163525.3-475155	31	248.855625	-47.865385	0.88	2.4	4.2	5.0	0.5	2.3	2.3	...
284	163525.3-473734	28	248.855756	-47.626381	2.24	7.5	3.7	2.5	2.7	8.3	8.3	nd
285	163525.7-465856	24	248.857335	-46.982484	6.61	10.5	0.9	0.0	1.1	15.1	15.1	...
286	163525.7-475116	31	248.857381	-47.854721	0.63	2.4	8.1	10.1	0.0	2.3	2.3	...
287	163525.8-472937	29,26	248.857605	-47.493832	1.11	5.7;6.5	7.1	0.0	7.2	5.4;6.4	5.4;6.4	...;...
288	163525.9-473800	29,28	248.857971	-47.633415	1.25	4.8;7.2	7.5	9.9	0.0	4.1;7.8	4.1;7.8	...;...
289	163526.3-471138	27	248.859597	-47.194020	2.33	7.0	1.8	1.6	1.1	15.3	7.5	e,nd
290	163526.5-471424	27,24	248.860809	-47.240078	0.87	5.0;7.1	9.7	13.0	0.0	4.4;7.3	4.4;7.3	...;...
291	163526.7-474856	31	248.861662	-47.815771	0.72	3.5	8.2	8.4	3.2	2.9	2.9	nd
292	163527.0-471138	24	248.862592	-47.194074	1.51	5.1	4.5	2.4	3.7	4.3	4.3	nd
293	163527.2-470258	24	248.863401	-47.049563	3.18	6.8	2.1	3.7	0.0	7.2	7.2	...
294	163527.6-470012	24	248.865039	-47.003459	3.99	9.2	2.3	0.0	2.5	12.0	12.0	...
295	163527.7-475833	31	248.865592	-47.976043	2.17	7.8	5.4	6.9	1.0	8.3	8.3	...
296	163527.8-471314	27	248.865912	-47.220738	1.69	5.9	4.5	5.2	1.4	5.8	5.8	nd
297	163527.9-474715	31,28	248.866409	-47.787609	1.96	4.9;7.2	4.7	6.0	0.7	4.3;7.4	4.3;7.4	...;...
298	163528.7-475540	31	248.869851	-47.927861	1.32	5.3	5.3	6.6	0.8	4.6	4.6	...
299	163528.8-473946	29,28	248.870209	-47.662983	1.63	6.6;5.8	6.0	7.2	1.7	6.5;5.6	6.5;5.6	...;vp
300	163528.9-465804	24	248.870710	-46.967962	12.47	11.1	0.6	1.3	0.0	16.9	16.9	...
301	163529.3-470716	24	248.872395	-47.121299	3.20	3.8	3.1	1.2	2.7	3.2	3.2	...
302	163529.5-474457	28	248.872974	-47.749275	1.28	5.7	6.1	6.6	2.2	5.2	5.2	nd
303	163529.5-470723	24	248.872995	-47.123077	1.43	3.7	1.9	0.0	2.1	3.1	3.1	...
304	163529.6-471643	24,27,26	248.873459	-47.278755	0.66	8.9;4.6;9.7	17.9	18.7	5.8	10.7;4.0;13.2	10.7;4.0;13.2	vl;vs,vl;vl
305	163529.7-474559	31,28	248.874100	-47.766472	2.43	6.1;6.2	3.5	5.7	0.0	6.2;5.9	6.2;5.9	...;...
306	163529.9-473805	29,28	248.874756	-47.634724	1.15	5.4;6.6	5.6	5.8	3.2	12.6;6.9	4.8;6.9	e,id;id

Chandra Catalog: Detection and Localization (continued)

No.	Source (CXOU J)	ObsID (125**)	R.A. (deg)	Dec. (deg)	Unc. (arcsec)	Offset (arcmin)	Sig. FB	Sig. SB	Sig. HB	Radius (arcsec)	PSF (arcsec)	Flags
307	163530.8-473125	26	248.878374	-47.523702	3.29	7.2	2.2	0.0	2.6	7.4	7.4	m3,nd
308	163531.2-473120	26	248.880214	-47.522237	4.57	7.1	3.0	0.0	3.5	7.3	7.3	m3,nd
309	163531.3-473605	28	248.880583	-47.601512	4.47	7.9	2.5	4.1	0.0	9.3	9.3	nd
310	163531.4-475748	31	248.881211	-47.963364	3.39	7.3	3.0	4.5	0.0	7.6	7.6	...
311	163531.5-475821	31	248.881359	-47.972664	5.18	7.8	1.7	3.9	0.0	8.5	8.5	...
312	163532.0-475320	31	248.883626	-47.888998	1.53	4.0	4.8	6.7	0.0	3.4	3.4	...
313	163532.1-474636	31,28	248.884079	-47.776844	1.33	5.8;6.2	6.2	6.8	2.7	5.7;6.0	5.7;6.0	...;...
314	163532.6-471228	24,27	248.886154	-47.207813	0.97	5.0;7.1	10.1	0.0	10.2	4.2;7.6	4.2;7.6	...;...
315	163533.1-472130	26,27	248.888214	-47.358437	0.84	5.4;6.6	9.9	12.3	1.7	5.0;6.6	5.0;6.6	...;...
316	163533.7-474006	29	248.890706	-47.668361	3.38	7.3	2.3	0.0	3.0	7.6	7.6	nd
317	163534.0-471126	24	248.891845	-47.190634	1.53	4.0	3.1	4.3	0.0	3.4	3.4	...
318	163534.0-470315	21	248.892012	-47.054267	17.09	11.5	2.0	0.0	0.0	17.1	17.1	nd
319	163534.1-473933	29,28	248.892487	-47.659344	0.48	6.9;5.2	39.2	32.5	23.3	7.1;4.6	7.1;4.6	...;...
320	163534.4-473305	29	248.893579	-47.551465	2.14	4.8	5.2	5.3	2.4	4.1	4.1	nd
321	163534.4-475133	31	248.893586	-47.859381	0.77	3.9	8.9	6.0	6.7	3.3	3.3	vp
322	163534.7-470930	24	248.894763	-47.158511	0.66	2.8	9.7	10.4	2.4	2.4	2.4	vs
323	163535.3-474426	28	248.897172	-47.740670	1.14	4.6	5.3	5.2	2.5	3.9	3.9	...
324	163536.1-473509	29	248.900745	-47.586099	1.92	5.0	3.0	4.8	0.0	4.3	4.3	nd
325	163536.2-470548	24	248.901036	-47.096680	0.56	3.6	22.6	4.3	22.6	3.0	3.0	...
326	163536.5-470508	24	248.902466	-47.085781	1.60	4.1	3.3	4.5	0.0	3.5	3.5	...
327	163536.8-471631	27	248.903386	-47.275519	1.38	5.8	5.8	3.8	4.3	5.6	5.6	nd
328	163537.0-471516	27	248.904348	-47.254493	2.26	6.2	3.8	0.1	3.9	6.2	6.2	nd
329	163537.6-471802	27	248.906870	-47.300681	3.68	6.0	2.2	3.2	0.4	5.7	5.7	nd
330	163537.8-470709	24	248.907733	-47.119317	0.81	2.5	4.8	0.0	5.0	2.3	2.3	...
331	163538.6-470956	24	248.911122	-47.165679	0.80	2.5	4.2	0.0	4.5	2.3	2.3	...
332	163538.8-471829	26	248.911679	-47.308194	3.86	7.5	1.5	0.0	2.1	8.4	8.4	nd
333	163539.0-474123	29	248.912571	-47.689804	7.77	8.9	1.1	2.9	0.0	10.7	10.7	...
334	163540.0-475728	31	248.917024	-47.957961	3.48	7.8	2.8	3.3	0.8	8.5	8.5	...
335	163540.4-475043	31	248.918376	-47.845401	1.60	4.9	4.2	5.4	0.3	4.2	4.2	nd
336	163540.6-473759	25	248.919309	-47.633056	14.77	12.1	2.0	0.0	0.0	18.9	18.9	...
337	163540.8-473722	29	248.920107	-47.623010	2.08	6.5	3.7	5.5	0.4	6.4	6.4	vs,nd
338	163540.8-465922	24	248.920181	-46.989580	1.25	9.3	15.3	16.9	3.8	12.3	12.3	vs
339	163541.0-475228	31	248.920866	-47.874662	1.72	5.1	4.6	4.8	1.9	4.4	4.4	...
340	163542.0-473341	29	248.925256	-47.561424	1.95	5.9	3.4	4.6	0.6	5.7	5.7	nd
341	163542.5-473344	28	248.927090	-47.562443	3.48	9.1	3.7	2.7	1.3	12.0	12.0	nd
342	163542.7-470258	21	248.927946	-47.049453	7.78	10.0	0.4	0.0	0.5	13.1	13.1	nd
343	163543.1-475225	31	248.929763	-47.873644	3.28	5.4	0.9	3.0	0.0	4.9	4.9	...
344	163543.2-473411	26	248.930065	-47.569853	1.84	9.0	7.6	2.8	7.0	10.8	10.8	nd
345	163543.3-471204	27	248.930483	-47.201269	6.86	8.7	2.0	0.0	2.4	10.8	10.8	...
346	163543.3-474737	28,31	248.930573	-47.793663	0.69	5.9;6.5	16.2	19.0	2.2	5.5;6.7	5.5;6.7	...;...
347	163543.5-470853	24	248.931394	-47.148158	0.69	1.2	1.5	0.2	1.5	8.7	2.1	e
348	163543.9-470201	24	248.933139	-47.033619	2.55	6.6	3.0	2.2	1.9	6.9	6.9	vp,nd
349	163544.5-475003	28	248.935758	-47.834172	4.15	8.0	3.1	1.1	2.8	8.9	8.9	m1,nd
350	163545.0-470509	24	248.937876	-47.085994	1.24	3.5	3.0	0.0	3.3	2.9	2.9	...

Chandra Catalog: Detection and Localization (continued)

No.	Source (CXOU J)	ObsID (125**)	R.A. (deg)	Dec. (deg)	Unc. (arcsec)	Offset (arcmin)	Sig. FB	Sig. SB	Sig. HB	Radius (arcsec)	PSF (arcsec)	Flags
351	163545.3-470136	21	248.938850	-47.026846	4.19	9.2	2.3	0.0	0.3	24.4	11.5	e,id,nd
352	163545.3-470138	24	248.938959	-47.027435	1.96	6.9	4.7	2.5	3.8	7.5	7.5	id,nd
353	163545.4-471121	24	248.939366	-47.189312	0.96	3.0	3.4	5.0	0.0	2.5	2.5	...
354	163545.7-470400	24	248.940501	-47.066849	1.88	4.6	2.4	4.1	0.0	4.0	4.0	nd
355	163545.8-473731	29	248.941056	-47.625451	2.54	7.3	4.9	0.0	5.1	7.6	7.6	nd
356	163545.9-474537	28	248.941365	-47.760315	1.34	4.0	4.2	0.0	4.7	3.3	3.3	m1,nd
357	163546.0-475011	28	248.941862	-47.836579	3.73	8.1	2.9	4.4	0.2	9.1	9.1	m1,nd
358	163546.1-474754	31	248.942208	-47.798588	2.14	6.7	4.6	3.0	3.4	7.0	7.0	nd
359	163546.3-474540	28	248.943221	-47.761330	2.99	4.0	2.5	2.1	1.4	3.3	3.3	m1,nd
360	163546.5-470524	24	248.943868	-47.090137	0.86	3.2	5.4	4.3	3.5	2.6	2.6	...
361	163546.5-473732	28	248.944135	-47.625820	1.70	5.3	3.4	0.0	3.6	4.9	4.9	nd
362	163546.8-471440	24	248.945072	-47.244652	1.89	6.2	4.5	1.0	4.4	5.9	5.9	nd
363	163546.8-472744	26	248.945343	-47.462413	0.81	2.7	5.3	7.0	0.0	2.4	2.4	...
364	163546.8-471024	24	248.945351	-47.173446	0.89	2.0	3.5	4.9	0.0	2.2	2.2	...
365	163547.0-473739	28,25	248.946121	-47.627659	—	5.2;10.7	6.6	0.0	7.6	45.3;49.7	4.7;14.9	c,e,s,id;c,e,s,id
366	163547.0-474024	28	248.946153	-47.673458	1.12	2.9	0.2	1.3	0.0	2.4	2.4	...
367	163547.2-470622	24	248.946743	-47.106202	0.69	2.2	5.8	7.3	0.0	2.2	2.2	...
368	163547.3-473725	29	248.947211	-47.623705	2.63	7.5	4.5	1.2	4.2	7.9	7.9	nd
369	163547.4-473608	29,28	248.947739	-47.602360	1.14	7.0;6.6	8.4	9.3	3.7	7.3;7.0	7.3;7.0	...;...
370	163547.7-471401	24	248.949038	-47.233792	1.89	5.5	3.9	0.4	3.9	5.0	5.0	nd
371	163548.3-472128	26	248.951348	-47.358029	0.82	4.1	7.5	0.0	8.0	3.5	3.5	id,nd
372	163548.3-473649	29,28	248.951370	-47.613770	1.52	7.3;5.9	5.9	5.8	3.8	7.8;5.8	7.8;5.8	...;vp
373	163548.4-472132	23	248.951799	-47.358978	2.88	10.4	6.0	1.2	5.8	14.3	14.3	id,nd
374	163548.9-471918	26	248.953872	-47.321716	1.80	6.2	4.3	2.8	2.4	6.4	6.4	nd
375	163548.9-471950	27	248.954127	-47.330680	2.94	8.2	2.8	1.8	2.1	9.5	9.5	nd
376	163549.1-474117	28	248.954759	-47.688073	0.56	2.1	15.6	13.5	8.5	2.2	2.2	vs
377	163549.4-473429	25	248.955928	-47.574998	12.94	9.9	1.6	2.4	0.5	12.9	12.9	nd
378	163549.7-472205	26	248.957304	-47.368195	0.97	3.5	4.4	2.2	3.7	2.9	2.9	...
379	163550.0-472817	26	248.958358	-47.471413	0.87	2.9	4.6	6.6	0.0	2.5	2.5	...
380	163550.0-473654	28	248.958628	-47.615067	3.01	5.8	2.1	3.6	0.1	5.6	5.6	nd
381	163550.1-475306	31	248.958765	-47.885237	2.87	6.7	3.7	2.1	3.0	6.9	6.9	...
382	163550.1-474556	31	248.958938	-47.765741	7.10	8.4	1.4	2.1	0.0	10.2	10.2	...
383	163550.4-471319	24	248.960360	-47.222211	1.27	4.8	6.2	2.0	5.8	4.0	4.0	vp,nd
384	163550.8-473739	25	248.961949	-47.627749	2.54	10.4	5.9	4.1	4.5	14.2	14.2	nd
385	163551.0-471056	24	248.962814	-47.182270	0.78	2.4	4.6	1.3	4.3	2.4	2.4	...
386	163551.1-470010	24	248.963138	-47.002862	4.61	8.3	2.5	0.0	2.8	10.3	10.3	nd
387	163551.2-472300	26	248.963362	-47.383405	0.59	2.5	9.4	0.0	9.8	2.3	2.3	...
388	163551.2-465822	21	248.963527	-46.972788	6.99	8.1	2.5	3.0	1.0	9.3	9.3	...
389	163551.2-474346	28	248.963727	-47.729717	0.52	2.0	30.9	14.3	27.2	2.2	2.2	...
390	163551.3-471111	24	248.963864	-47.186524	0.81	2.7	2.6	2.9	1.0	6.1	2.4	e
391	163551.8-473523	29,25,28	248.965942	-47.589813	0.72	7.6;9.6;7.1	19.3	1.0	19.8	8.3;12.3;7.9	8.3;12.3;7.9	id;id;id
392	163552.1-473518	26	248.967298	-47.588480	4.20	9.9	4.1	0.8	3.9	12.6	12.6	nb,id,nd
393	163552.4-470812	24	248.968385	-47.136720	0.65	0.5	5.0	6.2	0.0	2.0	2.0	...
394	163553.0-474614	31,28	248.971069	-47.770710	0.75	8.6;4.0	12.2	11.3	6.7	10.6;3.3	10.6;3.3	vs,vl;vl

Chandra Catalog: Detection and Localization (continued)

No.	Source (CXOU J)	ObsID (125**)	R.A. (deg)	Dec. (deg)	Unc. (arcsec)	Offset (arcmin)	Sig. FB	Sig. SB	Sig. HB	Radius (arcsec)	PSF (arcsec)	Flags
395	163553.3-470525	24,21	248.972473	-47.090469	0.73	3.1;9.5	8.5	2.1	8.4	2.6;12.0	2.6;12.0	...;...
396	163553.5-470037	24,21	248.973007	-47.010311	0.83	7.9;7.6	17.0	4.7	16.4	9.3;8.3	9.3;8.3	...;...
397	163553.8-470338	24,21	248.974518	-47.060715	0.61	4.9;8.5	20.9	20.7	8.9	4.3;10.0	4.3;10.0	...;...
398	163553.9-473602	25	248.974647	-47.600664	3.75	9.4	3.2	3.3	1.9	11.9	11.9	nd
399	163554.2-471844	24	248.976091	-47.312461	4.40	10.2	1.8	0.8	1.6	13.5	13.5	nd
400	163554.3-465740	21	248.976254	-46.961325	5.48	7.7	2.5	4.1	0.2	8.5	8.5	...
401	163555.2-470436	24	248.980248	-47.076853	1.11	4.0	4.9	4.3	2.6	3.4	3.4	nd
402	163555.2-471904	26,23	248.980286	-47.317921	1.21	6.4;8.4	7.7	0.0	8.0	6.6;9.8	6.6;9.8	id,vp;id
403	163555.2-470316	21	248.980312	-47.054544	3.28	8.1	3.4	3.7	1.1	9.2	9.2	nd
404	163555.4-471907	23,26	248.980835	-47.318779	—	8.4;6.3	9.7	0.1	10.6	47.8;60.9	9.9;6.5	c,e,s,id;c,e,s,id
405	163555.5-470614	24	248.981554	-47.103890	0.72	2.4	6.5	2.4	6.0	2.3	2.3	...
406	163555.5-472656	26	248.981561	-47.449020	0.55	1.5	7.3	0.0	7.7	2.2	2.2	...
407	163555.5-470631	24	248.981631	-47.108814	0.62	2.2	8.2	8.9	1.7	2.2	2.2	...
408	163555.9-474120	28	248.983187	-47.688979	0.75	1.3	1.4	2.9	0.0	6.8	2.0	e
409	163555.9-474549	28	248.983260	-47.763819	0.87	3.5	6.3	0.8	6.4	2.9	2.9	...
410	163556.0-475134	31	248.983364	-47.859578	1.73	7.5	6.0	4.5	4.2	8.0	8.0	...
411	163556.0-475122	28	248.983637	-47.856387	4.95	9.0	3.0	0.0	3.2	10.8	10.8	nd
412	163557.6-472026	26	248.990173	-47.340774	1.38	5.0	4.4	0.5	4.4	4.5	4.5	nd
413	163558.9-474103	28	248.995696	-47.684201	0.70	1.4	4.5	5.3	0.6	2.0	2.0	...
414	163559.0-473131	25	248.996180	-47.525502	7.11	8.4	0.6	0.0	0.9	10.1	10.1	nd
415	163559.2-470517	21,24	248.996765	-47.088135	1.19	8.7;3.6	5.6	2.7	4.2	10.3;3.0	10.3;3.0	...;...
416	163600.0-475221	28	249.000365	-47.872755	7.41	9.9	0.8	0.0	0.7	12.8	12.8	nd
417	163601.2-474853	28	249.005345	-47.814953	1.32	6.5	7.4	2.7	6.8	6.3	6.3	vp,nd
418	163601.9-474556	28	249.007946	-47.765621	1.28	3.5	3.1	4.1	0.1	3.0	3.0	...
419	163601.9-470247	24,21	249.008301	-47.046520	1.27	6.1;6.9	7.3	9.8	1.5	6.1;7.0	6.1;7.0	...;...
420	163603.3-474416	28	249.014032	-47.737949	0.81	2.0	1.7	0.0	1.8	5.3	2.2	e
421	163603.3-470840	24	249.014058	-47.144614	0.67	2.2	6.2	1.2	6.0	2.3	2.3	...
422	163603.5-471955	26	249.014862	-47.332163	2.26	5.7	0.6	2.7	0.0	14.7	5.6	e,nd
423	163603.7-472136	26,23	249.015594	-47.360245	0.72	4.1;8.3	11.0	0.4	10.9	3.6;9.5	3.6;9.5	...;...
424	163604.5-472753	26	249.018932	-47.464775	0.75	2.9	7.4	0.0	7.7	2.5	2.5	...
425	163604.6-474458	28	249.019179	-47.749668	0.75	2.7	1.9	0.1	2.0	12.2	2.4	e
426	163604.7-471215	24	249.019610	-47.204174	1.36	4.4	3.9	0.9	3.7	3.7	3.7	nd
427	163604.8-465236	21	249.020372	-46.876798	4.09	9.0	3.8	1.1	3.5	11.6	11.6	m3
428	163604.9-465246	21	249.020698	-46.879614	4.72	8.9	1.6	0.0	2.3	11.3	11.3	m3
429	163605.2-465744	21	249.022027	-46.962464	3.29	5.9	3.2	0.0	3.4	5.6	5.6	...
430	163605.6-470841	24	249.023524	-47.144910	0.87	2.6	4.6	4.2	2.4	2.4	2.4	...
431	163605.8-473933	25	249.024206	-47.659346	5.53	9.3	1.1	0.1	1.1	11.5	11.5	m1,nd
432	163605.9-473953	25	249.024862	-47.664856	3.95	9.5	3.3	1.4	2.9	11.9	11.9	m1
433	163606.0-470709	24	249.025309	-47.119358	1.07	3.0	4.6	6.6	0.0	2.5	2.5	...
434	163606.1-474400	28	249.025770	-47.733458	0.62	1.9	8.7	9.3	1.8	2.2	2.2	...
435	163606.2-471050	24	249.026095	-47.180821	0.87	3.6	6.6	6.8	2.4	3.0	3.0	...
436	163606.5-470141	21	249.027234	-47.028315	1.79	5.7	1.4	0.5	1.2	12.6	5.3	e,nd
437	163607.0-471434	27,23,24	249.029282	-47.242996	0.89	11.2;6.4;6.7	12.2	7.1	10.2	16.8;6.4;6.7	16.8;6.4;6.7	id;id;id
438	163607.5-465637	21	249.031479	-46.943764	1.82	6.0	4.6	0.0	4.9	5.8	5.8	...

Chandra Catalog: Detection and Localization (continued)

No.	Source (CXOU J)	ObsID (125**)	R.A. (deg)	Dec. (deg)	Unc. (arcsec)	Offset (arcmin)	Sig. FB	Sig. SB	Sig. HB	Radius (arcsec)	PSF (arcsec)	Flags
439	163607.6-474025	28	249.031975	-47.673718	1.00	2.4	3.7	4.9	0.0	2.3	2.3	...
440	163607.6-474028	28	249.032037	-47.674533	0.68	2.4	0.0	0.0	0.0	21.8	2.3	e,s
441	163609.1-472628	26	249.038162	-47.441162	0.86	2.6	4.1	0.0	4.4	2.4	2.4	...
442	163609.3-470730	24	249.038913	-47.125135	0.87	3.4	3.1	0.0	3.9	8.1	2.8	e
443	163610.8-471923	23	249.045360	-47.323230	1.60	6.1	4.6	1.2	4.3	5.8	5.8	nd
444	163611.0-474136	28	249.046009	-47.693544	0.72	2.1	5.6	5.8	1.9	2.2	2.2	...
445	163611.2-473046	25	249.046703	-47.512862	2.31	6.7	3.6	2.2	2.8	7.0	7.0	nd
446	163611.2-472042	26	249.046836	-47.345126	2.04	5.5	2.7	0.8	2.5	15.6	5.2	e
447	163611.8-471509	24	249.049434	-47.252720	7.52	7.6	1.4	0.0	1.6	8.0	8.0	nd
448	163611.9-470224	24,21	249.049820	-47.040146	0.71	7.1;5.2	14.2	13.6	7.2	7.8;4.5	7.8;4.5	id;id
449	163612.1-465841	21	249.050499	-46.978256	1.37	4.5	3.9	2.7	2.7	3.8	3.8	...
450	163612.3-472611	26	249.051363	-47.436593	0.80	3.0	6.4	2.7	5.7	2.5	2.5	...
451	163613.1-464959	21	249.054887	-46.833102	15.39	10.5	0.0	0.0	0.0	15.4	15.4	...
452	163613.2-465749	21	249.055263	-46.963646	1.18	4.6	5.7	0.0	6.0	3.9	3.9	...
453	163613.5-473851	28	249.056430	-47.647664	1.01	4.3	3.1	0.7	2.9	3.7	3.7	nd
454	163614.2-465222	21	249.059258	-46.873031	1.97	8.3	6.3	1.1	6.3	10.1	10.1	...
455	163614.3-465955	21	249.059771	-46.998729	0.93	4.0	6.2	2.8	5.4	3.4	3.4	...
456	163614.3-475129	28	249.059879	-47.858321	4.60	9.4	2.9	3.7	0.8	11.7	11.7	...
457	163614.6-473531	25,28	249.061050	-47.592220	1.40	5.9;7.3	6.5	4.8	4.8	5.6;8.2	5.6;8.2	...;...
458	163614.7-465821	21	249.061330	-46.972505	1.31	4.2	5.0	5.2	1.7	3.5	3.5	...
459	163614.8-470803	24	249.061911	-47.134409	1.35	4.2	3.5	5.2	0.0	3.6	3.6	nd
460	163615.7-475154	28	249.065456	-47.865226	2.18	9.9	7.6	8.9	1.6	12.6	12.6	...
461	163616.5-473022	26	249.068973	-47.506192	1.55	6.1	3.9	2.5	2.9	5.9	5.9	nd
462	163616.5-470509	21,24	249.069122	-47.085850	1.57	6.6;5.6	4.6	5.1	1.1	6.5;5.3	6.5;5.3	...;...
463	163616.9-475353	28	249.070826	-47.898247	4.32	11.8	3.4	1.2	3.0	17.8	17.8	...
464	163617.1-472428	26	249.071510	-47.408041	0.97	3.9	5.1	5.6	1.7	3.3	3.3	...
465	163617.1-471815	23	249.071659	-47.304258	1.46	4.6	3.9	5.4	0.6	3.9	3.9	nd
466	163617.3-474425	28	249.072132	-47.740499	0.97	3.6	5.4	6.2	1.4	3.0	3.0	...
467	163617.6-473254	25,26	249.073669	-47.548595	1.03	5.1;8.4	8.2	10.8	0.5	4.4;9.6	4.4;9.6	...;...
468	163619.4-472103	26,23	249.080948	-47.350876	0.85	6.0;6.0	10.6	4.5	9.7	6.0;5.6	6.0;5.6	...;...
469	163619.7-471436	24,23	249.082169	-47.243401	0.80	7.8;4.4	9.6	12.3	1.2	8.6;3.7	8.6;3.7	...;...
470	163620.2-470808	24	249.084355	-47.135662	1.63	5.1	5.6	6.4	1.1	4.4	4.4	id,m3,nd
471	163620.2-471324	23,24	249.084564	-47.223553	2.02	5.0;7.1	5.2	6.3	1.4	4.3;7.3	4.3;7.3	...;...
472	163620.4-470807	23,21	249.085251	-47.135281	5.20	9.3;8.9	2.5	5.2	0.0	12.3;10.7	12.3;10.7	b,id;b,id
473	163620.5-470807	24	249.085575	-47.135492	0.75	5.1	15.3	15.5	6.4	4.5	4.5	id,m3,vp,nd
474	163620.6-465734	21	249.086115	-46.959658	1.02	3.6	4.5	5.8	0.9	3.0	3.0	...
475	163620.8-475342	28	249.086842	-47.895230	12.44	11.8	1.2	0.0	1.4	17.8	17.8	m3
476	163621.1-471113	24,23	249.087967	-47.187206	0.81	5.9;6.5	12.1	3.9	11.5	5.5;6.7	5.5;6.7	id;id
477	163621.2-470144	21	249.088737	-47.029152	0.83	3.5	6.4	7.4	1.2	2.9	2.9	...
478	163621.3-471433	24	249.088977	-47.242657	4.35	8.0	2.9	4.8	0.0	8.9	8.9	id,nd
479	163621.8-471430	23	249.090874	-47.241850	1.73	4.1	0.0	1.2	0.0	10.6	3.5	e,id,nd
480	163621.8-474611	28	249.091018	-47.769772	2.70	5.3	2.6	3.1	0.8	4.7	4.7	...
481	163621.8-475325	28	249.091110	-47.890331	11.78	11.6	2.6	0.1	2.8	17.2	17.2	m3
482	163622.1-465654	21	249.092393	-46.948527	1.43	3.8	3.9	4.9	0.9	3.2	3.2	...

Chandra Catalog: Detection and Localization (continued)

No.	Source (CXOU J)	ObsID (125**)	R.A. (deg)	Dec. (deg)	Unc. (arcsec)	Offset (arcmin)	Sig. FB	Sig. SB	Sig. HB	Radius (arcsec)	PSF (arcsec)	Flags
483	163622.4-473730	25,28	249.093369	-47.625271	1.13	5.8;6.2	7.2	0.0	7.7	5.4;6.3	5.4;6.3	...;...
484	163623.4-474041	28	249.097554	-47.678288	1.33	4.3	4.2	2.8	3.1	3.7	3.7	nd
485	163623.9-470135	21	249.099888	-47.026447	0.86	3.1	4.7	4.8	2.0	2.5	2.5	...
486	163624.2-464959	21	249.101086	-46.833152	5.39	9.9	1.9	0.0	2.5	13.7	13.7	...
487	163624.7-471727	23	249.103265	-47.290868	0.56	3.2	16.5	6.7	15.0	2.6	2.6	...
488	163625.6-474106	28	249.106871	-47.685159	0.96	4.6	7.5	4.4	6.0	3.9	3.9	vp
489	163625.6-472805	25	249.106995	-47.468085	3.21	6.6	1.7	4.0	0.0	6.9	6.9	nd
490	163625.9-473124	25,26	249.107956	-47.523335	0.87	4.2;7.9	8.1	10.2	1.0	3.6;8.8	3.6;8.8	id;id
491	163626.2-474232	28	249.109389	-47.709043	1.29	4.5	0.4	0.0	0.6	10.8	3.8	e,s,vp
492	163626.4-465523	18	249.110229	-46.923274	11.81	11.1	0.3	0.6	0.0	16.1	16.1	m2,nd
493	163626.5-474229	28	249.110554	-47.708314	1.12	4.5	5.6	5.6	2.7	3.9	3.9	vs
494	163627.2-465544	18	249.113405	-46.928903	15.33	11.1	0.8	0.2	0.7	16.1	16.1	m2,nd
495	163627.2-472949	26,25	249.113586	-47.496956	1.01	7.0;5.1	7.8	7.5	4.9	7.1;4.4	7.1;4.4	...;vs
496	163628.0-465725	21	249.116871	-46.957042	0.91	2.8	4.6	5.4	0.5	2.4	2.4	...
497	163628.2-473733	28	249.117586	-47.625840	7.29	6.8	2.8	2.5	1.6	7.3	7.3	m3,nd
498	163628.2-473745	28	249.117796	-47.629253	3.60	6.7	0.6	2.4	0.0	15.5	7.1	e,m1,nd
499	163628.2-471051	23,24	249.117798	-47.180847	1.84	6.2;6.9	4.4	5.6	1.2	6.4;7.0	6.4;7.0	...;...
500	163628.4-473536	25	249.118369	-47.593406	1.27	3.8	3.5	3.1	1.9	3.2	3.2	...
501	163628.5-474739	28	249.119074	-47.794400	4.17	7.1	2.4	3.4	0.4	7.4	7.4	...
502	163629.3-470001	21	249.122350	-47.000413	0.58	1.5	7.0	8.5	0.4	2.1	2.1	...
503	163629.4-465229	21	249.122516	-46.874782	1.70	7.3	6.6	0.6	6.7	8.1	8.1	...
504	163629.5-465640	18	249.123172	-46.944484	16.41	11.2	2.2	0.0	0.6	16.4	16.4	nd
505	163629.8-474100	28,25	249.124374	-47.683521	0.92	5.3;8.0	10.6	5.6	9.1	4.7;8.9	4.7;8.9	...;...
506	163629.9-465617	21	249.124844	-46.938122	0.85	3.6	6.0	7.4	0.0	3.0	3.0	nd
507	163630.5-473228	25,26	249.127136	-47.541134	0.59	3.1;9.2	12.5	13.7	4.0	2.5;11.4	2.5;11.4	...;m1
508	163631.0-473208	26	249.129248	-47.535741	1.89	9.0	7.0	0.9	7.1	11.0	11.0	m1,nd
509	163631.3-473212	25	249.130589	-47.536865	0.63	3.0	11.8	1.2	11.8	2.5	2.5	nd
510	163631.5-470929	24	249.131328	-47.158137	3.50	7.0	2.8	4.0	0.1	7.4	7.4	nd
511	163631.8-472028	23	249.132623	-47.341320	1.06	4.3	2.9	0.0	3.0	9.8	3.6	e
512	163632.3-474315	28	249.134878	-47.721085	1.64	5.6	3.0	2.1	2.2	14.0	5.1	e
513	163632.7-470205	21	249.136534	-47.034850	0.77	2.6	6.0	2.6	5.3	2.4	2.4	...
514	163632.9-473245	25	249.137320	-47.545932	0.72	2.6	5.9	0.0	6.0	2.3	2.3	...
515	163633.7-472124	26	249.140706	-47.356917	4.62	7.7	2.2	4.0	0.0	8.7	8.7	nd
516	163633.9-470239	21	249.141474	-47.044344	0.71	3.1	8.0	0.0	8.4	2.6	2.6	...
517	163634.7-465802	21	249.144975	-46.967383	0.76	1.7	3.7	3.5	1.7	2.0	2.0	...
518	163635.0-470808	23	249.145948	-47.135794	3.93	8.5	1.8	1.9	0.8	10.7	10.7	nd
519	163635.6-472625	25,26	249.148514	-47.440361	1.10	7.4;6.9	9.4	13.0	0.4	8.2;7.2	8.2;7.2	...;...
520	163636.1-471801	23	249.150650	-47.300402	0.58	1.8	7.3	0.0	7.8	2.2	2.2	...
521	163636.3-470853	24,23	249.151398	-47.148270	3.00	7.8;7.8	4.3	0.0	4.9	8.7;9.0	8.7;9.0	...;...
522	163636.6-471315	23	249.152850	-47.220914	1.66	3.5	2.5	0.0	2.7	2.9	2.9	...
523	163636.9-471314	23	249.154058	-47.220778	1.26	3.5	0.0	0.0	0.0	8.3	2.9	e,s
524	163637.0-470253	21	249.154225	-47.048259	0.83	3.3	6.5	0.7	6.8	2.7	2.7	...
525	163637.7-465436	21	249.157096	-46.910227	2.67	5.0	1.8	3.0	0.0	4.4	4.4	nd
526	163638.2-473510	25	249.159476	-47.586190	0.67	2.3	8.8	0.0	9.2	2.3	2.3	vp

Chandra Catalog: Detection and Localization (continued)

No.	Source (CXOU J)	ObsID (125**)	R.A. (deg)	Dec. (deg)	Unc. (arcsec)	Offset (arcmin)	Sig. FB	Sig. SB	Sig. HB	Radius (arcsec)	PSF (arcsec)	Flags
527	163638.3-473958	28,25	249.159592	-47.666115	1.43	6.9;6.6	6.9	0.3	7.2	7.4;6.5	7.4;6.5	vp;...
528	163638.6-470159	21	249.160882	-47.033262	0.70	2.4	5.7	6.6	0.5	2.3	2.3	...
529	163638.7-473922	28,25	249.161514	-47.656219	0.81	7.2;6.0	14.5	13.3	7.7	7.8;5.7	7.8;5.7	vl;vs,vl
530	163638.9-471957	23	249.162438	-47.332702	0.78	3.4	6.8	4.9	4.9	2.9	2.9	...
531	163639.8-473213	25	249.166200	-47.537069	0.65	1.9	7.6	0.0	8.0	2.1	2.1	...
532	163639.9-473709	25	249.166657	-47.619349	1.17	3.8	4.1	2.2	3.3	3.2	3.2	m2
533	163640.0-470051	21	249.166718	-47.014178	0.58	1.3	7.0	7.6	2.0	2.2	2.2	...
534	163640.3-473442	25	249.167941	-47.578410	0.65	1.7	5.9	5.3	3.3	2.2	2.2	vp
535	163640.3-473718	25	249.168249	-47.621908	0.86	4.0	2.1	0.6	1.9	7.5	3.3	e,m1,nd
536	163640.4-470151	21	249.168583	-47.030938	0.75	2.3	5.8	7.0	0.5	2.3	2.3	...
537	163640.5-471221	23	249.168751	-47.206049	1.25	4.2	3.8	0.9	3.6	3.7	3.7	nd
538	163640.8-472314	23,26	249.170105	-47.387436	1.55	6.7;8.1	5.0	5.0	2.9	6.6;9.5	6.6;9.5	...;...
539	163641.0-465343	21	249.171220	-46.895326	3.29	6.0	2.0	4.3	0.0	5.9	5.9	nd
540	163641.9-465008	18	249.174910	-46.835794	3.91	7.4	1.8	0.0	2.1	7.9	7.9	vp
541	163643.6-473027	25	249.182007	-47.507771	1.01	3.1	3.9	1.1	3.6	2.6	2.6	...
542	163643.8-470359	21	249.182758	-47.066428	1.37	4.5	4.7	2.8	3.7	3.7	3.7	...
543	163644.5-474516	28	249.185430	-47.754528	3.13	8.1	4.1	3.0	2.8	9.2	9.2	vp
544	163645.1-471932	23	249.187966	-47.325666	1.07	3.0	3.5	3.4	1.5	2.5	2.5	...
545	163645.6-471148	23,20	249.190353	-47.196743	1.11	4.8;8.6	6.6	8.7	0.9	4.2;10.1	4.2;10.1	...;...
546	163646.2-472903	25	249.192863	-47.484220	0.96	4.5	7.1	7.1	2.9	3.9	3.9	nd
547	163646.5-473540	25	249.193906	-47.594573	1.40	2.1	4.9	2.6	4.0	2.3	2.3	...
548	163646.6-472815	25,22	249.194183	-47.470863	1.00	5.3;9.0	8.8	4.5	7.2	4.8;11.0	4.8;11.0	...;...
549	163646.6-470506	24	249.194509	-47.085094	11.05	10.2	0.0	0.0	0.6	14.0	14.0	m3,nd
550	163646.8-474101	28	249.195165	-47.683744	5.01	8.0	1.8	3.8	0.0	9.3	9.3	...
551	163647.4-471430	23	249.197654	-47.241718	0.70	2.2	2.0	2.0	1.1	7.9	2.2	e
552	163647.4-465153	21,18	249.197906	-46.864754	1.42	7.9;6.5	6.3	9.0	0.0	9.3;6.6	9.3;6.6	...;...
553	163647.5-473427	25	249.198264	-47.574342	1.09	0.9	1.5	2.0	0.3	8.3	2.1	e
554	163648.0-470746	24	249.200298	-47.129608	11.77	9.8	1.3	2.6	0.0	13.0	13.0	nd
555	163648.1-470505	24	249.200819	-47.084723	14.67	10.4	0.3	0.0	0.8	14.7	14.7	m3,nd
556	163648.2-473033	25	249.201130	-47.509333	0.72	3.0	7.0	0.0	7.3	2.5	2.5	...
557	163648.6-470551	21	249.202893	-47.097613	3.10	6.5	2.1	4.1	0.0	6.3	6.3	nd
558	163649.0-470655	21	249.204257	-47.115403	5.18	7.5	2.2	4.2	0.0	7.8	7.8	m1,nd
559	163649.1-471815	23	249.204611	-47.304424	1.08	2.0	2.4	3.5	0.0	2.2	2.2	...
560	163649.2-465531	21	249.205179	-46.925382	1.25	4.6	3.1	2.6	1.8	4.0	4.0	nd
561	163649.2-465620	18	249.205386	-46.939100	2.80	8.3	3.0	0.0	3.2	9.6	9.6	...
562	163649.3-464559	18	249.205598	-46.766601	5.65	7.7	2.8	4.2	0.1	8.7	8.7	...
563	163650.1-474220	28	249.208953	-47.705563	4.25	8.5	2.0	0.1	2.1	10.2	10.2	...
564	163650.1-470705	20,24,21	249.209137	-47.118073	1.50	6.8;10.3;7.7	7.5	6.2	5.7	7.0;14.2;8.3	7.0;14.2;8.3	...;...;m1
565	163650.4-471840	23	249.210360	-47.311352	0.83	2.5	4.3	0.0	4.5	2.4	2.4	...
566	163650.5-472145	22	249.210506	-47.362508	4.22	8.1	2.1	0.8	1.9	9.4	9.4	nd
567	163651.0-473606	25	249.212682	-47.601834	0.76	2.6	5.3	0.0	5.5	2.4	2.4	...
568	163651.0-474317	28,25	249.212830	-47.721653	1.00	8.7;9.8	18.1	2.1	18.0	10.6;12.4	10.6;12.4	vl;vp,vl
569	163651.1-465231	21,18	249.213074	-46.875446	0.63	7.5;6.1	21.3	17.4	13.2	8.3;5.9	8.3;5.9	vl;vl
570	163651.8-471734	23	249.216019	-47.292793	0.68	1.8	5.6	2.9	4.7	2.2	2.2	vp

Chandra Catalog: Detection and Localization (continued)

No.	Source (CXOU J)	ObsID (125**)	R.A. (deg)	Dec. (deg)	Unc. (arcsec)	Offset (arcmin)	Sig. FB	Sig. SB	Sig. HB	Radius (arcsec)	PSF (arcsec)	Flags
571	163652.4-471845	23	249.218366	-47.312650	0.83	2.7	4.5	5.3	1.3	2.4	2.4	...
572	163653.7-465834	21	249.224115	-46.976374	0.90	2.9	3.9	1.0	3.7	2.5	2.5	...
573	163653.8-464713	18	249.224168	-46.787030	2.25	6.4	3.4	3.9	1.4	6.5	6.5	...
574	163654.6-473339	25	249.227590	-47.560849	0.54	1.2	8.0	8.8	2.0	2.1	2.1	vp
575	163654.9-470348	21,20	249.229004	-47.063496	0.83	5.1;7.1	10.8	0.0	11.6	4.3;7.6	4.3;7.6	...;...
576	163655.0-473803	25	249.229421	-47.634264	1.59	4.7	1.0	0.0	1.0	9.2	3.9	e
577	163655.3-473124	25	249.230449	-47.523351	0.79	2.5	1.9	0.0	2.0	12.0	2.3	e
578	163655.5-474232	28,25	249.231506	-47.709042	0.86	9.4;9.1	25.1	23.3	12.9	12.1;11.1	12.1;11.1	id,vl;id,vl
579	163655.7-470101	20	249.232172	-47.017178	6.00	8.9	0.6	0.0	1.0	11.3	11.3	nd
580	163655.8-472710	23	249.232836	-47.452968	8.59	10.8	3.2	0.0	2.4	15.0	15.0	nd
581	163655.9-472817	25	249.233147	-47.471543	1.49	5.4	0.9	1.1	0.3	17.1	5.1	e,nd
582	163656.3-470225	21	249.234786	-47.040387	1.65	4.2	3.9	4.2	1.4	3.5	3.5	nd
583	163656.9-471613	23	249.237315	-47.270424	0.75	2.4	3.3	0.0	3.5	6.9	2.3	e
584	163657.0-471612	23	249.237728	-47.270105	0.69	2.5	0.0	0.0	0.0	15.8	2.3	e,s
585	163657.1-464903	18	249.238205	-46.817655	2.13	5.0	3.7	0.0	4.2	4.4	4.4	...
586	163658.5-472643	22	249.244144	-47.445330	2.26	6.5	3.8	0.0	4.1	6.5	6.5	nd
587	163658.7-473146	25	249.244691	-47.529634	0.86	2.6	4.3	1.2	4.0	2.3	2.3	...
588	163658.8-471515	23	249.245217	-47.254394	0.68	3.0	3.7	0.8	3.6	18.9	2.5	e
589	163658.8-471826	22	249.245234	-47.307425	7.40	8.7	1.7	0.9	1.2	11.0	11.0	...
590	163659.3-471451	23	249.247267	-47.247702	0.93	3.3	5.3	7.1	0.0	2.8	2.8	nd
591	163659.5-465753	21	249.248068	-46.964894	1.29	4.1	3.7	5.8	0.0	3.5	3.5	nd
592	163659.9-470914	20	249.249783	-47.153889	1.67	5.4	2.4	4.0	0.1	12.6	4.8	e,nd
593	163700.1-471102	23,20	249.250763	-47.184090	1.23	6.3;6.1	7.6	10.2	0.6	6.5;5.8	6.5;5.8	vp;...
594	163700.3-470546	20	249.251289	-47.096265	3.18	5.4	2.5	3.7	0.0	4.9	4.9	...
595	163700.3-465705	18	249.251648	-46.951609	2.85	7.7	3.2	5.5	0.0	8.2	8.2	...
596	163701.2-473413	25	249.255123	-47.570413	0.75	2.4	6.1	2.7	5.3	2.3	2.3	...
597	163701.2-464141	18	249.255154	-46.694767	3.74	9.9	2.8	0.4	2.6	13.6	13.6	m3
598	163701.2-470854	20	249.255274	-47.148432	1.34	5.1	5.2	3.9	3.8	4.3	4.3	nd
599	163701.4-470338	21	249.256191	-47.060599	1.73	5.7	4.0	4.5	1.6	5.2	5.2	vp,nd
600	163702.0-473818	25	249.258718	-47.638436	2.01	5.4	3.3	2.6	2.1	4.7	4.7	...
601	163702.3-473149	25	249.259876	-47.530493	0.98	3.0	4.0	4.2	1.5	2.5	2.5	nd
602	163702.4-470223	20,21	249.260071	-47.039917	1.30	7.1;5.0	5.5	0.0	5.9	7.7;4.3	7.7;4.3	m3;...
603	163702.5-470052	20,21	249.260635	-47.014465	1.92	8.3;4.4	4.6	6.2	0.8	10.1;3.7	10.1;3.7	...;...
604	163702.6-464145	18	249.261055	-46.695998	4.80	9.7	1.8	0.0	2.6	13.3	13.3	m3
605	163702.8-465222	18	249.262062	-46.872998	1.16	4.2	5.3	3.6	3.9	3.5	3.5	...
606	163702.9-470223	20	249.262304	-47.039964	3.38	7.0	1.3	0.0	1.6	7.6	7.6	m3
607	163703.8-464940	18	249.266087	-46.827939	0.93	3.8	5.4	6.4	0.9	3.2	3.2	...
608	163704.8-464332	18	249.270109	-46.725586	3.24	7.9	3.1	4.0	0.8	9.4	9.4	...
609	163704.9-470757	20	249.270467	-47.132746	0.84	4.3	8.2	9.9	1.3	3.6	3.6	nd
610	163705.3-470759	21	249.272096	-47.133165	2.73	9.6	5.0	3.7	2.5	12.0	12.0	nd
611	163705.5-470753	20	249.273284	-47.131414	1.66	4.2	2.8	4.2	0.0	3.5	3.5	nd
612	163705.8-470158	20	249.274194	-47.032976	3.09	7.1	3.2	5.1	0.0	7.6	7.6	nd
613	163706.2-464725	18	249.275880	-46.790475	1.88	4.6	2.8	4.3	0.0	3.9	3.9	...
614	163706.4-470955	23	249.276711	-47.165521	4.69	7.8	1.9	1.9	0.7	9.0	9.0	...

Chandra Catalog: Detection and Localization (continued)

No.	Source (CXOU J)	ObsID (125**)	R.A. (deg)	Dec. (deg)	Unc. (arcsec)	Offset (arcmin)	Sig. FB	Sig. SB	Sig. HB	Radius (arcsec)	PSF (arcsec)	Flags
615	163707.0-464622	18	249.279497	-46.773041	1.63	5.3	3.6	2.8	2.3	4.8	4.8	...
616	163707.4-465109	18	249.281157	-46.852734	0.88	3.1	4.6	0.0	4.9	2.5	2.5	...
617	163708.0-473220	25	249.283610	-47.539112	1.52	3.7	2.3	3.8	0.0	3.1	3.1	nd
618	163708.4-472131	22	249.285281	-47.358848	1.18	5.5	7.1	6.3	4.2	5.1	5.1	nd
619	163709.2-465826	20	249.288553	-46.974158	4.90	9.9	3.6	1.6	2.0	13.7	13.7	nd
620	163709.7-473157	25	249.290588	-47.532603	0.68	4.1	11.4	0.9	11.6	3.5	3.5	nd
621	163709.8-473154	22	249.290930	-47.531671	1.89	8.4	6.6	1.0	6.6	9.7	9.7	nd
622	163710.5-470750	20	249.293756	-47.130579	0.55	3.3	24.2	25.8	5.4	2.8	2.8	...
623	163711.4-472455	22	249.297893	-47.415455	0.75	4.0	9.9	2.0	9.7	3.4	3.4	nd
624	163711.9-465248	18	249.299979	-46.880242	1.26	3.1	2.8	0.0	3.1	2.6	2.6	...
625	163712.0-472343	22	249.300385	-47.395506	1.54	4.0	3.3	4.0	0.9	3.4	3.4	nd
626	163712.1-465501	18,21	249.300781	-46.917007	1.54	4.9;7.5	5.3	0.0	5.4	4.1;8.2	4.1;8.2	...;...
627	163712.2-472442	23	249.301090	-47.411867	11.99	9.5	2.1	0.0	2.7	12.0	12.0	nd
628	163712.4-464834	18	249.301687	-46.809717	0.65	3.0	9.8	2.2	9.7	2.5	2.5	vs
629	163712.7-465627	18	249.302976	-46.940838	1.89	6.2	3.1	0.0	3.5	5.9	5.9	nd
630	163713.0-465627	18	249.304481	-46.940868	1.25	6.1	1.0	0.5	1.0	18.5	5.8	e,s,nd
631	163713.7-465506	18	249.307342	-46.918371	2.61	4.8	1.4	3.5	0.0	4.1	4.1	nd
632	163713.7-473358	25	249.307394	-47.566145	1.14	4.4	5.3	0.9	5.2	3.8	3.8	...
633	163713.8-464619	18	249.307869	-46.772086	1.63	4.8	3.4	1.6	2.9	4.1	4.1	nd
634	163713.8-465801	18	249.307915	-46.966977	3.47	7.6	2.0	1.4	1.4	8.0	8.0	nd
635	163713.9-464532	18	249.308280	-46.758922	2.40	5.5	2.3	3.7	0.0	5.2	5.2	...
636	163714.0-471407	22	249.308724	-47.235369	17.11	11.1	1.0	0.9	0.5	17.1	17.1	m2,nd
637	163714.1-465142	18	249.309124	-46.861866	0.78	2.1	4.8	0.0	5.0	2.3	2.3	...
638	163714.3-471429	20,23,22	249.309738	-47.241486	1.97	7.3;5.8;10.7	4.8	7.2	0.0	7.5;5.5;16.0	7.5;5.5;16.0	...;...;m2
639	163714.5-472924	22	249.310738	-47.490110	2.48	5.9	1.6	4.2	0.0	5.5	5.5	nd
640	163714.9-465444	21	249.312311	-46.912273	5.27	8.0	0.9	0.0	1.0	9.4	9.4	nd
641	163715.2-465157	18	249.313617	-46.865945	0.77	2.1	4.3	2.6	3.2	2.3	2.3	...
642	163716.3-464606	18	249.318267	-46.768400	2.12	4.8	2.8	2.4	1.5	4.2	4.2	nd
643	163717.6-470337	17	249.323705	-47.060458	16.73	11.3	0.9	0.0	1.1	16.7	16.7	nd
644	163717.8-465759	20	249.324281	-46.966619	7.67	9.9	0.0	0.0	0.6	13.7	13.7	nd
645	163717.9-471131	23,20	249.324814	-47.192127	1.39	7.8;4.4	5.5	0.6	5.6	9.0;3.6	9.0;3.6	id,vp;id
646	163718.0-470031	21,20	249.325363	-47.008713	1.95	6.9;7.5	4.9	6.5	1.0	7.2;8.4	7.2;8.4	...;...
647	163718.1-471330	20,23	249.325653	-47.225147	0.87	6.2;6.8	11.2	11.7	5.3	5.9;7.1	5.9;7.1	...;...
648	163718.1-472851	22	249.325829	-47.480887	2.21	5.1	2.7	0.0	3.1	4.3	4.3	nd
649	163718.8-471435	22	249.328429	-47.243168	14.32	10.4	0.0	0.0	0.2	15.2	15.2	nd
650	163718.9-464523	18	249.329004	-46.756537	1.18	5.4	6.0	4.4	4.2	5.0	5.0	nd
651	163720.0-471222	20	249.333643	-47.206324	1.78	5.0	3.0	0.0	3.4	4.2	4.2	nd
652	163720.1-472149	22	249.333919	-47.363876	1.30	3.8	4.1	0.9	3.9	3.2	3.2	nd
653	163720.5-472150	22	249.335667	-47.363922	0.95	3.8	0.0	0.0	0.3	13.5	3.2	e,s,vp,nd
654	163720.5-471027	20	249.335738	-47.174374	0.72	3.2	7.9	8.3	2.8	2.7	2.7	...
655	163720.8-464435	15,18	249.336838	-46.743080	1.09	9.2;6.1	10.8	11.6	4.0	11.6;6.2	11.6;6.2	vs,vl;vl
656	163721.2-472704	22	249.338562	-47.451140	1.02	3.4	4.3	3.3	2.8	2.8	2.8	...
657	163721.3-470657	20	249.339084	-47.116085	0.67	1.7	2.2	0.0	2.8	5.8	2.1	e
658	163722.0-472137	22	249.341687	-47.360533	1.01	3.8	5.4	0.0	5.9	3.2	3.2	nd

Chandra Catalog: Detection and Localization (continued)

No.	Source (CXOU J)	ObsID (125**)	R.A. (deg)	Dec. (deg)	Unc. (arcsec)	Offset (arcmin)	Sig. FB	Sig. SB	Sig. HB	Radius (arcsec)	PSF (arcsec)	Flags
659	163722.0-464551	15,18	249.342056	-46.764397	0.60	9.5;4.8	23.9	23.3	9.2	12.1;4.2	12.1;4.2	vl;vp,vl
660	163722.4-473517	25	249.343377	-47.588176	2.62	6.1	2.8	3.4	0.7	6.0	6.0	...
661	163722.4-471539	23	249.343701	-47.260964	1.92	6.8	5.1	5.7	1.9	7.1	7.1	nd
662	163722.8-472712	22	249.345355	-47.453543	0.76	3.3	7.2	8.1	2.0	2.8	2.8	...
663	163723.4-472436	22	249.347791	-47.410097	0.64	2.0	2.3	0.8	2.1	9.5	2.2	e
664	163723.5-470616	20	249.348035	-47.104536	0.64	1.8	3.2	0.0	3.6	4.6	2.1	e
665	163723.6-472903	22	249.348362	-47.484394	1.19	4.8	7.2	1.2	7.1	4.1	4.1	...
666	163724.5-470859	20	249.352437	-47.149762	0.63	1.6	6.5	7.0	1.7	2.2	2.2	...
667	163724.8-465323	18	249.353597	-46.889725	0.74	2.7	6.0	8.0	0.0	2.4	2.4	vp
668	163725.7-465917	17	249.357183	-46.988227	5.75	8.8	1.5	0.0	2.3	10.9	10.9	nd
669	163725.9-471733	22,19	249.358200	-47.292648	2.71	7.3;9.8	3.7	6.0	0.0	8.0;12.7	8.0;12.7	...;...
670	163726.1-465316	18	249.358856	-46.887780	0.82	2.6	5.0	0.0	5.3	2.4	2.4	...
671	163726.1-464022	15	249.358884	-46.673027	1.96	8.0	5.5	2.4	4.8	9.2	9.2	...
672	163726.2-470505	20	249.359497	-47.084772	1.09	2.7	3.7	4.5	0.5	2.3	2.3	nd
673	163726.4-465525	18	249.360090	-46.923873	1.14	4.8	5.6	4.3	3.9	4.0	4.0	...
674	163726.6-471816	19,22,23	249.361237	-47.304527	2.07	9.8;6.5;7.7	5.5	8.7	0.0	12.8;6.9;8.4	12.8;6.9;8.4	...;...;...
675	163726.8-471135	20	249.362032	-47.193065	0.67	3.9	12.6	12.9	5.0	3.3	3.3	vp
676	163727.3-472236	22	249.363808	-47.376944	0.75	2.4	5.2	6.6	0.3	2.3	2.3	...
677	163728.0-472143	22	249.366979	-47.362012	0.97	3.2	4.3	5.4	0.2	2.6	2.6	...
678	163729.3-464713	18,15	249.372177	-46.787117	0.73	3.5;9.1	9.4	9.0	4.3	3.0;11.2	3.0;11.2	...;...
679	163729.3-465446	18	249.372432	-46.913020	0.94	4.2	6.9	2.8	6.2	3.5	3.5	vs
680	163729.7-463750	15	249.373991	-46.630674	2.00	8.2	5.5	5.5	2.6	9.8	9.8	vs
681	163729.8-464518	18,15	249.374344	-46.755085	0.91	5.4;8.0	10.1	10.9	3.7	5.1;9.1	5.1;9.1	...;...
682	163730.2-464338	18	249.376054	-46.727378	3.56	7.1	0.6	0.4	0.3	7.7	7.7	m3,vp,nd
683	163730.5-465038	18	249.377233	-46.844040	0.73	0.9	3.1	4.8	0.0	2.1	2.1	...
684	163730.6-464336	18	249.377815	-46.726884	2.19	7.1	4.3	3.1	3.4	7.8	7.8	m3,nd
685	163730.8-472640	22	249.378661	-47.444469	0.76	2.2	3.1	1.8	2.4	7.3	2.3	e
686	163731.0-472329	22	249.379335	-47.391478	0.60	1.4	6.7	7.0	2.7	2.0	2.0	...
687	163731.0-470940	20	249.379451	-47.161335	0.82	2.0	3.4	4.2	1.0	4.6	2.2	e
688	163731.2-472102	22	249.380148	-47.350600	1.12	3.7	4.0	0.0	4.3	3.1	3.1	nd
689	163731.5-471639	19,22	249.381378	-47.277538	2.34	8.8;8.0	5.3	6.9	1.4	10.6;9.5	10.6;9.5	...;vp
690	163731.8-470021	17	249.382531	-47.005860	3.37	7.9	1.7	0.4	1.6	21.1	9.0	e,nd
691	163733.2-472746	22	249.388689	-47.462947	1.01	3.1	6.0	5.7	2.6	2.6	2.6	...
692	163733.7-465956	17	249.390762	-46.999130	7.80	7.5	3.3	4.9	0.4	8.1	8.1	nd
693	163733.8-472013	22	249.391094	-47.337213	1.04	4.4	6.0	1.9	5.6	3.8	3.8	nd
694	163734.1-464630	18,15	249.392120	-46.775036	0.72	4.4;8.0	15.0	14.6	6.5	3.9;9.0	3.9;9.0	...;vp
695	163734.1-464050	15	249.392419	-46.680763	2.31	6.6	3.0	4.4	0.0	6.7	6.7	vp
696	163735.3-465549	18	249.397298	-46.930379	1.59	5.4	4.6	5.2	1.4	4.8	4.8	nd
697	163735.4-465516	17,18	249.397568	-46.921337	1.52	7.9;4.9	4.6	6.1	0.0	9.2;4.1	9.2;4.1	...;...
698	163735.7-472043	22	249.398854	-47.345279	1.52	3.9	2.7	4.2	0.0	3.4	3.4	nd
699	163735.7-470621	20	249.398921	-47.106001	0.75	1.6	4.4	6.2	0.0	2.1	2.1	...
700	163735.7-465642	21	249.399089	-46.945176	14.35	10.3	0.0	0.0	0.0	14.4	14.4	m1,nd
701	163735.8-470226	20,17	249.399246	-47.040810	1.14	5.3;8.0	7.9	10.1	1.3	4.9;9.0	4.9;9.0	...;...
702	163736.4-465618	21	249.401942	-46.938389	13.82	10.5	0.0	0.0	0.2	15.0	15.0	m1,nd

Chandra Catalog: Detection and Localization (continued)

No.	Source (CXOU J)	ObsID (125**)	R.A. (deg)	Dec. (deg)	Unc. (arcsec)	Offset (arcmin)	Sig. FB	Sig. SB	Sig. HB	Radius (arcsec)	PSF (arcsec)	Flags
703	163736.9-472951	25,22	249.403824	-47.497723	0.92	9.1;5.2	10.5	13.8	0.0	11.7;4.5	11.7;4.5	...;...
704	163737.0-470349	20	249.404385	-47.063772	1.86	4.0	3.0	3.6	0.8	3.5	3.5	nd
705	163737.6-463347	15	249.406771	-46.563165	6.69	9.9	3.5	0.8	3.4	13.7	13.7	...
706	163738.2-470033	17	249.409513	-47.009175	2.52	6.9	3.0	0.0	3.5	7.1	7.1	nd
707	163738.5-465630	21	249.410607	-46.941761	4.38	10.8	3.4	1.9	2.7	15.8	15.8	m1,nd
708	163739.2-464937	18	249.413632	-46.827112	0.83	2.6	4.6	2.4	3.8	2.4	2.4	...
709	163739.3-464551	18	249.414119	-46.764418	2.20	5.4	2.0	0.0	2.5	5.0	5.0	nd
710	163739.4-465101	18	249.414300	-46.850540	1.19	2.5	2.4	3.5	0.0	2.4	2.4	...
711	163739.6-465722	21	249.415308	-46.956375	15.21	10.8	0.3	0.0	0.3	15.6	15.6	nd
712	163740.0-465029	18	249.416724	-46.841390	0.58	2.6	12.1	11.1	6.1	2.4	2.4	...
713	163740.9-473421	25	249.420720	-47.572752	2.81	9.0	3.5	0.0	4.0	11.3	11.3	nd
714	163741.0-472756	22	249.421226	-47.465631	1.22	3.4	3.3	4.8	0.0	2.9	2.9	...
715	163741.4-470104	18	249.422705	-47.017842	14.46	10.8	0.7	0.0	1.1	14.9	14.9	nd
716	163741.5-473424	22	249.423284	-47.573524	3.89	9.8	4.7	0.7	3.9	12.5	12.5	...
717	163742.2-465304	17,18	249.425873	-46.884514	1.07	8.3;3.8	5.8	5.1	3.5	10.0;3.2	10.0;3.2	...;vp
718	163742.5-463823	15	249.427087	-46.639750	2.70	6.1	2.5	3.3	0.4	6.0	6.0	...
719	163742.5-470241	20,17	249.427231	-47.044861	1.27	5.4;7.1	6.4	9.4	0.0	5.1;7.4	5.1;7.4	id;id,vp
720	163743.1-463716	15	249.429734	-46.621225	2.74	6.7	4.5	0.6	4.6	7.0	7.0	...
721	163743.1-465148	18	249.429737	-46.863536	1.08	3.3	4.1	5.2	0.1	2.8	2.8	nd
722	163743.5-472556	22	249.431570	-47.432367	0.89	1.9	2.5	3.6	0.0	5.1	2.2	e
723	163743.6-464515	15	249.431793	-46.754327	1.79	6.0	5.1	3.1	3.9	5.7	5.7	vs,nd
724	163743.9-472417	22	249.433015	-47.404786	0.59	1.5	7.8	4.7	6.2	2.1	2.1	...
725	163744.0-464128	15	249.433669	-46.691176	1.11	4.8	6.0	6.7	1.4	4.1	4.1	...
726	163744.2-472022	22	249.434274	-47.339520	1.31	4.5	3.9	0.5	3.9	4.0	4.0	nd
727	163744.2-472159	19	249.434458	-47.366411	4.12	9.0	1.9	3.3	0.2	11.0	11.0	...
728	163744.3-470324	17,20	249.434647	-47.056927	2.16	7.3;4.9	4.0	4.5	1.6	7.7;4.3	7.7;4.3	m3;...
729	163744.3-464922	18	249.434879	-46.822779	1.28	3.5	3.4	4.4	0.1	3.0	3.0	vp,nd
730	163744.6-470331	17	249.436239	-47.058720	3.87	7.4	2.7	4.9	0.0	7.7	7.7	m3
731	163744.9-471833	20	249.437133	-47.309435	15.89	11.2	0.0	0.0	0.0	15.9	15.9	nd
732	163745.0-465027	17	249.437819	-46.840933	9.04	9.9	0.9	3.5	0.0	13.7	13.7	nd
733	163745.3-465832	17	249.439124	-46.975801	2.35	5.5	2.8	1.7	2.0	5.0	5.0	nd
734	163745.4-463652	15	249.439572	-46.614596	1.73	6.7	5.4	5.7	2.2	7.0	7.0	...
735	163745.8-470125	17	249.441206	-47.023684	4.16	6.0	2.8	4.0	0.0	5.8	5.8	nd
736	163746.4-463824	15	249.443443	-46.640096	1.22	5.5	6.8	4.2	5.3	5.2	5.2	...
737	163746.6-464514	18	249.444310	-46.753991	2.55	6.6	2.3	0.0	2.8	6.9	6.9	nd
738	163746.6-465404	18,17	249.444366	-46.901249	0.83	5.0;7.0	11.3	5.5	9.9	4.2;7.5	4.2;7.5	...;...
739	163746.9-465721	17	249.445668	-46.956097	2.14	5.4	5.3	1.5	5.1	4.8	4.8	nd
740	163747.3-463648	15	249.447428	-46.613420	3.60	6.5	1.7	3.5	0.0	6.8	6.8	...
741	163747.5-465616	18	249.448220	-46.937864	3.95	6.8	2.4	3.7	0.0	6.8	6.8	nd
742	163747.9-464053	15	249.449674	-46.681503	1.36	4.2	4.5	3.5	2.9	3.6	3.6	...
743	163748.1-464813	18,15	249.450699	-46.803856	1.48	4.6;7.6	5.3	5.7	1.0	4.0;8.1	4.0;8.1	...;vp
744	163748.2-472220	19,22	249.451202	-47.372253	0.46	8.8;3.2	42.4	28.2	33.2	10.5;2.7	10.5;2.7	vl;vl
745	163748.3-465859	17	249.451403	-46.983181	1.49	5.0	4.2	0.0	4.5	4.2	4.2	vp,nd
746	163748.4-470646	20	249.451981	-47.112904	1.07	3.2	3.7	5.1	0.1	2.7	2.7	...

Chandra Catalog: Detection and Localization (continued)

No.	Source (CXOU J)	ObsID (125**)	R.A. (deg)	Dec. (deg)	Unc. (arcsec)	Offset (arcmin)	Sig. FB	Sig. SB	Sig. HB	Radius (arcsec)	PSF (arcsec)	Flags
747	163748.9-471429	19	249.453801	-47.241458	2.76	5.9	2.1	4.0	0.0	5.6	5.6	nd
748	163750.1-472046	22	249.459031	-47.346233	1.51	4.6	3.0	0.1	3.1	9.0	4.0	e,nd
749	163750.2-464430	15	249.459475	-46.741821	1.76	4.6	3.3	5.0	0.0	3.9	3.9	nd
750	163750.8-465545	18,17	249.461761	-46.929237	0.44	6.7;5.4	53.1	53.1	53.1	6.7;5.0	6.7;5.0	vs,vl;vs,vl
751	163751.6-472538	22	249.465083	-47.427435	1.43	2.9	2.2	3.7	0.0	2.5	2.5	...
752	163751.6-464735	18	249.465101	-46.793178	2.39	5.5	3.1	3.7	0.7	5.1	5.1	nd
753	163751.8-464029	15	249.465949	-46.674955	1.05	3.7	4.3	5.3	0.9	3.1	3.1	...
754	163752.7-473115	22	249.469893	-47.520855	1.67	7.2	6.3	2.9	5.5	7.5	7.5	...
755	163753.6-470102	20	249.473380	-47.017499	4.69	7.8	1.9	0.0	2.0	8.9	8.9	nd
756	163753.7-464950	18	249.473833	-46.830748	1.55	5.0	3.8	3.5	2.0	4.3	4.3	nd
757	163754.8-465504	17	249.478491	-46.917946	2.77	5.3	2.2	3.2	0.1	4.8	4.8	nd
758	163754.9-465012	15	249.478952	-46.836735	2.26	8.9	5.8	6.4	2.4	10.7	10.7	vs,nd
759	163755.0-471109	19	249.479291	-47.185955	2.05	6.5	4.0	3.4	2.5	6.8	6.8	nd
760	163755.4-464832	18	249.480872	-46.808899	2.49	5.6	2.6	4.1	0.0	5.3	5.3	nd
761	163755.6-464106	15	249.481943	-46.685029	0.71	2.9	7.6	8.9	1.4	2.4	2.4	vp
762	163755.6-464558	18,15	249.481964	-46.766232	1.22	7.0;5.1	6.3	7.5	1.3	7.5;4.3	7.5;4.3	...;...
763	163756.0-470457	20,17	249.483704	-47.082569	0.79	5.2;7.2	11.7	1.2	11.8	4.6;7.4	4.6;7.4	...;...
764	163756.4-471949	19,22	249.485321	-47.330547	0.54	6.0;6.0	26.7	29.1	6.0	5.7;6.0	5.7;6.0	vs;...
765	163756.5-473224	22	249.485733	-47.540121	2.87	8.6	3.3	3.9	1.1	10.0	10.0	...
766	163757.1-473419	22	249.488101	-47.572015	2.79	10.4	5.6	2.7	4.9	13.8	13.8	...
767	163757.2-471336	19	249.488411	-47.226784	1.56	4.8	4.0	0.0	4.4	4.1	4.1	nd
768	163757.9-463519	12	249.491271	-46.588877	11.05	10.7	2.6	3.8	0.1	14.9	14.9	nd
769	163758.0-470122	20	249.491850	-47.022954	4.83	7.9	1.7	1.1	1.2	9.2	9.2	nd
770	163758.1-463405	15	249.492252	-46.568078	2.77	8.0	3.4	1.6	2.8	9.6	9.6	vs,nd
771	163758.8-472052	22	249.495112	-47.347803	0.98	5.5	9.4	9.4	4.3	5.2	5.2	vp,nd
772	163758.8-463902	15	249.495151	-46.650558	0.90	3.5	6.0	5.8	2.7	3.0	3.0	...
773	163759.2-471232	19	249.496948	-47.208970	2.98	5.1	1.7	2.9	0.0	4.4	4.4	nd
774	163759.2-464338	15	249.497026	-46.727343	0.72	2.9	7.9	4.3	6.5	2.5	2.5	vp
775	163759.3-465824	18,17	249.497223	-46.973362	1.27	9.7;3.1	6.0	7.5	0.6	12.3;2.5	12.3;2.5	...;...
776	163800.2-470210	17,20	249.501068	-47.036343	1.08	4.5;7.5	7.8	9.7	1.8	3.8;8.4	3.8;8.4	...;...
777	163800.3-464228	15	249.501555	-46.708035	0.74	2.1	5.1	4.3	2.8	2.2	2.2	...
778	163800.8-464012	15	249.503678	-46.670149	0.51	2.5	29.1	3.4	29.1	2.3	2.3	...
779	163800.9-464956	18	249.504165	-46.832466	4.43	6.2	2.0	3.5	0.0	6.1	6.1	nd
780	163801.0-470301	17	249.504473	-47.050522	2.30	5.1	1.5	4.1	0.0	11.3	4.4	e,nd
781	163801.1-465347	17	249.504729	-46.896437	2.27	5.6	3.0	5.4	0.0	5.4	5.4	vp
782	163801.7-464605	15	249.507216	-46.768123	1.95	4.7	2.1	3.9	0.0	3.9	3.9	nd
783	163802.4-463657	15	249.510330	-46.615921	1.91	5.1	3.0	0.0	3.6	4.5	4.5	...
784	163802.6-471356	20	249.511021	-47.232454	1.13	8.3	15.4	0.0	15.8	9.6	9.6	b,id,nd
785	163802.6-465805	17	249.511107	-46.968087	1.15	2.6	2.8	4.0	0.0	2.3	2.3	nd
786	163802.6-471358	19	249.511123	-47.232890	0.59	3.8	21.6	1.1	21.9	3.2	3.2	id,nd
787	163802.6-471345	19	249.511135	-47.229360	—	3.9	8.8	0.4	9.1	9.3	3.3	c,e,nd
788	163802.9-472716	22	249.512265	-47.454496	1.79	5.4	3.5	3.7	1.4	4.8	4.8	...
789	163803.2-463859	15	249.513454	-46.649807	0.67	3.2	9.4	8.5	4.8	2.6	2.6	...
790	163803.2-464055	15	249.513529	-46.682163	0.72	1.7	4.6	5.3	0.5	2.1	2.1	...

Chandra Catalog: Detection and Localization (continued)

No.	Source (CXOU J)	ObsID (125**)	R.A. (deg)	Dec. (deg)	Unc. (arcsec)	Offset (arcmin)	Sig. FB	Sig. SB	Sig. HB	Radius (arcsec)	PSF (arcsec)	Flags
791	163803.9-464002	15	249.516541	-46.667486	0.72	2.2	5.3	6.8	0.0	2.2	2.2	...
792	163804.4-471002	19	249.518437	-47.167295	1.96	6.5	4.0	3.9	2.1	6.7	6.7	vp,nd
793	163804.4-471657	19	249.518440	-47.282618	1.11	3.3	3.9	3.5	2.1	2.8	2.8	...
794	163804.8-465117	17,18	249.520172	-46.854900	1.58	7.7;6.8	6.4	9.1	0.0	8.9;7.0	8.9;7.0	vp;...
795	163805.1-464328	15	249.521357	-46.724502	0.83	2.1	4.7	4.2	2.4	2.3	2.3	...
796	163805.6-470202	20	249.523499	-47.034056	6.99	8.3	2.2	0.0	2.7	10.0	10.0	...
797	163806.5-471255	19	249.527194	-47.215367	1.22	3.9	4.1	3.8	2.0	3.3	3.3	vs,nd
798	163807.4-465729	17	249.530972	-46.958205	0.87	2.1	4.3	4.4	1.6	2.2	2.2	...
799	163807.7-463716	15	249.532190	-46.621136	1.94	4.6	4.7	1.6	4.2	4.0	4.0	...
800	163807.9-470555	19	249.533294	-47.098821	14.19	10.1	1.1	0.7	0.8	14.2	14.2	nd
801	163808.3-471853	19	249.534759	-47.314779	1.15	4.0	4.3	5.7	0.0	3.3	3.3	...
802	163808.3-471208	19,16	249.534988	-47.202267	0.90	4.3;11.7	3.0	2.0	2.4	17.2;17.9	3.7;17.9	e,id;id
803	163808.6-473029	22	249.536076	-47.508332	2.82	8.1	3.9	0.0	4.2	9.2	9.2	...
804	163808.8-465532	17	249.536793	-46.925657	0.96	3.5	3.8	0.0	4.0	2.9	2.9	nd
805	163808.9-471022	20,19	249.537125	-47.173023	2.21	7.1;5.8	4.2	5.8	0.0	7.4;5.7	7.4;5.7	...;...
806	163808.9-471755	19	249.537469	-47.298804	0.98	3.2	4.6	3.5	3.0	2.7	2.7	vp
807	163809.0-470102	17	249.537835	-47.017357	0.71	2.7	14.2	14.3	5.1	2.4	2.4	...
808	163809.4-463838	15	249.539415	-46.643905	0.75	3.2	7.2	2.2	6.8	2.6	2.6	...
809	163809.5-472823	22	249.539797	-47.473067	2.31	6.9	2.2	0.6	2.0	22.4	7.1	e
810	163809.5-472921	22	249.539872	-47.489268	0.91	7.5	19.9	9.8	17.3	7.9	7.9	vp
811	163809.9-471857	22,19	249.541656	-47.315968	0.67	8.2;3.9	13.2	12.5	7.2	9.8;3.2	9.8;3.2	...;...
812	163810.3-472202	19	249.543246	-47.367426	2.31	6.7	3.7	0.0	4.1	6.6	6.6	nd
813	163810.5-464353	15	249.543865	-46.731537	0.74	2.1	4.6	1.0	4.5	2.3	2.3	...
814	163810.5-470108	17	249.544092	-47.019059	1.00	2.7	3.9	5.3	0.0	2.4	2.4	...
815	163810.6-470847	20,19	249.544434	-47.146526	1.49	7.0;7.2	6.7	3.8	5.8	7.3;8.0	7.3;8.0	...;...
816	163811.0-463544	15,12	249.545868	-46.595810	0.98	6.0;8.6	10.3	7.3	7.2	6.0;10.1	6.0;10.1	...;...
817	163811.0-463443	15	249.546047	-46.578880	2.51	7.0	3.4	2.1	2.5	7.7	7.7	nd
818	163811.0-464823	18,15	249.546112	-46.806614	1.32	8.2;6.6	7.7	10.4	0.4	9.6;6.6	9.6;6.6	...;...
819	163811.6-472400	22	249.548374	-47.400111	2.43	6.2	2.9	0.0	3.4	6.1	6.1	nd
820	163812.2-464115	15	249.550891	-46.687768	0.63	0.5	4.6	0.0	5.0	2.0	2.0	...
821	163812.4-464527	15	249.551989	-46.757510	0.76	3.7	8.5	10.0	1.7	3.1	3.1	nd
822	163813.9-470432	17,20	249.558151	-47.075821	2.61	5.9;8.1	3.7	5.6	0.2	5.5;9.5	5.5;9.5	...;...
823	163814.7-471633	19	249.561296	-47.276077	0.74	1.6	1.9	3.5	0.0	6.8	2.2	e
824	163814.7-465554	17	249.561329	-46.931789	1.10	2.8	2.6	4.3	0.0	6.2	2.4	e,nd
825	163814.9-465129	18,14	249.562332	-46.858173	1.87	8.5;8.6	6.9	0.7	6.6	10.2;10.3	10.2;10.3	...;...
826	163815.6-465413	17	249.565105	-46.903648	1.17	4.5	6.0	6.2	2.2	3.9	3.9	vs,nd
827	163816.0-471710	19	249.566975	-47.286171	0.70	1.8	4.7	4.2	2.5	2.2	2.2	...
828	163816.3-470241	17	249.568293	-47.044944	1.11	4.0	5.1	0.0	5.5	3.4	3.4	...
829	163816.8-472404	22	249.570090	-47.401372	2.65	7.1	3.5	3.3	1.7	7.5	7.5	...
830	163817.2-462900	12	249.571959	-46.483564	4.04	8.1	2.0	0.1	2.1	9.5	9.5	...
831	163817.5-472120	19,22	249.572937	-47.355598	1.72	5.7;7.9	4.8	7.8	0.0	5.2;9.1	5.2;9.1	...;...
832	163817.5-464529	15	249.572990	-46.758267	1.04	3.9	5.0	0.0	5.5	3.2	3.2	nd
833	163817.5-464124	15	249.573070	-46.690004	0.66	1.0	3.5	4.6	0.0	2.0	2.0	...
834	163817.8-464540	18	249.574564	-46.761245	10.09	10.3	3.2	1.6	2.7	14.5	14.5	nd

No.	Source (CXOU J)	ObsID (125**)	R.A. (deg)	Dec. (deg)	Unc. (arcsec)	Offset (arcmin)	Sig. FB	Sig. SB	Sig. HB	Radius (arcsec)	PSF (arcsec)	Flags
835	163817.9-471846	19	249.574604	-47.312896	0.90	3.2	5.3	6.4	1.2	2.6	2.6	...
836	163818.2-463228	12	249.575902	-46.541150	2.97	6.9	0.5	2.3	0.0	19.1	7.2	e,m1
837	163818.3-463556	12	249.576267	-46.599143	1.07	7.5	14.6	9.9	10.5	7.9	7.9	nd
838	163818.3-465602	17,14	249.576553	-46.933941	0.82	2.7;10.0	7.8	9.4	0.0	2.3;13.0	2.3;13.0	...;vp
839	163818.6-471809	19	249.577708	-47.302576	1.03	2.5	3.6	4.6	0.4	2.4	2.4	...
840	163818.8-465515	14	249.578629	-46.921024	3.98	9.5	2.6	2.1	1.8	12.0	12.0	nd
841	163819.5-470837	20,19	249.581436	-47.143707	2.07	8.4;7.1	4.3	6.1	0.4	10.0;7.8	10.0;7.8	...;...
842	163820.0-462740	12	249.583446	-46.461281	9.79	8.5	1.6	0.8	1.1	10.3	10.3	...
843	163820.4-471733	19	249.585067	-47.292530	0.88	1.9	3.2	3.8	0.7	2.2	2.2	...
844	163820.5-463225	12	249.585702	-46.540518	3.72	6.5	3.2	3.3	1.3	6.6	6.6	m2
845	163820.6-463851	15,12	249.585938	-46.647743	0.82	3.3;8.7	6.5	0.0	7.4	2.7;10.3	2.7;10.3	...;...
846	163820.7-471327	19	249.586362	-47.224281	0.58	2.3	11.8	12.1	3.9	2.2	2.2	vs,nd
847	163821.3-465140	14	249.589086	-46.861263	4.02	7.6	2.9	4.4	0.0	8.2	8.2	nd
848	163821.7-464013	15	249.590652	-46.670301	0.60	2.3	9.3	1.3	9.4	2.3	2.3	...
849	163822.0-471643	19	249.591668	-47.278861	0.75	1.0	4.2	3.0	2.9	2.1	2.1	...
850	163822.0-464902	15	249.591705	-46.817309	2.99	7.5	5.1	4.6	2.9	7.8	7.8	nd
851	163822.3-465420	17,14	249.593292	-46.905781	0.93	4.4;8.5	8.8	0.0	9.1	3.9;9.9	3.9;9.9	...;...
852	163822.6-464502	15	249.594403	-46.750817	1.38	3.8	2.9	4.6	0.0	3.2	3.2	nd
853	163823.0-464701	18	249.596142	-46.783883	5.56	10.6	0.5	1.9	0.0	15.1	15.1	nd
854	163823.2-464133	15	249.596807	-46.692746	0.54	1.9	13.4	1.2	13.7	2.2	2.2	...
855	163823.2-465339	17,14	249.597031	-46.894257	1.00	5.1;8.0	8.9	10.8	1.9	4.6;8.9	4.6;8.9	vp;...
856	163823.5-465146	14	249.598236	-46.862958	3.16	7.2	2.8	1.6	2.2	7.6	7.6	nd
857	163824.0-463411	15	249.600096	-46.569839	2.35	7.8	1.3	0.0	1.3	9.2	9.2	m3
858	163824.0-463422	15	249.600231	-46.573026	4.27	7.7	2.8	1.4	2.2	8.8	8.8	m3,nd
859	163824.3-463917	15	249.601315	-46.654831	0.77	3.3	7.3	4.0	6.0	2.7	2.7	...
860	163824.4-463621	15	249.601670	-46.606067	2.32	5.8	2.8	4.2	0.0	5.7	5.7	m3,nd
861	163824.6-462826	12	249.602690	-46.474087	3.91	7.4	3.4	3.9	1.1	8.0	8.0	vp
862	163824.6-465917	17	249.602733	-46.988083	0.83	1.4	4.5	6.0	0.0	2.2	2.2	...
863	163824.8-463623	15	249.603559	-46.606544	4.08	5.8	1.5	0.0	1.5	5.7	5.7	m3,nd
864	163824.8-463809	15,12	249.603653	-46.636051	1.19	4.2;7.7	6.0	7.2	1.2	3.6;8.3	3.6;8.3	...;...
865	163825.2-470134	17	249.605036	-47.026142	0.87	3.2	7.5	6.1	4.6	2.7	2.7	...
866	163825.9-470245	17	249.608061	-47.046040	1.36	4.3	4.0	0.7	3.9	3.6	3.6	...
867	163825.9-463030	12	249.608223	-46.508423	1.56	6.1	5.4	0.0	5.8	6.0	6.0	...
868	163826.2-465300	14	249.609215	-46.883581	2.63	7.3	3.2	3.2	1.6	7.6	7.6	nd
869	163826.2-472349	22,19	249.609375	-47.397045	2.42	8.6;8.1	5.5	6.7	1.9	10.5;9.1	10.5;9.1	...;...
870	163826.6-464049	15	249.611214	-46.680331	0.89	2.7	4.0	0.0	4.4	2.4	2.4	...
871	163826.7-470403	20	249.611640	-47.067501	13.54	10.3	0.0	0.4	0.0	14.4	14.4	nd
872	163826.8-465754	17	249.612054	-46.965013	0.76	1.8	6.3	7.8	0.5	2.2	2.2	...
873	163827.0-471839	19	249.612640	-47.311090	0.92	3.0	4.4	5.6	0.2	2.5	2.5	...
874	163827.3-464741	14	249.613990	-46.794787	1.58	6.6	6.2	5.7	3.2	6.8	6.8	m2,vp,nd
875	163827.4-463808	15	249.614379	-46.635597	1.46	4.5	3.2	1.5	2.6	3.9	3.9	vp,nd
876	163828.3-464756	14	249.618223	-46.799157	2.58	6.4	1.6	0.3	1.2	13.5	6.5	e,m1,nd
877	163829.1-472025	19	249.621267	-47.340516	1.72	4.8	3.0	4.4	0.0	4.1	4.1	...
878	163829.1-465431	17	249.621298	-46.908782	1.64	4.6	4.0	1.8	3.4	4.0	4.0	nd

Chandra Catalog: Detection and Localization (continued)

No.	Source (CXOU J)	ObsID (125**)	R.A. (deg)	Dec. (deg)	Unc. (arcsec)	Offset (arcmin)	Sig. FB	Sig. SB	Sig. HB	Radius (arcsec)	PSF (arcsec)	Flags
879	163830.5-471239	19	249.627499	-47.211084	0.91	3.3	4.0	0.0	4.3	2.8	2.8	nd
880	163831.6-470310	16	249.631865	-47.052879	5.91	7.4	2.4	3.5	0.0	8.1	8.1	nd
881	163832.2-470339	17,16	249.634186	-47.060890	0.58	5.6;7.1	30.4	14.6	26.6	5.0;7.6	5.0;7.6	...;...
882	163832.5-470651	17	249.635830	-47.114199	3.69	8.6	3.6	2.5	2.6	10.0	10.0	nd
883	163833.2-464406	15	249.638711	-46.735266	1.56	4.3	3.0	4.1	0.0	3.7	3.7	nd
884	163833.7-462934	12	249.640720	-46.492781	1.76	5.5	4.1	5.4	0.1	5.0	5.0	...
885	163833.8-464020	12,15,14	249.641037	-46.672382	0.84	8.5;4.0;10.8	9.2	4.7	8.2	9.8;3.4;16.0	9.8;3.4;16.0	...;...;m3
886	163834.3-463933	12	249.643184	-46.659252	3.21	7.7	2.8	2.4	1.6	8.3	8.3	nd
887	163834.6-464003	14	249.644517	-46.667653	12.01	10.9	0.0	0.0	0.0	16.6	16.6	m3,nd
888	163835.1-464104	12,15	249.646637	-46.684662	0.77	9.0;4.0	9.8	6.2	7.6	10.8;3.4	10.8;3.4	...;vp
889	163835.2-463731	15	249.646813	-46.625448	2.57	5.8	1.6	2.4	0.0	5.7	5.7	...
890	163835.4-464116	15	249.647816	-46.687802	0.94	4.1	6.3	5.3	3.7	3.5	3.5	nd
891	163835.6-464302	15,14	249.648407	-46.717327	1.54	4.2;8.3	4.0	4.4	1.3	3.6;10.1	3.6;10.1	...;...
892	163835.8-470617	16	249.649248	-47.104886	2.18	5.8	3.7	0.4	3.7	5.5	5.5	nd
893	163835.8-472145	22,19	249.649567	-47.362682	0.70	10.7;6.4	25.5	1.7	26.0	15.4;6.3	15.4;6.3	...;m1
894	163836.6-471542	19	249.652538	-47.261853	0.68	2.4	7.3	5.8	4.8	2.3	2.3	...
895	163836.6-464142	12	249.652594	-46.695249	8.69	9.5	2.0	0.9	1.6	11.8	11.8	nd
896	163836.9-472140	19	249.654070	-47.361362	3.49	6.4	2.5	3.6	0.1	6.3	6.3	m1,nd
897	163837.0-470938	16	249.654437	-47.160659	3.03	6.3	1.6	3.1	0.0	6.2	6.2	nd
898	163837.4-464114	15	249.656143	-46.687296	1.09	4.4	0.9	0.0	1.6	14.0	3.8	e,nd
899	163837.6-464726	15,14	249.656998	-46.790703	0.60	7.2;5.1	20.9	2.2	21.3	7.4;4.5	7.4;4.5	...;...
900	163837.7-463400	12	249.657107	-46.566775	1.14	3.7	5.3	0.6	5.6	3.1	3.1	...
901	163837.9-465213	15	249.658160	-46.870286	15.02	11.4	0.0	0.0	0.8	16.5	16.5	nd
902	163838.1-465830	17,16	249.658768	-46.975040	0.81	3.5;9.8	9.9	12.3	0.4	3.0;13.5	3.0;13.5	id;id
903	163838.4-470649	17,16	249.660156	-47.113831	1.19	8.9;5.3	6.6	0.0	7.0	10.6;4.8	10.6;4.8	...;...
904	163838.6-472623	19	249.661140	-47.439728	15.52	11.0	0.0	0.0	0.3	15.5	15.5	...
905	163838.7-465447	14	249.661398	-46.913102	3.33	6.6	1.6	3.9	0.0	6.6	6.6	nd
906	163839.2-470617	16,17	249.663422	-47.104843	0.71	5.2;8.4	16.2	13.7	9.7	4.6;9.7	4.6;9.7	...;...
907	163839.6-470341	17,16	249.665070	-47.061657	1.46	6.3;6.0	3.7	6.2	0.0	6.1;5.8	6.1;5.8	vp;...
908	163840.5-465253	14	249.668868	-46.881625	1.39	5.1	1.1	0.7	0.7	12.5	4.4	e,nd
909	163840.7-464352	14	249.669609	-46.731169	2.48	7.1	3.0	0.0	3.6	7.8	7.8	...
910	163840.9-471952	19	249.670821	-47.331357	0.87	5.2	10.9	11.4	3.7	4.5	4.5	vs
911	163842.2-463903	12	249.676023	-46.650988	2.87	6.6	3.0	2.8	0.1	14.7	6.6	e,nd
912	163842.3-465341	14,17	249.676254	-46.894829	1.71	5.4;6.6	4.4	6.0	0.2	4.8;6.9	4.8;6.9	...;...
913	163842.3-465159	17	249.676506	-46.866537	4.26	8.0	2.0	0.0	2.4	9.4	9.4	nd
914	163842.4-470429	16	249.676954	-47.074919	1.85	5.2	4.4	1.3	4.2	4.6	4.6	nd
915	163843.0-465400	17,14	249.679459	-46.900192	0.82	6.4;5.6	11.9	13.4	3.9	6.6;5.0	6.6;5.0	...;...
916	163843.5-465703	17	249.681487	-46.951098	1.47	4.8	4.5	5.6	1.1	4.1	4.1	nd
917	163843.6-472023	19	249.681983	-47.339998	5.52	5.9	4.7	1.5	4.3	5.5	5.5	...
918	163844.0-470915	17	249.683580	-47.154174	6.48	11.5	1.9	0.0	3.3	16.9	16.9	nd
919	163844.2-463310	12	249.684191	-46.552920	0.92	2.5	4.7	6.5	0.0	2.3	2.3	...
920	163844.2-465838	17	249.684340	-46.977324	1.20	4.6	1.2	1.5	0.5	17.5	3.9	e,nd
921	163845.2-472004	19	249.688462	-47.334456	2.70	5.8	4.0	4.0	2.0	5.4	5.4	...
922	163845.3-470652	16	249.688861	-47.114603	1.00	4.2	6.2	0.0	6.5	3.5	3.5	nd

Chandra Catalog: Detection and Localization (continued)

No.	Source (CXOU J)	ObsID (125**)	R.A. (deg)	Dec. (deg)	Unc. (arcsec)	Offset (arcmin)	Sig. FB	Sig. SB	Sig. HB	Radius (arcsec)	PSF (arcsec)	Flags
923	163845.3-464027	12	249.689089	-46.674336	2.13	7.8	3.7	1.7	2.0	18.3	8.3	e,nd
924	163845.4-464735	15,14	249.689270	-46.793320	0.78	8.2;3.9	8.9	7.1	5.8	9.2;3.3	9.2;3.3	...;...
925	163845.6-463100	12	249.690358	-46.516935	0.98	3.0	4.7	5.5	0.5	2.5	2.5	vp
926	163845.7-465248	17	249.690523	-46.880056	3.12	7.6	0.2	0.0	0.5	18.2	8.6	e,m1,nd
927	163846.1-465337	14	249.692469	-46.893658	1.80	4.9	3.9	2.4	2.9	9.8	4.2	e,nd
928	163846.2-472042	19	249.692807	-47.345191	1.71	6.4	4.9	5.5	1.9	6.3	6.3	...
929	163846.7-464825	15	249.694713	-46.807061	3.52	8.9	3.0	2.9	1.8	10.8	10.8	m1,nd
930	163847.0-464842	15	249.695874	-46.811732	4.21	9.2	3.2	3.3	2.1	11.3	11.3	m1,nd
931	163847.4-463714	12	249.697582	-46.620671	2.32	4.6	3.9	3.2	2.2	3.9	3.9	nd
932	163847.7-470812	16	249.698838	-47.136707	1.53	4.0	3.1	4.6	0.0	3.4	3.4	nd
933	163847.7-465001	14	249.699060	-46.833851	0.88	2.8	5.4	0.0	5.7	2.4	2.4	nd
934	163848.2-465243	17	249.701026	-46.878875	5.62	8.0	1.0	2.4	0.0	9.3	9.3	m2,nd
935	163849.6-471759	19	249.706767	-47.299945	1.97	5.1	5.7	0.0	6.1	4.4	4.4	vp
936	163849.8-465545	17	249.707877	-46.929341	1.77	6.3	4.7	3.4	3.3	6.3	6.3	vp,nd
937	163850.0-465801	13	249.708433	-46.967174	6.79	11.3	1.4	0.5	1.3	16.7	16.7	vp,nd
938	163850.2-464639	14	249.709317	-46.777565	1.05	3.9	4.8	0.7	4.8	3.3	3.3	nd
939	163850.3-462627	12	249.709827	-46.441052	3.48	6.7	2.0	3.4	0.0	7.1	7.1	...
940	163850.5-471125	16	249.710691	-47.190381	2.63	5.7	1.9	3.7	0.0	5.3	5.3	nd
941	163850.9-463110	12	249.712359	-46.519653	0.97	2.3	4.5	4.4	1.8	2.2	2.2	...
942	163851.0-463055	12	249.712792	-46.515441	0.86	2.5	4.3	5.5	0.0	2.3	2.3	...
943	163851.2-463617	12	249.713702	-46.604830	2.94	3.5	0.0	1.1	0.0	2.9	2.9	nd
944	163851.4-465543	14	249.714327	-46.928710	1.52	6.3	5.4	7.1	0.6	6.1	6.1	vs,nd
945	163851.7-464428	14	249.715776	-46.741332	1.54	5.7	4.7	5.2	1.7	5.5	5.5	vp,nd
946	163852.4-471102	19	249.718422	-47.183977	2.46	6.9	3.8	4.5	1.2	7.4	7.4	nd
947	163852.5-470141	17	249.718848	-47.028113	2.86	6.7	3.3	1.0	3.0	6.8	6.8	nd
948	163852.9-471145	19	249.720492	-47.195941	3.04	6.5	1.9	1.9	1.0	6.7	6.7	nd
949	163853.0-465903	17,16	249.721207	-46.984402	1.10	6.1;8.1	9.7	6.2	7.3	6.0;9.8	6.0;9.8	...;...
950	163853.1-471935	19	249.721420	-47.326504	2.71	6.5	3.8	3.1	2.0	6.4	6.4	m1
951	163853.5-471945	19	249.723255	-47.329249	2.25	6.6	4.0	0.0	4.5	6.6	6.6	m1
952	163853.8-462843	12	249.724504	-46.478618	1.75	4.4	2.9	4.0	0.0	3.8	3.8	nd
953	163854.2-465241	17	249.726218	-46.878209	3.60	8.7	3.5	0.7	3.4	10.9	10.9	...
954	163854.3-464844	14	249.726336	-46.812483	0.72	2.0	4.8	5.5	0.6	2.2	2.2	...
955	163854.4-465824	13	249.726740	-46.973337	7.36	10.6	3.0	0.0	2.1	14.7	14.7	m3,nd
956	163854.7-471526	19	249.728152	-47.257243	1.52	5.5	4.9	5.7	2.0	5.0	5.0	...
957	163854.8-465405	14	249.728468	-46.901467	0.98	4.6	7.3	7.3	3.5	3.9	3.9	nd
958	163854.8-463259	12	249.728630	-46.549779	0.65	0.6	4.6	6.2	0.0	2.0	2.0	...
959	163855.0-464622	14	249.729426	-46.772881	0.83	3.7	7.0	7.9	1.7	3.2	3.2	nd
960	163855.0-462856	12	249.729575	-46.482293	1.47	4.1	3.0	5.0	0.0	3.5	3.5	nd
961	163855.1-470145	17,16	249.729706	-47.029339	0.58	7.1;5.5	27.0	22.5	16.4	7.4;5.2	7.4;5.2	vp,vl;vp,vl
962	163855.5-464517	14	249.731306	-46.754792	1.16	4.7	5.5	2.4	4.8	4.1	4.1	nd
963	163855.6-464411	15,14,11	249.731674	-46.736485	0.98	7.8;5.8;10.0	9.7	7.8	6.6	8.7;5.6;13.1	8.7;5.6;13.1	id;id;id
964	163855.9-465829	13	249.733261	-46.974797	4.88	10.3	3.4	1.4	1.4	14.0	14.0	m3,nd
965	163856.1-463217	12	249.733863	-46.538258	0.66	0.8	5.0	1.2	4.9	2.0	2.0	...
966	163856.3-463522	12	249.734782	-46.589447	0.61	2.4	2.2	0.0	2.5	17.9	2.3	e

Chandra Catalog: Detection and Localization (continued)

No.	Source (CXOU J)	ObsID (125**)	R.A. (deg)	Dec. (deg)	Unc. (arcsec)	Offset (arcmin)	Sig. FB	Sig. SB	Sig. HB	Radius (arcsec)	PSF (arcsec)	Flags
967	163856.5-464821	14	249.735571	-46.805985	0.68	1.9	5.7	6.1	1.6	2.1	2.1	...
968	163856.5-465800	13	249.735804	-46.966770	6.84	10.2	1.2	0.0	1.4	13.7	13.7	nd
969	163857.1-465649	13	249.737969	-46.947204	5.32	10.2	2.3	0.5	2.2	13.7	13.7	nd
970	163857.3-463948	12	249.738910	-46.663467	2.94	6.8	4.6	4.3	1.5	6.8	6.8	vp,nd
971	163858.2-463840	15	249.742516	-46.644674	3.81	8.5	2.2	3.6	0.0	10.3	10.3	nd
972	163859.1-470538	16	249.746596	-47.094029	0.73	2.1	5.6	0.0	5.9	2.2	2.2	...
973	163859.6-463538	12	249.748548	-46.594110	1.07	2.6	3.4	5.0	0.0	2.4	2.4	...
974	163859.9-471239	19	249.749717	-47.210911	2.69	7.0	4.0	0.0	4.5	7.5	7.5	...
975	163859.9-471541	19	249.749999	-47.261510	1.79	6.3	4.7	5.7	1.4	6.3	6.3	...
976	163900.0-470321	17	249.750380	-47.055883	10.30	8.6	0.7	2.8	0.0	10.3	10.3	vp,nd
977	163900.0-462049	09	249.750415	-46.347082	7.56	8.3	2.8	2.7	1.4	10.0	10.0	...
978	163900.3-471358	16	249.751414	-47.232813	5.94	7.4	2.7	4.0	0.2	7.7	7.7	nd
979	163900.5-464713	14	249.752484	-46.787179	0.65	2.6	9.4	11.0	0.4	2.3	2.3	...
980	163900.9-463754	15	249.754066	-46.631869	7.45	9.2	3.2	1.0	3.0	11.9	11.9	m2,nd
981	163901.2-471503	19	249.755188	-47.251068	3.21	6.6	3.3	2.9	2.1	6.7	6.7	...
982	163901.6-463804	12,15	249.756699	-46.634525	2.11	5.1;9.3	7.1	1.7	6.9	4.3;12.0	4.3;12.0	id;id,m2
983	163901.7-464253	14	249.757311	-46.714747	2.30	6.9	0.5	4.6	0.0	7.4	7.4	nd
984	163901.7-464739	14	249.757410	-46.794173	0.76	2.2	4.7	0.0	5.0	2.2	2.2	...
985	163902.2-470811	16	249.759437	-47.136494	0.71	2.0	4.4	5.5	0.6	2.2	2.2	...
986	163902.5-471135	19,16	249.760803	-47.193127	1.36	7.9;5.0	6.8	7.3	2.8	9.2;4.2	9.2;4.2	vp;...
987	163902.6-462341	09	249.760910	-46.394936	5.72	7.3	2.5	4.6	0.0	7.8	7.8	nd
988	163902.7-464213	15	249.761338	-46.703759	4.14	8.7	7.0	0.1	7.7	10.4	10.6	nb,nd
989	163903.0-462254	09	249.762841	-46.381903	4.75	7.3	3.2	4.0	1.2	7.8	7.8	...
990	163903.3-463015	12	249.764042	-46.504374	0.90	2.9	5.2	0.0	5.6	2.4	2.4	nd
991	163903.6-463116	12	249.765304	-46.521251	0.58	2.0	11.4	12.7	0.7	2.1	2.1	...
992	163904.1-471542	16	249.767127	-47.261804	4.52	9.1	1.8	1.4	1.2	11.0	11.0	nd
993	163904.5-470647	16	249.769111	-47.113235	0.65	0.9	5.2	0.0	5.3	2.1	2.1	...
994	163904.7-463720	12	249.769784	-46.622262	2.21	4.4	3.1	3.6	0.7	3.7	3.7	nd
995	163904.8-471556	19	249.770229	-47.265631	3.39	7.2	3.4	4.5	0.7	7.6	7.6	...
996	163905.0-464031	15	249.771097	-46.675512	4.55	9.2	1.7	0.8	1.4	11.7	11.7	m3,nd
997	163905.2-470839	16	249.771713	-47.144280	0.74	2.1	4.9	2.7	4.0	2.3	2.3	...
998	163905.3-465021	14	249.772174	-46.839431	0.69	0.6	4.4	0.0	4.6	2.1	2.1	...
999	163905.4-464212	14,12,11	249.772842	-46.703495	0.34	7.6;9.3;7.9	120.7	9.9	120.6	8.5;11.4;8.8	8.5;11.4;8.8	id,vs,vl;id,vs,vl;id,vs,vl
1000	163905.8-465646	17	249.774378	-46.946118	4.63	8.5	2.1	0.0	2.6	10.3	10.3	nd
1001	163905.8-464356	12	249.774522	-46.732491	4.30	11.0	2.1	0.4	2.0	15.5	15.5	nd
1002	163906.0-464404	14,11	249.775162	-46.734467	0.80	5.7;8.3	13.0	4.2	12.4	5.5;9.6	5.5;9.6	vp;...
1003	163906.2-462341	09	249.775943	-46.394820	1.85	6.7	4.6	3.0	3.5	6.9	6.9	...
1004	163906.6-464034	15,11,12	249.777802	-46.676353	1.03	9.4;7.6;7.7	12.7	16.7	0.7	12.2;8.2;8.2	12.2;8.2;8.2	m2;...;...
1005	163906.8-465739	17	249.778612	-46.961006	10.28	8.5	3.2	0.0	3.7	10.3	10.3	m3,nd
1006	163907.2-465015	14	249.780278	-46.837708	0.70	0.7	1.2	2.0	0.0	11.2	2.1	e
1007	163907.3-464959	14	249.780522	-46.833285	0.63	0.6	6.0	3.3	4.9	2.1	2.1	vp
1008	163907.5-462751	12	249.781429	-46.464415	1.30	5.4	5.7	7.3	0.6	5.0	5.0	nd
1009	163907.6-465741	17	249.781845	-46.961432	7.25	8.6	4.6	1.6	4.3	10.5	10.5	m3,nd
1010	163908.0-463643	15	249.783591	-46.612044	15.97	10.9	0.0	0.1	0.0	16.0	16.0	vp

Chandra Catalog: Detection and Localization (continued)

No.	Source (CXOU J)	ObsID (125**)	R.A. (deg)	Dec. (deg)	Unc. (arcsec)	Offset (arcmin)	Sig. FB	Sig. SB	Sig. HB	Radius (arcsec)	PSF (arcsec)	Flags
1011	163908.1-463613	12	249.783959	-46.603870	1.18	3.6	3.6	4.8	0.0	3.0	3.0	vp
1012	163909.2-463223	12	249.788347	-46.539798	0.77	2.0	4.2	3.2	2.5	2.2	2.2	...
1013	163909.3-464333	11	249.788916	-46.726004	6.57	7.6	0.9	1.8	0.0	8.1	8.1	nd
1014	163910.1-461917	09	249.792495	-46.321573	4.94	7.6	1.0	2.0	0.0	8.4	8.4	...
1015	163910.7-470552	16	249.794732	-47.098053	0.65	0.8	4.2	3.0	2.9	2.0	2.0	...
1016	163910.9-462946	09,12	249.795746	-46.496181	1.22	8.3;3.9	6.5	0.0	6.4	9.6;3.3	9.6;3.3	...;...
1017	163911.2-464659	14	249.796961	-46.783139	0.95	3.0	3.3	0.0	3.7	14.4	2.5	e,nd
1018	163911.5-462640	12	249.797926	-46.444707	1.31	6.7	7.2	0.0	8.1	7.2	7.2	nd
1019	163911.5-464235	11	249.798170	-46.709851	2.14	6.9	1.6	5.2	0.0	7.1	7.1	nd
1020	163911.6-462349	09	249.798517	-46.397137	1.42	5.8	5.5	6.3	1.3	5.4	5.4	...
1021	163911.7-463539	11	249.799126	-46.594342	7.83	8.5	1.0	0.6	0.6	10.4	10.4	...
1022	163912.1-462608	12,09	249.800629	-46.435822	1.24	7.3;6.1	6.7	1.7	6.7	8.0;5.9	8.0;5.9	id;id
1023	163912.1-471031	16	249.800754	-47.175529	0.73	3.8	9.9	5.0	8.4	3.2	3.2	...
1024	163912.9-462357	09	249.803930	-46.399252	0.66	5.5	32.0	5.7	32.1	5.1	5.1	...
1025	163913.3-463212	12	249.805589	-46.536819	0.72	2.7	6.8	0.0	7.3	2.4	2.4	...
1026	163914.4-470021	13,16	249.810333	-47.005848	0.82	7.6;6.4	16.0	18.1	3.7	8.0;6.7	8.0;6.7	vl;vl
1027	163914.6-470154	13	249.811122	-47.031749	3.93	8.1	1.6	3.6	0.0	9.2	9.2	nd
1028	163914.7-471307	16	249.811432	-47.218855	2.90	6.5	2.2	0.0	2.4	6.3	6.3	nd
1029	163914.7-464254	11	249.811535	-46.715084	2.37	6.5	2.8	0.0	3.3	6.5	6.5	nd
1030	163914.9-464940	14	249.812215	-46.828015	0.76	1.8	1.7	2.9	0.0	8.9	2.2	e
1031	163915.0-462806	12	249.812684	-46.468385	2.59	5.7	2.7	4.5	0.0	5.5	5.5	nd
1032	163915.2-461447	09	249.813669	-46.246481	3.03	10.4	5.6	7.0	0.4	15.1	15.1	...
1033	163915.3-462906	09,12	249.814011	-46.485050	1.28	7.3;4.9	6.1	7.0	1.9	7.6;4.3	7.6;4.3	m3;...
1034	163915.9-462910	09	249.816305	-46.486157	3.56	7.3	2.2	1.8	1.3	7.6	7.6	m3,nd
1035	163916.2-463238	12	249.817890	-46.544048	0.70	3.1	8.8	8.8	3.0	2.6	2.6	vp
1036	163916.4-465512	13	249.818377	-46.920137	5.73	7.4	2.1	2.6	0.6	7.9	7.9	nd
1037	163916.5-463810	12	249.819133	-46.636229	4.36	6.0	1.1	2.7	0.0	5.7	5.7	nd
1038	163916.8-463027	09	249.820282	-46.507652	3.14	8.2	3.9	0.5	4.0	9.3	9.3	...
1039	163920.4-465006	14	249.835116	-46.835169	0.61	2.8	13.8	1.4	13.8	2.5	2.5	...
1040	163920.5-470526	16	249.835617	-47.090596	0.73	2.2	3.6	4.7	0.4	2.3	2.3	...
1041	163920.5-465436	14	249.835648	-46.910106	2.85	5.6	2.6	3.7	0.1	5.0	5.0	nd
1042	163921.2-462230	09	249.838538	-46.375242	1.17	4.3	5.3	7.0	0.0	3.7	3.7	...
1043	163921.3-465046	14	249.839124	-46.846161	1.14	3.1	3.1	0.0	3.3	6.0	2.6	e
1044	163921.4-465758	14,13	249.839340	-46.966263	1.07	8.7;6.0	11.1	13.3	2.4	10.3;5.7	10.3;5.7	...;...
1045	163921.7-464332	14,11	249.840775	-46.725582	0.59	6.9;5.6	24.6	18.4	16.7	7.4;5.2	7.4;5.2	vl;vl
1046	163921.8-461709	09	249.840928	-46.285836	3.57	7.8	1.9	3.9	0.0	9.1	9.1	...
1047	163922.0-471007	16	249.841751	-47.168885	1.79	4.0	2.6	3.8	0.0	3.4	3.4	...
1048	163922.2-470400	13	249.842539	-47.066902	3.50	8.4	3.5	3.0	2.2	9.7	9.7	nd
1049	163922.3-464911	14	249.843324	-46.819874	0.84	3.2	5.9	6.5	1.4	2.7	2.7	...
1050	163922.5-470534	16	249.843852	-47.092987	0.84	2.4	4.1	5.7	0.0	2.3	2.3	...
1051	163922.6-470827	16	249.844205	-47.140894	0.86	2.8	5.7	6.2	1.6	2.5	2.5	...
1052	163923.3-465227	14	249.847159	-46.874223	1.52	4.2	3.4	0.0	3.6	3.6	3.6	nd
1053	163923.4-463228	12,11	249.847794	-46.541351	1.10	4.3;9.6	6.3	4.8	4.6	3.7;13.0	3.7;13.0	...;...
1054	163923.7-464830	14	249.849102	-46.808497	1.10	3.6	4.4	2.1	3.8	3.0	3.0	nd

Chandra Catalog: Detection and Localization (continued)

No.	Source (CXOU J)	ObsID (125**)	R.A. (deg)	Dec. (deg)	Unc. (arcsec)	Offset (arcmin)	Sig. FB	Sig. SB	Sig. HB	Radius (arcsec)	PSF (arcsec)	Flags
1055	163924.1-462503	09	249.850572	-46.417738	1.62	3.8	3.0	4.5	0.0	3.2	3.2	...
1056	163924.3-464237	11	249.851493	-46.710294	1.48	4.8	3.8	0.5	3.8	4.1	4.1	...
1057	163925.4-462859	09	249.856223	-46.483131	4.43	6.1	2.4	3.8	0.0	5.9	5.9	nd
1058	163925.5-471413	16	249.856531	-47.237023	2.94	8.0	3.3	0.0	4.0	8.8	8.8	...
1059	163925.7-465303	13,14	249.857193	-46.884331	0.52	7.2;4.9	30.5	34.3	3.1	7.7;4.2	7.7;4.2	vp;vp
1060	163925.8-462832	09,12	249.857727	-46.475769	1.45	5.7;6.5	6.2	3.9	5.2	5.3;6.8	5.3;6.8	...;...
1061	163926.4-470012	14,13	249.860077	-47.003525	1.93	11.1;5.6	5.2	4.5	3.5	15.8;5.1	15.8;5.1	m1;...
1062	163926.9-463403	12	249.862470	-46.567672	1.33	5.0	5.2	3.4	3.9	4.3	4.3	nd
1063	163927.0-463517	12	249.862613	-46.588115	2.18	5.4	3.1	0.9	3.0	4.9	4.9	nd
1064	163927.4-464751	14	249.864495	-46.797763	0.91	4.4	7.9	4.9	6.1	3.8	3.8	nd
1065	163927.9-462316	09	249.866271	-46.387890	1.01	3.0	4.1	5.8	0.0	2.5	2.5	...
1066	163928.1-464821	14	249.867285	-46.805895	1.44	4.3	3.0	0.0	3.5	3.7	3.7	nd
1067	163928.3-464823	14	249.868327	-46.806500	1.12	4.4	0.8	0.6	0.5	13.3	3.7	e,s,nd
1068	163928.5-471405	16	249.869071	-47.234978	5.07	8.0	1.7	3.2	0.0	8.9	8.9	...
1069	163928.7-465336	13	249.869680	-46.893570	1.60	6.4	3.4	3.5	1.6	6.5	6.5	nd
1070	163928.7-470019	16,13,14	249.869705	-47.005314	0.74	7.2;5.3;11.4	15.4	15.7	6.4	7.9;4.6;16.6	7.9;4.6;16.6	vl;vs,vl;m1,vl
1071	163929.4-463859	11	249.872584	-46.649824	0.97	4.1	3.0	2.5	1.8	13.8	3.5	e
1072	163929.5-465151	13	249.873001	-46.864377	3.05	7.6	3.2	1.1	3.0	8.5	8.5	...
1073	163929.7-463838	11,12	249.873825	-46.644157	0.68	4.2;7.8	13.7	14.1	6.1	3.6;8.5	3.6;8.5	...;...
1074	163929.8-465911	14	249.874335	-46.986433	3.40	10.4	4.9	4.8	1.7	13.9	13.9	nd
1075	163929.9-464448	14,11	249.874908	-46.746777	1.10	6.6;5.3	7.5	0.0	8.1	6.9;4.6	6.9;4.6	...;...
1076	163930.7-464427	11	249.878013	-46.741096	1.31	5.0	4.6	2.2	3.9	4.2	4.2	vp,nd
1077	163930.8-470852	16	249.878608	-47.147820	0.88	4.2	8.2	0.0	8.5	3.5	3.5	...
1078	163930.9-464350	14	249.879111	-46.730824	4.54	7.5	2.3	3.3	0.2	8.3	8.3	...
1079	163931.3-470736	16	249.880657	-47.126861	1.60	3.8	2.5	4.3	0.0	3.2	3.2	...
1080	163931.6-464232	11	249.881801	-46.709057	1.14	3.7	3.7	0.0	4.2	3.1	3.1	...
1081	163931.7-463631	11	249.882113	-46.608758	1.88	5.5	3.2	1.6	2.6	5.1	5.1	vp,nd
1082	163931.7-464633	14	249.882366	-46.775852	2.18	5.7	2.4	1.9	1.5	5.5	5.5	nd
1083	163931.9-463154	11	249.883040	-46.531769	2.65	9.5	3.9	5.7	0.2	12.9	12.9	vp,nd
1084	163931.9-470059	13	249.883138	-47.016418	1.49	5.2	0.4	0.1	0.3	11.3	4.4	e,nd
1085	163932.1-464859	14	249.884150	-46.816480	1.60	4.8	3.6	4.6	0.3	4.2	4.2	nd
1086	163932.4-470911	16	249.885088	-47.153201	1.02	4.6	4.8	5.7	1.0	3.9	3.9	...
1087	163932.7-463625	11	249.886657	-46.606989	2.04	5.4	3.8	1.9	3.2	5.0	5.0	nd
1088	163932.8-461859	09	249.886671	-46.316635	1.54	5.3	4.9	1.7	4.5	4.9	4.9	...
1089	163932.9-470303	16,13	249.887222	-47.050884	0.71	5.4;6.5	14.0	1.6	14.2	4.9;6.3	4.9;6.3	...;...
1090	163933.2-465530	14,13	249.888428	-46.925037	1.21	7.6;4.7	8.0	2.2	7.7	8.0;4.0	8.0;4.0	...;...
1091	163933.2-464121	11	249.888484	-46.689393	0.81	3.0	6.4	3.1	5.5	2.5	2.5	...
1092	163933.9-463649	11,12	249.891342	-46.613754	1.71	5.0;7.2	4.3	6.5	0.0	4.3;7.6	4.3;7.6	...;...
1093	163934.7-462126	09	249.894823	-46.357248	1.01	3.0	4.3	5.2	0.6	2.5	2.5	...
1094	163935.1-470913	16	249.896426	-47.153687	1.77	5.0	3.2	0.0	3.5	4.2	4.2	...
1095	163935.3-464547	14	249.897213	-46.763232	1.80	6.6	3.7	2.9	2.4	6.9	6.9	nd
1096	163935.8-464756	14	249.899562	-46.799019	2.30	5.7	2.6	1.3	2.2	5.4	5.4	nd
1097	163936.4-462924	09	249.901864	-46.490101	2.01	5.7	4.0	0.2	4.2	5.2	5.2	vp
1098	163936.8-462551	09	249.903390	-46.430953	1.04	2.4	4.1	4.8	0.5	2.3	2.3	...

Chandra Catalog: Detection and Localization (continued)

No.	Source (CXOU J)	ObsID (125**)	R.A. (deg)	Dec. (deg)	Unc. (arcsec)	Offset (arcmin)	Sig. FB	Sig. SB	Sig. HB	Radius (arcsec)	PSF (arcsec)	Flags
1099	163936.8-463058	11	249.903741	-46.516247	6.90	10.2	2.3	2.1	1.4	14.5	14.5	nd
1100	163937.0-465204	13	249.904545	-46.867788	3.52	6.8	3.9	0.0	4.2	7.1	7.1	nd
1101	163937.2-465650	13	249.905367	-46.947320	1.25	3.5	3.4	2.5	2.2	2.9	2.9	nd
1102	163938.2-465438	13	249.909335	-46.910558	1.42	4.5	4.4	2.6	3.4	3.9	3.9	nd
1103	163938.3-461914	09	249.909732	-46.320615	1.09	4.8	6.2	8.2	0.0	4.2	4.2	...
1104	163938.4-463507	12	249.910042	-46.585392	2.61	7.2	2.3	0.0	3.2	7.6	7.6	nd
1105	163939.0-463922	11	249.912501	-46.656162	0.83	2.5	5.4	5.4	2.2	2.3	2.3	...
1106	163939.1-463451	11	249.913186	-46.581043	1.64	6.3	4.7	5.4	1.3	6.6	6.6	nd
1107	163939.1-464727	11	249.913322	-46.791014	2.53	6.9	3.5	5.8	0.0	6.9	6.9	...
1108	163939.4-462918	12	249.914168	-46.488588	3.38	8.0	3.3	0.0	4.0	9.3	9.3	nd
1109	163939.7-470747	16	249.915665	-47.129840	1.06	5.2	8.2	0.6	8.4	4.6	4.6	...
1110	163940.5-463701	12	249.918951	-46.616987	2.26	8.3	4.6	4.5	2.2	9.6	9.6	nd
1111	163940.8-471726	16	249.920131	-47.290731	7.62	12.0	1.6	0.1	1.6	18.1	18.1	...
1112	163941.2-462018	09	249.921784	-46.338603	1.01	3.6	0.2	2.7	0.0	18.5	3.1	e
1113	163941.2-464746	11	249.922016	-46.796175	1.96	7.1	0.8	1.7	0.0	20.8	7.2	e
1114	163941.3-471309	16	249.922360	-47.219359	9.67	8.4	2.4	1.4	1.9	9.7	9.7	...
1115	163941.3-471122	16	249.922383	-47.189558	2.02	7.1	4.8	2.6	3.9	7.3	7.3	...
1116	163941.5-463816	11,08	249.923203	-46.637871	0.88	3.1;11.5	3.6	3.0	2.5	11.6;17.0	2.5;17.0	e,id;id
1117	163941.8-461907	09	249.924236	-46.318846	2.39	4.8	0.9	3.8	0.0	8.5	4.2	e,m1
1118	163941.8-464556	11	249.924289	-46.765657	1.54	5.3	4.3	4.0	2.3	4.6	4.6	nd
1119	163942.2-470543	16	249.926080	-47.095356	2.48	5.6	3.0	3.9	0.5	5.2	5.2	nd
1120	163942.3-471257	16	249.926453	-47.216077	—	8.3	3.1	1.9	2.0	44.0	9.6	c,e,s
1121	163942.4-470711	13	249.926792	-47.119836	11.91	9.5	1.5	3.0	0.0	11.9	11.9	vp
1122	163942.6-463346	12,08,11	249.927811	-46.563030	1.29	7.6;9.6;7.2	8.3	4.7	7.0	8.5;12.4;8.0	8.5;12.4;8.0	...;...;...
1123	163942.7-461902	09	249.928315	-46.317390	1.47	4.8	3.8	3.4	2.5	4.2	4.2	m2
1124	163943.4-471249	16	249.931150	-47.213612	2.80	8.4	3.9	1.0	3.8	9.6	9.6	...
1125	163943.7-464855	11,13	249.932495	-46.815498	4.56	8.1;9.3	5.0	4.9	0.8	9.1;12.2	9.1;12.2	...;...
1126	163944.1-463357	11	249.933823	-46.565870	2.35	7.0	3.5	2.4	2.5	7.7	7.7	nd
1127	163944.3-465714	13	249.934680	-46.953916	0.75	2.2	5.7	6.5	1.0	2.2	2.2	...
1128	163944.3-465614	13	249.934965	-46.937460	0.50	2.7	37.5	24.5	30.9	2.4	2.4	...
1129	163944.7-465005	14,13,11	249.936386	-46.834827	1.72	6.9;8.1;9.3	6.7	6.6	4.0	7.2;9.7;11.5	7.2;9.7;11.5	...;...;...
1130	163944.9-463317	09	249.937091	-46.554797	2.57	9.4	4.8	2.0	4.3	11.7	11.7	vp,nd
1131	163944.9-465151	13,14	249.937149	-46.864235	1.37	6.4;7.3	4.2	5.2	1.1	6.6;7.6	6.6;7.6	...;...
1132	163944.9-464213	11	249.937387	-46.703614	0.78	1.7	3.6	1.1	3.3	2.2	2.2	...
1133	163945.3-463100	12	249.939137	-46.516817	4.08	8.3	2.8	2.5	1.6	10.0	10.0	nd
1134	163945.4-470259	13	249.939191	-47.049747	1.95	5.4	3.3	4.8	0.0	4.7	4.7	nd
1135	163945.6-464103	11	249.940215	-46.684416	0.54	0.9	12.7	12.7	4.6	2.1	2.1	...
1136	163945.8-461923	09	249.940956	-46.323191	1.31	4.5	4.0	0.0	4.4	3.9	3.9	...
1137	163946.1-462359	09	249.942130	-46.399965	0.59	0.2	9.5	0.0	9.8	2.0	2.0	...
1138	163946.2-464726	13	249.942542	-46.790707	10.93	10.7	0.0	0.0	0.0	15.7	15.7	nd
1139	163947.0-470132	13,16	249.945862	-47.025616	0.89	3.9;8.2	6.8	9.4	0.0	3.3;9.8	3.3;9.8	...;...
1140	163947.7-463504	12	249.948757	-46.584637	2.41	8.7	4.7	4.1	2.6	10.7	10.7	nd
1141	163947.8-465325	13	249.949277	-46.890465	1.41	4.8	4.4	0.0	5.0	4.1	4.1	nd
1142	163947.9-464114	11	249.949739	-46.687226	0.54	0.6	12.1	10.8	6.2	2.1	2.1	...

Chandra Catalog: Detection and Localization (continued)

No.	Source (CXOU J)	ObsID (125**)	R.A. (deg)	Dec. (deg)	Unc. (arcsec)	Offset (arcmin)	Sig. FB	Sig. SB	Sig. HB	Radius (arcsec)	PSF (arcsec)	Flags
1143	163948.2-465941	13	249.950934	-46.994825	0.72	2.2	1.1	0.3	0.9	17.0	2.3	e
1144	163948.2-463214	11	249.950990	-46.537406	4.58	8.7	2.4	0.0	2.7	11.0	11.0	nd
1145	163948.2-470551	16	249.951008	-47.097749	1.05	6.6	11.2	8.2	7.8	6.7	6.7	vs,nd
1146	163948.5-462737	09	249.952357	-46.460387	1.20	3.8	4.8	5.5	1.0	3.2	3.2	...
1147	163948.6-470325	16	249.952915	-47.056986	4.36	7.4	3.0	2.1	2.0	8.0	8.0	nd
1148	163948.9-463048	08	249.953804	-46.513434	3.84	8.4	2.6	1.1	2.2	10.0	10.0	nd
1149	163949.7-470413	16,13	249.957138	-47.070385	1.54	7.2;6.4	6.7	8.0	2.3	7.7;6.2	7.7;6.2	...;...
1150	163949.9-462332	09	249.958035	-46.392416	0.59	0.9	9.5	10.8	1.7	2.0	2.0	...
1151	163950.0-462526	09	249.958678	-46.423931	0.66	1.8	6.9	7.6	1.7	2.2	2.2	...
1152	163950.0-465238	13,10,14	249.958710	-46.877403	0.82	5.4;9.9;8.4	13.0	12.4	6.5	5.0;12.9;9.8	5.0;12.9;9.8	...;...;vp
1153	163950.1-465446	10	249.958857	-46.912940	5.13	10.9	3.1	0.0	4.5	15.5	15.5	nd
1154	163950.2-465211	13	249.959468	-46.869933	3.20	5.9	1.9	3.5	0.0	5.7	5.7	nd
1155	163950.8-463822	11	249.961815	-46.639479	0.76	2.5	5.6	0.0	6.0	2.3	2.3	nd
1156	163951.4-462014	09	249.964412	-46.337438	1.29	3.8	3.8	2.4	2.8	3.2	3.2	...
1157	163951.5-463037	09,08	249.964584	-46.510479	1.12	6.9;7.9	9.7	11.6	2.3	6.9;9.1	6.9;9.1	...;...
1158	163951.6-470022	13	249.965398	-47.006269	0.72	2.6	6.1	7.8	0.0	2.4	2.4	...
1159	163951.8-470133	16	249.966045	-47.025927	6.47	8.8	1.1	3.1	0.0	11.1	11.1	nd
1160	163952.5-462236	09	249.969119	-46.376930	0.73	1.8	0.4	1.9	0.0	13.6	2.1	e
1161	163952.6-463937	11	249.969441	-46.660454	0.70	1.3	2.2	0.0	2.4	5.3	2.0	e
1162	163953.3-465912	13	249.972171	-46.986693	0.57	1.4	8.5	9.3	1.9	2.2	2.2	...
1163	163953.9-465152	13	249.974984	-46.864454	1.98	6.1	3.5	4.0	1.3	6.1	6.1	nd
1164	163954.2-464834	13,14,11	249.975891	-46.809639	2.04	9.4;8.6;7.7	6.0	6.3	2.0	12.6;10.5;8.3	12.6;10.5;8.3	id;id;id
1165	163954.5-462341	09	249.977240	-46.394724	0.67	1.6	7.2	7.6	2.5	2.2	2.2	...
1166	163954.5-464718	13	249.977321	-46.788600	11.49	10.6	0.0	0.0	0.0	15.7	15.7	vp,nd
1167	163954.7-465431	13	249.978144	-46.908634	1.45	3.4	3.3	4.4	0.2	2.9	2.9	nd
1168	163955.2-463145	08,09	249.980194	-46.529377	0.61	7.2;8.1	29.9	27.0	15.4	7.7;9.0	7.7;9.0	vp,vl;vl
1169	163955.2-462450	09	249.980207	-46.414155	0.85	2.0	4.5	2.6	3.4	2.2	2.2	...
1170	163955.6-464418	11	249.981961	-46.738352	1.09	3.5	3.8	5.6	0.0	3.0	3.0	...
1171	163955.9-465234	10,13	249.982956	-46.876312	1.08	9.0;5.4	8.3	7.4	4.2	11.0;5.0	11.0;5.0	...;vs
1172	163955.9-465642	13	249.983080	-46.945260	0.67	1.2	4.6	0.0	4.8	2.0	2.0	vs
1173	163955.9-462921	09,08	249.983124	-46.489189	0.98	5.8;7.5	11.1	11.8	4.6	5.3;8.2	5.3;8.2	...;...
1174	163956.2-470250	13	249.984448	-47.047294	1.77	4.9	3.1	2.5	2.1	8.3	4.1	e,nd
1175	163956.3-470025	13	249.984950	-47.007000	0.86	2.5	4.2	0.0	4.5	2.4	2.4	...
1176	163956.8-465918	13	249.986827	-46.988357	0.62	1.3	0.0	0.0	0.0	15.4	2.2	e,s
1177	163956.8-463155	12	249.987028	-46.532172	12.17	10.1	1.4	1.3	0.7	13.9	13.9	m1,nd
1178	163956.8-465915	13	249.987055	-46.987719	0.68	1.3	7.3	7.5	2.3	2.2	2.2	...
1179	163957.0-465923	13	249.987756	-46.989930	0.80	1.4	3.4	0.0	3.7	2.2	2.2	...
1180	163957.2-465126	10,13,11	249.988724	-46.857368	0.56	8.3;6.5;10.6	32.8	0.8	33.8	9.7;6.8;14.4	9.7;6.8;14.4	id;id;id
1181	163957.8-462549	09,08	249.991119	-46.430534	0.62	3.0;9.0	15.8	0.0	16.4	2.5;11.6	2.5;11.6	...;...
1182	163958.1-464505	14	249.992392	-46.751500	12.36	10.4	0.4	0.0	0.0	14.5	14.5	nd
1183	163958.3-463229	08,12	249.993301	-46.541462	2.24	6.7;10.5	4.5	1.3	4.4	6.9;14.9	6.9;14.9	id;id,m3
1184	163958.5-462435	09	249.993880	-46.409877	1.21	2.4	4.9	6.0	0.3	2.4	2.4	...
1185	163958.6-462113	09	249.994399	-46.353746	0.87	3.5	6.5	7.7	1.2	3.0	3.0	...
1186	163958.7-463931	11	249.994982	-46.658770	0.82	1.9	6.4	4.3	4.6	2.1	2.1	...

Chandra Catalog: Detection and Localization (continued)

No.	Source (CXOU J)	ObsID (125**)	R.A. (deg)	Dec. (deg)	Unc. (arcsec)	Offset (arcmin)	Sig. FB	Sig. SB	Sig. HB	Radius (arcsec)	PSF (arcsec)	Flags
1187	163958.7-463311	08	249.994991	-46.553086	3.69	6.7	1.9	2.8	0.0	6.9	6.9	nd
1188	163958.9-463213	12	249.995611	-46.537071	14.79	10.4	1.6	1.0	1.1	14.8	14.8	id,m3,nd
1189	163959.0-470112	16	249.995919	-47.020161	13.67	10.0	2.2	1.5	1.4	13.7	13.7	...
1190	163959.0-462415	09	249.996021	-46.404227	0.87	2.4	4.7	1.2	4.4	2.4	2.4	...
1191	163959.3-465038	13,10	249.997375	-46.844006	1.62	7.3;7.7	6.2	0.0	7.1	8.1;8.5	8.1;8.5	...;...
1192	163959.3-462755	09	249.997458	-46.465499	1.55	4.8	4.5	2.5	3.7	4.0	4.0	nd
1193	163959.7-463435	08	249.998779	-46.576614	3.50	7.0	1.5	3.2	0.0	7.2	7.2	vp,nd
1194	164000.1-470142	16	250.000439	-47.028458	5.91	9.9	2.1	1.5	1.4	13.4	13.4	nd
1195	164000.1-465152	13	250.000500	-46.864508	1.62	6.1	5.1	1.0	5.1	6.2	6.2	nd
1196	164000.3-463917	11	250.001471	-46.654833	0.66	2.3	7.5	6.8	3.9	2.2	2.2	...
1197	164000.5-463233	12	250.002258	-46.542703	15.47	10.7	0.0	0.0	0.0	15.5	15.5	m3,nd
1198	164000.8-465922	13	250.003533	-46.989545	0.75	1.6	4.2	3.9	2.0	2.2	2.2	...
1199	164000.9-464633	10	250.003758	-46.775863	4.27	7.6	3.0	3.8	0.9	8.4	8.4	vp,nd
1200	164001.7-470154	13	250.007477	-47.031859	1.30	4.1	4.3	5.9	0.0	3.4	3.4	nd
1201	164002.1-462826	09	250.008806	-46.473891	1.22	5.4	6.3	6.1	3.0	4.8	4.8	nd
1202	164002.3-462121	09	250.009922	-46.356103	1.22	3.9	3.5	0.5	3.5	11.1	3.3	e
1203	164002.4-463200	08,09	250.010117	-46.533497	0.53	6.0;8.7	32.5	27.5	18.3	5.8;10.2	5.8;10.2	...;...
1204	164003.5-463850	11	250.014900	-46.647307	0.74	3.0	7.0	7.4	2.8	2.5	2.5	nd
1205	164003.6-465939	13	250.015023	-46.994438	0.92	2.1	4.5	5.2	0.7	2.3	2.3	...
1206	164003.6-462442	09	250.015117	-46.411869	1.03	3.3	4.3	2.3	3.5	2.8	2.8	nd
1207	164003.6-463844	11	250.015401	-46.645695	1.12	3.1	3.3	5.1	0.0	2.6	2.6	nd
1208	164003.7-470401	16	250.015616	-47.067064	5.07	9.6	2.9	0.6	2.9	12.5	12.5	m2,nd
1209	164004.0-463501	11	250.016718	-46.583867	1.73	6.3	4.6	1.3	3.6	6.5	6.5	nd
1210	164004.1-470418	13,16	250.017487	-47.071884	0.82	6.5;9.6	17.0	19.6	3.6	6.4;12.5	6.4;12.5	...;m2
1211	164005.5-464950	13,10	250.023132	-46.830795	1.74	8.3;6.5	5.2	3.0	4.3	10.1;6.6	10.1;6.6	...;...
1212	164005.8-462238	08	250.024309	-46.377410	3.97	10.7	2.5	0.0	3.2	15.8	15.8	m3,nd
1213	164006.1-462224	08	250.025598	-46.373379	10.51	10.9	0.0	0.3	0.0	16.3	16.3	m3,nd
1214	164006.3-462203	09	250.026306	-46.367616	1.15	4.1	3.6	0.0	3.9	3.5	3.5	nd
1215	164006.6-462239	09	250.027816	-46.377536	1.38	3.9	4.0	1.0	3.7	3.4	3.4	nd
1216	164006.8-462913	09,08	250.028717	-46.487190	0.92	6.5;5.8	13.1	0.7	13.6	6.5;5.6	6.5;5.6	vl;vp,vl
1217	164007.3-464036	10	250.030485	-46.676835	14.48	10.2	0.1	1.6	0.0	14.5	14.5	...
1218	164008.0-462714	09,08	250.033630	-46.454159	0.70	5.2;6.8	14.4	15.1	5.3	4.5;7.2	4.5;7.2	...;...
1219	164008.3-461704	09	250.034821	-46.284451	4.06	7.9	2.6	0.0	2.8	9.2	9.2	...
1220	164009.1-462946	08,09	250.038086	-46.496372	0.93	5.3;7.2	8.3	9.3	2.7	4.7;7.4	4.7;7.4	...;vp
1221	164009.8-462637	08	250.041006	-46.443730	4.69	7.0	1.6	2.5	0.0	7.6	7.6	...
1222	164010.0-462426	08	250.041773	-46.407334	2.70	8.8	4.7	2.2	3.2	11.1	11.1	nd
1223	164010.0-464348	11	250.042065	-46.730277	1.33	4.4	4.1	5.0	1.2	3.7	3.7	nd
1224	164010.6-465220	13,10	250.044479	-46.872303	2.05	6.1;6.6	4.0	6.5	0.0	6.2;6.6	6.2;6.6	...;...
1225	164010.9-462901	09	250.045700	-46.483868	3.51	6.8	2.6	1.8	1.9	6.9	6.9	nd
1226	164011.0-464247	11	250.046217	-46.713308	1.03	4.0	5.7	4.6	3.4	3.4	3.4	nd
1227	164011.1-465706	13	250.046340	-46.951931	0.56	2.6	16.7	18.5	0.6	2.4	2.4	...
1228	164011.8-463601	11	250.049213	-46.600349	1.28	6.1	2.7	0.0	1.6	22.8	6.1	e,nd
1229	164012.0-461945	09	250.050136	-46.329431	2.36	6.2	3.0	1.9	2.3	6.3	6.3	...
1230	164012.0-463507	08	250.050227	-46.585449	1.49	5.4	4.6	3.1	3.3	4.9	4.9	nd

Chandra Catalog: Detection and Localization (continued)

No.	Source (CXOU J)	ObsID (125**)	R.A. (deg)	Dec. (deg)	Unc. (arcsec)	Offset (arcmin)	Sig. FB	Sig. SB	Sig. HB	Radius (arcsec)	PSF (arcsec)	Flags
1231	164012.4-464138	11	250.051750	-46.694009	1.31	3.8	0.0	1.6	0.0	10.2	3.2	e,nd
1232	164012.4-463505	08	250.051805	-46.584980	1.21	5.4	0.0	0.0	0.2	23.3	4.8	e,s,nd
1233	164012.6-463901	11,08,10	250.052719	-46.650379	0.82	4.2;8.3;11.0	9.8	10.4	3.2	3.6;9.5;16.8	3.6;9.5;16.8	...;...;...
1234	164013.1-462657	09	250.054889	-46.449388	1.47	5.7	4.8	2.9	3.8	5.3	5.3	nd
1235	164013.2-462654	08	250.055364	-46.448432	1.61	6.4	3.7	3.9	1.5	6.6	6.6	nd
1236	164014.1-462949	09	250.058877	-46.497171	1.79	7.8	6.0	7.3	1.3	8.4	8.4	nd
1237	164014.4-464850	10,11	250.060120	-46.814041	1.16	4.9;8.9	6.8	8.4	0.0	4.2;10.8	4.2;10.8	...;...
1238	164014.6-470241	13	250.061086	-47.044999	3.09	5.7	3.4	4.0	1.0	5.2	5.2	...
1239	164014.7-470237	13	250.061259	-47.043875	1.27	5.6	0.0	0.0	0.0	20.2	5.1	e,s
1240	164014.8-470600	13	250.062010	-47.100082	2.31	8.6	6.2	1.2	6.2	10.2	10.2	...
1241	164015.8-465258	13	250.065871	-46.882798	1.91	6.0	3.4	0.0	4.1	6.0	6.0	nd
1242	164015.8-463453	08	250.066219	-46.581596	1.29	4.8	4.7	2.4	4.0	4.0	4.0	nd
1243	164016.2-465719	13	250.067690	-46.955509	1.52	3.4	3.9	3.8	1.8	2.9	2.9	...
1244	164016.2-470200	13	250.067811	-47.033453	3.05	5.3	1.6	2.3	0.1	9.8	4.7	e
1245	164016.4-464520	10	250.068399	-46.755614	2.59	5.7	2.1	0.0	2.5	5.5	5.5	nd
1246	164016.4-464236	11	250.068708	-46.710176	1.81	4.7	3.2	3.6	0.9	4.0	4.0	nd
1247	164016.6-463629	11	250.069485	-46.608069	2.33	6.3	2.5	3.8	0.0	6.4	6.4	nd
1248	164016.7-465621	13,10	250.069809	-46.939247	0.83	3.8;8.8	8.6	5.2	6.6	3.3;10.5	3.3;10.5	...;...
1249	164016.8-464817	10	250.070192	-46.804874	1.52	4.6	3.4	4.0	0.7	3.9	3.9	...
1250	164017.3-462514	09	250.072127	-46.420774	1.33	5.7	6.5	4.3	4.8	5.4	5.4	nd
1251	164017.7-464133	11,10	250.073761	-46.692551	0.87	4.7;8.4	8.9	11.5	0.0	4.0;10.4	4.0;10.4	...;...
1252	164017.9-462406	09	250.074755	-46.401689	1.70	5.7	3.5	1.8	2.9	5.3	5.3	nd
1253	164018.1-463506	08	250.075741	-46.585173	0.65	4.6	14.3	11.2	9.3	3.9	3.9	...
1254	164018.2-462409	08	250.075882	-46.402525	2.20	8.4	2.3	0.8	0.1	21.5	10.3	e,m1,nd
1255	164018.3-462507	09	250.076585	-46.418755	1.88	5.9	5.4	4.8	3.0	5.6	5.6	nd
1256	164018.5-463345	09	250.077378	-46.562527	7.23	11.4	2.8	1.9	2.0	16.7	16.7	...
1257	164018.9-463105	08	250.078943	-46.518298	1.02	3.2	3.9	4.9	0.3	2.7	2.7	nd
1258	164019.4-465537	13	250.081075	-46.927072	0.98	4.6	6.7	7.2	2.4	4.0	4.0	vs,nd
1259	164019.6-462350	08,09	250.081711	-46.397446	1.07	8.6;6.0	8.7	3.4	8.2	10.7;5.8	10.7;5.8	id,m3;id
1260	164019.9-463438	11	250.083112	-46.577370	9.47	8.0	1.3	0.0	1.2	9.5	9.5	...
1261	164020.5-464000	11,10	250.085556	-46.666794	1.75	5.2;9.6	3.1	4.0	0.7	13.0;13.0	4.6;13.0	e,id;id
1262	164022.1-463013	08	250.092197	-46.503672	1.07	3.1	4.2	5.0	0.5	2.5	2.5	nd
1263	164022.2-464131	11	250.092853	-46.692117	1.37	5.4	4.9	0.1	5.1	5.0	5.0	nd
1264	164022.6-462836	08,09	250.094360	-46.476719	0.60	4.1;8.0	13.9	8.9	10.9	3.5;9.0	3.5;9.0	id;id
1265	164022.7-463046	08	250.094584	-46.512950	0.84	2.7	4.1	5.6	0.0	2.4	2.4	nd
1266	164022.9-465351	13	250.095485	-46.897596	2.16	6.1	1.7	2.6	0.0	6.1	6.1	m1,nd
1267	164023.1-465341	13	250.096279	-46.894724	2.19	6.2	2.4	0.0	2.7	6.4	6.4	m1,nd
1268	164024.3-465715	10	250.101453	-46.954337	3.81	9.1	2.7	0.3	2.7	11.0	11.0	...
1269	164024.4-465842	13	250.101832	-46.978589	1.83	4.8	3.0	4.9	0.0	4.2	4.2	...
1270	164024.8-463236	08	250.103366	-46.543430	0.67	2.3	0.9	0.0	1.7	11.6	2.3	e
1271	164024.9-462322	09,08	250.103897	-46.389450	1.52	6.9;8.7	5.5	7.5	1.3	7.1;11.1	7.1;11.1	...;...
1272	164026.8-465535	13	250.111837	-46.926533	1.90	5.7	4.5	0.0	5.1	5.5	5.5	nd
1273	164027.6-464814	10	250.115249	-46.804054	0.54	2.7	16.4	0.9	17.0	2.4	2.4	...
1274	164027.7-462851	09	250.115505	-46.480957	4.06	8.9	0.8	0.0	1.0	29.0	10.7	e,nd

Chandra Catalog: Detection and Localization (continued)

No.	Source (CXOU J)	ObsID (125**)	R.A. (deg)	Dec. (deg)	Unc. (arcsec)	Offset (arcmin)	Sig. FB	Sig. SB	Sig. HB	Radius (arcsec)	PSF (arcsec)	Flags
1275	164027.7-465522	13	250.115692	-46.922864	1.73	5.9	3.0	0.0	3.5	5.8	5.8	m3,nd
1276	164027.8-462513	09,08	250.115845	-46.420464	0.84	7.5;6.8	13.5	0.0	14.2	8.0;7.3	8.0;7.3	...;...
1277	164028.1-465522	13	250.117180	-46.922956	1.68	6.0	1.9	1.1	1.4	5.9	5.9	m3,nd
1278	164029.4-462328	09	250.122642	-46.391346	0.80	7.7	26.6	0.2	27.6	8.4	8.4	b,id,nd
1279	164029.5-462329	08	250.123115	-46.391536	0.81	8.5	21.8	3.2	21.8	10.5	10.5	b,id,nd
1280	164029.8-463027	08	250.124562	-46.507514	0.65	1.9	1.9	1.5	1.2	5.4	2.1	e
1281	164030.0-463436	08	250.125193	-46.576680	0.73	3.0	0.3	0.3	0.1	12.0	2.5	e
1282	164030.1-463804	11	250.125433	-46.634689	3.17	7.3	4.2	4.3	2.2	7.9	7.9	nd
1283	164030.1-465726	10	250.125778	-46.957263	5.89	8.9	2.6	0.0	2.9	10.7	10.7	nd
1284	164030.2-464107	10	250.126108	-46.685331	2.33	8.0	3.3	4.8	0.6	9.4	9.4	nd
1285	164030.3-464617	10	250.126392	-46.771540	0.82	3.3	6.2	7.2	1.3	2.8	2.8	nd
1286	164030.3-465058	10	250.126498	-46.849673	0.93	3.1	4.4	3.3	2.9	2.6	2.6	...
1287	164030.7-464001	08	250.128093	-46.667164	9.02	8.3	2.3	0.0	2.7	9.3	9.3	nd
1288	164030.7-464520	07	250.128150	-46.755740	8.60	11.5	3.2	3.2	0.3	17.2	17.2	nd
1289	164030.8-470117	13	250.128560	-47.021613	1.71	6.8	5.5	7.4	0.4	6.9	6.9	...
1290	164031.0-462023	09	250.129182	-46.339855	4.37	8.7	1.9	3.8	0.0	10.7	10.7	...
1291	164031.0-464845	10	250.129396	-46.812666	0.61	2.1	8.5	0.0	8.8	2.2	2.2	...
1292	164031.5-462501	08	250.131358	-46.417002	2.63	6.9	4.2	3.6	2.5	7.4	7.4	nd
1293	164032.1-465518	13	250.134109	-46.921685	2.56	6.7	1.0	0.7	0.7	19.5	7.0	e
1294	164032.2-465343	13	250.134308	-46.895547	2.03	7.4	1.4	1.0	0.9	20.6	8.2	e,nd
1295	164032.8-463836	08	250.137047	-46.643490	3.24	6.8	2.4	3.6	0.0	6.8	6.8	nd
1296	164033.2-464359	07	250.138346	-46.733132	10.28	10.5	2.5	2.4	1.4	14.6	14.6	vp,nd
1297	164033.3-462700	08	250.138872	-46.450174	1.11	4.9	5.7	1.4	5.5	4.3	4.3	...
1298	164033.4-462026	09	250.139397	-46.340639	1.53	9.0	9.7	5.3	7.6	11.4	11.4	...
1299	164034.1-465728	13	250.142309	-46.957804	1.98	6.5	4.2	0.0	4.6	6.6	6.6	nd
1300	164034.3-464044	10	250.143296	-46.679099	3.15	8.2	3.0	1.5	2.4	9.9	9.9	vp,nd
1301	164035.5-462951	08	250.148144	-46.497512	0.54	2.0	7.5	1.2	7.5	2.1	2.1	...
1302	164035.6-470251	13	250.148673	-47.047700	2.55	8.3	3.8	5.4	0.7	9.6	9.6	...
1303	164035.7-464431	11	250.148924	-46.741976	7.38	8.5	2.4	0.9	2.1	10.1	10.1	nd
1304	164035.7-463520	08	250.149014	-46.589098	0.85	3.5	6.2	0.0	6.7	2.9	2.9	...
1305	164036.0-463021	08	250.150102	-46.506061	0.45	1.5	10.1	11.8	1.5	2.0	2.0	...
1306	164037.3-464636	10	250.155501	-46.776737	0.77	2.4	4.8	0.0	5.1	2.2	2.2	...
1307	164037.6-463716	08	250.156934	-46.621268	1.78	5.4	3.8	4.6	0.4	4.8	4.8	nd
1308	164038.0-464249	10	250.158570	-46.713696	1.90	6.0	2.4	3.3	0.3	6.0	6.0	vp,nd
1309	164038.7-463147	08	250.161386	-46.529904	—	0.3	9.5	0.5	10.5	102.0	2.0	c,e,s
1310	164038.8-464729	10	250.161757	-46.791485	0.55	1.5	8.3	8.3	3.2	2.0	2.0	...
1311	164038.8-462526	08	250.161969	-46.423976	1.53	6.4	5.4	3.8	3.8	6.6	6.6	...
1312	164038.9-463128	08	250.162319	-46.524682	0.58	0.5	4.3	1.7	3.8	2.0	2.0	...
1313	164039.0-464833	10	250.162716	-46.809256	0.58	0.8	5.4	6.2	0.6	2.0	2.0	...
1314	164040.0-464615	10	250.166783	-46.771109	0.62	2.6	9.6	8.5	5.2	2.3	2.3	nd
1315	164040.4-463929	11,07,08	250.168671	-46.658108	1.46	8.6;8.4;7.7	8.2	0.0	8.5	10.5;10.1;8.1	10.5;10.1;8.1	...;...;...
1316	164040.8-465539	10	250.170258	-46.927698	3.45	6.9	1.8	2.8	0.2	16.3	6.9	e,nd
1317	164042.6-465238	10	250.177645	-46.877327	1.44	3.9	3.5	4.1	0.8	3.2	3.2	...
1318	164043.0-463407	08	250.179195	-46.568882	0.87	2.5	4.4	6.0	0.0	2.4	2.4	...

Chandra Catalog: Detection and Localization (continued)

No.	Source (CXOU J)	ObsID (125**)	R.A. (deg)	Dec. (deg)	Unc. (arcsec)	Offset (arcmin)	Sig. FB	Sig. SB	Sig. HB	Radius (arcsec)	PSF (arcsec)	Flags
1319	164043.2-464943	10	250.180244	-46.828780	0.56	1.0	8.7	9.4	2.2	2.1	2.1	...
1320	164043.3-461859	09	250.180817	-46.316512	7.41	11.2	0.6	0.0	0.8	16.8	16.8	...
1321	164043.5-463135	08	250.181317	-46.526572	0.38	1.1	19.4	0.0	19.9	2.1	2.1	...
1322	164044.0-462838	08	250.183364	-46.477444	0.90	3.4	5.9	3.7	4.5	2.9	2.9	...
1323	164044.4-464502	10	250.185046	-46.750708	1.05	3.7	4.7	1.0	4.6	3.2	3.2	nd
1324	164044.8-463509	08	250.187083	-46.586085	0.72	3.6	7.4	3.0	6.7	3.0	3.0	...
1325	164045.5-465116	10	250.189736	-46.854630	0.69	2.5	3.3	1.0	3.1	8.5	2.4	e
1326	164045.5-464607	10	250.189760	-46.768642	0.58	2.7	11.8	0.0	12.4	2.4	2.4	vs,nd
1327	164045.6-462450	08	250.190274	-46.414127	3.51	7.1	3.0	0.0	3.5	7.8	7.8	...
1328	164045.9-463723	08	250.191356	-46.623061	2.21	5.7	3.5	0.0	4.1	5.3	5.3	nd
1329	164046.3-465508	10	250.193287	-46.918892	4.90	6.4	1.8	3.9	0.0	6.2	6.2	...
1330	164046.6-464436	10,07	250.194504	-46.743538	0.63	4.2;8.8	16.7	19.4	2.4	3.6;10.6	3.6;10.6	vl;vp,vl
1331	164046.8-465049	10	250.195248	-46.847116	0.83	2.1	5.0	1.2	4.7	2.3	2.3	...
1332	164047.1-464134	10	250.196299	-46.692945	3.27	7.2	3.0	4.9	0.0	8.0	8.0	nd
1333	164047.5-463545	07	250.198182	-46.596052	3.33	8.3	1.8	0.0	2.5	9.9	9.9	nd
1334	164048.4-462458	08	250.201682	-46.416151	2.47	7.1	2.9	0.8	2.7	7.8	7.8	...
1335	164048.5-463500	08	250.202238	-46.583608	0.77	3.7	6.6	0.7	6.7	3.1	3.1	vp,nd
1336	164049.4-465159	10	250.205965	-46.866421	0.95	3.4	4.9	5.4	1.1	2.8	2.8	...
1337	164050.5-464055	10,07	250.210724	-46.681950	1.96	7.9;6.8	6.5	4.9	4.8	9.3;7.0	9.3;7.0	...;...
1338	164050.9-462806	08	250.212495	-46.468433	1.08	4.4	6.0	5.8	3.0	3.8	3.8	...
1339	164051.6-465222	10	250.215362	-46.872784	0.94	3.9	5.7	0.0	6.1	3.2	3.2	...
1340	164052.5-465606	10	250.219114	-46.935065	1.75	7.5	5.6	6.8	1.6	7.8	7.8	vp
1341	164053.4-465408	10	250.222802	-46.902255	1.21	5.6	7.0	2.8	6.3	5.1	5.1	...
1342	164053.8-463825	07	250.224357	-46.640533	2.82	6.3	2.6	4.4	0.0	6.3	6.3	nd
1343	164054.6-464422	10	250.227547	-46.739632	1.26	4.8	4.6	6.2	0.3	4.2	4.2	nd
1344	164055.5-465257	10	250.231561	-46.882638	1.50	4.7	3.5	0.0	4.0	3.9	3.9	...
1345	164058.0-463843	08	250.241701	-46.645305	2.27	7.7	3.8	0.4	3.9	8.3	8.3	...
1346	164100.2-465123	10	250.251218	-46.856564	1.73	3.9	3.5	3.7	1.1	3.3	3.3	...
1347	164100.5-464028	07	250.252410	-46.674721	2.01	5.0	2.2	1.7	1.4	11.4	4.3	e,nd
1348	164100.9-465205	10	250.254132	-46.868313	1.39	4.5	3.8	0.0	4.2	3.8	3.8	...
1349	164101.0-463751	07	250.254456	-46.631101	3.77	5.3	4.0	5.1	0.7	4.7	4.7	nd
1350	164101.4-462517	08	250.256227	-46.421495	2.69	7.8	0.3	0.5	0.0	20.9	8.9	e,vp
1351	164101.6-462618	08	250.256808	-46.438375	1.59	7.0	5.8	4.3	3.9	7.5	7.5	...
1352	164102.5-462937	08	250.260473	-46.493876	2.10	4.9	2.4	4.1	0.0	4.2	4.2	...
1353	164102.7-463609	07	250.261283	-46.602527	1.81	5.9	4.6	3.3	3.2	5.7	5.7	vs,nd
1354	164103.3-465416	10	250.263919	-46.904563	2.17	6.5	3.2	3.3	1.5	6.3	6.3	...
1355	164104.5-463900	07,08	250.268784	-46.650131	1.41	4.4;8.6	5.8	3.0	5.1	3.7;10.0	3.7;10.0	...;...
1356	164104.9-463156	08	250.270737	-46.532492	0.96	4.8	6.9	4.0	5.5	4.1	4.1	vp,nd
1357	164105.1-464027	07	250.271627	-46.674267	1.20	4.2	4.5	3.0	3.3	3.6	3.6	nd
1358	164105.5-465108	10	250.273101	-46.852330	0.56	4.5	28.4	25.1	14.4	3.8	3.8	...
1359	164106.2-464259	10,07	250.275955	-46.716393	1.52	7.0;5.1	5.1	7.0	0.0	7.5;4.4	7.5;4.4	...;...
1360	164107.1-464129	07	250.279865	-46.691612	1.53	4.2	3.0	3.3	0.8	3.5	3.5	nd
1361	164107.8-463638	07	250.282856	-46.610645	2.13	4.9	2.6	0.5	2.5	4.2	4.2	nd
1362	164109.9-465454	10	250.291489	-46.915232	3.57	7.6	3.5	0.7	2.3	19.5	8.1	e

Chandra Catalog: Detection and Localization (continued)

No.	Source (CXOU J)	ObsID (125**)	R.A. (deg)	Dec. (deg)	Unc. (arcsec)	Offset (arcmin)	Sig. FB	Sig. SB	Sig. HB	Radius (arcsec)	PSF (arcsec)	Flags
1363	164114.9-463133	08,07	250.312134	-46.526009	0.81	6.5;8.6	15.0	17.8	2.6	6.5;10.8	6.5;10.8	vs;...
1364	164114.9-463256	07	250.312448	-46.549069	3.39	7.3	1.9	0.8	1.6	8.0	8.0	...
1365	164116.1-463231	07	250.317302	-46.542007	2.44	7.6	4.2	4.0	2.4	8.7	8.7	nd
1366	164116.7-465113	10	250.319661	-46.853873	1.66	6.2	5.8	1.4	5.5	6.1	6.1	...
1367	164117.4-463326	07,08	250.322678	-46.557274	1.08	6.7;7.1	10.8	12.1	4.2	7.1;7.4	7.1;7.4	...;...
1368	164117.6-464320	10,07	250.323639	-46.722279	0.71	8.0;4.1	12.3	15.6	0.0	9.4;3.4	9.4;3.4	...;...
1369	164118.1-465449	10	250.325621	-46.913805	1.67	8.5	8.3	10.3	1.4	9.9	9.9	...
1370	164118.7-462855	08	250.328178	-46.482114	6.60	7.7	0.7	2.0	0.0	8.6	8.6	...
1371	164119.4-464511	07	250.331166	-46.753109	2.74	5.7	4.0	0.0	4.4	5.2	5.2	...
1372	164122.7-463839	07	250.344617	-46.644439	0.56	1.6	13.2	12.7	5.4	2.1	2.1	...
1373	164122.8-464116	07	250.345066	-46.688024	0.76	1.9	4.3	0.0	4.5	2.2	2.2	...
1374	164122.8-464529	10,07	250.345276	-46.758179	0.65	7.5;5.8	35.4	28.5	22.5	8.3;5.4	8.3;5.4	vs,vl;vl
1375	164124.0-463144	07	250.350050	-46.529007	4.49	8.1	1.5	0.2	1.4	9.7	9.7	nd
1376	164124.1-464636	10	250.350723	-46.776759	1.28	7.3	8.7	9.8	2.4	7.9	7.9	vs
1377	164124.8-463125	08	250.353549	-46.523837	5.04	8.2	1.8	2.7	0.0	9.5	9.5	...
1378	164125.3-463943	07	250.355769	-46.662014	0.62	0.7	5.4	6.6	0.5	2.0	2.0	...
1379	164130.8-463048	08	250.378682	-46.513559	0.91	9.3	30.4	27.9	13.7	11.8	11.8	...
1380	164131.4-463935	07	250.380840	-46.659726	0.61	0.4	6.9	8.3	0.0	2.0	2.0	...
1381	164133.3-464815	07	250.389093	-46.804331	3.57	8.5	2.5	0.0	2.8	9.8	9.8	nd
1382	164133.7-463906	07	250.390633	-46.651880	0.56	1.0	9.6	10.8	1.8	2.0	2.0	vp
1383	164133.9-463452	07	250.391633	-46.581381	1.43	5.0	4.7	1.4	4.4	4.4	4.4	...
1384	164134.8-464024	07	250.395031	-46.673595	0.74	1.1	1.1	2.3	0.0	6.7	2.1	e
1385	164134.8-464003	07	250.395059	-46.667532	0.63	0.9	5.6	4.2	3.5	2.1	2.1	...
1386	164135.0-463935	07	250.396141	-46.659925	0.62	1.0	2.0	2.4	0.8	19.0	2.1	e
1387	164135.9-464502	10	250.399620	-46.750735	11.20	9.7	1.7	1.5	0.9	13.0	13.0	nd
1388	164137.1-463346	07	250.404679	-46.562828	1.08	6.1	9.0	10.8	1.2	6.2	6.2	...
1389	164137.4-463359	07	250.405994	-46.566409	1.90	6.0	3.9	4.6	1.0	5.9	5.9	...
1390	164137.4-463724	07	250.406237	-46.623343	1.14	2.7	2.6	3.9	0.0	2.4	2.4	...
1391	164137.6-464538	07,10	250.407043	-46.760651	1.31	6.0;9.8	7.1	0.0	7.8	5.7;13.1	5.7;13.1	...;...
1392	164140.0-464013	07	250.416784	-46.670363	0.84	1.8	3.2	4.4	0.0	2.2	2.2	...
1393	164140.3-464134	07	250.418077	-46.692890	0.97	2.6	1.7	3.0	0.0	6.2	2.4	e,m2
1394	164140.4-464901	07	250.418474	-46.817172	11.14	9.4	0.0	2.6	0.0	11.7	11.7	...
1395	164140.4-464128	07	250.418634	-46.691140	1.10	2.5	2.4	2.6	0.9	5.1	2.4	e,m3
1396	164145.4-464053	07	250.439547	-46.681424	2.53	2.9	0.4	0.0	0.5	2.5	2.5	...
1397	164145.9-464050	07	250.441578	-46.680794	1.20	3.0	3.7	3.6	2.0	14.7	2.5	e,s
1398	164146.7-464021	07	250.444715	-46.672536	1.23	3.0	3.2	4.6	0.0	2.5	2.5	...
1399	164147.6-464549	07	250.448379	-46.763846	2.51	6.8	3.7	5.0	0.3	6.8	6.8	...
1400	164150.5-463523	07	250.460798	-46.589851	3.46	5.7	2.5	0.2	2.5	5.4	5.4	...
1401	164154.0-464147	07	250.475362	-46.696503	1.34	4.7	5.6	7.6	0.0	4.0	4.0	...
1402	164155.7-464652	07	250.482121	-46.781225	4.50	8.4	2.3	2.7	0.7	9.6	9.6	...
1403	164156.1-463515	07	250.483920	-46.587708	3.46	6.4	3.6	4.9	0.2	6.6	6.6	...
1404	164201.4-463625	07	250.505872	-46.607008	1.70	6.4	5.1	1.6	4.8	6.5	6.5	...
1405	164202.6-464534	07	250.510885	-46.759611	1.44	8.1	10.2	4.6	9.0	9.1	9.1	...
1406	164203.0-463544	07	250.512791	-46.595728	1.84	7.0	2.3	0.0	0.5	25.8	7.5	e

Chandra Catalog: Detection and Localization (continued)

No.	Source (CXOU J)	ObsID (125**)	R.A. (deg)	Dec. (deg)	Unc. (arcsec)	Offset (arcmin)	Sig. FB	Sig. SB	Sig. HB	Radius (arcsec)	PSF (arcsec)	Flags
1407	164203.4-464427	07	250.514284	-46.740924	1.06	7.5	14.5	13.6	6.6	7.8	7.8	...
1408	164204.5-464341	07	250.519111	-46.728140	1.05	7.2	12.9	2.9	12.7	7.4	7.4	...
1409	164206.8-464420	07	250.528699	-46.739107	2.43	7.9	3.7	1.7	3.2	8.6	8.6	...
1410	164207.8-464505	07	250.532892	-46.751639	5.39	8.5	3.1	3.1	1.5	9.8	9.8	...
1411	164216.6-464150	07	250.569399	-46.697474	4.16	8.3	3.4	5.3	0.0	9.7	9.7	...
1412	164218.9-463543	07	250.578793	-46.595525	3.47	9.4	3.5	3.4	1.7	12.2	12.2	vs
1413	164220.2-463850	07	250.584341	-46.647449	3.46	8.7	3.3	4.5	0.4	10.7	10.7	...
1414	164221.0-463655	07	250.587592	-46.615401	11.94	9.3	0.0	0.0	0.0	11.9	11.9	m1
1415	164222.7-463709	07	250.594905	-46.619428	7.56	9.5	1.6	2.7	0.1	12.4	12.4	m1

A.2 Photometry Table

(1) NARCS catalog source number.
(2–4) Net source counts in the full 0.5–10 keV band and corresponding 1σ errors, calculated as described in §2.2.4. For cases in which the estimated background counts in a source aperture region were determined to be greater than or equal to the total number of counts in the source region, then the catalog presents the 90% upper confidence limit to the net source counts based on the method described in Kraft et al. (1991); in such cases, the error columns are left blank. For sources detected in multiple observations, net counts from different observations were added together and errors combined in quadrature.
(5–7) Net source counts in soft 0.5–2 keV band. Same details as discussed for Columns 2–4 apply.
(8–10) Net source counts in hard 2–10 keV band. Same details as discussed for Columns 2–4 apply.
(11–13) Photon flux in the full 0.5–10 keV band and corresponding 1σ errors. The photon flux was calculated by dividing the net counts by the exposure time and the mean effective area within the source region. For sources with zero or negative net counts, the catalog provides the 90% upper limit on the photon flux and leaves the error columns blank. For sources detected in multiple observations, the average photon fluxes are reported; if a source was found to be variable between observations (flagged as "vl") then its photon fluxes from individual observations were simply averaged, but otherwise its photon fluxes were weight-averaged.
(14–16) Photon flux in the soft 0.5–10 keV band. Same details as discussed for Columns 11–13 apply.
(17–19) Photon flux in the hard 2–10 keV band. Same details as discussed for Columns 11–13 apply.
(20–21) The median energy of the source and corresponding 1σ error. It is determined from the total counts (not background corrected) in the source region. For sources detected in multiple observations, the simple average of the energies from individual observations is reported if a source is found to be variable between observations or the weighted-average is reported otherwise.
(22–23) The energy below which 25% of the total source counts reside and corresponding 1σ error. Same details as discussed for Columns 20–21 apply.
(24–25) The energy below which 75% of the total source counts reside and corresponding 1σ error. Same details as discussed for Columns 20–21 apply.
(26–28) The energy flux in the full 0.5–10 keV band and corresponding 1σ errors. This estimate of the energy flux is calculated by multiplying the full band photon flux and the median energy of the source provided in the catalog. In cases where only an upper limit to the photon flux is available, the 90% upper limit to the energy flux is reported and the error columns are left blank.
(29) Photometric flags. If the photometric values provided for a source are 90% upper limits in the full, soft, or hard energy bands, this column displays an F, S, or H, respectively.
(30) The spectral group defined using quantile diagrams to which the source belongs. See

§2.2.8 for details about quantile analysis and the spectral groups defined in this work.

Table A.2: *Chandra* Catalog of Point and Extended Sources: Photometry

No.	C_{net} FB	C_{net} SB	C_{net} HB	$f_{\rm ph}$FB(10^{-6} cm^{-2} s^{-1})	$f_{\rm ph}$SB(10^{-6} cm^{-2} s^{-1})	$f_{\rm ph}$HB(10^{-6} cm^{-2} s^{-1})	E_{50} (keV)	E_{25} (keV)	E_{75} (keV)	f_X(10^{-14}erg cm^{-2} s^{-1})	Phot. Flag	Quantile Group
(1)	(2-4)	(5-7)	(8-10)	(11-13)	(14-16)	(17-19)	(20-21)	(22-23)	(24-25)	(26-28)	(29)	(30)
1	16^{+7}_{-6}	6^{+4}_{-3}	10^{+6}_{-5}	$3.76^{+1.57}_{-1.32}$	$0.76^{+0.55}_{-0.40}$	$2.47^{+1.39}_{-1.13}$	2.9±1.8	1.6±0.8	5.6±2.4	$1.75^{+1.31}_{-1.25}$	- - -	C
2	47^{+9}_{-8}	37^{+7}_{-6}	10^{+6}_{-5}	$10.55^{+1.99}_{-1.76}$	$4.68^{+0.93}_{-0.80}$	$2.28^{+1.31}_{-1.07}$	1.4±0.1	1.0±0.1	1.8±0.5	$2.35^{+0.49}_{-0.44}$	- - -	A
3	9^{+5}_{-4}	3	9^{+5}_{-4}	$3.48^{+2.15}_{-1.71}$	0.69	$3.88^{+2.14}_{-1.69}$	5.4±0.9	4.5±1.3	6.1±0.9	$3.03^{+1.93}_{-1.56}$	- S -	D
4	36^{+8}_{-7}	2^{+3}_{-2}	34^{+7}_{-6}	$7.95^{+1.69}_{-1.46}$	$0.28^{+0.40}_{-0.24}$	$7.60^{+1.66}_{-1.42}$	4.6±0.3	3.7±0.3	5.2±0.5	$5.90^{+1.33}_{-1.17}$	- - -	D
5	13^{+6}_{-5}	13^{+5}_{-4}	6	$2.85^{+1.36}_{-1.12}$	$1.70^{+0.65}_{-0.51}$	1.32	1.0±0.1	0.9±0.2	1.1±0.1	$0.44^{+0.21}_{-0.18}$	- - H	A
6	22^{+7}_{-6}	4^{+4}_{-2}	19^{+6}_{-5}	$6.00^{+1.82}_{-1.53}$	$0.59^{+0.55}_{-0.36}$	$5.07^{+1.71}_{-1.41}$	3.0±0.7	2.2±0.4	5.7±1.2	$2.90^{+1.10}_{-0.99}$	- - -	C
7	20^{+6}_{-5}	12^{+5}_{-3}	9^{+4}_{-3}	$4.70^{+1.35}_{-1.10}$	$1.53^{+0.60}_{-0.46}$	$2.08^{+1.04}_{-0.78}$	1.8±0.6	1.5±0.1	3.5±0.5	$1.37^{+0.57}_{-0.53}$	- - -	B
8	8^{+5}_{-4}	7^{+4}_{-3}	1^{+4}_{-1}	$1.82^{+1.17}_{-0.92}$	$0.85^{+0.51}_{-0.37}$	$0.33^{+0.93}_{-0.33}$	1.6±0.9	1.4±0.3	1.8±3.8	$0.47^{+0.40}_{-0.35}$	- - -	A
9	7	2^{+3}_{-2}	5	1.74	$0.27^{+0.48}_{-0.27}$	1.23	5.2±4.8	2.9±7.1	7.6±7.1	1.46	F - H	C
10	6^{+4}_{-3}	1^{+2}_{-1}	5^{+4}_{-2}	$1.11^{+0.74}_{-0.50}$	$0.08^{+0.26}_{-0.08}$	$0.98^{+0.72}_{-0.47}$	5.1±0.8	4.4±1.4	5.4±0.3	$0.91^{+0.62}_{-0.44}$	- - -	E
11	9^{+5}_{-4}	3^{+3}_{-2}	6^{+5}_{-4}	$2.25^{+1.32}_{-1.06}$	$0.39^{+0.47}_{-0.30}$	$1.58^{+1.19}_{-0.92}$	2.3±0.3	1.9±0.8	2.5±1.2	$0.82^{+0.50}_{-0.41}$	- - -	E
12	182^{+15}_{-14}	68^{+10}_{-9}	114^{+13}_{-12}	$22.55^{+1.83}_{-1.77}$	$5.84^{+0.70}_{-0.60}$	$14.31^{+1.62}_{-1.44}$	2.7±0.2	1.7±0.1	3.9±0.2	$9.59^{+1.11}_{-1.09}$	- - -	C
13	9^{+4}_{-3}	2^{+3}_{-1}	7^{+4}_{-3}	$1.77^{+0.82}_{-0.61}$	$0.21^{+0.30}_{-0.14}$	$1.44^{+0.77}_{-0.55}$	3.2±0.3	3.0±0.7	3.6±0.3	$0.91^{+0.43}_{-0.32}$	- - -	E
14	9^{+5}_{-4}	3^{+3}_{-2}	6^{+5}_{-4}	$1.87^{+1.14}_{-0.92}$	$0.36^{+0.42}_{-0.27}$	$1.28^{+1.03}_{-0.80}$	7.7±3.9	1.8±2.2	9.3±1.6	$2.29^{+1.83}_{-1.62}$	- - -	C
15	5^{+4}_{-2}	2^{+3}_{-1}	3^{+3}_{-2}	$1.08^{+0.73}_{-0.48}$	$0.22^{+0.31}_{-0.15}$	$0.72^{+0.66}_{-0.40}$	2.4±0.6	1.9±0.3	3.2±0.5	$0.42^{+0.30}_{-0.21}$	- - -	E
16	8^{+4}_{-3}	3	8^{+4}_{-3}	$1.85^{+0.97}_{-0.71}$	0.35	$1.92^{+0.99}_{-0.72}$	4.9±0.5	4.5±0.6	5.8±0.4	$1.46^{+0.78}_{-0.58}$	- S -	E
17	8^{+4}_{-3}	3	8^{+4}_{-3}	$1.59^{+0.78}_{-0.57}$	0.29	$1.65^{+0.80}_{-0.58}$	3.3±0.3	3.1±0.4	3.6±0.6	$0.84^{+0.42}_{-0.31}$	- S -	E
18	12	4	11	2.77	0.56	2.54	5.2±4.8	2.9±7.1	7.6±7.1	2.33	F S H	C
19	12^{+5}_{-4}	8^{+4}_{-3}	5^{+3}_{-2}	$2.33^{+0.88}_{-0.67}$	$0.86^{+0.43}_{-0.31}$	$0.86^{+0.65}_{-0.41}$	1.8±0.3	1.1±0.2	2.1±0.4	$0.68^{+0.28}_{-0.23}$	- - -	B
20	22^{+8}_{-6}	17^{+6}_{-5}	5^{+6}_{-3}	$2.90^{+0.95}_{-0.75}$	$1.89^{+0.45}_{-0.33}$	$0.54^{+0.61}_{-0.34}$	1.3±0.2	1.0±0.1	1.8±0.4	$0.59^{+0.21}_{-0.18}$	- - -	B
21	58^{+9}_{-8}	55^{+8}_{-7}	3^{+3}_{-2}	$11.69^{+1.78}_{-1.57}$	$6.35^{+0.98}_{-0.86}$	$0.63^{+0.71}_{-0.45}$	1.2±0.1	1.0±0.1	1.5±0.1	$2.25^{+0.38}_{-0.34}$	- - -	A
22	6^{+4}_{-2}	3	6^{+4}_{-2}	$1.10^{+0.72}_{-0.47}$	0.30	$1.14^{+0.73}_{-0.48}$	5.1±0.9	4.9±0.7	7.0±0.7	$0.90^{+0.61}_{-0.42}$	- S -	D
23	7^{+4}_{-3}	3	7^{+4}_{-3}	$1.48^{+0.85}_{-0.58}$	0.35	$1.53^{+0.87}_{-0.59}$	4.8±0.5	4.5±0.3	5.6±0.6	$1.15^{+0.67}_{-0.46}$	- S -	E
24	4^{+3}_{-2}	4^{+3}_{-2}	3	$1.13^{+0.97}_{-0.58}$	$0.70^{+0.56}_{-0.34}$	0.78	1.2±0.2	1.0±0.1	1.4±0.1	$0.22^{+0.19}_{-0.12}$	- - H	A
25	7^{+4}_{-3}	8^{+4}_{-3}	2	$1.49^{+0.84}_{-0.60}$	$0.96^{+0.49}_{-0.35}$	0.50	1.0±0.1	0.8±0.1	1.1±0.1	$0.25^{+0.14}_{-0.11}$	- - H	A
26	3^{+5}_{-3}	5^{+4}_{-3}	4	$0.60^{+1.03}_{-0.60}$	$0.63^{+0.48}_{-0.33}$	0.97	1.1±0.3	0.9±0.2	1.3±0.1	$0.11^{+0.19}_{-0.11}$	- - H	A
27	9^{+6}_{-4}	7^{+4}_{-3}	2^{+4}_{-2}	$2.32^{+1.36}_{-1.09}$	$0.96^{+0.58}_{-0.42}$	$0.63^{+1.09}_{-0.63}$	1.5±0.2	1.3±0.2	1.7±0.5	$0.56^{+0.34}_{-0.28}$	- - -	A
28	9^{+4}_{-3}	4^{+3}_{-2}	5^{+4}_{-2}	$1.79^{+0.83}_{-0.62}$	$0.43^{+0.36}_{-0.21}$	$1.06^{+0.71}_{-0.47}$	2.1±1.1	1.9±0.2	5.7±1.6	$0.61^{+0.43}_{-0.39}$	- - -	B
29	46^{+8}_{-7}	42^{+8}_{-6}	4^{+3}_{-2}	$9.01^{+1.55}_{-1.34}$	$4.72^{+0.85}_{-0.73}$	$0.85^{+0.68}_{-0.43}$	1.1±0.1	0.9±0.1	1.3±0.1	$1.54^{+0.28}_{-0.24}$	- - -	A
30	6^{+5}_{-4}	3^{+3}_{-2}	3^{+4}_{-3}	$1.60^{+1.33}_{-1.03}$	$0.39^{+0.50}_{-0.31}$	$0.92^{+1.19}_{-0.88}$	5.8±2.6	1.7±2.1	6.0±1.7	$1.49^{+1.40}_{-1.16}$	- - -	C
31	7^{+4}_{-3}	6^{+4}_{-2}	2^{+3}_{-1}	$1.40^{+0.75}_{-0.54}$	$0.65^{+0.40}_{-0.26}$	$0.30^{+0.51}_{-0.25}$	1.4±0.4	1.2±0.3	1.7±0.8	$0.30^{+0.19}_{-0.15}$	- - -	A
32	6^{+4}_{-3}	1^{+2}_{-1}	5^{+4}_{-2}	$1.24^{+0.75}_{-0.51}$	$0.09^{+0.27}_{-0.09}$	$1.10^{+0.73}_{-0.48}$	3.0±2.3	2.2±0.8	7.7±2.4	$0.59^{+0.59}_{-0.52}$	- - -	C
33	52^{+9}_{-8}	12^{+5}_{-4}	40^{+8}_{-7}	$17.88^{+3.15}_{-2.79}$	$2.24^{+0.94}_{-0.73}$	$14.20^{+2.89}_{-2.52}$	3.4±0.4	2.4±0.4	5.0±0.3	$9.69^{+1.99}_{-1.82}$	- - -	C
34	10^{+6}_{-5}	4^{+4}_{-2}	6^{+5}_{-4}	$3.35^{+1.87}_{-1.52}$	$0.79^{+0.67}_{-0.45}$	$1.99^{+1.67}_{-1.30}$	2.1±0.9	1.8±0.6	4.0±1.0	$1.13^{+0.80}_{-0.71}$	- - -	B
35	6^{+5}_{-4}	4^{+4}_{-2}	2^{+4}_{-2}	$1.16^{+1.02}_{-0.81}$	$0.48^{+0.41}_{-0.27}$	$0.33^{+0.88}_{-0.33}$	1.7±0.5	1.7±0.3	2.4±0.5	$0.32^{+0.29}_{-0.24}$	- - -	A
36	6^{+4}_{-2}	3	6^{+4}_{-2}	$1.07^{+0.69}_{-0.46}$	0.30	$1.10^{+0.71}_{-0.47}$	4.4±1.6	3.9±0.8	7.0±2.0	$0.76^{+0.56}_{-0.42}$	- S -	D
37	7^{+4}_{-3}	2^{+3}_{-1}	6^{+4}_{-3}	$1.52^{+0.84}_{-0.61}$	$0.20^{+0.31}_{-0.15}$	$1.20^{+0.79}_{-0.54}$	3.2±0.6	2.7±0.6	3.7±0.8	$0.78^{+0.46}_{-0.35}$	- - -	E
38	122^{+11}_{-11}	2^{+3}_{-1}	120^{+11}_{-11}	$24.35^{+2.21}_{-2.21}$	$0.22^{+0.31}_{-0.15}$	$24.45^{+2.24}_{-2.24}$	4.4±0.1	3.5±0.1	5.4±0.2	$17.20^{+1.63}_{-1.63}$	- - -	D

No.	C_{net} FB	C_{net} SB	C_{net} HB	$f_{\rm ph}$FB(10^{-6} cm^{-2} s^{-1})	$f_{\rm ph}$SB(10^{-6} cm^{-2} s^{-1})	$f_{\rm ph}$HB(10^{-6} cm^{-2} s^{-1})	E_{50} (keV)	E_{25} (keV)	E_{75} (keV)	f_X(10^{-14}erg cm^{-2} s^{-1})	Phot. Flag	Quantile Group
39	14^{+5}_{-4}	3^{+3}_{-2}	12^{+5}_{-3}	$2.75^{+0.95}_{-0.74}$	$0.32^{+0.33}_{-0.18}$	$2.24^{+0.89}_{-0.67}$	2.1±0.4	2.1±0.2	3.5±0.7	$0.93^{+0.37}_{-0.31}$	- - -	A
40	138^{+12}_{-12}	31^{+7}_{-6}	108^{+11}_{-11}	$30.72^{+2.67}_{-2.67}$	$3.89^{+0.85}_{-0.72}$	$24.40^{+2.40}_{-2.40}$	3.4±0.2	2.1±0.2	4.3±0.2	$16.77^{+1.75}_{-1.75}$	- - -	C
41	9^{+5}_{-4}	8^{+4}_{-3}	1^{+4}_{-1}	$1.91^{+1.06}_{-0.82}$	$0.95^{+0.50}_{-0.36}$	$0.25^{+0.78}_{-0.25}$	1.5±0.3	1.3±0.2	1.7±1.1	$0.45^{+0.26}_{-0.21}$	- - -	A
42	16^{+6}_{-5}	2	18^{+6}_{-5}	$3.49^{+1.43}_{-1.19}$	0.29	$4.07^{+1.46}_{-1.22}$	5.3±0.6	4.3±0.6	6.1±0.5	$2.96^{+1.25}_{-1.06}$	- S -	D
43	16^{+5}_{-4}	3	17^{+5}_{-4}	$3.27^{+1.04}_{-0.82}$	0.29	$3.37^{+1.06}_{-0.84}$	4.5±0.5	4.1±0.2	6.3±0.9	$2.34^{+0.79}_{-0.64}$	- S -	D
44	6^{+4}_{-3}	4^{+3}_{-2}	2^{+3}_{-2}	$2.47^{+1.73}_{-1.25}$	$0.87^{+0.79}_{-0.47}$	$0.97^{+1.43}_{-0.88}$	1.6±0.5	1.4±0.3	2.3±0.5	$0.63^{+0.48}_{-0.37}$	- - -	A
45	9^{+4}_{-3}	5^{+4}_{-2}	3^{+3}_{-2}	$4.89^{+2.42}_{-1.81}$	$1.73^{+1.13}_{-0.74}$	$1.91^{+1.90}_{-1.20}$	1.9±0.7	1.6±0.3	2.1±1.5	$1.52^{+0.94}_{-0.80}$	- - -	A
46	22^{+6}_{-5}	5^{+3}_{-2}	17^{+5}_{-4}	$4.32^{+1.14}_{-0.93}$	$0.55^{+0.38}_{-0.24}$	$3.44^{+1.05}_{-0.84}$	3.4±0.4	2.6±0.5	4.4±1.2	$2.34^{+0.69}_{-0.59}$	- - -	E
47	67^{+10}_{-8}	38^{+7}_{-6}	29^{+7}_{-6}	$17.03^{+2.43}_{-2.17}$	$5.52^{+1.06}_{-0.91}$	$7.48^{+1.78}_{-1.50}$	1.8±0.1	1.4±0.1	3.0±0.5	$4.98^{+0.80}_{-0.73}$	- - -	B
48	17^{+7}_{-6}	9^{+5}_{-4}	8^{+6}_{-5}	$5.37^{+2.23}_{-1.90}$	$1.67^{+0.84}_{-0.65}$	$2.44^{+1.88}_{-1.54}$	1.9±0.6	1.5±0.2	3.2±1.1	$1.61^{+0.84}_{-0.76}$	- - -	B
49	18^{+6}_{-5}	14^{+5}_{-4}	4^{+4}_{-3}	$3.86^{+1.27}_{-1.04}$	$1.72^{+0.61}_{-0.47}$	$0.85^{+0.88}_{-0.63}$	1.3±0.3	1.1±0.1	1.9±0.9	$0.82^{+0.32}_{-0.28}$	- - -	A
50	5^{+4}_{-2}	1^{+2}_{-1}	5^{+3}_{-2}	$1.04^{+0.68}_{-0.45}$	$0.10^{+0.26}_{-0.09}$	$0.89^{+0.66}_{-0.42}$	5.5±1.9	2.1±1.3	6.0±1.7	$0.93^{+0.69}_{-0.51}$	- - -	C
51	7^{+5}_{-4}	4^{+4}_{-2}	2^{+4}_{-2}	$1.38^{+1.11}_{-0.88}$	$0.50^{+0.44}_{-0.30}$	$0.52^{+0.96}_{-0.52}$	7.5±5.2	0.7±3.1	8.6±2.0	$1.67^{+1.76}_{-1.56}$	- - -	C
52	42^{+8}_{-7}	10^{+4}_{-3}	32^{+7}_{-6}	$9.71^{+1.81}_{-1.57}$	$1.35^{+0.59}_{-0.44}$	$7.51^{+1.64}_{-1.39}$	2.9±0.2	2.0±0.2	3.5±0.3	$4.47^{+0.91}_{-0.81}$	- - -	E
53	16^{+6}_{-5}	10^{+5}_{-3}	6^{+5}_{-4}	$3.44^{+1.37}_{-1.14}$	$1.24^{+0.56}_{-0.43}$	$1.27^{+1.12}_{-0.88}$	1.9±0.4	1.7±0.3	3.1±0.7	$1.03^{+0.46}_{-0.40}$	- - -	A
54	13^{+5}_{-4}	3^{+3}_{-2}	11^{+4}_{-3}	$2.63^{+0.95}_{-0.73}$	$0.32^{+0.33}_{-0.18}$	$2.11^{+0.88}_{-0.66}$	2.8±0.3	2.2±0.4	3.3±1.1	$1.16^{+0.44}_{-0.35}$	- - -	E
55	8^{+5}_{-4}	7^{+4}_{-3}	1^{+4}_{-1}	$1.86^{+1.20}_{-0.95}$	$0.93^{+0.54}_{-0.39}$	$0.24^{+0.93}_{-0.24}$	1.1±1.3	1.0±0.3	1.3±4.2	$0.31^{+0.45}_{-0.43}$	- - -	A
56	7^{+5}_{-4}	3^{+3}_{-2}	5^{+5}_{-4}	$1.69^{+1.26}_{-1.00}$	$0.34^{+0.43}_{-0.26}$	$1.11^{+1.17}_{-0.90}$	3.7±2.4	1.7±1.1	5.8±3.8	$0.99^{+0.99}_{-0.88}$	- - -	C
57	22^{+7}_{-6}	3^{+3}_{-2}	19^{+6}_{-5}	$4.75^{+1.49}_{-1.26}$	$0.35^{+0.42}_{-0.27}$	$4.22^{+1.42}_{-1.19}$	3.1±0.4	2.4±0.4	4.2±0.4	$2.34^{+0.81}_{-0.71}$	- - -	E
58	12^{+5}_{-4}	3	12^{+5}_{-4}	$2.77^{+1.17}_{-0.93}$	0.43	$2.82^{+1.17}_{-0.92}$	5.6±0.7	4.3±0.9	6.5±1.5	$2.50^{+1.11}_{-0.90}$	- S -	D
59	22^{+6}_{-5}	3	23^{+6}_{-5}	$4.41^{+1.16}_{-0.94}$	0.29	$4.53^{+1.18}_{-0.96}$	3.9±0.5	3.1±0.3	5.3±0.5	$2.76^{+0.81}_{-0.70}$	- S -	D
60	5^{+4}_{-3}	2	6^{+4}_{-3}	$1.41^{+1.02}_{-0.69}$	0.36	$1.54^{+1.04}_{-0.71}$	4.1±1.3	3.8±0.5	6.0±1.3	$0.93^{+0.74}_{-0.55}$	- S -	D
61	7^{+4}_{-3}	2	8^{+4}_{-3}	$1.49^{+0.91}_{-0.69}$	0.27	$1.73^{+0.93}_{-0.70}$	4.9±1.1	2.7±0.9	5.2±0.7	$1.16^{+0.76}_{-0.60}$	- S -	C
62	12^{+5}_{-4}	2^{+3}_{-2}	10^{+5}_{-4}	$2.62^{+1.12}_{-0.88}$	$0.27^{+0.37}_{-0.20}$	$2.19^{+1.06}_{-0.81}$	3.2±0.9	2.1±0.9	5.2±2.2	$1.33^{+0.69}_{-0.59}$	- - -	C
63	5^{+4}_{-2}	4^{+3}_{-2}	2^{+3}_{-1}	$1.16^{+0.77}_{-0.51}$	$0.48^{+0.39}_{-0.24}$	$0.34^{+0.58}_{-0.28}$	1.5±1.2	0.9±0.4	3.3±1.4	$0.29^{+0.30}_{-0.26}$	- - -	B
64	5^{+4}_{-2}	5^{+3}_{-2}	4	$1.06^{+0.72}_{-0.48}$	$0.56^{+0.39}_{-0.25}$	0.78	1.7±0.3	1.5±0.4	1.9±0.2	$0.28^{+0.20}_{-0.14}$	- - H	A
65	5^{+4}_{-2}	5^{+3}_{-2}	4	$1.06^{+0.72}_{-0.48}$	$0.56^{+0.39}_{-0.25}$	0.78	1.1±0.2	1.0±0.1	1.3±0.3	$0.19^{+0.13}_{-0.09}$	- - H	A
66	3^{+7}_{-3}	1^{+4}_{-1}	1^{+6}_{-1}	$0.76^{+1.97}_{-0.76}$	$0.22^{+0.61}_{-0.22}$	$0.37^{+1.83}_{-0.37}$	1.0±9.0	0.8±4.2	9.6±8.2	$0.12^{+1.14}_{-1.11}$	- - -	B
67	5^{+4}_{-3}	2	5^{+4}_{-3}	$0.93^{+0.77}_{-0.52}$	0.27	$1.04^{+0.78}_{-0.53}$	3.7±1.7	3.1±0.6	6.2±2.1	$0.55^{+0.52}_{-0.40}$	- S -	C
68	21^{+7}_{-6}	12^{+5}_{-4}	9^{+5}_{-4}	$4.54^{+1.40}_{-1.17}$	$1.48^{+0.59}_{-0.45}$	$1.97^{+1.11}_{-0.88}$	1.6±0.8	1.3±0.1	4.7±3.1	$1.20^{+0.67}_{-0.64}$	- - -	B
69	9^{+4}_{-3}	7^{+4}_{-3}	1^{+3}_{-1}	$1.76^{+0.90}_{-0.68}$	$0.87^{+0.46}_{-0.33}$	$0.26^{+0.61}_{-0.26}$	1.6±0.3	1.3±0.2	1.8±0.8	$0.45^{+0.25}_{-0.20}$	- - -	A
70	17^{+7}_{-6}	12^{+5}_{-4}	6^{+6}_{-5}	$3.53^{+1.53}_{-1.32}$	$1.37^{+0.60}_{-0.46}$	$1.16^{+1.28}_{-1.07}$	1.7±0.5	1.1±0.4	2.1±4.0	$0.95^{+0.49}_{-0.44}$	- - -	B
71	13^{+7}_{-6}	1^{+3}_{-1}	11^{+6}_{-5}	$4.97^{+2.68}_{-2.26}$	$0.28^{+0.75}_{-0.28}$	$4.57^{+2.57}_{-2.13}$	4.8±1.0	3.5±1.4	6.2±2.0	$3.79^{+2.20}_{-1.90}$	- - -	D
72	165^{+13}_{-13}	2^{+3}_{-2}	163^{+13}_{-13}	$35.95^{+2.83}_{-2.83}$	$0.26^{+0.37}_{-0.20}$	$36.23^{+2.86}_{-2.86}$	4.2±0.1	3.4±0.1	5.2±0.2	$24.25^{+2.06}_{-2.06}$	- - -	D
73	19^{+7}_{-5}	20^{+6}_{-5}	5	$4.25^{+1.48}_{-1.24}$	$2.58^{+0.74}_{-0.60}$	1.21	0.9±0.1	0.8±0.1	1.3±0.2	$0.63^{+0.23}_{-0.20}$	- - H	A
74	7^{+6}_{-5}	4	7^{+6}_{-5}	$2.54^{+2.38}_{-1.96}$	0.92	$2.71^{+2.29}_{-1.86}$	9.7±2.3	6.6±4.2	9.7±0.4	$3.93^{+3.79}_{-3.17}$	- S -	D
75	8^{+4}_{-3}	5^{+3}_{-2}	3^{+3}_{-2}	$1.82^{+1.00}_{-0.73}$	$0.64^{+0.47}_{-0.30}$	$0.72^{+0.79}_{-0.47}$	1.9±1.6	1.6±0.3	5.7±2.6	$0.55^{+0.55}_{-0.51}$	- - -	B
76	10^{+5}_{-4}	2	11^{+5}_{-4}	$2.43^{+1.26}_{-0.99}$	0.32	$2.82^{+1.28}_{-1.01}$	4.9±1.0	3.4±0.6	5.7±1.3	$1.91^{+1.06}_{-0.87}$	- S -	D

No.	C_{net} FB	C_{net} SB	C_{net} HB	$f_{\rm ph}$FB(10^{-6} cm^{-2} s^{-1})	$f_{\rm ph}$SB(10^{-6} cm^{-2} s^{-1})	$f_{\rm ph}$HB(10^{-6} cm^{-2} s^{-1})	E_{50} (keV)	E_{25} (keV)	E_{75} (keV)	f_X(10^{-14}erg cm^{-2} s^{-1})	Phot. Flag	Quantile Group
77	13^{+7}_{-6}	13^{+6}_{-4}	1^{+5}_{-1}	$1.36^{+0.73}_{-0.52}$	$1.47^{+0.37}_{-0.26}$	$0.30^{+1.22}_{-0.30}$	0.9±0.1	0.9±0.1	1.1±0.1	$0.20^{+0.11}_{-0.08}$	- - -	A
78	529^{+23}_{-23}	68^{+10}_{-8}	462^{+22}_{-22}	$75.82^{+3.31}_{-3.31}$	$6.80^{+0.80}_{-0.68}$	$67.51^{+3.16}_{-3.16}$	3.8±0.1	2.8±0.1	4.9±0.1	$46.21^{+2.22}_{-2.22}$	- - -	D
79	11^{+7}_{-6}	3^{+4}_{-3}	9^{+6}_{-5}	$2.24^{+1.35}_{-1.14}$	$0.29^{+0.43}_{-0.29}$	$1.79^{+1.26}_{-1.04}$	5.1±2.7	2.3±1.0	7.7±2.3	$1.82^{+1.48}_{-1.35}$	- - -	C
80	8^{+4}_{-3}	2^{+3}_{-1}	6^{+4}_{-3}	$1.77^{+0.89}_{-0.65}$	$0.23^{+0.33}_{-0.16}$	$1.39^{+0.84}_{-0.57}$	3.1±0.7	2.0±0.5	3.8±0.5	$0.87^{+0.48}_{-0.38}$	- - -	D
81	161^{+14}_{-13}	4^{+4}_{-2}	157^{+13}_{-13}	$28.26^{+2.40}_{-2.27}$	$0.76^{+0.38}_{-0.20}$	$28.17^{+2.41}_{-2.28}$	3.9±0.1	3.4±0.1	4.7±0.2	$17.50^{+1.52}_{-1.44}$	- - -	E
82	6^{+4}_{-3}	7^{+4}_{-3}	2	$1.24^{+0.72}_{-0.49}$	$0.77^{+0.42}_{-0.29}$	0.44	1.0±0.1	0.9±0.1	1.1±0.1	$0.21^{+0.12}_{-0.08}$	- - H	A
83	11^{+7}_{-6}	3	13^{+6}_{-5}	$2.60^{+1.56}_{-1.31}$	0.44	$3.15^{+1.54}_{-1.29}$	5.2±3.8	2.7±1.4	8.6±1.8	$2.17^{+2.05}_{-1.93}$	- S -	C
84	11^{+5}_{-4}	4	10^{+5}_{-4}	$2.48^{+1.13}_{-0.88}$	0.48	$2.47^{+1.13}_{-0.86}$	5.0±0.9	4.5±1.0	6.8±0.8	$1.98^{+0.98}_{-0.79}$	- S -	D
85	8^{+5}_{-4}	1^{+3}_{-1}	8^{+5}_{-4}	$2.42^{+1.44}_{-1.12}$	$0.11^{+0.44}_{-0.11}$	$2.28^{+1.39}_{-1.06}$	7.5±2.5	2.5±2.0	7.7±1.7	$2.90^{+1.98}_{-1.66}$	- - -	C
86	11^{+5}_{-3}	3	11^{+5}_{-3}	$2.23^{+0.91}_{-0.69}$	0.30	$2.30^{+0.93}_{-0.70}$	3.3±0.4	3.0±0.4	4.2±1.5	$1.16^{+0.50}_{-0.39}$	- S -	E
87	10^{+5}_{-4}	4	10^{+5}_{-4}	$2.22^{+1.17}_{-0.94}$	0.51	$2.23^{+1.14}_{-0.90}$	5.7±1.5	3.4±1.3	6.4±1.8	$2.03^{+1.19}_{-1.00}$	- S -	D
88	33^{+9}_{-8}	25^{+7}_{-6}	8^{+6}_{-3}	$2.33^{+0.70}_{-0.55}$	$1.40^{+0.32}_{-0.23}$	$1.14^{+0.82}_{-0.35}$	1.1±0.2	1.0±0.1	1.4±0.5	$0.42^{+0.14}_{-0.12}$	- - -	B
89	7^{+4}_{-3}	5^{+3}_{-2}	2^{+3}_{-2}	$1.60^{+0.94}_{-0.67}$	$0.65^{+0.46}_{-0.29}$	$0.48^{+0.71}_{-0.39}$	1.2±0.9	1.0±0.2	2.7±1.8	$0.30^{+0.30}_{-0.27}$	- - -	B
90	6^{+4}_{-3}	6^{+4}_{-2}	4	$1.20^{+0.71}_{-0.49}$	$0.65^{+0.39}_{-0.26}$	0.74	1.7±0.3	1.3±0.3	1.8±0.3	$0.32^{+0.20}_{-0.14}$	- - H	A
91	8	3	8	2.04	0.42	2.10	5.2±4.8	2.9±7.1	7.6±7.1	1.72	F S H	C
92	7^{+4}_{-3}	2	8^{+4}_{-3}	$1.55^{+0.92}_{-0.69}$	0.28	$1.77^{+0.94}_{-0.70}$	4.6±1.6	3.1±0.8	6.2±1.5	$1.15^{+0.79}_{-0.64}$	- S -	C
93	5^{+4}_{-2}	3	5^{+4}_{-2}	$1.02^{+0.68}_{-0.45}$	0.29	$1.06^{+0.70}_{-0.46}$	3.8±1.0	2.8±0.7	4.3±1.0	$0.63^{+0.45}_{-0.32}$	- S -	D
94	81^{+15}_{-13}	12^{+7}_{-4}	70^{+13}_{-12}	$6.12^{+1.01}_{-0.86}$	$1.07^{+0.29}_{-0.13}$	$5.28^{+0.95}_{-0.80}$	3.1±0.2	2.2±0.2	4.2±0.3	$3.03^{+0.54}_{-0.47}$	- - -	C
95	12^{+5}_{-4}	12^{+5}_{-3}	1^{+3}_{-1}	$2.68^{+1.07}_{-0.83}$	$1.46^{+0.58}_{-0.44}$	$0.15^{+0.60}_{-0.15}$	1.2±0.2	1.1±0.1	1.5±0.7	$0.52^{+0.22}_{-0.17}$	- - -	A
96	11^{+5}_{-4}	13^{+5}_{-4}	4	$2.55^{+1.22}_{-0.98}$	$1.72^{+0.64}_{-0.50}$	0.85	1.2±0.1	1.0±0.2	1.4±0.1	$0.49^{+0.24}_{-0.20}$	- - H	A
97	11^{+5}_{-4}	2^{+3}_{-2}	10^{+5}_{-4}	$2.56^{+1.20}_{-0.95}$	$0.20^{+0.37}_{-0.20}$	$2.24^{+1.14}_{-0.89}$	3.5±0.6	2.3±0.5	3.6±1.0	$1.42^{+0.71}_{-0.59}$	- - -	E
98	32^{+7}_{-6}	4^{+3}_{-2}	28^{+6}_{-5}	$11.88^{+2.51}_{-2.11}$	$0.86^{+0.69}_{-0.42}$	$10.61^{+2.42}_{-2.02}$	3.1±0.3	2.4±0.2	4.1±0.6	$5.92^{+1.37}_{-1.19}$	- - -	D
99	7^{+4}_{-3}	6^{+4}_{-2}	1^{+2}_{-1}	$3.24^{+1.79}_{-1.22}$	$1.64^{+0.99}_{-0.65}$	$0.42^{+1.12}_{-0.40}$	1.5±0.8	1.0±0.2	1.8±1.5	$0.79^{+0.59}_{-0.50}$	- - -	A
100	14^{+6}_{-5}	10^{+4}_{-3}	5^{+4}_{-3}	$3.69^{+1.44}_{-1.16}$	$1.43^{+0.65}_{-0.49}$	$1.21^{+1.09}_{-0.80}$	1.6±0.5	1.3±0.2	2.1±1.8	$0.93^{+0.45}_{-0.40}$	- - -	A
101	114^{+11}_{-11}	5^{+4}_{-2}	108^{+11}_{-11}	$23.36^{+2.22}_{-2.22}$	$0.62^{+0.42}_{-0.28}$	$22.75^{+2.21}_{-2.21}$	4.1±0.2	3.2±0.2	5.3±0.2	$15.45^{+1.74}_{-1.74}$	- - -	D
102	7^{+4}_{-3}	2^{+3}_{-2}	5^{+4}_{-3}	$2.58^{+1.76}_{-1.33}$	$0.43^{+0.66}_{-0.37}$	$1.85^{+1.61}_{-1.16}$	4.0±2.5	1.6±1.2	6.1±2.0	$1.67^{+1.54}_{-1.34}$	- - -	C
103	27^{+6}_{-5}	17^{+5}_{-4}	10^{+4}_{-3}	$5.23^{+1.22}_{-1.01}$	$1.87^{+0.58}_{-0.46}$	$2.05^{+0.86}_{-0.65}$	1.7±0.2	1.3±0.1	2.6±0.4	$1.39^{+0.38}_{-0.34}$	- - -	B
104	6^{+4}_{-3}	6^{+4}_{-2}	4	$1.40^{+0.97}_{-0.69}$	$0.79^{+0.50}_{-0.33}$	0.98	1.2±0.2	0.9±0.2	1.4±0.2	$0.28^{+0.20}_{-0.15}$	- - H	A
105	13^{+6}_{-5}	6^{+4}_{-3}	7^{+5}_{-4}	$2.86^{+1.31}_{-1.07}$	$0.74^{+0.49}_{-0.35}$	$1.58^{+1.13}_{-0.89}$	2.1±0.6	1.0±0.6	2.5±1.6	$0.95^{+0.50}_{-0.44}$	- - -	B
106	4^{+4}_{-3}	6^{+4}_{-3}	2	$0.89^{+0.81}_{-0.56}$	$0.79^{+0.46}_{-0.32}$	0.50	1.0±0.3	0.7±0.2	1.2±0.1	$0.14^{+0.14}_{-0.10}$	- - H	B
107	6^{+4}_{-2}	3	6^{+4}_{-2}	$1.31^{+0.84}_{-0.56}$	0.36	$1.35^{+0.86}_{-0.57}$	3.2±0.6	2.4±0.4	3.7±0.7	$0.67^{+0.45}_{-0.31}$	- S -	E
108	4^{+4}_{-3}	4	4^{+4}_{-3}	$0.77^{+0.76}_{-0.55}$	0.43	$0.69^{+0.74}_{-0.51}$	2.6±1.6	1.3±0.8	4.7±1.3	$0.33^{+0.37}_{-0.30}$	- S -	C
109	4^{+4}_{-3}	5^{+4}_{-2}	4	$0.92^{+0.86}_{-0.63}$	$0.62^{+0.43}_{-0.28}$	0.86	0.8±0.2	0.7±0.1	1.0±0.2	$0.11^{+0.11}_{-0.08}$	- - H	A
110	6^{+4}_{-2}	3	6^{+4}_{-2}	$1.17^{+0.76}_{-0.50}$	0.32	$1.22^{+0.77}_{-0.51}$	5.1±1.9	3.3±0.9	8.2±1.3	$0.95^{+0.71}_{-0.54}$	- S -	C
111	9^{+4}_{-3}	5^{+3}_{-2}	4^{+3}_{-2}	$1.71^{+0.83}_{-0.61}$	$0.57^{+0.40}_{-0.25}$	$0.74^{+0.65}_{-0.39}$	1.8±0.7	1.1±0.3	2.9±1.3	$0.50^{+0.31}_{-0.27}$	- - -	B
112	6^{+4}_{-3}	2^{+3}_{-1}	5^{+3}_{-2}	$1.36^{+0.80}_{-0.54}$	$0.23^{+0.33}_{-0.16}$	$0.98^{+0.73}_{-0.46}$	3.2±0.5	2.1±0.5	3.4±0.5	$0.69^{+0.42}_{-0.30}$	- - -	E
113	15^{+5}_{-4}	11^{+4}_{-3}	4^{+3}_{-2}	$2.73^{+0.93}_{-0.73}$	$1.19^{+0.48}_{-0.36}$	$0.69^{+0.61}_{-0.37}$	1.3±0.4	1.0±0.1	2.5±1.0	$0.58^{+0.25}_{-0.22}$	- - -	B
114	10^{+5}_{-4}	1^{+3}_{-1}	9^{+5}_{-4}	$2.00^{+1.04}_{-0.81}$	$0.07^{+0.32}_{-0.07}$	$1.91^{+1.00}_{-0.77}$	2.9±0.5	2.3±0.4	3.6±0.7	$0.92^{+0.50}_{-0.40}$	- - -	E
115	13^{+6}_{-5}	4^{+4}_{-2}	9^{+5}_{-4}	$4.00^{+1.89}_{-1.56}$	$0.67^{+0.65}_{-0.43}$	$2.86^{+1.72}_{-1.37}$	2.4±1.6	1.6±0.5	4.7±3.8	$1.56^{+1.26}_{-1.19}$	- - -	C

Chandra Catalog: Photometry (continued)

No.	C_{net} FB	C_{net} SB	C_{net} HB	$f_{\rm ph}$FB(10^{-6} cm^{-2} s^{-1})	$f_{\rm ph}$SB(10^{-6} cm^{-2} s^{-1})	$f_{\rm ph}$HB(10^{-6} cm^{-2} s^{-1})	E_{50} (keV)	E_{25} (keV)	E_{75} (keV)	f_X(10^{-14}erg cm^{-2} s^{-1})	Phot. Flag	Quantile Group
116	15^{+5}_{-4}	7^{+4}_{-3}	8^{+4}_{-3}	$3.13^{+1.13}_{-0.90}$	$0.87^{+0.47}_{-0.33}$	$1.65^{+0.93}_{-0.69}$	2.1±0.7	1.7±0.4	3.9±1.0	$1.04^{+0.52}_{-0.46}$	- - -	B
117	6^{+4}_{-3}	1^{+2}_{-1}	6^{+4}_{-3}	$1.36^{+0.90}_{-0.66}$	$0.10^{+0.30}_{-0.10}$	$1.20^{+0.87}_{-0.63}$	4.8±0.8	3.5±0.7	5.1±0.6	$1.03^{+0.71}_{-0.54}$	- - -	D
118	40^{+9}_{-8}	11^{+6}_{-4}	30^{+8}_{-7}	$3.76^{+0.99}_{-0.80}$	$1.29^{+0.37}_{-0.25}$	$2.50^{+0.87}_{-0.67}$	3.7±0.5	2.0±0.3	5.4±1.2	$2.21^{+0.66}_{-0.56}$	- - -	C
119	24^{+7}_{-6}	2^{+4}_{-2}	21^{+7}_{-5}	$2.48^{+0.77}_{-0.60}$	$0.29^{+0.22}_{-0.07}$	$2.31^{+0.76}_{-0.58}$	3.9±0.4	2.9±0.6	4.6±0.4	$1.57^{+0.52}_{-0.42}$	- - -	D
120	2^{+4}_{-2}	4^{+3}_{-2}	3	$0.37^{+0.82}_{-0.37}$	$0.50^{+0.44}_{-0.28}$	0.65	0.8±0.1	0.7±9.3	0.8±9.2	$0.04^{+0.10}_{-0.05}$	- - H	A
121	11^{+5}_{-4}	7^{+4}_{-3}	4^{+4}_{-3}	$2.78^{+1.33}_{-1.05}$	$0.95^{+0.57}_{-0.41}$	$1.13^{+1.08}_{-0.79}$	1.7±1.4	1.4±0.4	4.0±3.1	$0.76^{+0.71}_{-0.67}$	- - -	B
122	5^{+3}_{-2}	2^{+3}_{-1}	3^{+3}_{-2}	$0.91^{+0.67}_{-0.43}$	$0.22^{+0.30}_{-0.15}$	$0.54^{+0.59}_{-0.33}$	3.5±1.5	1.6±0.8	5.1±1.1	$0.51^{+0.44}_{-0.32}$	- - -	C
123	8^{+5}_{-3}	5^{+4}_{-2}	2^{+4}_{-2}	$1.61^{+0.97}_{-0.74}$	$0.64^{+0.44}_{-0.29}$	$0.51^{+0.78}_{-0.51}$	1.6±0.4	1.1±0.4	2.3±0.4	$0.41^{+0.27}_{-0.22}$	- - -	B
124	6^{+4}_{-2}	4^{+3}_{-2}	2^{+3}_{-1}	$1.36^{+0.87}_{-0.58}$	$0.55^{+0.45}_{-0.27}$	$0.42^{+0.66}_{-0.32}$	1.2±1.4	1.0±0.3	3.6±1.9	$0.27^{+0.34}_{-0.32}$	- - -	B
125	32^{+7}_{-6}	18^{+5}_{-4}	14^{+5}_{-4}	$6.70^{+1.46}_{-1.24}$	$2.19^{+0.65}_{-0.52}$	$2.94^{+1.09}_{-0.85}$	1.9±0.3	1.2±0.2	2.6±0.2	$2.00^{+0.51}_{-0.46}$	- - -	B
126	11^{+5}_{-4}	3^{+3}_{-2}	7^{+4}_{-3}	$2.43^{+1.11}_{-0.86}$	$0.42^{+0.42}_{-0.25}$	$1.73^{+1.00}_{-0.74}$	2.9±0.8	1.8±0.6	4.6±1.3	$1.14^{+0.60}_{-0.51}$	- - -	C
127	19^{+6}_{-5}	4	19^{+6}_{-5}	$4.40^{+1.31}_{-1.07}$	0.50	$4.39^{+1.31}_{-1.06}$	3.8±0.3	2.8±0.4	4.2±0.2	$2.68^{+0.83}_{-0.68}$	- S -	E
128	5^{+4}_{-3}	6^{+4}_{-2}	3	$1.07^{+0.76}_{-0.52}$	$0.65^{+0.42}_{-0.27}$	0.63	1.4±0.2	1.3±0.1	1.5±0.2	$0.23^{+0.17}_{-0.12}$	- - H	A
129	5^{+4}_{-2}	1^{+2}_{-1}	4^{+3}_{-2}	$1.22^{+0.92}_{-0.61}$	$0.11^{+0.34}_{-0.11}$	$1.04^{+0.89}_{-0.56}$	2.9±0.5	2.5±0.6	3.2±0.2	$0.56^{+0.44}_{-0.30}$	- - -	E
130	24^{+6}_{-5}	2^{+3}_{-2}	22^{+6}_{-5}	$5.36^{+1.41}_{-1.17}$	$0.26^{+0.37}_{-0.21}$	$5.01^{+1.37}_{-1.13}$	4.6±0.4	3.6±0.5	5.4±0.5	$3.96^{+1.08}_{-0.92}$	- - -	D
131	11^{+5}_{-4}	4	10^{+5}_{-3}	$2.42^{+1.06}_{-0.81}$	0.50	$2.36^{+1.05}_{-0.80}$	4.0±1.0	2.5±0.6	5.2±1.4	$1.55^{+0.77}_{-0.64}$	- S -	C
132	37^{+8}_{-7}	6^{+3}_{-2}	34^{+8}_{-6}	$4.65^{+1.04}_{-0.84}$	$1.33^{+0.46}_{-0.26}$	$4.45^{+1.02}_{-0.82}$	3.8±0.5	3.2±0.3	5.6±0.4	$2.86^{+0.73}_{-0.63}$	- - -	D
133	11^{+6}_{-4}	12^{+5}_{-4}	5^{+3}_{-1}	$1.19^{+0.62}_{-0.45}$	$1.13^{+0.31}_{-0.21}$	$0.25^{+0.65}_{-0.25}$	1.4±0.4	0.9±0.2	1.7±0.3	$0.26^{+0.15}_{-0.12}$	- - -	B
134	12^{+5}_{-4}	5^{+3}_{-2}	8^{+4}_{-3}	$2.89^{+1.10}_{-0.84}$	$0.65^{+0.46}_{-0.29}$	$1.80^{+0.94}_{-0.67}$	2.0±0.4	1.1±0.3	2.9±0.8	$0.93^{+0.40}_{-0.33}$	- - -	B
135	10^{+7}_{-6}	1^{+4}_{-1}	9^{+6}_{-5}	$3.14^{+2.01}_{-1.70}$	$0.20^{+0.62}_{-0.20}$	$2.85^{+1.87}_{-1.55}$	2.8±1.0	2.2±0.4	4.1±1.6	$1.40^{+1.03}_{-0.91}$	- - -	E
136	13^{+6}_{-5}	2^{+4}_{-1}	11^{+6}_{-4}	$1.31^{+0.64}_{-0.46}$	$0.57^{+0.22}_{-0.08}$	$1.15^{+0.62}_{-0.43}$	2.6±0.3	2.1±0.2	2.8±0.2	$0.54^{+0.27}_{-0.20}$	- - -	E
137	9^{+5}_{-3}	2	10^{+5}_{-3}	$1.97^{+1.00}_{-0.76}$	0.28	$2.16^{+1.02}_{-0.77}$	4.2±0.6	4.0±0.3	5.6±1.1	$1.34^{+0.71}_{-0.55}$	- S -	E
138	4^{+4}_{-3}	5^{+4}_{-2}	3	$1.00^{+0.94}_{-0.68}$	$0.72^{+0.49}_{-0.32}$	0.85	1.3±0.3	1.1±0.2	1.6±0.1	$0.20^{+0.20}_{-0.15}$	- - H	A
139	38^{+7}_{-6}	2	38^{+7}_{-6}	$7.66^{+1.49}_{-1.27}$	0.28	$7.88^{+1.52}_{-1.30}$	5.2±0.4	4.1±0.1	5.8±0.3	$6.32^{+1.31}_{-1.14}$	- S -	D
140	8^{+7}_{-6}	3^{+4}_{-3}	5^{+6}_{-5}	$2.84^{+2.33}_{-1.96}$	$0.63^{+0.81}_{-0.58}$	$1.75^{+2.08}_{-1.70}$	3.9±4.2	1.3±2.0	8.1±3.3	$1.78^{+2.42}_{-2.28}$	- - -	C
141	7^{+4}_{-3}	4^{+3}_{-2}	3^{+3}_{-2}	$1.37^{+0.80}_{-0.57}$	$0.45^{+0.37}_{-0.22}$	$0.61^{+0.65}_{-0.39}$	1.5±0.5	1.0±0.2	2.3±0.3	$0.32^{+0.22}_{-0.17}$	- - -	B
142	13^{+5}_{-4}	1^{+3}_{-1}	12^{+5}_{-4}	$3.20^{+1.32}_{-1.05}$	$0.16^{+0.41}_{-0.16}$	$2.98^{+1.26}_{-0.98}$	4.2±0.6	3.2±0.8	4.8±0.5	$2.17^{+0.95}_{-0.78}$	- - -	D
143	8^{+5}_{-3}	1^{+3}_{-1}	7^{+4}_{-3}	$1.62^{+0.94}_{-0.71}$	$0.15^{+0.31}_{-0.15}$	$1.40^{+0.90}_{-0.66}$	3.8±1.8	3.1±1.0	5.5±2.5	$0.98^{+0.73}_{-0.63}$	- - -	D
144	20^{+7}_{-6}	3^{+3}_{-2}	17^{+6}_{-5}	$4.57^{+1.49}_{-1.26}$	$0.41^{+0.44}_{-0.28}$	$3.93^{+1.42}_{-1.17}$	3.9±0.7	2.3±0.7	4.9±1.6	$2.89^{+1.08}_{-0.95}$	- - -	C
145	22^{+6}_{-5}	22^{+6}_{-5}	4	$4.98^{+1.33}_{-1.08}$	$2.84^{+0.75}_{-0.61}$	0.85	1.1±0.1	1.0±0.1	1.4±0.1	$0.87^{+0.25}_{-0.21}$	- - H	A
146	42^{+8}_{-7}	26^{+7}_{-5}	16^{+6}_{-5}	$4.19^{+0.89}_{-0.72}$	$1.98^{+0.39}_{-0.28}$	$1.76^{+0.68}_{-0.50}$	1.3±0.2	1.1±0.1	2.4±0.4	$0.90^{+0.24}_{-0.22}$	- - -	B
147	16^{+5}_{-4}	7^{+4}_{-3}	8^{+4}_{-3}	$3.50^{+1.20}_{-0.96}$	$0.95^{+0.51}_{-0.37}$	$1.89^{+0.98}_{-0.73}$	2.2±0.6	1.4±0.3	3.5±0.7	$1.23^{+0.55}_{-0.48}$	- - -	B
148	3^{+3}_{-2}	2^{+3}_{-1}	2^{+3}_{-2}	$0.69^{+0.72}_{-0.46}$	$0.18^{+0.32}_{-0.16}$	$0.37^{+0.63}_{-0.35}$	2.2±0.7	1.7±0.3	2.9±0.4	$0.24^{+0.26}_{-0.18}$	- - -	A
149	13^{+7}_{-6}	2^{+4}_{-2}	11^{+6}_{-5}	$2.57^{+1.36}_{-1.15}$	$0.22^{+0.40}_{-0.22}$	$2.24^{+1.29}_{-1.08}$	2.2±0.4	2.1±0.2	2.5±1.7	$0.89^{+0.50}_{-0.44}$	- - -	A
150	5^{+4}_{-2}	4^{+3}_{-2}	1^{+3}_{-1}	$1.13^{+0.80}_{-0.53}$	$0.48^{+0.40}_{-0.24}$	$0.29^{+0.60}_{-0.29}$	0.9±0.7	0.9±0.2	2.1±0.9	$0.17^{+0.17}_{-0.14}$	- - -	B
151	46^{+9}_{-8}	9^{+5}_{-3}	37^{+8}_{-7}	$5.22^{+1.02}_{-0.85}$	$0.88^{+0.32}_{-0.21}$	$4.30^{+0.96}_{-0.78}$	3.0±0.2	2.1±0.3	4.3±0.4	$2.50^{+0.52}_{-0.44}$	- - -	C
152	31^{+7}_{-6}	27^{+6}_{-5}	4^{+3}_{-2}	$6.17^{+1.35}_{-1.13}$	$3.07^{+0.72}_{-0.60}$	$0.83^{+0.70}_{-0.44}$	1.1±0.1	0.9±0.1	1.4±0.3	$1.10^{+0.26}_{-0.23}$	- - -	A
153	31^{+8}_{-6}	2^{+4}_{-2}	28^{+7}_{-6}	$3.40^{+0.88}_{-0.70}$	$0.35^{+0.24}_{-0.09}$	$3.24^{+0.87}_{-0.68}$	3.6±0.3	3.0±0.3	4.4±0.4	$1.96^{+0.53}_{-0.43}$	- - -	E

No.	C_{net} FB	C_{net} SB	C_{net} HB	$f_{\rm ph}$FB(10^{-6} cm^{-2} s^{-1})	$f_{\rm ph}$SB(10^{-6} cm^{-2} s^{-1})	$f_{\rm ph}$HB(10^{-6} cm^{-2} s^{-1})	E_{50} (keV)	E_{25} (keV)	E_{75} (keV)	f_X(10^{-14}erg cm^{-2} s^{-1})	Phot. Flag	Quantile Group
154	7^{+4}_{-3}	2	7^{+4}_{-3}	$1.36^{+0.80}_{-0.57}$	0.29	$1.43^{+0.81}_{-0.58}$	5.1±1.2	4.3±0.9	6.8±1.8	$1.11^{+0.70}_{-0.53}$	- S -	D
155	10^{+4}_{-3}	10^{+4}_{-3}	4	$2.15^{+0.93}_{-0.70}$	$1.21^{+0.52}_{-0.39}$	0.80	1.1±0.2	0.9±0.1	1.5±0.3	$0.39^{+0.18}_{-0.14}$	- - H	A
156	7^{+5}_{-4}	3	8^{+5}_{-3}	$1.56^{+0.99}_{-0.76}$	0.37	$1.68^{+0.98}_{-0.75}$	5.7±2.0	3.4±1.4	8.2±2.0	$1.41^{+1.03}_{-0.85}$	- S -	C
157	6^{+4}_{-3}	4^{+3}_{-2}	2^{+3}_{-2}	$1.16^{+0.77}_{-0.52}$	$0.43^{+0.37}_{-0.22}$	$0.41^{+0.61}_{-0.34}$	1.1±0.6	0.9±0.2	2.1±0.8	$0.21^{+0.18}_{-0.15}$	- - -	B
158	56^{+10}_{-8}	12^{+5}_{-4}	44^{+9}_{-7}	$5.76^{+1.04}_{-0.87}$	$0.99^{+0.34}_{-0.23}$	$4.19^{+0.92}_{-0.74}$	3.1±0.4	2.3±0.2	4.6±0.5	$2.87^{+0.64}_{-0.57}$	- - -	C
159	35^{+8}_{-7}	29^{+7}_{-6}	6^{+4}_{-3}	$7.77^{+1.66}_{-1.43}$	$3.64^{+0.83}_{-0.70}$	$1.39^{+1.00}_{-0.75}$	1.1±0.1	0.9±0.1	1.5±0.5	$1.39^{+0.34}_{-0.30}$	- - -	A
160	57^{+10}_{-8}	19^{+6}_{-5}	38^{+8}_{-7}	$7.55^{+1.27}_{-1.08}$	$1.92^{+0.47}_{-0.35}$	$4.99^{+1.09}_{-0.89}$	2.7±0.4	1.8±0.2	4.0±0.4	$3.24^{+0.70}_{-0.63}$	- - -	C
161	12^{+5}_{-4}	2^{+3}_{-2}	10^{+5}_{-4}	$2.65^{+1.15}_{-0.91}$	$0.22^{+0.37}_{-0.21}$	$2.31^{+1.09}_{-0.85}$	2.5±0.6	2.2±0.3	3.8±1.4	$1.06^{+0.52}_{-0.44}$	- - -	E
162	8^{+4}_{-3}	5^{+3}_{-2}	3^{+3}_{-2}	$1.73^{+0.92}_{-0.67}$	$0.61^{+0.44}_{-0.28}$	$0.70^{+0.73}_{-0.44}$	1.8±1.4	1.4±0.5	5.2±1.4	$0.51^{+0.46}_{-0.43}$	- - -	B
163	7^{+4}_{-3}	2^{+3}_{-1}	5^{+4}_{-2}	$1.41^{+0.85}_{-0.61}$	$0.21^{+0.33}_{-0.16}$	$1.06^{+0.79}_{-0.52}$	2.9±0.9	1.5±0.7	4.2±1.1	$0.65^{+0.44}_{-0.34}$	- - -	C
164	26^{+7}_{-6}	5^{+3}_{-2}	24^{+7}_{-6}	$3.10^{+0.88}_{-0.69}$	$0.98^{+0.46}_{-0.28}$	$2.89^{+0.86}_{-0.67}$	4.2±0.3	3.3±0.4	5.1±0.8	$2.07^{+0.61}_{-0.49}$	- - -	D
165	10^{+5}_{-4}	7^{+4}_{-3}	3^{+3}_{-2}	$2.05^{+0.98}_{-0.75}$	$0.86^{+0.47}_{-0.34}$	$0.56^{+0.72}_{-0.46}$	1.7±0.6	0.9±0.2	2.3±1.8	$0.56^{+0.34}_{-0.30}$	- - -	B
166	13^{+5}_{-4}	11^{+4}_{-3}	2^{+3}_{-1}	$3.54^{+1.32}_{-1.01}$	$1.77^{+0.72}_{-0.54}$	$0.50^{+0.76}_{-0.37}$	1.4±0.2	1.0±0.2	1.6±2.0	$0.77^{+0.31}_{-0.25}$	- - -	A
167	31^{+8}_{-6}	21^{+6}_{-5}	9^{+5}_{-4}	$3.23^{+0.82}_{-0.65}$	$1.71^{+0.38}_{-0.27}$	$1.04^{+0.61}_{-0.42}$	1.4±0.2	1.0±0.1	2.0±0.5	$0.73^{+0.22}_{-0.18}$	- - -	B
168	9^{+4}_{-3}	2^{+3}_{-1}	7^{+4}_{-3}	$2.03^{+1.02}_{-0.75}$	$0.21^{+0.36}_{-0.17}$	$1.70^{+0.96}_{-0.69}$	3.4±1.0	2.3±0.8	5.3±0.9	$1.10^{+0.64}_{-0.52}$	- - -	C
169	8^{+4}_{-3}	9^{+4}_{-3}	3	$1.66^{+0.84}_{-0.62}$	$0.97^{+0.47}_{-0.34}$	0.65	0.9±0.2	0.9±0.0	1.3±0.3	$0.24^{+0.13}_{-0.10}$	- - H	A
170	17^{+6}_{-5}	5^{+4}_{-3}	11^{+5}_{-4}	$3.98^{+1.50}_{-1.24}$	$0.73^{+0.54}_{-0.39}$	$2.75^{+1.32}_{-1.06}$	2.6±0.5	1.5±0.5	3.3±0.7	$1.63^{+0.68}_{-0.59}$	- - -	C
171	9^{+5}_{-4}	1^{+3}_{-1}	8^{+5}_{-4}	$1.97^{+1.11}_{-0.87}$	$0.10^{+0.34}_{-0.10}$	$1.82^{+1.07}_{-0.82}$	5.9±1.8	4.3±1.9	8.0±1.6	$1.84^{+1.19}_{-1.00}$	- - -	D
172	29^{+7}_{-6}	2^{+3}_{-2}	27^{+7}_{-6}	$5.72^{+1.46}_{-1.26}$	$0.18^{+0.36}_{-0.18}$	$5.52^{+1.43}_{-1.22}$	3.5±0.5	2.8±0.3	4.8±0.5	$3.19^{+0.92}_{-0.82}$	- - -	D
173	5^{+4}_{-2}	1^{+3}_{-1}	4^{+3}_{-2}	$1.01^{+0.71}_{-0.47}$	$0.15^{+0.29}_{-0.12}$	$0.76^{+0.66}_{-0.41}$	3.6±1.3	1.5±0.8	4.6±0.9	$0.58^{+0.47}_{-0.35}$	- - -	C
174	25^{+7}_{-6}	5^{+4}_{-3}	20^{+7}_{-5}	$1.69^{+0.64}_{-0.44}$	$0.70^{+0.24}_{-0.12}$	$1.34^{+0.60}_{-0.39}$	3.2±0.6	2.6±0.4	3.8±0.3	$0.88^{+0.37}_{-0.28}$	- - -	D
175	14^{+6}_{-5}	13^{+5}_{-4}	5^{+4}_{-2}	$1.36^{+0.64}_{-0.45}$	$1.09^{+0.33}_{-0.22}$	$0.40^{+0.91}_{-0.40}$	1.0±0.1	0.8±0.1	1.2±0.1	$0.22^{+0.11}_{-0.08}$	- - -	A
176	32^{+8}_{-7}	14^{+6}_{-4}	18^{+7}_{-5}	$3.00^{+0.79}_{-0.62}$	$1.37^{+0.33}_{-0.23}$	$1.64^{+0.65}_{-0.46}$	2.5±0.4	1.8±0.1	3.8±0.6	$1.18^{+0.36}_{-0.31}$	- - -	C
177	71^{+10}_{-9}	35^{+7}_{-6}	36^{+7}_{-6}	$15.78^{+2.13}_{-1.90}$	$4.41^{+0.89}_{-0.75}$	$8.25^{+1.64}_{-1.40}$	2.2±0.3	1.6±0.1	3.3±0.4	$5.56^{+1.02}_{-0.96}$	- - -	B
178	8^{+5}_{-3}	2^{+3}_{-2}	6^{+4}_{-3}	$1.69^{+0.93}_{-0.71}$	$0.22^{+0.35}_{-0.19}$	$1.34^{+0.86}_{-0.62}$	4.0±1.9	1.9±1.3	6.3±2.1	$1.08^{+0.79}_{-0.69}$	- - -	C
179	11^{+7}_{-6}	5^{+4}_{-3}	5^{+6}_{-5}	$2.98^{+2.00}_{-1.69}$	$0.85^{+0.66}_{-0.47}$	$1.51^{+1.82}_{-1.50}$	1.6±2.0	1.3±0.4	4.6±3.4	$0.75^{+1.08}_{-1.04}$	- - -	B
180	11^{+5}_{-4}	5^{+4}_{-2}	6^{+4}_{-3}	$2.35^{+1.05}_{-0.82}$	$0.64^{+0.44}_{-0.29}$	$1.26^{+0.89}_{-0.65}$	2.4±0.9	1.1±0.4	3.4±1.8	$0.91^{+0.53}_{-0.46}$	- - -	C
181	9^{+5}_{-4}	6^{+4}_{-3}	2^{+4}_{-2}	$1.93^{+1.08}_{-0.83}$	$0.80^{+0.48}_{-0.32}$	$0.54^{+0.86}_{-0.54}$	1.5±0.8	1.1±0.2	3.2±2.1	$0.48^{+0.36}_{-0.32}$	- - -	B
182	7^{+4}_{-3}	8^{+4}_{-3}	2	$1.44^{+0.82}_{-0.59}$	$0.93^{+0.47}_{-0.34}$	0.48	0.8±0.2	0.8±0.1	1.3±0.2	$0.19^{+0.12}_{-0.09}$	- - H	A
183	50^{+9}_{-8}	7^{+5}_{-3}	43^{+9}_{-7}	$5.14^{+0.93}_{-0.78}$	$0.82^{+0.28}_{-0.17}$	$4.45^{+0.88}_{-0.72}$	3.7±0.3	2.6±0.3	4.5±0.2	$3.02^{+0.60}_{-0.51}$	- - -	D
184	11^{+5}_{-3}	8^{+4}_{-3}	3^{+3}_{-2}	$2.50^{+1.03}_{-0.78}$	$1.02^{+0.52}_{-0.37}$	$0.75^{+0.73}_{-0.44}$	1.6±0.2	1.4±0.2	2.0±0.4	$0.62^{+0.27}_{-0.21}$	- - -	A
185	15^{+6}_{-5}	6^{+4}_{-3}	9^{+5}_{-4}	$3.40^{+1.28}_{-1.04}$	$0.80^{+0.51}_{-0.36}$	$2.03^{+1.09}_{-0.84}$	2.4±0.8	1.8±0.2	4.9±2.5	$1.30^{+0.65}_{-0.59}$	- - -	C
186	11^{+5}_{-4}	8^{+4}_{-3}	3^{+4}_{-2}	$2.73^{+1.23}_{-0.96}$	$1.16^{+0.58}_{-0.42}$	$0.71^{+0.92}_{-0.61}$	1.1±0.5	0.9±0.1	2.0±3.0	$0.50^{+0.31}_{-0.27}$	- - -	B
187	7^{+5}_{-4}	1^{+3}_{-1}	6^{+4}_{-3}	$2.52^{+1.71}_{-1.30}$	$0.25^{+0.56}_{-0.25}$	$2.12^{+1.64}_{-1.22}$	7.2±2.4	6.3±2.9	9.3±1.1	$2.92^{+2.20}_{-1.78}$	- - -	D
188	20^{+7}_{-5}	20^{+6}_{-5}	6	$2.29^{+0.80}_{-0.61}$	$1.81^{+0.43}_{-0.32}$	0.75	1.0±0.1	0.8±0.1	1.2±0.1	$0.35^{+0.13}_{-0.10}$	- - H	A
189	14^{+5}_{-4}	9^{+4}_{-3}	5^{+4}_{-3}	$3.20^{+1.23}_{-0.98}$	$1.17^{+0.56}_{-0.41}$	$1.16^{+0.94}_{-0.67}$	1.3±0.5	0.9±0.2	2.5±0.8	$0.65^{+0.35}_{-0.31}$	- - -	B
190	9^{+5}_{-4}	4^{+3}_{-2}	5^{+4}_{-3}	$2.26^{+1.14}_{-0.87}$	$0.57^{+0.46}_{-0.29}$	$1.28^{+0.98}_{-0.70}$	3.0±1.7	1.6±0.6	6.2±1.5	$1.09^{+0.81}_{-0.73}$	- - -	C
191	7^{+4}_{-3}	3	7^{+4}_{-3}	$1.53^{+0.83}_{-0.59}$	0.31	$1.60^{+0.85}_{-0.61}$	4.4±1.6	2.7±0.7	6.7±1.9	$1.08^{+0.71}_{-0.58}$	- S -	C

No.	C_{net} FB	C_{net} SB	C_{net} HB	$f_{\rm ph}$FB(10^{-6} cm^{-2} s^{-1})	$f_{\rm ph}$SB(10^{-6} cm^{-2} s^{-1})	$f_{\rm ph}$HB(10^{-6} cm^{-2} s^{-1})	E_{50} (keV)	E_{25} (keV)	E_{75} (keV)	f_X(10^{-14}erg cm^{-2} s^{-1})	Phot. Flag	Quantile Group
192	1^{+3}_{-1}	2	1^{+3}_{-1}	$0.22^{+1.05}_{-0.22}$	0.43	$0.48^{+1.07}_{-0.48}$	8.9±8.4	5.4±4.9	9.9±9.4	$0.31^{+1.51}_{-0.42}$	- S -	D
193	5^{+4}_{-3}	6^{+4}_{-2}	3	$1.26^{+0.88}_{-0.60}$	$0.75^{+0.48}_{-0.32}$	0.75	1.2±0.3	1.1±0.3	1.4±0.2	$0.25^{+0.18}_{-0.13}$	- - H	A
194	11^{+5}_{-3}	3	12^{+5}_{-3}	$2.21^{+0.88}_{-0.67}$	0.29	$2.28^{+0.90}_{-0.68}$	3.6±0.5	3.0±0.3	4.5±1.5	$1.26^{+0.53}_{-0.42}$	- S -	E
195	24^{+7}_{-6}	18^{+6}_{-4}	7^{+5}_{-3}	$2.65^{+0.78}_{-0.61}$	$1.60^{+0.37}_{-0.27}$	$0.71^{+0.57}_{-0.34}$	1.0±0.2	0.9±0.1	1.3±0.5	$0.44^{+0.16}_{-0.14}$	- - -	B
196	14^{+5}_{-4}	13^{+5}_{-4}	1^{+2}_{-1}	$3.01^{+1.07}_{-0.83}$	$1.67^{+0.61}_{-0.46}$	$0.15^{+0.52}_{-0.15}$	1.2±0.1	0.9±0.1	1.3±0.3	$0.56^{+0.21}_{-0.17}$	- - -	A
197	11^{+4}_{-3}	3^{+3}_{-2}	8^{+4}_{-3}	$2.07^{+0.87}_{-0.65}$	$0.33^{+0.33}_{-0.19}$	$1.54^{+0.79}_{-0.56}$	3.1±0.5	2.4±0.6	4.2±0.5	$1.02^{+0.45}_{-0.36}$	- - -	E
198	12^{+5}_{-4}	3	12^{+5}_{-4}	$2.38^{+0.91}_{-0.70}$	0.30	$2.44^{+0.93}_{-0.71}$	5.4±0.6	4.5±0.7	6.6±1.2	$2.05^{+0.81}_{-0.64}$	- S -	D
199	10^{+5}_{-4}	12^{+6}_{-4}	7^{+4}_{-2}	$2.48^{+1.17}_{-0.90}$	$1.33^{+0.40}_{-0.29}$	$0.79^{+0.89}_{-0.59}$	1.7±0.5	1.0±0.3	3.1±2.3	$0.67^{+0.38}_{-0.32}$	- - -	B
200	9^{+5}_{-4}	3^{+3}_{-2}	6^{+4}_{-3}	$1.98^{+1.11}_{-0.87}$	$0.35^{+0.40}_{-0.24}$	$1.40^{+1.01}_{-0.76}$	3.1±1.2	1.8±0.6	5.0±0.8	$0.97^{+0.66}_{-0.56}$	- - -	C
201	18^{+7}_{-5}	6^{+5}_{-3}	12^{+6}_{-4}	$2.00^{+0.73}_{-0.56}$	$0.65^{+0.27}_{-0.16}$	$1.31^{+0.65}_{-0.48}$	2.9±0.9	1.9±0.4	4.6±1.0	$0.94^{+0.44}_{-0.38}$	- - -	C
202	6^{+4}_{-3}	6^{+4}_{-2}	3	$1.17^{+0.78}_{-0.53}$	$0.68^{+0.43}_{-0.28}$	0.69	0.9±1.3	0.8±0.1	1.3±4.1	$0.18^{+0.27}_{-0.26}$	- - H	A
203	16^{+5}_{-4}	20^{+7}_{-5}	3^{+3}_{-2}	$3.50^{+1.15}_{-0.91}$	$1.58^{+0.42}_{-0.32}$	$0.72^{+0.72}_{-0.43}$	1.1±0.1	1.1±0.1	1.7±1.0	$0.60^{+0.20}_{-0.16}$	- - -	A
204	5^{+4}_{-2}	3^{+3}_{-2}	3^{+3}_{-2}	$1.03^{+0.68}_{-0.45}$	$0.32^{+0.32}_{-0.18}$	$0.49^{+0.56}_{-0.31}$	1.9±0.6	1.5±0.3	2.6±0.7	$0.31^{+0.23}_{-0.17}$	- - -	A
205	8^{+4}_{-3}	1^{+2}_{-1}	7^{+4}_{-3}	$1.44^{+0.75}_{-0.54}$	$0.10^{+0.26}_{-0.09}$	$1.29^{+0.73}_{-0.50}$	4.0±0.8	3.1±0.7	5.0±0.5	$0.93^{+0.52}_{-0.39}$	- - -	D
206	10^{+6}_{-5}	10^{+5}_{-4}	7	$2.25^{+1.39}_{-1.16}$	$1.25^{+0.60}_{-0.46}$	1.70	1.5±0.3	1.1±0.4	1.7±0.2	$0.54^{+0.35}_{-0.29}$	- - H	A
207	5	2^{+3}_{-2}	3	1.14	$0.24^{+0.38}_{-0.21}$	0.76	5.2±4.8	2.9±7.1	7.6±7.1	0.96	F - H	C
208	34^{+9}_{-8}	4^{+2}_{-1}	36^{+9}_{-7}	$3.85^{+0.96}_{-0.79}$	$0.94^{+0.27}_{-0.08}$	$4.04^{+0.95}_{-0.79}$	5.0±0.3	4.7±0.2	5.5±0.2	$3.08^{+0.78}_{-0.66}$	- - -	E
209	6^{+4}_{-3}	6^{+4}_{-3}	4	$1.45^{+0.97}_{-0.72}$	$0.80^{+0.49}_{-0.33}$	1.02	1.1±2.2	0.8±0.4	1.5±4.9	$0.25^{+0.55}_{-0.54}$	- - H	B
210	6^{+5}_{-4}	4^{+4}_{-2}	1^{+4}_{-1}	$1.33^{+1.08}_{-0.83}$	$0.57^{+0.47}_{-0.31}$	$0.34^{+0.89}_{-0.34}$	1.3±1.0	1.1±0.3	2.6±1.4	$0.27^{+0.31}_{-0.28}$	- - -	B
211	11^{+5}_{-3}	8^{+4}_{-3}	3^{+3}_{-2}	$2.22^{+0.91}_{-0.69}$	$0.90^{+0.46}_{-0.33}$	$0.68^{+0.65}_{-0.39}$	1.8±0.2	1.5±0.3	2.3±0.3	$0.64^{+0.28}_{-0.22}$	- - -	A
212	11^{+5}_{-4}	6^{+4}_{-2}	5^{+4}_{-3}	$2.28^{+0.98}_{-0.75}$	$0.66^{+0.43}_{-0.28}$	$1.15^{+0.80}_{-0.55}$	2.0±1.2	1.3±0.4	4.6±2.9	$0.73^{+0.54}_{-0.50}$	- - -	B
213	6^{+4}_{-2}	3	6^{+4}_{-2}	$1.06^{+0.69}_{-0.46}$	0.29	$1.10^{+0.70}_{-0.47}$	4.7±1.0	3.4±0.6	6.0±0.8	$0.80^{+0.55}_{-0.39}$	- S -	D
214	2^{+4}_{-2}	2	4^{+4}_{-3}	$0.82^{+1.92}_{-0.82}$	0.59	$1.64^{+1.96}_{-1.43}$	9.6±1.9	7.6±7.1	9.6±9.1	$1.25^{+2.97}_{-1.28}$	- S -	D
215	11^{+5}_{-3}	3	12^{+5}_{-3}	$2.19^{+0.87}_{-0.66}$	0.29	$2.26^{+0.89}_{-0.68}$	4.3±0.7	3.1±0.5	5.4±0.8	$1.51^{+0.66}_{-0.53}$	- S -	D
216	7^{+4}_{-3}	5^{+3}_{-2}	2^{+3}_{-2}	$1.42^{+0.79}_{-0.57}$	$0.55^{+0.39}_{-0.25}$	$0.47^{+0.60}_{-0.33}$	1.1±0.6	0.9±0.2	2.5±0.8	$0.25^{+0.19}_{-0.17}$	- - -	B
217	8^{+5}_{-4}	6^{+4}_{-3}	1^{+4}_{-1}	$1.74^{+1.10}_{-0.85}$	$0.79^{+0.50}_{-0.36}$	$0.34^{+0.83}_{-0.34}$	1.8±1.5	1.1±0.3	2.5±4.3	$0.51^{+0.52}_{-0.48}$	- - -	B
218	5^{+3}_{-2}	3^{+3}_{-2}	2^{+3}_{-1}	$1.02^{+0.74}_{-0.47}$	$0.38^{+0.38}_{-0.21}$	$0.38^{+0.59}_{-0.29}$	1.9±0.7	1.4±0.6	3.0±0.4	$0.31^{+0.25}_{-0.18}$	- - -	B
219	6^{+4}_{-2}	3	6^{+4}_{-2}	$1.06^{+0.68}_{-0.45}$	0.29	$1.10^{+0.70}_{-0.46}$	3.3±1.8	2.9±0.6	5.6±1.9	$0.56^{+0.47}_{-0.39}$	- S -	D
220	8^{+4}_{-3}	4^{+3}_{-2}	4^{+3}_{-2}	$2.85^{+1.44}_{-1.03}$	$0.84^{+0.68}_{-0.41}$	$1.44^{+1.18}_{-0.71}$	1.8±0.6	1.3±0.3	2.8±1.1	$0.81^{+0.49}_{-0.40}$	- - -	B
221	9^{+6}_{-4}	4^{+4}_{-2}	5^{+5}_{-4}	$2.42^{+1.47}_{-1.19}$	$0.64^{+0.54}_{-0.36}$	$1.31^{+1.31}_{-1.01}$	2.8±2.5	1.4±0.7	6.6±2.5	$1.07^{+1.16}_{-1.10}$	- - -	C
222	27^{+8}_{-6}	3^{+4}_{-2}	24^{+7}_{-6}	$3.12^{+0.89}_{-0.72}$	$0.71^{+0.26}_{-0.10}$	$2.81^{+0.86}_{-0.68}$	4.2±0.5	3.5±0.6	5.2±0.9	$2.11^{+0.65}_{-0.54}$	- - -	D
223	6^{+4}_{-2}	1^{+2}_{-1}	5^{+3}_{-2}	$1.15^{+0.73}_{-0.48}$	$0.11^{+0.27}_{-0.10}$	$0.98^{+0.71}_{-0.45}$	4.2±0.7	3.3±1.0	4.5±0.6	$0.77^{+0.51}_{-0.35}$	- - -	E
224	4^{+3}_{-2}	4^{+3}_{-2}	3	$1.22^{+1.04}_{-0.62}$	$0.75^{+0.60}_{-0.36}$	0.84	0.8±0.2	0.7±0.1	1.1±0.1	$0.17^{+0.15}_{-0.09}$	- - H	A
225	9^{+4}_{-3}	3^{+3}_{-2}	6^{+4}_{-2}	$1.75^{+0.84}_{-0.61}$	$0.35^{+0.35}_{-0.19}$	$1.18^{+0.75}_{-0.49}$	2.1±0.7	1.8±0.2	3.9±0.9	$0.60^{+0.35}_{-0.29}$	- - -	B
226	40^{+7}_{-6}	37^{+7}_{-6}	3^{+3}_{-2}	$8.09^{+1.51}_{-1.29}$	$4.36^{+0.84}_{-0.72}$	$0.57^{+0.61}_{-0.34}$	1.0±0.1	0.9±0.1	1.4±0.1	$1.31^{+0.26}_{-0.22}$	- - -	A
227	21^{+7}_{-6}	12^{+5}_{-4}	9^{+6}_{-4}	$2.27^{+0.81}_{-0.63}$	$1.09^{+0.35}_{-0.24}$	$0.97^{+0.67}_{-0.46}$	1.3±1.0	1.0±0.2	5.1±2.0	$0.46^{+0.41}_{-0.40}$	- - -	B
228	2^{+4}_{-2}	5^{+4}_{-2}	2	$0.37^{+0.72}_{-0.37}$	$0.58^{+0.42}_{-0.27}$	0.47	1.1±0.0	1.1±8.9	1.1±8.9	$0.06^{+0.12}_{-0.06}$	- - H	A
229	58^{+9}_{-8}	49^{+8}_{-7}	9^{+5}_{-4}	$13.50^{+2.09}_{-1.84}$	$6.49^{+1.08}_{-0.94}$	$2.16^{+1.12}_{-0.86}$	1.2±0.1	1.0±0.0	1.6±0.2	$2.64^{+0.45}_{-0.40}$	- - -	A

No.	C_{net} FB	C_{net} SB	C_{net} HB	$f_{\rm ph}$FB(10^{-6} cm^{-2} s^{-1})	$f_{\rm ph}$SB(10^{-6} cm^{-2} s^{-1})	$f_{\rm ph}$HB(10^{-6} cm^{-2} s^{-1})	E_{50} (keV)	E_{25} (keV)	E_{75} (keV)	f_X(10^{-14}erg cm^{-2} s^{-1})	Phot. Flag	Quantile Group
230	6^{+4}_{-2}	2^{+3}_{-1}	4^{+3}_{-2}	$1.52^{+0.97}_{-0.64}$	$0.30^{+0.42}_{-0.20}$	$1.02^{+0.88}_{-0.53}$	2.8±0.7	1.8±0.4	2.9±1.1	$0.68^{+0.46}_{-0.33}$	- - -	E
231	10^{+5}_{-4}	4^{+3}_{-2}	6^{+5}_{-4}	$3.63^{+1.96}_{-1.55}$	$0.82^{+0.71}_{-0.45}$	$2.22^{+1.76}_{-1.34}$	2.2±2.2	1.8±0.4	7.6±3.3	$1.29^{+1.47}_{-1.41}$	- - -	B
232	7^{+4}_{-3}	6^{+4}_{-2}	1^{+2}_{-1}	$1.49^{+0.86}_{-0.58}$	$0.77^{+0.47}_{-0.31}$	$0.17^{+0.54}_{-0.17}$	1.2±0.2	1.0±0.1	1.5±0.3	$0.29^{+0.17}_{-0.13}$	- - -	A
233	8^{+7}_{-6}	4^{+4}_{-3}	3^{+6}_{-3}	$1.79^{+1.54}_{-1.30}$	$0.57^{+0.57}_{-0.42}$	$0.81^{+1.35}_{-0.81}$	1.6±2.4	1.5±0.3	3.3±6.4	$0.46^{+0.79}_{-0.76}$	- - -	B
234	10^{+4}_{-3}	3^{+3}_{-2}	7^{+4}_{-3}	$2.04^{+0.88}_{-0.66}$	$0.33^{+0.34}_{-0.19}$	$1.51^{+0.80}_{-0.57}$	2.4±0.3	1.9±0.3	2.9±0.5	$0.79^{+0.36}_{-0.28}$	- - -	E
235	5^{+4}_{-3}	5^{+3}_{-2}	1^{+3}_{-1}	$1.18^{+0.83}_{-0.57}$	$0.58^{+0.43}_{-0.27}$	$0.17^{+0.60}_{-0.17}$	1.4±0.6	0.9±0.3	1.8±0.7	$0.27^{+0.22}_{-0.17}$	- - -	B
236	7^{+5}_{-4}	1^{+3}_{-1}	7^{+5}_{-4}	$2.53^{+1.74}_{-1.37}$	$0.12^{+0.58}_{-0.12}$	$2.36^{+1.64}_{-1.25}$	6.9±4.0	2.3±2.5	9.8±1.9	$2.78^{+2.51}_{-2.21}$	- - -	C
237	6^{+4}_{-3}	5^{+3}_{-2}	1^{+3}_{-1}	$1.28^{+0.80}_{-0.54}$	$0.58^{+0.41}_{-0.26}$	$0.28^{+0.57}_{-0.28}$	1.4±0.4	1.4±0.3	1.8±0.7	$0.29^{+0.20}_{-0.15}$	- - -	A
238	20^{+7}_{-6}	20^{+6}_{-5}	1^{+4}_{-1}	$2.23^{+0.79}_{-0.62}$	$1.55^{+0.38}_{-0.27}$	$0.15^{+0.95}_{-0.15}$	1.1±0.1	0.9±0.1	1.4±0.1	$0.40^{+0.15}_{-0.12}$	- - -	A
239	68^{+12}_{-10}	6	71^{+11}_{-10}	$5.49^{+0.93}_{-0.77}$	0.30	$5.84^{+0.94}_{-0.78}$	4.0±0.2	3.4±0.2	5.2±0.6	$3.56^{+0.64}_{-0.55}$	- S -	D
240	8^{+4}_{-3}	3^{+3}_{-2}	5^{+3}_{-2}	$3.62^{+1.84}_{-1.32}$	$0.79^{+0.79}_{-0.44}$	$2.29^{+1.61}_{-1.02}$	2.3±0.5	1.9±0.6	3.1±1.2	$1.36^{+0.76}_{-0.59}$	- - -	E
241	2^{+4}_{-2}	5^{+4}_{-2}	3	$0.62^{+1.39}_{-0.62}$	$0.90^{+0.70}_{-0.46}$	1.10	1.0±0.3	0.8±9.2	1.1±8.9	$0.10^{+0.22}_{-0.10}$	- - H	A
242	11^{+6}_{-5}	6^{+5}_{-3}	5^{+5}_{-4}	$2.32^{+1.28}_{-1.06}$	$0.77^{+0.54}_{-0.41}$	$1.01^{+1.03}_{-0.80}$	1.1±2.6	1.0±0.6	5.0±3.1	$0.42^{+0.99}_{-0.98}$	- - -	B
243	9^{+5}_{-4}	8^{+4}_{-3}	1^{+3}_{-1}	$1.81^{+0.99}_{-0.76}$	$0.97^{+0.49}_{-0.36}$	$0.12^{+0.68}_{-0.12}$	1.3±0.6	1.1±0.2	1.5±3.8	$0.39^{+0.28}_{-0.24}$	- - -	A
244	2^{+5}_{-2}	3^{+4}_{-2}	6	$0.73^{+1.83}_{-0.73}$	$0.53^{+0.74}_{-0.49}$	2.23	1.5±0.1	1.5±8.5	1.6±8.4	$0.18^{+0.44}_{-0.18}$	- - H	A
245	5^{+4}_{-2}	3^{+3}_{-2}	2^{+3}_{-2}	$2.30^{+1.71}_{-1.13}$	$0.76^{+0.81}_{-0.45}$	$1.01^{+1.43}_{-0.79}$	1.6±2.6	1.4±0.6	2.4±3.9	$0.58^{+1.06}_{-1.01}$	- - -	A
246	10^{+4}_{-3}	1^{+2}_{-1}	9^{+4}_{-3}	$1.87^{+0.84}_{-0.62}$	$0.09^{+0.26}_{-0.09}$	$1.74^{+0.82}_{-0.60}$	4.4±0.6	3.1±0.8	5.0±0.8	$1.30^{+0.61}_{-0.47}$	- - -	D
247	5^{+4}_{-2}	2	5^{+4}_{-2}	$1.03^{+0.80}_{-0.53}$	0.30	$1.14^{+0.82}_{-0.54}$	6.6±1.7	3.2±1.5	7.5±0.8	$1.09^{+0.89}_{-0.63}$	- S -	C
248	41^{+9}_{-7}	33^{+7}_{-6}	7^{+6}_{-4}	$4.74^{+0.99}_{-0.82}$	$2.92^{+0.49}_{-0.39}$	$0.90^{+0.61}_{-0.39}$	1.6±0.1	1.3±0.1	2.0±0.2	$1.22^{+0.28}_{-0.24}$	- - -	A
249	38^{+9}_{-7}	8^{+5}_{-3}	30^{+8}_{-6}	$4.05^{+0.90}_{-0.74}$	$0.88^{+0.26}_{-0.14}$	$3.37^{+0.86}_{-0.69}$	2.8±0.4	2.2±0.2	3.9±0.6	$1.82^{+0.48}_{-0.41}$	- - -	E
250	4^{+4}_{-3}	6^{+4}_{-3}	2	$1.01^{+0.88}_{-0.60}$	$0.84^{+0.50}_{-0.34}$	0.54	0.9±0.1	0.8±0.1	1.0±0.1	$0.15^{+0.13}_{-0.09}$	- - H	A
251	5^{+7}_{-5}	11^{+5}_{-4}	8	$0.99^{+1.60}_{-0.99}$	$1.34^{+0.64}_{-0.50}$	1.84	0.8±0.6	0.6±0.3	1.2±0.5	$0.13^{+0.23}_{-0.16}$	- - H	B
252	10^{+5}_{-4}	2	10^{+5}_{-4}	$2.02^{+1.03}_{-0.80}$	0.28	$2.20^{+1.05}_{-0.81}$	6.1±0.8	4.6±0.8	6.4±0.4	$1.99^{+1.04}_{-0.82}$	- S -	D
253	6^{+4}_{-3}	4	6^{+4}_{-3}	$1.11^{+0.79}_{-0.57}$	0.39	$1.11^{+0.77}_{-0.55}$	4.4±1.6	3.6±0.8	6.6±1.9	$0.79^{+0.63}_{-0.50}$	- S -	D
254	2^{+3}_{-2}	3^{+3}_{-2}	3	$0.98^{+1.98}_{-0.98}$	$1.07^{+1.04}_{-0.63}$	1.71	1.5±0.0	1.5±8.5	1.6±8.4	$0.24^{+0.49}_{-0.24}$	- - H	A
255	41^{+7}_{-6}	39^{+7}_{-6}	2^{+3}_{-1}	$8.21^{+1.51}_{-1.30}$	$4.56^{+0.86}_{-0.73}$	$0.34^{+0.55}_{-0.27}$	1.1±0.1	0.9±0.0	1.4±0.1	$1.39^{+0.27}_{-0.24}$	- - -	A
256	11^{+5}_{-4}	1^{+3}_{-1}	10^{+5}_{-3}	$2.45^{+1.04}_{-0.80}$	$0.17^{+0.32}_{-0.16}$	$2.20^{+1.00}_{-0.76}$	2.9±0.6	2.4±0.3	4.0±2.1	$1.14^{+0.53}_{-0.44}$	- - -	E
257	12^{+6}_{-5}	16^{+5}_{-4}	5	$3.14^{+1.54}_{-1.27}$	$2.22^{+0.75}_{-0.59}$	1.22	1.5±0.2	1.1±0.3	1.5±0.1	$0.73^{+0.37}_{-0.30}$	- - H	A
258	9^{+4}_{-3}	6^{+4}_{-2}	4^{+3}_{-2}	$1.78^{+0.81}_{-0.60}$	$0.64^{+0.39}_{-0.26}$	$0.69^{+0.61}_{-0.37}$	1.7±0.5	1.3±0.3	2.5±1.0	$0.48^{+0.26}_{-0.21}$	- - -	B
259	12^{+5}_{-4}	1^{+3}_{-1}	10^{+5}_{-4}	$2.66^{+1.18}_{-0.94}$	$0.18^{+0.34}_{-0.17}$	$2.39^{+1.15}_{-0.90}$	3.3±0.7	2.2±0.3	4.5±1.8	$1.39^{+0.69}_{-0.58}$	- - -	C
260	20^{+7}_{-5}	14^{+6}_{-4}	5^{+5}_{-3}	$2.30^{+0.80}_{-0.61}$	$1.44^{+0.38}_{-0.27}$	$0.58^{+0.59}_{-0.23}$	1.4±0.2	1.2±0.1	2.1±0.3	$0.50^{+0.19}_{-0.15}$	- - -	A
261	8^{+5}_{-4}	5^{+4}_{-2}	3^{+4}_{-3}	$1.67^{+1.05}_{-0.81}$	$0.60^{+0.45}_{-0.30}$	$0.63^{+0.86}_{-0.59}$	2.0±0.5	1.6±0.3	2.7±0.6	$0.53^{+0.35}_{-0.28}$	- - -	A
262	13^{+6}_{-5}	14^{+6}_{-4}	3^{+3}_{-1}	$1.48^{+0.72}_{-0.53}$	$1.39^{+0.37}_{-0.26}$	$0.13^{+0.70}_{-0.13}$	0.9±0.1	0.8±0.1	1.1±0.1	$0.20^{+0.11}_{-0.08}$	- - -	A
263	10^{+5}_{-3}	2^{+3}_{-1}	8^{+4}_{-3}	$2.09^{+0.98}_{-0.75}$	$0.19^{+0.33}_{-0.16}$	$1.80^{+0.94}_{-0.70}$	3.1±1.5	2.2±0.6	5.9±1.9	$1.03^{+0.69}_{-0.62}$	- - -	C
264	9^{+5}_{-3}	5^{+4}_{-2}	4^{+4}_{-2}	$3.25^{+1.64}_{-1.25}$	$1.09^{+0.74}_{-0.49}$	$1.36^{+1.32}_{-0.88}$	1.5±1.5	1.1±0.4	5.0±1.6	$0.76^{+0.88}_{-0.84}$	- - -	B
265	5^{+4}_{-3}	5^{+4}_{-2}	1^{+3}_{-1}	$1.48^{+1.27}_{-0.96}$	$0.74^{+0.58}_{-0.38}$	$0.18^{+1.00}_{-0.18}$	1.0±0.9	0.8±0.2	1.3±1.2	$0.23^{+0.29}_{-0.25}$	- - -	A
266	11^{+5}_{-3}	10^{+4}_{-3}	2^{+3}_{-1}	$2.71^{+1.09}_{-0.83}$	$1.35^{+0.59}_{-0.43}$	$0.37^{+0.65}_{-0.31}$	1.2±0.2	0.9±0.1	1.5±0.9	$0.51^{+0.23}_{-0.19}$	- - -	A
267	8^{+5}_{-4}	7^{+4}_{-3}	1^{+4}_{-1}	$1.77^{+1.08}_{-0.85}$	$0.91^{+0.51}_{-0.37}$	$0.17^{+0.80}_{-0.17}$	1.5±0.3	1.3±0.3	1.8±0.2	$0.41^{+0.27}_{-0.21}$	- - -	A

No.	C_{net} FB	C_{net} SB	C_{net} HB	$f_{\rm ph}$FB(10^{-6} cm^{-2} s^{-1})	$f_{\rm ph}$SB(10^{-6} cm^{-2} s^{-1})	$f_{\rm ph}$HB(10^{-6} cm^{-2} s^{-1})	E_{50} (keV)	E_{25} (keV)	E_{75} (keV)	f_X(10^{-14}erg cm^{-2} s^{-1})	Phot. Flag	Quantile Group
268	30^{+7}_{-5}	13^{+5}_{-4}	17^{+5}_{-4}	$5.77^{+1.28}_{-1.07}$	$1.45^{+0.53}_{-0.41}$	$3.32^{+1.04}_{-0.82}$	2.1±0.2	1.6±0.2	2.6±0.3	$1.93^{+0.46}_{-0.39}$	- - -	A
269	54^{+10}_{-8}	48^{+9}_{-7}	6^{+5}_{-3}	$6.02^{+1.05}_{-0.88}$	$3.78^{+0.54}_{-0.45}$	$0.73^{+0.58}_{-0.35}$	1.0±0.1	0.8±0.0	1.3±0.2	$0.94^{+0.17}_{-0.14}$	- - -	A
270	9^{+5}_{-4}	9^{+4}_{-3}	4	$2.05^{+1.06}_{-0.81}$	$1.18^{+0.55}_{-0.40}$	0.95	1.5±0.3	1.1±0.2	1.7±0.2	$0.49^{+0.27}_{-0.21}$	- - H	A
271	3^{+4}_{-3}	6^{+4}_{-3}	3	$0.64^{+1.01}_{-0.64}$	$0.76^{+0.52}_{-0.36}$	0.78	1.1±0.2	1.0±0.1	1.2±0.1	$0.11^{+0.17}_{-0.11}$	- - H	A
272	13^{+5}_{-4}	8^{+4}_{-3}	5^{+4}_{-3}	$2.80^{+1.14}_{-0.91}$	$0.98^{+0.50}_{-0.37}$	$1.11^{+0.90}_{-0.66}$	1.7±0.3	1.5±0.1	2.1±0.7	$0.75^{+0.34}_{-0.28}$	- - -	A
273	14^{+5}_{-4}	5^{+4}_{-2}	9^{+4}_{-3}	$3.22^{+1.22}_{-0.97}$	$0.70^{+0.48}_{-0.32}$	$2.04^{+1.06}_{-0.80}$	3.1±0.9	1.9±0.5	4.4±1.1	$1.60^{+0.76}_{-0.66}$	- - -	C
274	23^{+7}_{-5}	20^{+6}_{-5}	3^{+5}_{-2}	$2.71^{+0.83}_{-0.64}$	$1.89^{+0.42}_{-0.31}$	$0.39^{+0.55}_{-0.23}$	1.2±0.1	1.0±0.1	1.3±0.1	$0.51^{+0.16}_{-0.13}$	- - -	A
275	7^{+4}_{-3}	1^{+2}_{-1}	6^{+4}_{-3}	$1.40^{+0.81}_{-0.59}$	$0.08^{+0.26}_{-0.08}$	$1.29^{+0.80}_{-0.57}$	4.9±1.0	4.5±1.4	6.0±0.8	$1.10^{+0.68}_{-0.52}$	- - -	E
276	7^{+6}_{-5}	1^{+3}_{-1}	6^{+6}_{-5}	$2.58^{+2.18}_{-1.82}$	$0.20^{+0.68}_{-0.20}$	$2.27^{+2.03}_{-1.66}$	4.2±3.5	2.2±2.3	7.0±3.3	$1.75^{+2.07}_{-1.91}$	- - -	C
277	7	6^{+4}_{-3}	3	1.61	$0.78^{+0.51}_{-0.37}$	0.72	5.2±4.8	2.9±7.1	7.6±7.1	1.35	F - H	C
278	33^{+7}_{-6}	29^{+7}_{-5}	5^{+4}_{-3}	$6.99^{+1.51}_{-1.29}$	$3.46^{+0.78}_{-0.66}$	$0.97^{+0.85}_{-0.61}$	1.2±0.1	0.9±0.1	1.6±0.4	$1.35^{+0.32}_{-0.28}$	- - -	A
279	1^{+4}_{-1}	3	1^{+3}_{-1}	$0.17^{+0.87}_{-0.17}$	0.44	$0.22^{+0.84}_{-0.22}$	2.3±1.3	0.6±9.4	2.5±7.5	$0.06^{+0.32}_{-0.07}$	- S -	C
280	8^{+5}_{-4}	2	9^{+5}_{-4}	$1.88^{+1.16}_{-0.89}$	0.32	$2.15^{+1.18}_{-0.91}$	7.0±2.5	2.5±1.9	7.9±1.2	$2.10^{+1.49}_{-1.24}$	- S -	C
281	7^{+4}_{-3}	2	7^{+4}_{-3}	$2.12^{+1.19}_{-0.85}$	0.42	$2.23^{+1.21}_{-0.87}$	3.7±0.9	3.2±0.3	5.3±0.8	$1.26^{+0.76}_{-0.58}$	- S -	D
282	12^{+6}_{-5}	4^{+4}_{-3}	8^{+5}_{-4}	$5.07^{+2.45}_{-2.02}$	$1.03^{+0.88}_{-0.60}$	$3.30^{+2.18}_{-1.72}$	3.6±1.6	1.7±0.8	5.5±2.1	$2.94^{+1.94}_{-1.76}$	- - -	C
283	6^{+4}_{-2}	5^{+3}_{-2}	1^{+2}_{-1}	$1.30^{+0.85}_{-0.56}$	$0.66^{+0.46}_{-0.29}$	$0.15^{+0.56}_{-0.15}$	1.5±0.3	1.3±0.4	1.8±0.2	$0.32^{+0.22}_{-0.15}$	- - -	A
284	12^{+5}_{-4}	4^{+3}_{-2}	8^{+5}_{-4}	$2.67^{+1.19}_{-0.95}$	$0.51^{+0.43}_{-0.27}$	$1.82^{+1.08}_{-0.83}$	2.3±0.5	1.6±0.6	3.2±2.1	$1.00^{+0.50}_{-0.42}$	- - -	C
285	4^{+6}_{-4}	4	5^{+5}_{-4}	$1.14^{+1.51}_{-1.14}$	0.62	$1.28^{+1.44}_{-1.15}$	4.0±4.9	2.6±2.1	7.4±4.8	$0.72^{+1.32}_{-1.15}$	- S -	C
286	14^{+5}_{-4}	14^{+5}_{-4}	2	$2.95^{+1.05}_{-0.81}$	$1.74^{+0.61}_{-0.47}$	0.52	1.3±0.1	1.2±0.1	1.5±0.1	$0.60^{+0.22}_{-0.18}$	- - H	A
287	23^{+7}_{-6}	5	24^{+7}_{-5}	$2.54^{+0.78}_{-0.61}$	0.30	$2.66^{+0.78}_{-0.61}$	4.7±0.3	4.1±0.2	5.3±0.4	$1.92^{+0.60}_{-0.47}$	- S -	E
288	23^{+7}_{-6}	23^{+6}_{-5}	1^{+3}_{-1}	$2.52^{+0.76}_{-0.59}$	$1.90^{+0.40}_{-0.30}$	$0.14^{+0.78}_{-0.14}$	0.9±0.1	0.8±0.1	1.2±0.2	$0.38^{+0.12}_{-0.10}$	- - -	A
289	10^{+7}_{-6}	5^{+4}_{-3}	5^{+6}_{-5}	$2.44^{+1.68}_{-1.42}$	$0.64^{+0.59}_{-0.43}$	$1.33^{+1.50}_{-1.22}$	2.9±1.3	1.5±0.8	3.3±4.3	$1.14^{+0.93}_{-0.83}$	- - -	C
290	34^{+8}_{-6}	35^{+8}_{-6}	4^{+3}_{-1}	$3.69^{+0.88}_{-0.71}$	$2.80^{+0.48}_{-0.38}$	$0.18^{+0.63}_{-0.18}$	0.9±0.1	0.8±0.0	1.0±0.1	$0.52^{+0.13}_{-0.11}$	- - -	A
291	16^{+5}_{-4}	12^{+5}_{-3}	4^{+3}_{-2}	$3.26^{+1.05}_{-0.83}$	$1.37^{+0.53}_{-0.40}$	$0.89^{+0.70}_{-0.44}$	1.8±0.1	1.4±0.3	2.0±0.5	$0.94^{+0.31}_{-0.25}$	- - -	A
292	9^{+4}_{-3}	3^{+3}_{-2}	7^{+4}_{-3}	$1.83^{+0.87}_{-0.66}$	$0.30^{+0.33}_{-0.18}$	$1.34^{+0.80}_{-0.57}$	2.3±0.6	1.9±0.3	3.4±1.3	$0.67^{+0.36}_{-0.30}$	- - -	E
293	6^{+4}_{-3}	6^{+4}_{-3}	4	$1.19^{+0.91}_{-0.67}$	$0.73^{+0.46}_{-0.31}$	0.90	1.4±0.2	1.1±0.2	1.5±0.1	$0.27^{+0.21}_{-0.15}$	- - H	A
294	9^{+6}_{-5}	4	9^{+5}_{-4}	$2.14^{+1.33}_{-1.08}$	0.49	$2.23^{+1.30}_{-1.04}$	4.4±1.0	3.8±0.4	5.8±0.8	$1.51^{+0.99}_{-0.83}$	- S -	D
295	18^{+6}_{-5}	16^{+5}_{-4}	3^{+4}_{-3}	$4.19^{+1.37}_{-1.12}$	$2.04^{+0.67}_{-0.53}$	$0.61^{+0.89}_{-0.61}$	1.4±0.3	1.0±0.1	1.8±0.8	$0.92^{+0.34}_{-0.30}$	- - -	A
296	11^{+5}_{-4}	8^{+4}_{-3}	3^{+3}_{-2}	$2.53^{+1.10}_{-0.85}$	$1.08^{+0.53}_{-0.39}$	$0.63^{+0.79}_{-0.50}$	1.6±0.3	1.1±0.3	1.9±0.3	$0.64^{+0.30}_{-0.24}$	- - -	A
297	13^{+6}_{-4}	12^{+5}_{-4}	2^{+4}_{-1}	$1.55^{+0.69}_{-0.50}$	$1.29^{+0.35}_{-0.23}$	$0.20^{+0.48}_{-0.13}$	1.2±0.5	1.0±0.1	1.7±1.4	$0.30^{+0.19}_{-0.17}$	- - -	A
298	12^{+5}_{-4}	11^{+4}_{-3}	1^{+3}_{-1}	$2.43^{+0.98}_{-0.76}$	$1.23^{+0.52}_{-0.39}$	$0.30^{+0.61}_{-0.30}$	1.2±0.2	1.0±0.1	1.4±0.9	$0.48^{+0.21}_{-0.17}$	- - -	A
299	18^{+6}_{-5}	15^{+6}_{-4}	4^{+5}_{-2}	$1.94^{+0.68}_{-0.52}$	$1.30^{+0.34}_{-0.24}$	$0.38^{+0.49}_{-0.21}$	1.4±0.3	1.1±0.1	2.4±0.7	$0.43^{+0.18}_{-0.15}$	- - -	B
300	3^{+6}_{-3}	4^{+4}_{-3}	7	$1.03^{+1.90}_{-1.03}$	$0.75^{+0.77}_{-0.56}$	2.12	1.9±0.5	1.4±0.4	1.9±0.2	$0.31^{+0.57}_{-0.32}$	- - H	A
301	4^{+3}_{-2}	1^{+2}_{-1}	3^{+3}_{-2}	$1.19^{+1.06}_{-0.63}$	$0.17^{+0.45}_{-0.16}$	$0.92^{+0.99}_{-0.55}$	2.4±2.9	1.6±1.0	5.9±3.0	$0.45^{+0.69}_{-0.61}$	- - -	C
302	16^{+5}_{-4}	11^{+5}_{-3}	4^{+4}_{-2}	$3.18^{+1.09}_{-0.87}$	$1.34^{+0.54}_{-0.41}$	$0.87^{+0.75}_{-0.50}$	1.1±0.4	0.9±0.1	2.0±1.9	$0.58^{+0.30}_{-0.27}$	- - -	B
303	2^{+3}_{-1}	3	2^{+3}_{-1}	$0.82^{+1.27}_{-0.61}$	0.73	$0.88^{+1.29}_{-0.63}$	2.7±0.0	2.6±7.4	2.7±7.3	$0.35^{+0.54}_{-0.26}$	- S -	E
304	82^{+12}_{-10}	71^{+10}_{-9}	19^{+6}_{-4}	$6.07^{+0.94}_{-0.80}$	$3.00^{+0.46}_{-0.37}$	$1.28^{+0.73}_{-0.39}$	1.3±0.1	1.0±0.1	1.5±1.4	$1.22^{+0.22}_{-0.20}$	- - -	A
305	10^{+5}_{-4}	11^{+5}_{-3}	6	$1.20^{+0.69}_{-0.48}$	$1.27^{+0.37}_{-0.24}$	0.73	1.2±0.1	1.1±0.1	1.3±0.1	$0.23^{+0.14}_{-0.10}$	- - H	A

No.	C_{net} FB	C_{net} SB	C_{net} HB	$f_{\rm ph}$FB(10^{-6} cm^{-2} s^{-1})	$f_{\rm ph}$SB(10^{-6} cm^{-2} s^{-1})	$f_{\rm ph}$HB(10^{-6} cm^{-2} s^{-1})	E_{50} (keV)	E_{25} (keV)	E_{75} (keV)	f_X(10^{-14}erg cm^{-2} s^{-1})	Phot. Flag	Quantile Group
306	24^{+8}_{-6}	14^{+6}_{-4}	10^{+6}_{-5}	$2.73^{+0.88}_{-0.70}$	$1.28^{+0.36}_{-0.25}$	$1.22^{+0.73}_{-0.55}$	1.9±0.4	1.1±0.1	2.8±1.8	$0.83^{+0.33}_{-0.29}$	- - -	B
307	6^{+4}_{-3}	2	7^{+4}_{-3}	$1.36^{+0.98}_{-0.74}$	0.28	$1.57^{+1.00}_{-0.75}$	3.9±0.4	3.6±0.3	4.3±0.3	$0.85^{+0.62}_{-0.47}$	- S -	E
308	8^{+5}_{-3}	2	8^{+5}_{-3}	$1.71^{+1.02}_{-0.77}$	0.29	$1.92^{+1.04}_{-0.79}$	6.9±2.0	4.6±1.5	9.3±1.3	$1.88^{+1.25}_{-1.01}$	- S -	C
309	8^{+5}_{-4}	8^{+4}_{-3}	5	$1.88^{+1.18}_{-0.91}$	$1.10^{+0.58}_{-0.43}$	1.18	1.0±0.1	0.9±0.2	1.2±0.4	$0.30^{+0.19}_{-0.15}$	- - H	A
310	8^{+5}_{-3}	8^{+4}_{-3}	4	$1.93^{+1.12}_{-0.85}$	$1.11^{+0.57}_{-0.41}$	1.04	1.1±0.1	1.0±0.2	1.2±0.1	$0.34^{+0.20}_{-0.15}$	- - H	A
311	5^{+4}_{-3}	6^{+4}_{-3}	4	$1.22^{+1.08}_{-0.80}$	$0.89^{+0.54}_{-0.37}$	0.98	0.9±0.3	0.8±0.1	1.1±0.4	$0.17^{+0.16}_{-0.12}$	- - H	A
312	8^{+4}_{-3}	9^{+4}_{-3}	2	$1.76^{+0.89}_{-0.65}$	$1.09^{+0.51}_{-0.37}$	0.51	1.1±0.1	1.0±0.1	1.4±0.2	$0.30^{+0.16}_{-0.12}$	- - H	A
313	21^{+7}_{-5}	15^{+6}_{-4}	7^{+5}_{-3}	$2.17^{+0.72}_{-0.55}$	$1.28^{+0.34}_{-0.24}$	$0.64^{+0.54}_{-0.30}$	1.5±0.2	1.1±0.2	1.8±0.4	$0.51^{+0.19}_{-0.16}$	- - -	A
314	38^{+8}_{-7}	2^{+3}_{-2}	36^{+8}_{-6}	$4.24^{+0.93}_{-0.75}$	$0.28^{+0.40}_{-0.22}$	$4.21^{+0.93}_{-0.75}$	4.6±0.4	3.0±0.4	5.7±0.5	$3.09^{+0.75}_{-0.63}$	- - -	D
315	36^{+8}_{-6}	32^{+7}_{-6}	4^{+5}_{-2}	$3.92^{+0.91}_{-0.72}$	$2.63^{+0.48}_{-0.37}$	$0.42^{+0.54}_{-0.17}$	1.2±0.1	0.9±0.1	1.5±0.3	$0.75^{+0.18}_{-0.15}$	- - -	A
316	6^{+4}_{-3}	2	8^{+4}_{-3}	$1.40^{+0.98}_{-0.74}$	0.29	$1.72^{+1.00}_{-0.75}$	4.9±0.5	4.4±0.6	5.1±0.2	$1.09^{+0.77}_{-0.59}$	- S -	E
317	5^{+4}_{-2}	5^{+3}_{-2}	4	$1.03^{+0.75}_{-0.50}$	$0.58^{+0.41}_{-0.26}$	0.75	0.9±0.2	0.8±0.1	1.2±0.2	$0.14^{+0.11}_{-0.08}$	- - H	A
318	9	5	7	2.25	0.74	1.88	5.2±4.8	2.9±7.1	7.6±7.1	1.90	F S H	C
319	293^{+17}_{-17}	171^{+15}_{-13}	122^{+13}_{-11}	$31.00^{+1.83}_{-1.83}$	$11.58^{+0.89}_{-0.80}$	$13.12^{+1.37}_{-1.21}$	1.8±0.1	1.3±0.0	2.8±0.2	$8.79^{+0.61}_{-0.61}$	- - -	B
320	11^{+5}_{-3}	7^{+4}_{-3}	4^{+3}_{-2}	$2.30^{+1.00}_{-0.76}$	$0.84^{+0.47}_{-0.32}$	$0.85^{+0.76}_{-0.48}$	1.7±1.1	1.2±0.3	4.3±2.3	$0.64^{+0.49}_{-0.46}$	- - -	B
321	18^{+5}_{-4}	7^{+4}_{-3}	11^{+5}_{-3}	$3.83^{+1.15}_{-0.92}$	$0.83^{+0.46}_{-0.31}$	$2.44^{+0.98}_{-0.74}$	2.2±0.5	1.6±0.3	4.0±1.2	$1.38^{+0.52}_{-0.46}$	- - -	C
322	18^{+5}_{-4}	16^{+5}_{-4}	3^{+3}_{-2}	$3.51^{+1.04}_{-0.83}$	$1.76^{+0.56}_{-0.44}$	$0.51^{+0.57}_{-0.32}$	1.4±0.1	1.1±0.1	1.8±0.7	$0.77^{+0.24}_{-0.20}$	- - -	A
323	11^{+5}_{-3}	7^{+4}_{-3}	4^{+3}_{-2}	$2.12^{+0.91}_{-0.69}$	$0.77^{+0.44}_{-0.30}$	$0.80^{+0.69}_{-0.44}$	1.6±0.5	1.2±0.1	3.0±0.6	$0.54^{+0.28}_{-0.24}$	- - -	B
324	5^{+4}_{-3}	6^{+4}_{-2}	3	$1.20^{+0.84}_{-0.57}$	$0.73^{+0.46}_{-0.30}$	0.69	0.9±0.3	0.8±0.1	1.3±0.4	$0.18^{+0.14}_{-0.10}$	- - H	A
325	78^{+10}_{-9}	5^{+3}_{-2}	73^{+10}_{-9}	$15.26^{+1.94}_{-1.73}$	$0.54^{+0.38}_{-0.24}$	$14.63^{+1.92}_{-1.71}$	4.3±0.2	3.3±0.2	5.1±0.4	$10.56^{+1.44}_{-1.31}$	- - -	D
326	5^{+4}_{-2}	5^{+3}_{-2}	4	$1.00^{+0.71}_{-0.47}$	$0.55^{+0.39}_{-0.25}$	0.73	1.3±2.0	1.0±0.4	1.6±3.1	$0.21^{+0.36}_{-0.34}$	- - H	A
327	15^{+5}_{-4}	5^{+4}_{-2}	9^{+4}_{-3}	$3.16^{+1.13}_{-0.89}$	$0.67^{+0.44}_{-0.29}$	$2.03^{+0.98}_{-0.74}$	2.4±0.5	1.7±0.3	3.1±0.4	$1.21^{+0.50}_{-0.42}$	- - -	E
328	9^{+5}_{-3}	4	9^{+4}_{-3}	$2.14^{+1.07}_{-0.81}$	0.50	$2.09^{+1.06}_{-0.80}$	5.4±1.3	4.3±1.1	7.4±1.5	$1.86^{+1.03}_{-0.83}$	- S -	D
329	5^{+4}_{-3}	4^{+3}_{-2}	1^{+3}_{-1}	$0.98^{+0.81}_{-0.55}$	$0.44^{+0.38}_{-0.23}$	$0.20^{+0.64}_{-0.20}$	1.3±0.9	1.1±0.3	1.5±1.3	$0.21^{+0.22}_{-0.18}$	- - -	A
330	7^{+4}_{-3}	3	7^{+4}_{-3}	$1.24^{+0.72}_{-0.49}$	0.29	$1.28^{+0.73}_{-0.50}$	4.8±0.5	3.9±0.5	5.1±0.7	$0.95^{+0.56}_{-0.39}$	- S -	E
331	6^{+4}_{-2}	3	6^{+4}_{-2}	$1.13^{+0.73}_{-0.48}$	0.31	$1.17^{+0.75}_{-0.49}$	2.7±0.6	2.4±0.2	3.4±0.7	$0.49^{+0.34}_{-0.23}$	- S -	E
332	4^{+4}_{-3}	2	6^{+4}_{-3}	$0.96^{+0.96}_{-0.71}$	0.29	$1.26^{+0.98}_{-0.72}$	4.6±3.8	4.4±2.4	9.2±1.9	$0.70^{+0.91}_{-0.79}$	- S -	C
333	4^{+4}_{-3}	6^{+4}_{-3}	4	$0.95^{+1.12}_{-0.85}$	$0.78^{+0.54}_{-0.37}$	1.05	1.3±0.5	1.2±0.5	1.4±0.2	$0.20^{+0.24}_{-0.19}$	- - H	A
334	9^{+5}_{-4}	6^{+4}_{-3}	2^{+4}_{-2}	$1.90^{+1.09}_{-0.85}$	$0.79^{+0.49}_{-0.35}$	$0.51^{+0.85}_{-0.51}$	1.5±0.4	1.2±0.3	1.9±0.6	$0.45^{+0.28}_{-0.23}$	- - -	A
335	8^{+4}_{-3}	8^{+4}_{-3}	1^{+3}_{-1}	$1.71^{+0.88}_{-0.65}$	$0.89^{+0.46}_{-0.33}$	$0.15^{+0.56}_{-0.15}$	1.5±0.2	1.3±0.2	1.5±0.7	$0.41^{+0.22}_{-0.16}$	- - -	A
336	7	4	7	3.48	0.92	3.33	5.2±4.8	2.9±7.1	7.6±7.1	2.92	F S H	C
337	10^{+5}_{-4}	9^{+4}_{-3}	1^{+3}_{-1}	$2.12^{+1.04}_{-0.80}$	$1.07^{+0.52}_{-0.38}$	$0.23^{+0.72}_{-0.23}$	1.3±0.3	1.1±0.1	1.9±1.5	$0.43^{+0.24}_{-0.19}$	- - -	A
338	103^{+11}_{-11}	87^{+11}_{-10}	16^{+6}_{-5}	$23.87^{+2.52}_{-2.52}$	$11.35^{+1.38}_{-1.24}$	$3.85^{+1.51}_{-1.26}$	1.3±0.1	1.0±0.0	1.6±0.1	$4.95^{+0.56}_{-0.56}$	- - -	A
339	9^{+4}_{-3}	6^{+4}_{-2}	3^{+3}_{-2}	$2.11^{+1.04}_{-0.77}$	$0.80^{+0.50}_{-0.33}$	$0.73^{+0.79}_{-0.48}$	1.7±0.6	1.1±0.3	2.8±1.4	$0.57^{+0.35}_{-0.30}$	- - -	B
340	9^{+5}_{-3}	7^{+4}_{-3}	1^{+3}_{-1}	$1.89^{+1.00}_{-0.76}$	$0.91^{+0.49}_{-0.35}$	$0.29^{+0.71}_{-0.29}$	1.2±0.5	0.9±0.2	1.6±2.2	$0.37^{+0.24}_{-0.20}$	- - -	A
341	11^{+6}_{-5}	6^{+4}_{-3}	5^{+5}_{-4}	$2.76^{+1.46}_{-1.20}$	$0.88^{+0.58}_{-0.42}$	$1.22^{+1.23}_{-0.96}$	1.9±2.1	1.4±0.6	7.5±3.2	$0.84^{+1.01}_{-0.98}$	- - -	B
342	2^{+5}_{-2}	4	2^{+5}_{-2}	$0.39^{+1.23}_{-0.39}$	0.49	$0.49^{+1.19}_{-0.49}$	4.0±6.0	3.8±6.2	9.9±9.4	$0.25^{+0.86}_{-0.45}$	- S -	C
343	2^{+3}_{-2}	4^{+3}_{-2}	2	$0.40^{+0.71}_{-0.40}$	$0.45^{+0.40}_{-0.24}$	0.52	1.3±0.1	1.3±8.7	1.3±8.7	$0.08^{+0.15}_{-0.08}$	- - H	A
344	34^{+8}_{-7}	6^{+4}_{-3}	28^{+7}_{-6}	$8.95^{+2.00}_{-1.73}$	$0.89^{+0.59}_{-0.42}$	$7.54^{+1.88}_{-1.59}$	3.3±0.3	2.7±0.4	4.3±0.9	$4.73^{+1.12}_{-0.99}$	- - -	E

No.	C_{net} FB	C_{net} SB	C_{net} HB	$f_{\rm ph}$FB(10^{-6} cm^{-2} s^{-1})	$f_{\rm ph}$SB(10^{-6} cm^{-2} s^{-1})	$f_{\rm ph}$HB(10^{-6} cm^{-2} s^{-1})	E_{50} (keV)	E_{25} (keV)	E_{75} (keV)	f_X(10^{-14}erg cm^{-2} s^{-1})	Phot. Flag	Quantile Group
345	4^{+4}_{-3}	2	5^{+4}_{-3}	$3.40^{+2.93}_{-2.00}$	0.99	$3.86^{+3.00}_{-2.04}$	4.6±2.4	3.4±1.3	7.8±1.5	$2.53^{+2.53}_{-1.97}$	- S -	C
346	79^{+11}_{-9}	73^{+10}_{-9}	5^{+5}_{-3}	$9.17^{+1.26}_{-1.08}$	$5.72^{+0.68}_{-0.58}$	$0.61^{+0.57}_{-0.36}$	1.1±0.1	1.0±0.0	1.5±0.1	$1.66^{+0.25}_{-0.22}$	- - -	A
347	4^{+4}_{-3}	1^{+3}_{-1}	4^{+4}_{-3}	$1.05^{+1.03}_{-0.75}$	$0.09^{+0.39}_{-0.09}$	$0.91^{+0.96}_{-0.66}$	5.2±2.0	3.1±1.6	6.2±0.9	$0.87^{+0.92}_{-0.71}$	- - -	C
348	8^{+5}_{-3}	4^{+3}_{-2}	4^{+4}_{-3}	$1.69^{+0.98}_{-0.74}$	$0.45^{+0.41}_{-0.26}$	$0.92^{+0.83}_{-0.57}$	1.9±0.6	1.3±0.5	2.5±0.6	$0.52^{+0.34}_{-0.28}$	- - -	B
349	10^{+5}_{-4}	2^{+3}_{-2}	8^{+5}_{-4}	$2.30^{+1.18}_{-0.93}$	$0.24^{+0.39}_{-0.22}$	$1.91^{+1.12}_{-0.86}$	2.7±0.6	2.2±0.6	3.5±1.7	$1.00^{+0.56}_{-0.46}$	- - -	E
350	4^{+3}_{-2}	3	4^{+3}_{-2}	$0.93^{+0.75}_{-0.47}$	0.32	$0.98^{+0.76}_{-0.48}$	3.1±0.3	3.0±0.2	3.2±0.3	$0.46^{+0.37}_{-0.24}$	- S -	E
351	2^{+9}_{-2}	6	3^{+8}_{-3}	$0.54^{+2.06}_{-0.54}$	0.80	$0.69^{+1.91}_{-0.69}$	8.3±7.8	3.2±6.8	8.4±7.9	$0.71^{+2.82}_{-0.98}$	- S -	C
352	14^{+5}_{-4}	4^{+3}_{-2}	10^{+5}_{-4}	$3.12^{+1.21}_{-0.97}$	$0.52^{+0.44}_{-0.28}$	$2.26^{+1.09}_{-0.84}$	2.7±0.4	1.7±0.5	3.3±0.4	$1.35^{+0.56}_{-0.46}$	- - -	C
353	4^{+3}_{-2}	5^{+3}_{-2}	2	$0.90^{+0.69}_{-0.44}$	$0.58^{+0.40}_{-0.26}$	0.48	1.2±0.2	1.1±0.2	1.3±0.1	$0.18^{+0.14}_{-0.09}$	- - H	A
354	4^{+3}_{-2}	5^{+3}_{-2}	2	$0.90^{+0.80}_{-0.51}$	$0.64^{+0.46}_{-0.29}$	0.55	1.4±0.3	1.1±0.2	1.6±0.1	$0.20^{+0.18}_{-0.12}$	- - H	A
355	17^{+6}_{-5}	3	17^{+6}_{-5}	$3.75^{+1.31}_{-1.07}$	0.44	$3.80^{+1.32}_{-1.07}$	5.2±0.4	4.4±0.3	5.9±0.3	$3.12^{+1.12}_{-0.93}$	- S -	D
356	7^{+4}_{-3}	3	7^{+4}_{-3}	$1.41^{+0.83}_{-0.57}$	0.31	$1.48^{+0.84}_{-0.58}$	3.3±1.7	2.7±0.5	5.7±2.6	$0.75^{+0.58}_{-0.48}$	- S -	C
357	10^{+5}_{-4}	9^{+4}_{-3}	1^{+4}_{-1}	$2.22^{+1.18}_{-0.93}$	$1.14^{+0.56}_{-0.41}$	$0.20^{+0.86}_{-0.20}$	1.3±1.1	1.2±0.1	1.8±3.9	$0.46^{+0.45}_{-0.42}$	- - -	A
358	13^{+5}_{-4}	5^{+4}_{-2}	8^{+4}_{-3}	$2.98^{+1.18}_{-0.94}$	$0.64^{+0.46}_{-0.31}$	$1.90^{+1.03}_{-0.77}$	2.9±1.0	1.5±0.4	4.1±1.7	$1.39^{+0.73}_{-0.65}$	- - -	C
359	4^{+3}_{-2}	2^{+3}_{-1}	2^{+3}_{-1}	$0.79^{+0.72}_{-0.44}$	$0.24^{+0.35}_{-0.17}$	$0.37^{+0.61}_{-0.30}$	2.2±2.2	1.0±1.0	5.0±1.4	$0.28^{+0.37}_{-0.32}$	- - -	B
360	8^{+4}_{-3}	4^{+3}_{-2}	4^{+3}_{-2}	$1.94^{+0.95}_{-0.69}$	$0.52^{+0.43}_{-0.26}$	$1.06^{+0.80}_{-0.51}$	2.6±1.0	1.2±0.4	3.6±1.6	$0.80^{+0.50}_{-0.42}$	- - -	C
361	8^{+4}_{-3}	2	8^{+4}_{-3}	$1.81^{+1.00}_{-0.75}$	0.31	$1.92^{+1.03}_{-0.77}$	4.8±0.6	3.9±0.4	5.2±1.1	$1.38^{+0.79}_{-0.60}$	- S -	E
362	11^{+5}_{-4}	1^{+3}_{-1}	10^{+5}_{-3}	$2.31^{+1.00}_{-0.77}$	$0.16^{+0.31}_{-0.15}$	$2.08^{+0.96}_{-0.73}$	4.3±0.7	3.9±0.8	5.8±0.7	$1.60^{+0.73}_{-0.59}$	- - -	D
363	8^{+4}_{-3}	8^{+4}_{-3}	2	$1.49^{+0.78}_{-0.56}$	$0.91^{+0.45}_{-0.33}$	0.47	1.3±0.2	1.0±0.1	1.6±0.1	$0.32^{+0.17}_{-0.13}$	- - H	A
364	4^{+3}_{-2}	4^{+3}_{-2}	2	$1.19^{+1.01}_{-0.61}$	$0.73^{+0.59}_{-0.35}$	0.81	0.9±0.3	0.8±0.1	1.4±0.3	$0.17^{+0.16}_{-0.11}$	- - H	B
365	194^{+29}_{-29}	9^{+10}_{-9}	194^{+26}_{-26}	$22.18^{+3.21}_{-3.21}$	$1.19^{+1.27}_{-1.12}$	$22.82^{+3.05}_{-3.05}$	5.2±0.2	4.6±0.2	5.3±0.2	$18.56^{+2.77}_{-2.77}$	- - -	D
366	4	1^{+2}_{-1}	2	0.75	$0.10^{+0.26}_{-0.09}$	0.46	5.2±4.8	2.9±7.1	7.6±7.1	0.63	F - H	C
367	9^{+4}_{-3}	9^{+4}_{-3}	2	$1.76^{+0.85}_{-0.62}$	$1.06^{+0.49}_{-0.36}$	0.50	1.3±0.2	1.1±0.2	1.5±0.1	$0.36^{+0.18}_{-0.14}$	- - H	A
368	17^{+6}_{-5}	2^{+3}_{-2}	15^{+6}_{-5}	$3.85^{+1.40}_{-1.15}$	$0.26^{+0.39}_{-0.22}$	$3.47^{+1.36}_{-1.10}$	4.6±0.4	3.5±1.1	5.1±0.7	$2.85^{+1.07}_{-0.89}$	- - -	D
369	38^{+9}_{-7}	26^{+7}_{-5}	12^{+6}_{-5}	$4.34^{+0.97}_{-0.79}$	$2.24^{+0.44}_{-0.34}$	$1.41^{+0.71}_{-0.53}$	1.6±0.2	1.2±0.1	2.7±0.6	$1.11^{+0.30}_{-0.26}$	- - -	B
370	8^{+4}_{-3}	1^{+2}_{-1}	7^{+4}_{-3}	$1.78^{+0.95}_{-0.70}$	$0.07^{+0.29}_{-0.07}$	$1.69^{+0.93}_{-0.68}$	4.3±1.3	2.3±0.8	5.2±0.6	$1.24^{+0.76}_{-0.62}$	- - -	C
371	17^{+5}_{-4}	2	17^{+5}_{-4}	$3.42^{+1.09}_{-0.87}$	0.29	$3.54^{+1.11}_{-0.89}$	4.3±0.2	3.7±0.4	4.7±0.3	$2.33^{+0.76}_{-0.61}$	- S -	E
372	24^{+7}_{-6}	12^{+5}_{-4}	11^{+6}_{-4}	$2.73^{+0.86}_{-0.68}$	$1.10^{+0.34}_{-0.23}$	$1.18^{+0.71}_{-0.36}$	1.7±0.4	1.2±0.4	2.2±0.4	$0.76^{+0.29}_{-0.25}$	- - -	B
373	28^{+8}_{-7}	3^{+3}_{-2}	26^{+7}_{-6}	$6.84^{+1.89}_{-1.64}$	$0.35^{+0.46}_{-0.30}$	$6.35^{+1.84}_{-1.58}$	4.6±0.6	3.2±0.6	6.4±1.7	$5.08^{+1.55}_{-1.38}$	- - -	C
374	10^{+5}_{-4}	4^{+3}_{-2}	6^{+4}_{-3}	$2.19^{+1.08}_{-0.84}$	$0.51^{+0.42}_{-0.27}$	$1.33^{+0.95}_{-0.70}$	3.9±1.4	1.4±1.0	4.7±2.0	$1.37^{+0.84}_{-0.72}$	- - -	C
375	11^{+6}_{-5}	3^{+3}_{-2}	7^{+5}_{-4}	$2.63^{+1.39}_{-1.13}$	$0.46^{+0.47}_{-0.30}$	$1.86^{+1.28}_{-1.01}$	4.6±2.3	1.9±1.0	6.7±2.3	$1.96^{+1.43}_{-1.30}$	- - -	C
376	36^{+7}_{-6}	23^{+6}_{-5}	13^{+5}_{-4}	$6.89^{+1.36}_{-1.16}$	$2.58^{+0.66}_{-0.54}$	$2.51^{+0.93}_{-0.71}$	1.6±0.2	1.2±0.1	3.1±0.8	$1.76^{+0.40}_{-0.36}$	- - -	B
377	4^{+4}_{-3}	3^{+3}_{-2}	1^{+3}_{-1}	$2.29^{+2.23}_{-1.60}$	$0.85^{+0.92}_{-0.51}$	$0.80^{+1.96}_{-0.80}$	1.4±3.7	1.1±1.3	5.1±3.6	$0.52^{+1.44}_{-1.40}$	- - -	B
378	7^{+4}_{-3}	2^{+3}_{-1}	5^{+4}_{-2}	$1.60^{+0.89}_{-0.64}$	$0.24^{+0.35}_{-0.17}$	$1.22^{+0.83}_{-0.55}$	3.0±0.6	1.6±0.6	3.1±0.2	$0.76^{+0.45}_{-0.34}$	- - -	C
379	6^{+4}_{-3}	7^{+4}_{-3}	2	$1.34^{+0.79}_{-0.54}$	$0.84^{+0.46}_{-0.31}$	0.49	1.3±0.2	0.9±0.2	1.4±0.1	$0.28^{+0.17}_{-0.12}$	- - H	A
380	5^{+4}_{-3}	5^{+3}_{-2}	1^{+3}_{-1}	$1.11^{+0.88}_{-0.64}$	$0.56^{+0.41}_{-0.26}$	$0.14^{+0.70}_{-0.14}$	1.8±2.9	1.5±0.6	5.6±4.4	$0.32^{+0.57}_{-0.54}$	- - -	B
381	10^{+5}_{-4}	3^{+3}_{-2}	6^{+4}_{-3}	$2.24^{+1.10}_{-0.85}$	$0.41^{+0.42}_{-0.25}$	$1.55^{+0.99}_{-0.72}$	3.0±0.9	1.3±0.6	3.7±1.1	$1.08^{+0.61}_{-0.51}$	- - -	C
382	4^{+5}_{-3}	4^{+4}_{-2}	5	$1.37^{+1.39}_{-1.05}$	$0.74^{+0.63}_{-0.42}$	1.59	1.3±3.4	1.3±0.9	1.5±3.6	$0.29^{+0.80}_{-0.77}$	- - H	A

No.	C_{net} FB	C_{net} SB	C_{net} HB	$f_{\rm ph}$FB(10^{-6} cm^{-2} s^{-1})	$f_{\rm ph}$SB(10^{-6} cm^{-2} s^{-1})	$f_{\rm ph}$HB(10^{-6} cm^{-2} s^{-1})	E_{50} (keV)	E_{25} (keV)	E_{75} (keV)	f_X(10^{-14}erg cm^{-2} s^{-1})	Phot. Flag	Quantile Group
383	13^{+5}_{-4}	2^{+3}_{-1}	11^{+5}_{-3}	$2.96^{+1.13}_{-0.87}$	$0.24^{+0.36}_{-0.17}$	$2.59^{+1.09}_{-0.82}$	3.7±0.8	3.0±0.8	5.4±0.9	$1.73^{+0.77}_{-0.65}$	- - -	D
384	36^{+9}_{-8}	12^{+5}_{-4}	24^{+8}_{-7}	$8.32^{+2.03}_{-1.79}$	$1.53^{+0.66}_{-0.52}$	$5.71^{+1.82}_{-1.57}$	2.9±0.5	1.9±0.3	4.4±0.4	$3.90^{+1.18}_{-1.09}$	- - -	C
385	6^{+4}_{-3}	1^{+2}_{-1}	6^{+4}_{-2}	$1.23^{+0.72}_{-0.49}$	$0.10^{+0.26}_{-0.09}$	$1.08^{+0.70}_{-0.46}$	5.0±1.0	4.3±1.2	6.0±0.9	$0.98^{+0.60}_{-0.43}$	- - -	D
386	9^{+5}_{-4}	4	9^{+5}_{-4}	$2.15^{+1.24}_{-0.99}$	0.50	$2.19^{+1.21}_{-0.95}$	7.4±1.4	5.7±2.7	9.1±0.8	$2.55^{+1.55}_{-1.28}$	- S -	D
387	17^{+5}_{-4}	3	18^{+5}_{-4}	$3.46^{+1.05}_{-0.84}$	0.30	$3.55^{+1.08}_{-0.86}$	4.8±0.7	3.9±0.3	6.5±0.9	$2.66^{+0.90}_{-0.75}$	- S -	D
388	8^{+5}_{-4}	5^{+4}_{-2}	3^{+4}_{-3}	$1.83^{+1.12}_{-0.87}$	$0.66^{+0.47}_{-0.31}$	$0.69^{+0.94}_{-0.68}$	1.4±0.9	1.0±0.3	2.8±0.9	$0.42^{+0.37}_{-0.33}$	- - -	B
389	113^{+11}_{-11}	25^{+6}_{-5}	88^{+10}_{-9}	$21.59^{+2.04}_{-2.04}$	$2.79^{+0.68}_{-0.56}$	$17.15^{+2.04}_{-1.83}$	2.9±0.2	2.3±0.2	4.6±0.2	$10.04^{+1.14}_{-1.14}$	- - -	C
390	6^{+4}_{-3}	4^{+3}_{-2}	2^{+3}_{-2}	$1.24^{+0.82}_{-0.61}$	$0.47^{+0.38}_{-0.24}$	$0.44^{+0.66}_{-0.42}$	1.5±0.7	1.3±0.2	2.2±1.6	$0.30^{+0.24}_{-0.20}$	- - -	A
391	150^{+15}_{-13}	6^{+3}_{-2}	148^{+15}_{-13}	$11.21^{+1.15}_{-1.01}$	$0.31^{+0.37}_{-0.21}$	$11.22^{+1.15}_{-1.01}$	3.8±0.1	3.2±0.1	4.7±0.2	$6.83^{+0.73}_{-0.65}$	- - -	E
392	14^{+6}_{-5}	1^{+3}_{-1}	13^{+6}_{-4}	$5.92^{+2.34}_{-1.90}$	$0.29^{+0.62}_{-0.29}$	$5.52^{+2.30}_{-1.85}$	3.1±0.4	2.9±0.7	4.3±1.3	$2.98^{+1.24}_{-1.03}$	- - -	E
393	5^{+3}_{-2}	5^{+3}_{-2}	3	$2.89^{+2.01}_{-1.28}$	$1.71^{+1.17}_{-0.74}$	1.58	1.2±0.2	0.9±0.2	1.3±0.1	$0.55^{+0.40}_{-0.26}$	- - H	A
394	63^{+10}_{-9}	38^{+8}_{-6}	25^{+7}_{-6}	$8.14^{+1.30}_{-1.13}$	$2.75^{+0.57}_{-0.46}$	$3.34^{+0.98}_{-0.79}$	1.5±0.3	1.2±0.1	3.0±0.4	$1.99^{+0.46}_{-0.43}$	- - -	B
395	33^{+8}_{-7}	4^{+4}_{-2}	29^{+8}_{-6}	$3.01^{+0.81}_{-0.63}$	$0.66^{+0.23}_{-0.09}$	$2.80^{+0.79}_{-0.61}$	4.1±0.4	3.0±0.5	5.0±0.3	$1.97^{+0.56}_{-0.46}$	- - -	D
396	103^{+12}_{-11}	11^{+5}_{-4}	92^{+12}_{-10}	$12.23^{+1.48}_{-1.30}$	$1.23^{+0.37}_{-0.25}$	$11.11^{+1.43}_{-1.24}$	3.4±0.2	2.7±0.1	4.2±0.2	$6.73^{+0.87}_{-0.77}$	- - -	D
397	111^{+13}_{-11}	81^{+11}_{-9}	30^{+8}_{-6}	$11.95^{+1.36}_{-1.20}$	$5.81^{+0.66}_{-0.56}$	$3.37^{+0.86}_{-0.69}$	1.5±0.1	1.2±0.1	2.1±0.3	$2.88^{+0.36}_{-0.32}$	- - -	A
398	13^{+6}_{-5}	6^{+4}_{-3}	7^{+5}_{-4}	$3.22^{+1.47}_{-1.22}$	$0.81^{+0.52}_{-0.36}$	$1.81^{+1.32}_{-1.05}$	2.1±2.6	1.5±0.5	6.8±2.9	$1.08^{+1.44}_{-1.41}$	- - -	B
399	9^{+6}_{-5}	1^{+3}_{-1}	7^{+6}_{-5}	$2.37^{+1.68}_{-1.40}$	$0.23^{+0.45}_{-0.23}$	$2.01^{+1.63}_{-1.34}$	3.5±1.0	2.3±1.5	4.2±1.4	$1.33^{+1.02}_{-0.88}$	- - -	D
400	8^{+5}_{-4}	7^{+4}_{-3}	1^{+4}_{-1}	$1.88^{+1.15}_{-0.89}$	$0.95^{+0.53}_{-0.38}$	$0.20^{+0.88}_{-0.20}$	1.3±0.2	1.2±0.2	1.5±0.4	$0.39^{+0.25}_{-0.19}$	- - -	A
401	8^{+4}_{-3}	5^{+3}_{-2}	3^{+3}_{-2}	$1.96^{+0.99}_{-0.72}$	$0.66^{+0.47}_{-0.30}$	$0.82^{+0.78}_{-0.47}$	1.9±0.4	1.4±0.4	2.5±0.4	$0.60^{+0.33}_{-0.26}$	- - -	A
402	45^{+10}_{-8}	1^{+3}_{-1}	46^{+10}_{-8}	$4.40^{+1.04}_{-0.86}$	$0.07^{+0.33}_{-0.07}$	$4.63^{+1.05}_{-0.87}$	4.4±0.3	3.9±0.2	5.6±0.8	$3.14^{+0.76}_{-0.64}$	- - -	D
403	11^{+5}_{-4}	8^{+4}_{-3}	3^{+4}_{-3}	$2.88^{+1.39}_{-1.10}$	$1.20^{+0.64}_{-0.48}$	$0.78^{+1.03}_{-0.71}$	1.5±0.5	1.0±0.2	2.4±2.7	$0.69^{+0.40}_{-0.35}$	- - -	B
404	320^{+34}_{-34}	2^{+11}_{-2}	322^{+32}_{-32}	$35.56^{+3.78}_{-3.78}$	$0.23^{+1.34}_{-0.23}$	$36.73^{+3.63}_{-3.63}$	4.7±0.1	3.9±0.2	5.5±0.3	$27.02^{+2.94}_{-2.94}$	- - -	E
405	10^{+4}_{-3}	2^{+3}_{-1}	8^{+4}_{-3}	$2.18^{+0.97}_{-0.72}$	$0.25^{+0.35}_{-0.17}$	$1.79^{+0.91}_{-0.65}$	2.8±0.3	2.5±0.4	3.3±1.0	$0.98^{+0.45}_{-0.34}$	- - -	E
406	12^{+5}_{-3}	3	12^{+5}_{-3}	$2.51^{+0.99}_{-0.75}$	0.33	$2.59^{+1.01}_{-0.77}$	4.8±0.4	4.2±0.4	5.4±1.1	$1.92^{+0.78}_{-0.60}$	- S -	E
407	14^{+5}_{-4}	12^{+5}_{-3}	2^{+3}_{-1}	$2.64^{+0.94}_{-0.73}$	$1.34^{+0.52}_{-0.39}$	$0.34^{+0.53}_{-0.26}$	1.5±0.2	1.1±0.2	1.8±0.6	$0.62^{+0.24}_{-0.19}$	- - -	A
408	4^{+4}_{-3}	5^{+4}_{-2}	3	$0.71^{+0.77}_{-0.56}$	$0.56^{+0.41}_{-0.27}$	0.69	1.4±4.4	1.2±1.3	1.5±4.6	$0.16^{+0.52}_{-0.51}$	- - H	A
409	11^{+5}_{-3}	1^{+2}_{-1}	10^{+4}_{-3}	$2.23^{+0.91}_{-0.69}$	$0.09^{+0.27}_{-0.09}$	$2.12^{+0.90}_{-0.67}$	4.8±0.5	4.0±0.9	5.5±1.5	$1.72^{+0.73}_{-0.56}$	- - -	E
410	20^{+6}_{-5}	8^{+4}_{-3}	12^{+5}_{-4}	$4.83^{+1.46}_{-1.21}$	$1.06^{+0.55}_{-0.40}$	$3.00^{+1.26}_{-1.00}$	3.1±0.9	1.8±0.5	4.5±1.5	$2.41^{+0.99}_{-0.90}$	- - -	C
411	10^{+5}_{-4}	4	10^{+5}_{-4}	$2.80^{+1.44}_{-1.15}$	0.62	$2.79^{+1.40}_{-1.11}$	3.9±1.1	2.6±0.7	5.7±1.7	$1.75^{+1.03}_{-0.88}$	- S -	C
412	10^{+5}_{-3}	1^{+2}_{-1}	9^{+4}_{-3}	$2.07^{+0.97}_{-0.73}$	$0.08^{+0.28}_{-0.08}$	$1.97^{+0.96}_{-0.72}$	4.4±0.9	3.4±1.1	5.3±1.9	$1.45^{+0.74}_{-0.60}$	- - -	D
413	6^{+4}_{-2}	5^{+3}_{-2}	1^{+2}_{-1}	$1.10^{+0.70}_{-0.46}$	$0.56^{+0.39}_{-0.24}$	$0.14^{+0.46}_{-0.14}$	1.3±0.6	0.7±0.3	1.9±0.7	$0.23^{+0.18}_{-0.14}$	- - -	B
414	2^{+4}_{-2}	2	3^{+4}_{-3}	$0.57^{+1.16}_{-0.57}$	0.39	$0.79^{+1.19}_{-0.79}$	6.8±1.7	6.2±5.7	8.5±8.0	$0.63^{+1.28}_{-0.65}$	- S -	D
415	15^{+7}_{-5}	5^{+4}_{-3}	10^{+6}_{-4}	$1.54^{+0.70}_{-0.49}$	$0.44^{+0.26}_{-0.11}$	$1.11^{+0.65}_{-0.44}$	2.5±0.4	2.1±0.2	3.1±0.3	$0.62^{+0.30}_{-0.22}$	- - -	E
416	3^{+5}_{-3}	5	3^{+5}_{-3}	$0.89^{+1.39}_{-0.89}$	0.71	$0.79^{+1.31}_{-0.79}$	5.7±1.1	5.2±0.5	6.4±0.6	$0.81^{+1.27}_{-0.82}$	- S -	E
417	23^{+6}_{-5}	3^{+3}_{-2}	19^{+6}_{-5}	$4.80^{+1.32}_{-1.09}$	$0.42^{+0.39}_{-0.23}$	$4.15^{+1.26}_{-1.02}$	4.2±0.8	2.2±0.5	5.2±1.8	$3.26^{+1.07}_{-0.94}$	- - -	C
418	4^{+3}_{-2}	4^{+3}_{-2}	4	$0.90^{+0.72}_{-0.46}$	$0.47^{+0.39}_{-0.23}$	0.82	1.0±2.7	0.9±0.7	1.5±2.9	$0.14^{+0.40}_{-0.39}$	- - H	A
419	26^{+7}_{-6}	23^{+6}_{-5}	4^{+5}_{-3}	$2.92^{+0.81}_{-0.64}$	$1.98^{+0.41}_{-0.31}$	$0.40^{+0.52}_{-0.25}$	1.4±0.1	1.1±0.1	1.7±0.7	$0.64^{+0.19}_{-0.15}$	- - -	A
420	4^{+4}_{-2}	4	3^{+3}_{-2}	$0.88^{+0.89}_{-0.59}$	0.53	$0.82^{+0.86}_{-0.55}$	4.1±1.0	3.0±0.8	4.5±0.5	$0.57^{+0.60}_{-0.41}$	- S -	D

No.	C_{net} FB	C_{net} SB	C_{net} HB	$f_{\rm ph}$FB(10^{-6} cm^{-2} s^{-1})	$f_{\rm ph}$SB(10^{-6} cm^{-2} s^{-1})	$f_{\rm ph}$HB(10^{-6} cm^{-2} s^{-1})	E_{50} (keV)	E_{25} (keV)	E_{75} (keV)	f_X(10^{-14}erg cm^{-2} s^{-1})	Phot. Flag	Quantile Group
421	9^{+4}_{-3}	1^{+2}_{-1}	9^{+4}_{-3}	$1.96^{+0.89}_{-0.65}$	$0.11^{+0.28}_{-0.10}$	$1.82^{+0.87}_{-0.63}$	3.5±0.9	2.5±0.6	4.4±2.0	$1.10^{+0.57}_{-0.47}$	- - -	D
422	3^{+6}_{-3}	7^{+4}_{-3}	7	$0.72^{+1.37}_{-0.72}$	$0.89^{+0.56}_{-0.41}$	1.50	0.8±0.5	0.7±9.3	1.1±8.9	$0.09^{+0.18}_{-0.11}$	- - H	B
423	42^{+9}_{-7}	4^{+2}_{-1}	41^{+9}_{-7}	$4.66^{+0.96}_{-0.79}$	$0.87^{+0.30}_{-0.10}$	$4.67^{+0.96}_{-0.79}$	5.0±0.4	3.7±0.4	6.3±0.3	$3.76^{+0.83}_{-0.70}$	- - -	D
424	12^{+5}_{-3}	3	12^{+5}_{-3}	$2.66^{+1.05}_{-0.79}$	0.35	$2.73^{+1.07}_{-0.81}$	4.3±0.4	4.0±0.4	5.2±1.5	$1.83^{+0.74}_{-0.57}$	- S -	E
425	9^{+6}_{-5}	1^{+3}_{-1}	9^{+6}_{-5}	$1.79^{+1.21}_{-1.00}$	$0.07^{+0.37}_{-0.07}$	$1.70^{+1.15}_{-0.93}$	3.6±3.3	2.9±1.7	8.3±2.9	$1.03^{+1.16}_{-1.10}$	- - -	C
426	7^{+4}_{-3}	1^{+2}_{-1}	6^{+4}_{-3}	$1.36^{+0.79}_{-0.56}$	$0.09^{+0.27}_{-0.09}$	$1.22^{+0.77}_{-0.52}$	2.8±0.2	2.7±0.3	3.1±0.4	$0.61^{+0.36}_{-0.26}$	- - -	E
427	12^{+5}_{-4}	1^{+3}_{-1}	10^{+5}_{-4}	$4.14^{+1.87}_{-1.48}$	$0.26^{+0.57}_{-0.26}$	$3.75^{+1.79}_{-1.39}$	5.1±2.0	2.4±1.0	7.3±1.2	$3.38^{+2.03}_{-1.80}$	- - -	C
428	5^{+5}_{-3}	2	7^{+5}_{-3}	$1.42^{+1.22}_{-0.92}$	0.35	$1.88^{+1.24}_{-0.94}$	7.5±1.9	5.2±1.2	8.7±1.3	$1.70^{+1.53}_{-1.19}$	- S -	D
429	6^{+4}_{-3}	3	6^{+4}_{-3}	$2.02^{+1.36}_{-0.93}$	0.52	$2.14^{+1.39}_{-0.95}$	5.4±2.0	4.0±1.0	8.7±1.4	$1.76^{+1.35}_{-1.03}$	- S -	C
430	6^{+4}_{-3}	4^{+3}_{-2}	3^{+3}_{-2}	$1.34^{+0.78}_{-0.53}$	$0.46^{+0.38}_{-0.23}$	$0.55^{+0.62}_{-0.34}$	1.7±1.7	1.0±0.3	2.4±3.5	$0.36^{+0.42}_{-0.39}$	- - -	B
431	5^{+5}_{-4}	1^{+3}_{-1}	4^{+5}_{-4}	$1.14^{+1.17}_{-0.93}$	$0.09^{+0.38}_{-0.09}$	$1.00^{+1.10}_{-0.85}$	2.2±0.5	2.1±0.5	2.4±0.9	$0.41^{+0.43}_{-0.35}$	- - -	E
432	13^{+6}_{-5}	3^{+3}_{-2}	10^{+5}_{-4}	$3.57^{+1.65}_{-1.34}$	$0.40^{+0.54}_{-0.34}$	$2.93^{+1.53}_{-1.22}$	7.2±2.1	3.9±2.5	9.3±0.9	$4.12^{+2.25}_{-1.96}$	- - -	C
433	6^{+4}_{-3}	7^{+4}_{-3}	2	$1.28^{+0.75}_{-0.51}$	$0.79^{+0.43}_{-0.29}$	0.46	1.4±0.3	0.9±0.2	1.7±0.2	$0.28^{+0.18}_{-0.13}$	- - H	B
434	15^{+5}_{-4}	13^{+5}_{-4}	2^{+3}_{-1}	$3.86^{+1.31}_{-1.02}$	$1.98^{+0.72}_{-0.56}$	$0.46^{+0.72}_{-0.35}$	1.3±0.1	1.1±0.2	1.6±1.3	$0.82^{+0.29}_{-0.23}$	- - -	A
435	10^{+4}_{-3}	8^{+4}_{-3}	3^{+3}_{-2}	$2.95^{+1.25}_{-0.93}$	$1.28^{+0.64}_{-0.46}$	$0.75^{+0.84}_{-0.47}$	1.7±0.2	1.5±0.2	2.0±0.6	$0.81^{+0.35}_{-0.27}$	- - -	A
436	6^{+6}_{-5}	1^{+3}_{-1}	4^{+5}_{-4}	$1.48^{+1.40}_{-1.13}$	$0.21^{+0.50}_{-0.21}$	$1.15^{+1.27}_{-0.99}$	2.5±1.7	1.4±1.2	3.8±1.0	$0.59^{+0.69}_{-0.61}$	- - -	C
437	66^{+11}_{-9}	17^{+7}_{-5}	48^{+10}_{-8}	$5.59^{+0.94}_{-0.78}$	$1.02^{+0.33}_{-0.23}$	$4.02^{+0.83}_{-0.67}$	2.9±0.4	2.0±0.1	4.6±0.4	$2.57^{+0.54}_{-0.48}$	- - -	C
438	11^{+5}_{-4}	4	11^{+5}_{-4}	$2.34^{+1.01}_{-0.78}$	0.43	$2.33^{+1.00}_{-0.77}$	3.9±0.7	2.9±0.6	4.8±1.6	$1.47^{+0.68}_{-0.55}$	- S -	D
439	5^{+3}_{-2}	5^{+3}_{-2}	2	$1.21^{+0.90}_{-0.57}$	$0.74^{+0.52}_{-0.33}$	0.65	1.0±0.1	0.9±0.1	1.1±0.1	$0.20^{+0.15}_{-0.10}$	- - H	A
440	12	6	9	3.25	0.85	2.53	5.2±4.8	2.9±7.1	7.6±7.1	2.74	F S H	C
441	5^{+4}_{-2}	3	6^{+4}_{-2}	$1.08^{+0.71}_{-0.47}$	0.30	$1.13^{+0.72}_{-0.48}$	4.9±0.7	3.4±0.6	5.3±0.4	$0.85^{+0.57}_{-0.39}$	- S -	D
442	10^{+5}_{-4}	2	12^{+5}_{-4}	$2.05^{+1.04}_{-0.83}$	0.26	$2.44^{+1.07}_{-0.84}$	8.9±1.1	7.1±0.9	9.5±0.4	$2.91^{+1.52}_{-1.23}$	- S -	D
443	11^{+5}_{-4}	1^{+3}_{-1}	9^{+4}_{-3}	$2.49^{+1.11}_{-0.85}$	$0.20^{+0.36}_{-0.17}$	$2.19^{+1.06}_{-0.80}$	2.9±0.6	2.1±0.6	4.0±1.3	$1.14^{+0.57}_{-0.46}$	- - -	D
444	8^{+4}_{-3}	6^{+4}_{-2}	2^{+3}_{-1}	$1.58^{+0.82}_{-0.59}$	$0.70^{+0.43}_{-0.28}$	$0.37^{+0.56}_{-0.27}$	1.4±0.5	1.0±0.2	2.0±1.1	$0.36^{+0.22}_{-0.18}$	- - -	B
445	10^{+5}_{-4}	3^{+3}_{-2}	7^{+4}_{-3}	$2.05^{+1.00}_{-0.78}$	$0.38^{+0.38}_{-0.23}$	$1.42^{+0.91}_{-0.67}$	3.4±1.2	1.7±0.7	4.8±1.6	$1.11^{+0.68}_{-0.58}$	- - -	C
446	13^{+6}_{-5}	2^{+3}_{-2}	11^{+6}_{-5}	$4.12^{+2.07}_{-1.72}$	$0.33^{+0.60}_{-0.33}$	$3.62^{+1.97}_{-1.61}$	3.1±0.5	2.2±0.7	3.3±2.1	$2.05^{+1.09}_{-0.93}$	- - -	E
447	4^{+4}_{-3}	3	4^{+4}_{-3}	$0.88^{+0.97}_{-0.69}$	0.45	$0.92^{+0.94}_{-0.65}$	9.4±0.3	9.3±0.2	9.5±0.2	$1.32^{+1.45}_{-1.05}$	- S -	D
448	59^{+10}_{-8}	38^{+8}_{-6}	21^{+7}_{-5}	$6.47^{+1.09}_{-0.91}$	$2.97^{+0.49}_{-0.39}$	$2.46^{+0.79}_{-0.61}$	1.6±0.1	1.3±0.1	2.5±0.3	$1.70^{+0.32}_{-0.28}$	- - -	B
449	7^{+4}_{-3}	3^{+3}_{-2}	4^{+3}_{-2}	$1.50^{+0.87}_{-0.63}$	$0.35^{+0.37}_{-0.21}$	$0.92^{+0.77}_{-0.49}$	3.1±1.2	1.6±0.6	4.8±1.2	$0.74^{+0.52}_{-0.42}$	- - -	C
450	9^{+4}_{-3}	2^{+3}_{-1}	7^{+4}_{-3}	$2.47^{+1.17}_{-0.85}$	$0.31^{+0.43}_{-0.21}$	$1.97^{+1.10}_{-0.75}$	4.0±1.0	2.9±1.2	5.8±0.9	$1.59^{+0.85}_{-0.68}$	- - -	C
451	5	3	4	1.28	0.51	1.21	5.2±4.8	2.9±7.1	7.6±7.1	1.07	F S H	C
452	12^{+5}_{-4}	2	12^{+5}_{-4}	$2.33^{+0.95}_{-0.72}$	0.29	$2.43^{+0.97}_{-0.74}$	5.0±0.5	4.4±0.4	6.3±1.1	$1.86^{+0.78}_{-0.61}$	- S -	D
453	5^{+4}_{-2}	1^{+2}_{-1}	4^{+3}_{-2}	$1.17^{+0.86}_{-0.57}$	$0.10^{+0.32}_{-0.10}$	$1.02^{+0.83}_{-0.52}$	3.8±1.2	3.0±0.8	5.7±1.3	$0.72^{+0.58}_{-0.42}$	- - -	D
454	25^{+7}_{-6}	2^{+3}_{-2}	23^{+6}_{-5}	$5.70^{+1.55}_{-1.31}$	$0.28^{+0.41}_{-0.25}$	$5.31^{+1.50}_{-1.25}$	3.9±0.6	3.0±0.3	5.1±0.5	$3.54^{+1.10}_{-0.97}$	- - -	D
455	12^{+5}_{-4}	3^{+3}_{-2}	9^{+4}_{-3}	$2.35^{+0.93}_{-0.71}$	$0.31^{+0.34}_{-0.19}$	$1.84^{+0.86}_{-0.64}$	3.1±0.5	2.1±0.3	3.4±1.2	$1.17^{+0.51}_{-0.41}$	- - -	E
456	11^{+6}_{-5}	8^{+4}_{-3}	3^{+4}_{-3}	$2.69^{+1.39}_{-1.12}$	$1.13^{+0.60}_{-0.44}$	$0.69^{+1.10}_{-0.69}$	1.8±0.5	1.0±0.4	2.4±0.7	$0.77^{+0.44}_{-0.38}$	- - -	B
457	24^{+7}_{-6}	8^{+5}_{-3}	15^{+6}_{-5}	$2.76^{+0.84}_{-0.66}$	$0.85^{+0.31}_{-0.18}$	$1.67^{+0.72}_{-0.51}$	2.3±0.7	1.6±0.3	4.1±0.8	$1.01^{+0.43}_{-0.38}$	- - -	C
458	7^{+4}_{-3}	5^{+3}_{-2}	2^{+3}_{-1}	$3.26^{+1.87}_{-1.27}$	$1.40^{+0.97}_{-0.62}$	$0.85^{+1.34}_{-0.65}$	1.6±1.4	1.4±0.3	4.7±2.8	$0.86^{+0.89}_{-0.82}$	- - -	B
459	6^{+4}_{-3}	6^{+4}_{-2}	3	$1.18^{+0.76}_{-0.52}$	$0.67^{+0.42}_{-0.27}$	0.70	1.4±0.2	1.3±0.1	1.8±0.1	$0.27^{+0.18}_{-0.12}$	- - H	A

No.	C_{net} FB	C_{net} SB	C_{net} HB	$f_{\rm ph}$FB(10^{-6} cm^{-2} s^{-1})	$f_{\rm ph}$SB(10^{-6} cm^{-2} s^{-1})	$f_{\rm ph}$HB(10^{-6} cm^{-2} s^{-1})	E_{50} (keV)	E_{25} (keV)	E_{75} (keV)	f_X(10^{-14}erg cm^{-2} s^{-1})	Phot. Flag	Quantile Group
460	36^{+8}_{-7}	30^{+7}_{-6}	6^{+5}_{-4}	$9.27^{+2.08}_{-1.81}$	$4.33^{+0.98}_{-0.83}$	$1.59^{+1.36}_{-1.08}$	1.0±0.1	0.9±0.1	1.8±1.7	$1.55^{+0.38}_{-0.34}$	- - -	B
461	9^{+5}_{-3}	3^{+3}_{-2}	6^{+4}_{-3}	$2.09^{+1.03}_{-0.78}$	$0.43^{+0.41}_{-0.25}$	$1.37^{+0.91}_{-0.65}$	3.6±2.2	1.6±1.2	9.0±2.0	$1.19^{+0.95}_{-0.87}$	- - -	C
462	12^{+6}_{-4}	9^{+5}_{-3}	4^{+3}_{-2}	$1.43^{+0.71}_{-0.50}$	$1.07^{+0.35}_{-0.22}$	$0.87^{+0.83}_{-0.53}$	1.0±0.5	0.9±0.2	1.9±0.4	$0.22^{+0.15}_{-0.13}$	- - -	B
463	19^{+8}_{-6}	3^{+4}_{-3}	16^{+7}_{-6}	$6.70^{+2.64}_{-2.26}$	$0.67^{+0.77}_{-0.53}$	$5.62^{+2.48}_{-2.09}$	2.5±0.4	2.1±0.4	3.4±2.3	$2.70^{+1.13}_{-0.99}$	- - -	E
464	9^{+4}_{-3}	7^{+4}_{-3}	2^{+3}_{-2}	$1.85^{+0.88}_{-0.65}$	$0.80^{+0.45}_{-0.30}$	$0.47^{+0.62}_{-0.34}$	1.5±0.3	1.1±0.3	1.9±0.5	$0.45^{+0.23}_{-0.18}$	- - -	A
465	7^{+4}_{-3}	6^{+4}_{-2}	1^{+3}_{-1}	$1.45^{+0.85}_{-0.61}$	$0.72^{+0.44}_{-0.29}$	$0.21^{+0.58}_{-0.21}$	1.1±1.1	1.0±0.2	1.6±3.3	$0.27^{+0.29}_{-0.27}$	- - -	A
466	8^{+4}_{-3}	7^{+4}_{-3}	2^{+3}_{-1}	$2.35^{+1.15}_{-0.84}$	$1.10^{+0.61}_{-0.41}$	$0.43^{+0.76}_{-0.37}$	1.3±0.4	1.2±0.2	1.7±0.9	$0.49^{+0.29}_{-0.24}$	- - -	A
467	28^{+7}_{-6}	26^{+7}_{-5}	1^{+4}_{-1}	$3.12^{+0.84}_{-0.66}$	$2.36^{+0.44}_{-0.34}$	$0.16^{+0.47}_{-0.11}$	1.1±0.1	0.9±0.1	1.5±0.2	$0.54^{+0.15}_{-0.13}$	- - -	A
468	41^{+8}_{-7}	7^{+4}_{-3}	34^{+8}_{-6}	$4.46^{+0.91}_{-0.75}$	$0.75^{+0.27}_{-0.16}$	$3.81^{+0.87}_{-0.70}$	3.0±0.2	2.3±0.2	3.8±0.3	$2.12^{+0.46}_{-0.39}$	- - -	E
469	34^{+8}_{-6}	31^{+7}_{-6}	3^{+5}_{-2}	$3.51^{+0.82}_{-0.66}$	$2.41^{+0.43}_{-0.34}$	$0.27^{+0.45}_{-0.19}$	1.0±0.1	0.9±0.1	1.3±0.3	$0.56^{+0.14}_{-0.11}$	- - -	A
470	11^{+5}_{-4}	9^{+4}_{-3}	2^{+3}_{-2}	$2.30^{+0.96}_{-0.73}$	$1.07^{+0.49}_{-0.36}$	$0.44^{+0.63}_{-0.36}$	0.9±0.1	0.8±0.0	1.1±0.2	$0.33^{+0.14}_{-0.11}$	- - -	A
471	16^{+6}_{-5}	13^{+5}_{-4}	3^{+4}_{-3}	$1.59^{+0.64}_{-0.47}$	$1.22^{+0.32}_{-0.22}$	$0.30^{+0.45}_{-0.15}$	1.2±0.7	0.8±0.1	2.3±1.4	$0.30^{+0.21}_{-0.20}$	- - -	B
472	11^{+7}_{-6}	15^{+6}_{-4}	8	$1.34^{+0.89}_{-0.70}$	$1.45^{+0.41}_{-0.29}$	1.05	1.2±0.3	1.1±0.2	1.5±0.2	$0.26^{+0.18}_{-0.15}$	- - H	A
473	50^{+8}_{-7}	37^{+7}_{-6}	14^{+5}_{-4}	$10.39^{+1.71}_{-1.49}$	$4.33^{+0.84}_{-0.72}$	$2.85^{+1.05}_{-0.82}$	1.4±0.2	0.9±0.1	2.1±0.6	$2.30^{+0.46}_{-0.42}$	- - -	B
474	7^{+4}_{-3}	6^{+4}_{-2}	1^{+3}_{-1}	$1.42^{+0.78}_{-0.56}$	$0.68^{+0.41}_{-0.27}$	$0.25^{+0.54}_{-0.25}$	1.1±0.6	1.0±0.1	1.6±1.3	$0.26^{+0.19}_{-0.16}$	- - -	A
475	6^{+6}_{-5}	4	7^{+6}_{-5}	$2.25^{+2.14}_{-1.75}$	0.82	$2.41^{+2.06}_{-1.66}$	8.8±1.7	7.2±2.0	9.5±0.6	$3.18^{+3.09}_{-2.56}$	- S -	D
476	52^{+9}_{-8}	7^{+5}_{-3}	46^{+9}_{-7}	$5.44^{+0.96}_{-0.80}$	$0.77^{+0.27}_{-0.16}$	$4.82^{+0.92}_{-0.76}$	3.7±0.2	2.8±0.3	4.5±0.2	$3.20^{+0.59}_{-0.50}$	- - -	D
477	11^{+5}_{-3}	10^{+4}_{-3}	1^{+3}_{-1}	$2.40^{+0.98}_{-0.74}$	$1.22^{+0.53}_{-0.39}$	$0.31^{+0.58}_{-0.28}$	1.1±0.2	1.0±0.1	1.5±1.3	$0.42^{+0.20}_{-0.16}$	- - -	A
478	9^{+5}_{-4}	9^{+4}_{-3}	5	$2.01^{+1.11}_{-0.87}$	$1.14^{+0.54}_{-0.40}$	1.16	0.9±0.7	0.8±0.2	1.3±4.5	$0.28^{+0.27}_{-0.26}$	- - H	A
479	8	3^{+3}_{-2}	5	1.50	$0.30^{+0.40}_{-0.26}$	1.01	0.8±9.2	0.7±9.3	1.0±9.0	0.20	F - H	A
480	5^{+4}_{-3}	4^{+3}_{-2}	1^{+3}_{-1}	$1.13^{+0.85}_{-0.58}$	$0.47^{+0.41}_{-0.25}$	$0.33^{+0.68}_{-0.33}$	1.5±1.9	1.4±0.6	4.6±1.9	$0.26^{+0.40}_{-0.37}$	- - -	B
481	14^{+7}_{-6}	1^{+4}_{-1}	13^{+6}_{-5}	$3.82^{+1.89}_{-1.60}$	$0.17^{+0.56}_{-0.17}$	$3.60^{+1.78}_{-1.47}$	8.0±3.1	4.3±2.5	9.7±0.7	$4.87^{+3.06}_{-2.76}$	- - -	C
482	6^{+4}_{-3}	5^{+3}_{-2}	1^{+3}_{-1}	$1.22^{+0.76}_{-0.52}$	$0.56^{+0.39}_{-0.25}$	$0.25^{+0.54}_{-0.25}$	1.5±0.4	1.2±0.2	1.9±0.5	$0.29^{+0.19}_{-0.14}$	- - -	A
483	24^{+7}_{-5}	4	25^{+7}_{-5}	$2.78^{+0.81}_{-0.63}$	0.29	$2.88^{+0.81}_{-0.63}$	4.2±0.3	3.6±0.2	4.8±0.3	$1.88^{+0.56}_{-0.45}$	- S -	D
484	8^{+4}_{-3}	3^{+3}_{-2}	5^{+4}_{-2}	$1.63^{+0.87}_{-0.63}$	$0.33^{+0.35}_{-0.20}$	$1.07^{+0.77}_{-0.51}$	2.6±0.8	1.6±0.5	3.7±0.9	$0.68^{+0.42}_{-0.34}$	- - -	C
485	7^{+4}_{-3}	5^{+3}_{-2}	2^{+3}_{-2}	$1.48^{+0.80}_{-0.57}$	$0.57^{+0.40}_{-0.25}$	$0.50^{+0.61}_{-0.34}$	1.6±0.5	1.1±0.2	2.6±0.4	$0.37^{+0.23}_{-0.19}$	- - -	B
486	8^{+6}_{-5}	3	10^{+6}_{-5}	$2.18^{+1.54}_{-1.26}$	0.41	$2.74^{+1.54}_{-1.25}$	5.7±1.3	5.1±0.8	6.9±2.3	$2.00^{+1.48}_{-1.24}$	- S -	D
487	43^{+8}_{-7}	8^{+4}_{-3}	36^{+7}_{-6}	$8.56^{+1.52}_{-1.31}$	$0.90^{+0.45}_{-0.32}$	$7.15^{+1.42}_{-1.21}$	3.6±0.4	2.4±0.3	4.9±0.2	$4.98^{+1.05}_{-0.95}$	- - -	C
488	16^{+5}_{-4}	5^{+3}_{-2}	11^{+5}_{-3}	$3.57^{+1.17}_{-0.93}$	$0.62^{+0.44}_{-0.28}$	$2.55^{+1.05}_{-0.80}$	3.5±0.8	2.0±0.4	4.5±0.8	$2.01^{+0.80}_{-0.69}$	- - -	C
489	5^{+4}_{-3}	6^{+4}_{-3}	3	$0.96^{+0.87}_{-0.63}$	$0.75^{+0.45}_{-0.31}$	0.72	1.1±0.2	1.0±0.1	1.3±0.3	$0.17^{+0.16}_{-0.12}$	- - H	A
490	26^{+7}_{-6}	24^{+7}_{-5}	2^{+4}_{-2}	$2.74^{+0.76}_{-0.60}$	$2.01^{+0.40}_{-0.30}$	$0.23^{+0.44}_{-0.17}$	1.0±0.1	0.9±0.0	1.1±0.6	$0.44^{+0.13}_{-0.10}$	- - -	A
491	2^{+5}_{-2}	3	2^{+4}_{-2}	$0.44^{+0.96}_{-0.44}$	0.38	$0.52^{+0.94}_{-0.52}$	2.2±7.8	1.6±8.4	2.4±7.6	$0.15^{+0.64}_{-0.57}$	- S -	A
492	2^{+6}_{-2}	1^{+3}_{-1}	8	$0.48^{+1.60}_{-0.48}$	$0.20^{+0.52}_{-0.20}$	2.44	9.7±5.8	9.2±6.4	9.7±1.6	$0.75^{+2.51}_{-0.87}$	- - H	D
493	11^{+5}_{-3}	7^{+4}_{-3}	4^{+3}_{-2}	$2.26^{+0.95}_{-0.72}$	$0.81^{+0.45}_{-0.31}$	$0.86^{+0.72}_{-0.46}$	1.6±0.3	1.5±0.2	2.4±0.9	$0.58^{+0.27}_{-0.22}$	- - -	A
494	5^{+7}_{-5}	1^{+4}_{-1}	4^{+6}_{-4}	$1.25^{+1.58}_{-1.25}$	$0.11^{+0.46}_{-0.11}$	$1.07^{+1.49}_{-1.07}$	3.7±4.2	3.2±2.5	8.6±5.0	$0.75^{+1.26}_{-1.12}$	- - -	C
495	27^{+7}_{-6}	14^{+5}_{-4}	12^{+6}_{-4}	$2.86^{+0.80}_{-0.62}$	$0.98^{+0.32}_{-0.20}$	$1.44^{+0.67}_{-0.48}$	2.1±0.4	1.2±0.2	3.3±0.7	$0.96^{+0.32}_{-0.27}$	- - -	B
496	6^{+4}_{-3}	6^{+4}_{-2}	1^{+2}_{-1}	$1.27^{+0.75}_{-0.51}$	$0.67^{+0.41}_{-0.27}$	$0.12^{+0.47}_{-0.12}$	0.9±0.2	0.9±0.1	1.0±0.5	$0.19^{+0.12}_{-0.09}$	- - -	A
497	8^{+5}_{-4}	4^{+3}_{-2}	4^{+4}_{-3}	$1.94^{+1.11}_{-0.85}$	$0.57^{+0.46}_{-0.30}$	$0.95^{+0.93}_{-0.64}$	4.1±1.9	1.8±1.2	6.2±2.1	$1.28^{+0.94}_{-0.82}$	- - -	C

No.	C_{net} FB	C_{net} SB	C_{net} HB	$f_{\rm ph}$FB(10^{-6} cm^{-2} s^{-1})	$f_{\rm ph}$SB(10^{-6} cm^{-2} s^{-1})	$f_{\rm ph}$HB(10^{-6} cm^{-2} s^{-1})	E_{50} (keV)	E_{25} (keV)	E_{75} (keV)	f_X(10^{-14}erg cm^{-2} s^{-1})	Phot. Flag	Quantile Group
498	3^{+6}_{-3}	8^{+5}_{-4}	6	$0.78^{+1.49}_{-0.78}$	$1.03^{+0.63}_{-0.48}$	1.49	1.1±0.3	1.0±0.2	1.2±0.4	$0.13^{+0.26}_{-0.14}$	- - H	A
499	14^{+6}_{-5}	11^{+5}_{-4}	3^{+5}_{-2}	$1.66^{+0.73}_{-0.55}$	$1.20^{+0.35}_{-0.23}$	$0.34^{+0.56}_{-0.16}$	1.3±0.3	1.0±0.2	1.4±0.4	$0.34^{+0.16}_{-0.13}$	- - -	B
500	5^{+4}_{-2}	3^{+3}_{-2}	2^{+3}_{-2}	$1.24^{+0.86}_{-0.57}$	$0.39^{+0.41}_{-0.22}$	$0.57^{+0.71}_{-0.40}$	1.7±1.0	1.2±0.3	3.3±1.2	$0.33^{+0.30}_{-0.25}$	- - -	B
501	6^{+4}_{-3}	5^{+4}_{-2}	1^{+3}_{-1}	$1.41^{+0.98}_{-0.73}$	$0.65^{+0.45}_{-0.30}$	$0.27^{+0.77}_{-0.27}$	1.3±0.3	1.2±0.1	1.8±0.6	$0.30^{+0.22}_{-0.17}$	- - -	A
502	11^{+5}_{-3}	11^{+4}_{-3}	1^{+2}_{-1}	$2.20^{+0.88}_{-0.66}$	$1.22^{+0.50}_{-0.37}$	$0.11^{+0.45}_{-0.11}$	1.1±0.2	0.9±0.1	1.3±2.4	$0.39^{+0.17}_{-0.14}$	- - -	A
503	23^{+6}_{-5}	1^{+3}_{-1}	22^{+6}_{-5}	$5.34^{+1.49}_{-1.24}$	$0.14^{+0.36}_{-0.14}$	$5.20^{+1.48}_{-1.22}$	4.9±0.6	3.4±0.5	6.3±0.6	$4.15^{+1.28}_{-1.10}$	- - -	D
504	12	4	3^{+6}_{-3}	2.82	0.50	$0.79^{+1.39}_{-0.79}$	5.2±4.8	2.9±7.1	7.6±7.1	2.37	F S -	C
505	44^{+9}_{-7}	12^{+5}_{-4}	32^{+8}_{-6}	$5.10^{+1.02}_{-0.84}$	$1.29^{+0.35}_{-0.24}$	$3.81^{+0.92}_{-0.74}$	3.5±0.3	1.9±0.3	4.1±0.9	$2.84^{+0.61}_{-0.52}$	- - -	C
506	11^{+5}_{-3}	11^{+4}_{-3}	4	$2.39^{+0.99}_{-0.75}$	$1.34^{+0.56}_{-0.42}$	0.81	1.2±0.1	1.1±0.2	1.3±0.2	$0.47^{+0.20}_{-0.15}$	- - H	A
507	42^{+9}_{-7}	31^{+7}_{-6}	11^{+6}_{-4}	$4.94^{+0.99}_{-0.82}$	$2.82^{+0.49}_{-0.38}$	$0.92^{+0.57}_{-0.35}$	1.1±0.1	0.9±0.1	1.5±0.3	$0.85^{+0.19}_{-0.17}$	- - -	B
508	30^{+7}_{-6}	2^{+3}_{-2}	28^{+7}_{-6}	$7.71^{+1.85}_{-1.57}$	$0.31^{+0.45}_{-0.26}$	$7.33^{+1.81}_{-1.53}$	4.4±0.4	3.2±0.4	4.9±0.4	$5.45^{+1.39}_{-1.21}$	- - -	D
509	27^{+6}_{-5}	1^{+2}_{-1}	26^{+6}_{-5}	$5.20^{+1.21}_{-1.01}$	$0.10^{+0.26}_{-0.09}$	$5.13^{+1.22}_{-1.01}$	4.8±0.4	3.9±0.4	5.9±1.0	$4.03^{+1.00}_{-0.85}$	- - -	D
510	8^{+5}_{-3}	7^{+4}_{-3}	1^{+3}_{-1}	$1.65^{+0.99}_{-0.75}$	$0.86^{+0.48}_{-0.35}$	$0.13^{+0.71}_{-0.13}$	1.2±0.6	1.1±0.1	1.4±2.5	$0.33^{+0.24}_{-0.21}$	- - -	A
511	7^{+4}_{-3}	4	7^{+4}_{-3}	$3.46^{+2.15}_{-1.59}$	1.06	$3.38^{+2.12}_{-1.54}$	5.0±1.9	3.1±1.1	7.2±1.7	$2.79^{+2.02}_{-1.65}$	- S -	C
512	15^{+7}_{-6}	5^{+4}_{-3}	9^{+6}_{-5}	$3.19^{+1.44}_{-1.22}$	$0.68^{+0.52}_{-0.38}$	$2.04^{+1.28}_{-1.03}$	3.3±1.8	1.0±1.0	5.5±2.0	$1.70^{+1.19}_{-1.12}$	- - -	C
513	9^{+4}_{-3}	2^{+3}_{-1}	7^{+4}_{-3}	$2.20^{+1.06}_{-0.77}$	$0.28^{+0.40}_{-0.19}$	$1.75^{+0.99}_{-0.67}$	2.4±0.5	2.0±0.2	3.4±0.7	$0.86^{+0.45}_{-0.35}$	- - -	E
514	9^{+4}_{-3}	3	9^{+4}_{-3}	$1.81^{+0.87}_{-0.63}$	0.33	$1.86^{+0.89}_{-0.65}$	4.4±0.4	4.1±0.1	4.9±1.9	$1.27^{+0.62}_{-0.46}$	- S -	E
515	7^{+5}_{-4}	7^{+4}_{-3}	5	$1.66^{+1.14}_{-0.88}$	$0.96^{+0.54}_{-0.38}$	1.24	1.5±1.4	1.2±0.3	1.8±4.5	$0.40^{+0.47}_{-0.44}$	- - H	A
516	14^{+5}_{-4}	3	15^{+5}_{-4}	$2.96^{+1.02}_{-0.80}$	0.31	$3.06^{+1.04}_{-0.81}$	4.0±0.8	2.9±0.4	5.7±0.9	$1.92^{+0.77}_{-0.65}$	- S -	D
517	5^{+3}_{-2}	3^{+3}_{-2}	2^{+3}_{-1}	$0.89^{+0.66}_{-0.42}$	$0.33^{+0.33}_{-0.18}$	$0.33^{+0.53}_{-0.26}$	1.7±0.3	1.6±0.2	2.3±0.3	$0.24^{+0.19}_{-0.12}$	- - -	A
518	7^{+5}_{-4}	4^{+4}_{-2}	3^{+4}_{-3}	$1.54^{+1.20}_{-0.95}$	$0.52^{+0.48}_{-0.32}$	$0.64^{+1.03}_{-0.64}$	1.6±0.7	1.3±0.3	2.4±1.1	$0.41^{+0.36}_{-0.31}$	- - -	A
519	44^{+9}_{-7}	42^{+8}_{-7}	6^{+4}_{-1}	$4.79^{+0.97}_{-0.81}$	$3.28^{+0.51}_{-0.41}$	$0.28^{+0.80}_{-0.28}$	1.1±0.1	0.8±0.1	1.3±0.2	$0.82^{+0.17}_{-0.14}$	- - -	A
520	12^{+5}_{-4}	3	13^{+5}_{-4}	$2.39^{+0.90}_{-0.69}$	0.29	$2.46^{+0.92}_{-0.71}$	4.9±0.2	4.7±0.6	5.5±0.4	$1.88^{+0.72}_{-0.55}$	- S -	E
521	16^{+7}_{-5}	5	18^{+7}_{-5}	$1.82^{+0.82}_{-0.64}$	0.32	$2.12^{+0.83}_{-0.64}$	4.6±0.5	4.2±0.5	5.8±0.4	$1.34^{+0.62}_{-0.49}$	- S -	E
522	3^{+3}_{-2}	3	3^{+3}_{-2}	$0.75^{+0.72}_{-0.43}$	0.34	$0.78^{+0.73}_{-0.44}$	5.4±0.7	4.5±0.4	6.2±0.4	$0.65^{+0.63}_{-0.38}$	- S -	D
523	5	2	5	1.07	0.31	1.17	5.2±4.8	2.9±7.1	7.6±7.1	0.90	F S H	C
524	11^{+5}_{-3}	1^{+2}_{-1}	11^{+4}_{-3}	$2.37^{+0.96}_{-0.73}$	$0.09^{+0.28}_{-0.09}$	$2.26^{+0.95}_{-0.71}$	4.4±0.4	3.8±0.7	5.2±0.9	$1.66^{+0.69}_{-0.53}$	- - -	E
525	3^{+3}_{-2}	4^{+3}_{-2}	3	$0.69^{+0.72}_{-0.46}$	$0.43^{+0.39}_{-0.23}$	0.66	1.1±0.2	0.9±0.1	1.2±0.1	$0.13^{+0.13}_{-0.09}$	- - H	A
526	15^{+5}_{-4}	3	15^{+5}_{-4}	$3.00^{+1.02}_{-0.79}$	0.31	$3.08^{+1.04}_{-0.81}$	4.8±0.4	4.1±0.4	5.3±0.6	$2.33^{+0.82}_{-0.65}$	- S -	E
527	26^{+7}_{-6}	1^{+3}_{-1}	25^{+7}_{-6}	$3.05^{+0.86}_{-0.68}$	$0.13^{+0.33}_{-0.13}$	$2.97^{+0.85}_{-0.66}$	4.0±0.3	3.2±0.3	4.5±0.4	$1.97^{+0.57}_{-0.46}$	- - -	E
528	8^{+4}_{-3}	8^{+4}_{-3}	1^{+2}_{-1}	$1.65^{+0.80}_{-0.58}$	$0.89^{+0.45}_{-0.32}$	$0.13^{+0.46}_{-0.13}$	1.0±0.2	0.8±0.1	1.3±0.6	$0.26^{+0.14}_{-0.10}$	- - -	A
529	60^{+10}_{-8}	38^{+8}_{-6}	21^{+7}_{-5}	$6.21^{+1.02}_{-0.86}$	$2.30^{+0.47}_{-0.38}$	$2.23^{+0.73}_{-0.51}$	1.5±0.6	1.1±0.1	1.8±1.3	$1.45^{+0.63}_{-0.62}$	- - -	A
530	12^{+5}_{-4}	5^{+3}_{-2}	7^{+4}_{-3}	$2.44^{+0.94}_{-0.72}$	$0.56^{+0.39}_{-0.25}$	$1.50^{+0.80}_{-0.57}$	2.4±0.6	1.6±0.3	3.8±1.7	$0.95^{+0.44}_{-0.37}$	- - -	C
531	13^{+5}_{-4}	3	13^{+5}_{-4}	$2.36^{+0.89}_{-0.68}$	0.29	$2.43^{+0.91}_{-0.69}$	4.2±0.3	3.8±0.6	5.0±0.9	$1.61^{+0.62}_{-0.48}$	- S -	E
532	6^{+4}_{-3}	2^{+3}_{-1}	4^{+3}_{-2}	$1.29^{+0.79}_{-0.54}$	$0.22^{+0.32}_{-0.15}$	$0.93^{+0.72}_{-0.46}$	3.4±1.1	2.0±0.7	4.8±0.6	$0.71^{+0.49}_{-0.37}$	- - -	C
533	10^{+4}_{-3}	8^{+4}_{-3}	2^{+3}_{-1}	$2.55^{+1.12}_{-0.83}$	$1.21^{+0.61}_{-0.43}$	$0.47^{+0.71}_{-0.34}$	1.3±0.4	1.0±0.2	1.8±1.4	$0.54^{+0.28}_{-0.23}$	- - -	A
534	9^{+4}_{-3}	5^{+3}_{-2}	4^{+3}_{-2}	$1.72^{+0.83}_{-0.60}$	$0.58^{+0.40}_{-0.25}$	$0.75^{+0.65}_{-0.39}$	1.9±0.9	1.7±0.3	3.7±1.6	$0.54^{+0.36}_{-0.31}$	- - -	B
535	6^{+4}_{-3}	1^{+3}_{-1}	5^{+4}_{-3}	$1.24^{+0.92}_{-0.69}$	$0.13^{+0.33}_{-0.13}$	$1.04^{+0.87}_{-0.63}$	4.1±3.9	2.2±2.2	9.1±2.4	$0.81^{+0.97}_{-0.89}$	- - -	C
536	9^{+4}_{-3}	8^{+4}_{-3}	1^{+2}_{-1}	$1.65^{+0.80}_{-0.58}$	$0.89^{+0.45}_{-0.32}$	$0.12^{+0.46}_{-0.12}$	1.1±0.3	1.0±0.1	1.6±1.4	$0.29^{+0.16}_{-0.13}$	- - -	A

No.	C_{net} FB	C_{net} SB	C_{net} HB	$f_{\rm ph}$FB(10^{-6} cm^{-2} s^{-1})	$f_{\rm ph}$SB(10^{-6} cm^{-2} s^{-1})	$f_{\rm ph}$HB(10^{-6} cm^{-2} s^{-1})	E_{50} (keV)	E_{25} (keV)	E_{75} (keV)	f_X(10^{-14}erg cm^{-2} s^{-1})	Phot. Flag	Quantile Group
537	6^{+4}_{-3}	1^{+2}_{-1}	5^{+4}_{-2}	$1.42^{+0.89}_{-0.60}$	$0.11^{+0.31}_{-0.11}$	$1.26^{+0.86}_{-0.57}$	4.5±0.9	4.1±1.0	5.8±0.5	$1.02^{+0.67}_{-0.48}$	- - -	E
538	18^{+7}_{-5}	10^{+5}_{-3}	8^{+6}_{-3}	$2.01^{+0.78}_{-0.61}$	$1.10^{+0.32}_{-0.21}$	$0.88^{+0.66}_{-0.31}$	1.4±0.3	1.1±0.2	1.6±0.2	$0.45^{+0.20}_{-0.17}$	- - -	B
539	5^{+4}_{-3}	6^{+4}_{-3}	3	$1.06^{+0.89}_{-0.63}$	$0.81^{+0.48}_{-0.33}$	0.66	1.1±0.2	1.0±0.2	1.3±0.3	$0.18^{+0.16}_{-0.12}$	- - H	A
540	5^{+4}_{-3}	3	5^{+4}_{-3}	$1.06^{+0.91}_{-0.68}$	0.37	$1.14^{+0.90}_{-0.66}$	6.8±1.5	6.5±0.6	9.4±1.3	$1.16^{+1.03}_{-0.78}$	- S -	D
541	5^{+4}_{-2}	1^{+2}_{-1}	5^{+3}_{-2}	$1.25^{+0.84}_{-0.55}$	$0.12^{+0.31}_{-0.11}$	$1.07^{+0.81}_{-0.51}$	2.7±1.0	2.0±0.4	3.8±1.2	$0.54^{+0.42}_{-0.32}$	- - -	E
542	9^{+4}_{-3}	3^{+3}_{-2}	6^{+4}_{-3}	$1.78^{+0.87}_{-0.65}$	$0.32^{+0.34}_{-0.19}$	$1.24^{+0.79}_{-0.54}$	3.2±1.3	1.6±0.8	5.2±0.8	$0.90^{+0.57}_{-0.49}$	- - -	C
543	12^{+5}_{-4}	6^{+4}_{-3}	7^{+4}_{-3}	$3.11^{+1.31}_{-1.04}$	$0.78^{+0.54}_{-0.37}$	$1.75^{+1.10}_{-0.82}$	2.2±1.0	1.4±0.4	4.5±1.2	$1.10^{+0.68}_{-0.62}$	- - -	B
544	4^{+3}_{-2}	3^{+3}_{-2}	2^{+3}_{-1}	$0.88^{+0.67}_{-0.42}$	$0.33^{+0.34}_{-0.19}$	$0.32^{+0.53}_{-0.26}$	1.6±0.2	1.4±0.1	2.0±0.2	$0.23^{+0.18}_{-0.11}$	- - -	A
545	22^{+7}_{-6}	18^{+6}_{-4}	4^{+4}_{-3}	$2.40^{+0.78}_{-0.60}$	$1.53^{+0.37}_{-0.26}$	$1.01^{+1.06}_{-0.80}$	1.1±0.2	0.9±0.1	1.6±0.3	$0.40^{+0.15}_{-0.12}$	- - -	B
546	15^{+5}_{-4}	11^{+4}_{-3}	4^{+3}_{-2}	$3.58^{+1.23}_{-0.97}$	$1.48^{+0.61}_{-0.46}$	$1.02^{+0.84}_{-0.53}$	1.7±0.3	1.3±0.2	2.7±0.6	$1.00^{+0.38}_{-0.32}$	- - -	B
547	7^{+4}_{-3}	2^{+3}_{-1}	5^{+3}_{-2}	$1.24^{+0.71}_{-0.49}$	$0.21^{+0.29}_{-0.14}$	$0.90^{+0.65}_{-0.41}$	4.1±1.2	1.8±1.1	5.2±0.8	$0.82^{+0.53}_{-0.40}$	- - -	C
548	37^{+9}_{-7}	7^{+5}_{-3}	30^{+8}_{-6}	$3.95^{+0.92}_{-0.76}$	$0.87^{+0.30}_{-0.18}$	$3.07^{+0.84}_{-0.67}$	3.3±0.2	2.0±0.2	3.8±0.8	$2.07^{+0.50}_{-0.42}$	- - -	D
549	1^{+5}_{-1}	3	3^{+5}_{-3}	$0.18^{+1.45}_{-0.18}$	0.41	$0.88^{+1.45}_{-0.88}$	8.8±1.0	8.5±8.0	9.5±9.0	$0.26^{+2.06}_{-0.26}$	- S -	D
550	6^{+5}_{-4}	7^{+4}_{-3}	4	$1.39^{+1.15}_{-0.88}$	$0.97^{+0.56}_{-0.40}$	1.08	0.8±0.2	0.7±0.1	1.1±0.2	$0.19^{+0.17}_{-0.13}$	- - H	A
551	6^{+4}_{-3}	3^{+3}_{-2}	3^{+4}_{-3}	$1.18^{+0.90}_{-0.67}$	$0.36^{+0.37}_{-0.22}$	$0.58^{+0.78}_{-0.54}$	2.1±3.2	1.8±1.6	7.8±2.0	$0.40^{+0.67}_{-0.64}$	- - -	B
552	24^{+8}_{-6}	26^{+7}_{-5}	5	$2.91^{+0.90}_{-0.72}$	$2.26^{+0.47}_{-0.36}$	0.65	1.0±0.0	0.9±0.1	1.1±0.1	$0.47^{+0.15}_{-0.12}$	- - H	A
553	3^{+4}_{-2}	2^{+3}_{-2}	1^{+3}_{-1}	$1.42^{+1.59}_{-1.05}$	$0.63^{+0.75}_{-0.42}$	$0.35^{+1.32}_{-0.35}$	1.6±4.7	1.1±1.8	9.3±3.3	$0.35^{+1.14}_{-1.11}$	- - -	B
554	6^{+5}_{-4}	5^{+4}_{-3}	7	$1.64^{+1.60}_{-1.28}$	$0.89^{+0.63}_{-0.43}$	2.04	1.1±2.5	0.9±0.4	1.3±5.6	$0.29^{+0.72}_{-0.70}$	- - H	A
555	2^{+6}_{-2}	3	4^{+5}_{-4}	$0.49^{+1.45}_{-0.49}$	0.42	$0.97^{+1.45}_{-0.97}$	9.9±0.9	9.1±8.6	10.0±9.5	$0.78^{+2.31}_{-0.78}$	- S -	D
556	11^{+5}_{-3}	3	12^{+5}_{-3}	$2.53^{+1.01}_{-0.77}$	0.33	$2.61^{+1.03}_{-0.78}$	5.2±0.8	4.0±0.5	6.6±0.7	$2.12^{+0.90}_{-0.72}$	- S -	D
557	5^{+4}_{-3}	6^{+4}_{-3}	3	$1.15^{+0.93}_{-0.67}$	$0.84^{+0.51}_{-0.35}$	0.70	1.1±0.1	1.0±0.1	1.1±0.1	$0.20^{+0.16}_{-0.12}$	- - H	A
558	6^{+4}_{-3}	6^{+4}_{-3}	4	$1.30^{+0.95}_{-0.70}$	$0.80^{+0.47}_{-0.32}$	0.94	1.0±0.1	0.9±0.1	1.1±0.1	$0.20^{+0.15}_{-0.11}$	- - H	A
559	3^{+3}_{-2}	3^{+3}_{-2}	2	$0.56^{+0.63}_{-0.35}$	$0.36^{+0.36}_{-0.20}$	0.53	0.9±0.0	0.9±0.0	0.9±0.0	$0.08^{+0.09}_{-0.05}$	- - H	A
560	6^{+4}_{-3}	3^{+3}_{-2}	3^{+3}_{-2}	$1.28^{+0.87}_{-0.60}$	$0.36^{+0.39}_{-0.22}$	$0.67^{+0.75}_{-0.45}$	3.2±1.8	1.4±0.8	4.9±2.2	$0.65^{+0.59}_{-0.49}$	- - -	C
561	10^{+5}_{-4}	4	9^{+5}_{-4}	$2.09^{+1.11}_{-0.87}$	0.52	$2.05^{+1.08}_{-0.83}$	9.2±1.4	8.1±3.6	9.7±0.3	$3.08^{+1.70}_{-1.37}$	- S -	D
562	8^{+5}_{-4}	8^{+4}_{-3}	1^{+3}_{-1}	$1.81^{+1.04}_{-0.81}$	$0.95^{+0.50}_{-0.37}$	$0.14^{+0.75}_{-0.14}$	1.7±1.9	1.3±0.5	1.8±3.9	$0.48^{+0.61}_{-0.59}$	- - -	A
563	6^{+5}_{-4}	4	6^{+4}_{-3}	$2.05^{+1.57}_{-1.20}$	0.82	$1.94^{+1.51}_{-1.12}$	5.4±1.4	3.8±0.8	6.4±1.3	$1.78^{+1.45}_{-1.14}$	- S -	D
564	38^{+10}_{-8}	18^{+7}_{-5}	21^{+8}_{-5}	$2.82^{+0.73}_{-0.58}$	$0.86^{+0.27}_{-0.16}$	$1.71^{+0.66}_{-0.32}$	2.1±0.1	1.4±0.1	2.7±0.2	$0.95^{+0.25}_{-0.21}$	- - -	A
565	6^{+4}_{-2}	3	6^{+4}_{-2}	$1.21^{+0.79}_{-0.52}$	0.33	$1.26^{+0.80}_{-0.53}$	2.6±0.4	2.1±0.2	3.1±0.4	$0.51^{+0.34}_{-0.23}$	- S -	E
566	6^{+4}_{-3}	1^{+3}_{-1}	5^{+4}_{-3}	$2.05^{+1.54}_{-1.14}$	$0.24^{+0.54}_{-0.24}$	$1.66^{+1.45}_{-1.04}$	3.4±1.7	1.8±0.9	4.6±1.8	$1.11^{+1.00}_{-0.83}$	- - -	C
567	8^{+4}_{-3}	3	8^{+4}_{-3}	$1.43^{+0.76}_{-0.54}$	0.29	$1.48^{+0.77}_{-0.55}$	3.8±0.7	3.0±0.5	5.0±0.6	$0.88^{+0.49}_{-0.37}$	- S -	D
568	130^{+14}_{-12}	5^{+5}_{-2}	126^{+13}_{-12}	$17.50^{+1.88}_{-1.67}$	$0.40^{+0.37}_{-0.21}$	$17.17^{+1.86}_{-1.65}$	4.3±0.2	3.2±0.2	5.3±0.3	$11.97^{+1.41}_{-1.28}$	- - -	D
569	129^{+13}_{-12}	67^{+10}_{-8}	62^{+10}_{-8}	$14.35^{+1.47}_{-1.31}$	$4.22^{+0.62}_{-0.52}$	$7.10^{+1.12}_{-0.95}$	2.0±0.1	1.5±0.1	2.9±0.3	$4.64^{+0.55}_{-0.51}$	- - -	A
570	8^{+4}_{-3}	2^{+3}_{-1}	6^{+4}_{-2}	$1.49^{+0.77}_{-0.55}$	$0.22^{+0.30}_{-0.15}$	$1.13^{+0.72}_{-0.47}$	3.0±0.7	2.0±0.6	3.9±0.4	$0.70^{+0.40}_{-0.31}$	- - -	C
571	6^{+4}_{-3}	5^{+3}_{-2}	2^{+3}_{-1}	$1.42^{+0.83}_{-0.57}$	$0.63^{+0.44}_{-0.28}$	$0.34^{+0.60}_{-0.29}$	1.5±0.6	1.0±0.2	2.0±0.8	$0.35^{+0.24}_{-0.19}$	- - -	B
572	5^{+4}_{-2}	1^{+2}_{-1}	5^{+3}_{-2}	$1.09^{+0.73}_{-0.48}$	$0.10^{+0.27}_{-0.10}$	$0.94^{+0.70}_{-0.44}$	3.1±1.7	2.5±0.8	6.5±1.5	$0.53^{+0.46}_{-0.38}$	- - -	C
573	9^{+5}_{-3}	5^{+4}_{-2}	3^{+4}_{-2}	$1.84^{+0.99}_{-0.75}$	$0.67^{+0.44}_{-0.29}$	$0.68^{+0.79}_{-0.53}$	1.5±2.2	1.2±0.4	6.0±3.1	$0.45^{+0.70}_{-0.68}$	- - -	B
574	12^{+5}_{-3}	10^{+4}_{-3}	2^{+3}_{-1}	$2.94^{+1.15}_{-0.87}$	$1.45^{+0.62}_{-0.46}$	$0.45^{+0.68}_{-0.33}$	1.5±0.1	1.3±0.3	1.7±0.7	$0.70^{+0.28}_{-0.22}$	- - -	A

No.	C_{net} FB	C_{net} SB	C_{net} HB	$f_{\rm ph}$FB(10^{-6} cm^{-2} s^{-1})	$f_{\rm ph}$SB(10^{-6} cm^{-2} s^{-1})	$f_{\rm ph}$HB(10^{-6} cm^{-2} s^{-1})	E_{50} (keV)	E_{25} (keV)	E_{75} (keV)	f_X(10^{-14}erg cm^{-2} s^{-1})	Phot. Flag	Quantile Group
575	43^{+9}_{-7}	5	44^{+9}_{-7}	$4.52^{+0.91}_{-0.75}$	0.28	$4.77^{+0.92}_{-0.76}$	4.8±0.3	3.4±0.3	5.6±0.5	$3.49^{+0.74}_{-0.62}$	- S -	D
576	3^{+4}_{-3}	4	3^{+4}_{-3}	$0.62^{+0.83}_{-0.61}$	0.41	$0.59^{+0.82}_{-0.59}$	3.9±0.7	3.8±0.3	4.3±0.5	$0.39^{+0.53}_{-0.39}$	- S -	E
577	6^{+5}_{-4}	4	5^{+4}_{-3}	$2.45^{+1.94}_{-1.48}$	1.02	$2.34^{+1.85}_{-1.37}$	9.0±3.9	2.1±3.6	9.2±1.0	$3.54^{+3.18}_{-2.62}$	- S -	C
578	208^{+16}_{-15}	134^{+12}_{-12}	74^{+11}_{-9}	$30.10^{+2.50}_{-2.31}$	$10.51^{+1.08}_{-0.97}$	$11.64^{+1.83}_{-1.56}$	1.6±0.1	1.3±0.1	2.7±0.2	$7.84^{+0.97}_{-0.94}$	- - -	B
579	2^{+4}_{-2}	2	3^{+4}_{-3}	$0.67^{+1.32}_{-0.67}$	0.39	$1.00^{+1.35}_{-1.00}$	2.4±2.0	2.2±7.8	4.5±5.5	$0.26^{+0.55}_{-0.34}$	- S -	C
580	8^{+6}_{-5}	3	9^{+6}_{-4}	$2.64^{+1.82}_{-1.48}$	0.54	$3.07^{+1.82}_{-1.47}$	5.9±1.8	4.1±1.1	6.5±1.0	$2.49^{+1.87}_{-1.58}$	- S -	D
581	5^{+7}_{-5}	4^{+4}_{-3}	2^{+6}_{-2}	$1.13^{+1.42}_{-1.13}$	$0.44^{+0.52}_{-0.38}$	$0.38^{+1.26}_{-0.38}$	1.7±2.6	0.8±1.1	3.6±2.6	$0.30^{+0.61}_{-0.57}$	- - -	B
582	7^{+4}_{-3}	5^{+3}_{-2}	2^{+3}_{-2}	$1.44^{+0.84}_{-0.60}$	$0.58^{+0.41}_{-0.26}$	$0.44^{+0.63}_{-0.35}$	1.5±2.7	0.9±0.8	8.0±2.4	$0.35^{+0.65}_{-0.63}$	- - -	B
583	8^{+5}_{-3}	3	8^{+4}_{-3}	$1.80^{+0.98}_{-0.74}$	0.43	$1.81^{+0.97}_{-0.73}$	5.8±1.7	3.0±1.3	7.5±1.4	$1.67^{+1.04}_{-0.85}$	- S -	C
584	5	4	4	0.99	0.43	0.90	5.2±4.8	2.9±7.1	7.6±7.1	0.83	F S H	C
585	7^{+4}_{-3}	2	8^{+4}_{-3}	$1.45^{+0.82}_{-0.60}$	0.26	$1.56^{+0.83}_{-0.61}$	4.8±0.8	4.4±0.4	6.1±0.6	$1.12^{+0.66}_{-0.50}$	- S -	D
586	10^{+5}_{-4}	3	10^{+5}_{-4}	$2.14^{+1.01}_{-0.79}$	0.41	$2.17^{+1.01}_{-0.77}$	4.4±1.3	2.6±0.7	6.5±1.9	$1.50^{+0.84}_{-0.71}$	- S -	C
587	6^{+4}_{-2}	1^{+2}_{-1}	5^{+3}_{-2}	$1.09^{+0.71}_{-0.47}$	$0.10^{+0.26}_{-0.09}$	$0.94^{+0.68}_{-0.43}$	4.9±0.8	4.7±1.4	5.5±0.7	$0.86^{+0.57}_{-0.39}$	- - -	E
588	27^{+9}_{-8}	3^{+5}_{-3}	24^{+8}_{-7}	$5.49^{+1.85}_{-1.62}$	$0.36^{+0.53}_{-0.36}$	$4.97^{+1.74}_{-1.51}$	3.8±0.8	2.9±0.7	7.2±2.2	$3.38^{+1.36}_{-1.24}$	- - -	C
589	5^{+4}_{-3}	1^{+3}_{-1}	3^{+4}_{-3}	$1.74^{+1.60}_{-1.17}$	$0.29^{+0.58}_{-0.28}$	$1.26^{+1.50}_{-1.03}$	3.5±4.4	1.7±2.0	9.7±2.8	$0.99^{+1.53}_{-1.40}$	- - -	C
590	8^{+4}_{-3}	9^{+4}_{-3}	2	$1.71^{+0.84}_{-0.61}$	$1.04^{+0.48}_{-0.35}$	0.48	0.9±0.2	0.8±0.1	1.3±0.2	$0.25^{+0.13}_{-0.10}$	- - H	A
591	6^{+4}_{-3}	7^{+4}_{-3}	2	$1.26^{+0.80}_{-0.54}$	$0.82^{+0.45}_{-0.31}$	0.49	1.0±0.2	0.9±0.1	1.2±0.2	$0.20^{+0.13}_{-0.09}$	- - H	A
592	11^{+6}_{-5}	10^{+5}_{-4}	1^{+5}_{-1}	$2.25^{+1.28}_{-1.05}$	$1.18^{+0.55}_{-0.42}$	$0.19^{+1.01}_{-0.19}$	1.5±0.5	1.3±0.5	1.8±3.8	$0.55^{+0.35}_{-0.31}$	- - -	A
593	24^{+7}_{-5}	22^{+6}_{-5}	5^{+3}_{-2}	$3.40^{+1.03}_{-0.80}$	$2.37^{+0.55}_{-0.42}$	$0.93^{+1.59}_{-0.88}$	1.3±0.1	1.1±0.1	1.6±0.1	$0.72^{+0.23}_{-0.18}$	- - -	A
594	4^{+3}_{-2}	4^{+3}_{-2}	3	$1.55^{+1.36}_{-0.87}$	$0.88^{+0.73}_{-0.44}$	1.41	0.9±0.2	0.8±0.1	1.1±0.1	$0.23^{+0.21}_{-0.14}$	- - H	A
595	10^{+5}_{-4}	12^{+5}_{-4}	4	$2.12^{+1.09}_{-0.86}$	$1.40^{+0.57}_{-0.43}$	0.82	1.1±0.1	0.9±0.2	1.2±0.2	$0.36^{+0.19}_{-0.15}$	- - H	A
596	9^{+4}_{-3}	2^{+3}_{-1}	7^{+4}_{-3}	$2.16^{+1.03}_{-0.75}$	$0.28^{+0.38}_{-0.19}$	$1.71^{+0.97}_{-0.66}$	2.3±0.7	2.1±0.3	3.7±1.9	$0.78^{+0.45}_{-0.36}$	- - -	E
597	13^{+6}_{-5}	2^{+4}_{-2}	11^{+6}_{-5}	$3.04^{+1.51}_{-1.27}$	$0.22^{+0.47}_{-0.22}$	$2.70^{+1.42}_{-1.16}$	3.3±1.1	2.2±0.9	5.0±2.3	$1.63^{+0.97}_{-0.86}$	- - -	C
598	11^{+5}_{-3}	4^{+3}_{-2}	7^{+4}_{-3}	$2.47^{+1.07}_{-0.81}$	$0.52^{+0.43}_{-0.26}$	$1.61^{+0.94}_{-0.67}$	2.5±1.4	1.1±0.6	5.4±1.9	$1.00^{+0.72}_{-0.66}$	- - -	C
599	9^{+5}_{-3}	6^{+4}_{-3}	3^{+3}_{-2}	$2.00^{+0.97}_{-0.74}$	$0.79^{+0.46}_{-0.31}$	$0.64^{+0.74}_{-0.47}$	1.8±0.9	1.2±0.2	2.2±2.9	$0.57^{+0.40}_{-0.36}$	- - -	A
600	6^{+4}_{-3}	3^{+3}_{-2}	4^{+3}_{-2}	$1.28^{+0.80}_{-0.58}$	$0.32^{+0.34}_{-0.19}$	$0.74^{+0.71}_{-0.45}$	4.0±2.3	1.1±1.2	5.8±1.8	$0.82^{+0.69}_{-0.59}$	- - -	C
601	5^{+4}_{-2}	4^{+3}_{-2}	2^{+3}_{-1}	$1.08^{+0.71}_{-0.47}$	$0.44^{+0.36}_{-0.22}$	$0.32^{+0.54}_{-0.26}$	1.8±0.2	1.7±0.1	2.1±0.2	$0.32^{+0.21}_{-0.14}$	- - -	A
602	13^{+6}_{-4}	3	14^{+6}_{-4}	$1.65^{+0.85}_{-0.64}$	0.28	$1.82^{+0.87}_{-0.65}$	4.5±0.4	3.6±0.3	4.9±0.3	$1.20^{+0.63}_{-0.47}$	- S -	E
603	15^{+6}_{-5}	12^{+5}_{-4}	6^{+4}_{-3}	$1.32^{+0.65}_{-0.43}$	$1.00^{+0.33}_{-0.21}$	$0.75^{+1.00}_{-0.72}$	1.4±0.4	1.3±0.1	1.7±0.5	$0.30^{+0.17}_{-0.13}$	- - -	A
604	9^{+6}_{-5}	3	11^{+6}_{-5}	$2.04^{+1.41}_{-1.17}$	0.36	$2.71^{+1.42}_{-1.16}$	3.7±1.7	3.6±1.0	4.0±3.1	$1.21^{+1.01}_{-0.90}$	- S -	E
605	10^{+4}_{-3}	4^{+3}_{-2}	6^{+4}_{-3}	$2.00^{+0.89}_{-0.67}$	$0.44^{+0.37}_{-0.22}$	$1.26^{+0.78}_{-0.53}$	2.4±0.7	1.8±0.3	3.7±0.4	$0.77^{+0.42}_{-0.35}$	- - -	C
606	3^{+4}_{-3}	2	4^{+4}_{-3}	$0.70^{+0.88}_{-0.64}$	0.28	$0.84^{+0.90}_{-0.65}$	5.0±2.3	3.9±1.0	5.3±2.2	$0.55^{+0.75}_{-0.57}$	- S -	D
607	10^{+4}_{-3}	9^{+4}_{-3}	1^{+3}_{-1}	$1.92^{+0.85}_{-0.64}$	$0.97^{+0.46}_{-0.34}$	$0.24^{+0.52}_{-0.24}$	1.1±0.5	1.0±0.1	1.4±2.8	$0.34^{+0.22}_{-0.20}$	- - -	A
608	11^{+5}_{-4}	8^{+4}_{-3}	2^{+4}_{-2}	$2.50^{+1.25}_{-1.00}$	$1.10^{+0.57}_{-0.42}$	$0.58^{+0.95}_{-0.58}$	1.2±0.7	1.0±0.2	1.5±2.8	$0.47^{+0.35}_{-0.32}$	- - -	A
609	19^{+6}_{-4}	17^{+5}_{-4}	2^{+3}_{-2}	$3.84^{+1.14}_{-0.92}$	$1.99^{+0.62}_{-0.49}$	$0.40^{+0.62}_{-0.34}$	1.1±0.1	0.9±0.1	1.5±0.4	$0.66^{+0.21}_{-0.18}$	- - -	A
610	19^{+7}_{-6}	10^{+5}_{-4}	9^{+5}_{-4}	$4.56^{+1.62}_{-1.37}$	$1.33^{+0.64}_{-0.49}$	$2.25^{+1.33}_{-1.07}$	1.5±1.6	0.9±0.2	5.4±3.0	$1.08^{+1.20}_{-1.18}$	- - -	B
611	5^{+4}_{-2}	5^{+3}_{-2}	3	$0.93^{+0.71}_{-0.47}$	$0.54^{+0.39}_{-0.25}$	0.67	1.1±0.2	0.8±0.2	1.1±0.2	$0.16^{+0.13}_{-0.09}$	- - H	A
612	9^{+5}_{-4}	8^{+4}_{-3}	5	$1.96^{+1.05}_{-0.81}$	$1.07^{+0.52}_{-0.38}$	1.14	0.8±0.2	0.8±0.1	1.2±0.5	$0.26^{+0.15}_{-0.12}$	- - H	A
613	5^{+4}_{-2}	5^{+3}_{-2}	3	$0.94^{+0.72}_{-0.47}$	$0.55^{+0.39}_{-0.25}$	0.67	1.3±0.2	1.1±0.2	1.6±0.2	$0.19^{+0.15}_{-0.10}$	- - H	A

No.	C_{net} FB	C_{net} SB	C_{net} HB	$f_{\rm ph}$FB(10^{-6} cm^{-2} s^{-1})	$f_{\rm ph}$SB(10^{-6} cm^{-2} s^{-1})	$f_{\rm ph}$HB(10^{-6} cm^{-2} s^{-1})	E_{50} (keV)	E_{25} (keV)	E_{75} (keV)	f_X(10^{-14}erg cm^{-2} s^{-1})	Phot. Flag	Quantile Group
614	5^{+4}_{-3}	3^{+3}_{-2}	2^{+3}_{-2}	$2.02^{+1.76}_{-1.27}$	$0.74^{+0.79}_{-0.48}$	$0.70^{+1.45}_{-0.70}$	1.4±3.2	0.7±0.8	2.9±4.4	$0.47^{+1.10}_{-1.06}$	- - -	B
615	8^{+4}_{-3}	3^{+3}_{-2}	4^{+4}_{-2}	$1.57^{+0.87}_{-0.64}$	$0.41^{+0.37}_{-0.22}$	$0.88^{+0.75}_{-0.49}$	2.2±2.1	1.2±0.8	5.9±1.2	$0.54^{+0.60}_{-0.57}$	- - -	B
616	6^{+4}_{-3}	3	7^{+4}_{-3}	$1.42^{+0.83}_{-0.57}$	0.33	$1.47^{+0.85}_{-0.58}$	4.4±0.9	3.4±0.9	5.4±0.6	$0.99^{+0.61}_{-0.44}$	- S -	D
617	3^{+3}_{-2}	4^{+3}_{-2}	2	$0.63^{+0.64}_{-0.38}$	$0.44^{+0.36}_{-0.22}$	0.47	0.9±0.1	0.9±0.0	1.0±0.0	$0.09^{+0.09}_{-0.06}$	- - H	A
618	18^{+6}_{-4}	10^{+4}_{-3}	8^{+4}_{-3}	$3.69^{+1.14}_{-0.92}$	$1.14^{+0.51}_{-0.37}$	$1.75^{+0.90}_{-0.67}$	2.0±0.4	1.2±0.2	2.9±0.6	$1.16^{+0.42}_{-0.36}$	- - -	B
619	12^{+6}_{-5}	4^{+4}_{-2}	8^{+6}_{-5}	$2.84^{+1.51}_{-1.26}$	$0.48^{+0.49}_{-0.33}$	$2.03^{+1.39}_{-1.13}$	5.2±2.1	1.3±1.7	6.9±1.8	$2.35^{+1.58}_{-1.42}$	- - -	C
620	29^{+7}_{-5}	1^{+2}_{-1}	28^{+6}_{-5}	$6.36^{+1.44}_{-1.21}$	$0.10^{+0.29}_{-0.10}$	$6.32^{+1.45}_{-1.21}$	4.4±0.3	3.1±0.4	5.1±0.6	$4.44^{+1.07}_{-0.91}$	- - -	D
621	27^{+7}_{-6}	2^{+3}_{-2}	25^{+7}_{-6}	$6.07^{+1.57}_{-1.33}$	$0.21^{+0.37}_{-0.21}$	$5.81^{+1.54}_{-1.30}$	3.9±0.3	3.3±0.4	4.8±0.5	$3.76^{+1.03}_{-0.89}$	- - -	E
622	83^{+10}_{-9}	75^{+10}_{-9}	8^{+4}_{-3}	$17.54^{+2.15}_{-1.93}$	$9.16^{+1.19}_{-1.06}$	$1.80^{+0.89}_{-0.64}$	1.2±0.1	0.9±0.0	1.4±0.1	$3.29^{+0.44}_{-0.40}$	- - -	A
623	23^{+6}_{-5}	2^{+3}_{-1}	21^{+6}_{-5}	$4.52^{+1.18}_{-0.97}$	$0.20^{+0.30}_{-0.15}$	$4.26^{+1.16}_{-0.94}$	4.0±0.6	2.9±0.3	5.6±0.5	$2.90^{+0.87}_{-0.75}$	- - -	D
624	3^{+3}_{-2}	3	4^{+3}_{-2}	$0.70^{+0.65}_{-0.39}$	0.31	$0.74^{+0.66}_{-0.40}$	4.0±0.6	3.1±0.4	4.2±0.3	$0.45^{+0.42}_{-0.26}$	- S -	E
625	5^{+4}_{-2}	4^{+3}_{-2}	1^{+3}_{-1}	$1.08^{+0.76}_{-0.50}$	$0.47^{+0.39}_{-0.23}$	$0.27^{+0.57}_{-0.27}$	1.6±1.2	0.9±0.4	3.9±1.3	$0.28^{+0.29}_{-0.25}$	- - -	B
626	19^{+7}_{-5}	2^{+3}_{-2}	17^{+6}_{-5}	$1.74^{+0.70}_{-0.50}$	$0.22^{+0.41}_{-0.22}$	$1.75^{+0.71}_{-0.50}$	4.3±0.5	3.8±0.4	5.2±0.6	$1.20^{+0.50}_{-0.37}$	- - -	E
627	8^{+5}_{-4}	2	10^{+5}_{-4}	$2.18^{+1.44}_{-1.16}$	0.34	$2.67^{+1.47}_{-1.18}$	6.7±3.2	3.5±1.6	9.5±1.9	$2.33^{+1.90}_{-1.66}$	- S -	C
628	19^{+6}_{-4}	2^{+3}_{-1}	18^{+5}_{-4}	$3.73^{+1.07}_{-0.86}$	$0.20^{+0.30}_{-0.14}$	$3.45^{+1.05}_{-0.83}$	4.2±0.5	3.6±0.5	5.8±0.5	$2.53^{+0.78}_{-0.65}$	- - -	D
629	8^{+4}_{-3}	2	8^{+4}_{-3}	$1.55^{+0.91}_{-0.68}$	0.27	$1.73^{+0.93}_{-0.70}$	4.8±1.1	4.0±1.0	5.8±2.0	$1.20^{+0.76}_{-0.60}$	- S -	D
630	7^{+7}_{-6}	1^{+4}_{-1}	6^{+7}_{-6}	$1.68^{+1.74}_{-1.51}$	$0.15^{+0.50}_{-0.15}$	$1.44^{+1.67}_{-1.41}$	4.0±2.9	1.2±1.8	4.6±1.3	$1.08^{+1.36}_{-1.25}$	- - -	C
631	2^{+3}_{-2}	4^{+3}_{-2}	2	$0.53^{+0.69}_{-0.41}$	$0.47^{+0.39}_{-0.24}$	0.51	0.9±0.0	0.9±9.1	1.0±9.0	$0.08^{+0.10}_{-0.06}$	- - H	A
632	10^{+4}_{-3}	1^{+2}_{-1}	9^{+4}_{-3}	$2.08^{+0.94}_{-0.70}$	$0.10^{+0.28}_{-0.10}$	$1.95^{+0.93}_{-0.68}$	4.2±0.9	2.7±0.9	5.5±1.3	$1.39^{+0.69}_{-0.55}$	- - -	C
633	6^{+4}_{-3}	2^{+3}_{-1}	4^{+3}_{-2}	$1.37^{+0.89}_{-0.61}$	$0.22^{+0.36}_{-0.18}$	$1.00^{+0.82}_{-0.52}$	3.2±0.9	2.1±0.6	4.3±0.6	$0.71^{+0.50}_{-0.37}$	- - -	C
634	6^{+4}_{-3}	2^{+3}_{-2}	4^{+4}_{-3}	$1.40^{+1.10}_{-0.83}$	$0.28^{+0.41}_{-0.23}$	$0.91^{+1.00}_{-0.72}$	7.2±2.1	4.8±3.0	7.5±1.4	$1.60^{+1.35}_{-1.06}$	- - -	D
635	5^{+4}_{-3}	5^{+4}_{-2}	3	$0.98^{+0.78}_{-0.54}$	$0.63^{+0.43}_{-0.28}$	0.64	1.1±0.1	1.0±0.1	1.2±0.1	$0.16^{+0.13}_{-0.09}$	- - H	A
636	4^{+5}_{-4}	1^{+3}_{-1}	3^{+5}_{-3}	$2.09^{+2.52}_{-1.98}$	$0.38^{+0.81}_{-0.38}$	$1.45^{+2.40}_{-1.45}$	3.3±3.2	3.0±1.8	7.9±2.3	$1.12^{+1.72}_{-1.51}$	- - -	C
637	7^{+4}_{-3}	3	7^{+4}_{-3}	$1.29^{+0.75}_{-0.51}$	0.30	$1.34^{+0.77}_{-0.52}$	4.3±1.0	3.2±0.7	5.7±1.3	$0.88^{+0.55}_{-0.40}$	- S -	D
638	23^{+9}_{-7}	18^{+7}_{-5}	10^{+6}_{-5}	$1.47^{+0.63}_{-0.46}$	$1.18^{+0.31}_{-0.21}$	$1.80^{+1.59}_{-1.30}$	1.3±0.1	1.2±0.1	1.5±0.1	$0.30^{+0.13}_{-0.10}$	- - -	A
639	4^{+4}_{-3}	6^{+4}_{-3}	2	$0.77^{+0.79}_{-0.54}$	$0.75^{+0.45}_{-0.31}$	0.49	0.8±0.1	0.7±0.1	0.9±0.1	$0.10^{+0.10}_{-0.07}$	- - H	A
640	3^{+4}_{-3}	3	3^{+4}_{-3}	$0.75^{+1.12}_{-0.75}$	0.45	$0.83^{+1.10}_{-0.80}$	2.2±0.1	2.1±0.1	2.2±0.0	$0.26^{+0.38}_{-0.26}$	- S -	A
641	6^{+4}_{-2}	2^{+3}_{-1}	4^{+3}_{-2}	$1.04^{+0.67}_{-0.44}$	$0.21^{+0.29}_{-0.14}$	$0.69^{+0.61}_{-0.36}$	3.7±1.5	1.9±0.8	5.3±0.8	$0.61^{+0.47}_{-0.36}$	- - -	C
642	5^{+4}_{-2}	3^{+3}_{-2}	2^{+3}_{-2}	$1.15^{+0.88}_{-0.58}$	$0.36^{+0.41}_{-0.23}$	$0.52^{+0.73}_{-0.41}$	2.0±2.1	1.5±0.6	3.6±2.9	$0.36^{+0.48}_{-0.43}$	- - -	B
643	4^{+6}_{-4}	4	5^{+5}_{-4}	$1.40^{+1.82}_{-1.40}$	0.67	$1.60^{+1.78}_{-1.42}$	9.7±0.4	9.6±0.4	9.7±0.1	$2.17^{+2.82}_{-2.17}$	- S -	D
644	6	2	2^{+4}_{-2}	2.22	0.45	$0.80^{+1.58}_{-0.80}$	5.2±4.8	2.9±7.1	7.6±7.1	1.87	F S -	C
645	17^{+6}_{-5}	1^{+2}_{-1}	16^{+6}_{-5}	$2.15^{+0.84}_{-0.60}$	$0.13^{+0.39}_{-0.13}$	$2.04^{+0.82}_{-0.58}$	4.5±0.9	3.9±0.4	6.2±0.5	$1.55^{+0.67}_{-0.52}$	- - -	D
646	18^{+7}_{-5}	15^{+6}_{-4}	3^{+5}_{-2}	$1.93^{+0.77}_{-0.59}$	$1.32^{+0.36}_{-0.25}$	$0.32^{+0.57}_{-0.17}$	1.4±0.2	1.1±0.2	1.4±0.8	$0.43^{+0.19}_{-0.15}$	- - -	A
647	50^{+9}_{-8}	34^{+7}_{-6}	17^{+6}_{-5}	$5.02^{+0.96}_{-0.79}$	$2.67^{+0.46}_{-0.36}$	$1.44^{+0.65}_{-0.45}$	1.7±0.1	1.4±0.1	2.3±0.2	$1.35^{+0.28}_{-0.24}$	- - -	A
648	5^{+4}_{-2}	2	5^{+4}_{-2}	$1.07^{+0.84}_{-0.55}$	0.31	$1.18^{+0.86}_{-0.57}$	7.5±1.3	6.5±1.5	7.7±1.1	$1.29^{+1.04}_{-0.71}$	- S -	D
649	8	3	1^{+5}_{-1}	2.84	0.61	$0.42^{+1.79}_{-0.42}$	6.9±6.4	4.3±5.7	9.6±9.1	3.12	F S -	C
650	15^{+5}_{-4}	6^{+4}_{-3}	9^{+4}_{-3}	$3.21^{+1.11}_{-0.88}$	$0.77^{+0.45}_{-0.31}$	$1.91^{+0.94}_{-0.70}$	2.6±1.0	1.7±0.3	5.0±1.3	$1.36^{+0.70}_{-0.64}$	- - -	C
651	5^{+4}_{-3}	2	6^{+4}_{-3}	$1.24^{+0.86}_{-0.58}$	0.31	$1.33^{+0.87}_{-0.60}$	3.3±0.5	3.3±0.4	3.7±0.6	$0.66^{+0.47}_{-0.32}$	- S -	E

No.	C_{net} FB	C_{net} SB	C_{net} HB	$f_{\rm ph}$FB(10^{-6} cm^{-2} s^{-1})	$f_{\rm ph}$SB(10^{-6} cm^{-2} s^{-1})	$f_{\rm ph}$HB(10^{-6} cm^{-2} s^{-1})	E_{50} (keV)	E_{25} (keV)	E_{75} (keV)	f_X(10^{-14}erg cm^{-2} s^{-1})	Phot. Flag	Quantile Group
652	7^{+4}_{-3}	1^{+2}_{-1}	6^{+4}_{-3}	$1.42^{+0.81}_{-0.58}$	$0.10^{+0.28}_{-0.10}$	$1.28^{+0.79}_{-0.54}$	5.7±1.1	4.4±1.4	6.2±1.6	$1.29^{+0.78}_{-0.59}$	- - -	D
653	9	3	2^{+5}_{-2}	1.80	0.33	$0.34^{+1.13}_{-0.34}$	5.2±4.8	2.9±7.1	7.6±7.1	1.51	F S -	C
654	14^{+5}_{-4}	11^{+4}_{-3}	3^{+3}_{-2}	$3.02^{+1.04}_{-0.81}$	$1.33^{+0.54}_{-0.40}$	$0.75^{+0.68}_{-0.41}$	1.6±0.2	1.3±0.1	2.0±0.8	$0.78^{+0.28}_{-0.22}$	- - -	A
655	57^{+10}_{-8}	42^{+8}_{-7}	15^{+7}_{-5}	$6.73^{+1.17}_{-1.00}$	$2.82^{+0.55}_{-0.45}$	$1.79^{+0.79}_{-0.61}$	1.4±0.2	1.1±0.1	2.1±0.3	$1.46^{+0.31}_{-0.28}$	- - -	A
656	6^{+4}_{-3}	3^{+3}_{-2}	3^{+3}_{-2}	$1.34^{+0.80}_{-0.55}$	$0.35^{+0.36}_{-0.20}$	$0.75^{+0.69}_{-0.41}$	2.3±0.5	1.8±0.3	3.2±0.4	$0.48^{+0.31}_{-0.23}$	- - -	E
657	5^{+4}_{-3}	2	6^{+4}_{-3}	$1.03^{+0.80}_{-0.58}$	0.26	$1.25^{+0.81}_{-0.59}$	9.2±1.9	6.1±1.4	9.7±0.7	$1.51^{+1.21}_{-0.91}$	- S -	D
658	10^{+4}_{-3}	2	10^{+4}_{-3}	$2.06^{+0.92}_{-0.69}$	0.29	$2.15^{+0.94}_{-0.70}$	3.9±0.8	3.0±0.4	5.3±0.9	$1.28^{+0.62}_{-0.50}$	- S -	D
659	133^{+13}_{-12}	101^{+12}_{-10}	31^{+8}_{-6}	$14.89^{+1.55}_{-1.37}$	$6.46^{+0.76}_{-0.66}$	$3.63^{+0.94}_{-0.75}$	1.6±0.1	1.2±0.1	2.1±0.2	$3.81^{+0.43}_{-0.39}$	- - -	A
660	6^{+4}_{-3}	5^{+3}_{-2}	1^{+3}_{-1}	$1.37^{+0.93}_{-0.67}$	$0.60^{+0.45}_{-0.29}$	$0.32^{+0.71}_{-0.32}$	1.7±0.5	1.5±0.2	2.3±0.9	$0.37^{+0.28}_{-0.22}$	- - -	A
661	13^{+5}_{-4}	9^{+4}_{-3}	4^{+4}_{-2}	$3.87^{+1.50}_{-1.18}$	$1.56^{+0.71}_{-0.53}$	$1.12^{+1.08}_{-0.72}$	1.3±0.4	1.0±0.1	2.1±1.0	$0.80^{+0.38}_{-0.33}$	- - -	B
662	13^{+5}_{-4}	11^{+4}_{-3}	2^{+3}_{-2}	$2.83^{+1.03}_{-0.80}$	$1.34^{+0.55}_{-0.41}$	$0.52^{+0.64}_{-0.36}$	1.1±0.2	0.9±0.1	1.4±1.1	$0.51^{+0.21}_{-0.17}$	- - -	A
663	7^{+5}_{-4}	2^{+3}_{-2}	6^{+4}_{-3}	$1.93^{+1.28}_{-0.98}$	$0.24^{+0.46}_{-0.24}$	$1.55^{+1.19}_{-0.88}$	2.6±2.2	1.5±1.0	6.3±2.7	$0.79^{+0.86}_{-0.79}$	- - -	C
664	7^{+4}_{-3}	2	7^{+4}_{-3}	$1.30^{+0.80}_{-0.58}$	0.26	$1.43^{+0.82}_{-0.60}$	8.1±0.5	7.4±0.9	8.2±0.5	$1.68^{+1.04}_{-0.76}$	- S -	D
665	12^{+5}_{-3}	1^{+2}_{-1}	11^{+4}_{-3}	$6.02^{+2.39}_{-1.81}$	$0.26^{+0.70}_{-0.25}$	$5.68^{+2.36}_{-1.77}$	4.4±0.4	3.7±0.6	5.0±0.7	$4.21^{+1.71}_{-1.32}$	- - -	E
666	10^{+4}_{-3}	8^{+4}_{-3}	2^{+3}_{-1}	$1.96^{+0.88}_{-0.65}$	$0.94^{+0.47}_{-0.34}$	$0.35^{+0.55}_{-0.27}$	1.5±0.4	1.1±0.2	1.8±1.0	$0.48^{+0.24}_{-0.19}$	- - -	A
667	9^{+4}_{-3}	10^{+4}_{-3}	2	$1.80^{+0.82}_{-0.60}$	$1.10^{+0.47}_{-0.35}$	0.44	1.0±0.1	0.9±0.1	1.2±0.2	$0.29^{+0.14}_{-0.10}$	- - H	A
668	5^{+5}_{-3}	2	6^{+4}_{-3}	$1.56^{+1.50}_{-1.13}$	0.43	$2.21^{+1.52}_{-1.15}$	9.5±1.3	7.4±1.3	9.7±0.4	$2.38^{+2.30}_{-1.75}$	- S -	D
669	18^{+8}_{-6}	19^{+6}_{-5}	1^{+5}_{-1}	$1.74^{+0.82}_{-0.63}$	$1.64^{+0.40}_{-0.30}$	$0.26^{+1.12}_{-0.26}$	1.0±0.1	1.0±0.1	1.1±0.1	$0.29^{+0.14}_{-0.11}$	- - -	A
670	7^{+4}_{-3}	3	8^{+4}_{-3}	$1.41^{+0.75}_{-0.54}$	0.29	$1.46^{+0.77}_{-0.55}$	4.9±0.9	3.5±0.8	5.7±0.7	$1.10^{+0.62}_{-0.46}$	- S -	D
671	20^{+6}_{-5}	5^{+4}_{-2}	15^{+6}_{-5}	$4.63^{+1.44}_{-1.19}$	$0.60^{+0.48}_{-0.32}$	$3.66^{+1.33}_{-1.07}$	3.4±0.5	2.4±0.5	4.5±0.4	$2.49^{+0.84}_{-0.72}$	- - -	D
672	5^{+3}_{-2}	4^{+3}_{-2}	1^{+2}_{-1}	$0.91^{+0.68}_{-0.43}$	$0.45^{+0.37}_{-0.22}$	$0.13^{+0.47}_{-0.13}$	1.2±0.4	0.8±0.2	1.7±0.5	$0.18^{+0.14}_{-0.10}$	- - -	B
673	12^{+5}_{-4}	5^{+3}_{-2}	7^{+4}_{-3}	$2.52^{+1.03}_{-0.79}$	$0.60^{+0.43}_{-0.27}$	$1.51^{+0.88}_{-0.63}$	2.1±0.3	1.6±0.3	2.4±1.3	$0.87^{+0.37}_{-0.29}$	- - -	A
674	24^{+9}_{-7}	27^{+8}_{-6}	12	$1.90^{+0.68}_{-0.53}$	$1.41^{+0.33}_{-0.25}$	0.95	1.1±0.1	1.0±0.1	1.1±0.0	$0.32^{+0.12}_{-0.09}$	- - H	A
675	32^{+7}_{-6}	24^{+6}_{-5}	8^{+4}_{-3}	$6.58^{+1.40}_{-1.18}$	$2.83^{+0.71}_{-0.58}$	$1.72^{+0.87}_{-0.63}$	1.3±0.2	1.1±0.1	2.0±0.3	$1.38^{+0.34}_{-0.30}$	- - -	A
676	7^{+4}_{-3}	7^{+4}_{-3}	1^{+2}_{-1}	$1.46^{+0.77}_{-0.55}$	$0.79^{+0.43}_{-0.29}$	$0.11^{+0.46}_{-0.11}$	1.0±0.1	0.9±0.1	1.1±0.3	$0.25^{+0.13}_{-0.10}$	- - -	A
677	6^{+4}_{-3}	6^{+4}_{-2}	4	$1.26^{+0.76}_{-0.51}$	$0.68^{+0.42}_{-0.27}$	0.78	0.9±0.2	0.8±0.1	1.1±0.2	$0.19^{+0.12}_{-0.08}$	- - H	A
678	28^{+8}_{-6}	19^{+6}_{-5}	9^{+6}_{-4}	$3.18^{+0.87}_{-0.70}$	$1.74^{+0.40}_{-0.30}$	$1.05^{+0.65}_{-0.44}$	1.6±0.3	1.2±0.1	2.4±0.7	$0.79^{+0.25}_{-0.22}$	- - -	B
679	14^{+5}_{-4}	3^{+3}_{-2}	11^{+5}_{-3}	$2.85^{+1.02}_{-0.79}$	$0.32^{+0.35}_{-0.19}$	$2.33^{+0.95}_{-0.72}$	3.0±0.5	2.1±0.5	4.0±1.1	$1.39^{+0.54}_{-0.45}$	- - -	D
680	22^{+7}_{-5}	13^{+5}_{-4}	8^{+5}_{-4}	$5.01^{+1.52}_{-1.27}$	$1.75^{+0.66}_{-0.51}$	$1.96^{+1.17}_{-0.90}$	1.6±0.3	1.2±0.2	2.4±0.4	$1.28^{+0.46}_{-0.41}$	- - -	B
681	43^{+9}_{-7}	34^{+8}_{-6}	10^{+6}_{-4}	$4.67^{+0.95}_{-0.78}$	$2.71^{+0.47}_{-0.37}$	$1.10^{+0.62}_{-0.44}$	1.3±0.1	1.0±0.1	2.1±0.6	$1.00^{+0.22}_{-0.19}$	- - -	A
682	2^{+4}_{-2}	1^{+3}_{-1}	1^{+3}_{-1}	$0.49^{+0.86}_{-0.49}$	$0.11^{+0.34}_{-0.11}$	$0.31^{+0.79}_{-0.31}$	1.7±1.7	1.7±0.6	4.4±1.2	$0.14^{+0.27}_{-0.19}$	- - -	B
683	4^{+3}_{-2}	4^{+3}_{-2}	2	$0.68^{+0.60}_{-0.36}$	$0.43^{+0.35}_{-0.21}$	0.45	0.8±0.2	0.7±0.1	1.0±0.2	$0.08^{+0.08}_{-0.05}$	- - H	A
684	14^{+6}_{-4}	5^{+4}_{-3}	9^{+5}_{-4}	$3.14^{+1.22}_{-0.98}$	$0.67^{+0.47}_{-0.32}$	$2.00^{+1.06}_{-0.82}$	2.3±0.7	1.9±0.3	3.3±1.4	$1.16^{+0.56}_{-0.49}$	- - -	E
685	7^{+4}_{-3}	2^{+3}_{-2}	4^{+4}_{-2}	$2.44^{+1.50}_{-1.10}$	$0.49^{+0.63}_{-0.35}$	$1.63^{+1.34}_{-0.89}$	2.1±1.9	1.1±0.6	3.9±3.1	$0.83^{+0.90}_{-0.83}$	- - -	B
686	10^{+4}_{-3}	7^{+4}_{-3}	3^{+3}_{-2}	$1.87^{+0.83}_{-0.61}$	$0.79^{+0.43}_{-0.29}$	$0.53^{+0.58}_{-0.32}$	1.1±0.6	0.9±0.1	1.9±2.8	$0.34^{+0.24}_{-0.22}$	- - -	B
687	6^{+4}_{-3}	5^{+3}_{-2}	2^{+3}_{-2}	$1.34^{+0.83}_{-0.59}$	$0.58^{+0.41}_{-0.26}$	$0.35^{+0.63}_{-0.35}$	1.6±1.0	1.1±0.4	1.9±2.1	$0.34^{+0.31}_{-0.27}$	- - -	A
688	6^{+4}_{-3}	2	6^{+4}_{-3}	$1.25^{+0.77}_{-0.52}$	0.29	$1.32^{+0.79}_{-0.54}$	6.2±0.5	5.6±0.5	6.8±0.3	$1.25^{+0.78}_{-0.53}$	- S -	D
689	25^{+8}_{-6}	20^{+6}_{-5}	5^{+4}_{-3}	$2.77^{+0.89}_{-0.72}$	$1.67^{+0.40}_{-0.30}$	$1.21^{+1.05}_{-0.79}$	1.0±0.1	0.8±0.1	1.1±0.1	$0.45^{+0.16}_{-0.13}$	- - -	B

No.	C_{net} FB	C_{net} SB	C_{net} HB	$f_{\rm ph}$FB(10^{-6} cm^{-2} s^{-1})	$f_{\rm ph}$SB(10^{-6} cm^{-2} s^{-1})	$f_{\rm ph}$HB(10^{-6} cm^{-2} s^{-1})	E_{50} (keV)	E_{25} (keV)	E_{75} (keV)	f_X(10^{-14}erg cm^{-2} s^{-1})	Phot. Flag	Quantile Group
690	13^{+9}_{-8}	2^{+5}_{-2}	11^{+8}_{-7}	$3.08^{+2.10}_{-1.87}$	$0.26^{+0.62}_{-0.26}$	$2.68^{+1.99}_{-1.71}$	3.6±3.4	2.7±1.4	7.5±3.0	$1.77^{+2.08}_{-2.00}$	- - -	C
691	9^{+4}_{-3}	6^{+4}_{-2}	3^{+3}_{-2}	$1.83^{+0.88}_{-0.64}$	$0.73^{+0.45}_{-0.29}$	$0.59^{+0.64}_{-0.35}$	1.3±0.6	1.2±0.2	2.9±1.0	$0.39^{+0.26}_{-0.23}$	- - -	B
692	10^{+5}_{-4}	9^{+4}_{-3}	1^{+4}_{-1}	$2.35^{+1.16}_{-0.91}$	$1.17^{+0.55}_{-0.41}$	$0.29^{+0.84}_{-0.29}$	1.3±0.9	0.9±0.2	1.7±2.0	$0.50^{+0.42}_{-0.39}$	- - -	B
693	12^{+5}_{-4}	2^{+3}_{-1}	10^{+4}_{-3}	$2.90^{+1.15}_{-0.88}$	$0.25^{+0.37}_{-0.18}$	$2.52^{+1.11}_{-0.83}$	3.1±0.6	2.8±0.6	4.1±1.4	$1.46^{+0.63}_{-0.51}$	- - -	E
694	66^{+10}_{-9}	46^{+8}_{-7}	20^{+7}_{-5}	$11.10^{+1.69}_{-1.43}$	$5.36^{+0.81}_{-0.67}$	$3.35^{+1.12}_{-0.81}$	1.5±0.1	1.1±0.1	2.2±0.3	$2.71^{+0.47}_{-0.41}$	- - -	B
695	8^{+5}_{-3}	8^{+4}_{-3}	4	$1.80^{+1.03}_{-0.78}$	$1.02^{+0.53}_{-0.39}$	1.00	0.9±0.2	0.8±0.1	1.0±0.4	$0.25^{+0.15}_{-0.12}$	- - H	A
696	10^{+5}_{-3}	8^{+4}_{-3}	2^{+3}_{-2}	$2.18^{+1.00}_{-0.76}$	$0.94^{+0.49}_{-0.35}$	$0.55^{+0.71}_{-0.43}$	1.3±0.4	1.0±0.2	2.2±1.2	$0.46^{+0.26}_{-0.22}$	- - -	B
697	12^{+6}_{-5}	13^{+5}_{-4}	2^{+3}_{-2}	$1.31^{+0.65}_{-0.48}$	$1.13^{+0.33}_{-0.23}$	$0.44^{+0.64}_{-0.36}$	1.0±0.2	0.8±0.1	1.1±0.1	$0.21^{+0.11}_{-0.08}$	- - -	A
698	4^{+3}_{-2}	5^{+3}_{-2}	2	$0.97^{+0.82}_{-0.52}$	$0.66^{+0.47}_{-0.30}$	0.56	1.0±0.1	1.0±0.0	1.1±0.1	$0.15^{+0.13}_{-0.08}$	- - H	A
699	5^{+3}_{-2}	5^{+3}_{-2}	3	$1.66^{+1.18}_{-0.75}$	$1.00^{+0.68}_{-0.43}$	0.89	1.0±0.1	1.0±0.1	1.2±0.2	$0.27^{+0.19}_{-0.13}$	- - H	A
700	5	4	4	1.31	0.57	1.17	5.2±4.8	2.9±7.1	7.6±7.1	1.10	F S H	C
701	31^{+8}_{-6}	26^{+7}_{-5}	6^{+4}_{-3}	$3.17^{+0.82}_{-0.65}$	$2.20^{+0.42}_{-0.33}$	$1.25^{+0.95}_{-0.71}$	1.0±0.1	0.9±0.1	1.1±0.0	$0.52^{+0.14}_{-0.11}$	- - -	A
702	8	3	1^{+5}_{-1}	2.27	0.50	$0.20^{+1.47}_{-0.20}$	5.2±4.8	2.9±7.1	7.6±7.1	1.91	F S -	C
703	46^{+9}_{-8}	46^{+8}_{-7}	4^{+4}_{-1}	$5.29^{+1.05}_{-0.87}$	$3.67^{+0.56}_{-0.46}$	$0.29^{+1.08}_{-0.29}$	1.0±0.1	0.9±0.0	1.2±0.1	$0.88^{+0.18}_{-0.15}$	- - -	A
704	5^{+4}_{-2}	4^{+3}_{-2}	1^{+3}_{-1}	$1.09^{+0.81}_{-0.53}$	$0.48^{+0.41}_{-0.25}$	$0.26^{+0.61}_{-0.26}$	1.7±2.2	1.3±0.5	2.5±3.3	$0.30^{+0.45}_{-0.41}$	- - -	B
705	16^{+7}_{-5}	2^{+3}_{-2}	14^{+6}_{-5}	$3.92^{+1.61}_{-1.34}$	$0.25^{+0.45}_{-0.25}$	$3.55^{+1.54}_{-1.27}$	6.0±1.2	4.8±1.8	8.2±1.6	$3.77^{+1.73}_{-1.50}$	- - -	D
706	8^{+5}_{-3}	2	9^{+5}_{-3}	$1.68^{+0.97}_{-0.74}$	0.28	$1.90^{+0.99}_{-0.75}$	6.8±2.2	4.4±1.3	8.7±1.0	$1.83^{+1.20}_{-0.99}$	- S -	C
707	20^{+7}_{-6}	6^{+4}_{-3}	14^{+7}_{-5}	$5.40^{+2.01}_{-1.70}$	$0.84^{+0.64}_{-0.45}$	$3.98^{+1.85}_{-1.52}$	7.0±1.5	2.2±2.1	7.5±0.9	$6.06^{+2.59}_{-2.29}$	- - -	C
708	6^{+4}_{-3}	2^{+3}_{-1}	5^{+3}_{-2}	$1.26^{+0.74}_{-0.50}$	$0.21^{+0.30}_{-0.14}$	$0.92^{+0.68}_{-0.43}$	3.4±1.2	1.6±0.7	4.7±0.9	$0.70^{+0.48}_{-0.37}$	- - -	C
709	4^{+4}_{-3}	2	5^{+4}_{-3}	$0.96^{+0.84}_{-0.57}$	0.29	$1.13^{+0.86}_{-0.59}$	5.5±0.4	5.3±0.2	5.7±0.4	$0.85^{+0.74}_{-0.51}$	- S -	E
710	3^{+3}_{-2}	3^{+3}_{-2}	2	$0.62^{+0.70}_{-0.39}$	$0.40^{+0.40}_{-0.22}$	0.59	0.9±0.1	0.8±0.1	1.1±0.1	$0.09^{+0.10}_{-0.06}$	- - H	A
711	2^{+5}_{-2}	4	2^{+5}_{-2}	$0.60^{+1.77}_{-0.60}$	0.72	$0.60^{+1.71}_{-0.60}$	9.9±8.2	2.5±7.5	10.0±9.5	$0.96^{+2.92}_{-1.24}$	- S -	C
712	26^{+6}_{-5}	17^{+5}_{-4}	9^{+4}_{-3}	$5.50^{+1.33}_{-1.10}$	$2.10^{+0.65}_{-0.51}$	$1.90^{+0.91}_{-0.66}$	1.5±0.3	1.1±0.1	3.0±0.6	$1.30^{+0.41}_{-0.37}$	- - -	B
713	14^{+6}_{-5}	4	14^{+6}_{-5}	$3.59^{+1.53}_{-1.25}$	0.54	$3.75^{+1.50}_{-1.22}$	4.7±1.0	2.8±1.1	7.9±2.9	$2.69^{+1.28}_{-1.10}$	- S -	C
714	4^{+3}_{-2}	5^{+3}_{-2}	2	$0.88^{+0.68}_{-0.43}$	$0.56^{+0.39}_{-0.25}$	0.46	1.1±0.2	0.9±0.1	1.1±0.1	$0.15^{+0.12}_{-0.08}$	- - H	A
715	3^{+5}_{-3}	3	4^{+5}_{-3}	$1.36^{+2.24}_{-1.36}$	0.81	$1.79^{+2.22}_{-1.67}$	9.6±3.1	6.4±5.9	9.6±9.1	$2.08^{+3.49}_{-2.19}$	- S -	D
716	16^{+6}_{-5}	2^{+3}_{-2}	15^{+6}_{-5}	$4.32^{+1.68}_{-1.40}$	$0.25^{+0.48}_{-0.25}$	$3.97^{+1.61}_{-1.32}$	4.8±0.5	4.2±0.6	5.4±0.6	$3.34^{+1.34}_{-1.13}$	- - -	E
717	17^{+6}_{-5}	9^{+5}_{-3}	7^{+5}_{-4}	$2.02^{+0.78}_{-0.58}$	$1.05^{+0.35}_{-0.22}$	$0.92^{+0.64}_{-0.41}$	2.1±1.0	1.4±0.4	5.8±1.9	$0.67^{+0.42}_{-0.38}$	- - -	B
718	5^{+4}_{-3}	4^{+3}_{-2}	1^{+3}_{-1}	$1.15^{+0.84}_{-0.60}$	$0.54^{+0.41}_{-0.26}$	$0.22^{+0.64}_{-0.22}$	1.3±0.8	1.2±0.2	2.0±1.1	$0.24^{+0.22}_{-0.19}$	- - -	A
719	23^{+7}_{-5}	24^{+7}_{-5}	1^{+3}_{-1}	$2.35^{+0.75}_{-0.58}$	$2.00^{+0.41}_{-0.31}$	$0.11^{+0.72}_{-0.11}$	1.0±0.1	0.8±0.1	1.2±0.2	$0.37^{+0.13}_{-0.10}$	- - -	A
720	13^{+5}_{-4}	1^{+3}_{-1}	12^{+5}_{-4}	$2.71^{+1.09}_{-0.87}$	$0.12^{+0.32}_{-0.12}$	$2.56^{+1.06}_{-0.83}$	4.3±0.4	3.8±0.7	4.9±1.3	$1.86^{+0.77}_{-0.62}$	- - -	E
721	6^{+4}_{-3}	6^{+4}_{-2}	4	$1.21^{+0.74}_{-0.50}$	$0.65^{+0.40}_{-0.27}$	0.75	1.3±0.4	1.1±0.2	1.4±0.8	$0.25^{+0.17}_{-0.13}$	- - H	A
722	4^{+3}_{-2}	4^{+3}_{-2}	3	$1.44^{+1.27}_{-0.80}$	$0.81^{+0.68}_{-0.41}$	1.32	1.3±0.5	0.7±0.3	1.7±0.3	$0.30^{+0.29}_{-0.20}$	- - H	B
723	13^{+5}_{-4}	4^{+3}_{-2}	9^{+4}_{-3}	$2.78^{+1.08}_{-0.85}$	$0.53^{+0.41}_{-0.26}$	$1.90^{+0.96}_{-0.72}$	2.5±0.4	1.7±0.4	3.2±1.8	$1.13^{+0.47}_{-0.39}$	- - -	E
724	12^{+5}_{-3}	4^{+3}_{-2}	8^{+4}_{-3}	$2.46^{+0.96}_{-0.73}$	$0.48^{+0.39}_{-0.23}$	$1.67^{+0.85}_{-0.61}$	2.7±0.5	1.8±0.4	3.7±0.4	$1.05^{+0.45}_{-0.37}$	- - -	C
725	13^{+5}_{-4}	11^{+4}_{-3}	2^{+3}_{-2}	$2.70^{+1.04}_{-0.80}$	$1.31^{+0.55}_{-0.41}$	$0.44^{+0.64}_{-0.36}$	1.3±0.2	1.0±0.2	1.6±1.5	$0.57^{+0.24}_{-0.19}$	- - -	A
726	7^{+4}_{-3}	1^{+2}_{-1}	7^{+4}_{-3}	$1.58^{+0.87}_{-0.64}$	$0.08^{+0.28}_{-0.08}$	$1.48^{+0.86}_{-0.61}$	3.2±0.5	3.0±0.5	3.8±1.1	$0.82^{+0.47}_{-0.35}$	- - -	E
727	8^{+6}_{-4}	7^{+4}_{-3}	1^{+5}_{-1}	$1.69^{+1.23}_{-0.99}$	$0.82^{+0.50}_{-0.36}$	$0.24^{+1.03}_{-0.24}$	1.4±0.6	1.1±0.3	1.8±0.8	$0.37^{+0.32}_{-0.27}$	- - -	A
728	10^{+6}_{-4}	7^{+4}_{-3}	3^{+5}_{-2}	$1.41^{+0.78}_{-0.55}$	$1.09^{+0.35}_{-0.21}$	$0.46^{+0.64}_{-0.32}$	1.3±0.7	1.1±0.2	3.1±0.7	$0.30^{+0.23}_{-0.19}$	- - -	B

No.	C_{net} FB	C_{net} SB	C_{net} HB	$f_{\rm ph}$FB(10^{-6} cm^{-2} s^{-1})	$f_{\rm ph}$SB(10^{-6} cm^{-2} s^{-1})	$f_{\rm ph}$HB(10^{-6} cm^{-2} s^{-1})	E_{50} (keV)	E_{25} (keV)	E_{75} (keV)	f_X(10^{-14}erg cm^{-2} s^{-1})	Phot. Flag	Quantile Group
729	5^{+4}_{-2}	5^{+3}_{-2}	4	$1.03^{+0.72}_{-0.47}$	$0.55^{+0.39}_{-0.25}$	0.76	1.0±0.2	0.8±0.2	1.1±0.2	$0.16^{+0.12}_{-0.08}$	- - H	A
730	8^{+5}_{-4}	8^{+4}_{-3}	4	$1.78^{+1.08}_{-0.82}$	$1.11^{+0.55}_{-0.40}$	0.98	1.4±0.5	1.1±0.3	1.5±1.3	$0.40^{+0.28}_{-0.23}$	- - H	A
731	8	3	8	2.44	0.51	2.56	5.2±4.8	2.9±7.1	7.6±7.1	2.05	F S H	C
732	4^{+5}_{-4}	8^{+4}_{-3}	5	$0.99^{+1.29}_{-0.99}$	$1.08^{+0.59}_{-0.43}$	1.12	0.8±0.4	0.6±0.2	1.1±0.3	$0.12^{+0.17}_{-0.14}$	- - H	B
733	5^{+4}_{-3}	2^{+3}_{-1}	4^{+3}_{-2}	$1.15^{+0.84}_{-0.57}$	$0.22^{+0.34}_{-0.16}$	$0.80^{+0.77}_{-0.49}$	3.1±1.9	1.2±0.9	4.1±2.3	$0.57^{+0.55}_{-0.45}$	- - -	C
734	16^{+6}_{-4}	11^{+5}_{-3}	5^{+4}_{-3}	$3.53^{+1.21}_{-0.98}$	$1.38^{+0.57}_{-0.43}$	$1.13^{+0.89}_{-0.64}$	1.5±0.7	1.0±0.2	3.9±2.6	$0.87^{+0.48}_{-0.45}$	- - -	B
735	6^{+4}_{-3}	5^{+4}_{-2}	4	$1.43^{+0.98}_{-0.70}$	$0.78^{+0.51}_{-0.34}$	1.05	1.1±0.9	0.8±0.2	1.8±1.7	$0.26^{+0.27}_{-0.24}$	- - H	B
736	18^{+6}_{-4}	6^{+4}_{-2}	12^{+5}_{-4}	$3.56^{+1.12}_{-0.90}$	$0.65^{+0.42}_{-0.28}$	$2.49^{+1.00}_{-0.77}$	3.0±0.5	2.0±0.4	3.8±0.8	$1.72^{+0.60}_{-0.51}$	- - -	C
737	6^{+4}_{-3}	2	7^{+4}_{-3}	$1.45^{+1.01}_{-0.76}$	0.30	$1.69^{+1.04}_{-0.78}$	5.7±1.7	3.6±1.5	7.0±1.2	$1.33^{+1.01}_{-0.80}$	- S -	C
738	45^{+9}_{-7}	10^{+5}_{-3}	35^{+8}_{-6}	$4.56^{+0.89}_{-0.73}$	$0.99^{+0.29}_{-0.19}$	$3.58^{+0.81}_{-0.65}$	3.5±0.2	2.1±0.4	4.3±0.5	$2.55^{+0.52}_{-0.44}$	- - -	C
739	12^{+5}_{-4}	2^{+3}_{-1}	10^{+5}_{-3}	$2.40^{+0.96}_{-0.74}$	$0.18^{+0.30}_{-0.15}$	$2.12^{+0.93}_{-0.70}$	5.1±1.4	2.7±1.1	7.8±1.3	$1.97^{+0.96}_{-0.81}$	- - -	C
740	4^{+4}_{-3}	5^{+4}_{-2}	4	$0.98^{+0.93}_{-0.66}$	$0.70^{+0.48}_{-0.32}$	0.83	0.9±0.2	0.7±0.1	1.0±0.1	$0.15^{+0.14}_{-0.10}$	- - H	A
741	6^{+4}_{-3}	6^{+4}_{-3}	4	$1.44^{+1.00}_{-0.74}$	$0.81^{+0.50}_{-0.34}$	1.04	1.4±0.2	1.2±0.2	1.5±0.3	$0.32^{+0.23}_{-0.17}$	- - H	A
742	8^{+4}_{-3}	4^{+3}_{-2}	4^{+3}_{-2}	$1.67^{+0.87}_{-0.63}$	$0.45^{+0.39}_{-0.23}$	$0.90^{+0.73}_{-0.46}$	2.3±1.3	1.9±0.4	5.1±1.5	$0.60^{+0.47}_{-0.42}$	- - -	C
743	13^{+6}_{-5}	11^{+5}_{-4}	2^{+4}_{-1}	$1.47^{+0.68}_{-0.49}$	$1.20^{+0.33}_{-0.22}$	$0.24^{+0.50}_{-0.15}$	1.3±0.3	1.0±0.1	1.4±0.6	$0.30^{+0.15}_{-0.12}$	- - -	A
744	304^{+18}_{-18}	118^{+12}_{-11}	186^{+15}_{-14}	$33.49^{+1.96}_{-1.96}$	$7.41^{+0.78}_{-0.69}$	$20.91^{+1.65}_{-1.57}$	2.6±0.2	1.7±0.1	3.8±0.2	$14.04^{+1.16}_{-1.16}$	- - -	C
745	8^{+4}_{-3}	2	9^{+4}_{-3}	$1.65^{+0.84}_{-0.62}$	0.28	$1.73^{+0.86}_{-0.63}$	6.1±0.6	5.3±1.0	6.7±1.2	$1.60^{+0.83}_{-0.63}$	- S -	D
746	5^{+4}_{-2}	5^{+3}_{-2}	4	$1.08^{+0.73}_{-0.48}$	$0.57^{+0.40}_{-0.25}$	0.79	1.1±0.3	0.9±0.1	1.4±0.4	$0.19^{+0.14}_{-0.10}$	- - H	A
747	4^{+4}_{-3}	6^{+4}_{-2}	3	$1.05^{+0.90}_{-0.61}$	$0.75^{+0.49}_{-0.32}$	0.72	1.0±0.1	0.9±0.1	1.0±0.1	$0.17^{+0.15}_{-0.10}$	- - H	A
748	9^{+5}_{-4}	4	9^{+5}_{-4}	$2.15^{+1.16}_{-0.91}$	0.57	$2.08^{+1.12}_{-0.86}$	5.4±0.9	4.7±1.2	6.6±0.5	$1.87^{+1.05}_{-0.84}$	- S -	D
749	6^{+4}_{-3}	6^{+4}_{-2}	3	$1.11^{+0.74}_{-0.50}$	$0.65^{+0.40}_{-0.27}$	0.65	0.9±0.1	0.8±0.0	1.0±0.1	$0.15^{+0.10}_{-0.07}$	- - H	A
750	1793^{+42}_{-42}	904^{+30}_{-30}	889^{+30}_{-30}	$189.24^{+4.48}_{-4.48}$	$54.63^{+1.82}_{-1.82}$	$95.78^{+3.22}_{-3.22}$	2.0±0.0	1.4±0.0	3.5±0.1	$60.37^{+2.05}_{-2.05}$	- - -	B
751	3^{+3}_{-2}	3^{+3}_{-2}	2	$0.57^{+0.66}_{-0.37}$	$0.38^{+0.38}_{-0.21}$	0.53	0.9±0.1	0.9±0.0	1.0±0.0	$0.08^{+0.10}_{-0.05}$	- - H	A
752	7^{+4}_{-3}	5^{+4}_{-2}	1^{+3}_{-1}	$1.46^{+0.90}_{-0.65}$	$0.66^{+0.45}_{-0.29}$	$0.30^{+0.65}_{-0.30}$	1.4±0.5	1.2±0.1	1.5±1.4	$0.32^{+0.23}_{-0.19}$	- - -	A
753	7^{+4}_{-3}	6^{+4}_{-2}	1^{+3}_{-1}	$1.37^{+0.77}_{-0.55}$	$0.66^{+0.40}_{-0.27}$	$0.24^{+0.53}_{-0.24}$	1.2±1.0	1.1±0.2	1.9±2.8	$0.27^{+0.26}_{-0.24}$	- - -	A
754	20^{+6}_{-5}	5^{+4}_{-2}	16^{+5}_{-4}	$4.82^{+1.44}_{-1.18}$	$0.65^{+0.48}_{-0.32}$	$3.75^{+1.32}_{-1.05}$	2.8±0.3	2.3±0.5	3.7±0.4	$2.19^{+0.70}_{-0.59}$	- - -	E
755	5^{+4}_{-3}	4	5^{+4}_{-3}	$2.15^{+1.80}_{-1.32}$	0.85	$2.13^{+1.76}_{-1.27}$	7.8±1.9	7.4±2.6	8.3±0.7	$2.68^{+2.33}_{-1.76}$	- S -	D
756	8^{+4}_{-3}	5^{+3}_{-2}	3^{+3}_{-2}	$1.64^{+0.88}_{-0.65}$	$0.53^{+0.40}_{-0.25}$	$0.73^{+0.71}_{-0.45}$	1.7±0.6	1.3±0.2	2.5±1.5	$0.43^{+0.28}_{-0.23}$	- - -	B
757	4^{+4}_{-2}	4^{+3}_{-2}	4	$0.82^{+0.73}_{-0.48}$	$0.42^{+0.37}_{-0.22}$	0.88	1.6±1.5	1.5±0.4	3.8±1.9	$0.21^{+0.27}_{-0.23}$	- - H	B
758	23^{+7}_{-6}	16^{+5}_{-4}	7^{+5}_{-4}	$7.34^{+2.12}_{-1.78}$	$2.81^{+0.94}_{-0.75}$	$2.39^{+1.57}_{-1.21}$	1.7±0.2	1.1±0.1	2.3±0.5	$1.97^{+0.63}_{-0.55}$	- - -	B
759	11^{+5}_{-4}	5^{+4}_{-2}	6^{+4}_{-3}	$2.31^{+1.04}_{-0.81}$	$0.62^{+0.43}_{-0.28}$	$1.25^{+0.88}_{-0.64}$	2.5±0.5	1.8±0.4	3.0±0.7	$0.93^{+0.47}_{-0.39}$	- - -	E
760	5^{+4}_{-3}	6^{+4}_{-2}	3	$1.19^{+0.89}_{-0.61}$	$0.74^{+0.48}_{-0.32}$	0.74	1.1±0.2	1.0±0.1	1.3±0.1	$0.22^{+0.17}_{-0.12}$	- - H	A
761	13^{+5}_{-4}	12^{+5}_{-3}	2^{+3}_{-1}	$2.54^{+0.92}_{-0.71}$	$1.31^{+0.50}_{-0.38}$	$0.29^{+0.51}_{-0.25}$	1.2±0.3	1.0±0.1	1.8±1.7	$0.49^{+0.22}_{-0.18}$	- - -	A
762	17^{+6}_{-5}	15^{+6}_{-4}	2^{+3}_{-2}	$1.99^{+0.74}_{-0.56}$	$1.45^{+0.37}_{-0.26}$	$0.45^{+0.67}_{-0.37}$	1.3±0.2	1.0±0.1	1.7±0.2	$0.40^{+0.17}_{-0.13}$	- - -	A
763	48^{+9}_{-7}	2^{+4}_{-1}	46^{+9}_{-7}	$5.35^{+1.00}_{-0.83}$	$0.59^{+0.22}_{-0.07}$	$5.26^{+1.00}_{-0.82}$	3.5±0.4	2.9±0.2	5.5±0.7	$3.01^{+0.64}_{-0.56}$	- - -	D
764	158^{+14}_{-13}	141^{+13}_{-12}	17^{+6}_{-5}	$17.29^{+1.58}_{-1.41}$	$9.96^{+0.84}_{-0.75}$	$1.97^{+0.71}_{-0.53}$	1.2±0.1	0.9±0.0	1.6±0.1	$3.27^{+0.33}_{-0.30}$	- - -	A
765	11^{+5}_{-4}	8^{+4}_{-3}	3^{+4}_{-3}	$2.71^{+1.30}_{-1.04}$	$1.09^{+0.57}_{-0.42}$	$0.80^{+1.00}_{-0.74}$	1.6±0.5	1.1±0.2	2.1±1.2	$0.68^{+0.38}_{-0.33}$	- - -	B
766	29^{+8}_{-7}	6^{+4}_{-3}	22^{+7}_{-6}	$7.26^{+1.96}_{-1.70}$	$0.89^{+0.59}_{-0.43}$	$5.79^{+1.82}_{-1.55}$	3.3±0.4	2.2±0.6	4.9±0.9	$3.87^{+1.16}_{-1.04}$	- - -	C
767	8^{+4}_{-3}	2	8^{+4}_{-3}	$1.49^{+0.82}_{-0.60}$	0.27	$1.59^{+0.84}_{-0.61}$	4.7±0.7	3.4±0.7	5.2±0.6	$1.12^{+0.64}_{-0.48}$	- S -	D

No.	C_{net} FB	C_{net} SB	C_{net} HB	$f_{\rm ph}$FB(10^{-6} cm^{-2} s^{-1})	$f_{\rm ph}$SB(10^{-6} cm^{-2} s^{-1})	$f_{\rm ph}$HB(10^{-6} cm^{-2} s^{-1})	E_{50} (keV)	E_{25} (keV)	E_{75} (keV)	f_X(10^{-14}erg cm^{-2} s^{-1})	Phot. Flag	Quantile Group
768	12^{+7}_{-6}	11^{+5}_{-4}	1^{+5}_{-1}	$2.67^{+1.50}_{-1.26}$	$1.41^{+0.64}_{-0.50}$	$0.16^{+1.16}_{-0.16}$	1.1±0.2	0.9±0.2	1.3±0.8	$0.49^{+0.29}_{-0.25}$	- - -	A
769	4^{+4}_{-3}	1^{+3}_{-1}	3^{+4}_{-2}	$2.38^{+2.23}_{-1.60}$	$0.45^{+0.83}_{-0.41}$	$1.62^{+2.07}_{-1.38}$	5.4±3.2	4.4±2.7	6.7±1.7	$2.08^{+2.28}_{-1.84}$	- - -	D
770	12^{+6}_{-5}	3^{+4}_{-2}	9^{+5}_{-4}	$2.80^{+1.28}_{-1.04}$	$0.44^{+0.46}_{-0.31}$	$2.06^{+1.15}_{-0.90}$	2.4±0.7	1.6±0.5	3.7±1.8	$1.07^{+0.58}_{-0.50}$	- - -	C
771	26^{+6}_{-5}	18^{+5}_{-4}	8^{+4}_{-3}	$6.04^{+1.48}_{-1.23}$	$2.32^{+0.70}_{-0.56}$	$2.00^{+1.02}_{-0.75}$	1.6±0.2	1.1±0.2	2.2±0.4	$1.53^{+0.42}_{-0.36}$	- - -	B
772	10^{+4}_{-3}	7^{+4}_{-3}	3^{+3}_{-2}	$2.00^{+0.86}_{-0.65}$	$0.77^{+0.43}_{-0.29}$	$0.68^{+0.63}_{-0.38}$	1.8±0.2	1.4±0.2	2.1±0.5	$0.57^{+0.26}_{-0.20}$	- - -	A
773	3^{+3}_{-2}	4^{+3}_{-2}	3	$0.62^{+0.68}_{-0.43}$	$0.41^{+0.37}_{-0.22}$	0.63	0.9±0.2	0.8±9.2	1.1±8.9	$0.09^{+0.10}_{-0.07}$	- - H	A
774	13^{+5}_{-4}	4^{+3}_{-2}	10^{+4}_{-3}	$2.82^{+1.01}_{-0.78}$	$0.47^{+0.39}_{-0.23}$	$2.05^{+0.91}_{-0.67}$	2.8±0.4	1.8±0.5	3.6±0.7	$1.26^{+0.49}_{-0.40}$	- - -	C
775	15^{+7}_{-5}	15^{+6}_{-4}	1^{+2}_{-1}	$2.39^{+1.08}_{-0.81}$	$2.09^{+0.52}_{-0.37}$	$0.47^{+1.28}_{-0.46}$	1.0±0.2	0.9±0.1	1.2±0.1	$0.39^{+0.19}_{-0.15}$	- - -	A
776	23^{+7}_{-6}	19^{+6}_{-4}	4^{+5}_{-3}	$2.96^{+0.89}_{-0.69}$	$1.85^{+0.43}_{-0.31}$	$0.46^{+0.57}_{-0.28}$	1.0±0.1	0.9±0.1	1.5±0.4	$0.49^{+0.15}_{-0.12}$	- - -	B
777	7^{+4}_{-3}	4^{+3}_{-2}	3^{+3}_{-2}	$1.59^{+0.90}_{-0.62}$	$0.54^{+0.44}_{-0.27}$	$0.67^{+0.72}_{-0.40}$	1.9±0.6	1.4±0.2	2.7±1.0	$0.48^{+0.31}_{-0.24}$	- - -	B
778	107^{+10}_{-10}	3^{+3}_{-2}	104^{+10}_{-10}	$20.25^{+1.97}_{-1.97}$	$0.32^{+0.32}_{-0.18}$	$20.10^{+1.98}_{-1.98}$	4.3±0.2	3.5±0.1	5.1±0.1	$14.05^{+1.47}_{-1.47}$	- - -	D
779	5^{+4}_{-3}	5^{+4}_{-2}	4	$1.01^{+0.84}_{-0.60}$	$0.63^{+0.43}_{-0.29}$	0.80	1.0±0.2	0.9±0.1	1.3±0.2	$0.16^{+0.14}_{-0.10}$	- - H	A
780	5^{+5}_{-4}	8^{+4}_{-3}	4	$1.15^{+1.09}_{-0.84}$	$1.03^{+0.54}_{-0.39}$	0.89	1.1±0.2	1.0±0.1	1.4±0.2	$0.20^{+0.19}_{-0.15}$	- - H	A
781	6^{+4}_{-3}	7^{+4}_{-3}	3	$1.44^{+0.96}_{-0.69}$	$0.94^{+0.53}_{-0.36}$	0.75	1.1±0.2	0.9±0.2	1.4±0.2	$0.26^{+0.18}_{-0.14}$	- - H	A
782	4^{+3}_{-2}	5^{+3}_{-2}	2	$0.69^{+0.67}_{-0.43}$	$0.53^{+0.39}_{-0.25}$	0.46	1.3±0.2	1.1±0.1	1.5±0.1	$0.14^{+0.14}_{-0.09}$	- - H	A
783	6^{+4}_{-3}	2	7^{+4}_{-3}	$1.30^{+0.85}_{-0.61}$	0.28	$1.44^{+0.87}_{-0.62}$	4.9±1.2	4.2±0.6	6.7±1.3	$1.01^{+0.71}_{-0.53}$	- S -	D
784	82^{+11}_{-10}	3	82^{+10}_{-9}	$18.76^{+2.42}_{-2.18}$	0.43	$19.19^{+2.46}_{-2.22}$	4.7±0.2	3.8±0.1	6.1±0.3	$14.11^{+1.94}_{-1.77}$	- S -	D
785	3^{+3}_{-2}	4^{+3}_{-2}	2	$0.66^{+0.60}_{-0.36}$	$0.42^{+0.35}_{-0.21}$	0.45	0.8±0.1	0.8±0.0	0.9±0.0	$0.09^{+0.08}_{-0.05}$	- - H	A
786	71^{+10}_{-8}	1^{+2}_{-1}	70^{+9}_{-8}	$13.92^{+1.86}_{-1.66}$	$0.10^{+0.26}_{-0.09}$	$14.04^{+1.89}_{-1.68}$	5.0±0.2	4.0±0.2	6.2±0.3	$11.07^{+1.57}_{-1.42}$	- - -	D
787	39^{+8}_{-7}	1^{+3}_{-1}	38^{+8}_{-7}	$7.56^{+1.54}_{-1.34}$	$0.09^{+0.30}_{-0.09}$	$7.56^{+1.55}_{-1.33}$	4.6±0.3	3.6±0.3	5.9±0.6	$5.56^{+1.20}_{-1.05}$	- - -	D
788	7^{+4}_{-3}	5^{+3}_{-2}	2^{+3}_{-2}	$1.58^{+0.93}_{-0.67}$	$0.59^{+0.43}_{-0.28}$	$0.56^{+0.73}_{-0.44}$	1.3±0.8	1.0±0.3	2.9±1.0	$0.34^{+0.29}_{-0.26}$	- - -	B
789	18^{+5}_{-4}	12^{+5}_{-3}	7^{+4}_{-3}	$3.59^{+1.06}_{-0.85}$	$1.34^{+0.52}_{-0.39}$	$1.30^{+0.75}_{-0.51}$	1.3±0.3	1.0±0.1	2.3±0.4	$0.74^{+0.29}_{-0.25}$	- - -	B
790	6^{+4}_{-3}	6^{+4}_{-2}	1^{+2}_{-1}	$1.21^{+0.71}_{-0.49}$	$0.64^{+0.39}_{-0.26}$	$0.12^{+0.45}_{-0.12}$	1.1±0.7	1.0±0.1	1.4±1.4	$0.21^{+0.18}_{-0.16}$	- - -	A
791	8^{+4}_{-3}	8^{+4}_{-3}	2	$1.43^{+0.75}_{-0.54}$	$0.87^{+0.44}_{-0.31}$	0.46	1.0±0.2	0.7±0.2	1.4±0.1	$0.23^{+0.13}_{-0.10}$	- - H	B
792	10^{+5}_{-4}	5^{+4}_{-2}	4^{+4}_{-3}	$2.43^{+1.15}_{-0.88}$	$0.76^{+0.50}_{-0.33}$	$1.12^{+0.95}_{-0.65}$	1.9±0.7	1.5±0.2	3.5±1.1	$0.74^{+0.44}_{-0.38}$	- - -	B
793	5^{+4}_{-2}	3^{+3}_{-2}	2^{+3}_{-2}	$1.11^{+0.74}_{-0.49}$	$0.35^{+0.35}_{-0.20}$	$0.53^{+0.62}_{-0.34}$	2.1±2.5	1.4±0.9	7.3±2.2	$0.38^{+0.51}_{-0.47}$	- - -	B
794	26^{+8}_{-6}	26^{+7}_{-5}	5^{+4}_{-2}	$2.99^{+0.89}_{-0.71}$	$2.13^{+0.44}_{-0.34}$	$0.43^{+0.92}_{-0.43}$	1.0±0.1	1.0±0.1	1.1±0.1	$0.50^{+0.15}_{-0.12}$	- - -	A
795	7^{+4}_{-3}	4^{+3}_{-2}	3^{+3}_{-2}	$1.22^{+0.71}_{-0.48}$	$0.42^{+0.35}_{-0.21}$	$0.50^{+0.56}_{-0.31}$	1.6±0.6	1.2±0.2	2.6±0.7	$0.31^{+0.22}_{-0.17}$	- - -	B
796	6^{+4}_{-3}	2	6^{+4}_{-3}	$2.83^{+2.12}_{-1.55}$	0.65	$3.30^{+2.16}_{-1.58}$	6.0±1.9	3.6±1.2	7.8±1.5	$2.74^{+2.21}_{-1.72}$	- S -	C
797	6^{+4}_{-3}	4^{+3}_{-2}	2^{+3}_{-2}	$1.23^{+0.75}_{-0.51}$	$0.43^{+0.36}_{-0.22}$	$0.49^{+0.59}_{-0.33}$	1.9±0.8	1.1±0.3	3.0±0.8	$0.37^{+0.27}_{-0.22}$	- - -	B
798	6^{+4}_{-2}	4^{+3}_{-2}	2^{+3}_{-1}	$1.05^{+0.68}_{-0.45}$	$0.43^{+0.35}_{-0.21}$	$0.32^{+0.51}_{-0.25}$	1.5±0.5	1.2±0.2	2.5±0.6	$0.25^{+0.18}_{-0.14}$	- - -	B
799	9^{+4}_{-3}	2^{+3}_{-1}	7^{+4}_{-3}	$1.90^{+0.94}_{-0.69}$	$0.21^{+0.33}_{-0.16}$	$1.57^{+0.88}_{-0.63}$	2.4±0.8	2.0±0.3	4.2±1.2	$0.73^{+0.43}_{-0.36}$	- - -	C
800	5^{+6}_{-5}	2^{+3}_{-2}	3^{+5}_{-3}	$1.47^{+1.66}_{-1.35}$	$0.30^{+0.58}_{-0.30}$	$0.95^{+1.51}_{-0.95}$	9.5±6.9	1.3±4.9	9.7±2.6	$2.24^{+3.00}_{-2.62}$	- - -	C
801	7^{+4}_{-3}	7^{+4}_{-3}	4	$1.50^{+0.84}_{-0.60}$	$0.83^{+0.46}_{-0.31}$	0.79	1.1±0.2	0.9±0.1	1.4±0.3	$0.25^{+0.15}_{-0.11}$	- - H	A
802	21^{+10}_{-8}	7^{+6}_{-4}	14^{+9}_{-7}	$2.74^{+1.29}_{-1.11}$	$0.75^{+0.44}_{-0.31}$	$1.88^{+1.18}_{-0.98}$	4.7±1.9	1.2±1.1	5.7±1.5	$2.05^{+1.28}_{-1.18}$	- - -	C
803	13^{+5}_{-4}	3	13^{+5}_{-4}	$3.00^{+1.28}_{-1.03}$	0.44	$3.08^{+1.28}_{-1.02}$	4.6±0.9	3.6±0.4	6.2±1.2	$2.20^{+1.03}_{-0.87}$	- S -	D
804	5^{+4}_{-2}	3	5^{+4}_{-2}	$1.17^{+0.79}_{-0.52}$	0.33	$1.22^{+0.80}_{-0.53}$	3.2±0.9	2.8±0.4	4.1±1.7	$0.60^{+0.44}_{-0.32}$	- S -	E
805	12^{+6}_{-4}	11^{+5}_{-3}	5^{+3}_{-2}	$1.48^{+0.74}_{-0.52}$	$1.29^{+0.38}_{-0.25}$	$0.63^{+0.98}_{-0.63}$	1.1±0.3	0.9±0.2	1.6±0.2	$0.27^{+0.15}_{-0.12}$	- - -	B

No.	C_{net} FB	C_{net} SB	C_{net} HB	$f_{\rm ph}$FB(10^{-6} cm^{-2} s^{-1})	$f_{\rm ph}$SB(10^{-6} cm^{-2} s^{-1})	$f_{\rm ph}$HB(10^{-6} cm^{-2} s^{-1})	E_{50} (keV)	E_{25} (keV)	E_{75} (keV)	f_X(10^{-14}erg cm^{-2} s^{-1})	Phot. Flag	Quantile Group
806	6^{+4}_{-3}	3^{+3}_{-2}	4^{+3}_{-2}	$1.33^{+0.78}_{-0.53}$	$0.35^{+0.35}_{-0.19}$	$0.75^{+0.67}_{-0.40}$	2.1±1.1	1.2±0.5	3.9±0.9	$0.46^{+0.35}_{-0.29}$	- - -	B
807	33^{+7}_{-6}	26^{+6}_{-5}	7^{+4}_{-3}	$6.20^{+1.30}_{-1.10}$	$2.87^{+0.68}_{-0.57}$	$1.29^{+0.74}_{-0.50}$	1.3±0.1	1.0±0.1	1.8±0.4	$1.31^{+0.29}_{-0.25}$	- - -	A
808	12^{+5}_{-4}	2^{+3}_{-1}	11^{+4}_{-3}	$2.45^{+0.93}_{-0.71}$	$0.21^{+0.30}_{-0.15}$	$2.13^{+0.89}_{-0.67}$	3.4±0.4	3.0±0.7	3.9±0.7	$1.33^{+0.52}_{-0.41}$	- - -	E
809	12^{+7}_{-6}	2^{+4}_{-2}	10^{+7}_{-5}	$4.93^{+2.85}_{-2.41}$	$0.42^{+0.82}_{-0.42}$	$4.29^{+2.71}_{-2.26}$	7.6±1.5	5.5±3.4	8.3±0.8	$5.98^{+3.66}_{-3.16}$	- - -	D
810	101^{+10}_{-10}	23^{+6}_{-5}	78^{+10}_{-9}	$25.63^{+2.60}_{-2.60}$	$3.33^{+0.86}_{-0.70}$	$20.18^{+2.61}_{-2.34}$	3.2±0.2	2.1±0.2	4.3±0.2	$12.93^{+1.55}_{-1.55}$	- - -	C
811	43^{+9}_{-7}	29^{+7}_{-5}	14^{+6}_{-4}	$5.56^{+1.08}_{-0.89}$	$2.59^{+0.51}_{-0.40}$	$1.84^{+0.77}_{-0.38}$	1.5±0.2	1.2±0.1	2.9±0.4	$1.34^{+0.33}_{-0.29}$	- - -	B
812	9^{+5}_{-3}	2	10^{+5}_{-3}	$2.12^{+1.07}_{-0.82}$	0.31	$2.28^{+1.10}_{-0.83}$	5.4±0.7	4.4±1.1	6.0±1.6	$1.83^{+0.96}_{-0.74}$	- S -	D
813	6^{+4}_{-3}	1^{+2}_{-1}	6^{+4}_{-2}	$1.22^{+0.71}_{-0.49}$	$0.09^{+0.26}_{-0.09}$	$1.08^{+0.69}_{-0.46}$	3.5±0.5	3.4±0.7	4.0±0.6	$0.69^{+0.42}_{-0.29}$	- - -	E
814	5^{+3}_{-2}	5^{+3}_{-2}	2	$0.91^{+0.67}_{-0.42}$	$0.56^{+0.39}_{-0.25}$	0.48	1.2±0.1	1.1±0.1	1.4±0.1	$0.17^{+0.13}_{-0.08}$	- - H	A
815	27^{+8}_{-6}	7^{+5}_{-3}	20^{+7}_{-5}	$3.02^{+0.84}_{-0.67}$	$0.73^{+0.29}_{-0.17}$	$2.27^{+0.77}_{-0.60}$	3.1±0.4	2.0±0.4	4.1±0.9	$1.51^{+0.47}_{-0.40}$	- - -	C
816	48^{+9}_{-8}	20^{+6}_{-5}	28^{+8}_{-6}	$5.10^{+1.00}_{-0.84}$	$1.70^{+0.39}_{-0.29}$	$3.00^{+0.84}_{-0.68}$	2.1±0.2	1.4±0.2	4.1±0.4	$1.68^{+0.37}_{-0.32}$	- - -	B
817	10^{+5}_{-4}	4^{+3}_{-2}	6^{+4}_{-3}	$2.10^{+1.07}_{-0.83}$	$0.46^{+0.43}_{-0.27}$	$1.33^{+0.93}_{-0.68}$	2.3±0.4	1.8±0.3	2.6±0.7	$0.78^{+0.41}_{-0.33}$	- - -	E
818	33^{+8}_{-7}	31^{+7}_{-6}	6^{+4}_{-2}	$3.71^{+0.92}_{-0.75}$	$2.50^{+0.47}_{-0.37}$	$0.44^{+0.99}_{-0.44}$	1.2±0.1	1.0±0.1	1.4±0.6	$0.70^{+0.18}_{-0.15}$	- - -	A
819	7^{+4}_{-3}	2	8^{+4}_{-3}	$1.52^{+0.94}_{-0.70}$	0.28	$1.69^{+0.96}_{-0.71}$	4.9±0.7	4.4±0.6	5.7±0.8	$1.19^{+0.75}_{-0.57}$	- S -	E
820	6^{+4}_{-2}	3	6^{+4}_{-2}	$1.28^{+0.81}_{-0.54}$	0.35	$1.33^{+0.83}_{-0.55}$	4.7±1.9	3.5±0.8	8.6±1.8	$0.97^{+0.73}_{-0.56}$	- S -	C
821	18^{+5}_{-4}	16^{+5}_{-4}	2^{+3}_{-2}	$3.51^{+1.06}_{-0.85}$	$1.78^{+0.57}_{-0.45}$	$0.44^{+0.58}_{-0.32}$	1.0±0.1	0.9±0.1	1.2±0.6	$0.58^{+0.18}_{-0.14}$	- - -	A
822	13^{+6}_{-5}	11^{+5}_{-3}	2^{+4}_{-2}	$1.30^{+0.67}_{-0.49}$	$1.18^{+0.32}_{-0.21}$	$0.52^{+1.02}_{-0.52}$	1.2±0.3	1.1±0.2	1.8±0.3	$0.25^{+0.15}_{-0.12}$	- - -	B
823	5^{+4}_{-3}	5^{+4}_{-2}	4	$1.03^{+0.89}_{-0.64}$	$0.69^{+0.47}_{-0.31}$	0.83	0.9±0.1	0.8±0.2	1.0±0.0	$0.16^{+0.14}_{-0.10}$	- - H	A
824	6^{+4}_{-3}	6^{+4}_{-2}	5	$1.33^{+0.92}_{-0.67}$	$0.73^{+0.46}_{-0.31}$	1.04	1.1±0.5	1.0±0.1	1.3±1.1	$0.23^{+0.20}_{-0.16}$	- - H	A
825	34^{+9}_{-7}	6^{+3}_{-2}	32^{+8}_{-7}	$4.22^{+1.09}_{-0.91}$	$1.02^{+0.42}_{-0.25}$	$4.03^{+1.07}_{-0.88}$	4.0±0.4	3.6±0.3	5.2±0.5	$2.70^{+0.75}_{-0.64}$	- - -	E
826	12^{+5}_{-4}	9^{+4}_{-3}	3^{+3}_{-2}	$2.41^{+0.96}_{-0.74}$	$1.02^{+0.48}_{-0.35}$	$0.65^{+0.66}_{-0.40}$	1.5±0.2	1.2±0.2	2.0±1.0	$0.57^{+0.25}_{-0.20}$	- - -	A
827	7^{+4}_{-3}	4^{+3}_{-2}	3^{+3}_{-2}	$1.23^{+0.72}_{-0.49}$	$0.43^{+0.35}_{-0.21}$	$0.51^{+0.57}_{-0.31}$	1.8±0.9	1.5±0.2	3.2±1.3	$0.36^{+0.28}_{-0.23}$	- - -	B
828	9^{+4}_{-3}	2	9^{+4}_{-3}	$1.88^{+0.89}_{-0.66}$	0.30	$1.97^{+0.91}_{-0.67}$	3.9±0.2	3.5±0.2	3.9±0.4	$1.17^{+0.56}_{-0.42}$	- S -	E
829	9^{+5}_{-3}	5^{+4}_{-2}	4^{+4}_{-2}	$2.23^{+1.17}_{-0.88}$	$0.74^{+0.52}_{-0.34}$	$0.93^{+0.94}_{-0.62}$	1.6±0.3	1.2±0.2	2.1±0.4	$0.56^{+0.32}_{-0.25}$	- - -	A
830	7^{+5}_{-4}	4	7^{+5}_{-4}	$1.50^{+1.06}_{-0.83}$	0.52	$1.43^{+1.03}_{-0.79}$	9.7±1.1	8.5±2.4	9.7±0.3	$2.32^{+1.66}_{-1.31}$	- S -	D
831	16^{+6}_{-5}	17^{+6}_{-4}	4	$1.71^{+0.71}_{-0.53}$	$1.66^{+0.38}_{-0.28}$	0.49	1.1±0.2	0.9±0.1	1.2±0.1	$0.30^{+0.14}_{-0.11}$	- - H	B
832	8^{+4}_{-3}	2	8^{+4}_{-3}	$1.60^{+0.81}_{-0.59}$	0.28	$1.68^{+0.82}_{-0.60}$	5.2±0.8	4.8±0.7	6.8±0.6	$1.34^{+0.70}_{-0.53}$	- S -	D
833	4^{+3}_{-2}	4^{+3}_{-2}	2	$1.00^{+0.85}_{-0.51}$	$0.61^{+0.50}_{-0.30}$	0.68	1.0±0.2	0.9±0.1	1.2±0.1	$0.15^{+0.14}_{-0.08}$	- - H	A
834	16^{+7}_{-6}	4^{+4}_{-3}	12^{+6}_{-5}	$4.18^{+1.78}_{-1.51}$	$0.57^{+0.57}_{-0.39}$	$3.23^{+1.65}_{-1.36}$	3.7±1.0	2.6±1.0	5.7±1.8	$2.49^{+1.27}_{-1.14}$	- - -	C
835	8^{+4}_{-3}	7^{+4}_{-3}	1^{+3}_{-1}	$1.62^{+0.80}_{-0.58}$	$0.78^{+0.43}_{-0.29}$	$0.29^{+0.53}_{-0.26}$	1.1±0.4	0.9±0.1	1.9±0.9	$0.29^{+0.18}_{-0.15}$	- - -	B
836	4^{+8}_{-4}	10^{+6}_{-5}	8	$0.92^{+1.83}_{-0.92}$	$1.29^{+0.76}_{-0.61}$	2.02	1.1±8.9	0.9±2.6	1.2±8.8	$0.17^{+1.35}_{-1.32}$	- - H	A
837	66^{+9}_{-8}	27^{+6}_{-5}	39^{+8}_{-7}	$14.44^{+2.09}_{-1.86}$	$3.34^{+0.80}_{-0.66}$	$8.74^{+1.72}_{-1.48}$	2.3±0.3	1.5±0.1	4.0±0.4	$5.31^{+1.02}_{-0.96}$	- - -	C
838	18^{+7}_{-6}	18^{+6}_{-5}	5	$2.06^{+0.78}_{-0.61}$	$1.66^{+0.39}_{-0.29}$	0.54	1.0±0.2	0.9±0.1	1.3±1.9	$0.33^{+0.14}_{-0.11}$	- - H	A
839	5^{+3}_{-2}	4^{+3}_{-2}	1^{+2}_{-1}	$0.86^{+0.65}_{-0.41}$	$0.44^{+0.35}_{-0.21}$	$0.11^{+0.45}_{-0.11}$	1.5±0.3	1.2±0.2	1.7±0.3	$0.21^{+0.16}_{-0.11}$	- - -	A
840	12^{+6}_{-5}	5^{+4}_{-3}	7^{+5}_{-4}	$2.51^{+1.32}_{-1.09}$	$0.57^{+0.47}_{-0.32}$	$1.53^{+1.18}_{-0.94}$	4.5±1.7	1.8±1.0	5.7±1.7	$1.81^{+1.17}_{-1.04}$	- - -	C
841	19^{+7}_{-6}	17^{+6}_{-5}	3^{+4}_{-3}	$2.23^{+0.88}_{-0.69}$	$1.51^{+0.40}_{-0.30}$	$0.79^{+0.93}_{-0.67}$	1.2±0.2	1.0±0.1	1.3±0.1	$0.42^{+0.17}_{-0.14}$	- - -	A
842	3^{+4}_{-2}	1^{+3}_{-1}	2^{+3}_{-2}	$1.87^{+1.97}_{-1.31}$	$0.38^{+0.83}_{-0.38}$	$1.22^{+1.78}_{-1.08}$	4.5±4.1	0.8±2.1	6.9±2.4	$1.35^{+1.89}_{-1.56}$	- - -	C
843	4^{+3}_{-2}	3^{+3}_{-2}	1^{+2}_{-1}	$0.69^{+0.60}_{-0.36}$	$0.33^{+0.33}_{-0.18}$	$0.14^{+0.45}_{-0.14}$	1.5±0.5	1.4±0.2	1.9±0.7	$0.16^{+0.15}_{-0.10}$	- - -	A

No.	C_{net} FB	C_{net} SB	C_{net} HB	$f_{\rm ph}$FB(10^{-6} cm^{-2} s^{-1})	$f_{\rm ph}$SB(10^{-6} cm^{-2} s^{-1})	$f_{\rm ph}$HB(10^{-6} cm^{-2} s^{-1})	E_{50} (keV)	E_{25} (keV)	E_{75} (keV)	f_X(10^{-14}erg cm^{-2} s^{-1})	Phot. Flag	Quantile Group
844	9^{+5}_{-4}	6^{+4}_{-3}	3^{+4}_{-2}	$1.74^{+0.95}_{-0.73}$	$0.70^{+0.44}_{-0.30}$	$0.54^{+0.73}_{-0.48}$	1.5±0.6	1.1±0.3	2.0±2.3	$0.41^{+0.28}_{-0.24}$	- - -	A
845	18^{+7}_{-5}	5	20^{+7}_{-5}	$1.89^{+0.69}_{-0.53}$	0.28	$2.11^{+0.71}_{-0.54}$	4.5±0.3	4.1±0.2	5.5±0.5	$1.37^{+0.51}_{-0.39}$	- S -	E
846	25^{+6}_{-5}	20^{+6}_{-4}	5^{+3}_{-2}	$4.77^{+1.18}_{-0.97}$	$2.24^{+0.63}_{-0.51}$	$0.92^{+0.67}_{-0.43}$	1.2±0.1	1.0±0.1	1.6±0.7	$0.92^{+0.24}_{-0.21}$	- - -	A
847	8^{+5}_{-3}	8^{+4}_{-3}	4	$1.93^{+1.14}_{-0.87}$	$1.13^{+0.58}_{-0.42}$	1.09	1.0±0.2	0.9±0.2	1.3±0.2	$0.31^{+0.19}_{-0.15}$	- - H	A
848	17^{+5}_{-4}	1^{+2}_{-1}	16^{+5}_{-4}	$3.23^{+1.02}_{-0.80}$	$0.10^{+0.26}_{-0.09}$	$3.12^{+1.01}_{-0.80}$	3.2±0.4	2.5±0.3	4.1±1.3	$1.66^{+0.57}_{-0.47}$	- - -	E
849	5^{+3}_{-2}	2^{+3}_{-1}	3^{+3}_{-2}	$1.25^{+0.90}_{-0.57}$	$0.30^{+0.41}_{-0.20}$	$0.75^{+0.79}_{-0.44}$	2.3±0.7	1.7±0.4	3.5±0.6	$0.45^{+0.36}_{-0.25}$	- - -	C
850	15^{+6}_{-4}	8^{+4}_{-3}	7^{+4}_{-3}	$3.34^{+1.20}_{-0.97}$	$0.99^{+0.51}_{-0.37}$	$1.62^{+0.98}_{-0.74}$	2.0±0.6	1.5±0.2	3.3±1.4	$1.07^{+0.50}_{-0.44}$	- - -	B
851	32^{+8}_{-6}	4^{+3}_{-1}	32^{+8}_{-6}	$3.56^{+0.88}_{-0.71}$	$0.83^{+0.31}_{-0.15}$	$3.53^{+0.87}_{-0.69}$	4.3±0.5	3.3±0.4	5.5±0.7	$2.45^{+0.67}_{-0.56}$	- - -	D
852	4^{+3}_{-2}	5^{+3}_{-2}	2	$0.82^{+0.67}_{-0.42}$	$0.55^{+0.38}_{-0.24}$	0.46	1.2±0.3	0.9±0.2	1.3±0.1	$0.16^{+0.14}_{-0.09}$	- - H	A
853	3^{+6}_{-3}	5^{+4}_{-3}	7	$0.71^{+1.59}_{-0.71}$	$0.77^{+0.63}_{-0.46}$	1.81	1.1±8.9	0.7±3.7	9.8±7.1	$0.12^{+1.05}_{-1.02}$	- - H	B
854	29^{+6}_{-5}	1^{+2}_{-1}	28^{+6}_{-5}	$5.83^{+1.32}_{-1.10}$	$0.10^{+0.27}_{-0.10}$	$5.77^{+1.32}_{-1.10}$	5.3±0.5	3.5±0.4	6.5±0.3	$4.94^{+1.22}_{-1.05}$	- - -	D
855	39^{+9}_{-7}	34^{+8}_{-6}	5^{+5}_{-3}	$3.68^{+0.84}_{-0.68}$	$2.52^{+0.44}_{-0.34}$	$0.46^{+0.51}_{-0.31}$	1.0±0.0	0.9±0.0	1.4±0.5	$0.60^{+0.14}_{-0.11}$	- - -	A
856	7^{+4}_{-3}	2^{+3}_{-2}	5^{+4}_{-3}	$1.75^{+1.07}_{-0.80}$	$0.30^{+0.40}_{-0.22}$	$1.24^{+0.98}_{-0.70}$	3.2±1.5	2.5±0.8	6.1±1.7	$0.89^{+0.69}_{-0.58}$	- - -	C
857	3^{+3}_{-2}	4	2^{+3}_{-2}	$1.85^{+2.30}_{-1.47}$	1.39	$1.67^{+2.20}_{-1.33}$	6.1±2.9	1.5±1.9	7.6±1.3	$1.82^{+2.42}_{-1.69}$	- S -	C
858	9^{+5}_{-4}	3^{+3}_{-2}	6^{+4}_{-3}	$2.61^{+1.45}_{-1.13}$	$0.46^{+0.54}_{-0.33}$	$1.83^{+1.30}_{-0.97}$	3.4±1.5	1.6±1.0	4.2±2.7	$1.44^{+1.02}_{-0.89}$	- - -	C
859	12^{+5}_{-4}	4^{+3}_{-2}	9^{+4}_{-3}	$2.68^{+1.02}_{-0.78}$	$0.48^{+0.39}_{-0.24}$	$1.89^{+0.91}_{-0.66}$	2.4±0.6	1.9±0.3	3.7±0.5	$1.02^{+0.47}_{-0.40}$	- - -	E
860	6^{+4}_{-3}	6^{+4}_{-3}	4	$1.50^{+0.99}_{-0.73}$	$0.86^{+0.51}_{-0.35}$	0.99	1.0±0.2	0.9±0.1	1.4±0.2	$0.24^{+0.17}_{-0.13}$	- - H	A
861	10^{+5}_{-4}	7^{+4}_{-3}	3^{+4}_{-2}	$2.26^{+1.15}_{-0.89}$	$0.94^{+0.54}_{-0.38}$	$0.63^{+0.88}_{-0.58}$	1.3±0.4	1.1±0.2	2.1±1.0	$0.46^{+0.29}_{-0.24}$	- - -	A
862	6^{+4}_{-2}	6^{+4}_{-2}	2	$1.06^{+0.68}_{-0.45}$	$0.65^{+0.39}_{-0.26}$	0.46	1.1±0.2	0.8±0.2	1.3±0.2	$0.19^{+0.13}_{-0.09}$	- - H	B
863	4^{+4}_{-3}	4	3^{+4}_{-2}	$0.81^{+0.86}_{-0.59}$	0.47	$0.75^{+0.83}_{-0.55}$	5.0±3.0	3.6±2.0	9.5±1.7	$0.65^{+0.79}_{-0.61}$	- S -	C
864	20^{+7}_{-5}	17^{+6}_{-4}	3^{+4}_{-3}	$2.46^{+0.84}_{-0.62}$	$1.74^{+0.42}_{-0.30}$	$0.66^{+0.83}_{-0.60}$	1.2±0.2	0.8±0.1	1.6±0.3	$0.49^{+0.19}_{-0.15}$	- - -	B
865	13^{+5}_{-4}	7^{+4}_{-3}	6^{+4}_{-3}	$2.57^{+0.93}_{-0.72}$	$0.77^{+0.42}_{-0.29}$	$1.27^{+0.75}_{-0.51}$	1.9±0.5	1.7±0.2	3.4±1.5	$0.78^{+0.35}_{-0.30}$	- - -	B
866	7^{+4}_{-3}	1^{+2}_{-1}	6^{+4}_{-3}	$1.36^{+0.78}_{-0.56}$	$0.08^{+0.27}_{-0.08}$	$1.24^{+0.77}_{-0.52}$	4.9±1.0	4.0±1.6	6.1±0.6	$1.07^{+0.65}_{-0.49}$	- - -	D
867	14^{+5}_{-4}	2	15^{+5}_{-4}	$2.71^{+1.00}_{-0.79}$	0.25	$2.86^{+1.02}_{-0.81}$	3.7±0.9	3.2±0.3	5.9±1.0	$1.62^{+0.72}_{-0.62}$	- S -	D
868	10^{+5}_{-4}	6^{+4}_{-3}	4^{+4}_{-3}	$2.24^{+1.15}_{-0.90}$	$0.75^{+0.50}_{-0.34}$	$0.95^{+0.94}_{-0.67}$	1.5±0.6	1.4±0.3	2.5±0.9	$0.52^{+0.35}_{-0.31}$	- - -	A
869	23^{+8}_{-6}	18^{+6}_{-4}	6^{+4}_{-3}	$2.66^{+0.91}_{-0.73}$	$1.69^{+0.41}_{-0.31}$	$1.46^{+1.05}_{-0.79}$	1.1±0.2	1.2±0.1	1.2±0.3	$0.49^{+0.18}_{-0.15}$	- - -	A
870	5^{+4}_{-2}	3	6^{+4}_{-2}	$1.12^{+0.74}_{-0.49}$	0.30	$1.17^{+0.76}_{-0.50}$	5.0±0.7	4.3±0.8	5.4±0.5	$0.90^{+0.61}_{-0.42}$	- S -	E
871	9	1^{+3}_{-1}	7	2.58	$0.20^{+0.55}_{-0.20}$	2.08	5.2±4.8	2.9±7.1	7.6±7.1	2.17	F - H	C
872	10^{+4}_{-3}	9^{+4}_{-3}	1^{+2}_{-1}	$1.95^{+0.87}_{-0.65}$	$1.05^{+0.49}_{-0.35}$	$0.13^{+0.48}_{-0.13}$	1.1±0.2	0.9±0.1	1.5±0.3	$0.34^{+0.16}_{-0.13}$	- - -	A
873	6^{+4}_{-3}	6^{+4}_{-2}	4	$1.24^{+0.74}_{-0.50}$	$0.67^{+0.41}_{-0.27}$	0.77	1.1±0.4	1.0±0.1	2.0±0.3	$0.23^{+0.15}_{-0.12}$	- - H	B
874	19^{+6}_{-5}	11^{+5}_{-3}	8^{+4}_{-3}	$3.78^{+1.18}_{-0.96}$	$1.28^{+0.53}_{-0.40}$	$1.58^{+0.90}_{-0.67}$	1.8±0.3	1.5±0.1	2.5±0.4	$1.09^{+0.39}_{-0.33}$	- - -	A
875	6^{+4}_{-3}	2^{+3}_{-1}	4^{+3}_{-2}	$1.21^{+0.82}_{-0.56}$	$0.20^{+0.33}_{-0.16}$	$0.88^{+0.75}_{-0.48}$	4.4±1.3	1.9±1.1	5.0±0.7	$0.85^{+0.62}_{-0.46}$	- - -	C
876	8^{+6}_{-5}	2^{+4}_{-2}	6^{+6}_{-5}	$1.61^{+1.31}_{-1.09}$	$0.19^{+0.44}_{-0.19}$	$1.30^{+1.19}_{-0.97}$	3.1±0.9	2.3±1.1	4.1±0.6	$0.80^{+0.69}_{-0.59}$	- - -	D
877	5^{+4}_{-3}	6^{+4}_{-2}	3	$1.11^{+0.77}_{-0.52}$	$0.66^{+0.42}_{-0.28}$	0.67	1.1±0.4	0.9±0.2	1.8±0.3	$0.19^{+0.15}_{-0.11}$	- - H	B
878	8^{+4}_{-3}	2^{+3}_{-1}	6^{+4}_{-3}	$1.66^{+0.91}_{-0.66}$	$0.22^{+0.33}_{-0.16}$	$1.30^{+0.85}_{-0.58}$	4.1±1.2	2.1±0.9	5.0±1.2	$1.09^{+0.67}_{-0.54}$	- - -	C
879	5^{+4}_{-2}	3	6^{+4}_{-2}	$1.24^{+0.82}_{-0.54}$	0.34	$1.29^{+0.84}_{-0.55}$	4.3±1.0	4.1±0.5	6.6±0.9	$0.85^{+0.59}_{-0.42}$	- S -	D
880	7^{+5}_{-4}	7^{+4}_{-3}	5	$1.49^{+1.01}_{-0.76}$	$0.82^{+0.49}_{-0.35}$	1.07	1.4±0.6	1.3±0.3	1.7±1.5	$0.34^{+0.27}_{-0.22}$	- - H	A
881	200^{+15}_{-14}	46^{+8}_{-7}	154^{+14}_{-13}	$21.54^{+1.63}_{-1.54}$	$3.54^{+0.52}_{-0.43}$	$16.67^{+1.54}_{-1.38}$	3.3±0.2	2.1±0.2	4.4±0.2	$11.39^{+1.05}_{-1.02}$	- - -	C

No.	C_{net} FB	C_{net} SB	C_{net} HB	$f_{\rm ph}$FB(10^{-6} cm^{-2} s^{-1})	$f_{\rm ph}$SB(10^{-6} cm^{-2} s^{-1})	$f_{\rm ph}$HB(10^{-6} cm^{-2} s^{-1})	E_{50} (keV)	E_{25} (keV)	E_{75} (keV)	f_X(10^{-14}erg cm^{-2} s^{-1})	Phot. Flag	Quantile Group
882	12^{+5}_{-4}	5^{+4}_{-2}	8^{+5}_{-4}	$2.88^{+1.28}_{-1.03}$	$0.60^{+0.48}_{-0.32}$	$1.85^{+1.13}_{-0.87}$	2.5±1.2	1.5±0.4	3.6±3.1	$1.14^{+0.75}_{-0.69}$	- - -	C
883	5^{+4}_{-2}	5^{+3}_{-2}	4	$1.11^{+0.82}_{-0.54}$	$0.62^{+0.44}_{-0.28}$	0.82	1.5±2.1	1.3±0.4	1.8±3.3	$0.26^{+0.42}_{-0.40}$	- - H	A
884	9^{+4}_{-3}	8^{+4}_{-3}	4	$1.68^{+0.84}_{-0.63}$	$0.92^{+0.45}_{-0.33}$	0.83	1.1±0.2	0.9±0.1	1.3±1.0	$0.29^{+0.16}_{-0.12}$	- - H	A
885	47^{+11}_{-9}	15^{+7}_{-5}	32^{+10}_{-8}	$3.13^{+0.72}_{-0.58}$	$0.64^{+0.25}_{-0.15}$	$2.35^{+0.66}_{-0.52}$	2.7±0.5	1.9±0.3	4.5±1.2	$1.33^{+0.38}_{-0.34}$	- - -	C
886	9^{+5}_{-4}	4^{+4}_{-2}	4^{+4}_{-3}	$1.83^{+1.04}_{-0.82}$	$0.53^{+0.43}_{-0.28}$	$0.92^{+0.89}_{-0.65}$	2.1±1.1	1.3±0.4	3.4±3.4	$0.61^{+0.48}_{-0.43}$	- - -	B
887	7	4	6	3.29	1.07	3.08	8.2±7.7	1.9±8.1	8.9±8.4	4.33	F S H	C
888	28^{+8}_{-6}	10^{+5}_{-3}	18^{+7}_{-5}	$3.36^{+0.89}_{-0.71}$	$0.97^{+0.34}_{-0.23}$	$2.21^{+0.78}_{-0.60}$	2.8±0.4	1.6±0.3	3.7±0.7	$1.50^{+0.46}_{-0.39}$	- - -	C
889	4^{+4}_{-3}	4^{+3}_{-2}	4	$0.86^{+0.87}_{-0.59}$	$0.50^{+0.44}_{-0.28}$	0.88	0.9±3.7	0.8±1.0	0.9±4.0	$0.12^{+0.52}_{-0.51}$	- - H	A
890	12^{+5}_{-4}	7^{+4}_{-3}	5^{+4}_{-2}	$2.45^{+0.96}_{-0.73}$	$0.78^{+0.44}_{-0.30}$	$1.10^{+0.75}_{-0.49}$	1.8±0.4	1.2±0.3	2.3±0.7	$0.70^{+0.31}_{-0.26}$	- - -	B
891	10^{+6}_{-4}	10^{+4}_{-2}	4^{+4}_{-3}	$1.08^{+0.61}_{-0.43}$	$1.48^{+0.41}_{-0.27}$	$0.92^{+0.96}_{-0.71}$	1.6±0.2	1.3±0.2	1.7±0.2	$0.27^{+0.16}_{-0.12}$	- - -	A
892	9^{+4}_{-3}	1^{+2}_{-1}	8^{+4}_{-3}	$1.98^{+1.03}_{-0.77}$	$0.08^{+0.31}_{-0.08}$	$1.88^{+1.02}_{-0.75}$	3.4±0.4	2.9±0.5	3.9±0.6	$1.06^{+0.57}_{-0.43}$	- - -	E
893	187^{+15}_{-14}	3^{+4}_{-3}	183^{+15}_{-14}	$24.02^{+1.93}_{-1.84}$	$0.40^{+0.30}_{-0.16}$	$24.06^{+1.94}_{-1.85}$	4.6±0.1	3.8±0.1	5.4±0.1	$17.67^{+1.50}_{-1.44}$	- - -	D
894	11^{+4}_{-3}	5^{+3}_{-2}	6^{+4}_{-2}	$2.55^{+1.06}_{-0.79}$	$0.68^{+0.47}_{-0.30}$	$1.40^{+0.88}_{-0.58}$	2.0±0.5	1.6±0.2	3.1±0.7	$0.81^{+0.40}_{-0.33}$	- - -	B
895	8^{+5}_{-4}	2^{+3}_{-2}	6^{+5}_{-4}	$1.89^{+1.33}_{-1.06}$	$0.27^{+0.45}_{-0.27}$	$1.45^{+1.23}_{-0.95}$	4.9±2.7	3.0±2.1	8.5±2.1	$1.49^{+1.34}_{-1.18}$	- - -	C
896	6^{+4}_{-3}	5^{+4}_{-2}	5	$1.33^{+0.96}_{-0.70}$	$0.70^{+0.47}_{-0.31}$	1.11	1.3±0.2	1.1±0.1	1.5±0.3	$0.27^{+0.20}_{-0.15}$	- - H	A
897	3^{+4}_{-2}	4^{+3}_{-2}	4	$0.69^{+0.75}_{-0.50}$	$0.43^{+0.38}_{-0.23}$	0.80	1.3±0.2	1.2±0.1	1.4±0.1	$0.15^{+0.16}_{-0.11}$	- - H	A
898	5^{+6}_{-5}	3	8^{+6}_{-5}	$1.04^{+1.27}_{-1.04}$	0.37	$1.58^{+1.24}_{-1.01}$	7.4±0.9	6.8±1.0	7.5±0.8	$1.23^{+1.52}_{-1.24}$	- S -	E
899	109^{+12}_{-11}	3^{+4}_{-2}	105^{+12}_{-10}	$11.39^{+1.29}_{-1.13}$	$0.40^{+0.24}_{-0.12}$	$11.29^{+1.30}_{-1.13}$	4.8±0.2	3.9±0.2	6.0±0.2	$8.67^{+1.05}_{-0.93}$	- - -	D
900	9^{+4}_{-3}	1^{+2}_{-1}	8^{+4}_{-3}	$1.68^{+0.79}_{-0.58}$	$0.07^{+0.25}_{-0.07}$	$1.59^{+0.77}_{-0.56}$	3.5±0.5	3.3±1.0	4.3±1.1	$0.95^{+0.47}_{-0.36}$	- - -	E
901	9	4	8	2.70	0.64	2.58	5.2±4.8	2.9±7.1	7.6±7.1	2.27	F S H	C
902	36^{+9}_{-7}	34^{+8}_{-6}	1^{+5}_{-1}	$3.85^{+0.93}_{-0.75}$	$2.90^{+0.49}_{-0.39}$	$0.36^{+1.19}_{-0.36}$	1.2±0.1	1.0±0.1	1.6±0.1	$0.75^{+0.20}_{-0.17}$	- - -	A
903	23^{+7}_{-6}	4^{+3}_{-1}	23^{+7}_{-6}	$2.65^{+0.82}_{-0.65}$	$1.01^{+0.42}_{-0.18}$	$2.62^{+0.81}_{-0.64}$	4.0±0.2	3.7±0.4	5.0±0.5	$1.68^{+0.53}_{-0.42}$	- - -	E
904	9	3	1^{+5}_{-1}	2.48	0.44	$0.41^{+1.48}_{-0.41}$	5.2±4.8	2.9±7.1	7.6±7.1	2.08	F S -	C
905	4^{+4}_{-3}	6^{+4}_{-3}	3	$0.81^{+0.80}_{-0.57}$	$0.71^{+0.44}_{-0.30}$	0.58	1.0±0.1	0.9±0.0	1.1±0.0	$0.13^{+0.13}_{-0.09}$	- - H	A
906	88^{+11}_{-10}	46^{+8}_{-7}	42^{+9}_{-7}	$9.52^{+1.25}_{-1.08}$	$3.63^{+0.54}_{-0.44}$	$4.42^{+0.94}_{-0.76}$	1.9±0.2	1.4±0.1	3.4±0.2	$2.83^{+0.48}_{-0.45}$	- - -	B
907	11^{+6}_{-4}	13^{+5}_{-4}	1^{+3}_{-1}	$1.10^{+0.59}_{-0.43}$	$1.10^{+0.31}_{-0.21}$	$0.17^{+0.61}_{-0.17}$	1.0±0.1	0.8±0.1	1.1±0.1	$0.18^{+0.10}_{-0.07}$	- - -	A
908	4^{+5}_{-4}	2^{+3}_{-2}	3^{+5}_{-3}	$1.05^{+1.25}_{-1.00}$	$0.22^{+0.45}_{-0.22}$	$0.68^{+1.16}_{-0.68}$	9.1±5.3	5.0±4.6	9.6±2.0	$1.53^{+2.03}_{-1.71}$	- - -	C
909	9^{+5}_{-4}	2	10^{+5}_{-4}	$1.97^{+1.05}_{-0.82}$	0.27	$2.23^{+1.07}_{-0.84}$	4.0±1.0	3.6±0.6	4.6±2.3	$1.27^{+0.75}_{-0.62}$	- S -	E
910	31^{+7}_{-6}	25^{+6}_{-5}	7^{+4}_{-3}	$6.40^{+1.40}_{-1.18}$	$2.89^{+0.72}_{-0.59}$	$1.39^{+0.83}_{-0.59}$	1.3±0.1	1.1±0.1	1.8±0.5	$1.35^{+0.32}_{-0.27}$	- - -	A
911	10^{+7}_{-6}	9^{+5}_{-4}	1^{+5}_{-1}	$1.90^{+1.37}_{-1.16}$	$1.00^{+0.56}_{-0.44}$	$0.14^{+1.10}_{-0.14}$	0.9±2.4	0.7±0.3	1.4±6.2	$0.28^{+0.76}_{-0.76}$	- - -	B
912	13^{+6}_{-4}	11^{+5}_{-3}	2^{+3}_{-2}	$1.37^{+0.65}_{-0.46}$	$1.20^{+0.33}_{-0.22}$	$0.52^{+0.83}_{-0.52}$	1.0±0.1	1.0±0.1	1.1±0.1	$0.23^{+0.11}_{-0.08}$	- - -	A
913	5^{+4}_{-3}	2	6^{+4}_{-3}	$1.80^{+1.43}_{-1.06}$	0.42	$2.11^{+1.46}_{-1.08}$	5.2±1.7	5.1±0.5	7.6±2.0	$1.51^{+1.30}_{-1.02}$	- S -	D
914	9^{+4}_{-3}	1^{+3}_{-1}	8^{+4}_{-3}	$1.85^{+0.89}_{-0.67}$	$0.17^{+0.31}_{-0.15}$	$1.58^{+0.84}_{-0.61}$	3.6±1.2	2.6±0.7	5.6±1.5	$1.06^{+0.61}_{-0.51}$	- - -	C
915	46^{+9}_{-7}	39^{+8}_{-6}	8^{+4}_{-3}	$5.11^{+0.98}_{-0.81}$	$3.18^{+0.50}_{-0.41}$	$1.73^{+0.94}_{-0.68}$	1.2±0.1	1.0±0.1	1.5±0.2	$0.98^{+0.20}_{-0.17}$	- - -	B
916	9^{+4}_{-3}	7^{+4}_{-3}	2^{+3}_{-2}	$1.92^{+0.96}_{-0.71}$	$0.87^{+0.48}_{-0.33}$	$0.41^{+0.67}_{-0.37}$	1.3±1.0	0.9±0.1	1.6±3.3	$0.39^{+0.36}_{-0.34}$	- - -	A
917	12^{+5}_{-4}	2^{+3}_{-1}	10^{+5}_{-3}	$2.41^{+1.01}_{-0.78}$	$0.20^{+0.32}_{-0.15}$	$2.11^{+0.98}_{-0.74}$	3.6±0.8	2.8±0.7	4.9±0.8	$1.41^{+0.66}_{-0.54}$	- - -	D
918	10^{+7}_{-6}	4	11^{+6}_{-5}	$2.77^{+1.92}_{-1.62}$	0.63	$3.14^{+1.88}_{-1.57}$	7.1±1.7	5.5±3.4	8.9±1.6	$3.13^{+2.30}_{-1.98}$	- S -	D
919	6^{+4}_{-3}	7^{+4}_{-3}	2	$1.28^{+0.75}_{-0.51}$	$0.80^{+0.44}_{-0.30}$	0.46	1.3±0.2	1.0±0.1	1.6±0.2	$0.27^{+0.17}_{-0.12}$	- - H	A
920	8^{+7}_{-6}	4^{+4}_{-3}	3^{+7}_{-3}	$1.64^{+1.56}_{-1.34}$	$0.52^{+0.51}_{-0.37}$	$0.74^{+1.44}_{-0.74}$	1.7±2.7	0.8±0.6	2.2±6.0	$0.44^{+0.82}_{-0.79}$	- - -	B

No.	C_{net} FB	C_{net} SB	C_{net} HB	$f_{\rm ph}$FB(10^{-6} cm^{-2} s^{-1})	$f_{\rm ph}$SB(10^{-6} cm^{-2} s^{-1})	$f_{\rm ph}$HB(10^{-6} cm^{-2} s^{-1})	E_{50} (keV)	E_{25} (keV)	E_{75} (keV)	f_X(10^{-14}erg cm^{-2} s^{-1})	Phot. Flag	Quantile Group
921	9^{+5}_{-3}	6^{+4}_{-2}	4^{+4}_{-2}	$1.98^{+0.96}_{-0.73}$	$0.66^{+0.43}_{-0.28}$	$0.84^{+0.77}_{-0.51}$	1.7±1.8	1.1±0.5	5.0±2.9	$0.55^{+0.61}_{-0.59}$	- - -	B
922	11^{+5}_{-3}	3	11^{+5}_{-3}	$2.57^{+1.05}_{-0.80}$	0.34	$2.66^{+1.08}_{-0.82}$	3.2±0.4	2.7±0.2	3.9±1.0	$1.32^{+0.57}_{-0.44}$	- S -	E
923	17^{+8}_{-7}	6^{+5}_{-3}	12^{+7}_{-6}	$3.83^{+1.80}_{-1.58}$	$0.70^{+0.58}_{-0.44}$	$2.66^{+1.63}_{-1.40}$	2.4±1.2	1.3±0.9	4.7±1.3	$1.49^{+1.01}_{-0.95}$	- - -	C
924	22^{+7}_{-6}	12^{+5}_{-4}	10^{+6}_{-3}	$2.23^{+0.74}_{-0.58}$	$1.03^{+0.32}_{-0.22}$	$1.05^{+0.61}_{-0.19}$	1.9±0.3	1.8±0.1	2.3±0.3	$0.68^{+0.26}_{-0.21}$	- - -	A
925	6^{+4}_{-3}	6^{+4}_{-2}	1^{+2}_{-1}	$1.18^{+0.69}_{-0.47}$	$0.62^{+0.38}_{-0.25}$	$0.12^{+0.43}_{-0.12}$	1.0±1.6	0.9±0.2	1.6±3.4	$0.18^{+0.32}_{-0.31}$	- - -	A
926	3^{+7}_{-3}	5	4^{+6}_{-4}	$0.65^{+1.75}_{-0.65}$	0.69	$0.93^{+1.60}_{-0.93}$	6.5±1.2	5.7±0.8	6.6±0.5	$0.68^{+1.82}_{-0.69}$	- S -	E
927	15^{+6}_{-5}	5^{+4}_{-3}	10^{+5}_{-4}	$2.91^{+1.17}_{-0.96}$	$0.57^{+0.43}_{-0.29}$	$1.95^{+1.03}_{-0.82}$	2.3±1.1	1.6±0.4	5.2±1.6	$1.09^{+0.69}_{-0.64}$	- - -	C
928	14^{+5}_{-4}	9^{+4}_{-3}	4^{+4}_{-3}	$2.88^{+1.11}_{-0.88}$	$1.14^{+0.52}_{-0.38}$	$0.91^{+0.83}_{-0.57}$	1.7±0.3	1.4±0.2	2.1±1.1	$0.80^{+0.33}_{-0.27}$	- - -	A
929	11^{+6}_{-4}	5^{+4}_{-2}	6^{+5}_{-4}	$2.62^{+1.34}_{-1.08}$	$0.71^{+0.50}_{-0.33}$	$1.39^{+1.18}_{-0.91}$	2.3±0.7	1.6±0.6	3.1±0.9	$0.96^{+0.57}_{-0.48}$	- - -	C
930	12^{+6}_{-5}	6^{+4}_{-3}	7^{+5}_{-4}	$3.18^{+1.46}_{-1.19}$	$0.83^{+0.55}_{-0.37}$	$1.75^{+1.29}_{-1.00}$	3.1±1.8	1.3±0.6	5.8±1.4	$1.57^{+1.18}_{-1.10}$	- - -	C
931	7^{+4}_{-3}	4^{+3}_{-2}	3^{+3}_{-2}	$1.53^{+0.89}_{-0.64}$	$0.47^{+0.41}_{-0.25}$	$0.72^{+0.73}_{-0.44}$	1.5±1.8	1.2±0.5	5.5±2.6	$0.38^{+0.50}_{-0.47}$	- - -	B
932	5^{+4}_{-2}	5^{+3}_{-2}	3	$0.94^{+0.69}_{-0.46}$	$0.54^{+0.38}_{-0.24}$	0.68	1.3±0.2	1.2±0.1	1.6±0.2	$0.19^{+0.15}_{-0.10}$	- - H	A
933	8^{+4}_{-3}	3	8^{+4}_{-3}	$1.62^{+0.85}_{-0.61}$	0.33	$1.67^{+0.86}_{-0.62}$	5.2±0.8	4.2±0.5	6.3±1.0	$1.35^{+0.73}_{-0.54}$	- S -	D
934	3^{+4}_{-3}	5^{+4}_{-3}	3	$0.75^{+1.04}_{-0.75}$	$0.69^{+0.53}_{-0.36}$	0.84	1.0±0.1	0.9±0.1	1.1±0.1	$0.12^{+0.16}_{-0.12}$	- - H	A
935	13^{+5}_{-4}	2	13^{+5}_{-4}	$2.68^{+1.02}_{-0.80}$	0.27	$2.82^{+1.05}_{-0.81}$	4.3±0.5	3.3±0.5	5.2±0.6	$1.84^{+0.74}_{-0.60}$	- S -	D
936	13^{+5}_{-4}	5^{+4}_{-2}	7^{+4}_{-3}	$2.90^{+1.17}_{-0.92}$	$0.68^{+0.47}_{-0.31}$	$1.74^{+1.00}_{-0.74}$	2.2±0.7	1.3±0.4	3.9±1.7	$1.01^{+0.52}_{-0.46}$	- - -	B
937	7^{+6}_{-5}	2^{+4}_{-2}	6^{+6}_{-5}	$2.16^{+1.84}_{-1.53}$	$0.25^{+0.58}_{-0.25}$	$1.74^{+1.72}_{-1.39}$	2.4±3.9	1.8±1.6	7.4±3.4	$0.83^{+1.51}_{-1.46}$	- - -	C
938	9^{+4}_{-3}	1^{+2}_{-1}	8^{+4}_{-3}	$1.72^{+0.83}_{-0.62}$	$0.08^{+0.26}_{-0.08}$	$1.61^{+0.82}_{-0.60}$	3.2±1.6	2.3±0.5	5.9±2.5	$0.87^{+0.62}_{-0.55}$	- - -	C
939	5^{+4}_{-3}	6^{+4}_{-3}	4	$1.12^{+0.91}_{-0.66}$	$0.73^{+0.48}_{-0.32}$	0.81	0.9±0.3	0.8±0.1	1.3±0.3	$0.16^{+0.14}_{-0.11}$	- - H	A
940	4^{+4}_{-2}	5^{+4}_{-2}	2	$0.83^{+0.80}_{-0.53}$	$0.68^{+0.46}_{-0.30}$	0.52	1.3±0.2	1.1±0.2	1.4±0.1	$0.17^{+0.17}_{-0.11}$	- - H	A
941	6^{+4}_{-2}	4^{+3}_{-2}	2^{+3}_{-1}	$1.01^{+0.65}_{-0.43}$	$0.41^{+0.33}_{-0.20}$	$0.32^{+0.49}_{-0.24}$	1.4±1.3	1.2±0.3	2.7±2.3	$0.22^{+0.25}_{-0.23}$	- - -	B
942	6^{+4}_{-2}	6^{+4}_{-2}	2	$1.01^{+0.65}_{-0.43}$	$0.62^{+0.38}_{-0.25}$	0.44	1.2±0.1	1.0±0.1	1.4±0.1	$0.20^{+0.13}_{-0.09}$	- - H	A
943	4	1^{+2}_{-1}	2	0.66	$0.09^{+0.25}_{-0.09}$	0.43	5.2±4.8	2.9±7.1	7.6±7.1	0.55	F - H	C
944	15^{+5}_{-4}	13^{+5}_{-4}	1^{+3}_{-1}	$3.27^{+1.19}_{-0.95}$	$1.70^{+0.62}_{-0.48}$	$0.31^{+0.73}_{-0.31}$	1.4±0.2	1.1±0.1	1.7±0.3	$0.75^{+0.28}_{-0.23}$	- - -	A
945	12^{+5}_{-4}	8^{+4}_{-3}	4^{+4}_{-2}	$2.45^{+1.02}_{-0.80}$	$0.99^{+0.49}_{-0.35}$	$0.75^{+0.76}_{-0.50}$	1.5±0.6	1.3±0.2	2.8±1.8	$0.58^{+0.35}_{-0.31}$	- - -	B
946	11^{+5}_{-4}	8^{+4}_{-3}	3^{+4}_{-2}	$2.49^{+1.15}_{-0.90}$	$1.05^{+0.54}_{-0.39}$	$0.65^{+0.85}_{-0.56}$	1.0±0.8	0.8±0.1	1.9±3.6	$0.40^{+0.38}_{-0.36}$	- - -	B
947	8^{+4}_{-3}	1^{+3}_{-1}	7^{+4}_{-3}	$1.93^{+1.08}_{-0.81}$	$0.18^{+0.37}_{-0.18}$	$1.65^{+1.02}_{-0.75}$	4.0±2.0	2.7±1.3	7.6±2.4	$1.23^{+0.93}_{-0.81}$	- - -	C
948	5^{+4}_{-3}	2^{+3}_{-2}	2^{+3}_{-2}	$1.03^{+0.90}_{-0.65}$	$0.31^{+0.38}_{-0.21}$	$0.50^{+0.79}_{-0.50}$	1.8±3.0	1.0±1.2	6.8±2.3	$0.30^{+0.57}_{-0.54}$	- - -	B
949	43^{+9}_{-7}	15^{+6}_{-4}	29^{+8}_{-6}	$4.96^{+1.02}_{-0.85}$	$1.42^{+0.37}_{-0.27}$	$3.35^{+0.90}_{-0.72}$	2.3±0.2	1.9±0.1	3.2±0.2	$1.87^{+0.43}_{-0.37}$	- - -	E
950	9^{+5}_{-4}	5^{+3}_{-2}	5^{+4}_{-3}	$2.18^{+1.09}_{-0.83}$	$0.61^{+0.46}_{-0.29}$	$1.13^{+0.92}_{-0.64}$	2.0±0.4	1.6±0.3	2.5±1.1	$0.69^{+0.37}_{-0.30}$	- - -	A
951	10^{+5}_{-4}	2	11^{+5}_{-4}	$2.48^{+1.16}_{-0.89}$	0.32	$2.69^{+1.18}_{-0.91}$	4.3±0.9	3.0±0.6	5.8±0.6	$1.69^{+0.86}_{-0.70}$	- S -	D
952	5^{+4}_{-2}	5^{+3}_{-2}	3	$0.91^{+0.69}_{-0.45}$	$0.52^{+0.37}_{-0.24}$	0.67	1.1±0.1	0.9±0.1	1.1±0.1	$0.16^{+0.12}_{-0.08}$	- - H	A
953	12^{+6}_{-4}	1^{+3}_{-1}	11^{+5}_{-4}	$3.60^{+1.61}_{-1.29}$	$0.24^{+0.49}_{-0.24}$	$3.24^{+1.54}_{-1.21}$	2.8±1.9	2.1±0.4	6.0±3.1	$1.62^{+1.30}_{-1.23}$	- - -	C
954	7^{+4}_{-3}	6^{+4}_{-2}	1^{+2}_{-1}	$1.21^{+0.70}_{-0.48}$	$0.63^{+0.39}_{-0.26}$	$0.13^{+0.44}_{-0.13}$	1.0±0.2	0.9±0.1	1.3±0.4	$0.20^{+0.12}_{-0.09}$	- - -	A
955	9^{+7}_{-6}	4	11^{+7}_{-6}	$1.93^{+1.54}_{-1.31}$	0.45	$2.40^{+1.50}_{-1.27}$	4.3±3.5	3.1±1.3	9.3±3.9	$1.34^{+1.53}_{-1.42}$	- S -	C
956	10^{+5}_{-3}	7^{+4}_{-3}	3^{+3}_{-2}	$2.18^{+0.97}_{-0.73}$	$0.82^{+0.46}_{-0.31}$	$0.74^{+0.74}_{-0.47}$	1.2±0.8	0.8±0.3	3.1±1.0	$0.44^{+0.33}_{-0.30}$	- - -	B
957	17^{+5}_{-4}	11^{+4}_{-3}	6^{+4}_{-3}	$3.24^{+1.04}_{-0.83}$	$1.21^{+0.50}_{-0.37}$	$1.16^{+0.76}_{-0.51}$	1.6±0.4	1.3±0.2	3.2±0.9	$0.84^{+0.35}_{-0.31}$	- - -	B
958	6^{+4}_{-2}	6^{+4}_{-2}	2	$1.01^{+0.64}_{-0.42}$	$0.62^{+0.38}_{-0.25}$	0.45	1.1±0.2	1.0±0.1	1.4±0.1	$0.19^{+0.12}_{-0.08}$	- - H	A

No.	C_{net} FB	C_{net} SB	C_{net} HB	$f_{\rm ph}$FB(10^{-6} cm^{-2} s^{-1})	$f_{\rm ph}$SB(10^{-6} cm^{-2} s^{-1})	$f_{\rm ph}$HB(10^{-6} cm^{-2} s^{-1})	E_{50} (keV)	E_{25} (keV)	E_{75} (keV)	f_X(10^{-14}erg cm^{-2} s^{-1})	Phot. Flag	Quantile Group
959	14^{+5}_{-4}	12^{+5}_{-3}	2^{+3}_{-2}	$2.73^{+0.97}_{-0.76}$	$1.32^{+0.51}_{-0.39}$	$0.45^{+0.58}_{-0.32}$	1.4±0.2	1.3±0.1	1.8±1.3	$0.62^{+0.24}_{-0.19}$	- - -	A
960	5^{+4}_{-2}	6^{+4}_{-2}	2	$0.94^{+0.70}_{-0.46}$	$0.65^{+0.40}_{-0.27}$	0.45	1.4±0.3	1.0±0.2	1.5±0.1	$0.21^{+0.16}_{-0.11}$	- - H	A
961	157^{+13}_{-13}	86^{+11}_{-9}	71^{+10}_{-9}	$19.11^{+1.65}_{-1.56}$	$5.95^{+0.75}_{-0.65}$	$8.90^{+1.28}_{-1.09}$	1.9±0.1	1.3±0.0	3.2±0.4	$5.85^{+0.67}_{-0.65}$	- - -	B
962	11^{+5}_{-4}	3^{+3}_{-2}	9^{+4}_{-3}	$2.71^{+1.12}_{-0.86}$	$0.36^{+0.40}_{-0.22}$	$2.13^{+1.04}_{-0.77}$	3.2±0.9	2.2±0.6	5.2±1.0	$1.38^{+0.70}_{-0.59}$	- - -	C
963	53^{+11}_{-9}	23^{+7}_{-5}	30^{+9}_{-7}	$3.85^{+0.78}_{-0.65}$	$1.19^{+0.30}_{-0.22}$	$2.15^{+0.65}_{-0.51}$	2.1±0.3	1.6±0.1	3.4±0.5	$1.28^{+0.33}_{-0.29}$	- - -	B
964	12^{+7}_{-6}	4^{+4}_{-3}	8^{+6}_{-5}	$2.60^{+1.54}_{-1.31}$	$0.51^{+0.49}_{-0.34}$	$1.73^{+1.41}_{-1.17}$	3.0±3.2	1.9±1.0	7.7±3.0	$1.23^{+1.51}_{-1.46}$	- - -	C
965	7^{+4}_{-3}	1^{+2}_{-1}	6^{+4}_{-2}	$1.19^{+0.68}_{-0.46}$	$0.09^{+0.24}_{-0.09}$	$1.05^{+0.66}_{-0.44}$	6.3±1.9	2.7±1.3	7.2±0.8	$1.20^{+0.77}_{-0.59}$	- - -	C
966	16^{+8}_{-8}	6	16^{+8}_{-7}	$2.91^{+1.56}_{-1.38}$	0.63	$3.03^{+1.48}_{-1.27}$	4.1±1.0	3.2±1.3	5.4±3.1	$1.93^{+1.15}_{-1.04}$	- S -	D
967	9^{+4}_{-3}	7^{+4}_{-3}	2^{+3}_{-1}	$1.59^{+0.77}_{-0.56}$	$0.75^{+0.41}_{-0.28}$	$0.31^{+0.51}_{-0.25}$	1.3±0.3	1.1±0.1	1.8±0.3	$0.34^{+0.18}_{-0.14}$	- - -	A
968	6^{+6}_{-5}	4	6^{+6}_{-5}	$1.41^{+1.41}_{-1.17}$	0.56	$1.50^{+1.37}_{-1.11}$	8.7±3.8	4.0±3.0	9.7±1.4	$1.97^{+2.15}_{-1.84}$	- S -	C
969	11^{+6}_{-5}	1^{+3}_{-1}	10^{+6}_{-5}	$2.69^{+1.53}_{-1.28}$	$0.17^{+0.44}_{-0.17}$	$2.45^{+1.47}_{-1.21}$	5.0±1.1	4.3±2.4	5.9±1.4	$2.17^{+1.32}_{-1.13}$	- - -	D
970	11^{+5}_{-4}	7^{+4}_{-3}	4^{+4}_{-3}	$2.47^{+1.16}_{-0.90}$	$0.94^{+0.52}_{-0.37}$	$0.83^{+0.90}_{-0.62}$	1.7±1.9	1.2±0.4	6.2±2.1	$0.66^{+0.82}_{-0.80}$	- - -	B
971	9^{+6}_{-5}	9^{+5}_{-3}	6	$2.13^{+1.33}_{-1.08}$	$1.21^{+0.61}_{-0.46}$	1.46	1.5±0.3	0.9±0.3	1.6±0.2	$0.50^{+0.33}_{-0.28}$	- - H	B
972	8^{+4}_{-3}	3	8^{+4}_{-3}	$1.45^{+0.75}_{-0.54}$	0.29	$1.50^{+0.77}_{-0.55}$	5.7±0.7	4.4±0.8	6.2±0.5	$1.33^{+0.71}_{-0.52}$	- S -	D
973	4^{+3}_{-2}	5^{+3}_{-2}	2	$0.82^{+0.63}_{-0.40}$	$0.53^{+0.37}_{-0.23}$	0.43	1.0±0.2	0.8±0.1	1.2±0.1	$0.13^{+0.10}_{-0.07}$	- - H	A
974	12^{+5}_{-4}	2	12^{+5}_{-4}	$2.71^{+1.19}_{-0.94}$	0.30	$2.93^{+1.22}_{-0.96}$	4.7±0.8	3.8±0.6	6.0±1.0	$2.03^{+0.96}_{-0.78}$	- S -	D
975	11^{+5}_{-4}	9^{+4}_{-3}	3^{+3}_{-2}	$2.65^{+1.13}_{-0.87}$	$1.14^{+0.54}_{-0.39}$	$0.66^{+0.81}_{-0.52}$	1.6±0.6	1.4±0.3	3.3±2.3	$0.66^{+0.38}_{-0.33}$	- - -	B
976	3^{+4}_{-3}	5^{+4}_{-2}	4	$0.59^{+1.02}_{-0.59}$	$0.64^{+0.47}_{-0.31}$	0.93	1.2±0.4	0.7±0.3	1.2±0.2	$0.11^{+0.19}_{-0.12}$	- - H	B
977	8^{+5}_{-4}	5^{+4}_{-2}	3^{+4}_{-3}	$3.43^{+1.99}_{-1.53}$	$1.13^{+0.86}_{-0.57}$	$1.46^{+1.64}_{-1.12}$	1.9±0.3	1.7±0.2	2.2±0.5	$1.07^{+0.65}_{-0.51}$	- - -	A
978	7^{+4}_{-3}	6^{+4}_{-3}	1^{+3}_{-1}	$1.59^{+1.00}_{-0.75}$	$0.80^{+0.48}_{-0.33}$	$0.18^{+0.74}_{-0.18}$	1.1±0.3	1.0±0.2	1.3±0.9	$0.28^{+0.19}_{-0.16}$	- - -	A
979	17^{+5}_{-4}	17^{+5}_{-4}	1^{+2}_{-1}	$3.35^{+1.02}_{-0.81}$	$1.87^{+0.58}_{-0.46}$	$0.12^{+0.45}_{-0.12}$	0.9±0.1	0.8±0.1	1.2±0.3	$0.48^{+0.16}_{-0.14}$	- - -	A
980	14^{+6}_{-5}	3^{+4}_{-2}	11^{+6}_{-5}	$3.33^{+1.53}_{-1.27}$	$0.35^{+0.50}_{-0.34}$	$2.77^{+1.40}_{-1.13}$	2.2±1.4	2.0±0.6	5.1±2.7	$1.17^{+0.91}_{-0.86}$	- - -	B
981	8^{+4}_{-3}	4^{+3}_{-2}	4^{+4}_{-3}	$1.99^{+1.10}_{-0.82}$	$0.50^{+0.45}_{-0.27}$	$1.12^{+0.96}_{-0.66}$	2.0±0.6	1.5±0.4	2.9±0.7	$0.65^{+0.41}_{-0.33}$	- - -	B
982	22^{+8}_{-6}	4^{+4}_{-3}	18^{+7}_{-5}	$2.50^{+0.81}_{-0.65}$	$0.58^{+0.56}_{-0.39}$	$2.00^{+0.76}_{-0.56}$	3.9±0.5	2.9±0.5	5.0±1.3	$1.55^{+0.55}_{-0.46}$	- - -	C
983	2^{+6}_{-2}	11^{+5}_{-4}	4	$0.50^{+1.28}_{-0.50}$	$1.39^{+0.61}_{-0.47}$	0.91	1.0±9.0	1.0±9.0	1.0±9.0	$0.08^{+0.75}_{-0.73}$	- - H	A
984	7^{+4}_{-3}	3	7^{+4}_{-3}	$1.24^{+0.72}_{-0.49}$	0.29	$1.28^{+0.73}_{-0.50}$	3.6±0.3	3.3±0.4	4.0±0.3	$0.71^{+0.42}_{-0.29}$	- S -	E
985	6^{+4}_{-2}	5^{+3}_{-2}	1^{+2}_{-1}	$1.05^{+0.67}_{-0.44}$	$0.54^{+0.37}_{-0.23}$	$0.13^{+0.44}_{-0.13}$	1.5±0.3	1.0±0.2	1.7±0.2	$0.25^{+0.17}_{-0.12}$	- - -	A
986	23^{+7}_{-6}	15^{+6}_{-4}	8^{+5}_{-4}	$3.11^{+0.97}_{-0.74}$	$1.77^{+0.45}_{-0.32}$	$0.88^{+0.70}_{-0.38}$	1.2±0.5	1.0±0.1	2.3±1.5	$0.61^{+0.30}_{-0.27}$	- - -	B
987	7^{+4}_{-3}	7^{+4}_{-3}	4	$1.43^{+0.94}_{-0.71}$	$0.89^{+0.48}_{-0.34}$	0.88	1.3±0.3	0.8±0.2	1.4±0.1	$0.31^{+0.21}_{-0.17}$	- - H	B
988	37^{+8}_{-7}	1^{+3}_{-1}	36^{+8}_{-7}	$10.49^{+2.36}_{-2.07}$	$0.10^{+0.47}_{-0.10}$	$10.55^{+2.35}_{-2.05}$	5.3±0.3	4.5±0.3	5.9±0.2	$8.92^{+2.08}_{-1.84}$	- - -	D
989	8^{+5}_{-3}	6^{+4}_{-2}	3^{+4}_{-2}	$2.06^{+1.14}_{-0.86}$	$0.79^{+0.51}_{-0.34}$	$0.69^{+0.92}_{-0.61}$	1.7±3.5	1.1±0.9	9.5±2.7	$0.56^{+1.19}_{-1.17}$	- - -	B
990	7^{+4}_{-3}	3	8^{+4}_{-3}	$1.50^{+0.79}_{-0.57}$	0.30	$1.56^{+0.81}_{-0.58}$	4.5±0.5	3.8±0.5	4.9±1.1	$1.08^{+0.58}_{-0.42}$	- S -	E
991	23^{+6}_{-5}	22^{+6}_{-5}	1^{+2}_{-1}	$4.16^{+1.08}_{-0.88}$	$2.34^{+0.62}_{-0.50}$	$0.14^{+0.44}_{-0.14}$	1.1±0.1	0.9±0.1	1.4±0.2	$0.72^{+0.20}_{-0.16}$	- - -	A
992	6^{+5}_{-4}	2^{+3}_{-2}	4^{+5}_{-3}	$1.65^{+1.31}_{-1.02}$	$0.36^{+0.47}_{-0.28}$	$1.03^{+1.19}_{-0.90}$	8.0±5.1	0.9±3.2	9.5±1.9	$2.13^{+2.16}_{-1.89}$	- - -	C
993	7^{+4}_{-3}	3	7^{+4}_{-3}	$1.25^{+0.71}_{-0.48}$	0.29	$1.28^{+0.72}_{-0.49}$	6.5±1.0	4.4±1.5	6.6±0.3	$1.29^{+0.76}_{-0.54}$	- S -	D
994	6^{+4}_{-3}	5^{+3}_{-2}	1^{+3}_{-1}	$1.06^{+0.72}_{-0.49}$	$0.50^{+0.37}_{-0.24}$	$0.20^{+0.52}_{-0.20}$	1.1±1.8	1.0±0.2	1.3±4.0	$0.18^{+0.32}_{-0.31}$	- - -	A
995	9^{+5}_{-4}	7^{+4}_{-3}	2^{+3}_{-2}	$2.15^{+1.12}_{-0.86}$	$0.98^{+0.53}_{-0.38}$	$0.43^{+0.83}_{-0.43}$	1.1±0.4	0.9±0.1	1.3±0.8	$0.37^{+0.23}_{-0.19}$	- - -	A
996	7^{+5}_{-4}	2^{+3}_{-2}	5^{+5}_{-4}	$2.46^{+1.93}_{-1.55}$	$0.44^{+0.66}_{-0.41}$	$1.72^{+1.77}_{-1.38}$	5.3±4.0	1.8±2.4	8.2±2.5	$2.07^{+2.25}_{-2.03}$	- - -	C

No.	C_{net} FB	C_{net} SB	C_{net} HB	$f_{\rm ph}$FB(10^{-6} cm^{-2} s^{-1})	$f_{\rm ph}$SB(10^{-6} cm^{-2} s^{-1})	$f_{\rm ph}$HB(10^{-6} cm^{-2} s^{-1})	E_{50} (keV)	E_{25} (keV)	E_{75} (keV)	f_X(10^{-14}erg cm^{-2} s^{-1})	Phot. Flag	Quantile Group
997	7^{+4}_{-3}	2^{+3}_{-1}	5^{+3}_{-2}	$1.24^{+0.71}_{-0.48}$	$0.21^{+0.29}_{-0.14}$	$0.89^{+0.65}_{-0.41}$	2.5±1.3	2.1±0.4	5.0±1.8	$0.49^{+0.38}_{-0.32}$	- - -	C
998	5^{+3}_{-2}	3	5^{+3}_{-2}	$1.53^{+1.09}_{-0.69}$	0.49	$1.58^{+1.11}_{-0.70}$	5.6±0.6	5.2±0.3	6.7±0.4	$1.38^{+0.99}_{-0.64}$	- S -	D
999	14716^{+122}_{-122}	46^{+9}_{-7}	14670^{+122}_{-122}	$1062.62^{+8.80}_{-8.80}$	$1.86^{+0.38}_{-0.30}$	$1082.41^{+8.98}_{-8.98}$	5.4±0.0	4.6±0.0	6.3±0.0	$923.27^{+7.92}_{-7.92}$	- - -	D
1000	8^{+5}_{-4}	3	9^{+5}_{-4}	$1.97^{+1.30}_{-1.04}$	0.40	$2.28^{+1.30}_{-1.03}$	3.9±2.0	3.8±0.5	7.7±3.2	$1.22^{+1.03}_{-0.91}$	- S -	C
1001	11^{+7}_{-6}	1^{+3}_{-1}	10^{+7}_{-6}	$3.51^{+2.19}_{-1.86}$	$0.22^{+0.60}_{-0.22}$	$3.17^{+2.09}_{-1.76}$	3.9±1.2	2.7±1.0	5.0±2.6	$2.21^{+1.54}_{-1.37}$	- - -	D
1002	66^{+11}_{-9}	8^{+5}_{-3}	59^{+10}_{-8}	$7.47^{+1.19}_{-1.03}$	$0.87^{+0.32}_{-0.18}$	$6.75^{+1.15}_{-0.97}$	3.9±0.3	3.0±0.3	5.3±0.4	$4.68^{+0.84}_{-0.74}$	- - -	D
1003	13^{+5}_{-4}	4^{+3}_{-2}	8^{+4}_{-3}	$2.60^{+1.06}_{-0.83}$	$0.51^{+0.40}_{-0.26}$	$1.74^{+0.94}_{-0.70}$	2.6±0.5	2.0±0.4	3.4±0.5	$1.07^{+0.48}_{-0.40}$	- - -	E
1004	73^{+11}_{-10}	70^{+10}_{-9}	10^{+6}_{-4}	$7.30^{+1.14}_{-0.97}$	$4.09^{+0.58}_{-0.47}$	$1.21^{+0.99}_{-0.66}$	0.9±0.0	0.8±0.0	0.9±0.0	$1.06^{+0.17}_{-0.15}$	- - -	A
1005	12^{+6}_{-5}	2	13^{+6}_{-5}	$2.98^{+1.42}_{-1.15}$	0.33	$3.35^{+1.46}_{-1.18}$	9.2±1.4	6.3±1.8	9.6±0.3	$4.38^{+2.20}_{-1.82}$	- S -	D
1006	5^{+5}_{-4}	5^{+4}_{-3}	6	$1.04^{+1.05}_{-0.83}$	$0.55^{+0.45}_{-0.31}$	1.25	1.4±2.4	1.1±0.5	2.1±3.7	$0.23^{+0.46}_{-0.44}$	- - H	A
1007	9^{+4}_{-3}	3^{+3}_{-2}	6^{+4}_{-2}	$1.60^{+0.76}_{-0.56}$	$0.31^{+0.32}_{-0.17}$	$1.09^{+0.68}_{-0.45}$	3.3±0.8	1.6±0.6	4.0±1.4	$0.83^{+0.45}_{-0.36}$	- - -	C
1008	14^{+5}_{-4}	13^{+5}_{-4}	1^{+3}_{-1}	$2.73^{+1.01}_{-0.80}$	$1.42^{+0.54}_{-0.41}$	$0.25^{+0.60}_{-0.25}$	1.3±0.1	1.2±0.1	1.7±0.3	$0.57^{+0.22}_{-0.18}$	- - -	A
1009	17^{+6}_{-5}	2^{+3}_{-2}	16^{+6}_{-5}	$4.47^{+1.58}_{-1.30}$	$0.25^{+0.41}_{-0.22}$	$4.11^{+1.55}_{-1.26}$	7.3±1.2	4.7±2.1	8.4±1.1	$5.23^{+2.04}_{-1.76}$	- - -	D
1010	5	1^{+3}_{-1}	4	2.19	$0.12^{+0.74}_{-0.12}$	1.66	5.2±4.8	2.9±7.1	7.6±7.1	1.84	F - H	C
1011	5^{+4}_{-2}	6^{+4}_{-2}	2	$1.15^{+0.79}_{-0.52}$	$0.73^{+0.46}_{-0.30}$	0.51	1.3±0.2	1.1±0.1	1.5±0.2	$0.23^{+0.16}_{-0.11}$	- - H	A
1012	6^{+4}_{-2}	3^{+3}_{-2}	3^{+3}_{-2}	$1.02^{+0.67}_{-0.44}$	$0.30^{+0.31}_{-0.17}$	$0.50^{+0.55}_{-0.31}$	1.8±0.8	1.1±0.4	2.7±0.7	$0.29^{+0.23}_{-0.18}$	- - -	B
1013	3^{+5}_{-3}	3^{+3}_{-2}	6	$0.64^{+1.04}_{-0.64}$	$0.43^{+0.44}_{-0.28}$	1.28	1.3±6.4	0.9±2.4	1.8±4.6	$0.13^{+0.70}_{-0.67}$	- - H	B
1014	3^{+4}_{-3}	4^{+3}_{-2}	5	$0.69^{+0.93}_{-0.69}$	$0.44^{+0.42}_{-0.27}$	1.10	1.4±0.2	1.3±0.1	1.6±0.1	$0.15^{+0.21}_{-0.16}$	- - H	A
1015	5^{+3}_{-2}	2^{+3}_{-1}	3^{+3}_{-2}	$1.03^{+0.74}_{-0.47}$	$0.25^{+0.34}_{-0.16}$	$0.62^{+0.65}_{-0.36}$	3.1±1.7	1.3±0.8	4.2±2.0	$0.51^{+0.46}_{-0.37}$	- - -	C
1016	21^{+7}_{-6}	5	21^{+7}_{-5}	$1.98^{+0.71}_{-0.53}$	0.31	$2.09^{+0.72}_{-0.53}$	6.6±1.2	4.1±0.8	9.0±0.8	$2.09^{+0.83}_{-0.67}$	- S -	C
1017	16^{+7}_{-6}	5	16^{+6}_{-5}	$4.26^{+1.79}_{-1.51}$	0.72	$4.31^{+1.72}_{-1.42}$	5.8±0.9	4.5±1.3	7.3±1.7	$3.96^{+1.77}_{-1.52}$	- S -	D
1018	24^{+6}_{-5}	2	26^{+6}_{-5}	$5.43^{+1.44}_{-1.21}$	0.29	$5.85^{+1.47}_{-1.23}$	4.3±0.3	3.7±0.4	5.8±0.6	$3.78^{+1.05}_{-0.89}$	- S -	D
1019	7^{+6}_{-5}	11^{+5}_{-3}	5	$1.40^{+1.17}_{-0.95}$	$1.28^{+0.54}_{-0.41}$	1.03	1.2±2.0	1.1±0.3	1.4±6.4	$0.27^{+0.51}_{-0.49}$	- - H	A
1020	14^{+5}_{-4}	11^{+5}_{-3}	2^{+3}_{-2}	$2.86^{+1.07}_{-0.84}$	$1.36^{+0.55}_{-0.42}$	$0.50^{+0.68}_{-0.41}$	1.0±0.2	0.8±0.1	1.6±0.6	$0.47^{+0.21}_{-0.17}$	- - -	B
1021	2^{+4}_{-2}	1^{+3}_{-1}	1^{+3}_{-1}	$1.19^{+1.79}_{-1.19}$	$0.28^{+0.75}_{-0.28}$	$0.71^{+1.62}_{-0.71}$	3.7±2.1	0.8±9.2	4.0±6.0	$0.71^{+1.14}_{-0.81}$	- - -	C
1022	25^{+7}_{-6}	3^{+4}_{-2}	22^{+7}_{-5}	$2.71^{+0.80}_{-0.63}$	$0.38^{+0.25}_{-0.12}$	$2.38^{+0.75}_{-0.58}$	4.3±0.5	3.5±0.6	5.8±0.6	$1.87^{+0.59}_{-0.49}$	- - -	D
1023	22^{+6}_{-5}	6^{+4}_{-2}	16^{+5}_{-4}	$4.31^{+1.15}_{-0.94}$	$0.65^{+0.41}_{-0.27}$	$3.25^{+1.04}_{-0.82}$	3.7±0.6	2.0±0.5	4.5±0.9	$2.56^{+0.81}_{-0.70}$	- - -	C
1024	185^{+14}_{-14}	10^{+4}_{-3}	175^{+13}_{-13}	$37.22^{+2.75}_{-2.75}$	$1.17^{+0.51}_{-0.38}$	$35.92^{+2.73}_{-2.73}$	4.1±0.2	3.1±0.1	5.3±0.2	$24.47^{+2.13}_{-2.13}$	- - -	D
1025	11^{+5}_{-3}	3	12^{+5}_{-3}	$2.16^{+0.86}_{-0.65}$	0.28	$2.23^{+0.88}_{-0.67}$	5.2±0.6	4.1±0.4	6.1±0.6	$1.79^{+0.75}_{-0.58}$	- S -	D
1026	74^{+10}_{-9}	66^{+10}_{-8}	9^{+4}_{-3}	$8.78^{+1.24}_{-1.07}$	$4.49^{+0.66}_{-0.56}$	$2.12^{+1.06}_{-0.80}$	1.0±0.1	0.9±0.0	1.4±0.2	$1.47^{+0.23}_{-0.20}$	- - -	A
1027	5^{+5}_{-4}	6^{+4}_{-3}	5	$1.13^{+0.98}_{-0.76}$	$0.71^{+0.45}_{-0.30}$	1.09	1.1±0.1	1.0±0.1	1.2±0.1	$0.20^{+0.18}_{-0.14}$	- - H	A
1028	5^{+4}_{-3}	3	5^{+4}_{-3}	$1.11^{+0.86}_{-0.63}$	0.41	$1.11^{+0.84}_{-0.60}$	4.9±0.6	4.6±0.3	5.7±0.6	$0.87^{+0.68}_{-0.50}$	- S -	E
1029	8^{+5}_{-4}	2	9^{+5}_{-4}	$1.74^{+1.00}_{-0.78}$	0.27	$1.97^{+1.02}_{-0.79}$	7.5±2.0	3.6±1.9	8.1±0.7	$2.08^{+1.32}_{-1.08}$	- S -	C
1030	5^{+5}_{-4}	6^{+4}_{-3}	5	$1.20^{+1.04}_{-0.79}$	$0.72^{+0.49}_{-0.34}$	1.16	1.7±0.3	1.4±0.2	1.8±0.1	$0.33^{+0.29}_{-0.22}$	- - H	A
1031	6^{+4}_{-3}	6^{+4}_{-2}	4	$1.21^{+0.85}_{-0.61}$	$0.69^{+0.44}_{-0.29}$	0.84	1.4±0.2	1.3±0.1	1.8±0.2	$0.27^{+0.19}_{-0.14}$	- - H	A
1032	26^{+8}_{-7}	24^{+6}_{-5}	2^{+5}_{-2}	$6.32^{+1.85}_{-1.60}$	$3.27^{+0.86}_{-0.72}$	$0.51^{+1.25}_{-0.51}$	1.4±0.1	1.1±0.1	1.6±0.2	$1.43^{+0.44}_{-0.39}$	- - -	A
1033	16^{+6}_{-5}	13^{+5}_{-4}	4^{+3}_{-2}	$1.62^{+0.69}_{-0.50}$	$1.20^{+0.34}_{-0.23}$	$0.73^{+0.69}_{-0.44}$	1.3±0.3	1.0±0.1	1.7±0.2	$0.33^{+0.16}_{-0.13}$	- - -	B
1034	5^{+4}_{-3}	2^{+3}_{-2}	3^{+4}_{-2}	$1.32^{+1.06}_{-0.78}$	$0.33^{+0.44}_{-0.25}$	$0.75^{+0.93}_{-0.61}$	2.2±3.6	1.6±1.4	6.3±3.1	$0.46^{+0.84}_{-0.81}$	- - -	B

No.	C_{net} FB	C_{net} SB	C_{net} HB	$f_{\rm ph}$FB(10^{-6} cm^{-2} s^{-1})	$f_{\rm ph}$SB(10^{-6} cm^{-2} s^{-1})	$f_{\rm ph}$HB(10^{-6} cm^{-2} s^{-1})	E_{50} (keV)	E_{25} (keV)	E_{75} (keV)	f_X(10^{-14}erg cm^{-2} s^{-1})	Phot. Flag	Quantile Group
1035	17^{+5}_{-4}	14^{+5}_{-4}	4^{+3}_{-2}	$3.27^{+1.01}_{-0.80}$	$1.49^{+0.53}_{-0.41}$	$0.68^{+0.62}_{-0.37}$	1.2±0.2	1.0±0.1	1.8±0.6	$0.64^{+0.22}_{-0.19}$	- - -	B
1036	6^{+4}_{-3}	4^{+3}_{-2}	2^{+3}_{-2}	$1.19^{+0.90}_{-0.66}$	$0.48^{+0.40}_{-0.26}$	$0.35^{+0.73}_{-0.35}$	1.7±1.3	1.3±0.2	2.0±2.9	$0.32^{+0.35}_{-0.31}$	- - -	A
1037	2^{+3}_{-2}	3^{+3}_{-2}	3	$0.52^{+0.78}_{-0.49}$	$0.45^{+0.41}_{-0.25}$	0.69	0.7±0.5	0.5±9.5	1.3±8.7	$0.06^{+0.09}_{-0.07}$	- - H	B
1038	14^{+6}_{-5}	1^{+3}_{-1}	13^{+5}_{-4}	$2.96^{+1.23}_{-1.00}$	$0.13^{+0.36}_{-0.13}$	$2.79^{+1.18}_{-0.94}$	8.0±1.9	2.4±2.3	8.6±0.6	$3.79^{+1.82}_{-1.57}$	- - -	C
1039	31^{+7}_{-6}	1^{+2}_{-1}	30^{+7}_{-5}	$7.07^{+1.54}_{-1.29}$	$0.12^{+0.31}_{-0.11}$	$7.00^{+1.55}_{-1.29}$	4.5±0.3	3.7±0.3	6.1±0.6	$5.05^{+1.14}_{-0.97}$	- - -	D
1040	5^{+3}_{-2}	4^{+3}_{-2}	1^{+2}_{-1}	$0.88^{+0.66}_{-0.42}$	$0.44^{+0.36}_{-0.21}$	$0.12^{+0.46}_{-0.12}$	1.0±1.4	0.8±0.4	1.4±2.2	$0.15^{+0.23}_{-0.21}$	- - -	B
1041	5^{+4}_{-3}	5^{+3}_{-2}	4	$1.06^{+0.81}_{-0.55}$	$0.56^{+0.41}_{-0.26}$	0.93	1.0±0.6	0.7±0.2	1.2±0.8	$0.18^{+0.17}_{-0.14}$	- - H	B
1042	10^{+4}_{-3}	10^{+4}_{-3}	3	$1.94^{+0.87}_{-0.65}$	$1.11^{+0.49}_{-0.36}$	0.70	1.0±0.2	1.0±0.0	1.3±1.3	$0.33^{+0.16}_{-0.12}$	- - H	A
1043	8^{+4}_{-3}	4	7^{+4}_{-3}	$1.48^{+0.85}_{-0.64}$	0.40	$1.46^{+0.84}_{-0.62}$	6.4±2.5	3.2±1.5	9.3±1.3	$1.52^{+1.06}_{-0.89}$	- S -	C
1044	51^{+9}_{-8}	43^{+8}_{-7}	8^{+6}_{-4}	$5.48^{+1.03}_{-0.86}$	$3.39^{+0.53}_{-0.43}$	$0.61^{+0.58}_{-0.31}$	1.0±0.1	0.8±0.0	1.5±0.5	$0.85^{+0.19}_{-0.16}$	- - -	A
1045	145^{+14}_{-12}	65^{+10}_{-8}	80^{+11}_{-9}	$15.52^{+1.49}_{-1.33}$	$3.95^{+0.59}_{-0.50}$	$8.79^{+1.20}_{-1.03}$	2.2±0.1	1.7±0.1	3.4±0.2	$5.38^{+0.62}_{-0.58}$	- - -	B
1046	6^{+5}_{-4}	8^{+4}_{-3}	4	$1.28^{+1.01}_{-0.77}$	$0.95^{+0.52}_{-0.38}$	0.84	1.2±0.3	0.9±0.2	1.5±0.3	$0.25^{+0.21}_{-0.17}$	- - H	A
1047	4^{+3}_{-2}	4^{+3}_{-2}	4	$0.78^{+0.67}_{-0.42}$	$0.43^{+0.36}_{-0.22}$	0.71	1.1±0.3	0.9±0.1	1.4±0.3	$0.13^{+0.12}_{-0.08}$	- - H	A
1048	12^{+5}_{-4}	6^{+4}_{-3}	6^{+5}_{-4}	$2.99^{+1.36}_{-1.10}$	$0.78^{+0.53}_{-0.36}$	$1.64^{+1.17}_{-0.89}$	2.2±0.9	1.3±0.4	3.4±0.9	$1.03^{+0.65}_{-0.59}$	- - -	B
1049	9^{+4}_{-3}	8^{+4}_{-3}	2^{+3}_{-1}	$1.90^{+0.87}_{-0.64}$	$0.91^{+0.46}_{-0.33}$	$0.32^{+0.55}_{-0.27}$	1.3±0.3	1.0±0.2	1.8±0.7	$0.38^{+0.20}_{-0.17}$	- - -	A
1050	5^{+4}_{-2}	6^{+4}_{-2}	2	$1.07^{+0.70}_{-0.46}$	$0.66^{+0.40}_{-0.27}$	0.46	0.9±0.1	0.9±0.1	1.0±0.1	$0.16^{+0.11}_{-0.07}$	- - H	A
1051	8^{+4}_{-3}	7^{+4}_{-3}	2^{+3}_{-1}	$1.91^{+0.93}_{-0.68}$	$0.90^{+0.49}_{-0.34}$	$0.37^{+0.61}_{-0.30}$	1.3±0.3	1.1±0.1	1.7±1.0	$0.40^{+0.22}_{-0.18}$	- - -	A
1052	6^{+4}_{-3}	3	6^{+4}_{-3}	$1.29^{+0.85}_{-0.58}$	0.33	$1.36^{+0.87}_{-0.59}$	6.0±1.1	4.2±0.7	6.6±0.9	$1.24^{+0.85}_{-0.60}$	- S -	D
1053	26^{+8}_{-7}	11^{+5}_{-4}	15^{+7}_{-6}	$2.34^{+0.77}_{-0.59}$	$1.09^{+0.30}_{-0.19}$	$1.43^{+0.67}_{-0.48}$	2.5±0.5	1.9±0.2	4.2±0.7	$0.94^{+0.37}_{-0.31}$	- - -	C
1054	7^{+4}_{-3}	2^{+3}_{-1}	5^{+4}_{-2}	$1.41^{+0.78}_{-0.56}$	$0.20^{+0.30}_{-0.15}$	$1.07^{+0.72}_{-0.48}$	3.9±1.0	2.0±0.8	4.6±0.5	$0.88^{+0.54}_{-0.42}$	- - -	C
1055	4^{+3}_{-2}	5^{+3}_{-2}	2	$0.89^{+0.72}_{-0.46}$	$0.59^{+0.42}_{-0.27}$	0.50	1.2±0.1	1.1±0.0	1.3±0.1	$0.17^{+0.14}_{-0.09}$	- - H	A
1056	8^{+4}_{-3}	1^{+2}_{-1}	7^{+4}_{-3}	$1.59^{+0.85}_{-0.63}$	$0.07^{+0.27}_{-0.07}$	$1.49^{+0.84}_{-0.61}$	2.9±0.3	2.5±0.6	3.1±0.5	$0.73^{+0.40}_{-0.30}$	- - -	E
1057	6^{+4}_{-3}	7^{+4}_{-3}	3	$1.16^{+0.84}_{-0.62}$	$0.80^{+0.46}_{-0.33}$	0.62	1.3±0.4	0.7±0.3	1.6±0.2	$0.24^{+0.19}_{-0.15}$	- - H	B
1058	11^{+5}_{-4}	2	12^{+5}_{-4}	$2.31^{+1.14}_{-0.90}$	0.28	$2.70^{+1.16}_{-0.92}$	4.6±0.5	3.9±0.4	5.2±0.7	$1.69^{+0.85}_{-0.69}$	- S -	E
1059	199^{+15}_{-14}	192^{+15}_{-14}	7^{+5}_{-3}	$19.99^{+1.51}_{-1.44}$	$12.19^{+0.84}_{-0.80}$	$0.69^{+0.54}_{-0.30}$	0.9±0.0	0.8±0.0	1.2±0.0	$3.02^{+0.24}_{-0.23}$	- - -	A
1060	20^{+7}_{-5}	6^{+4}_{-3}	13^{+6}_{-4}	$2.23^{+0.75}_{-0.57}$	$0.78^{+0.48}_{-0.33}$	$1.35^{+0.65}_{-0.45}$	1.9±0.2	1.8±0.2	2.4±0.4	$0.68^{+0.24}_{-0.19}$	- - -	A
1061	24^{+8}_{-7}	9^{+5}_{-4}	15^{+7}_{-6}	$2.26^{+0.84}_{-0.64}$	$0.81^{+0.35}_{-0.23}$	$1.14^{+0.70}_{-0.46}$	1.9±0.4	1.5±0.3	2.8±0.5	$0.69^{+0.30}_{-0.25}$	- - -	B
1062	12^{+5}_{-4}	4^{+3}_{-2}	7^{+4}_{-3}	$2.35^{+0.96}_{-0.74}$	$0.50^{+0.38}_{-0.24}$	$1.51^{+0.83}_{-0.61}$	2.8±0.7	1.7±0.4	3.7±0.6	$1.05^{+0.51}_{-0.43}$	- - -	C
1063	6^{+4}_{-3}	1^{+3}_{-1}	5^{+4}_{-2}	$1.24^{+0.80}_{-0.57}$	$0.15^{+0.31}_{-0.15}$	$1.01^{+0.74}_{-0.49}$	3.2±1.5	2.5±1.0	4.8±2.4	$0.63^{+0.51}_{-0.42}$	- - -	D
1064	17^{+5}_{-4}	6^{+4}_{-2}	11^{+5}_{-3}	$3.64^{+1.15}_{-0.91}$	$0.71^{+0.44}_{-0.29}$	$2.45^{+1.00}_{-0.76}$	3.2±0.8	1.8±0.4	4.6±1.4	$1.84^{+0.73}_{-0.64}$	- - -	C
1065	6^{+4}_{-3}	7^{+4}_{-3}	2	$1.19^{+0.72}_{-0.49}$	$0.76^{+0.42}_{-0.29}$	0.45	1.1±0.1	1.0±0.1	1.3±0.2	$0.22^{+0.13}_{-0.09}$	- - H	A
1066	5^{+4}_{-3}	2	6^{+4}_{-3}	$1.10^{+0.76}_{-0.52}$	0.26	$1.20^{+0.77}_{-0.53}$	5.7±1.0	4.5±0.8	5.9±1.0	$0.99^{+0.71}_{-0.50}$	- S -	D
1067	5^{+6}_{-5}	1^{+4}_{-1}	3^{+6}_{-3}	$0.93^{+1.28}_{-0.93}$	$0.16^{+0.45}_{-0.16}$	$0.65^{+1.15}_{-0.65}$	3.9±4.7	1.3±3.0	6.5±3.1	$0.58^{+1.06}_{-0.90}$	- - -	C
1068	6^{+5}_{-4}	6^{+4}_{-3}	5	$1.28^{+1.06}_{-0.83}$	$0.78^{+0.49}_{-0.35}$	1.16	1.1±0.2	1.1±0.2	1.3±0.3	$0.23^{+0.20}_{-0.16}$	- - H	A
1069	9^{+5}_{-4}	5^{+4}_{-2}	4^{+4}_{-3}	$1.78^{+0.93}_{-0.72}$	$0.60^{+0.41}_{-0.27}$	$0.75^{+0.77}_{-0.52}$	1.9±1.7	1.1±0.6	4.8±2.3	$0.54^{+0.56}_{-0.53}$	- - -	B
1070	71^{+12}_{-10}	54^{+10}_{-8}	17^{+8}_{-5}	$5.55^{+0.97}_{-0.83}$	$2.42^{+0.44}_{-0.35}$	$1.31^{+0.71}_{-0.41}$	1.6±0.1	1.2±0.1	1.9±0.3	$1.38^{+0.26}_{-0.23}$	- - -	A
1071	17^{+7}_{-6}	8^{+5}_{-4}	8^{+6}_{-5}	$3.27^{+1.44}_{-1.22}$	$0.96^{+0.57}_{-0.44}$	$1.64^{+1.19}_{-0.98}$	1.7±1.6	1.0±0.4	6.0±2.8	$0.92^{+0.91}_{-0.89}$	- - -	B
1072	11^{+5}_{-4}	2^{+3}_{-2}	8^{+5}_{-4}	$2.27^{+1.13}_{-0.89}$	$0.26^{+0.39}_{-0.24}$	$1.84^{+1.04}_{-0.80}$	2.6±0.8	2.1±0.8	3.8±0.8	$0.96^{+0.55}_{-0.47}$	- - -	E

No.	C_{net} FB	C_{net} SB	C_{net} HB	$f_{\rm ph}$FB(10^{-6} cm^{-2} s^{-1})	$f_{\rm ph}$SB(10^{-6} cm^{-2} s^{-1})	$f_{\rm ph}$HB(10^{-6} cm^{-2} s^{-1})	E_{50} (keV)	E_{25} (keV)	E_{75} (keV)	f_X(10^{-14}erg cm^{-2} s^{-1})	Phot. Flag	Quantile Group
1073	53^{+9}_{-8}	41^{+8}_{-6}	13^{+6}_{-4}	$6.24^{+1.08}_{-0.90}$	$3.49^{+0.53}_{-0.43}$	$1.42^{+0.68}_{-0.38}$	1.3±0.1	1.0±0.1	1.7±0.2	$1.26^{+0.24}_{-0.20}$	- - -	B
1074	21^{+7}_{-6}	14^{+5}_{-4}	7^{+6}_{-4}	$4.98^{+1.72}_{-1.47}$	$1.84^{+0.71}_{-0.56}$	$1.73^{+1.36}_{-1.10}$	1.9±0.3	1.5±0.2	2.1±1.6	$1.48^{+0.56}_{-0.50}$	- - -	A
1075	27^{+7}_{-6}	5	28^{+7}_{-6}	$3.05^{+0.84}_{-0.66}$	0.30	$3.19^{+0.85}_{-0.66}$	5.0±0.3	4.2±0.2	5.8±0.4	$2.44^{+0.68}_{-0.55}$	- S -	E
1076	10^{+5}_{-3}	3^{+3}_{-2}	7^{+4}_{-3}	$2.04^{+0.93}_{-0.71}$	$0.30^{+0.34}_{-0.19}$	$1.56^{+0.86}_{-0.63}$	2.9±1.0	2.0±0.5	4.4±2.0	$0.94^{+0.55}_{-0.47}$	- - -	C
1077	15^{+5}_{-4}	3	15^{+5}_{-4}	$4.01^{+1.33}_{-1.04}$	0.39	$4.13^{+1.36}_{-1.07}$	4.7±0.3	4.2±0.6	5.5±0.6	$3.00^{+1.02}_{-0.81}$	- S -	E
1078	7^{+5}_{-4}	6^{+4}_{-3}	1^{+4}_{-1}	$1.78^{+1.18}_{-0.92}$	$0.88^{+0.54}_{-0.39}$	$0.23^{+0.90}_{-0.23}$	1.3±1.6	1.1±0.2	1.4±5.2	$0.36^{+0.53}_{-0.50}$	- - -	A
1079	4^{+3}_{-2}	5^{+3}_{-2}	2	$0.77^{+0.67}_{-0.43}$	$0.54^{+0.39}_{-0.24}$	0.46	1.3±0.2	1.0±0.1	1.5±0.1	$0.16^{+0.14}_{-0.09}$	- - H	A
1080	6^{+4}_{-3}	2	6^{+4}_{-3}	$1.23^{+0.78}_{-0.53}$	0.29	$1.32^{+0.79}_{-0.54}$	3.5±1.3	3.2±0.5	4.7±2.4	$0.69^{+0.51}_{-0.40}$	- S -	E
1081	7^{+4}_{-3}	2^{+3}_{-2}	5^{+4}_{-3}	$1.64^{+0.97}_{-0.72}$	$0.28^{+0.38}_{-0.21}$	$1.17^{+0.88}_{-0.60}$	3.8±0.9	2.0±0.8	4.2±0.5	$1.01^{+0.65}_{-0.51}$	- - -	C
1082	5^{+4}_{-3}	2^{+3}_{-2}	3^{+3}_{-2}	$1.18^{+0.90}_{-0.64}$	$0.30^{+0.38}_{-0.21}$	$0.66^{+0.79}_{-0.50}$	2.9±1.3	1.9±0.9	4.5±1.3	$0.55^{+0.49}_{-0.39}$	- - -	C
1083	20^{+7}_{-6}	19^{+6}_{-5}	1^{+5}_{-1}	$4.77^{+1.73}_{-1.48}$	$2.51^{+0.80}_{-0.65}$	$0.32^{+1.21}_{-0.32}$	1.5±0.2	1.0±0.2	1.8±1.1	$1.17^{+0.46}_{-0.40}$	- - -	A
1084	2^{+5}_{-2}	1^{+3}_{-1}	1^{+4}_{-1}	$0.42^{+1.05}_{-0.42}$	$0.07^{+0.37}_{-0.07}$	$0.31^{+0.98}_{-0.31}$	5.2±4.8	4.6±3.0	7.6±2.6	$0.36^{+0.94}_{-0.48}$	- - -	D
1085	7^{+4}_{-3}	6^{+4}_{-3}	1^{+3}_{-1}	$1.45^{+0.84}_{-0.61}$	$0.75^{+0.44}_{-0.30}$	$0.14^{+0.55}_{-0.14}$	1.0±0.2	0.9±0.1	1.1±0.6	$0.24^{+0.14}_{-0.11}$	- - -	A
1086	8^{+4}_{-3}	7^{+4}_{-3}	1^{+3}_{-1}	$1.85^{+0.94}_{-0.68}$	$0.89^{+0.49}_{-0.34}$	$0.30^{+0.62}_{-0.30}$	1.4±0.7	0.8±0.3	1.9±1.8	$0.43^{+0.29}_{-0.25}$	- - -	B
1087	9^{+4}_{-3}	2^{+3}_{-2}	6^{+4}_{-3}	$2.00^{+1.03}_{-0.77}$	$0.32^{+0.39}_{-0.22}$	$1.47^{+0.94}_{-0.67}$	3.4±0.9	2.1±0.7	4.3±1.4	$1.11^{+0.64}_{-0.52}$	- - -	C
1088	10^{+5}_{-3}	2^{+3}_{-1}	9^{+4}_{-3}	$2.32^{+1.03}_{-0.78}$	$0.22^{+0.34}_{-0.17}$	$1.98^{+0.99}_{-0.73}$	2.7±0.5	2.2±0.5	3.5±0.6	$1.00^{+0.48}_{-0.38}$	- - -	E
1089	56^{+9}_{-8}	2^{+4}_{-1}	54^{+9}_{-8}	$5.94^{+0.99}_{-0.83}$	$0.56^{+0.21}_{-0.08}$	$5.81^{+0.99}_{-0.82}$	4.6±0.3	3.7±0.2	5.6±0.2	$4.36^{+0.79}_{-0.68}$	- - -	D
1090	27^{+7}_{-6}	3^{+4}_{-2}	24^{+7}_{-5}	$3.92^{+1.06}_{-0.82}$	$0.68^{+0.32}_{-0.14}$	$3.57^{+1.03}_{-0.77}$	5.2±0.4	4.4±0.7	5.9±0.3	$3.24^{+0.91}_{-0.71}$	- - -	D
1091	11^{+5}_{-3}	3^{+3}_{-2}	8^{+4}_{-3}	$2.15^{+0.87}_{-0.66}$	$0.31^{+0.33}_{-0.18}$	$1.64^{+0.80}_{-0.58}$	2.6±0.6	2.0±0.3	3.8±0.7	$0.89^{+0.42}_{-0.35}$	- - -	E
1092	13^{+6}_{-4}	13^{+5}_{-4}	2^{+3}_{-2}	$1.35^{+0.63}_{-0.46}$	$1.24^{+0.33}_{-0.23}$	$0.34^{+0.78}_{-0.34}$	1.4±0.1	1.2±0.1	1.5±0.1	$0.30^{+0.14}_{-0.11}$	- - -	A
1093	6^{+4}_{-2}	5^{+3}_{-2}	1^{+2}_{-1}	$1.09^{+0.70}_{-0.46}$	$0.55^{+0.38}_{-0.24}$	$0.13^{+0.46}_{-0.13}$	1.3±0.3	0.9±0.2	1.6±0.4	$0.23^{+0.15}_{-0.11}$	- - -	A
1094	6^{+4}_{-3}	3	6^{+4}_{-3}	$1.23^{+0.83}_{-0.56}$	0.31	$1.30^{+0.84}_{-0.57}$	3.7±0.9	3.5±0.3	5.4±1.0	$0.73^{+0.52}_{-0.37}$	- S -	E
1095	11^{+5}_{-4}	5^{+4}_{-2}	6^{+4}_{-3}	$2.36^{+1.10}_{-0.86}$	$0.59^{+0.44}_{-0.29}$	$1.34^{+0.94}_{-0.70}$	4.3±2.8	1.6±1.2	9.4±1.9	$1.61^{+1.29}_{-1.20}$	- - -	C
1096	6^{+4}_{-3}	2^{+3}_{-1}	5^{+4}_{-3}	$1.32^{+0.90}_{-0.66}$	$0.19^{+0.33}_{-0.16}$	$1.01^{+0.85}_{-0.58}$	5.1±1.9	3.1±1.5	6.3±2.1	$1.08^{+0.84}_{-0.67}$	- - -	C
1097	8^{+4}_{-3}	4	8^{+4}_{-3}	$2.73^{+1.43}_{-1.06}$	0.74	$2.62^{+1.41}_{-1.03}$	3.6±1.4	3.2±0.9	6.7±1.3	$1.56^{+1.01}_{-0.85}$	- S -	C
1098	5^{+4}_{-2}	5^{+3}_{-2}	1^{+2}_{-1}	$1.10^{+0.73}_{-0.48}$	$0.57^{+0.40}_{-0.25}$	$0.12^{+0.48}_{-0.12}$	1.1±0.5	1.1±0.1	1.3±0.7	$0.19^{+0.15}_{-0.12}$	- - -	A
1099	10^{+6}_{-5}	5^{+4}_{-3}	5^{+5}_{-4}	$3.77^{+2.23}_{-1.82}$	$1.02^{+0.83}_{-0.57}$	$2.00^{+1.96}_{-1.53}$	2.2±0.5	1.6±0.5	2.8±0.7	$1.34^{+0.85}_{-0.72}$	- - -	A
1100	10^{+5}_{-4}	4	10^{+5}_{-4}	$2.09^{+0.98}_{-0.76}$	0.41	$2.10^{+0.97}_{-0.74}$	6.2±1.2	4.1±1.3	7.4±1.4	$2.07^{+1.05}_{-0.85}$	- S -	D
1101	4^{+3}_{-2}	2^{+3}_{-1}	3^{+3}_{-2}	$1.01^{+0.78}_{-0.49}$	$0.25^{+0.35}_{-0.17}$	$0.59^{+0.68}_{-0.38}$	2.4±1.0	1.2±0.6	3.7±0.6	$0.39^{+0.34}_{-0.25}$	- - -	C
1102	8^{+4}_{-3}	3^{+3}_{-2}	6^{+4}_{-3}	$1.61^{+0.81}_{-0.60}$	$0.29^{+0.32}_{-0.18}$	$1.12^{+0.73}_{-0.50}$	2.5±0.5	1.9±0.5	3.4±0.7	$0.65^{+0.35}_{-0.27}$	- - -	E
1103	13^{+5}_{-4}	14^{+5}_{-4}	3	$2.98^{+1.10}_{-0.86}$	$1.73^{+0.62}_{-0.48}$	0.72	1.3±0.1	1.2±0.1	1.5±0.1	$0.64^{+0.24}_{-0.19}$	- - H	A
1104	7^{+5}_{-4}	2	9^{+5}_{-4}	$1.56^{+1.04}_{-0.80}$	0.28	$1.96^{+1.06}_{-0.82}$	4.7±0.8	3.5±0.6	5.0±0.5	$1.17^{+0.81}_{-0.63}$	- S -	D
1105	8^{+4}_{-3}	6^{+4}_{-2}	3^{+3}_{-2}	$1.61^{+0.79}_{-0.58}$	$0.65^{+0.40}_{-0.26}$	$0.50^{+0.57}_{-0.32}$	1.8±0.5	0.9±0.3	2.0±0.7	$0.45^{+0.26}_{-0.21}$	- - -	B
1106	14^{+5}_{-4}	11^{+5}_{-3}	3^{+4}_{-2}	$2.92^{+1.14}_{-0.90}$	$1.31^{+0.56}_{-0.42}$	$0.64^{+0.78}_{-0.52}$	1.0±0.4	0.9±0.1	1.9±2.0	$0.48^{+0.26}_{-0.24}$	- - -	B
1107	10^{+5}_{-4}	11^{+5}_{-3}	3	$2.28^{+1.13}_{-0.88}$	$1.47^{+0.61}_{-0.46}$	0.82	1.0±0.2	0.8±0.1	1.3±0.2	$0.36^{+0.19}_{-0.15}$	- - H	A
1108	11^{+5}_{-4}	3	12^{+5}_{-4}	$2.64^{+1.28}_{-1.01}$	0.41	$2.93^{+1.27}_{-1.00}$	6.5±1.1	5.7±1.4	8.6±1.3	$2.74^{+1.40}_{-1.15}$	- S -	D
1109	19^{+6}_{-4}	1^{+2}_{-1}	18^{+5}_{-4}	$4.62^{+1.37}_{-1.11}$	$0.10^{+0.33}_{-0.10}$	$4.55^{+1.37}_{-1.10}$	4.9±0.4	3.9±0.5	5.5±0.3	$3.60^{+1.10}_{-0.90}$	- - -	D
1110	17^{+6}_{-5}	11^{+5}_{-4}	6^{+4}_{-3}	$3.65^{+1.29}_{-1.06}$	$1.30^{+0.57}_{-0.44}$	$1.36^{+0.98}_{-0.74}$	1.6±0.3	1.1±0.2	2.2±1.4	$0.96^{+0.38}_{-0.32}$	- - -	B

No.	C_{net} FB	C_{net} SB	C_{net} HB	$f_{\rm ph}$FB(10^{-6} cm^{-2} s^{-1})	$f_{\rm ph}$SB(10^{-6} cm^{-2} s^{-1})	$f_{\rm ph}$HB(10^{-6} cm^{-2} s^{-1})	E_{50} (keV)	E_{25} (keV)	E_{75} (keV)	f_X(10^{-14}erg cm^{-2} s^{-1})	Phot. Flag	Quantile Group
1111	8^{+6}_{-5}	1^{+3}_{-1}	8^{+6}_{-5}	$2.64^{+2.03}_{-1.69}$	$0.11^{+0.54}_{-0.11}$	$2.49^{+1.98}_{-1.62}$	5.4±3.8	2.3±2.7	8.4±2.1	$2.28^{+2.38}_{-2.18}$	- - -	C
1112	2^{+7}_{-2}	10^{+5}_{-4}	6	$0.39^{+1.47}_{-0.39}$	$1.16^{+0.62}_{-0.48}$	1.29	0.8±9.2	0.7±9.3	8.2±7.7	$0.05^{+0.61}_{-0.58}$	- - H	B
1113	6^{+9}_{-6}	7^{+5}_{-4}	15	$1.44^{+2.01}_{-1.44}$	$0.92^{+0.71}_{-0.56}$	3.44	1.2±0.5	1.2±0.8	1.4±0.2	$0.28^{+0.41}_{-0.30}$	- - H	A
1114	9^{+6}_{-4}	3^{+3}_{-2}	6^{+5}_{-4}	$2.22^{+1.31}_{-1.06}$	$0.38^{+0.46}_{-0.29}$	$1.57^{+1.19}_{-0.93}$	3.9±1.4	1.8±0.8	4.9±1.5	$1.38^{+0.95}_{-0.82}$	- - -	C
1115	14^{+5}_{-4}	4^{+3}_{-2}	10^{+5}_{-4}	$3.24^{+1.23}_{-0.98}$	$0.51^{+0.43}_{-0.28}$	$2.39^{+1.11}_{-0.86}$	3.3±0.6	1.8±0.7	4.2±0.6	$1.69^{+0.70}_{-0.59}$	- - -	C
1116	21^{+9}_{-8}	9^{+6}_{-4}	12^{+8}_{-6}	$2.56^{+1.08}_{-0.90}$	$1.03^{+0.40}_{-0.26}$	$1.39^{+0.94}_{-0.75}$	4.2±1.5	1.7±1.0	5.9±0.8	$1.74^{+0.95}_{-0.86}$	- - -	C
1117	3^{+4}_{-3}	6^{+4}_{-2}	3	$0.58^{+0.84}_{-0.58}$	$0.67^{+0.43}_{-0.28}$	0.67	1.0±0.3	0.8±0.2	1.1±0.1	$0.09^{+0.14}_{-0.10}$	- - H	A
1118	10^{+5}_{-3}	5^{+4}_{-2}	4^{+4}_{-2}	$2.14^{+1.01}_{-0.76}$	$0.69^{+0.45}_{-0.30}$	$0.95^{+0.81}_{-0.54}$	1.5±1.0	1.1±0.3	4.1±1.3	$0.51^{+0.41}_{-0.38}$	- - -	B
1119	6^{+4}_{-3}	5^{+4}_{-2}	1^{+3}_{-1}	$1.36^{+0.87}_{-0.63}$	$0.65^{+0.43}_{-0.28}$	$0.22^{+0.63}_{-0.22}$	1.3±0.5	1.1±0.1	1.5±0.9	$0.29^{+0.21}_{-0.17}$	- - -	A
1120	64^{+17}_{-17}	14^{+9}_{-8}	26^{+14}_{-14}	$15.61^{+4.02}_{-4.02}$	$1.90^{+1.19}_{-1.06}$	$6.56^{+3.42}_{-3.42}$	2.8±0.7	1.7±0.3	4.3±0.5	$6.98^{+2.46}_{-2.46}$	- - -	C
1121	6^{+5}_{-4}	6^{+4}_{-3}	6	$1.61^{+1.43}_{-1.12}$	$0.89^{+0.61}_{-0.41}$	1.77	1.0±0.4	0.7±0.2	1.1±0.5	$0.26^{+0.25}_{-0.21}$	- - H	B
1122	43^{+10}_{-8}	16^{+6}_{-4}	30^{+9}_{-7}	$3.37^{+0.84}_{-0.67}$	$1.66^{+0.47}_{-0.34}$	$2.65^{+0.77}_{-0.60}$	2.6±0.3	1.9±0.1	3.8±0.3	$1.41^{+0.40}_{-0.34}$	- - -	C
1123	7^{+4}_{-3}	3^{+3}_{-2}	4^{+4}_{-2}	$1.53^{+0.86}_{-0.62}$	$0.35^{+0.35}_{-0.19}$	$0.95^{+0.76}_{-0.50}$	2.2±0.3	1.6±0.4	2.5±0.5	$0.53^{+0.31}_{-0.23}$	- - -	A
1124	15^{+6}_{-5}	2^{+3}_{-2}	13^{+6}_{-5}	$3.65^{+1.45}_{-1.19}$	$0.27^{+0.44}_{-0.26}$	$3.24^{+1.38}_{-1.11}$	3.3±0.6	2.8±0.6	4.8±1.2	$1.91^{+0.84}_{-0.72}$	- - -	E
1125	17^{+8}_{-6}	13^{+6}_{-4}	4^{+5}_{-4}	$1.82^{+0.87}_{-0.69}$	$1.19^{+0.36}_{-0.26}$	$0.95^{+1.14}_{-0.90}$	1.3±0.5	1.0±0.2	1.8±2.3	$0.38^{+0.24}_{-0.21}$	- - -	B
1126	11^{+5}_{-4}	4^{+4}_{-2}	7^{+4}_{-3}	$2.58^{+1.21}_{-0.96}$	$0.58^{+0.47}_{-0.31}$	$1.59^{+1.05}_{-0.79}$	4.2±2.0	1.8±1.1	6.0±1.3	$1.75^{+1.17}_{-1.06}$	- - -	C
1127	7^{+4}_{-3}	6^{+4}_{-2}	1^{+2}_{-1}	$2.38^{+1.33}_{-0.91}$	$1.22^{+0.74}_{-0.49}$	$0.29^{+0.83}_{-0.29}$	1.4±0.3	1.0±0.2	1.6±0.8	$0.55^{+0.33}_{-0.24}$	- - -	A
1128	177^{+13}_{-13}	65^{+9}_{-8}	112^{+11}_{-11}	$32.28^{+2.43}_{-2.43}$	$6.90^{+0.97}_{-0.86}$	$20.83^{+1.97}_{-1.97}$	2.5±0.1	1.8±0.1	3.7±0.2	$13.04^{+1.13}_{-1.13}$	- - -	C
1129	35^{+10}_{-8}	19^{+7}_{-5}	16^{+8}_{-6}	$2.59^{+0.71}_{-0.57}$	$1.08^{+0.29}_{-0.20}$	$1.19^{+0.60}_{-0.45}$	2.1±0.3	1.3±0.2	2.5±0.8	$0.86^{+0.26}_{-0.22}$	- - -	B
1130	20^{+7}_{-6}	5^{+4}_{-3}	16^{+6}_{-5}	$6.34^{+2.06}_{-1.73}$	$0.86^{+0.70}_{-0.50}$	$4.91^{+1.85}_{-1.51}$	2.9±0.9	2.1±0.5	4.9±1.0	$2.98^{+1.35}_{-1.24}$	- - -	C
1131	14^{+6}_{-5}	12^{+5}_{-4}	7^{+3}_{-2}	$1.51^{+0.67}_{-0.50}$	$1.12^{+0.32}_{-0.22}$	$0.50^{+0.72}_{-0.46}$	1.5±0.2	1.1±0.2	1.6±0.2	$0.35^{+0.16}_{-0.13}$	- - -	A
1132	5^{+3}_{-2}	1^{+2}_{-1}	4^{+3}_{-2}	$0.96^{+0.72}_{-0.46}$	$0.11^{+0.29}_{-0.10}$	$0.79^{+0.69}_{-0.41}$	2.5±0.3	2.3±0.2	2.9±0.3	$0.38^{+0.29}_{-0.19}$	- - -	E
1133	10^{+5}_{-4}	5^{+4}_{-3}	5^{+4}_{-3}	$2.35^{+1.27}_{-1.02}$	$0.67^{+0.51}_{-0.35}$	$1.17^{+1.08}_{-0.82}$	6.5±3.8	1.1±1.4	7.7±1.9	$2.45^{+1.96}_{-1.79}$	- - -	C
1134	6^{+4}_{-3}	7^{+4}_{-3}	3	$1.37^{+0.86}_{-0.62}$	$0.82^{+0.47}_{-0.32}$	0.69	0.9±0.1	0.9±0.1	1.1±0.1	$0.20^{+0.13}_{-0.09}$	- - H	A
1135	24^{+6}_{-5}	19^{+5}_{-4}	5^{+3}_{-2}	$9.42^{+2.37}_{-1.94}$	$4.38^{+1.26}_{-1.01}$	$1.95^{+1.37}_{-0.87}$	1.1±0.1	1.0±0.1	1.8±0.6	$1.62^{+0.45}_{-0.38}$	- - -	B
1136	8^{+4}_{-3}	2	8^{+4}_{-3}	$1.56^{+0.85}_{-0.62}$	0.29	$1.65^{+0.87}_{-0.63}$	3.8±1.0	2.4±0.6	5.2±0.6	$0.96^{+0.58}_{-0.45}$	- S -	C
1137	14^{+5}_{-4}	3	14^{+5}_{-4}	$6.18^{+2.16}_{-1.67}$	0.69	$6.32^{+2.21}_{-1.71}$	4.4±0.7	3.4±0.4	6.4±0.7	$4.40^{+1.71}_{-1.40}$	- S -	D
1138	7	4	6	2.24	0.78	1.97	5.2±4.8	2.9±7.1	7.6±7.1	1.88	F S H	C
1139	15^{+6}_{-5}	20^{+6}_{-5}	7	$1.66^{+0.68}_{-0.51}$	$1.74^{+0.38}_{-0.28}$	0.66	1.2±0.1	1.1±0.1	1.4±0.3	$0.32^{+0.13}_{-0.10}$	- - H	A
1140	19^{+6}_{-5}	10^{+5}_{-4}	9^{+5}_{-4}	$4.77^{+1.63}_{-1.36}$	$1.45^{+0.67}_{-0.52}$	$2.23^{+1.30}_{-1.02}$	1.9±1.2	1.4±0.3	5.6±1.8	$1.42^{+1.02}_{-0.99}$	- - -	B
1141	8^{+4}_{-3}	2	8^{+4}_{-3}	$1.73^{+0.91}_{-0.66}$	0.30	$1.85^{+0.93}_{-0.68}$	5.7±0.7	4.7±0.7	6.5±0.7	$1.59^{+0.86}_{-0.64}$	- S -	D
1142	23^{+6}_{-5}	15^{+5}_{-4}	8^{+4}_{-3}	$7.96^{+2.06}_{-1.68}$	$3.06^{+1.02}_{-0.79}$	$2.78^{+1.42}_{-1.01}$	1.5±0.3	1.2±0.2	2.8±0.6	$1.95^{+0.60}_{-0.53}$	- - -	B
1143	5^{+6}_{-5}	1^{+4}_{-1}	4^{+5}_{-4}	$1.45^{+1.66}_{-1.35}$	$0.18^{+0.59}_{-0.18}$	$1.17^{+1.51}_{-1.17}$	9.7±4.9	9.6±7.6	9.8±0.9	$2.26^{+2.82}_{-2.39}$	- - -	D
1144	10^{+6}_{-5}	4	11^{+6}_{-5}	$2.39^{+1.39}_{-1.14}$	0.56	$2.50^{+1.34}_{-1.08}$	7.3±2.9	3.2±2.4	9.6±1.1	$2.80^{+1.96}_{-1.73}$	- S -	C
1145	41^{+8}_{-7}	18^{+5}_{-4}	23^{+6}_{-5}	$8.96^{+1.69}_{-1.46}$	$2.23^{+0.67}_{-0.54}$	$5.13^{+1.38}_{-1.14}$	2.3±0.3	1.5±0.1	3.2±0.4	$3.23^{+0.71}_{-0.64}$	- - -	C
1146	8^{+4}_{-3}	7^{+4}_{-3}	1^{+3}_{-1}	$1.59^{+0.81}_{-0.59}$	$0.77^{+0.43}_{-0.29}$	$0.26^{+0.53}_{-0.26}$	1.5±0.8	1.0±0.2	1.7±3.3	$0.39^{+0.29}_{-0.26}$	- - -	B
1147	9^{+5}_{-4}	4^{+3}_{-2}	5^{+4}_{-3}	$2.15^{+1.19}_{-0.92}$	$0.50^{+0.47}_{-0.30}$	$1.28^{+1.04}_{-0.76}$	2.8±3.8	1.8±1.0	9.6±2.9	$0.98^{+1.42}_{-1.38}$	- - -	C
1148	8^{+5}_{-4}	2^{+3}_{-2}	6^{+4}_{-3}	$2.45^{+1.49}_{-1.15}$	$0.34^{+0.52}_{-0.29}$	$1.89^{+1.38}_{-1.03}$	7.4±2.2	3.7±2.5	7.9±1.2	$2.91^{+1.97}_{-1.61}$	- - -	C
1149	23^{+7}_{-6}	18^{+6}_{-4}	6^{+5}_{-3}	$2.52^{+0.77}_{-0.60}$	$1.51^{+0.37}_{-0.27}$	$0.62^{+0.55}_{-0.36}$	1.3±0.3	1.0±0.1	2.3±0.6	$0.51^{+0.20}_{-0.17}$	- - -	B

No.	C_{net} FB	C_{net} SB	C_{net} HB	$f_{\rm ph}$FB(10^{-6} cm^{-2} s^{-1})	$f_{\rm ph}$SB(10^{-6} cm^{-2} s^{-1})	$f_{\rm ph}$HB(10^{-6} cm^{-2} s^{-1})	E_{50} (keV)	E_{25} (keV)	E_{75} (keV)	f_X(10^{-14}erg cm^{-2} s^{-1})	Phot. Flag	Quantile Group
1150	17^{+5}_{-4}	15^{+5}_{-4}	2^{+3}_{-1}	$4.04^{+1.27}_{-1.00}$	$2.10^{+0.70}_{-0.54}$	$0.42^{+0.66}_{-0.32}$	1.1±0.1	0.9±0.1	1.5±0.3	$0.69^{+0.23}_{-0.19}$	- - -	A
1151	11^{+4}_{-3}	9^{+4}_{-3}	2^{+3}_{-1}	$2.24^{+0.94}_{-0.70}$	$1.10^{+0.51}_{-0.37}$	$0.36^{+0.57}_{-0.28}$	1.3±0.3	1.0±0.1	1.7±0.9	$0.48^{+0.22}_{-0.18}$	- - -	A
1152	69^{+11}_{-10}	46^{+9}_{-7}	23^{+8}_{-6}	$5.37^{+0.90}_{-0.75}$	$2.35^{+0.39}_{-0.31}$	$1.90^{+0.66}_{-0.51}$	1.3±0.2	1.1±0.1	3.0±0.6	$1.16^{+0.24}_{-0.22}$	- - -	B
1153	17^{+7}_{-6}	4	18^{+7}_{-6}	$3.80^{+1.64}_{-1.40}$	0.55	$4.10^{+1.59}_{-1.35}$	4.9±0.6	4.1±1.5	6.4±2.2	$3.01^{+1.35}_{-1.18}$	- S -	D
1154	4^{+4}_{-3}	5^{+3}_{-2}	4	$0.97^{+0.87}_{-0.59}$	$0.60^{+0.45}_{-0.28}$	0.88	0.9±0.5	0.8±0.2	1.8±0.4	$0.15^{+0.15}_{-0.12}$	- - H	B
1155	8^{+4}_{-3}	3	9^{+4}_{-3}	$1.68^{+0.82}_{-0.60}$	0.29	$1.74^{+0.84}_{-0.61}$	5.4±0.8	4.7±0.6	7.0±1.1	$1.46^{+0.74}_{-0.56}$	- S -	D
1156	5^{+4}_{-2}	2^{+3}_{-1}	3^{+3}_{-2}	$1.80^{+1.22}_{-0.80}$	$0.36^{+0.52}_{-0.25}$	$1.19^{+1.10}_{-0.66}$	2.7±0.7	1.8±0.4	3.1±0.6	$0.78^{+0.56}_{-0.40}$	- - -	E
1157	45^{+9}_{-8}	38^{+8}_{-6}	7^{+6}_{-4}	$5.24^{+1.05}_{-0.87}$	$3.22^{+0.52}_{-0.42}$	$0.74^{+0.65}_{-0.42}$	1.2±0.1	1.0±0.1	1.3±0.4	$0.99^{+0.21}_{-0.18}$	- - -	A
1158	9^{+4}_{-3}	10^{+4}_{-3}	2	$1.74^{+0.79}_{-0.58}$	$1.06^{+0.46}_{-0.34}$	0.43	1.0±0.1	0.8±0.1	1.1±0.1	$0.27^{+0.13}_{-0.10}$	- - H	A
1159	4^{+5}_{-4}	7^{+4}_{-3}	4	$1.07^{+1.22}_{-0.95}$	$0.98^{+0.60}_{-0.43}$	1.01	1.2±0.2	0.8±0.2	1.2±0.1	$0.20^{+0.23}_{-0.18}$	- - H	A
1160	2^{+6}_{-2}	5^{+4}_{-3}	6	$0.43^{+1.17}_{-0.43}$	$0.61^{+0.49}_{-0.36}$	1.24	1.4±8.6	1.2±8.8	9.9±9.4	$0.09^{+0.64}_{-0.59}$	- - H	B
1161	5^{+4}_{-3}	3	5^{+4}_{-3}	$1.04^{+0.80}_{-0.58}$	0.39	$1.04^{+0.78}_{-0.56}$	6.3±1.2	5.2±1.2	7.3±0.5	$1.05^{+0.83}_{-0.62}$	- S -	D
1162	14^{+5}_{-4}	12^{+5}_{-3}	2^{+3}_{-1}	$2.78^{+0.98}_{-0.76}$	$1.42^{+0.54}_{-0.41}$	$0.36^{+0.55}_{-0.27}$	1.3±0.2	1.1±0.1	1.8±0.5	$0.59^{+0.22}_{-0.18}$	- - -	A
1163	9^{+5}_{-4}	6^{+4}_{-3}	3^{+4}_{-2}	$1.87^{+0.96}_{-0.73}$	$0.73^{+0.44}_{-0.30}$	$0.60^{+0.75}_{-0.50}$	1.6±0.4	1.3±0.2	2.2±0.4	$0.47^{+0.27}_{-0.22}$	- - -	A
1164	28^{+9}_{-8}	21^{+7}_{-5}	7^{+6}_{-4}	$2.22^{+0.76}_{-0.61}$	$1.23^{+0.33}_{-0.24}$	$0.86^{+0.76}_{-0.47}$	1.4±0.4	1.1±0.1	3.4±1.2	$0.49^{+0.23}_{-0.21}$	- - -	B
1165	12^{+5}_{-3}	9^{+4}_{-3}	3^{+3}_{-2}	$2.55^{+1.01}_{-0.77}$	$1.14^{+0.53}_{-0.38}$	$0.60^{+0.66}_{-0.37}$	1.3±0.6	1.1±0.1	2.2±2.6	$0.53^{+0.32}_{-0.29}$	- - -	B
1166	9	4	8	2.82	0.78	2.52	5.2±4.8	2.9±7.1	7.6±7.1	2.38	F S H	C
1167	4^{+3}_{-2}	4^{+3}_{-2}	4	$0.97^{+0.75}_{-0.48}$	$0.50^{+0.41}_{-0.24}$	0.87	1.2±1.9	1.1±0.5	1.4±2.1	$0.18^{+0.33}_{-0.31}$	- - H	A
1168	228^{+16}_{-16}	146^{+13}_{-12}	82^{+11}_{-10}	$25.75^{+1.82}_{-1.75}$	$9.37^{+0.82}_{-0.78}$	$9.49^{+1.28}_{-1.11}$	1.6±0.1	1.2±0.0	2.7±0.4	$6.59^{+0.66}_{-0.65}$	- - -	B
1169	6^{+4}_{-2}	2^{+3}_{-1}	4^{+3}_{-2}	$1.15^{+0.74}_{-0.49}$	$0.23^{+0.31}_{-0.15}$	$0.78^{+0.67}_{-0.40}$	2.2±0.4	1.6±0.2	2.5±0.6	$0.41^{+0.27}_{-0.19}$	- - -	A
1170	6^{+4}_{-3}	7^{+4}_{-3}	2	$1.23^{+0.77}_{-0.52}$	$0.79^{+0.44}_{-0.30}$	0.47	1.1±0.2	1.0±0.2	1.4±0.1	$0.21^{+0.14}_{-0.10}$	- - H	A
1171	27^{+8}_{-6}	18^{+6}_{-5}	9^{+6}_{-3}	$2.96^{+0.86}_{-0.70}$	$1.50^{+0.39}_{-0.29}$	$1.01^{+0.66}_{-0.27}$	1.5±0.3	1.0±0.1	2.3±0.6	$0.71^{+0.24}_{-0.21}$	- - -	A
1172	6^{+4}_{-2}	3	6^{+4}_{-2}	$1.04^{+0.66}_{-0.44}$	0.28	$1.07^{+0.67}_{-0.44}$	5.0±0.5	4.6±0.3	5.4±0.7	$0.82^{+0.53}_{-0.36}$	- S -	E
1173	48^{+9}_{-8}	34^{+8}_{-6}	14^{+6}_{-4}	$5.23^{+0.99}_{-0.82}$	$2.84^{+0.48}_{-0.38}$	$1.41^{+0.66}_{-0.46}$	1.4±0.1	1.1±0.1	2.0±0.5	$1.19^{+0.25}_{-0.22}$	- - -	A
1174	10^{+5}_{-4}	4^{+3}_{-2}	6^{+4}_{-3}	$1.95^{+1.00}_{-0.79}$	$0.45^{+0.38}_{-0.24}$	$1.19^{+0.89}_{-0.67}$	2.6±1.6	1.5±0.7	5.9±2.7	$0.81^{+0.64}_{-0.59}$	- - -	C
1175	6^{+4}_{-2}	3	6^{+4}_{-2}	$1.02^{+0.66}_{-0.44}$	0.28	$1.06^{+0.68}_{-0.45}$	3.7±0.8	3.3±0.5	4.8±1.0	$0.60^{+0.41}_{-0.28}$	- S -	E
1176	5	3	5	1.58	0.57	1.45	5.2±4.8	2.9±7.1	7.6±7.1	1.33	F S H	C
1177	6^{+5}_{-4}	3^{+3}_{-2}	3^{+4}_{-3}	$1.68^{+1.58}_{-1.24}$	$0.48^{+0.59}_{-0.38}$	$0.84^{+1.40}_{-0.84}$	8.7±4.3	1.6±2.5	9.3±1.8	$2.34^{+2.48}_{-2.08}$	- - -	C
1178	10^{+4}_{-3}	8^{+4}_{-3}	2^{+3}_{-1}	$3.23^{+1.41}_{-1.04}$	$1.53^{+0.76}_{-0.54}$	$0.62^{+0.89}_{-0.43}$	1.4±0.4	0.9±0.2	1.7±0.9	$0.73^{+0.37}_{-0.30}$	- - -	B
1179	4^{+3}_{-2}	3	4^{+3}_{-2}	$0.94^{+0.81}_{-0.49}$	0.39	$0.98^{+0.83}_{-0.50}$	4.8±1.5	2.9±1.0	6.2±0.7	$0.73^{+0.67}_{-0.44}$	- S -	C
1180	335^{+19}_{-19}	4^{+5}_{-3}	332^{+19}_{-19}	$26.40^{+1.52}_{-1.52}$	$0.26^{+0.30}_{-0.17}$	$26.79^{+1.53}_{-1.53}$	4.3±0.1	3.6±0.1	5.2±0.1	$18.07^{+1.11}_{-1.11}$	- - -	E
1181	51^{+9}_{-8}	1^{+3}_{-1}	51^{+9}_{-8}	$7.09^{+1.26}_{-1.05}$	$0.13^{+0.56}_{-0.13}$	$7.12^{+1.27}_{-1.05}$	5.0±0.5	3.4±0.2	6.3±0.4	$5.70^{+1.15}_{-1.01}$	- - -	D
1182	8	4	8	2.18	0.56	2.04	5.2±4.8	2.9±7.1	7.6±7.1	1.83	F S H	C
1183	24^{+9}_{-7}	7^{+3}_{-2}	23^{+8}_{-7}	$2.42^{+0.92}_{-0.73}$	$1.13^{+0.43}_{-0.27}$	$1.86^{+0.82}_{-0.62}$	2.7±0.8	1.9±0.5	3.8±0.4	$1.03^{+0.51}_{-0.45}$	- - -	C
1184	7^{+4}_{-3}	7^{+4}_{-3}	1^{+2}_{-1}	$1.43^{+0.77}_{-0.55}$	$0.77^{+0.42}_{-0.29}$	$0.10^{+0.46}_{-0.10}$	1.2±0.2	1.0±0.1	1.5±0.3	$0.27^{+0.15}_{-0.12}$	- - -	A
1185	11^{+5}_{-3}	10^{+4}_{-3}	1^{+3}_{-1}	$2.30^{+0.93}_{-0.71}$	$1.15^{+0.50}_{-0.37}$	$0.30^{+0.55}_{-0.27}$	1.1±0.2	1.0±0.1	1.6±0.7	$0.41^{+0.18}_{-0.15}$	- - -	A
1186	10^{+4}_{-3}	4^{+3}_{-2}	6^{+4}_{-2}	$1.87^{+0.84}_{-0.62}$	$0.44^{+0.36}_{-0.22}$	$1.13^{+0.72}_{-0.47}$	2.9±0.5	1.8±0.4	3.1±0.4	$0.86^{+0.42}_{-0.32}$	- - -	E
1187	4^{+4}_{-3}	5^{+4}_{-2}	4	$1.10^{+0.98}_{-0.70}$	$0.67^{+0.51}_{-0.34}$	0.94	1.6±0.4	1.1±0.4	1.8±0.2	$0.28^{+0.26}_{-0.19}$	- - H	A
1188	7^{+6}_{-5}	2^{+4}_{-2}	5^{+5}_{-4}	$2.76^{+2.19}_{-1.78}$	$0.49^{+0.77}_{-0.49}$	$1.91^{+1.97}_{-1.54}$	3.8±3.4	2.1±1.7	6.0±3.1	$1.70^{+2.01}_{-1.85}$	- - -	C

No.	C_{net} FB	C_{net} SB	C_{net} HB	$f_{\rm ph}$FB(10^{-6} cm^{-2} s^{-1})	$f_{\rm ph}$SB(10^{-6} cm^{-2} s^{-1})	$f_{\rm ph}$HB(10^{-6} cm^{-2} s^{-1})	E_{50} (keV)	E_{25} (keV)	E_{75} (keV)	f_X(10^{-14}erg cm^{-2} s^{-1})	Phot. Flag	Quantile Group
1189	6^{+5}_{-3}	3^{+3}_{-2}	4^{+4}_{-3}	$2.97^{+2.09}_{-1.57}$	$0.71^{+0.83}_{-0.50}$	$1.73^{+1.83}_{-1.26}$	8.1±3.7	1.3±3.4	8.9±1.2	$3.84^{+3.23}_{-2.69}$	- - -	C
1190	6^{+4}_{-3}	1^{+2}_{-1}	6^{+4}_{-2}	$1.56^{+0.91}_{-0.62}$	$0.12^{+0.32}_{-0.11}$	$1.37^{+0.88}_{-0.58}$	3.6±1.2	2.6±0.8	5.1±1.1	$0.89^{+0.59}_{-0.46}$	- - -	C
1191	28^{+8}_{-6}	5	30^{+8}_{-6}	$3.25^{+0.92}_{-0.75}$	0.32	$3.56^{+0.93}_{-0.75}$	4.0±0.3	3.4±0.2	5.1±0.6	$2.08^{+0.61}_{-0.51}$	- S -	D
1192	9^{+4}_{-3}	3^{+3}_{-2}	6^{+4}_{-3}	$1.74^{+0.86}_{-0.64}$	$0.31^{+0.34}_{-0.19}$	$1.23^{+0.78}_{-0.53}$	2.6±1.2	1.6±0.5	5.2±2.1	$0.73^{+0.50}_{-0.43}$	- - -	C
1193	4^{+4}_{-3}	6^{+4}_{-3}	3	$0.95^{+0.93}_{-0.69}$	$0.78^{+0.49}_{-0.35}$	0.73	1.1±0.2	1.1±0.1	1.2±0.1	$0.17^{+0.17}_{-0.13}$	- - H	A
1194	8^{+6}_{-5}	3^{+3}_{-2}	5^{+5}_{-4}	$2.19^{+1.45}_{-1.17}$	$0.45^{+0.50}_{-0.32}$	$1.41^{+1.32}_{-1.03}$	2.9±1.4	1.4±0.9	4.0±3.6	$1.02^{+0.83}_{-0.73}$	- - -	C
1195	14^{+5}_{-4}	1^{+3}_{-1}	12^{+5}_{-4}	$2.81^{+1.06}_{-0.84}$	$0.15^{+0.31}_{-0.15}$	$2.60^{+1.03}_{-0.81}$	4.8±0.5	4.1±0.7	5.7±0.6	$2.16^{+0.85}_{-0.69}$	- - -	D
1196	13^{+5}_{-4}	8^{+4}_{-3}	5^{+3}_{-2}	$2.46^{+0.93}_{-0.71}$	$0.89^{+0.45}_{-0.32}$	$0.93^{+0.68}_{-0.43}$	1.8±0.4	1.3±0.2	2.9±0.8	$0.73^{+0.32}_{-0.27}$	- - -	B
1197	5	2	6	1.53	0.40	1.89	5.2±4.8	2.9±7.1	7.6±7.1	1.29	F S H	C
1198	5^{+3}_{-2}	3^{+3}_{-2}	2^{+3}_{-1}	$1.45^{+1.04}_{-0.66}$	$0.52^{+0.52}_{-0.29}$	$0.56^{+0.83}_{-0.40}$	1.7±1.2	1.1±0.5	4.0±0.9	$0.40^{+0.40}_{-0.33}$	- - -	B
1199	10^{+5}_{-4}	8^{+4}_{-3}	3^{+4}_{-3}	$2.09^{+1.08}_{-0.86}$	$0.88^{+0.49}_{-0.35}$	$0.55^{+0.84}_{-0.55}$	1.4±0.8	1.3±0.4	3.2±1.1	$0.47^{+0.35}_{-0.32}$	- - -	B
1200	7^{+4}_{-3}	7^{+4}_{-3}	4	$1.35^{+0.76}_{-0.54}$	$0.75^{+0.42}_{-0.28}$	0.71	1.1±0.3	1.0±0.1	1.4±0.8	$0.24^{+0.15}_{-0.12}$	- - H	A
1201	15^{+5}_{-4}	10^{+4}_{-3}	5^{+4}_{-3}	$3.08^{+1.07}_{-0.85}$	$1.12^{+0.50}_{-0.37}$	$1.14^{+0.79}_{-0.54}$	1.9±0.3	1.4±0.2	2.7±1.1	$0.92^{+0.35}_{-0.29}$	- - -	B
1202	14^{+6}_{-5}	1^{+3}_{-1}	13^{+6}_{-5}	$2.90^{+1.25}_{-1.02}$	$0.13^{+0.36}_{-0.13}$	$2.73^{+1.21}_{-0.97}$	4.2±1.2	2.6±1.0	7.1±2.7	$1.97^{+1.03}_{-0.90}$	- - -	C
1203	250^{+16}_{-16}	154^{+14}_{-13}	96^{+12}_{-10}	$28.25^{+1.83}_{-1.83}$	$11.20^{+0.90}_{-0.81}$	$11.06^{+1.35}_{-1.18}$	1.7±0.1	1.2±0.0	2.6±0.1	$7.57^{+0.60}_{-0.60}$	- - -	B
1204	12^{+5}_{-4}	9^{+4}_{-3}	3^{+3}_{-2}	$2.48^{+0.95}_{-0.72}$	$1.02^{+0.48}_{-0.35}$	$0.71^{+0.65}_{-0.39}$	1.3±0.3	1.0±0.1	2.0±0.4	$0.51^{+0.22}_{-0.18}$	- - -	B
1205	6^{+4}_{-2}	5^{+3}_{-2}	1^{+2}_{-1}	$1.11^{+0.71}_{-0.47}$	$0.56^{+0.39}_{-0.24}$	$0.15^{+0.47}_{-0.15}$	1.2±0.2	1.1±0.1	1.3±0.3	$0.21^{+0.14}_{-0.10}$	- - -	A
1206	6^{+4}_{-3}	2^{+3}_{-1}	4^{+3}_{-2}	$1.25^{+0.75}_{-0.51}$	$0.21^{+0.30}_{-0.15}$	$0.90^{+0.68}_{-0.43}$	2.6±1.2	1.8±0.6	4.2±1.6	$0.52^{+0.39}_{-0.32}$	- - -	C
1207	4^{+3}_{-2}	5^{+3}_{-2}	2	$0.99^{+0.77}_{-0.49}$	$0.63^{+0.44}_{-0.28}$	0.53	1.3±0.2	1.2±0.1	1.7±0.2	$0.21^{+0.17}_{-0.11}$	- - H	A
1208	12^{+6}_{-5}	1^{+3}_{-1}	11^{+6}_{-5}	$2.93^{+1.46}_{-1.21}$	$0.20^{+0.44}_{-0.20}$	$2.63^{+1.39}_{-1.13}$	4.6±2.4	2.3±1.0	7.3±2.3	$2.14^{+1.56}_{-1.43}$	- - -	C
1209	11^{+5}_{-4}	2^{+3}_{-2}	9^{+5}_{-4}	$2.65^{+1.20}_{-0.95}$	$0.26^{+0.40}_{-0.22}$	$2.24^{+1.14}_{-0.87}$	3.5±0.7	2.6±1.0	4.1±1.0	$1.49^{+0.73}_{-0.60}$	- - -	E
1210	94^{+12}_{-10}	85^{+11}_{-9}	8^{+6}_{-3}	$11.03^{+1.41}_{-1.23}$	$6.67^{+0.73}_{-0.63}$	$1.08^{+0.73}_{-0.17}$	1.1±0.0	1.0±0.0	1.4±0.1	$1.99^{+0.27}_{-0.24}$	- - -	A
1211	22^{+7}_{-6}	6^{+5}_{-3}	16^{+7}_{-5}	$2.10^{+0.76}_{-0.58}$	$0.53^{+0.26}_{-0.14}$	$1.62^{+0.70}_{-0.53}$	3.4±0.8	2.1±0.5	5.3±0.9	$1.14^{+0.48}_{-0.41}$	- - -	C
1212	14^{+8}_{-6}	3	18^{+7}_{-6}	$3.59^{+1.88}_{-1.63}$	0.41	$4.59^{+1.89}_{-1.61}$	8.7±1.2	7.2±2.4	9.0±0.6	$4.97^{+2.70}_{-2.36}$	- S -	D
1213	11	1^{+4}_{-1}	9	2.83	$0.09^{+0.54}_{-0.09}$	2.28	9.8±9.3	1.9±8.1	9.9±9.4	4.45	F - H	C
1214	6^{+4}_{-3}	3	6^{+4}_{-3}	$1.28^{+0.81}_{-0.55}$	0.31	$1.34^{+0.83}_{-0.57}$	4.4±0.9	3.5±0.7	5.4±0.8	$0.90^{+0.60}_{-0.43}$	- S -	D
1215	7^{+4}_{-3}	1^{+2}_{-1}	6^{+4}_{-3}	$1.39^{+0.80}_{-0.57}$	$0.10^{+0.27}_{-0.10}$	$1.24^{+0.78}_{-0.53}$	4.9±1.6	3.0±1.4	6.8±1.4	$1.08^{+0.72}_{-0.57}$	- - -	C
1216	55^{+9}_{-8}	5^{+3}_{-1}	54^{+9}_{-8}	$6.27^{+1.05}_{-0.89}$	$0.14^{+0.35}_{-0.14}$	$6.24^{+1.05}_{-0.89}$	4.2±0.5	3.3±0.4	5.5±0.9	$4.26^{+0.87}_{-0.78}$	- - -	D
1217	1^{+5}_{-1}	4^{+4}_{-2}	4	$0.21^{+1.49}_{-0.21}$	$0.65^{+0.65}_{-0.43}$	1.44	5.2±4.8	2.9±7.1	7.6±7.1	$0.17^{+1.27}_{-0.24}$	- - H	C
1218	65^{+10}_{-9}	48^{+9}_{-7}	17^{+6}_{-5}	$6.85^{+1.06}_{-0.90}$	$3.40^{+0.51}_{-0.42}$	$1.48^{+0.63}_{-0.44}$	1.2±0.1	1.1±0.0	1.8±0.2	$1.35^{+0.22}_{-0.19}$	- - -	B
1219	7^{+4}_{-3}	3	7^{+4}_{-3}	$2.54^{+1.64}_{-1.23}$	0.70	$2.59^{+1.62}_{-1.20}$	2.4±3.7	2.2±1.2	9.2±2.5	$0.97^{+1.63}_{-1.57}$	- S -	C
1220	30^{+8}_{-6}	23^{+7}_{-5}	7^{+5}_{-3}	$3.30^{+0.86}_{-0.68}$	$1.88^{+0.41}_{-0.31}$	$0.75^{+0.58}_{-0.38}$	1.5±0.2	1.1±0.1	1.8±0.6	$0.77^{+0.22}_{-0.19}$	- - -	A
1221	5^{+4}_{-3}	4^{+4}_{-2}	5	$1.20^{+1.09}_{-0.81}$	$0.65^{+0.52}_{-0.35}$	1.25	1.0±0.5	0.8±0.3	1.2±0.7	$0.20^{+0.20}_{-0.17}$	- - H	A
1222	16^{+6}_{-5}	5^{+4}_{-3}	11^{+5}_{-4}	$4.04^{+1.55}_{-1.29}$	$0.72^{+0.55}_{-0.40}$	$2.83^{+1.38}_{-1.11}$	3.6±0.7	1.8±1.0	4.2±1.1	$2.35^{+1.01}_{-0.88}$	- - -	C
1223	8^{+4}_{-3}	6^{+4}_{-2}	2^{+3}_{-2}	$1.78^{+0.97}_{-0.70}$	$0.78^{+0.49}_{-0.32}$	$0.44^{+0.70}_{-0.39}$	1.5±0.7	1.0±0.3	2.0±2.5	$0.42^{+0.30}_{-0.26}$	- - -	B
1224	12^{+6}_{-4}	14^{+5}_{-4}	6	$1.29^{+0.65}_{-0.47}$	$1.33^{+0.34}_{-0.24}$	0.64	0.9±0.1	0.8±0.0	1.1±0.1	$0.18^{+0.09}_{-0.07}$	- - H	A
1225	7^{+4}_{-3}	2^{+3}_{-2}	5^{+4}_{-3}	$1.48^{+0.95}_{-0.71}$	$0.28^{+0.36}_{-0.20}$	$1.00^{+0.87}_{-0.62}$	6.8±3.7	1.1±2.2	9.6±1.8	$1.61^{+1.36}_{-1.17}$	- - -	C
1226	11^{+5}_{-3}	6^{+4}_{-2}	5^{+4}_{-2}	$2.17^{+0.92}_{-0.69}$	$0.65^{+0.41}_{-0.27}$	$1.06^{+0.74}_{-0.49}$	2.0±0.8	1.1±0.3	3.0±1.3	$0.70^{+0.41}_{-0.36}$	- - -	B
1227	42^{+8}_{-6}	41^{+7}_{-6}	1^{+2}_{-1}	$7.92^{+1.44}_{-1.24}$	$4.48^{+0.82}_{-0.70}$	$0.13^{+0.45}_{-0.13}$	1.0±0.0	0.9±0.0	1.2±0.1	$1.26^{+0.23}_{-0.20}$	- - -	A

No.	C_{net} FB	C_{net} SB	C_{net} HB	$f_{\rm ph}$FB(10^{-6} cm^{-2} s^{-1})	$f_{\rm ph}$SB(10^{-6} cm^{-2} s^{-1})	$f_{\rm ph}$HB(10^{-6} cm^{-2} s^{-1})	E_{50} (keV)	E_{25} (keV)	E_{75} (keV)	f_X(10^{-14}erg cm^{-2} s^{-1})	Phot. Flag	Quantile Group
1228	10^{+10}_{-9}	6	13^{+9}_{-8}	$2.41^{+2.24}_{-2.02}$	0.77	$3.03^{+2.09}_{-1.86}$	6.3±1.6	5.1±0.9	7.3±2.0	$2.43^{+2.33}_{-2.12}$	- S -	D
1229	7^{+4}_{-3}	2^{+3}_{-2}	5^{+4}_{-3}	$1.67^{+0.99}_{-0.75}$	$0.30^{+0.37}_{-0.21}$	$1.16^{+0.91}_{-0.65}$	3.4±1.4	1.7±0.8	3.8±2.9	$0.90^{+0.65}_{-0.55}$	- - -	C
1230	10^{+5}_{-3}	4^{+3}_{-2}	6^{+4}_{-3}	$2.28^{+1.04}_{-0.79}$	$0.57^{+0.44}_{-0.28}$	$1.32^{+0.88}_{-0.60}$	2.0±0.6	1.3±0.3	2.9±2.1	$0.74^{+0.39}_{-0.33}$	- - -	B
1231	7	4^{+4}_{-3}	4	1.60	$0.49^{+0.49}_{-0.34}$	0.84	5.2±4.8	2.9±7.1	7.6±7.1	1.34	F - H	C
1232	18	4	3^{+8}_{-3}	4.18	0.56	$0.70^{+1.89}_{-0.70}$	5.2±4.8	2.9±7.1	7.6±7.1	3.52	F S -	C
1233	41^{+11}_{-9}	31^{+8}_{-6}	10^{+8}_{-4}	$3.53^{+0.82}_{-0.67}$	$1.87^{+0.37}_{-0.29}$	$0.70^{+0.52}_{-0.24}$	1.5±0.1	1.2±0.1	2.1±0.3	$0.82^{+0.20}_{-0.17}$	- - -	A
1234	12^{+5}_{-4}	4^{+3}_{-2}	8^{+4}_{-3}	$2.84^{+1.19}_{-0.92}$	$0.50^{+0.45}_{-0.27}$	$2.01^{+1.08}_{-0.80}$	2.3±0.4	1.9±0.2	3.1±0.2	$1.06^{+0.48}_{-0.39}$	- - -	E
1235	10^{+5}_{-4}	6^{+4}_{-3}	3^{+4}_{-2}	$2.31^{+1.15}_{-0.88}$	$0.86^{+0.53}_{-0.36}$	$0.82^{+0.90}_{-0.59}$	1.8±0.9	1.7±0.3	3.1±2.4	$0.67^{+0.47}_{-0.42}$	- - -	A
1236	21^{+6}_{-5}	18^{+5}_{-4}	4^{+4}_{-3}	$5.07^{+1.51}_{-1.25}$	$2.40^{+0.74}_{-0.59}$	$0.86^{+0.98}_{-0.70}$	1.3±0.2	0.8±0.1	1.6±0.3	$1.02^{+0.34}_{-0.30}$	- - -	B
1237	19^{+7}_{-6}	20^{+6}_{-5}	6	$2.21^{+0.79}_{-0.62}$	$1.86^{+0.41}_{-0.31}$	0.74	1.2±0.1	1.0±0.1	1.5±0.2	$0.43^{+0.16}_{-0.13}$	- - H	A
1238	6^{+4}_{-3}	5^{+3}_{-2}	2^{+3}_{-2}	$1.63^{+1.01}_{-0.72}$	$0.69^{+0.50}_{-0.31}$	$0.44^{+0.77}_{-0.43}$	1.8±0.5	1.0±0.3	2.0±0.4	$0.48^{+0.32}_{-0.24}$	- - -	B
1239	12	4	11	2.79	0.52	2.66	5.2±4.8	2.9±7.1	7.6±7.1	2.35	F S H	C
1240	24^{+7}_{-6}	2^{+3}_{-2}	22^{+6}_{-5}	$5.46^{+1.53}_{-1.28}$	$0.29^{+0.41}_{-0.25}$	$5.06^{+1.47}_{-1.22}$	5.5±0.6	4.1±1.0	6.8±1.3	$4.78^{+1.44}_{-1.25}$	- - -	D
1241	8^{+4}_{-3}	2	9^{+4}_{-3}	$1.67^{+0.92}_{-0.69}$	0.27	$1.89^{+0.94}_{-0.71}$	3.7±1.1	3.3±0.5	5.4±2.1	$0.98^{+0.62}_{-0.50}$	- S -	D
1242	9^{+4}_{-3}	3^{+3}_{-2}	6^{+4}_{-3}	$2.13^{+1.04}_{-0.77}$	$0.37^{+0.41}_{-0.23}$	$1.53^{+0.93}_{-0.64}$	4.0±1.7	1.6±1.0	6.5±2.2	$1.37^{+0.89}_{-0.77}$	- - -	C
1243	6^{+4}_{-3}	4^{+3}_{-2}	2^{+3}_{-2}	$1.19^{+0.73}_{-0.50}$	$0.42^{+0.35}_{-0.21}$	$0.46^{+0.58}_{-0.32}$	1.0±2.0	0.8±0.4	2.4±3.0	$0.18^{+0.41}_{-0.40}$	- - -	B
1244	4^{+4}_{-3}	3^{+3}_{-2}	5	$2.14^{+2.19}_{-1.49}$	$1.06^{+1.05}_{-0.63}$	2.79	1.2±0.5	0.9±0.3	1.8±0.4	$0.41^{+0.46}_{-0.34}$	- - H	B
1245	4^{+4}_{-3}	2	5^{+4}_{-3}	$0.87^{+0.75}_{-0.51}$	0.26	$1.00^{+0.77}_{-0.52}$	2.9±2.3	2.5±0.7	6.3±2.2	$0.41^{+0.47}_{-0.40}$	- S -	C
1246	5^{+4}_{-2}	4^{+3}_{-2}	1^{+3}_{-1}	$1.29^{+0.93}_{-0.61}$	$0.56^{+0.47}_{-0.28}$	$0.33^{+0.70}_{-0.33}$	1.2±0.9	1.0±0.3	1.9±1.3	$0.24^{+0.26}_{-0.23}$	- - -	B
1247	7^{+4}_{-3}	7^{+4}_{-3}	4	$1.50^{+1.01}_{-0.76}$	$0.88^{+0.51}_{-0.37}$	1.00	0.9±0.1	0.9±0.1	1.2±0.1	$0.22^{+0.15}_{-0.12}$	- - H	A
1248	25^{+8}_{-6}	10^{+5}_{-3}	15^{+7}_{-5}	$2.78^{+0.83}_{-0.66}$	$1.08^{+0.31}_{-0.20}$	$1.75^{+0.73}_{-0.56}$	2.0±0.2	1.8±0.2	2.6±0.4	$0.91^{+0.29}_{-0.24}$	- - -	A
1249	6^{+4}_{-3}	5^{+3}_{-2}	1^{+3}_{-1}	$1.49^{+0.98}_{-0.66}$	$0.70^{+0.51}_{-0.32}$	$0.29^{+0.70}_{-0.29}$	0.9±0.3	0.9±0.1	1.3±0.6	$0.23^{+0.17}_{-0.13}$	- - -	A
1250	16^{+5}_{-4}	6^{+4}_{-3}	10^{+4}_{-3}	$3.99^{+1.34}_{-1.07}$	$0.91^{+0.54}_{-0.37}$	$2.44^{+1.14}_{-0.85}$	2.6±0.6	1.6±0.4	4.2±1.4	$1.69^{+0.70}_{-0.61}$	- - -	C
1251	33^{+8}_{-7}	32^{+7}_{-6}	1^{+4}_{-1}	$3.65^{+0.90}_{-0.73}$	$2.67^{+0.47}_{-0.37}$	$0.21^{+0.96}_{-0.21}$	1.1±0.1	0.9±0.1	1.4±0.2	$0.63^{+0.16}_{-0.13}$	- - -	A
1252	9^{+5}_{-3}	2^{+3}_{-2}	6^{+4}_{-3}	$1.92^{+1.01}_{-0.77}$	$0.29^{+0.37}_{-0.20}$	$1.45^{+0.93}_{-0.68}$	2.5±0.7	1.9±0.2	3.5±1.3	$0.77^{+0.46}_{-0.37}$	- - -	E
1253	41^{+8}_{-6}	21^{+6}_{-5}	20^{+6}_{-5}	$10.67^{+1.97}_{-1.69}$	$3.12^{+0.85}_{-0.69}$	$5.36^{+1.51}_{-1.22}$	2.0±0.4	1.5±0.1	3.6±0.4	$3.38^{+0.96}_{-0.90}$	- - -	B
1254	4^{+9}_{-4}	3^{+5}_{-3}	1^{+8}_{-1}	$1.09^{+2.20}_{-1.09}$	$0.48^{+0.72}_{-0.48}$	$0.25^{+1.98}_{-0.25}$	2.2±4.1	1.9±0.7	3.1±6.9	$0.39^{+1.06}_{-0.81}$	- - -	A
1255	13^{+5}_{-4}	7^{+4}_{-3}	5^{+4}_{-3}	$3.38^{+1.31}_{-1.02}$	$1.11^{+0.59}_{-0.42}$	$1.46^{+1.02}_{-0.70}$	1.7±0.8	1.5±0.2	3.5±2.9	$0.93^{+0.55}_{-0.50}$	- - -	B
1256	13^{+7}_{-6}	5^{+4}_{-3}	8^{+6}_{-5}	$4.67^{+2.34}_{-1.96}$	$0.98^{+0.83}_{-0.61}$	$2.98^{+2.06}_{-1.67}$	3.2±1.3	1.4±0.6	3.8±0.4	$2.38^{+1.52}_{-1.38}$	- - -	C
1257	5^{+4}_{-2}	5^{+3}_{-2}	1^{+2}_{-1}	$1.08^{+0.72}_{-0.48}$	$0.57^{+0.40}_{-0.25}$	$0.10^{+0.48}_{-0.10}$	1.0±0.4	0.8±0.1	1.4±0.4	$0.17^{+0.13}_{-0.10}$	- - -	A
1258	15^{+5}_{-4}	11^{+4}_{-3}	4^{+3}_{-2}	$3.06^{+1.07}_{-0.84}$	$1.28^{+0.53}_{-0.40}$	$0.83^{+0.73}_{-0.46}$	1.7±0.2	1.4±0.2	2.1±0.5	$0.83^{+0.30}_{-0.24}$	- - -	A
1259	44^{+9}_{-8}	6^{+5}_{-3}	37^{+9}_{-7}	$4.75^{+1.01}_{-0.84}$	$0.63^{+0.30}_{-0.19}$	$4.08^{+0.95}_{-0.77}$	3.5±0.3	2.7±0.3	4.1±0.2	$2.65^{+0.60}_{-0.51}$	- - -	E
1260	3^{+4}_{-2}	4	3^{+3}_{-2}	$1.87^{+2.31}_{-1.53}$	1.32	$1.70^{+2.23}_{-1.42}$	8.2±1.1	7.4±0.6	9.2±0.7	$2.44^{+3.04}_{-2.04}$	- S -	D
1261	17^{+9}_{-6}	14^{+6}_{-5}	13^{+6}_{-5}	$1.78^{+0.99}_{-0.65}$	$1.18^{+0.40}_{-0.30}$	$1.68^{+1.28}_{-1.03}$	1.0±0.4	0.7±0.2	1.2±0.2	$0.27^{+0.19}_{-0.15}$	- - -	B
1262	6^{+4}_{-2}	5^{+3}_{-2}	1^{+2}_{-1}	$1.12^{+0.73}_{-0.48}$	$0.57^{+0.40}_{-0.25}$	$0.13^{+0.48}_{-0.13}$	1.4±0.6	0.9±0.3	1.9±0.9	$0.25^{+0.19}_{-0.15}$	- - -	B
1263	12^{+5}_{-4}	4	12^{+5}_{-4}	$2.56^{+1.04}_{-0.81}$	0.45	$2.52^{+1.04}_{-0.80}$	4.7±0.8	3.7±0.8	6.4±0.9	$1.91^{+0.85}_{-0.69}$	- S -	D
1264	58^{+10}_{-8}	21^{+6}_{-5}	37^{+8}_{-7}	$6.19^{+1.03}_{-0.87}$	$1.83^{+0.39}_{-0.29}$	$4.04^{+0.89}_{-0.72}$	2.3±0.2	1.8±0.2	3.1±0.5	$2.23^{+0.43}_{-0.38}$	- - -	E
1265	5^{+4}_{-2}	6^{+4}_{-2}	2	$1.10^{+0.72}_{-0.48}$	$0.68^{+0.42}_{-0.28}$	0.47	1.0±0.1	0.8±0.1	1.1±0.1	$0.17^{+0.11}_{-0.08}$	- - H	A
1266	4^{+4}_{-3}	4^{+3}_{-2}	4	$0.93^{+0.89}_{-0.64}$	$0.51^{+0.43}_{-0.27}$	1.00	1.3±2.2	1.3±0.6	1.8±3.4	$0.20^{+0.38}_{-0.36}$	- - H	A

No.	C_{net} FB	C_{net} SB	C_{net} HB	$f_{\rm ph}$FB(10^{-6} cm^{-2} s^{-1})	$f_{\rm ph}$SB(10^{-6} cm^{-2} s^{-1})	$f_{\rm ph}$HB(10^{-6} cm^{-2} s^{-1})	E_{50} (keV)	E_{25} (keV)	E_{75} (keV)	f_X(10^{-14}erg cm^{-2} s^{-1})	Phot. Flag	Quantile Group
1267	7^{+4}_{-3}	3	7^{+4}_{-3}	$1.44^{+0.95}_{-0.71}$	0.40	$1.49^{+0.94}_{-0.69}$	6.0±1.2	5.3±1.4	7.4±1.1	$1.38^{+0.95}_{-0.73}$	- S -	D
1268	10^{+5}_{-4}	1^{+3}_{-1}	9^{+5}_{-4}	$3.53^{+1.96}_{-1.55}$	$0.15^{+0.56}_{-0.15}$	$3.34^{+1.90}_{-1.49}$	5.9±1.6	3.9±1.7	7.8±1.1	$3.31^{+2.05}_{-1.72}$	- - -	C
1269	5^{+4}_{-3}	7^{+4}_{-3}	2	$1.08^{+0.75}_{-0.51}$	$0.75^{+0.43}_{-0.29}$	0.47	0.9±0.0	0.8±0.0	0.9±0.0	$0.15^{+0.11}_{-0.07}$	- - H	A
1270	4^{+5}_{-4}	2	6^{+5}_{-4}	$0.85^{+1.15}_{-0.85}$	0.31	$1.42^{+1.17}_{-0.91}$	6.4±3.2	3.3±6.7	6.6±6.1	$0.87^{+1.25}_{-0.97}$	- S -	C
1271	29^{+9}_{-7}	22^{+7}_{-5}	6^{+6}_{-5}	$3.20^{+0.97}_{-0.80}$	$1.96^{+0.43}_{-0.33}$	$1.57^{+1.40}_{-1.14}$	1.4±0.3	1.0±0.1	1.7±0.2	$0.70^{+0.25}_{-0.22}$	- - -	A
1272	10^{+5}_{-3}	2	10^{+5}_{-3}	$2.15^{+0.99}_{-0.75}$	0.28	$2.33^{+1.02}_{-0.77}$	5.5±0.7	4.6±0.7	6.3±0.8	$1.89^{+0.90}_{-0.70}$	- S -	D
1273	43^{+8}_{-7}	1^{+2}_{-1}	43^{+8}_{-7}	$8.01^{+1.42}_{-1.22}$	$0.09^{+0.25}_{-0.09}$	$8.02^{+1.43}_{-1.24}$	4.8±0.4	3.4±0.3	6.0±0.4	$6.11^{+1.20}_{-1.07}$	- - -	D
1274	6^{+9}_{-6}	6	7^{+8}_{-7}	$1.81^{+2.49}_{-1.81}$	0.93	$2.12^{+2.29}_{-1.95}$	3.2±3.0	2.5±2.1	4.2±5.8	$0.93^{+1.54}_{-1.26}$	- S -	E
1275	7^{+4}_{-3}	2	8^{+4}_{-3}	$1.52^{+0.91}_{-0.68}$	0.28	$1.70^{+0.93}_{-0.69}$	5.1±2.2	3.9±1.1	8.8±1.9	$1.24^{+0.93}_{-0.78}$	- S -	C
1276	72^{+11}_{-9}	6	73^{+11}_{-9}	$8.59^{+1.27}_{-1.09}$	0.41	$8.85^{+1.29}_{-1.10}$	4.4±0.2	3.7±0.2	5.8±0.3	$6.03^{+0.94}_{-0.82}$	- S -	D
1277	4^{+4}_{-3}	1^{+3}_{-1}	3^{+3}_{-2}	$0.83^{+0.82}_{-0.55}$	$0.13^{+0.32}_{-0.13}$	$0.61^{+0.76}_{-0.49}$	3.3±2.3	1.9±8.1	6.2±5.7	$0.44^{+0.53}_{-0.43}$	- - -	C
1278	191^{+14}_{-14}	1^{+3}_{-1}	190^{+14}_{-14}	$42.72^{+3.16}_{-3.16}$	$0.09^{+0.37}_{-0.09}$	$43.50^{+3.21}_{-3.21}$	4.0±0.1	3.2±0.1	4.8±0.1	$27.19^{+2.08}_{-2.08}$	- - -	D
1279	185^{+14}_{-14}	8^{+4}_{-3}	177^{+14}_{-14}	$45.56^{+3.50}_{-3.50}$	$1.14^{+0.62}_{-0.47}$	$44.50^{+3.48}_{-3.48}$	3.7±0.2	3.0±0.1	4.5±0.1	$27.29^{+2.37}_{-2.37}$	- - -	E
1280	5^{+4}_{-3}	2^{+3}_{-2}	2^{+3}_{-2}	$0.91^{+0.79}_{-0.57}$	$0.25^{+0.34}_{-0.19}$	$0.50^{+0.69}_{-0.44}$	2.1±2.1	1.2±0.9	5.3±1.5	$0.31^{+0.41}_{-0.36}$	- - -	B
1281	2^{+5}_{-2}	1^{+3}_{-1}	1^{+5}_{-1}	$0.34^{+1.11}_{-0.34}$	$0.11^{+0.40}_{-0.11}$	$0.15^{+1.02}_{-0.15}$	2.3±1.2	1.8±8.2	2.8±7.2	$0.13^{+0.42}_{-0.14}$	- - -	E
1282	14^{+6}_{-5}	8^{+4}_{-3}	7^{+5}_{-4}	$3.29^{+1.30}_{-1.06}$	$1.02^{+0.53}_{-0.39}$	$1.52^{+1.07}_{-0.82}$	1.7±1.1	1.4±0.2	3.9±3.0	$0.91^{+0.67}_{-0.64}$	- - -	B
1283	11^{+6}_{-5}	4	11^{+6}_{-4}	$2.69^{+1.46}_{-1.18}$	0.53	$2.81^{+1.43}_{-1.15}$	5.1±2.8	2.9±1.2	8.4±1.3	$2.17^{+1.68}_{-1.54}$	- S -	C
1284	12^{+6}_{-5}	10^{+5}_{-3}	2^{+4}_{-2}	$2.71^{+1.24}_{-1.01}$	$1.29^{+0.57}_{-0.43}$	$0.45^{+0.93}_{-0.45}$	1.0±0.2	1.0±0.1	1.3±2.7	$0.45^{+0.22}_{-0.18}$	- - -	A
1285	10^{+4}_{-3}	9^{+4}_{-3}	1^{+3}_{-1}	$1.97^{+0.85}_{-0.63}$	$0.98^{+0.46}_{-0.33}$	$0.29^{+0.52}_{-0.25}$	1.3±0.4	1.1±0.2	1.7±1.6	$0.41^{+0.22}_{-0.18}$	- - -	A
1286	6^{+4}_{-3}	3^{+3}_{-2}	4^{+3}_{-2}	$1.26^{+0.74}_{-0.51}$	$0.33^{+0.34}_{-0.19}$	$0.71^{+0.64}_{-0.38}$	2.5±1.0	1.4±0.5	3.8±1.1	$0.51^{+0.36}_{-0.29}$	- - -	C
1287	8^{+5}_{-4}	3	8^{+5}_{-4}	$1.81^{+1.17}_{-0.92}$	0.40	$2.00^{+1.17}_{-0.91}$	4.4±1.4	4.0±0.8	5.5±2.4	$1.27^{+0.92}_{-0.77}$	- S -	E
1288	12^{+7}_{-6}	10^{+5}_{-4}	2^{+6}_{-2}	$2.82^{+1.74}_{-1.49}$	$1.32^{+0.67}_{-0.52}$	$0.47^{+1.44}_{-0.47}$	1.5±0.4	1.3±0.5	1.6±3.8	$0.67^{+0.45}_{-0.39}$	- - -	A
1289	16^{+6}_{-4}	15^{+5}_{-4}	1^{+3}_{-1}	$3.52^{+1.21}_{-0.98}$	$1.86^{+0.63}_{-0.49}$	$0.23^{+0.71}_{-0.23}$	1.4±0.2	1.1±0.2	1.8±1.2	$0.82^{+0.30}_{-0.25}$	- - -	A
1290	7^{+5}_{-4}	9^{+5}_{-3}	5	$1.81^{+1.32}_{-1.06}$	$1.28^{+0.63}_{-0.48}$	1.17	1.2±0.1	1.1±0.2	1.2±0.1	$0.34^{+0.25}_{-0.20}$	- - H	A
1291	13^{+5}_{-4}	3	13^{+5}_{-4}	$4.93^{+1.82}_{-1.39}$	0.60	$5.05^{+1.86}_{-1.42}$	4.3±0.6	3.5±0.3	5.6±0.5	$3.36^{+1.34}_{-1.08}$	- S -	D
1292	12^{+5}_{-4}	6^{+4}_{-3}	6^{+4}_{-3}	$2.99^{+1.26}_{-1.00}$	$0.83^{+0.52}_{-0.35}$	$1.56^{+1.06}_{-0.79}$	2.1±0.9	1.6±0.4	4.7±2.8	$1.01^{+0.59}_{-0.53}$	- - -	B
1293	7^{+8}_{-7}	2^{+4}_{-2}	5^{+7}_{-5}	$1.58^{+1.72}_{-1.48}$	$0.31^{+0.54}_{-0.31}$	$1.05^{+1.59}_{-1.05}$	4.3±3.9	3.0±2.3	7.6±4.0	$1.09^{+1.55}_{-1.42}$	- - -	C
1294	10^{+8}_{-7}	4^{+5}_{-4}	6^{+7}_{-6}	$2.37^{+1.95}_{-1.69}$	$0.53^{+0.64}_{-0.49}$	$1.47^{+1.76}_{-1.47}$	3.8±3.4	1.1±2.0	5.8±1.7	$1.44^{+1.75}_{-1.65}$	- - -	C
1295	6^{+4}_{-3}	6^{+4}_{-3}	4	$1.50^{+1.07}_{-0.79}$	$0.84^{+0.54}_{-0.37}$	1.10	1.3±0.2	1.1±0.1	1.4±0.2	$0.31^{+0.22}_{-0.17}$	- - H	A
1296	12^{+6}_{-5}	6^{+4}_{-3}	6^{+5}_{-4}	$2.94^{+1.57}_{-1.31}$	$0.83^{+0.59}_{-0.43}$	$1.49^{+1.37}_{-1.09}$	2.7±1.5	1.3±0.5	3.6±3.0	$1.28^{+0.99}_{-0.91}$	- - -	C
1297	13^{+5}_{-4}	2^{+3}_{-1}	11^{+5}_{-4}	$2.82^{+1.08}_{-0.84}$	$0.19^{+0.33}_{-0.16}$	$2.53^{+1.04}_{-0.80}$	3.8±0.7	2.7±0.5	5.2±0.8	$1.71^{+0.72}_{-0.60}$	- - -	D
1298	49^{+9}_{-8}	15^{+5}_{-4}	34^{+8}_{-7}	$11.92^{+2.16}_{-1.90}$	$2.06^{+0.73}_{-0.58}$	$8.42^{+1.89}_{-1.63}$	3.4±0.5	1.9±0.2	4.3±0.3	$6.57^{+1.47}_{-1.36}$	- - -	C
1299	11^{+5}_{-4}	2	12^{+5}_{-4}	$2.60^{+1.14}_{-0.89}$	0.30	$2.77^{+1.16}_{-0.91}$	3.7±0.4	3.3±0.4	4.5±0.4	$1.54^{+0.69}_{-0.55}$	- S -	E
1300	11^{+6}_{-5}	3^{+3}_{-2}	8^{+5}_{-4}	$2.53^{+1.26}_{-1.03}$	$0.38^{+0.43}_{-0.27}$	$1.91^{+1.16}_{-0.92}$	3.0±2.4	2.4±0.5	9.7±3.7	$1.21^{+1.13}_{-1.07}$	- - -	C
1301	12^{+5}_{-4}	1^{+2}_{-1}	12^{+5}_{-3}	$2.53^{+0.95}_{-0.73}$	$0.10^{+0.27}_{-0.10}$	$2.40^{+0.94}_{-0.72}$	4.3±0.3	3.3±0.7	4.7±0.2	$1.73^{+0.67}_{-0.52}$	- - -	E
1302	13^{+6}_{-5}	11^{+5}_{-3}	2^{+4}_{-2}	$3.41^{+1.43}_{-1.16}$	$1.59^{+0.66}_{-0.50}$	$0.59^{+1.05}_{-0.59}$	1.5±0.2	1.1±0.2	1.8±0.3	$0.82^{+0.37}_{-0.31}$	- - -	A
1303	7^{+5}_{-4}	1^{+3}_{-1}	6^{+4}_{-3}	$2.32^{+1.50}_{-1.16}$	$0.23^{+0.47}_{-0.23}$	$1.95^{+1.44}_{-1.09}$	5.8±3.0	2.5±2.0	9.7±2.4	$2.15^{+1.78}_{-1.55}$	- - -	C
1304	11^{+5}_{-3}	3	11^{+5}_{-3}	$2.28^{+0.94}_{-0.71}$	0.30	$2.37^{+0.95}_{-0.72}$	3.8±0.8	2.8±0.5	5.3±1.4	$1.38^{+0.63}_{-0.52}$	- S -	D

No.	C_{net} FB	C_{net} SB	C_{net} HB	$f_{\rm ph}$FB(10^{-6} cm^{-2} s^{-1})	$f_{\rm ph}$SB(10^{-6} cm^{-2} s^{-1})	$f_{\rm ph}$HB(10^{-6} cm^{-2} s^{-1})	E_{50} (keV)	E_{25} (keV)	E_{75} (keV)	f_X(10^{-14}erg cm^{-2} s^{-1})	Phot. Flag	Quantile Group
1305	19^{+6}_{-4}	18^{+5}_{-4}	2^{+3}_{-1}	$3.94^{+1.12}_{-0.90}$	$2.10^{+0.63}_{-0.50}$	$0.32^{+0.55}_{-0.27}$	1.1±0.1	0.9±0.1	1.4±0.2	$0.67^{+0.20}_{-0.17}$	- - -	A
1306	7^{+4}_{-3}	3	7^{+4}_{-3}	$1.23^{+0.71}_{-0.48}$	0.28	$1.27^{+0.73}_{-0.49}$	4.5±0.9	4.2±0.3	5.7±2.0	$0.89^{+0.54}_{-0.39}$	- S -	E
1307	7^{+4}_{-3}	6^{+4}_{-3}	1^{+3}_{-1}	$1.71^{+0.96}_{-0.70}$	$0.87^{+0.51}_{-0.34}$	$0.20^{+0.63}_{-0.20}$	1.1±1.3	0.9±0.2	1.9±3.9	$0.31^{+0.40}_{-0.38}$	- - -	B
1308	6^{+4}_{-3}	5^{+4}_{-2}	1^{+3}_{-1}	$1.25^{+0.89}_{-0.66}$	$0.61^{+0.43}_{-0.28}$	$0.19^{+0.67}_{-0.19}$	1.4±0.4	1.3±0.1	1.5±0.7	$0.27^{+0.21}_{-0.16}$	- - -	A
1309	273^{+30}_{-30}	5^{+12}_{-5}	267^{+28}_{-28}	$63.82^{+7.05}_{-7.05}$	$0.72^{+1.67}_{-0.72}$	$63.69^{+6.56}_{-6.56}$	4.5±0.2	3.6±0.1	5.5±0.3	$45.83^{+5.49}_{-5.49}$	- - -	D
1310	14^{+5}_{-4}	11^{+4}_{-3}	4^{+3}_{-2}	$2.69^{+0.92}_{-0.72}$	$1.17^{+0.48}_{-0.36}$	$0.69^{+0.60}_{-0.36}$	1.7±0.2	1.3±0.2	2.0±0.6	$0.72^{+0.27}_{-0.22}$	- - -	A
1311	15^{+5}_{-4}	6^{+4}_{-3}	9^{+5}_{-3}	$3.66^{+1.30}_{-1.05}$	$0.84^{+0.52}_{-0.35}$	$2.24^{+1.12}_{-0.85}$	2.1±0.5	1.2±0.3	2.7±0.5	$1.25^{+0.52}_{-0.45}$	- - -	B
1312	5^{+3}_{-2}	1^{+2}_{-1}	4^{+3}_{-2}	$2.81^{+2.01}_{-1.28}$	$0.33^{+0.80}_{-0.28}$	$2.29^{+1.92}_{-1.15}$	3.6±0.6	3.0±0.7	4.2±0.3	$1.62^{+1.19}_{-0.78}$	- - -	E
1313	8^{+4}_{-3}	7^{+4}_{-3}	1^{+2}_{-1}	$1.39^{+0.73}_{-0.52}$	$0.74^{+0.41}_{-0.28}$	$0.13^{+0.44}_{-0.13}$	1.3±0.3	0.9±0.2	1.6±0.5	$0.29^{+0.16}_{-0.12}$	- - -	B
1314	18^{+5}_{-4}	11^{+4}_{-3}	7^{+4}_{-3}	$3.34^{+1.01}_{-0.81}$	$1.20^{+0.49}_{-0.37}$	$1.29^{+0.73}_{-0.50}$	1.8±0.3	1.4±0.3	2.6±0.4	$0.95^{+0.33}_{-0.28}$	- - -	A
1315	42^{+10}_{-8}	9	43^{+10}_{-8}	$3.38^{+0.82}_{-0.67}$	0.42	$3.56^{+0.82}_{-0.66}$	4.6±0.2	3.9±0.3	4.7±0.1	$2.47^{+0.61}_{-0.50}$	- S -	E
1316	10^{+7}_{-6}	9^{+5}_{-4}	1^{+6}_{-1}	$2.22^{+1.55}_{-1.32}$	$1.11^{+0.62}_{-0.48}$	$0.28^{+1.29}_{-0.28}$	1.6±0.9	1.1±0.3	1.8±4.9	$0.58^{+0.53}_{-0.48}$	- - -	A
1317	6^{+4}_{-3}	5^{+3}_{-2}	1^{+3}_{-1}	$1.11^{+0.72}_{-0.49}$	$0.52^{+0.38}_{-0.24}$	$0.22^{+0.52}_{-0.22}$	1.2±0.4	1.1±0.1	1.8±0.5	$0.21^{+0.15}_{-0.11}$	- - -	A
1318	6^{+4}_{-3}	7^{+4}_{-3}	2	$1.28^{+0.76}_{-0.52}$	$0.80^{+0.44}_{-0.30}$	0.47	1.2±0.1	1.1±0.0	1.3±0.1	$0.24^{+0.14}_{-0.10}$	- - H	A
1319	13^{+5}_{-4}	11^{+4}_{-3}	2^{+3}_{-1}	$4.28^{+1.58}_{-1.21}$	$2.14^{+0.87}_{-0.65}$	$0.62^{+0.91}_{-0.44}$	1.4±0.2	1.1±0.1	1.9±1.2	$0.95^{+0.38}_{-0.31}$	- - -	A
1320	3^{+6}_{-3}	5	4^{+5}_{-4}	$1.20^{+2.26}_{-1.20}$	0.98	$1.46^{+2.12}_{-1.46}$	4.0±1.5	2.7±1.1	4.1±0.6	$0.77^{+1.48}_{-0.83}$	- S -	D
1321	56^{+9}_{-8}	3	56^{+9}_{-8}	$14.69^{+2.24}_{-1.97}$	0.40	$15.01^{+2.29}_{-2.01}$	4.6±0.3	3.4±0.2	5.8±0.4	$10.83^{+1.83}_{-1.65}$	- S -	D
1322	8^{+4}_{-3}	3^{+3}_{-2}	5^{+3}_{-2}	$4.13^{+2.12}_{-1.52}$	$0.89^{+0.90}_{-0.50}$	$2.62^{+1.86}_{-1.18}$	2.1±0.7	1.7±0.3	2.8±2.6	$1.39^{+0.86}_{-0.70}$	- - -	A
1323	7^{+4}_{-3}	1^{+2}_{-1}	6^{+4}_{-3}	$1.67^{+0.90}_{-0.65}$	$0.11^{+0.30}_{-0.11}$	$1.51^{+0.88}_{-0.60}$	2.8±0.4	2.0±0.3	3.2±0.3	$0.74^{+0.42}_{-0.31}$	- - -	E
1324	14^{+5}_{-4}	3^{+3}_{-2}	11^{+5}_{-3}	$3.12^{+1.09}_{-0.85}$	$0.36^{+0.37}_{-0.21}$	$2.55^{+1.03}_{-0.78}$	3.2±0.5	2.1±0.3	3.8±0.2	$1.57^{+0.61}_{-0.50}$	- - -	D
1325	12^{+6}_{-5}	2^{+3}_{-2}	10^{+5}_{-4}	$2.22^{+1.04}_{-0.84}$	$0.21^{+0.35}_{-0.21}$	$1.89^{+0.97}_{-0.77}$	5.1±1.9	2.7±1.3	6.8±2.1	$1.83^{+1.09}_{-0.97}$	- - -	C
1326	25^{+6}_{-5}	3	25^{+6}_{-5}	$5.10^{+1.26}_{-1.04}$	0.31	$5.23^{+1.29}_{-1.06}$	4.0±0.6	3.7±0.2	6.1±0.5	$3.27^{+0.95}_{-0.83}$	- S -	D
1327	9^{+5}_{-4}	2	10^{+5}_{-4}	$2.18^{+1.18}_{-0.92}$	0.30	$2.47^{+1.20}_{-0.94}$	3.9±0.7	3.4±0.5	5.2±0.8	$1.35^{+0.77}_{-0.62}$	- S -	E
1328	7^{+4}_{-3}	2	8^{+4}_{-3}	$1.83^{+1.07}_{-0.78}$	0.34	$2.02^{+1.09}_{-0.79}$	5.6±0.7	5.2±0.6	6.8±0.7	$1.64^{+0.98}_{-0.73}$	- S -	D
1329	4^{+4}_{-3}	6^{+4}_{-3}	3	$0.89^{+0.80}_{-0.58}$	$0.71^{+0.44}_{-0.30}$	0.59	1.0±0.2	0.9±0.1	1.1±0.1	$0.14^{+0.13}_{-0.09}$	- - H	A
1330	90^{+11}_{-10}	84^{+11}_{-9}	6^{+5}_{-3}	$10.08^{+1.30}_{-1.13}$	$5.38^{+0.69}_{-0.60}$	$0.62^{+0.60}_{-0.38}$	1.1±0.0	1.0±0.0	1.3±0.2	$1.72^{+0.23}_{-0.21}$	- - -	A
1331	7^{+4}_{-3}	1^{+2}_{-1}	7^{+4}_{-3}	$1.38^{+0.74}_{-0.53}$	$0.10^{+0.25}_{-0.09}$	$1.24^{+0.72}_{-0.49}$	4.0±1.3	2.4±1.0	5.8±1.1	$0.87^{+0.55}_{-0.45}$	- - -	C
1332	9^{+5}_{-4}	10^{+4}_{-3}	5	$2.04^{+1.09}_{-0.85}$	$1.21^{+0.55}_{-0.41}$	1.02	1.4±0.2	1.1±0.1	1.5±0.2	$0.46^{+0.25}_{-0.20}$	- - H	A
1333	6^{+5}_{-4}	2	8^{+5}_{-4}	$1.44^{+1.15}_{-0.89}$	0.30	$1.89^{+1.17}_{-0.91}$	7.7±1.7	6.4±1.2	9.7±1.2	$1.78^{+1.46}_{-1.16}$	- S -	D
1334	9^{+5}_{-4}	2^{+3}_{-2}	7^{+4}_{-3}	$2.04^{+1.15}_{-0.89}$	$0.21^{+0.40}_{-0.21}$	$1.71^{+1.08}_{-0.81}$	3.2±0.7	2.5±0.8	3.7±1.5	$1.04^{+0.63}_{-0.51}$	- - -	E
1335	13^{+5}_{-4}	1^{+2}_{-1}	12^{+5}_{-4}	$2.67^{+1.00}_{-0.77}$	$0.09^{+0.28}_{-0.09}$	$2.57^{+0.99}_{-0.76}$	3.4±0.8	2.5±0.4	5.8±1.3	$1.44^{+0.64}_{-0.54}$	- - -	C
1336	8^{+4}_{-3}	7^{+4}_{-3}	1^{+3}_{-1}	$1.59^{+0.80}_{-0.58}$	$0.76^{+0.43}_{-0.29}$	$0.28^{+0.53}_{-0.26}$	1.5±0.3	1.3±0.1	1.7±0.9	$0.38^{+0.21}_{-0.16}$	- - -	A
1337	22^{+7}_{-5}	9^{+5}_{-3}	13^{+6}_{-4}	$3.26^{+1.08}_{-0.84}$	$1.15^{+0.45}_{-0.29}$	$1.76^{+0.90}_{-0.66}$	2.7±0.3	1.6±0.3	3.1±0.5	$1.41^{+0.50}_{-0.40}$	- - -	E
1338	13^{+5}_{-4}	8^{+4}_{-3}	5^{+4}_{-2}	$2.77^{+1.07}_{-0.83}$	$0.97^{+0.50}_{-0.36}$	$1.10^{+0.81}_{-0.54}$	1.6±0.6	1.3±0.2	3.6±1.0	$0.72^{+0.39}_{-0.35}$	- - -	B
1339	10^{+4}_{-3}	3	10^{+4}_{-3}	$2.06^{+0.90}_{-0.68}$	0.30	$2.14^{+0.92}_{-0.69}$	4.8±0.9	3.9±0.5	6.8±0.8	$1.59^{+0.76}_{-0.61}$	- S -	D
1340	18^{+6}_{-5}	14^{+5}_{-4}	4^{+4}_{-3}	$3.92^{+1.28}_{-1.05}$	$1.74^{+0.61}_{-0.48}$	$0.88^{+0.88}_{-0.63}$	1.2±0.4	1.0±0.1	1.7±2.9	$0.75^{+0.35}_{-0.32}$	- - -	A
1341	18^{+6}_{-4}	3^{+3}_{-2}	14^{+5}_{-4}	$3.80^{+1.19}_{-0.96}$	$0.43^{+0.39}_{-0.23}$	$3.12^{+1.11}_{-0.88}$	3.1±0.6	2.4±0.4	4.3±0.4	$1.90^{+0.70}_{-0.60}$	- - -	D
1342	5^{+4}_{-3}	6^{+4}_{-3}	2	$2.11^{+1.57}_{-1.07}$	$1.53^{+0.90}_{-0.61}$	0.97	1.0±0.2	0.9±0.1	1.1±0.2	$0.33^{+0.25}_{-0.18}$	- - H	A

No.	C_{net} FB	C_{net} SB	C_{net} HB	$f_{\rm ph}$FB(10^{-6} cm^{-2} s^{-1})	$f_{\rm ph}$SB(10^{-6} cm^{-2} s^{-1})	$f_{\rm ph}$HB(10^{-6} cm^{-2} s^{-1})	E_{50} (keV)	E_{25} (keV)	E_{75} (keV)	f_X(10^{-14}erg cm^{-2} s^{-1})	Phot. Flag	Quantile Group
1343	9^{+4}_{-3}	9^{+4}_{-3}	1^{+3}_{-1}	$2.09^{+0.99}_{-0.74}$	$1.10^{+0.52}_{-0.38}$	$0.16^{+0.61}_{-0.16}$	1.2±0.2	1.0±0.1	1.4±0.5	$0.41^{+0.20}_{-0.16}$	- - -	A
1344	6^{+4}_{-3}	2	7^{+4}_{-3}	$1.27^{+0.77}_{-0.55}$	0.26	$1.37^{+0.79}_{-0.56}$	6.7±1.1	6.0±1.6	7.9±0.7	$1.36^{+0.86}_{-0.63}$	- S -	D
1345	13^{+5}_{-4}	1^{+3}_{-1}	12^{+5}_{-4}	$2.89^{+1.24}_{-1.00}$	$0.10^{+0.34}_{-0.10}$	$2.77^{+1.22}_{-0.96}$	4.5±0.7	3.2±1.0	5.6±1.1	$2.09^{+0.96}_{-0.79}$	- - -	D
1346	5^{+4}_{-2}	4^{+3}_{-2}	1^{+3}_{-1}	$1.15^{+0.80}_{-0.53}$	$0.49^{+0.41}_{-0.25}$	$0.31^{+0.61}_{-0.29}$	1.5±0.8	1.1±0.3	2.6±0.9	$0.28^{+0.24}_{-0.19}$	- - -	B
1347	9^{+6}_{-5}	4^{+4}_{-3}	5^{+5}_{-4}	$1.97^{+1.22}_{-1.00}$	$0.49^{+0.47}_{-0.32}$	$1.14^{+1.07}_{-0.83}$	3.9±2.7	1.0±1.6	7.2±1.5	$1.24^{+1.13}_{-1.05}$	- - -	C
1348	7^{+4}_{-3}	2	7^{+4}_{-3}	$1.32^{+0.77}_{-0.55}$	0.27	$1.41^{+0.79}_{-0.57}$	4.4±0.9	3.8±0.6	6.1±0.8	$0.93^{+0.57}_{-0.43}$	- S -	D
1349	9^{+4}_{-3}	7^{+4}_{-3}	1^{+3}_{-1}	$1.81^{+0.91}_{-0.69}$	$0.89^{+0.47}_{-0.34}$	$0.27^{+0.62}_{-0.27}$	1.4±0.5	1.1±0.2	1.7±1.1	$0.41^{+0.25}_{-0.21}$	- - -	A
1350	3^{+9}_{-3}	2^{+5}_{-2}	1^{+8}_{-1}	$0.84^{+2.61}_{-0.84}$	$0.36^{+0.78}_{-0.36}$	$0.21^{+2.48}_{-0.21}$	9.8±9.3	0.9±9.1	9.9±9.4	$1.32^{+4.29}_{-1.82}$	- - -	C
1351	20^{+6}_{-5}	9^{+4}_{-3}	11^{+5}_{-4}	$4.81^{+1.50}_{-1.24}$	$1.19^{+0.60}_{-0.44}$	$2.76^{+1.25}_{-0.98}$	2.0±0.9	1.5±0.2	4.2±0.5	$1.56^{+0.86}_{-0.82}$	- - -	B
1352	4^{+4}_{-2}	6^{+4}_{-2}	2	$1.01^{+0.85}_{-0.56}$	$0.74^{+0.48}_{-0.32}$	0.55	0.9±0.3	0.7±0.2	1.3±0.2	$0.14^{+0.13}_{-0.09}$	- - H	B
1353	12^{+5}_{-4}	5^{+4}_{-2}	7^{+4}_{-3}	$2.50^{+1.05}_{-0.82}$	$0.62^{+0.44}_{-0.29}$	$1.45^{+0.89}_{-0.65}$	2.7±0.7	1.8±0.3	3.4±2.1	$1.09^{+0.54}_{-0.46}$	- - -	D
1354	8^{+5}_{-3}	5^{+4}_{-2}	3^{+4}_{-2}	$1.84^{+1.01}_{-0.77}$	$0.65^{+0.45}_{-0.30}$	$0.72^{+0.82}_{-0.54}$	1.8±0.7	1.6±0.2	3.3±1.2	$0.54^{+0.36}_{-0.30}$	- - -	B
1355	20^{+7}_{-5}	5^{+4}_{-3}	14^{+6}_{-5}	$2.75^{+0.99}_{-0.72}$	$1.02^{+0.36}_{-0.16}$	$2.12^{+0.92}_{-0.65}$	3.3±0.6	2.0±0.6	4.4±0.4	$1.46^{+0.58}_{-0.46}$	- - -	C
1356	15^{+5}_{-4}	5^{+3}_{-2}	11^{+5}_{-3}	$3.60^{+1.22}_{-0.96}$	$0.62^{+0.45}_{-0.29}$	$2.56^{+1.09}_{-0.83}$	3.4±0.7	1.9±0.4	4.1±0.7	$1.96^{+0.77}_{-0.65}$	- - -	C
1357	8^{+4}_{-3}	3^{+3}_{-2}	5^{+4}_{-2}	$1.58^{+0.83}_{-0.60}$	$0.33^{+0.34}_{-0.19}$	$1.04^{+0.74}_{-0.49}$	3.5±1.3	1.7±0.9	5.1±0.6	$0.89^{+0.57}_{-0.48}$	- - -	C
1358	131^{+11}_{-11}	89^{+10}_{-9}	42^{+8}_{-7}	$27.06^{+2.38}_{-2.38}$	$10.58^{+1.25}_{-1.13}$	$8.86^{+1.61}_{-1.39}$	1.5±0.1	1.2±0.0	2.1±0.2	$6.49^{+0.64}_{-0.64}$	- - -	A
1359	16^{+6}_{-5}	15^{+6}_{-4}	4^{+4}_{-2}	$1.82^{+0.74}_{-0.53}$	$1.52^{+0.39}_{-0.28}$	$0.44^{+0.86}_{-0.44}$	1.0±0.1	0.9±0.1	1.4±0.2	$0.30^{+0.13}_{-0.10}$	- - -	A
1360	5^{+4}_{-2}	4^{+3}_{-2}	1^{+3}_{-1}	$1.02^{+0.76}_{-0.50}$	$0.45^{+0.39}_{-0.23}$	$0.25^{+0.57}_{-0.25}$	1.8±0.4	1.5±0.2	2.3±0.5	$0.29^{+0.23}_{-0.16}$	- - -	A
1361	5^{+4}_{-2}	1^{+2}_{-1}	4^{+3}_{-2}	$0.93^{+0.74}_{-0.49}$	$0.07^{+0.28}_{-0.07}$	$0.82^{+0.72}_{-0.45}$	4.9±1.3	3.6±1.4	6.0±0.6	$0.73^{+0.62}_{-0.43}$	- - -	D
1362	17^{+9}_{-8}	3^{+5}_{-3}	14^{+8}_{-7}	$3.98^{+1.98}_{-1.75}$	$0.36^{+0.60}_{-0.36}$	$3.42^{+1.83}_{-1.59}$	5.1±0.8	3.6±1.7	5.9±1.8	$3.27^{+1.70}_{-1.52}$	- - -	D
1363	84^{+11}_{-10}	75^{+10}_{-9}	9^{+6}_{-5}	$9.66^{+1.31}_{-1.14}$	$5.78^{+0.67}_{-0.57}$	$0.95^{+0.68}_{-0.47}$	1.1±0.0	0.9±0.0	1.4±0.1	$1.71^{+0.24}_{-0.22}$	- - -	A
1364	6^{+5}_{-4}	1^{+3}_{-1}	5^{+4}_{-3}	$1.40^{+1.09}_{-0.83}$	$0.16^{+0.36}_{-0.16}$	$1.15^{+1.04}_{-0.78}$	3.5±1.8	2.8±1.6	5.8±1.3	$0.79^{+0.74}_{-0.62}$	- - -	C
1365	14^{+6}_{-5}	7^{+4}_{-3}	7^{+5}_{-4}	$3.39^{+1.35}_{-1.09}$	$0.97^{+0.54}_{-0.39}$	$1.72^{+1.14}_{-0.87}$	1.9±0.7	1.2±0.2	2.7±2.5	$1.05^{+0.55}_{-0.49}$	- - -	B
1366	13^{+5}_{-4}	2^{+3}_{-1}	12^{+5}_{-4}	$5.52^{+2.10}_{-1.63}$	$0.38^{+0.64}_{-0.31}$	$4.96^{+2.03}_{-1.56}$	3.7±0.7	2.6±0.7	5.2±0.6	$3.28^{+1.39}_{-1.16}$	- - -	C
1367	46^{+9}_{-7}	34^{+7}_{-6}	12^{+6}_{-4}	$5.25^{+1.07}_{-0.87}$	$2.89^{+0.52}_{-0.40}$	$1.42^{+0.73}_{-0.50}$	1.6±0.1	1.2±0.1	2.4±0.6	$1.36^{+0.30}_{-0.25}$	- - -	B
1368	45^{+9}_{-7}	45^{+8}_{-7}	3^{+4}_{-1}	$5.34^{+1.06}_{-0.88}$	$3.74^{+0.57}_{-0.46}$	$0.12^{+0.95}_{-0.12}$	1.2±0.1	1.0±0.0	1.3±0.1	$1.00^{+0.21}_{-0.17}$	- - -	A
1369	34^{+7}_{-6}	30^{+7}_{-6}	4^{+4}_{-3}	$8.08^{+1.77}_{-1.52}$	$4.05^{+0.90}_{-0.76}$	$0.93^{+1.00}_{-0.73}$	1.2±0.1	0.9±0.1	1.5±0.2	$1.56^{+0.37}_{-0.32}$	- - -	A
1370	2^{+4}_{-2}	3^{+3}_{-2}	4	$0.57^{+1.05}_{-0.57}$	$0.51^{+0.50}_{-0.32}$	1.04	1.1±8.9	0.9±9.1	1.2±8.8	$0.10^{+0.84}_{-0.83}$	- - H	A
1371	7^{+4}_{-3}	2	7^{+4}_{-3}	$3.21^{+1.85}_{-1.32}$	0.66	$3.39^{+1.88}_{-1.35}$	4.3±1.2	3.4±0.8	6.5±0.8	$2.22^{+1.41}_{-1.09}$	- S -	D
1372	28^{+6}_{-5}	21^{+6}_{-5}	7^{+4}_{-3}	$5.41^{+1.25}_{-1.04}$	$2.38^{+0.65}_{-0.52}$	$1.35^{+0.76}_{-0.52}$	1.3±0.1	1.0±0.1	2.0±0.4	$1.14^{+0.29}_{-0.25}$	- - -	B
1373	6^{+4}_{-2}	3	6^{+4}_{-2}	$1.08^{+0.70}_{-0.46}$	0.30	$1.12^{+0.71}_{-0.47}$	5.0±1.2	3.7±0.9	6.8±1.1	$0.85^{+0.59}_{-0.42}$	- S -	D
1374	286^{+17}_{-17}	157^{+13}_{-13}	129^{+12}_{-12}	$33.05^{+2.01}_{-1.99}$	$10.22^{+0.84}_{-0.82}$	$15.28^{+1.41}_{-1.38}$	1.8±0.1	1.3±0.1	2.5±0.2	$9.43^{+0.81}_{-0.80}$	- - -	A
1375	5^{+5}_{-4}	1^{+3}_{-1}	4^{+4}_{-3}	$1.13^{+1.08}_{-0.83}$	$0.08^{+0.36}_{-0.08}$	$1.02^{+1.04}_{-0.77}$	7.9±2.7	7.2±3.9	8.6±0.8	$1.43^{+1.46}_{-1.16}$	- - -	D
1376	33^{+7}_{-6}	27^{+6}_{-5}	6^{+4}_{-3}	$8.09^{+1.79}_{-1.53}$	$3.70^{+0.89}_{-0.74}$	$1.55^{+1.09}_{-0.80}$	1.4±0.1	1.1±0.1	1.8±0.3	$1.80^{+0.43}_{-0.38}$	- - -	A
1377	6^{+5}_{-4}	6^{+4}_{-3}	5	$1.49^{+1.22}_{-0.95}$	$0.81^{+0.56}_{-0.40}$	1.39	1.3±0.3	1.0±0.2	1.5±0.2	$0.31^{+0.26}_{-0.21}$	- - H	A
1378	8^{+4}_{-3}	7^{+4}_{-3}	1^{+2}_{-1}	$1.47^{+0.77}_{-0.55}$	$0.78^{+0.43}_{-0.29}$	$0.13^{+0.46}_{-0.13}$	1.1±0.1	1.0±0.0	1.1±0.3	$0.25^{+0.13}_{-0.10}$	- - -	A
1379	233^{+15}_{-15}	172^{+13}_{-13}	61^{+9}_{-8}	$105.33^{+6.98}_{-6.98}$	$43.41^{+3.33}_{-3.33}$	$28.29^{+4.22}_{-3.74}$	1.5±0.1	1.1±0.0	2.1±0.2	$25.27^{+2.00}_{-2.00}$	- - -	B
1380	9^{+4}_{-3}	9^{+4}_{-3}	3	$2.87^{+1.34}_{-0.98}$	$1.69^{+0.78}_{-0.57}$	0.85	1.4±0.2	1.3±0.1	1.7±0.1	$0.65^{+0.31}_{-0.23}$	- - H	A

No.	C_{net} FB	C_{net} SB	C_{net} HB	$f_{\rm ph}$FB(10^{-6} cm^{-2} s^{-1})	$f_{\rm ph}$SB(10^{-6} cm^{-2} s^{-1})	$f_{\rm ph}$HB(10^{-6} cm^{-2} s^{-1})	E_{50} (keV)	E_{25} (keV)	E_{75} (keV)	f_X(10^{-14}erg cm^{-2} s^{-1})	Phot. Flag	Quantile Group
1381	9^{+5}_{-4}	4	9^{+5}_{-4}	$2.10^{+1.27}_{-1.01}$	0.51	$2.21^{+1.24}_{-0.97}$	4.1±0.7	3.6±0.5	4.9±1.0	$1.36^{+0.85}_{-0.69}$	- S -	E
1382	17^{+5}_{-4}	15^{+5}_{-4}	2^{+3}_{-1}	$3.85^{+1.20}_{-0.95}$	$2.00^{+0.66}_{-0.52}$	$0.40^{+0.63}_{-0.30}$	1.2±0.1	1.0±0.1	1.3±0.5	$0.72^{+0.23}_{-0.19}$	- - -	A
1383	10^{+5}_{-3}	2^{+3}_{-1}	9^{+4}_{-3}	$2.18^{+0.99}_{-0.75}$	$0.20^{+0.33}_{-0.16}$	$1.88^{+0.94}_{-0.70}$	4.1±0.9	2.5±0.7	4.8±1.1	$1.45^{+0.72}_{-0.58}$	- - -	C
1384	3^{+4}_{-2}	4^{+3}_{-2}	3	$0.55^{+0.77}_{-0.51}$	$0.47^{+0.42}_{-0.27}$	0.63	1.0±0.3	0.9±0.1	1.2±0.2	$0.09^{+0.13}_{-0.09}$	- - H	A
1385	8^{+4}_{-3}	4^{+3}_{-2}	4^{+3}_{-2}	$1.49^{+0.77}_{-0.55}$	$0.44^{+0.36}_{-0.22}$	$0.75^{+0.63}_{-0.38}$	2.2±1.0	1.6±0.4	4.0±2.2	$0.53^{+0.37}_{-0.32}$	- - -	C
1386	16^{+9}_{-8}	10^{+5}_{-4}	6^{+8}_{-6}	$3.72^{+2.15}_{-1.85}$	$1.32^{+0.72}_{-0.54}$	$1.48^{+1.93}_{-1.48}$	1.6±0.5	1.3±0.3	2.4±4.8	$0.93^{+0.62}_{-0.56}$	- - -	A
1387	8^{+6}_{-5}	4^{+4}_{-3}	4^{+5}_{-4}	$1.87^{+1.45}_{-1.20}$	$0.51^{+0.52}_{-0.35}$	$0.98^{+1.29}_{-0.98}$	4.6±3.0	1.9±1.5	7.7±3.4	$1.38^{+1.40}_{-1.26}$	- - -	C
1388	29^{+7}_{-6}	26^{+6}_{-5}	3^{+3}_{-2}	$6.65^{+1.55}_{-1.31}$	$3.45^{+0.82}_{-0.68}$	$0.60^{+0.80}_{-0.51}$	1.2±0.1	1.0±0.1	1.5±0.2	$1.23^{+0.30}_{-0.26}$	- - -	A
1389	9^{+5}_{-3}	7^{+4}_{-3}	2^{+3}_{-2}	$2.09^{+1.02}_{-0.78}$	$0.94^{+0.51}_{-0.36}$	$0.45^{+0.73}_{-0.44}$	1.1±0.3	1.0±0.1	1.5±0.4	$0.37^{+0.20}_{-0.16}$	- - -	A
1390	3^{+3}_{-2}	4^{+3}_{-2}	2	$0.69^{+0.65}_{-0.39}$	$0.45^{+0.37}_{-0.22}$	0.48	1.3±0.2	1.0±0.2	1.4±0.1	$0.14^{+0.14}_{-0.09}$	- - H	A
1391	37^{+9}_{-8}	2^{+4}_{-2}	35^{+9}_{-7}	$3.90^{+1.01}_{-0.81}$	$0.27^{+0.51}_{-0.27}$	$4.03^{+1.01}_{-0.81}$	3.6±0.3	2.6±0.3	4.2±0.4	$2.23^{+0.60}_{-0.50}$	- - -	D
1392	4^{+3}_{-2}	4^{+3}_{-2}	2	$0.71^{+0.63}_{-0.38}$	$0.44^{+0.36}_{-0.22}$	0.49	1.3±0.2	1.1±0.2	1.6±0.1	$0.15^{+0.14}_{-0.09}$	- - H	A
1393	3^{+4}_{-2}	4^{+3}_{-2}	3	$0.74^{+0.81}_{-0.53}$	$0.53^{+0.43}_{-0.26}$	0.76	1.2±0.1	1.1±0.0	1.3±0.1	$0.14^{+0.15}_{-0.10}$	- - H	A
1394	5	5^{+4}_{-3}	2	1.20	$0.74^{+0.55}_{-0.37}$	0.61	5.2±4.8	2.9±7.1	7.6±7.1	1.01	F - H	C
1395	5^{+4}_{-2}	3^{+3}_{-2}	2^{+3}_{-2}	$1.11^{+0.89}_{-0.59}$	$0.39^{+0.42}_{-0.23}$	$0.45^{+0.75}_{-0.42}$	1.2±2.9	1.1±0.8	7.0±3.2	$0.22^{+0.55}_{-0.53}$	- - -	B
1396	1^{+2}_{-1}	3	1^{+2}_{-1}	$0.11^{+0.47}_{-0.11}$	0.30	$0.13^{+0.48}_{-0.13}$	2.4±7.6	1.3±8.7	4.8±5.2	$0.04^{+0.23}_{-0.14}$	- S -	C
1397	20^{+7}_{-6}	11^{+5}_{-4}	9^{+6}_{-5}	$4.07^{+1.50}_{-1.27}$	$1.30^{+0.58}_{-0.45}$	$1.85^{+1.27}_{-1.03}$	2.0±1.1	1.1±0.3	6.6±3.7	$1.28^{+0.85}_{-0.82}$	- - -	B
1398	4^{+3}_{-2}	4^{+3}_{-2}	2	$0.90^{+0.79}_{-0.47}$	$0.56^{+0.45}_{-0.27}$	0.61	1.0±0.2	0.8±0.1	1.2±0.2	$0.14^{+0.13}_{-0.08}$	- - H	A
1399	9^{+5}_{-3}	8^{+4}_{-3}	1^{+3}_{-1}	$2.31^{+1.17}_{-0.89}$	$1.20^{+0.60}_{-0.44}$	$0.20^{+0.77}_{-0.20}$	0.8±0.2	0.8±0.1	1.3±0.3	$0.31^{+0.18}_{-0.14}$	- - -	A
1400	5^{+4}_{-3}	4	5^{+4}_{-3}	$1.25^{+0.92}_{-0.66}$	0.50	$1.17^{+0.90}_{-0.61}$	5.0±3.1	3.1±1.4	9.6±2.0	$1.01^{+0.96}_{-0.81}$	- S -	C
1401	8^{+4}_{-3}	9^{+4}_{-3}	2	$4.13^{+2.01}_{-1.47}$	$2.49^{+1.15}_{-0.84}$	1.14	1.1±0.2	1.0±0.1	1.5±0.2	$0.72^{+0.37}_{-0.28}$	- - H	A
1402	7^{+5}_{-4}	5^{+4}_{-3}	2^{+4}_{-2}	$1.73^{+1.15}_{-0.89}$	$0.70^{+0.50}_{-0.34}$	$0.51^{+0.92}_{-0.51}$	1.5±0.4	1.4±0.3	2.0±0.6	$0.40^{+0.29}_{-0.23}$	- - -	A
1403	9^{+5}_{-3}	8^{+4}_{-3}	1^{+3}_{-1}	$2.09^{+1.08}_{-0.82}$	$1.10^{+0.55}_{-0.40}$	$0.16^{+0.71}_{-0.16}$	1.0±0.2	0.9±0.1	1.4±0.3	$0.35^{+0.19}_{-0.15}$	- - -	A
1404	14^{+5}_{-4}	2^{+3}_{-2}	12^{+5}_{-4}	$3.34^{+1.26}_{-1.00}$	$0.30^{+0.40}_{-0.22}$	$2.86^{+1.20}_{-0.93}$	3.9±0.6	2.8±0.9	5.3±0.5	$2.09^{+0.86}_{-0.71}$	- - -	D
1405	43^{+8}_{-7}	10^{+5}_{-3}	33^{+7}_{-6}	$10.33^{+1.95}_{-1.69}$	$1.39^{+0.63}_{-0.47}$	$8.05^{+1.76}_{-1.50}$	2.6±0.2	2.1±0.2	3.4±0.3	$4.23^{+0.90}_{-0.81}$	- - -	E
1406	4^{+10}_{-4}	6	4^{+9}_{-4}	$0.85^{+2.35}_{-0.85}$	0.85	$1.07^{+2.21}_{-1.07}$	7.5±7.0	2.6±7.4	9.6±5.3	$1.02^{+2.98}_{-1.39}$	- S -	C
1407	66^{+9}_{-8}	46^{+8}_{-7}	20^{+6}_{-5}	$15.13^{+2.17}_{-1.93}$	$5.99^{+1.04}_{-0.90}$	$4.67^{+1.39}_{-1.13}$	1.6±0.1	1.2±0.1	2.4±0.4	$3.93^{+0.60}_{-0.54}$	- - -	B
1408	57^{+9}_{-8}	5^{+4}_{-2}	52^{+9}_{-7}	$12.67^{+1.99}_{-1.76}$	$0.62^{+0.46}_{-0.30}$	$11.84^{+1.95}_{-1.71}$	3.7±0.2	2.9±0.3	4.5±0.2	$7.43^{+1.22}_{-1.09}$	- - -	E
1409	13^{+6}_{-4}	3^{+3}_{-2}	9^{+5}_{-4}	$2.90^{+1.25}_{-1.00}$	$0.43^{+0.44}_{-0.28}$	$2.20^{+1.14}_{-0.88}$	3.2±1.0	1.8±0.6	4.4±1.6	$1.47^{+0.78}_{-0.68}$	- - -	C
1410	10^{+5}_{-4}	6^{+4}_{-3}	4^{+4}_{-3}	$2.45^{+1.24}_{-0.98}$	$0.84^{+0.53}_{-0.38}$	$0.99^{+1.00}_{-0.73}$	1.3±1.5	1.1±0.3	4.5±3.1	$0.51^{+0.64}_{-0.62}$	- - -	B
1411	10^{+5}_{-4}	11^{+5}_{-3}	4	$3.10^{+1.53}_{-1.19}$	$1.86^{+0.78}_{-0.59}$	1.27	1.3±0.2	1.0±0.2	1.4±0.1	$0.64^{+0.33}_{-0.26}$	- - H	A
1412	14^{+6}_{-5}	8^{+4}_{-3}	6^{+5}_{-4}	$3.61^{+1.54}_{-1.28}$	$1.17^{+0.63}_{-0.47}$	$1.55^{+1.26}_{-0.98}$	1.8±0.5	1.4±0.2	2.7±2.3	$1.02^{+0.53}_{-0.47}$	- - -	A
1413	12^{+6}_{-5}	11^{+5}_{-4}	2^{+4}_{-2}	$3.32^{+1.53}_{-1.24}$	$1.63^{+0.71}_{-0.54}$	$0.42^{+1.10}_{-0.42}$	0.8±0.3	0.8±0.0	1.0±3.8	$0.44^{+0.25}_{-0.22}$	- - -	A
1414	5	2	6	1.33	0.32	1.53	5.2±4.8	2.9±7.1	7.6±7.1	1.12	F S H	C
1415	7^{+6}_{-5}	6^{+4}_{-3}	1^{+5}_{-1}	$1.90^{+1.49}_{-1.22}$	$0.92^{+0.60}_{-0.44}$	$0.26^{+1.24}_{-0.26}$	1.9±1.9	1.6±0.5	2.0±6.1	$0.58^{+0.74}_{-0.69}$	- - -	A

A.3 Table of Infrared Counterparts

(1) NARCS catalog source number.
(2) Name of VVV source that is closest to the *Chandra* source position, within 3σ of the position provided in Table 2.3.
(3) Right ascension (J2000.0) of the VVV source.
(4) Declination (J2000.0) of the VVV source.
(5) Angular separation between the *Chandra* and VVV source.
(6) Probability that the VVV source is a noise fluctuation, provided in the VVV catalog.
(7) Reliability of the VVV counterpart calculated according to the method of Sutherland & Saunders (1992). The reliability depends on the distance between the X-ray and IR sources, the positional uncertainties of the X-ray and IR sources, and the spatial density of IR sources. The reliability is expressed as a fraction between zero and one; VVV sources with a higher reliability are more likely to be true IR counterparts to the *Chandra* sources.

Table A.3: *Chandra* Catalog of Point and Extended Sources: Infrared Counterparts

No.	VVV Source Name	R.A. (deg)	Dec. (deg)	Δ_{X-IR} (arcsec)	p_{noise}	Reliability
(1)	(2)	(3)	(4)	(5)	(6)	(7)
1	515727792649	248.117752	-47.631649	1.89	3.07e-03	0.3216
2	515726841264	248.172806	-47.677017	1.84	5.29e-07	0.8660
3	515726837733	248.185730	-47.693638	4.13	5.29e-07	0.3508
4	515727238897	248.203003	-47.505127	1.05	1.71e-04	0.7804
5	515726847521	248.212341	-47.693485	1.52	1.71e-04	0.9482
6	515727540494	248.220947	-47.700108	0.76	1.71e-04	0.9142
7	515726868309	248.246140	-47.638630	0.64	5.29e-07	0.9777
8	515726918176	248.247345	-47.468082	0.78	9.52e-06	0.4607
9	515726930863	248.262817	-47.429794	1.29	5.29e-07	0.0657
10	515727577185	248.276459	-47.544682	1.59	2.81e-04	0.8825
11	515726849311	248.284439	-47.720947	1.66	1.71e-04	0.4653
12	—	-	-	-	-	-
13	515726902991	248.301819	-47.556408	0.30	9.52e-06	0.9888
14	—	-	-	-	-	-
15	—	-	-	-	-	-
16	—	-	-	-	-	-
17	515726886955	248.315262	-47.624165	0.69	9.52e-06	0.9662
18	515727536700	248.316101	-47.778404	1.08	1.55e-03	0.0523
19	515726892336	248.319962	-47.608994	0.18	5.29e-07	0.9921
20	515726916284	248.320389	-47.522675	0.15	5.29e-07	0.9902
21	515726872863	248.321442	-47.673111	0.33	5.29e-07	0.9882
22	515726900711	248.325470	-47.579105	0.08	5.29e-07	0.9925
23	515727236656	248.331909	-47.619701	1.16	1.71e-04	0.8759
24	515726896348	248.342468	-47.606651	0.48	1.62e-04	0.9819
25	515726886643	248.343933	-47.651249	0.82	5.29e-07	0.9691
26	515726939169	248.344574	-47.450134	0.96	5.29e-07	0.1770
27	515726935318	248.346451	-47.465511	0.64	6.80e-07	0.1182
28	515726888298	248.346817	-47.641685	0.75	5.29e-07	0.9644
29	515726886646	248.348068	-47.646889	0.31	5.29e-07	0.9891
30	515727822171	248.349823	-47.435467	3.21	3.07e-03	0.4811
31	515726895046	248.354202	-47.624043	0.09	5.29e-07	0.9917
32	515726921314	248.354263	-47.527267	0.81	9.53e-06	0.9627
33	515726835781	248.356781	-47.809982	2.82	5.29e-07	0.5577
34	515726918568	248.359360	-47.534481	1.48	1.62e-04	0.4898

Chandra Catalog: Infrared Counterparts (continued)

No.	VVV Source Name	R.A. (deg)	Dec. (deg)	$\Delta_{\mathrm{X-IR}}$ (arcsec)	p_{noise}	Reliability
35	—	-	-	-	-	-
36	515726915754	248.368668	-47.550976	0.56	5.29e-07	0.9781
37	515726928476	248.372375	-47.507313	0.61	5.29e-07	0.9634
38	515727245968	248.373215	-47.559093	0.15	9.53e-06	0.9939
39	—	-	-	-	-	-
40	515726951422	248.378479	-47.426388	0.68	5.29e-07	0.9664
41	515726876489	248.386765	-47.700935	1.07	5.29e-07	0.5932
42	515726927264	248.387756	-47.530861	2.61	1.62e-04	0.3316
43	—	-	-	-	-	-
44	515727617958	248.397186	-47.395027	3.90	2.92e-03	0.3047
45	515726965153	248.397690	-47.393360	1.60	5.29e-07	0.7562
46	—	-	-	-	-	-
47	515726933821	248.398346	-47.503017	0.66	1.62e-04	0.9747
48	515726858944	248.399689	-47.763542	1.06	6.80e-07	0.6330
49	515726972327	248.400757	-47.373447	0.28	5.29e-07	0.9252
50	—	-	-	-	-	-
51	515726932059	248.403870	-47.519299	1.62	5.29e-07	0.7710
52	515726962286	248.406509	-47.411800	0.86	5.29e-07	0.9563
53	515726847345	248.407928	-47.808243	2.14	5.29e-07	0.8048
54	515726920408	248.411133	-47.560318	0.19	5.29e-07	0.9918
55	515727546584	248.411270	-47.788212	1.46	2.92e-03	0.2320
56	515726873309	248.412537	-47.729134	3.09	9.53e-06	0.0933
57	515726845546	248.417068	-47.813835	1.44	1.62e-04	0.8816
58	515727627704	248.420197	-47.361183	1.94	2.92e-03	0.7080
59	—	-	-	-	-	-
60	515727270718	248.424301	-47.405876	1.36	1.21e-04	0.4989
61	515726970209	248.425034	-47.392921	3.01	5.29e-07	0.5471
62	515732384008	248.425613	-47.757118	0.69	3.07e-03	0.5515
63	515726919982	248.430969	-47.576023	1.60	5.29e-07	0.7219
64	515726927774	248.432709	-47.554955	0.90	9.52e-06	0.9633
65	515726927788	248.436661	-47.557644	0.89	1.62e-04	0.9533
66	515731861511	248.438126	-47.772339	1.71	1.71e-04	0.0300
67	515726885017	248.441437	-47.712498	1.52	5.29e-07	0.7666
68	515731836990	248.444489	-47.813679	0.38	2.92e-03	0.7228
69	515726978475	248.449066	-47.382710	0.75	9.52e-06	0.9706
70	515726870055	248.448502	-47.759991	1.54	5.29e-07	0.8369
71	515727225879	248.453079	-47.772549	3.76	3.07e-03	0.0527
72	—	-	-	-	-	-
73	515727009631	248.467117	-47.304317	0.27	5.29e-07	0.9627
74	515727024557	248.467972	-47.261200	0.71	9.52e-06	0.1897
75	515726920702	248.475739	-47.615055	1.14	8.75e-07	0.6027
76	515727249359	248.478088	-47.616798	0.70	3.07e-03	0.9411
77	515726930329	248.478348	-47.567638	0.24	5.29e-07	0.9818
78	515726911773	248.479614	-47.634678	0.07	1.62e-04	0.9945
79	515727619083	248.482376	-47.443478	0.42	2.92e-03	0.9842
80	515726891995	248.491608	-47.714260	0.98	9.52e-06	0.9163
81	515727236330	248.495575	-47.704136	0.16	1.54e-03	0.9931
82	515726966091	248.495667	-47.450733	0.06	5.29e-07	0.9895
83	515727023388	248.497116	-47.279175	1.34	6.80e-07	0.5574
84	515727602199	248.508743	-47.545742	0.30	3.07e-03	0.6248
85	515726956974	248.509842	-47.489536	5.03	1.71e-04	0.2845
86	—	-	-	-	-	-
87	—	-	-	-	-	-
88	515726926068	248.519913	-47.617504	0.99	5.29e-07	0.9597
89	515726951465	248.524048	-47.515182	0.60	5.29e-07	0.9375
90	515726888585	248.527618	-47.750206	0.26	9.53e-06	0.9879
91	515732372434	248.531067	-47.912136	3.22	3.07e-03	0.0330
92	—	-	-	-	-	-
93	515727578573	248.542603	-47.701954	0.16	1.71e-04	0.9905

Chandra Catalog: Infrared Counterparts (continued)

No.	VVV Source Name	R.A. (deg)	Dec. (deg)	$\Delta_{\mathrm{X-IR}}$ (arcsec)	p_{noise}	Reliability
94	515726927377	248.551636	-47.622246	0.95	1.62e-04	0.8775
95	515726877136	248.555450	-47.803242	0.78	5.29e-07	0.9687
96	515731857641	248.556686	-47.853981	1.61	1.71e-04	0.6772
97	515721375089	248.566101	-47.269386	1.36	3.07e-03	0.8623
98	515727274310	248.567688	-47.454254	0.21	1.71e-04	0.9915
99	515726986399	248.569595	-47.433563	0.19	9.53e-06	0.9874
100	515727030236	248.570190	-47.304718	1.59	1.62e-04	0.7854
101	—	-	-	-	-	-
102	515719995615	248.574310	-47.234753	0.92	5.29e-07	0.2709
103	515726892227	248.574768	-47.766094	0.46	5.29e-07	0.9779
104	515726954807	248.575821	-47.535477	0.53	5.29e-07	0.9613
105	515727010007	248.575211	-47.372810	2.70	1.62e-04	0.5622
106	515727020542	248.582840	-47.341137	1.16	1.54e-03	0.3064
107	—	-	-	-	-	-
108	—	-	-	-	-	-
109	515731888973	248.589035	-47.829006	1.16	1.71e-04	0.5439
110	—	-	-	-	-	-
111	515727005478	248.590836	-47.390930	0.05	6.80e-07	0.9900
112	—	-	-	-	-	-
113	515726908002	248.594437	-47.721920	0.35	9.53e-06	0.9857
114	515727036512	248.595139	-47.301022	0.89	1.71e-04	0.5946
115	515727820877	248.597214	-47.606785	3.44	3.07e-03	0.2777
116	—	-	-	-	-	-
117	515727597156	248.597900	-47.628376	0.95	1.71e-04	0.3969
118	515726938431	248.605835	-47.616306	1.16	5.29e-07	0.9369
119	—	-	-	-	-	-
120	515726956310	248.609390	-47.552338	1.48	1.62e-04	0.7565
121	515719978197	248.610977	-47.311214	0.97	5.29e-07	0.5992
122	515727000452	248.611450	-47.418983	0.20	5.29e-07	0.9885
123	515726953188	248.611710	-47.562889	0.87	5.29e-07	0.7956
124	515726910695	248.612152	-47.722424	0.37	1.62e-04	0.9856
125	515727037379	248.612534	-47.310509	0.35	5.29e-07	0.9833
126	515727269852	248.621674	-47.537827	1.60	1.71e-04	0.5765
127	515719998064	248.627548	-47.266396	0.80	1.62e-04	0.9653
128	515731927781	248.630127	-47.794415	0.77	1.71e-04	0.8578
129	515727017501	248.631668	-47.381599	1.10	9.52e-06	0.9543
130	515721074747	248.633774	-47.217724	2.02	1.71e-04	0.3784
131	515726961170	248.637985	-47.553284	0.27	5.29e-07	0.9785
132	515727288954	248.637619	-47.325638	1.36	9.53e-06	0.6773
133	515727654625	248.639771	-47.360050	1.11	1.71e-04	0.5873
134	515726913635	248.639999	-47.729778	0.32	5.29e-07	0.9875
135	515732381884	248.640320	-47.905617	2.23	3.07e-03	0.1611
136	515726991911	248.642319	-47.462894	0.47	5.29e-07	0.9819
137	515720014326	248.642487	-47.221340	3.05	9.53e-06	0.4550
138	515727270761	248.644455	-47.541241	4.13	9.53e-06	0.3942
139	—	-	-	-	-	-
140	515726949540	248.644989	-47.597916	0.27	8.75e-07	0.4171
141	515719987007	248.649994	-47.308914	0.74	1.62e-04	0.9717
142	515731909689	248.651794	-47.832462	0.43	1.71e-04	0.8894
143	—	-	-	-	-	-
144	515720876334	248.659500	-47.158161	1.85	1.22e-05	0.6512
145	515719997468	248.660507	-47.283695	0.27	5.29e-07	0.9883
146	515727028863	248.662170	-47.365997	0.41	9.52e-06	0.9843
147	515731927232	248.664520	-47.831417	1.51	1.55e-03	0.7932
148	515727020965	248.664230	-47.390392	0.53	5.29e-07	0.9059
149	—	-	-	-	-	-
150	515726918170	248.670868	-47.730507	0.25	1.71e-04	0.5076
151	515727253034	248.671158	-47.695904	1.00	9.53e-06	0.6316
152	515726924172	248.672653	-47.708252	0.45	5.29e-07	0.9811

Chandra Catalog: Infrared Counterparts (continued)

No.	VVV Source Name	R.A. (deg)	Dec. (deg)	$\Delta_{\mathrm{X-IR}}$ (arcsec)	p_{noise}	Reliability
153	—	-	-	-	-	-
154	515719983536	248.674301	-47.331829	1.10	1.62e-04	0.9376
155	515719988309	248.676514	-47.321289	0.31	5.29e-07	0.9861
156	515731955313	248.678772	-47.770729	2.33	1.71e-04	0.4943
157	515726978466	248.678085	-47.526428	1.63	1.62e-04	0.6649
158	515727009565	248.679382	-47.434265	0.07	5.29e-07	0.9896
159	515720040214	248.680420	-47.171551	0.71	9.52e-06	0.9730
160	515726958100	248.682526	-47.591198	0.07	3.07e-03	0.9922
161	515731845105	248.683899	-47.948299	0.57	1.71e-04	0.9095
162	515726951760	248.683929	-47.612850	0.66	5.29e-07	0.9736
163	515726921715	248.685654	-47.728119	0.86	9.53e-06	0.9617
164	515727824795	248.687256	-47.613922	0.22	3.07e-03	0.9879
165	515720031250	248.688522	-47.205475	0.84	5.29e-07	0.7657
166	515720006635	248.689102	-47.274502	0.95	9.52e-06	0.8531
167	515726994090	248.689682	-47.486549	0.63	5.29e-07	0.9746
168	515726931885	248.689316	-47.690281	0.86	5.29e-07	0.9649
169	515731930854	248.693726	-47.822491	0.24	2.92e-03	0.9799
170	515731928607	248.696854	-47.841946	1.70	1.71e-04	0.9225
171	515727004931	248.696671	-47.458675	1.60	5.29e-07	0.5399
172	515727273626	248.699677	-47.545654	0.72	9.53e-06	0.9688
173	515727273626	248.699677	-47.545654	0.72	9.53e-06	0.9688
174	515726976188	248.699982	-47.546177	0.22	1.62e-04	0.9336
175	515719982095	248.701462	-47.355320	0.54	5.29e-07	0.9766
176	515726978416	248.702042	-47.541595	0.63	5.29e-07	0.9689
177	515732036896	248.703735	-47.644413	0.10	1.71e-04	0.9909
178	—	-	-	-	-	-
179	515726937573	248.709015	-47.681850	0.99	1.22e-05	0.0394
180	515720039772	248.709290	-47.193062	1.87	5.29e-07	0.8514
181	515731979258	248.710175	-47.747566	0.92	1.71e-04	0.2728
182	515719987272	248.710205	-47.344597	0.24	5.29e-07	0.9848
183	515731943086	248.710510	-47.809185	0.63	1.55e-03	0.9623
184	515719986515	248.711212	-47.346302	0.47	2.92e-03	0.9821
185	515726944973	248.711624	-47.655052	0.09	5.34e-04	0.5177
186	515731977032	248.711563	-47.753231	1.02	1.71e-04	0.8449
187	515727611684	248.711823	-47.620644	1.64	1.71e-04	0.6941
188	515731972036	248.712357	-47.772594	0.35	1.71e-04	0.9812
189	515727032894	248.713257	-47.389008	0.56	5.29e-07	0.9011
190	515727280596	248.713882	-47.471909	0.72	1.54e-03	0.8388
191	—	-	-	-	-	-
192	515731856307	248.721497	-47.956249	1.96	6.12e-04	0.2153
193	515720037527	248.722580	-47.211098	1.70	5.29e-07	0.9070
194	—	-	-	-	-	-
195	515726945138	248.724487	-47.669174	0.57	5.29e-07	0.9765
196	515726971924	248.724731	-47.573833	0.04	5.29e-07	0.9924
197	515719997400	248.725800	-47.324165	0.25	5.29e-07	0.9894
198	515727827306	248.727768	-47.602806	0.16	3.07e-03	0.9901
199	515727259403	248.728256	-47.690479	0.53	2.16e-04	0.8519
200	515727262707	248.729126	-47.667572	0.19	9.53e-06	0.5382
201	—	-	-	-	-	-
202	515727002049	248.732315	-47.500977	0.54	5.29e-07	0.9742
203	515720036180	248.733215	-47.216743	0.08	5.29e-07	0.9890
204	515731916357	248.733734	-47.870708	0.22	1.71e-04	0.9882
205	515721068178	248.733932	-47.319386	0.12	2.92e-03	0.9910
206	515720041355	248.734573	-47.206612	0.43	1.62e-04	0.2262
207	515731861894	248.734589	-47.960239	1.93	1.71e-04	0.1579
208	—	-	-	-	-	-
209	515720053128	248.738495	-47.177895	1.04	3.07e-03	0.2968
210	515727649348	248.740768	-47.447750	0.41	1.71e-04	0.4149
211	515720032769	248.741302	-47.231571	0.71	5.29e-07	0.9645

Chandra Catalog: Infrared Counterparts (continued)

No.	VVV Source Name	R.A. (deg)	Dec. (deg)	$\Delta_{\mathrm{X-IR}}$ (arcsec)	p_{noise}	Reliability
212	515726948542	248.742188	-47.660358	1.01	5.29e-07	0.9592
213	—	-	-	-	-	-
214	515732003691	248.752716	-47.731861	1.37	2.81e-04	0.0756
215	515720001217	248.753891	-47.329540	0.83	1.56e-05	0.8721
216	515726960020	248.759293	-47.632729	0.38	5.29e-07	0.9819
217	515732009667	248.765427	-47.730007	1.90	1.71e-04	0.5510
218	—	-	-	-	-	-
219	—	-	-	-	-	-
220	515731935369	248.767746	-47.859001	0.23	2.92e-03	0.9906
221	515731837735	248.768738	-48.010948	1.99	2.92e-03	0.0905
222	515727844660	248.769608	-47.406601	0.90	3.07e-03	0.8629
223	515721075338	248.772827	-47.300995	0.77	2.92e-03	0.8968
224	515731941796	248.776291	-47.856983	0.14	1.71e-04	0.9910
225	515726993046	248.777649	-47.543415	0.29	5.29e-07	0.9883
226	515720025405	248.780502	-47.278145	0.32	5.29e-07	0.9873
227	515732003337	248.785599	-47.755592	0.94	1.71e-04	0.9645
228	—	-	-	-	-	-
229	515720093414	248.791000	-47.104362	0.81	5.29e-07	0.9625
230	515720010415	248.790863	-47.326038	0.37	5.29e-07	0.9851
231	515720036176	248.793518	-47.252426	1.46	1.62e-04	0.0938
232	515726979513	248.796600	-47.596577	0.25	5.29e-07	0.9884
233	515727286032	248.799179	-47.460991	2.08	9.53e-06	0.6737
234	515726971018	248.800491	-47.624043	0.21	5.29e-07	0.9875
235	515731902524	248.804489	-47.940125	1.27	1.71e-04	0.9299
236	515732420758	248.807541	-47.720116	2.02	3.07e-03	0.1545
237	515726970055	248.810715	-47.635796	0.45	9.53e-06	0.9794
238	515731994482	248.810898	-47.784054	0.10	1.71e-04	0.9891
239	515720865399	248.813293	-47.384487	0.14	9.53e-06	0.9889
240	—	-	-	-	-	-
241	515720039153	248.815994	-47.260143	1.19	5.29e-07	0.1370
242	—	-	-	-	-	-
243	515720109142	248.821976	-47.074017	0.50	5.29e-07	0.8036
244	515732408188	248.822235	-47.828049	0.17	3.07e-03	0.9904
245	—	-	-	-	-	-
246	—	-	-	-	-	-
247	515720051620	248.823669	-47.227947	2.88	5.29e-07	0.4095
248	515727006204	248.826019	-47.535732	0.29	5.29e-07	0.9883
249	—	-	-	-	-	-
250	515732073827	248.828110	-47.662491	0.70	1.71e-04	0.9605
251	515719973711	248.828094	-47.457275	2.39	5.29e-07	0.4164
252	515721068519	248.828934	-47.376015	2.63	1.71e-04	0.4871
253	—	-	-	-	-	-
254	515720884674	248.832092	-47.168694	1.23	9.53e-06	0.1523
255	515731967336	248.833267	-47.852566	0.22	1.71e-04	0.9916
256	515720881053	248.833420	-47.212570	1.53	9.53e-06	0.8986
257	515719980215	248.833847	-47.440487	0.87	5.29e-07	0.4999
258	515731956293	248.834595	-47.864429	0.35	1.71e-04	0.9864
259	515732185036	248.835159	-47.465240	1.46	2.20e-04	0.3387
260	515727028129	248.835663	-47.475506	0.54	5.29e-07	0.4226
261	515732054042	248.835434	-47.696312	1.26	1.71e-04	0.4186
262	515732067980	248.835800	-47.674492	0.68	2.92e-03	0.9494
263	515719987619	248.836426	-47.420834	1.20	1.62e-04	0.9498
264	515732162909	248.836990	-47.515781	1.36	1.71e-04	0.4912
265	515732037899	248.837280	-47.724346	1.16	1.71e-04	0.2444
266	515720032005	248.838089	-47.295616	0.15	5.29e-07	0.9899
267	515731885333	248.839981	-47.984676	1.63	2.92e-03	0.4393
268	515731980319	248.840652	-47.827808	0.26	1.71e-04	0.9903
269	515720023597	248.840958	-47.321793	0.33	5.29e-07	0.9875
270	515721096433	248.840454	-47.227257	2.37	2.92e-03	0.8179

Chandra Catalog: Infrared Counterparts (continued)

No.	VVV Source Name	R.A. (deg)	Dec. (deg)	$\Delta_{\mathrm{X-IR}}$ (arcsec)	p_{noise}	Reliability
271	515720130362	248.844757	-47.035686	1.57	5.29e-07	0.3472
272	515732083934	248.844620	-47.654381	0.81	1.71e-04	0.8620
273	515724886301	248.846466	-47.472534	1.61	5.29e-07	0.4962
274	515732071629	248.849091	-47.679520	0.30	1.71e-04	0.9780
275	—	-	-	-	-	-
276	515727657182	248.851120	-47.477173	2.44	1.71e-04	0.0185
277	515719987064	248.851898	-47.431778	1.75	6.80e-07	0.2174
278	515720124625	248.851685	-47.056900	0.86	5.29e-07	0.9626
279	515720074177	248.853470	-47.188053	2.56	9.52e-06	0.6378
280	515720073957	248.852356	-47.186268	1.37	6.80e-07	0.1589
281	515720051419	248.852951	-47.248470	1.33	9.52e-06	0.9217
282	515732381537	248.854355	-48.042179	1.79	3.07e-03	0.0371
283	515731962796	248.855911	-47.865074	1.31	1.71e-04	0.5805
284	515732435856	248.856461	-47.626453	1.72	3.07e-03	0.8323
285	515720902172	248.856384	-46.983253	3.63	9.53e-06	0.1406
286	515731970035	248.857254	-47.854713	0.30	1.71e-04	0.9887
287	515727654559	248.857452	-47.494255	1.57	2.92e-03	0.5923
288	515732102614	248.858261	-47.633507	0.75	2.92e-03	0.9691
289	515720072762	248.859909	-47.193726	1.30	5.29e-07	0.5584
290	515720059099	248.860870	-47.239975	0.41	5.29e-07	0.9842
291	515731994386	248.861618	-47.815742	0.15	1.71e-04	0.9909
292	515720073318	248.863174	-47.193897	1.57	1.44e-06	0.5070
293	515720129524	248.863358	-47.049614	0.21	5.29e-07	0.5648
294	515720149224	248.864746	-47.003742	1.24	9.53e-06	0.5278
295	515731903338	248.865356	-47.975574	1.78	1.71e-04	0.5830
296	515720064674	248.866104	-47.220802	0.52	5.29e-07	0.9564
297	515732012299	248.866470	-47.787773	0.61	1.71e-04	0.9605
298	515731933308	248.869797	-47.927883	0.15	1.71e-04	0.9843
299	515732088827	248.870224	-47.663033	0.18	1.71e-04	0.9771
300	515720166055	248.871063	-46.968105	1.02	9.53e-06	0.0614
301	515720102721	248.872665	-47.121250	0.67	5.34e-04	0.7731
302	515732036446	248.872772	-47.749222	0.52	1.71e-04	0.9800
303	—	-	-	-	-	-
304	515720045238	248.873535	-47.278801	0.28	5.29e-07	0.9892
305	515732027680	248.874207	-47.766140	1.22	1.71e-04	0.8940
306	515732436459	248.874634	-47.634850	0.55	3.07e-03	0.9779
307	515732169976	248.878845	-47.523911	1.36	3.07e-03	0.7135
308	515732170999	248.879532	-47.522358	1.72	1.71e-04	0.2899
309	515732131652	248.880722	-47.601063	1.66	1.71e-04	0.4884
310	515732393401	248.881104	-47.963284	0.40	3.07e-03	0.5629
311	515731910512	248.881180	-47.972481	0.79	1.71e-04	0.5013
312	515731964505	248.883728	-47.888878	0.49	1.71e-04	0.9785
313	515732025092	248.883865	-47.776867	0.53	1.71e-04	0.9791
314	515720074429	248.886124	-47.208069	0.93	1.71e-04	0.7108
315	515720020099	248.888199	-47.358376	0.22	5.29e-07	0.9886
316	515732092389	248.891434	-47.668709	2.17	1.55e-03	0.4252
317	515720082972	248.891830	-47.190517	0.42	5.29e-07	0.9796
318	515720136518	248.893402	-47.053493	4.39	8.75e-07	0.0304
319	515732100727	248.892380	-47.659374	0.30	1.71e-04	0.9872
320	515727015651	248.894028	-47.551750	1.50	5.29e-07	0.5254
321	—	-	-	-	-	-
322	—	-	-	-	-	-
323	515732049697	248.897110	-47.740799	0.49	1.71e-04	0.9815
324	515732145281	248.900620	-47.586121	0.33	1.71e-04	0.9315
325	515720119160	248.901138	-47.096752	0.35	5.29e-07	0.9862
326	515720895917	248.902695	-47.085217	2.10	9.53e-06	0.4514
327	515720052381	248.903351	-47.275715	0.71	5.29e-07	0.9733
328	515720060536	248.903976	-47.254051	1.82	8.75e-07	0.8712
329	515720043917	248.907181	-47.301254	2.20	6.80e-07	0.3639

Chandra Catalog: Infrared Counterparts (continued)

No.	VVV Source Name	R.A. (deg)	Dec. (deg)	$\Delta_{\mathrm{X-IR}}$ (arcsec)	p_{noise}	Reliability
330	—	-	-	-	-	-
331	515720095589	248.911240	-47.165745	0.37	5.29e-07	0.9862
332	515721391165	248.911224	-47.308117	1.16	3.07e-03	0.4744
333	515732088573	248.912506	-47.689438	1.33	1.71e-04	0.1155
334	515731930432	248.916107	-47.957863	2.25	1.71e-04	0.7639
335	515731997298	248.918350	-47.845325	0.28	2.92e-03	0.9802
336	515732126350	248.923096	-47.632431	9.46	2.92e-03	0.1645
337	515732130818	248.920105	-47.622913	0.35	1.71e-04	0.8423
338	515720170385	248.920441	-46.989658	0.70	5.29e-07	0.9742
339	515731980548	248.920853	-47.874779	0.42	1.71e-04	0.9777
340	515732166177	248.925674	-47.561626	1.24	1.71e-04	0.9488
341	515732165794	248.927414	-47.562771	1.42	2.92e-03	0.6187
342	515720900228	248.928146	-47.049198	1.04	3.43e-05	0.1170
343	515731984608	248.930038	-47.873573	0.69	3.07e-03	0.5939
344	515732163126	248.930283	-47.569763	0.61	1.71e-04	0.9500
345	515720086780	248.930756	-47.200630	2.39	1.62e-04	0.2663
346	515732034350	248.930573	-47.793633	0.11	1.71e-04	0.9916
347	515721114893	248.931427	-47.148045	0.42	1.71e-04	0.9841
348	515720155486	248.933243	-47.033833	0.80	5.29e-07	0.8636
349	515732010861	248.934738	-47.834263	2.50	2.92e-03	0.3502
350	515721124762	248.938080	-47.085915	0.56	2.20e-04	0.6534
351	515720161333	248.939087	-47.026745	0.69	9.52e-06	0.3821
352	515720902796	248.938583	-47.027782	1.55	1.54e-03	0.6839
353	515720888891	248.939713	-47.189156	1.03	9.53e-06	0.9079
354	515720142415	248.940445	-47.067116	0.97	5.29e-07	0.9475
355	515732136668	248.940796	-47.625229	1.03	1.71e-04	0.7478
356	515732054208	248.941132	-47.759998	1.27	3.07e-03	0.9185
357	515732010598	248.941895	-47.836094	1.76	2.20e-04	0.6587
358	515732033464	248.941879	-47.798439	0.95	1.71e-04	0.8988
359	515732053442	248.942291	-47.761799	2.82	1.71e-04	0.5980
360	515721124750	248.943924	-47.090107	0.16	1.71e-04	0.9861
361	515732137601	248.944244	-47.625790	0.27	1.71e-04	0.9560
362	515720073473	248.945007	-47.244347	1.11	5.29e-07	0.6208
363	515719997510	248.945374	-47.462490	0.29	5.29e-07	0.9877
364	515720100906	248.945740	-47.173359	0.99	1.62e-04	0.9011
365	—	-	-	-	-	-
366	—	-	-	-	-	-
367	515720127548	248.946823	-47.106262	0.29	5.29e-07	0.9889
368	515732140206	248.946976	-47.622875	3.05	2.92e-03	0.4907
369	515732152481	248.947815	-47.602310	0.26	1.71e-04	0.9842
370	515720078855	248.949600	-47.233395	1.97	1.62e-04	0.7268
371	515721389020	248.951462	-47.358044	0.29	3.07e-03	0.9876
372	515732146789	248.951599	-47.613953	0.87	1.71e-04	0.9647
373	515721084910	248.952469	-47.358337	2.83	1.71e-04	0.3838
374	515720877915	248.953857	-47.322083	1.32	2.16e-04	0.9264
375	515720043823	248.954330	-47.329937	2.73	1.22e-05	0.6823
376	515732104330	248.954712	-47.688095	0.15	1.71e-04	0.9925
377	515732170991	248.957001	-47.574657	2.89	1.71e-04	0.0762
378	515720031123	248.957321	-47.368336	0.50	5.29e-07	0.9807
379	515719996033	248.958374	-47.471565	0.55	5.29e-07	0.6233
380	515732445238	248.958771	-47.614983	0.46	3.07e-03	0.5667
381	515731988503	248.959122	-47.884365	3.25	1.71e-04	0.3858
382	515732057788	248.959534	-47.766354	2.64	1.71e-04	0.1847
383	515720085994	248.960495	-47.222069	0.60	1.62e-04	0.9775
384	515732143663	248.962616	-47.627651	1.66	1.71e-04	0.6630
385	515721113327	248.962646	-47.182266	0.42	2.92e-03	0.9845
386	515721140040	248.964798	-47.002792	4.10	1.71e-04	0.3547
387	—	-	-	-	-	-
388	515720188425	248.962646	-46.972706	2.17	1.71e-04	0.3152

Chandra Catalog: Infrared Counterparts (continued)

No.	VVV Source Name	R.A. (deg)	Dec. (deg)	$\Delta_{\mathrm{X-IR}}$ (arcsec)	p_{noise}	Reliability
389	—	-	-	-	-	-
390	515720100154	248.963928	-47.186428	0.37	5.29e-07	0.9860
391	—	-	-	-	-	-
392	515732166039	248.966721	-47.588295	1.56	6.12e-04	0.4459
393	515720120252	248.968307	-47.136795	0.32	5.29e-07	0.9880
394	515732059728	248.971237	-47.770782	0.50	1.71e-04	0.9794
395	—	-	-	-	-	-
396	515720906266	248.972916	-47.010567	0.94	9.53e-06	0.8977
397	515720155530	248.974487	-47.060776	0.22	5.29e-07	0.9909
398	515732161491	248.974655	-47.599796	3.12	3.07e-03	0.5677
399	515720055706	248.975052	-47.312187	2.73	5.29e-07	0.2534
400	515720197603	248.976013	-46.961464	0.76	9.52e-06	0.2730
401	515720148302	248.980377	-47.076874	0.31	6.80e-07	0.9852
402	515720054266	248.979996	-47.317814	0.82	9.52e-06	0.9658
403	515720158664	248.980301	-47.054329	0.77	1.71e-04	0.6206
404	—	-	-	-	-	-
405	—	-	-	-	-	-
406	—	-	-	-	-	-
407	515720136437	248.981613	-47.108875	0.23	5.29e-07	0.9906
408	—	-	-	-	-	-
409	515732069048	248.983444	-47.764084	1.05	2.92e-03	0.8599
410	515732012362	248.983597	-47.860275	2.57	1.71e-04	0.4086
411	515732416593	248.983704	-47.856270	0.45	3.07e-03	0.5888
412	—	-	-	-	-	-
413	515732129285	248.995819	-47.684292	0.45	1.71e-04	0.9820
414	515724897196	248.997101	-47.525642	2.30	6.80e-07	0.2838
415	515720148545	248.996490	-47.088127	0.70	5.29e-07	0.9733
416	515732418811	249.000580	-47.873241	1.82	3.07e-03	0.2623
417	515732045388	249.005264	-47.815010	0.28	1.71e-04	0.9834
418	515732078081	249.008301	-47.765320	1.38	1.71e-04	0.8751
419	515720169097	249.008316	-47.046535	0.06	5.29e-07	0.9849
420	515732095686	249.014053	-47.738167	0.78	2.92e-03	0.9464
421	—	-	-	-	-	-
422	515725812244	249.014923	-47.332363	0.73	1.71e-04	0.3587
423	515724944189	249.015411	-47.360378	0.67	5.29e-07	0.9557
424	—	-	-	-	-	-
425	515732090747	249.018906	-47.749676	0.66	2.81e-04	0.9619
426	515720106559	249.019608	-47.204140	0.13	5.29e-07	0.9841
427	515720242627	249.020950	-46.876747	1.42	1.62e-04	0.3016
428	515721436904	249.021896	-46.879711	2.96	3.07e-03	0.3886
429	515720206314	249.022598	-46.963253	3.17	5.29e-07	0.5993
430	515720130878	249.023392	-47.144848	0.41	9.52e-06	0.9848
431	515732146909	249.024124	-47.659218	0.52	1.71e-04	0.2673
432	515732145381	249.024872	-47.664749	0.39	2.92e-03	0.4741
433	515720142307	249.025269	-47.119320	0.17	5.29e-07	0.9871
434	515732108366	249.025818	-47.733418	0.20	1.71e-04	0.9913
435	515720116495	249.026123	-47.180714	0.40	5.29e-07	0.9851
436	—	-	-	-	-	-
437	515720093751	249.029312	-47.242882	0.41	6.80e-07	0.9843
438	515720915548	249.031342	-46.943924	0.67	1.22e-05	0.9092
439	515732141878	249.032196	-47.673733	0.53	1.71e-04	0.9804
440	—	-	-	-	-	-
441	—	-	-	-	-	-
442	—	-	-	-	-	-
443	515720067425	249.045807	-47.323288	1.10	6.80e-07	0.9065
444	515732134867	249.046021	-47.693775	0.83	1.71e-04	0.9009
445	515724907512	249.045776	-47.512859	2.25	1.12e-06	0.7916
446	515720059043	249.045883	-47.345200	2.35	5.29e-07	0.6833
447	515721404166	249.049469	-47.252144	2.07	3.07e-03	0.1443

Chandra Catalog: Infrared Counterparts (continued)

No.	VVV Source Name	R.A. (deg)	Dec. (deg)	Δ_{X-IR} (arcsec)	p_{noise}	Reliability
448	515720182374	249.049881	-47.040188	0.20	5.29e-07	0.9905
449	515720206949	249.050629	-46.978340	0.45	8.75e-07	0.9779
450	515724927889	249.051056	-47.436462	0.88	3.40e-05	0.9083
451	515720272054	249.055191	-46.833179	0.80	5.29e-07	0.0426
452	515720214281	249.055023	-46.963814	0.84	5.29e-07	0.9605
453	515732163380	249.056793	-47.647984	1.45	2.20e-04	0.5787
454	515720257706	249.059372	-46.872715	1.18	2.92e-03	0.4628
455	—	-	-	-	-	-
456	515732426367	249.059784	-47.858116	0.78	3.07e-03	0.4758
457	515724890143	249.060944	-47.592270	0.34	5.29e-07	0.9838
458	515720214105	249.061401	-46.972649	0.54	9.53e-06	0.9790
459	515720145803	249.061859	-47.134422	0.13	5.29e-07	0.9842
460	515732038026	249.065445	-47.864979	0.89	1.71e-04	0.9140
461	—	-	-	-	-	-
462	515720168424	249.068802	-47.085751	0.86	9.52e-06	0.9117
463	515732024260	249.071777	-47.898083	2.37	6.12e-04	0.3588
464	515724940782	249.071701	-47.408062	0.46	9.52e-06	0.9822
465	515720080244	249.071442	-47.304394	0.71	5.29e-07	0.9758
466	515732116671	249.072113	-47.740463	0.13	1.71e-04	0.9884
467	515724903203	249.073608	-47.548725	0.50	5.29e-07	0.9834
468	515720066296	249.080750	-47.350937	0.54	1.62e-04	0.9781
469	515720108282	249.082367	-47.243420	0.46	5.29e-07	0.9828
470	515720152650	249.084457	-47.135689	0.27	9.53e-06	0.9797
471	515720115401	249.084549	-47.223469	0.31	5.29e-07	0.9777
472	515720901490	249.085358	-47.135098	0.72	1.54e-03	0.4868
473	—	-	-	-	-	-
474	515720224277	249.086044	-46.959698	0.21	9.52e-06	0.9785
475	515732027852	249.087692	-47.895588	2.41	1.71e-04	0.0721
476	515721123324	249.087982	-47.187393	0.67	2.81e-04	0.9655
477	515720197538	249.088730	-47.029129	0.09	5.29e-07	0.9901
478	515720892073	249.088394	-47.242523	1.50	1.71e-04	0.3858
479	515720108293	249.091202	-47.241528	1.42	1.62e-04	0.9276
480	515732105978	249.091644	-47.769962	1.66	1.71e-04	0.4855
481	515732033580	249.091553	-47.890438	1.14	1.71e-04	0.0803
482	515720230485	249.092468	-46.948616	0.37	5.29e-07	0.9801
483	—	-	-	-	-	-
484	—	-	-	-	-	-
485	515720200594	249.099762	-47.026379	0.39	5.29e-07	0.9850
486	515720930238	249.100098	-46.833572	2.88	9.53e-06	0.2447
487	—	-	-	-	-	-
488	—	-	-	-	-	-
489	515724929083	249.106842	-47.468323	0.93	5.29e-07	0.9263
490	515724914888	249.107819	-47.523438	0.52	5.29e-07	0.9820
491	—	-	-	-	-	-
492	515720246163	249.111465	-46.923542	3.19	1.62e-04	0.0697
493	515732150302	249.110550	-47.708370	0.20	1.71e-04	0.9863
494	515720243858	249.113693	-46.929314	1.64	1.62e-04	0.0342
495	515724921946	249.113815	-47.497047	0.64	5.29e-07	0.9744
496	515720233172	249.116913	-46.957218	0.64	5.29e-07	0.9718
497	515732191556	249.117844	-47.626019	0.91	1.71e-04	0.1604
498	515724889456	249.116882	-47.629704	2.74	5.29e-07	0.3338
499	515720140487	249.117752	-47.180855	0.14	5.29e-07	0.9799
500	515724898608	249.118530	-47.593502	0.52	5.29e-07	0.9820
501	515732101405	249.118774	-47.794201	1.02	2.92e-03	0.3955
502	515720218153	249.122284	-47.000443	0.20	5.29e-07	0.9915
503	515720270467	249.122513	-46.874691	0.33	8.75e-07	0.9757
504	515720920853	249.122757	-46.945145	2.60	9.53e-06	0.0323
505	515732165734	249.124146	-47.683514	0.53	1.71e-04	0.9799
506	515720243169	249.124710	-46.938114	0.32	5.29e-07	0.9869

Chandra Catalog: Infrared Counterparts (continued)

No.	VVV Source Name	R.A. (deg)	Dec. (deg)	$\Delta_{\mathrm{X-IR}}$ (arcsec)	p_{noise}	Reliability
507	515724916206	249.127213	-47.541203	0.30	5.29e-07	0.9900
508	515725793032	249.129578	-47.535233	1.99	2.92e-03	0.6158
509	—	-	-	-	-	-
510	515720902250	249.131195	-47.158421	1.06	1.71e-04	0.6014
511	515721400657	249.132614	-47.341660	1.22	3.07e-03	0.8731
512	515732150519	249.135590	-47.721256	1.82	2.92e-03	0.8261
513	515721152020	249.136093	-47.034760	1.14	2.92e-03	0.6144
514	—	-	-	-	-	-
515	515720076253	249.139816	-47.357056	2.21	5.29e-07	0.5918
516	515720912550	249.141525	-47.044315	0.17	1.71e-04	0.9907
517	515720236452	249.144882	-46.967361	0.23	9.53e-06	0.9893
518	515720167031	249.145844	-47.135757	0.29	1.62e-04	0.3730
519	515724945913	249.148239	-47.440449	0.74	5.29e-07	0.9735
520	—	-	-	-	-	-
521	515720903664	249.150558	-47.148373	2.12	2.92e-03	0.4888
522	—	-	-	-	-	-
523	—	-	-	-	-	-
524	—	-	-	-	-	-
525	515720263787	249.157349	-46.910229	0.63	6.80e-07	0.9354
526	—	-	-	-	-	-
527	515724885858	249.159149	-47.665913	1.33	1.62e-04	0.9082
528	515720213346	249.160934	-47.033241	0.14	5.29e-07	0.9911
529	515724889097	249.161392	-47.656342	0.55	5.29e-07	0.9775
530	515720097716	249.162415	-47.332787	0.32	5.29e-07	0.9886
531	515726072802	249.166351	-47.537273	0.83	3.07e-03	0.8591
532	515724901115	249.166489	-47.619526	0.76	5.29e-07	0.9733
533	515720222755	249.166672	-47.014179	0.12	5.29e-07	0.9926
534	515724909998	249.167969	-47.578453	0.16	1.22e-05	0.9923
535	—	-	-	-	-	-
536	515720216879	249.168457	-47.030846	0.45	5.29e-07	0.9824
537	515720143346	249.168304	-47.205711	1.65	9.52e-06	0.7266
538	515724966788	249.169769	-47.387352	0.85	5.29e-07	0.9568
539	515720274923	249.170959	-46.895279	0.67	5.29e-07	0.8732
540	515721449482	249.175949	-46.835365	2.99	3.07e-03	0.4033
541	515726077735	249.182312	-47.507824	0.75	3.07e-03	0.9703
542	515720204483	249.182846	-47.066235	0.73	5.29e-07	0.9729
543	515732148546	249.185928	-47.754539	1.21	1.71e-04	0.5371
544	515724990248	249.187790	-47.325607	0.47	5.29e-07	0.9807
545	515720153028	249.190430	-47.196701	0.28	5.29e-07	0.9867
546	515724939373	249.192886	-47.484303	0.31	9.52e-06	0.9829
547	515724910177	249.194000	-47.594296	1.03	5.29e-07	0.9278
548	515725621661	249.193863	-47.471081	1.13	2.92e-03	0.8885
549	515720911777	249.195236	-47.085205	1.84	1.71e-04	0.0787
550	515724887210	249.195496	-47.684166	1.71	5.29e-07	0.4566
551	—	-	-	-	-	-
552	515720295945	249.197998	-46.864697	0.30	1.71e-04	0.9820
553	—	-	-	-	-	-
554	515721423884	249.199707	-47.129383	1.67	3.07e-03	0.0975
555	515720201302	249.200317	-47.084721	1.25	3.40e-05	0.0488
556	515726079909	249.201187	-47.509350	0.16	3.07e-03	0.9919
557	515720197272	249.202896	-47.097733	0.43	8.75e-07	0.6226
558	515720192683	249.204514	-47.115482	0.70	6.80e-07	0.2907
559	515720111337	249.204819	-47.304268	0.77	5.29e-07	0.9669
560	515720270223	249.205048	-46.925480	0.47	5.29e-07	0.9807
561	515721441807	249.206482	-46.938778	2.92	3.07e-03	0.7478
562	515721200331	249.205231	-46.766151	1.85	1.71e-04	0.2126
563	515732453510	249.208862	-47.705822	0.96	3.07e-03	0.2327
564	515720909745	249.208817	-47.118050	0.79	1.71e-04	0.9495
565	515720892319	249.210144	-47.311420	0.58	9.53e-06	0.5935

Chandra Catalog: Infrared Counterparts (continued)

No.	VVV Source Name	R.A. (deg)	Dec. (deg)	$\Delta_{\mathrm{X-IR}}$ (arcsec)	p_{noise}	Reliability
566	515724982587	249.210571	-47.362900	1.41	9.52e-06	0.5063
567	—	-	-	-	-	-
568	—	-	-	-	-	-
569	515720296118	249.213058	-46.875580	0.49	5.29e-07	0.9770
570	515720118390	249.216095	-47.292747	0.24	5.29e-07	0.9908
571	515720111537	249.218246	-47.312550	0.47	5.29e-07	0.9838
572	—	-	-	-	-	-
573	515721199425	249.223877	-46.787167	0.88	1.71e-04	0.5154
574	515724923577	249.227554	-47.560837	0.11	5.29e-07	0.9940
575	515720217280	249.228668	-47.063328	1.01	2.92e-03	0.8517
576	—	-	-	-	-	-
577	—	-	-	-	-	-
578	515732184723	249.231812	-47.708950	0.79	3.07e-03	0.9503
579	515721165546	249.232193	-47.016762	1.50	1.71e-04	0.3506
580	515725624933	249.232330	-47.453514	2.32	3.07e-03	0.1342
581	515725623539	249.232727	-47.471066	2.00	1.71e-04	0.6047
582	515720228465	249.234863	-47.040588	0.75	9.52e-06	0.8321
583	—	-	-	-	-	-
584	—	-	-	-	-	-
585	515720327101	249.237289	-46.817364	2.47	5.29e-07	0.5732
586	515725815632	249.243805	-47.445656	1.44	3.07e-03	0.6165
587	—	-	-	-	-	-
588	—	-	-	-	-	-
589	515720119341	249.244995	-47.308006	2.18	5.29e-07	0.1652
590	515720146424	249.247177	-47.247803	0.43	5.29e-07	0.9851
591	515720264981	249.248138	-46.964821	0.32	5.29e-07	0.9829
592	515725056985	249.249435	-47.153648	1.21	5.29e-07	0.6357
593	515725047888	249.250900	-47.183926	0.66	5.29e-07	0.9775
594	515720209728	249.251526	-47.096092	0.84	5.29e-07	0.7004
595	515720272199	249.251755	-46.951454	0.61	1.62e-04	0.8444
596	515724925489	249.255020	-47.570324	0.41	5.29e-07	0.9862
597	515720387613	249.255630	-46.695210	1.99	1.71e-04	0.4757
598	515725059944	249.255402	-47.148273	0.65	5.29e-07	0.9774
599	515720225573	249.256607	-47.060959	1.65	5.29e-07	0.7837
600	515725789727	249.259094	-47.638348	0.96	1.71e-04	0.5482
601	515724937697	249.260040	-47.530712	0.88	9.53e-06	0.9054
602	515720235293	249.260300	-47.039978	0.62	5.29e-07	0.9767
603	515720247209	249.260559	-47.014755	1.06	5.29e-07	0.9642
604	515720389760	249.261597	-46.696289	1.70	5.29e-07	0.2791
605	515720309641	249.261932	-46.872944	0.38	5.29e-07	0.9825
606	515720235847	249.262787	-47.039463	2.16	9.53e-06	0.7041
607	515720330371	249.266129	-46.828033	0.35	5.29e-07	0.9848
608	515720377972	249.269424	-46.725529	1.68	5.29e-07	0.4275
609	515725069959	249.270447	-47.132717	0.11	9.52e-06	0.9907
610	515725861202	249.271698	-47.133347	1.17	2.92e-03	0.9101
611	515725069957	249.273361	-47.131233	0.67	5.29e-07	0.9761
612	515720242396	249.273605	-47.032948	1.46	5.29e-07	0.5073
613	515720349987	249.275970	-46.790188	1.06	5.29e-07	0.9163
614	515725058369	249.277145	-47.165653	1.16	5.29e-07	0.3092
615	515721461040	249.280136	-46.773251	1.73	3.07e-03	0.6058
616	—	-	-	-	-	-
617	515724940348	249.283554	-47.539314	0.74	5.29e-07	0.9492
618	515724998520	249.285156	-47.358986	0.58	5.29e-07	0.9814
619	515721177467	249.289001	-46.974834	2.67	1.71e-04	0.4107
620	515724942904	249.290588	-47.532536	0.24	5.29e-07	0.9910
621	515725807772	249.290680	-47.531811	0.79	3.07e-03	0.9547
622	515720211060	249.293762	-47.130573	0.02	9.52e-06	0.9941
623	—	-	-	-	-	-
624	515720316299	249.299835	-46.880089	0.65	5.29e-07	0.9740

Chandra Catalog: Infrared Counterparts (continued)

No.	VVV Source Name	R.A. (deg)	Dec. (deg)	$\Delta_{\mathrm{X-IR}}$ (arcsec)	p_{noise}	Reliability
625	515724991447	249.300827	-47.395355	1.22	5.29e-07	0.9244
626	—	-	-	-	-	-
627	515724984338	249.299973	-47.411667	2.81	1.71e-04	0.0804
628	—	-	-	-	-	-
629	515720290390	249.302887	-46.940868	0.23	9.53e-06	0.9538
630	—	-	-	-	-	-
631	515720301761	249.307098	-46.918213	0.83	5.29e-07	0.8878
632	515724935715	249.307190	-47.566078	0.54	1.62e-04	0.9820
633	515720371273	249.307465	-46.772045	1.02	5.29e-07	0.9583
634	515720280408	249.307968	-46.966370	2.19	5.29e-07	0.5225
635	515720374187	249.308167	-46.758747	0.69	5.29e-07	0.9278
636	515726118547	249.308548	-47.234848	1.93	3.07e-03	0.0533
637	—	-	-	-	-	-
638	515725041101	249.309448	-47.241631	0.86	5.29e-07	0.9634
639	515724961420	249.311005	-47.489975	0.82	1.62e-04	0.9007
640	515720304818	249.312088	-46.912670	1.53	1.71e-04	0.3926
641	515720326537	249.313568	-46.865971	0.16	9.52e-06	0.9893
642	515720372864	249.318451	-46.768192	0.86	1.22e-05	0.7989
643	515720243083	249.324402	-47.060371	1.73	5.29e-07	0.0735
644	515721181768	249.324356	-46.967121	1.82	1.71e-04	0.2879
645	—	-	-	-	-	-
646	515720266141	249.325089	-47.008671	0.67	3.07e-03	0.9718
647	515720175612	249.325531	-47.225090	0.39	5.29e-07	0.9865
648	515725817690	249.326813	-47.481369	2.95	2.92e-03	0.5871
649	515720168679	249.327759	-47.242439	3.10	9.52e-06	0.0645
650	515720383711	249.329147	-46.756416	0.55	5.29e-07	0.9780
651	515725856202	249.333282	-47.206051	1.33	1.71e-04	0.7549
652	515725006660	249.334198	-47.363964	0.74	5.29e-07	0.9760
653	—	-	-	-	-	-
654	515725068477	249.335648	-47.174309	0.33	5.29e-07	0.9885
655	515720392342	249.336655	-46.743141	0.50	1.54e-03	0.9775
656	515724979680	249.338394	-47.451092	0.43	5.29e-07	0.9856
657	—	-	-	-	-	-
658	—	-	-	-	-	-
659	515720381782	249.342072	-46.764351	0.18	5.29e-07	0.9901
660	515724937515	249.343613	-47.588268	0.67	9.52e-06	0.8521
661	515725041439	249.343903	-47.260960	0.48	5.29e-07	0.8855
662	515724982923	249.345230	-47.453609	0.38	5.29e-07	0.9876
663	—	-	-	-	-	-
664	—	-	-	-	-	-
665	—	-	-	-	-	-
666	515725079124	249.352478	-47.149704	0.22	9.53e-06	0.9915
667	515720327682	249.353622	-46.889778	0.20	5.29e-07	0.9894
668	515720930616	249.357635	-46.988300	1.14	1.71e-04	0.1863
669	515725034163	249.357758	-47.292580	1.10	5.29e-07	0.9231
670	—	-	-	-	-	-
671	—	-	-	-	-	-
672	515725102694	249.359451	-47.084740	0.15	5.29e-07	0.9879
673	515720313621	249.360123	-46.923710	0.59	5.29e-07	0.9767
674	515725031467	249.361328	-47.304470	0.32	5.29e-07	0.9778
675	515725066967	249.361954	-47.192951	0.45	5.29e-07	0.9830
676	515725010572	249.363785	-47.376850	0.35	9.53e-06	0.9887
677	515725014858	249.367004	-47.362183	0.62	9.52e-06	0.9783
678	515720379916	249.372025	-46.787155	0.42	5.29e-07	0.9831
679	515720938487	249.372757	-46.913124	0.87	9.53e-06	0.9423
680	515720452230	249.373459	-46.630745	1.35	5.29e-07	0.9010
681	515720394991	249.374573	-46.755085	0.54	5.29e-07	0.9778
682	515720406912	249.376175	-46.727020	1.32	6.80e-07	0.5313
683	515720354211	249.377197	-46.844021	0.12	5.29e-07	0.9904

Chandra Catalog: Infrared Counterparts (continued)

No.	VVV Source Name	R.A. (deg)	Dec. (deg)	Δ_{X-IR} (arcsec)	p_{noise}	Reliability
684	515720407806	249.378601	-46.727169	2.20	1.62e-04	0.7320
685	515724991027	249.378479	-47.444263	0.86	5.29e-07	0.9167
686	515725006718	249.379364	-47.391388	0.34	5.29e-07	0.9890
687	515726133806	249.379089	-47.161301	0.88	3.07e-03	0.8990
688	515725841379	249.380081	-47.350487	0.44	1.71e-04	0.9851
689	515725044280	249.381241	-47.277000	1.97	5.29e-07	0.7567
690	515720283013	249.381531	-47.006428	3.21	2.92e-03	0.2863
691	515724985484	249.388748	-47.462952	0.13	5.29e-07	0.9895
692	515720288575	249.389877	-46.999199	2.20	5.29e-07	0.1638
693	515725642378	249.391098	-47.337360	0.53	9.53e-06	0.9823
694	515720390344	249.392273	-46.774975	0.41	5.29e-07	0.9835
695	515720435098	249.392654	-46.680653	0.71	5.29e-07	0.7997
696	515720320326	249.397324	-46.930752	1.34	5.29e-07	0.7200
697	515720324625	249.397293	-46.921448	0.79	5.29e-07	0.8594
698	515725025255	249.398758	-47.345295	0.23	5.29e-07	0.9833
699	515725104431	249.398834	-47.105907	0.41	5.29e-07	0.9860
700	515721452114	249.399475	-46.944458	2.76	3.07e-03	0.0490
701	515725124908	249.399277	-47.040958	0.55	5.29e-07	0.9805
702	515721452890	249.402039	-46.938335	0.31	3.07e-03	0.0561
703	515724982779	249.403809	-47.497658	0.25	5.29e-07	0.9891
704	515720262902	249.404099	-47.063671	0.80	5.29e-07	0.9666
705	515720494602	249.407516	-46.563118	1.86	5.29e-07	0.1511
706	515720288963	249.408768	-47.009426	2.03	5.29e-07	0.8589
707	515720321285	249.409637	-46.941891	2.41	9.52e-06	0.3284
708	515721210255	249.413498	-46.827168	0.39	1.71e-04	0.9844
709	515720401013	249.414001	-46.764332	0.43	5.29e-07	0.9377
710	515720362163	249.414291	-46.850433	0.38	5.29e-07	0.9822
711	515721191690	249.415253	-46.956486	0.42	2.92e-03	0.0548
712	515720366508	249.416687	-46.841366	0.12	5.29e-07	0.9922
713	515725624896	249.420456	-47.573006	1.11	9.53e-06	0.9508
714	515724991300	249.421280	-47.465572	0.25	1.62e-04	0.9868
715	515725137611	249.422241	-47.018391	2.28	5.29e-07	0.0612
716	515724957139	249.424026	-47.574215	3.08	5.29e-07	0.6006
717	515720349112	249.425888	-46.884518	0.05	5.29e-07	0.9881
718	515720463509	249.426895	-46.639771	0.47	1.62e-04	0.8979
719	515725129528	249.426773	-47.045036	1.29	5.29e-07	0.8912
720	515720473269	249.429504	-46.620834	1.51	5.29e-07	0.7606
721	515720360138	249.429611	-46.863533	0.32	5.29e-07	0.9842
722	—	-	-	-	-	-
723	515720411515	249.431915	-46.754482	0.63	9.52e-06	0.9649
724	515725012942	249.433060	-47.404778	0.11	5.29e-07	0.9937
725	515720442832	249.433929	-46.691166	0.63	2.92e-03	0.9717
726	515726115121	249.434158	-47.339352	0.67	3.07e-03	0.9642
727	515725843355	249.434647	-47.366776	1.39	2.92e-03	0.5356
728	515725126792	249.434097	-47.057049	1.40	5.29e-07	0.6384
729	515720383220	249.435196	-46.822803	0.80	9.53e-06	0.9675
730	515725127068	249.436508	-47.058788	0.70	5.29e-07	0.6825
731	515725043682	249.436493	-47.309525	1.59	5.29e-07	0.0537
732	515720373581	249.438019	-46.840630	1.19	5.29e-07	0.1628
733	515720311655	249.438843	-46.976086	1.23	5.29e-07	0.9547
734	515720480742	249.439758	-46.614506	0.57	1.62e-04	0.8160
735	515725139596	249.441132	-47.024033	1.27	5.29e-07	0.5388
736	515720468396	249.443665	-46.639729	1.43	8.75e-07	0.5959
737	515720958194	249.443192	-46.753880	2.79	9.53e-06	0.4044
738	—	-	-	-	-	-
739	515720322836	249.445602	-46.955349	2.69	5.29e-07	0.4199
740	515720482584	249.447311	-46.613384	0.31	1.22e-05	0.5053
741	515720331617	249.447815	-46.938259	1.73	5.29e-07	0.3056
742	515721476446	249.450455	-46.681496	1.94	3.07e-03	0.5152

Chandra Catalog: Infrared Counterparts (continued)

No.	VVV Source Name	R.A. (deg)	Dec. (deg)	$\Delta_{\mathrm{X-IR}}$ (arcsec)	p_{noise}	Reliability
743	515720394093	249.450516	-46.803783	0.54	5.29e-07	0.9765
744	515725026645	249.451263	-47.372242	0.16	5.29e-07	0.9946
745	515720936505	249.451172	-46.983242	0.63	9.53e-06	0.9683
746	515725111635	249.451767	-47.112877	0.53	9.52e-06	0.9820
747	515725070912	249.454697	-47.241360	2.21	5.29e-07	0.4972
748	—	-	-	-	-	-
749	515720424597	249.459366	-46.741810	0.28	5.29e-07	0.9744
750	515720338856	249.461670	-46.929234	0.26	5.29e-07	0.9891
751	515725012074	249.465195	-47.427475	0.29	5.29e-07	0.9840
752	515720403515	249.465271	-46.793232	0.48	5.29e-07	0.9612
753	515720458505	249.466019	-46.674942	0.18	1.71e-04	0.9845
754	515724982579	249.469757	-47.520866	0.33	1.62e-04	0.9797
755	515726158952	249.473282	-47.017632	0.53	3.07e-03	0.3610
756	515721215799	249.473694	-46.830879	0.59	2.92e-03	0.9643
757	515720348476	249.478424	-46.918137	0.71	5.29e-07	0.9231
758	515720385672	249.478790	-46.836918	0.77	9.52e-06	0.9360
759	515725872245	249.479156	-47.185486	1.72	2.92e-03	0.6409
760	515720409938	249.481110	-46.808907	0.57	9.52e-06	0.9657
761	515720458238	249.481949	-46.684975	0.20	9.52e-06	0.9881
762	515720419547	249.481720	-46.766144	0.66	1.62e-04	0.9737
763	—	-	-	-	-	-
764	515725647384	249.485321	-47.330597	0.18	9.53e-06	0.9937
765	515724980138	249.485703	-47.539387	2.65	2.16e-04	0.6180
766	515724969695	249.488800	-47.571896	1.76	5.29e-07	0.5800
767	515726134131	249.489182	-47.226486	2.17	3.07e-03	0.5322
768	515720978328	249.491394	-46.588692	0.73	9.53e-06	0.0739
769	515726159954	249.492798	-47.023342	2.73	3.07e-03	0.3428
770	515721261351	249.491928	-46.567612	1.85	3.07e-03	0.6798
771	515725043311	249.495102	-47.347778	0.09	5.29e-07	0.9900
772	515720480093	249.495346	-46.650452	0.62	5.29e-07	0.9697
773	515725089829	249.496597	-47.209164	1.12	9.52e-06	0.9637
774	515720443274	249.497116	-46.727409	0.33	8.75e-07	0.9850
775	515725172153	249.496902	-46.973492	0.95	5.29e-07	0.9450
776	515725149698	249.500854	-47.036350	0.49	5.29e-07	0.9823
777	515720454683	249.501694	-46.707951	0.44	1.62e-04	0.9797
778	—	-	-	-	-	-
779	515720395265	249.504395	-46.832645	0.87	5.29e-07	0.3867
780	515725893211	249.504166	-47.050404	0.85	2.20e-04	0.7759
781	515720365641	249.504379	-46.896538	0.93	2.83e-04	0.9576
782	515720425785	249.507233	-46.767948	0.63	2.92e-03	0.5299
783	515720500473	249.510971	-46.615517	2.16	3.40e-05	0.7542
784	—	-	-	-	-	-
785	515720337310	249.511032	-46.968151	0.29	5.29e-07	0.7837
786	—	-	-	-	-	-
787	—	-	-	-	-	-
788	515725012241	249.512466	-47.454777	1.12	5.29e-07	0.8059
789	515720485727	249.513535	-46.649693	0.47	9.53e-06	0.9767
790	515720469451	249.513580	-46.682083	0.31	5.29e-07	0.9856
791	—	-	-	-	-	-
792	515725107085	249.518784	-47.167160	0.98	5.29e-07	0.9567
793	515725068660	249.518417	-47.282616	0.06	5.29e-07	0.9896
794	515720390260	249.520050	-46.854855	0.36	5.29e-07	0.9386
795	515720966028	249.521454	-46.724400	0.45	1.71e-04	0.9476
796	515725897162	249.522705	-47.033939	1.98	2.92e-03	0.1909
797	515725092878	249.527145	-47.215267	0.38	2.92e-03	0.9730
798	515725186017	249.530869	-46.958214	0.26	5.29e-07	0.9885
799	515720507860	249.532303	-46.621002	0.55	5.29e-07	0.9134
800	515725888846	249.532516	-47.098984	1.99	1.71e-04	0.0518
801	515725061720	249.534592	-47.314850	0.48	5.29e-07	0.9850

Chandra Catalog: Infrared Counterparts (continued)

No.	VVV Source Name	R.A. (deg)	Dec. (deg)	$\Delta_{\mathrm{X-IR}}$ (arcsec)	p_{noise}	Reliability
802	—	-	-	-	-	-
803	515724999378	249.536041	-47.508160	0.63	5.29e-07	0.9198
804	515721461614	249.537216	-46.925671	1.05	3.07e-03	0.9045
805	515725111412	249.536819	-47.173035	0.74	5.29e-07	0.9711
806	515725066962	249.537994	-47.299011	1.48	9.52e-06	0.5819
807	515725165094	249.537598	-47.017467	0.70	5.29e-07	0.9499
808	515720975550	249.539505	-46.643795	0.45	9.53e-06	0.9791
809	515725638717	249.539444	-47.473366	1.38	3.07e-03	0.7988
810	—	-	-	-	-	-
811	515725063944	249.541550	-47.316021	0.31	1.62e-04	0.9899
812	515725045763	249.543076	-47.367516	0.53	1.71e-04	0.7782
813	—	-	-	-	-	-
814	515720321386	249.544128	-47.019245	0.68	9.52e-06	0.9708
815	515725118896	249.544205	-47.146633	0.69	5.29e-07	0.9762
816	515720522703	249.546219	-46.595791	0.88	5.29e-07	0.9397
817	515720530857	249.545944	-46.578770	0.46	5.29e-07	0.9410
818	515720420063	249.546051	-46.806614	0.14	5.29e-07	0.9834
819	515725847995	249.549652	-47.399933	3.18	1.71e-04	0.5980
820	—	-	-	-	-	-
821	515720445141	249.552109	-46.757401	0.50	5.29e-07	0.9762
822	515725146870	249.557983	-47.076134	1.22	5.29e-07	0.5469
823	—	-	-	-	-	-
824	—	-	-	-	-	-
825	515721468438	249.561707	-46.858456	1.87	3.07e-03	0.8352
826	515720381034	249.564880	-46.903843	0.89	6.85e-06	0.9441
827	515725077186	249.566971	-47.286156	0.06	5.29e-07	0.9932
828	515726162570	249.568192	-47.045200	0.95	3.07e-03	0.9293
829	515725040714	249.570526	-47.401127	1.38	1.62e-04	0.8190
830	515721280417	249.571732	-46.483395	0.82	2.92e-03	0.4474
831	515725055489	249.572937	-47.355640	0.15	5.29e-07	0.9838
832	515720450690	249.572845	-46.758259	0.35	9.53e-06	0.9820
833	515720482766	249.572922	-46.690189	0.77	9.52e-06	0.8901
834	515720448578	249.575729	-46.761360	2.90	5.29e-07	0.0891
835	515725069856	249.574646	-47.313046	0.55	5.29e-07	0.9827
836	515720989181	249.575745	-46.541630	1.77	9.53e-06	0.5384
837	515720529482	249.576050	-46.599045	0.65	1.54e-03	0.9093
838	515725211630	249.576416	-46.933918	0.33	1.62e-04	0.9808
839	515725073868	249.577621	-47.302563	0.23	5.29e-07	0.9893
840	515725211645	249.577744	-46.920845	2.26	9.52e-06	0.5166
841	515725127739	249.580688	-47.143784	1.86	1.62e-04	0.8862
842	515720998755	249.583755	-46.461769	1.92	1.71e-04	0.1071
843	515725079033	249.585205	-47.292297	0.90	6.80e-07	0.9406
844	515720565459	249.585526	-46.540504	0.42	5.29e-07	0.4437
845	—	-	-	-	-	-
846	515725102456	249.586304	-47.224285	0.16	9.52e-06	0.9937
847	515720405672	249.589905	-46.861008	2.23	9.52e-06	0.4182
848	515721484122	249.590851	-46.670242	0.54	3.07e-03	0.9626
849	515725656799	249.591660	-47.278912	0.18	1.57e-05	0.9921
850	515721231044	249.591858	-46.817326	0.39	3.07e-03	0.6702
851	515725920135	249.593460	-46.906067	1.10	1.71e-04	0.8671
852	515720461702	249.594345	-46.750935	0.44	9.52e-06	0.9769
853	515720444366	249.596558	-46.783306	2.32	5.29e-07	0.2230
854	—	-	-	-	-	-
855	515725226081	249.597076	-46.894234	0.12	5.29e-07	0.9885
856	515720407004	249.598480	-46.863346	1.52	5.29e-07	0.6071
857	515721271681	249.600143	-46.569710	0.48	1.71e-04	0.8722
858	515720550483	249.599930	-46.572762	1.21	1.62e-04	0.5378
859	515721486823	249.601395	-46.654682	0.58	3.07e-03	0.9692
860	515720538039	249.601883	-46.605785	1.15	9.53e-06	0.7238

Chandra Catalog: Infrared Counterparts (continued)

No.	VVV Source Name	R.A. (deg)	Dec. (deg)	$\Delta_{\mathrm{X-IR}}$ (arcsec)	p_{noise}	Reliability
861	515720605137	249.602661	-46.474174	0.33	5.29e-07	0.7374
862	515720352453	249.602707	-46.988304	0.79	5.29e-07	0.9345
863	515721266020	249.603210	-46.606850	1.41	1.71e-04	0.3810
864	515720519091	249.603516	-46.636024	0.35	1.62e-04	0.9801
865	515725176581	249.605057	-47.026356	0.77	2.92e-03	0.9585
866	—	-	-	-	-	-
867	515720995402	249.609161	-46.508446	2.31	3.07e-03	0.3755
868	515725232108	249.609924	-46.882824	3.24	5.29e-07	0.4982
869	515725049489	249.609100	-47.396534	1.97	5.29e-07	0.8396
870	515720498694	249.611282	-46.680473	0.54	6.85e-06	0.9755
871	515726163071	249.611725	-47.067329	0.65	3.07e-03	0.0679
872	515725202229	249.612000	-46.965050	0.19	5.29e-07	0.9905
873	515725078287	249.612610	-47.311008	0.31	9.53e-06	0.9893
874	515720444417	249.613831	-46.794842	0.45	5.29e-07	0.9690
875	515720525215	249.614532	-46.635700	0.54	1.71e-04	0.9714
876	515721236586	249.618057	-46.799862	2.57	3.07e-03	0.3867
877	515725070166	249.621323	-47.340717	0.73	5.29e-07	0.9771
878	515720392829	249.621979	-46.908539	1.91	9.52e-06	0.6844
879	515725114261	249.627335	-47.211323	0.96	5.29e-07	0.9312
880	515725174209	249.632004	-47.052780	0.49	1.62e-04	0.2992
881	—	-	-	-	-	-
882	515725150630	249.636963	-47.114296	2.80	5.29e-07	0.7982
883	515720482166	249.638992	-46.735237	0.69	5.29e-07	0.9687
884	515720606803	249.640610	-46.492989	0.80	1.62e-04	0.8533
885	—	-	-	-	-	-
886	515720520382	249.643875	-46.658760	2.46	5.29e-07	0.4473
887	515720979986	249.644409	-46.668205	2.01	1.71e-04	0.0545
888	515720978267	249.646698	-46.684982	1.18	9.53e-06	0.4897
889	515720542009	249.646805	-46.625332	0.43	5.29e-07	0.8047
890	515720507686	249.648163	-46.687843	0.85	5.29e-07	0.9395
891	515720491701	249.648880	-46.717487	1.32	5.29e-07	0.8782
892	515725157520	249.649933	-47.104881	1.69	5.29e-07	0.7459
893	—	-	-	-	-	-
894	515725102720	249.652512	-47.261955	0.38	5.29e-07	0.9883
895	515720505455	249.652573	-46.694855	1.43	1.62e-04	0.1184
896	515725069692	249.653900	-47.361134	0.92	5.29e-07	0.6033
897	515725136747	249.653870	-47.160828	1.53	1.71e-04	0.7287
898	515721258809	249.656372	-46.686867	1.64	2.92e-03	0.4509
899	—	-	-	-	-	-
900	—	-	-	-	-	-
901	515725248496	249.658691	-46.870335	1.32	1.57e-05	0.0498
902	515725208441	249.658829	-46.975269	0.85	9.52e-06	0.9298
903	515726161425	249.659882	-47.113945	0.76	3.07e-03	0.9713
904	515725045316	249.660233	-47.440273	2.95	8.75e-07	0.0528
905	515720402298	249.661758	-46.913067	0.89	9.52e-06	0.5127
906	515725159893	249.663177	-47.105007	0.86	3.07e-03	0.8992
907	515725177482	249.665039	-47.062027	1.33	5.29e-07	0.9212
908	—	-	-	-	-	-
909	515720491675	249.669815	-46.731194	0.52	1.62e-04	0.7719
910	515725084462	249.670685	-47.331310	0.36	5.29e-07	0.9887
911	515720538257	249.675293	-46.650654	2.19	5.29e-07	0.4150
912	515725244481	249.676132	-46.894691	0.60	5.29e-07	0.9726
913	515720428199	249.677048	-46.866417	1.42	9.53e-06	0.4114
914	—	-	-	-	-	-
915	515725242618	249.679810	-46.899971	1.17	5.29e-07	0.6895
916	515725223092	249.681793	-46.951042	0.76	5.29e-07	0.9730
917	515725867659	249.681305	-47.339607	2.17	2.92e-03	0.5237
918	515725894042	249.683502	-47.153881	1.07	1.71e-04	0.2387
919	515720588952	249.684082	-46.552860	0.33	2.92e-03	0.9832

Chandra Catalog: Infrared Counterparts (continued)

No.	VVV Source Name	R.A. (deg)	Dec. (deg)	$\Delta_{\mathrm{X-IR}}$ (arcsec)	p_{noise}	Reliability
920	515725686540	249.684540	-46.977810	1.81	1.71e-04	0.4119
921	515725085557	249.688156	-47.334438	0.76	9.52e-06	0.6854
922	515725899976	249.688538	-47.114796	1.04	1.71e-04	0.9306
923	515720528512	249.690247	-46.674545	2.96	9.52e-06	0.4128
924	515720467451	249.689301	-46.793304	0.09	5.29e-07	0.9888
925	515720608874	249.690353	-46.516899	0.13	1.22e-05	0.9855
926	515725252240	249.690964	-46.880795	2.88	5.29e-07	0.5445
927	515725247711	249.692337	-46.893589	0.39	5.29e-07	0.9749
928	515725085179	249.692398	-47.345467	1.41	9.52e-06	0.9343
929	515721243404	249.695007	-46.807022	0.72	3.07e-03	0.5341
930	515725277817	249.695587	-46.811928	0.99	6.80e-07	0.4933
931	515720558746	249.697556	-46.620796	0.46	1.22e-05	0.7314
932	515725157325	249.699173	-47.136574	0.94	5.29e-07	0.9662
933	—	-	-	-	-	-
934	515726192646	249.700851	-46.878532	1.30	3.07e-03	0.2879
935	515725660754	249.707443	-47.300343	2.20	9.53e-06	0.8000
936	515725238275	249.707916	-46.929489	0.54	5.29e-07	0.9767
937	515726182356	249.709778	-46.966919	3.42	3.07e-03	0.1599
938	—	-	-	-	-	-
939	515720657827	249.709656	-46.441113	0.48	5.29e-07	0.6855
940	515725138852	249.710358	-47.190765	1.60	5.29e-07	0.7796
941	515720614721	249.712494	-46.519634	0.36	8.75e-07	0.9822
942	515720616750	249.712967	-46.515491	0.46	5.29e-07	0.9790
943	515720570249	249.713913	-46.604862	0.53	1.12e-06	0.6360
944	515725239248	249.714157	-46.928650	0.47	5.29e-07	0.9767
945	515720976670	249.716324	-46.741833	2.25	1.71e-04	0.4357
946	515725143579	249.718353	-47.183826	0.56	5.29e-07	0.9344
947	515725684380	249.719009	-47.027874	0.95	1.22e-05	0.5916
948	515725139004	249.721100	-47.196346	2.09	1.62e-04	0.5288
949	515725219337	249.721390	-46.984543	0.68	9.52e-06	0.9746
950	515725095440	249.721878	-47.326347	1.24	5.29e-07	0.9092
951	—	-	-	-	-	-
952	515720638205	249.724365	-46.478539	0.45	1.54e-03	0.9720
953	515725261006	249.726776	-46.878456	1.63	5.29e-07	0.6941
954	515720469453	249.726501	-46.812244	0.95	5.29e-07	0.7766
955	515725689078	249.726776	-46.973110	0.82	9.53e-06	0.1970
956	515725119425	249.728516	-47.257626	1.64	5.29e-07	0.8819
957	—	-	-	-	-	-
958	—	-	-	-	-	-
959	515720490380	249.729385	-46.772900	0.13	5.29e-07	0.9887
960	515720638538	249.729507	-46.482307	0.19	5.29e-07	0.9419
961	515725204199	249.729660	-47.029446	0.39	2.92e-03	0.9846
962	515720976221	249.731705	-46.755146	1.60	9.53e-06	0.6229
963	515720508049	249.731796	-46.736412	0.40	5.29e-07	0.9814
964	515725689319	249.733963	-46.974918	1.76	1.71e-04	0.3870
965	—	-	-	-	-	-
966	—	-	-	-	-	-
967	515725290196	249.735794	-46.805904	0.63	5.29e-07	0.9567
968	515725230436	249.736618	-46.966820	2.00	5.29e-07	0.2061
969	515725926597	249.737335	-46.947224	1.55	1.71e-04	0.3130
970	515721271125	249.738449	-46.663334	1.25	2.92e-03	0.5380
971	515720568510	249.742310	-46.644402	1.10	9.52e-06	0.3636
972	—	-	-	-	-	-
973	515720587145	249.748444	-46.594090	0.26	9.52e-06	0.9827
974	515725891460	249.749191	-47.211346	2.03	3.07e-03	0.8785
975	515725122048	249.749908	-47.262032	1.88	5.29e-07	0.8752
976	515725199090	249.751495	-47.056389	3.29	2.16e-04	0.1206
977	515720709459	249.750595	-46.346096	3.57	5.29e-07	0.1942
978	515725138334	249.751038	-47.232342	1.94	9.52e-06	0.5943

Chandra Catalog: Infrared Counterparts (continued)

No.	VVV Source Name	R.A. (deg)	Dec. (deg)	$\Delta_{\mathrm{X-IR}}$ (arcsec)	p_{noise}	Reliability
979	515720491026	249.752594	-46.787189	0.27	5.29e-07	0.5177
980	515720991588	249.754745	-46.632057	1.81	1.71e-04	0.1262
981	515725666886	249.755325	-47.251152	0.45	3.07e-03	0.7947
982	515720568506	249.755524	-46.634907	3.23	3.07e-03	0.2670
983	515720527943	249.757523	-46.714386	1.40	5.29e-07	0.6590
984	515725300140	249.757446	-46.794167	0.08	5.29e-07	0.9899
985	—	-	-	-	-	-
986	515725149355	249.760895	-47.193047	0.38	5.29e-07	0.9680
987	515720688626	249.760635	-46.394772	0.89	3.43e-05	0.2763
988	515721265539	249.761383	-46.703857	0.37	2.20e-04	0.4925
989	515720694419	249.762711	-46.381840	0.39	9.52e-06	0.4719
990	—	-	-	-	-	-
991	515720630796	249.765411	-46.521233	0.28	5.29e-07	0.9870
992	515725886206	249.767273	-47.261127	2.46	1.71e-04	0.5957
993	515726168994	249.769058	-47.113411	0.65	3.07e-03	0.9597
994	515720583767	249.770523	-46.622295	1.83	9.52e-06	0.8883
995	515725125664	249.770386	-47.264996	2.33	5.29e-07	0.8589
996	515720555018	249.771347	-46.676319	2.97	9.53e-06	0.3481
997	515725676900	249.771591	-47.144363	0.42	9.53e-06	0.9874
998	—	-	-	-	-	-
999	—	-	-	-	-	-
1000	515725246681	249.774048	-46.946152	0.80	6.80e-07	0.6133
1001	515720524731	249.775208	-46.732319	1.78	5.29e-07	0.5626
1002	515720522225	249.774826	-46.734467	0.85	1.12e-06	0.9159
1003	515720691824	249.775879	-46.394154	2.41	5.29e-07	0.5517
1004	515720555021	249.777802	-46.676304	0.18	9.53e-06	0.9850
1005	515725928126	249.778152	-46.960812	1.32	2.92e-03	0.1040
1006	—	-	-	-	-	-
1007	—	-	-	-	-	-
1008	515720661988	249.781296	-46.464352	0.40	9.52e-06	0.9775
1009	515725928281	249.781616	-46.961723	1.19	3.07e-03	0.2124
1010	515721280685	249.782913	-46.611687	2.12	1.71e-04	0.0383
1011	515720601376	249.784225	-46.604137	1.16	5.29e-07	0.9030
1012	—	-	-	-	-	-
1013	515720532037	249.788681	-46.726215	0.96	1.62e-04	0.1688
1014	515720728580	249.792603	-46.321533	0.32	6.85e-06	0.3500
1015	515725193290	249.794785	-47.098122	0.28	8.75e-07	0.9916
1016	515720652948	249.795074	-46.496323	1.74	5.29e-07	0.5106
1017	—	-	-	-	-	-
1018	—	-	-	-	-	-
1019	515720552244	249.798187	-46.710011	0.57	1.71e-04	0.9567
1020	515720696765	249.798370	-46.397129	0.38	5.29e-07	0.9760
1021	515720603000	249.797882	-46.594170	3.13	1.62e-04	0.1174
1022	—	-	-	-	-	-
1023	—	-	-	-	-	-
1024	—	-	-	-	-	-
1025	—	-	-	-	-	-
1026	515725232110	249.810318	-47.005810	0.14	5.29e-07	0.9908
1027	515725920925	249.810150	-47.032227	2.92	2.20e-04	0.4472
1028	515726159476	249.810730	-47.218273	2.70	3.07e-03	0.6182
1029	515720546331	249.811798	-46.715294	0.99	5.29e-07	0.7523
1030	—	-	-	-	-	-
1031	515720668187	249.812241	-46.468163	1.36	1.62e-04	0.4244
1032	515720776844	249.814102	-46.246727	1.39	5.29e-07	0.6564
1033	515720661660	249.814041	-46.485027	0.09	5.29e-07	0.9818
1034	515720661659	249.815842	-46.486588	1.93	5.29e-07	0.4439
1035	515720637381	249.817871	-46.543972	0.28	5.29e-07	0.9866
1036	515725266028	249.818558	-46.920170	0.48	5.29e-07	0.4406
1037	515720587090	249.818893	-46.636578	1.39	5.29e-07	0.2889

Chandra Catalog: Infrared Counterparts (continued)

No.	VVV Source Name	R.A. (deg)	Dec. (deg)	$\Delta_{\mathrm{X-IR}}$ (arcsec)	p_{noise}	Reliability
1038	515720653035	249.819626	-46.507729	1.66	9.53e-06	0.7207
1039	515720489725	249.835220	-46.835167	0.27	5.29e-07	0.9884
1040	—	-	-	-	-	-
1041	515725274397	249.835434	-46.910030	0.59	5.29e-07	0.9478
1042	515720717717	249.838562	-46.375259	0.10	1.71e-04	0.9562
1043	—	-	-	-	-	-
1044	515725254459	249.839508	-46.966343	0.49	5.29e-07	0.9794
1045	515725353017	249.840805	-46.725601	0.14	5.29e-07	0.9915
1046	515721343028	249.840546	-46.285446	1.70	1.71e-04	0.6816
1047	515725177232	249.841843	-47.169090	0.78	5.29e-07	0.9764
1048	515725215412	249.843033	-47.067802	3.46	1.62e-04	0.3193
1049	515725312738	249.843369	-46.819786	0.33	5.29e-07	0.9854
1050	515725206686	249.843903	-47.093105	0.44	5.29e-07	0.9869
1051	515725189241	249.844070	-47.140823	0.41	5.29e-07	0.9880
1052	515725945193	249.846436	-46.874222	1.78	3.07e-03	0.6689
1053	—	-	-	-	-	-
1054	515721258305	249.849167	-46.808498	0.17	3.07e-03	0.9851
1055	515720703031	249.850464	-46.417774	0.31	1.71e-04	0.8238
1056	515721272799	249.851425	-46.710178	0.45	1.71e-04	0.9384
1057	515720674761	249.856445	-46.483391	1.09	2.31e-05	0.2991
1058	515725153997	249.855667	-47.237171	2.17	1.22e-05	0.6804
1059	515725290815	249.857239	-46.884251	0.31	5.29e-07	0.9889
1060	515720678099	249.857971	-46.475811	0.62	5.29e-07	0.9709
1061	515725245291	249.860336	-47.003632	0.73	1.54e-03	0.9665
1062	515720636996	249.862000	-46.567638	1.19	5.29e-07	0.9131
1063	515720632867	249.862381	-46.587986	0.73	1.94e-05	0.9459
1064	515725711438	249.864807	-46.797962	1.05	1.71e-04	0.8696
1065	515720723464	249.866241	-46.388046	0.57	5.29e-07	0.9749
1066	515720979649	249.867538	-46.805794	0.72	9.53e-06	0.9463
1067	—	-	-	-	-	-
1068	515725158434	249.868591	-47.234940	1.18	9.52e-06	0.5414
1069	515725287633	249.870407	-46.893597	1.78	2.16e-04	0.5711
1070	515725246047	249.869690	-47.005367	0.19	9.53e-06	0.9914
1071	—	-	-	-	-	-
1072	515725949598	249.873093	-46.864399	0.23	2.92e-03	0.8133
1073	515720614074	249.873734	-46.644215	0.29	9.53e-06	0.9865
1074	515725254358	249.874191	-46.986324	0.54	5.29e-07	0.5057
1075	515721269457	249.875565	-46.746899	1.68	2.92e-03	0.3203
1076	515725354420	249.877914	-46.741447	1.28	9.53e-06	0.6969
1077	515726172633	249.878448	-47.147888	0.47	3.07e-03	0.9862
1078	515721493584	249.879410	-46.730820	0.73	3.07e-03	0.2561
1079	515725202658	249.880600	-47.126808	0.23	5.29e-07	0.9847
1080	515725369139	249.881668	-46.709103	0.35	3.07e-03	0.9707
1081	515720621831	249.882751	-46.608845	1.62	1.44e-06	0.6016
1082	515720534545	249.882294	-46.775608	0.90	5.29e-07	0.6971
1083	515720658551	249.882614	-46.532043	1.44	1.57e-05	0.6147
1084	—	-	-	-	-	-
1085	515725323307	249.883972	-46.816483	0.46	5.29e-07	0.9456
1086	515725682119	249.885529	-47.153435	1.38	1.22e-05	0.7580
1087	515720624293	249.886703	-46.606834	0.56	5.29e-07	0.9525
1088	515720761428	249.886459	-46.316734	0.64	5.29e-07	0.9680
1089	515725924877	249.887375	-47.050846	0.41	1.71e-04	0.9876
1090	—	-	-	-	-	-
1091	515726226364	249.888397	-46.689507	0.47	3.07e-03	0.9788
1092	515720622293	249.891357	-46.613663	0.33	5.29e-07	0.8645
1093	515720743364	249.894958	-46.357281	0.36	5.29e-07	0.9824
1094	515725682674	249.896164	-47.153141	2.07	2.16e-04	0.8139
1095	515725351222	249.896881	-46.762722	2.00	5.29e-07	0.4599
1096	515725335218	249.899811	-46.799034	0.61	1.71e-04	0.9384

Chandra Catalog: Infrared Counterparts (continued)

No.	VVV Source Name	R.A. (deg)	Dec. (deg)	$\Delta_{\mathrm{X-IR}}$ (arcsec)	p_{noise}	Reliability
1097	515720683319	249.901230	-46.489826	1.85	6.85e-06	0.8742
1098	515720710446	249.903336	-46.430962	0.12	9.52e-06	0.9853
1099	515720674355	249.905350	-46.516514	4.09	5.29e-07	0.1182
1100	515725308474	249.904633	-46.868454	2.41	9.53e-06	0.6837
1101	515726199917	249.905655	-46.947121	0.99	3.07e-03	0.9568
1102	515725703396	249.909149	-46.910648	0.55	1.54e-03	0.9799
1103	515720767717	249.909683	-46.320553	0.25	1.71e-04	0.9834
1104	515721006889	249.909866	-46.585213	0.78	1.71e-04	0.6923
1105	515720607010	249.912415	-46.656204	0.26	5.29e-07	0.9860
1106	515720646871	249.913055	-46.581009	0.34	5.29e-07	0.9755
1107	515725345452	249.913239	-46.790989	0.23	5.29e-07	0.8782
1108	515721315111	249.913025	-46.488918	3.06	3.07e-03	0.4652
1109	515725916590	249.915573	-47.129879	0.25	2.92e-03	0.9892
1110	515721004115	249.919189	-46.617020	0.59	5.34e-04	0.9498
1111	515725894944	249.919434	-47.290394	2.11	1.71e-04	0.3430
1112	515721342612	249.922012	-46.338272	1.31	2.92e-03	0.7374
1113	515725342296	249.922684	-46.795906	1.91	5.29e-07	0.3206
1114	515725904901	249.922028	-47.218918	1.78	2.20e-04	0.1044
1115	515725909052	249.922379	-47.189663	0.37	2.20e-04	0.9665
1116	—	-	-	-	-	-
1117	515720773612	249.925278	-46.318314	3.21	5.29e-07	0.3226
1118	515725356914	249.924500	-46.765575	0.61	5.29e-07	0.7533
1119	515725223964	249.925446	-47.095798	2.24	5.29e-07	0.9014
1120	—	-	-	-	-	-
1121	515725214656	249.926254	-47.120319	2.19	9.53e-06	0.1765
1122	515720657309	249.928177	-46.563007	0.92	3.07e-03	0.8597
1123	515720773995	249.928391	-46.317284	0.43	5.29e-07	0.9751
1124	515725906465	249.931137	-47.213390	0.79	2.92e-03	0.8107
1125	515725339096	249.932449	-46.815975	1.73	5.29e-07	0.4857
1126	515721303616	249.933777	-46.565220	2.34	3.07e-03	0.3811
1127	515725279802	249.934708	-46.953926	0.07	5.29e-07	0.9920
1128	515725286315	249.934982	-46.937469	0.06	5.29e-07	0.9945
1129	515725328997	249.936432	-46.835083	0.93	5.29e-07	0.9595
1130	515721510068	249.937119	-46.554733	0.23	3.07e-03	0.5643
1131	515725323031	249.937164	-46.864212	0.09	9.52e-06	0.9854
1132	515725387195	249.937363	-46.703564	0.19	5.29e-07	0.9878
1133	515721512955	249.938492	-46.517651	3.40	3.07e-03	0.4372
1134	515725245081	249.939148	-47.049854	0.41	5.29e-07	0.9501
1135	—	-	-	-	-	-
1136	515720775650	249.941025	-46.323383	0.71	1.71e-04	0.9632
1137	—	-	-	-	-	-
1138	515721491671	249.941986	-46.790424	1.71	3.07e-03	0.0785
1139	515725255511	249.945786	-47.025440	0.66	5.29e-07	0.9736
1140	515720652643	249.948990	-46.585320	2.52	1.12e-06	0.3803
1141	—	-	-	-	-	-
1142	515720606941	249.949799	-46.687160	0.28	5.29e-07	0.9873
1143	—	-	-	-	-	-
1144	515720676409	249.951447	-46.536846	2.31	9.52e-06	0.6460
1145	—	-	-	-	-	-
1146	515720710562	249.952316	-46.460327	0.25	5.29e-07	0.9822
1147	515725245992	249.952454	-47.056404	2.38	5.29e-07	0.3657
1148	515721315109	249.953094	-46.513466	1.77	1.71e-04	0.4274
1149	515725241554	249.957352	-47.070175	0.94	5.29e-07	0.9649
1150	515720745989	249.958115	-46.392399	0.22	5.29e-07	0.9894
1151	515720728627	249.958786	-46.423969	0.30	5.29e-07	0.9865
1152	515725317132	249.958954	-46.877514	0.74	5.29e-07	0.9602
1153	515725302171	249.958374	-46.912941	1.19	5.29e-07	0.3049
1154	515725321000	249.959152	-46.869823	0.86	5.29e-07	0.9368
1155	—	-	-	-	-	-

Chandra Catalog: Infrared Counterparts (continued)

No.	VVV Source Name	R.A. (deg)	Dec. (deg)	$\Delta_{\mathrm{X-IR}}$ (arcsec)	p_{noise}	Reliability
1156	515721346639	249.964218	-46.337456	0.50	1.71e-04	0.9594
1157	515720692626	249.964523	-46.510681	0.75	5.29e-07	0.9642
1158	515725267772	249.965454	-47.006252	0.14	5.29e-07	0.9918
1159	515725259625	249.966278	-47.025848	0.63	2.92e-03	0.1897
1160	—	-	-	-	-	-
1161	515721290805	249.969742	-46.660347	0.84	2.20e-04	0.8610
1162	515725277420	249.972107	-46.986622	0.30	5.29e-07	0.9898
1163	515725711664	249.974579	-46.863869	2.33	1.71e-04	0.6034
1164	515725352074	249.976013	-46.809776	0.57	5.29e-07	0.9745
1165	515720750173	249.977097	-46.394730	0.34	5.29e-07	0.9848
1166	515725360313	249.977020	-46.788708	0.84	8.75e-07	0.0774
1167	515725308260	249.978622	-46.908520	1.25	1.22e-05	0.9000
1168	515720689720	249.980209	-46.529305	0.27	5.29e-07	0.9865
1169	515720741117	249.980392	-46.414246	0.56	5.29e-07	0.9732
1170	—	-	-	-	-	-
1171	515725330087	249.982849	-46.876350	0.28	5.29e-07	0.9851
1172	—	-	-	-	-	-
1173	515720706709	249.983398	-46.489277	0.73	5.29e-07	0.9617
1174	515725255576	249.984100	-47.047737	1.82	1.62e-04	0.8732
1175	515725699018	249.984848	-47.006939	0.33	1.21e-04	0.9879
1176	—	-	-	-	-	-
1177	515720688090	249.987808	-46.532169	1.92	8.60e-05	0.0639
1178	515725281301	249.986862	-46.987785	0.53	5.29e-07	0.9768
1179	—	-	-	-	-	-
1180	515725333135	249.988754	-46.857475	0.39	6.80e-07	0.9829
1181	—	-	-	-	-	-
1182	515725380266	249.991287	-46.751759	2.89	5.29e-07	0.0623
1183	515720685046	249.993851	-46.542164	2.86	5.29e-07	0.4487
1184	515720747818	249.993820	-46.409744	0.49	5.29e-07	0.9774
1185	515720777148	249.994507	-46.353752	0.28	5.29e-07	0.9854
1186	515725421350	249.994858	-46.658829	0.37	1.12e-06	0.9831
1187	515720683062	249.994888	-46.552818	0.99	1.62e-04	0.5468
1188	515721016780	249.996033	-46.536537	2.19	1.71e-04	0.0473
1189	515725938134	249.997025	-47.020050	2.73	1.71e-04	0.0817
1190	—	-	-	-	-	-
1191	515725341460	249.997101	-46.843819	0.96	5.29e-07	0.9657
1192	515721329957	249.998077	-46.465347	1.64	2.20e-04	0.8307
1193	515725457121	249.999176	-46.576412	1.23	5.29e-07	0.3478
1194	515725266067	250.000717	-47.029472	3.72	1.22e-05	0.3504
1195	515725333467	250.000488	-46.864861	1.27	5.29e-07	0.6999
1196	515720640126	250.001572	-46.654797	0.28	5.29e-07	0.9869
1197	515721315516	250.003387	-46.542160	3.41	1.71e-04	0.0394
1198	515725281994	250.003647	-46.989632	0.41	3.40e-05	0.9859
1199	515725372362	250.003586	-46.776108	0.97	8.60e-05	0.4639
1200	515725266753	250.007141	-47.031860	0.81	5.29e-07	0.9714
1201	515720719643	250.009003	-46.474014	0.65	6.80e-07	0.9716
1202	515720779867	250.010574	-46.356274	1.73	9.52e-06	0.5559
1203	515720696577	250.010178	-46.533405	0.36	5.29e-07	0.9809
1204	515720643872	250.015045	-46.647270	0.40	5.29e-07	0.9822
1205	515725282910	250.015091	-46.994381	0.27	5.29e-07	0.9885
1206	515720756080	250.014923	-46.411747	0.65	5.29e-07	0.9606
1207	515720643873	250.015106	-46.645695	0.73	9.52e-06	0.9426
1208	515726192903	250.015594	-47.067272	0.75	3.07e-03	0.5865
1209	515725457918	250.016983	-46.584145	1.21	5.29e-07	0.9409
1210	515725255105	250.017563	-47.071945	0.31	5.29e-07	0.9886
1211	515725353857	250.023849	-46.830647	1.85	1.56e-05	0.4786
1212	515720773615	250.024323	-46.376888	1.88	1.91e-06	0.2891
1213	515720776007	250.024551	-46.373199	2.68	5.29e-07	0.1035
1214	—	-	-	-	-	-

Chandra Catalog: Infrared Counterparts (continued)

No.	VVV Source Name	R.A. (deg)	Dec. (deg)	$\Delta_{\mathrm{X-IR}}$ (arcsec)	p_{noise}	Reliability
1215	515720776795	250.027649	-46.377327	0.85	5.29e-07	0.9515
1216	—	-	-	-	-	-
1217	515725423248	250.030350	-46.676880	0.38	1.62e-04	0.0461
1218	515720737297	250.033585	-46.454121	0.17	5.29e-07	0.9892
1219	515721045650	250.034958	-46.284840	1.45	1.71e-04	0.4087
1220	515720718242	250.038177	-46.496284	0.39	5.29e-07	0.9804
1221	515720744600	250.041779	-46.443176	2.78	5.29e-07	0.4316
1222	515720765409	250.042389	-46.407417	1.57	1.71e-04	0.7758
1223	515725402657	250.042007	-46.729919	1.30	9.52e-06	0.7990
1224	515725343259	250.044342	-46.872562	0.98	5.29e-07	0.9545
1225	515721332159	250.046021	-46.483528	1.47	1.71e-04	0.5526
1226	515725413085	250.046738	-46.713352	1.29	9.53e-06	0.7777
1227	515725708206	250.046371	-46.951996	0.25	1.71e-04	0.9279
1228	515720674692	250.049591	-46.600468	1.03	1.62e-04	0.8303
1229	515721041595	250.050262	-46.330048	2.24	1.71e-04	0.4680
1230	515725468105	250.050049	-46.585285	0.74	1.62e-04	0.9616
1231	515720630300	250.051437	-46.694302	1.30	5.29e-07	0.8908
1232	515726007541	250.051559	-46.585449	1.80	1.55e-03	0.3221
1233	515720652021	250.052612	-46.650444	0.34	5.29e-07	0.9840
1234	515720744950	250.054794	-46.449368	0.26	1.22e-05	0.9785
1235	—	-	-	-	-	-
1236	515720723852	250.059387	-46.496960	1.46	5.29e-07	0.7716
1237	515725379575	250.060089	-46.813992	0.19	5.29e-07	0.9851
1238	515725276054	250.061340	-47.045135	0.80	5.29e-07	0.8520
1239	515725276066	250.060989	-47.043713	0.89	5.29e-07	0.9566
1240	515726192215	250.061966	-47.100788	2.54	3.07e-03	0.6652
1241	515725344863	250.065414	-46.882912	1.21	5.29e-07	0.8533
1242	515720692335	250.066986	-46.581497	1.91	1.91e-06	0.3255
1243	515725312176	250.068176	-46.955322	1.38	5.29e-07	0.6311
1244	515725942522	250.068405	-47.033295	1.58	1.71e-04	0.7149
1245	515725400661	250.068985	-46.756119	2.31	5.29e-07	0.8379
1246	515725420102	250.068939	-46.710365	0.89	5.29e-07	0.9600
1247	515720676755	250.069199	-46.607704	1.49	5.29e-07	0.5469
1248	—	-	-	-	-	-
1249	515725379615	250.070328	-46.804924	0.37	3.07e-03	0.9700
1250	515720766298	250.071915	-46.420689	0.63	5.29e-07	0.8678
1251	515725428038	250.073746	-46.692600	0.18	5.29e-07	0.9868
1252	515721035419	250.074783	-46.401764	0.28	9.53e-06	0.9525
1253	515720688501	250.075714	-46.585110	0.24	5.29e-07	0.9874
1254	515720776894	250.075348	-46.402493	1.34	1.62e-04	0.6139
1255	515720768905	250.076050	-46.418728	1.35	5.29e-07	0.9158
1256	515720699409	250.077072	-46.563202	2.55	5.29e-07	0.1210
1257	515725498011	250.078918	-46.518288	0.07	5.29e-07	0.9837
1258	515725711991	250.080978	-46.927124	0.29	2.20e-04	0.9730
1259	515721530611	250.081726	-46.397476	0.12	3.07e-03	0.9391
1260	515721515394	250.083252	-46.577957	2.15	3.07e-03	0.0705
1261	515720653734	250.085144	-46.666649	1.14	5.29e-07	0.9361
1262	515721522372	250.091568	-46.503544	1.61	3.07e-03	0.3126
1263	515725737687	250.093536	-46.692299	1.83	9.53e-06	0.6340
1264	—	-	-	-	-	-
1265	515720727205	250.094681	-46.512806	0.58	5.29e-07	0.9689
1266	515725343597	250.094681	-46.897591	2.00	5.29e-07	0.4653
1267	515725344712	250.095047	-46.894997	3.18	9.52e-06	0.4106
1268	515725320417	250.101730	-46.954800	1.80	5.29e-07	0.5900
1269	515725310498	250.101746	-46.978470	0.48	1.71e-04	0.8964
1270	—	-	-	-	-	-
1271	515720793249	250.104477	-46.389507	1.45	5.29e-07	0.7242
1272	515725335645	250.111908	-46.926060	1.71	2.01e-05	0.9073
1273	—	-	-	-	-	-

Chandra Catalog: Infrared Counterparts (continued)

No.	VVV Source Name	R.A. (deg)	Dec. (deg)	$\Delta_{\mathrm{X-IR}}$ (arcsec)	p_{noise}	Reliability
1274	515720748347	250.114990	-46.480415	2.34	5.29e-07	0.3226
1275	515725338396	250.114944	-46.923279	2.35	5.29e-07	0.3614
1276	—	-	-	-	-	-
1277	515725338334	250.116730	-46.923065	1.18	5.29e-07	0.9557
1278	515721039638	250.122757	-46.391678	1.23	3.07e-03	0.4995
1279	515721039638	250.122757	-46.391678	1.04	3.07e-03	0.5790
1280	515720739516	250.124588	-46.507507	0.05	5.29e-07	0.9901
1281	—	-	-	-	-	-
1282	515721512765	250.125961	-46.634529	1.43	3.07e-03	0.3897
1283	515725325068	250.125198	-46.957066	1.59	5.29e-07	0.2206
1284	515725741005	250.125946	-46.685524	0.80	9.53e-06	0.9653
1285	515725407239	250.126373	-46.771503	0.14	5.29e-07	0.9894
1286	515725373159	250.126389	-46.849628	0.32	5.29e-07	0.9859
1287	515726001471	250.129791	-46.667370	4.25	2.20e-04	0.1041
1288	515725414593	250.128922	-46.755047	3.15	2.16e-04	0.1303
1289	515725303312	250.128860	-47.021580	0.76	9.53e-06	0.9740
1290	515720825531	250.128754	-46.340179	1.59	2.92e-03	0.4797
1291	—	-	-	-	-	-
1292	515720787796	250.130966	-46.416676	1.53	5.29e-07	0.6565
1293	515725962874	250.134155	-46.922112	1.54	1.71e-04	0.8587
1294	515725354498	250.134552	-46.896202	2.44	1.62e-04	0.5980
1295	515725463697	250.137085	-46.643394	0.36	2.92e-03	0.7382
1296	515725426700	250.138779	-46.733253	1.17	9.52e-06	0.1198
1297	—	-	-	-	-	-
1298	515720828432	250.139359	-46.340252	1.40	1.54e-03	0.8638
1299	515725330303	250.142212	-46.957737	0.34	5.29e-07	0.9713
1300	515725450644	250.144226	-46.679020	2.31	5.29e-07	0.4295
1301	—	-	-	-	-	-
1302	515725293375	250.148132	-47.047157	2.36	1.62e-04	0.5641
1303	515725425567	250.149673	-46.741905	1.87	1.62e-04	0.2127
1304	515725492314	250.149002	-46.589108	0.06	5.29e-07	0.9872
1305	515720746327	250.150162	-46.505974	0.35	2.92e-03	0.9787
1306	515725986926	250.155502	-46.776657	0.28	1.71e-04	0.9878
1307	515725477584	250.157623	-46.621712	2.32	5.29e-07	0.5801
1308	515725441564	250.158203	-46.713177	2.08	9.53e-06	0.5427
1309	—	-	-	-	-	-
1310	515725407399	250.161713	-46.791451	0.17	9.52e-06	0.9919
1311	515720805685	250.161606	-46.423923	0.92	5.29e-07	0.9553
1312	—	-	-	-	-	-
1313	515725400470	250.162781	-46.809189	0.30	5.29e-07	0.9883
1314	515725418454	250.166779	-46.771095	0.06	5.29e-07	0.9924
1315	—	-	-	-	-	-
1316	515725350432	250.170441	-46.927402	1.16	1.71e-04	0.6822
1317	515725375315	250.177750	-46.877155	0.67	5.29e-07	0.9740
1318	515720727347	250.179276	-46.568943	0.30	9.52e-06	0.9836
1319	515725397917	250.180267	-46.828827	0.18	5.29e-07	0.9916
1320	515720852967	250.182175	-46.316296	3.47	5.29e-07	0.0894
1321	—	-	-	-	-	-
1322	515720771508	250.183319	-46.477341	0.40	5.29e-07	0.9805
1323	515725737773	250.185120	-46.750748	0.23	9.53e-06	0.9860
1324	515725496964	250.187119	-46.586102	0.09	5.29e-07	0.9888
1325	—	-	-	-	-	-
1326	515725424702	250.189789	-46.768692	0.19	9.52e-06	0.9913
1327	515720809599	250.189682	-46.413387	3.04	9.53e-06	0.6595
1328	—	-	-	-	-	-
1329	515725362993	250.193390	-46.919075	0.71	9.52e-06	0.5289
1330	515725436798	250.194580	-46.743565	0.20	5.29e-07	0.9907
1331	515725392665	250.195587	-46.846935	1.06	1.62e-04	0.8170
1332	515725458230	250.195847	-46.692898	1.15	5.29e-07	0.5843

Chandra Catalog: Infrared Counterparts (continued)

No.	VVV Source Name	R.A. (deg)	Dec. (deg)	$\Delta_{\mathrm{X-IR}}$ (arcsec)	p_{noise}	Reliability
1333	515725496864	250.198868	-46.596066	1.71	9.52e-06	0.7351
1334	515720809632	250.202484	-46.416302	2.07	5.29e-07	0.8532
1335	—	-	-	-	-	-
1336	515725389811	250.205978	-46.866478	0.22	9.52e-06	0.9867
1337	515725466553	250.210236	-46.681767	1.37	5.29e-07	0.9419
1338	515720787949	250.212570	-46.468334	0.41	9.52e-06	0.9787
1339	—	-	-	-	-	-
1340	515725361636	250.218887	-46.935146	0.62	1.71e-04	0.9733
1341	515725375282	250.222992	-46.902298	0.49	5.29e-07	0.9799
1342	515725485280	250.223907	-46.640762	1.38	5.29e-07	0.5511
1343	—	-	-	-	-	-
1344	—	-	-	-	-	-
1345	515725487884	250.241821	-46.645172	0.55	6.85e-06	0.8879
1346	515725402572	250.251007	-46.856606	0.56	6.80e-07	0.9746
1347	515725480333	250.252197	-46.674377	1.35	1.71e-04	0.5244
1348	—	-	-	-	-	-
1349	515725495512	250.254074	-46.630608	2.01	5.29e-07	0.5191
1350	515720823546	250.256805	-46.421593	1.47	9.52e-06	0.4027
1351	—	-	-	-	-	-
1352	515720788845	250.260132	-46.493755	0.94	5.29e-07	0.9116
1353	515725509067	250.261398	-46.603123	2.16	1.62e-04	0.7291
1354	515725385859	250.264008	-46.904724	0.62	1.62e-04	0.7714
1355	515725491664	250.269028	-46.650070	0.67	5.29e-07	0.9715
1356	515725542057	250.270813	-46.532524	0.23	5.29e-07	0.9839
1357	—	-	-	-	-	-
1358	515725732674	250.273132	-46.852352	0.11	9.53e-06	0.9926
1359	515725470938	250.276108	-46.716385	0.39	1.62e-04	0.8238
1360	515725479120	250.279648	-46.691792	0.85	9.53e-06	0.9660
1361	515725510257	250.283493	-46.609917	3.07	6.85e-06	0.3527
1362	515725388081	250.292023	-46.915203	1.30	5.29e-07	0.7050
1363	515725557851	250.311966	-46.526073	0.46	1.71e-04	0.9774
1364	515725763313	250.312836	-46.548931	1.09	1.71e-04	0.4661
1365	515725550906	250.318176	-46.542286	2.39	9.53e-06	0.4479
1366	515726237060	250.318878	-46.853573	2.23	3.07e-03	0.5954
1367	—	-	-	-	-	-
1368	515725481428	250.323730	-46.722191	0.41	9.53e-06	0.9839
1369	515725404383	250.325974	-46.913670	1.01	3.08e-03	0.9602
1370	515725576087	250.328049	-46.482143	0.35	5.29e-07	0.1243
1371	515726006840	250.332138	-46.753246	2.46	1.71e-04	0.7110
1372	515725516215	250.344757	-46.644428	0.36	9.52e-06	0.9846
1373	—	-	-	-	-	-
1374	515725467960	250.345245	-46.758133	0.18	5.29e-07	0.9909
1375	515726275232	250.350479	-46.528690	1.56	3.07e-03	0.3320
1376	515725465874	250.350861	-46.776630	0.57	1.71e-04	0.9731
1377	515725564998	250.353088	-46.523792	1.16	5.29e-07	0.4032
1378	515725507052	250.355881	-46.662048	0.30	9.53e-06	0.9878
1379	515725581165	250.378815	-46.513611	0.36	9.53e-06	0.9816
1380	515725516820	250.380951	-46.659634	0.44	5.29e-07	0.9793
1381	515726004632	250.388962	-46.804440	0.52	1.55e-03	0.8351
1382	515725520598	250.390701	-46.651855	0.20	9.52e-06	0.9909
1383	—	-	-	-	-	-
1384	515725512282	250.394791	-46.673698	0.69	5.29e-07	0.9533
1385	515725514125	250.395081	-46.667599	0.24	6.80e-07	0.9895
1386	—	-	-	-	-	-
1387	515725484007	250.400558	-46.750839	2.33	5.29e-07	0.0963
1388	515725564028	250.404572	-46.562969	0.58	5.29e-07	0.9766
1389	515725564017	250.405548	-46.566238	1.28	3.08e-03	0.9057
1390	515725538196	250.406555	-46.623428	0.85	5.29e-07	0.9592
1391	—	-	-	-	-	-

Chandra Catalog: Infrared Counterparts (continued)

No.	VVV Source Name	R.A. (deg)	Dec. (deg)	$\Delta_{\mathrm{X-IR}}$ (arcsec)	p_{noise}	Reliability
1392	—	-	-	-	-	-
1393	515725511146	250.418274	-46.692574	1.25	9.52e-06	0.5504
1394	515725462042	250.418640	-46.816730	1.64	5.29e-07	0.1061
1395	515726023847	250.418686	-46.690907	0.85	1.71e-04	0.9571
1396	515725519688	250.440155	-46.681316	1.57	2.20e-04	0.6663
1397	515725520234	250.441467	-46.680958	0.64	9.53e-06	0.9741
1398	515725529396	250.444931	-46.672462	0.58	5.29e-07	0.9765
1399	515725751382	250.448334	-46.763847	0.12	3.07e-03	0.9687
1400	515725767215	250.460709	-46.590271	1.53	1.71e-04	0.3741
1401	515725524359	250.475525	-46.696651	0.68	5.29e-07	0.9727
1402	515725490933	250.482132	-46.780788	1.57	5.29e-07	0.3071
1403	515725571376	250.483490	-46.588154	1.93	5.29e-07	0.6553
1404	515725569715	250.506546	-46.607452	2.31	9.53e-06	0.5694
1405	515725509306	250.510818	-46.759598	0.18	5.29e-07	0.9804
1406	515725575334	250.512604	-46.595982	1.02	6.80e-07	0.9579
1407	515725515726	250.514297	-46.740940	0.06	5.29e-07	0.9865
1408	515725521664	250.519241	-46.728081	0.39	3.08e-03	0.9828
1409	515726026038	250.528214	-46.738918	1.38	1.71e-04	0.5958
1410	515725513843	250.533112	-46.751823	0.85	5.29e-07	0.5249
1411	515726271337	250.568970	-46.697632	1.21	3.07e-03	0.7554
1412	515725591172	250.579208	-46.595829	1.50	5.29e-07	0.5310
1413	515725577848	250.583115	-46.647369	3.06	9.53e-06	0.7123
1414	515726047429	250.587677	-46.615616	0.80	2.92e-03	0.0897
1415	515725584528	250.595139	-46.619923	1.88	5.29e-07	0.1914

Appendix B

Additional *Chandra* and *NuSTAR* Spectra of Norma Region Sources

In this appendix, we present the *Chandra* and *NuSTAR* spectra of sources NNR 10–27 from the *NuSTAR* Norma Arm Region Survey. The plots show the data, the best-fitting spectral model, and the data residuals for each sources. The parameters of the best-fitting spectral models are provided in Table 2.21. Our spectral analysis is described in § 2.3.10. The spectra of NNR 1, 2, and 3 are shown in King et al. 2014, B16, and G14, respectively, while the spectra of sources NNR 4–9 are shown in Figure 2.27. In the figures below, *Chandra* data is shown in black, *NuSTAR* FPMA data is shown in red, and FPMB data is shown in blue. For NNR 19, black points show the *Chandra* spectrum from ObsID 7591 while orange points shows the *Chandra* spectrum from ObsID 16170. For NNR 21, black points denote the *Chandra* spectrum for the point source and extended emission combined while orange points display the point source contribution alone.

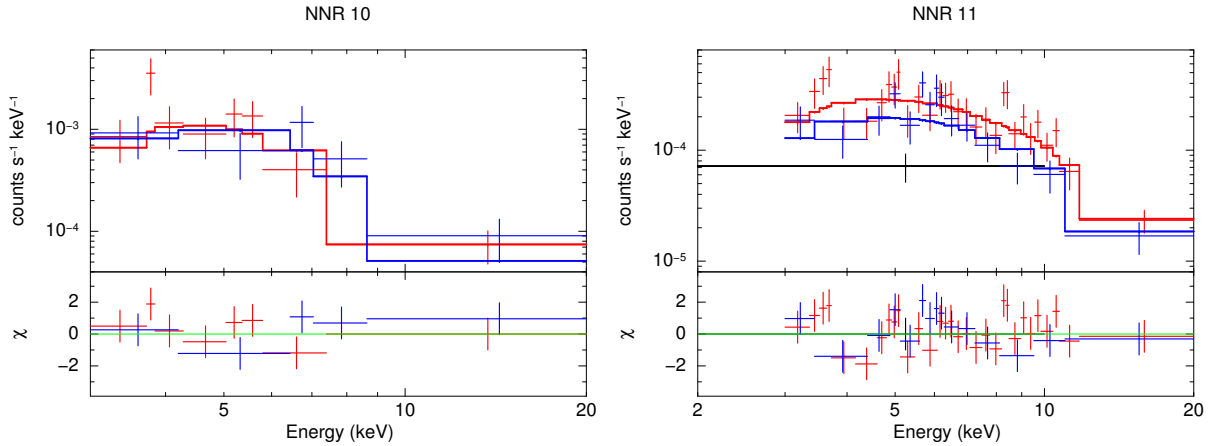

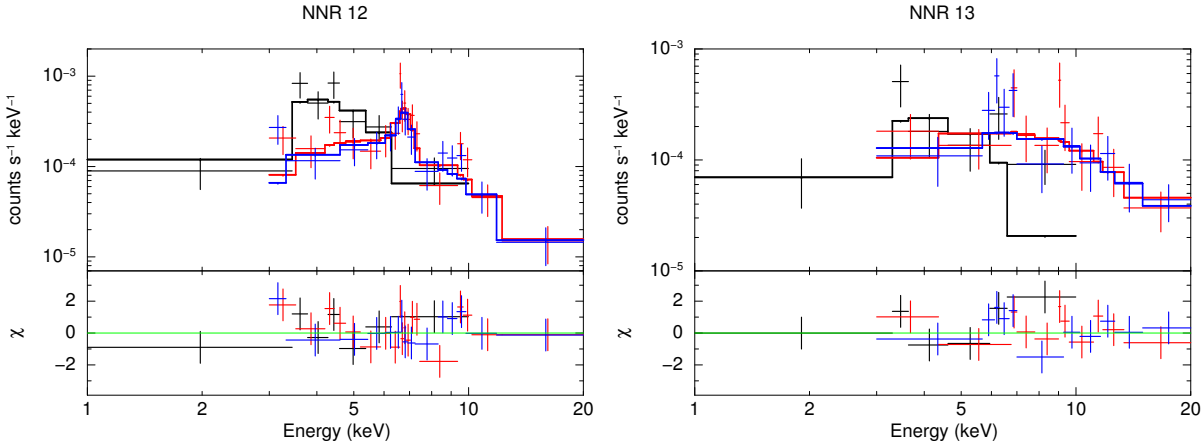
NNR 12
counts s⁻¹ keV⁻¹
χ
Energy (keV)

NNR 13
counts s⁻¹ keV⁻¹
χ
Energy (keV)

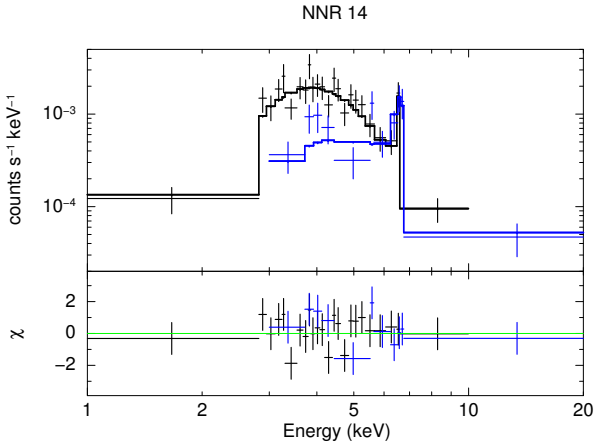
NNR 14
counts s⁻¹ keV⁻¹
χ
Energy (keV)

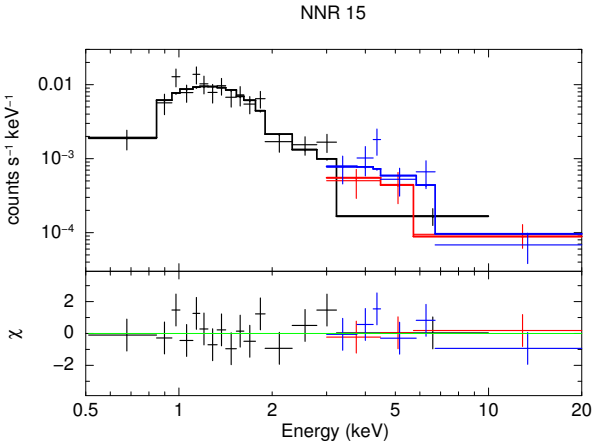
NNR 15
counts s⁻¹ keV⁻¹
χ
Energy (keV)

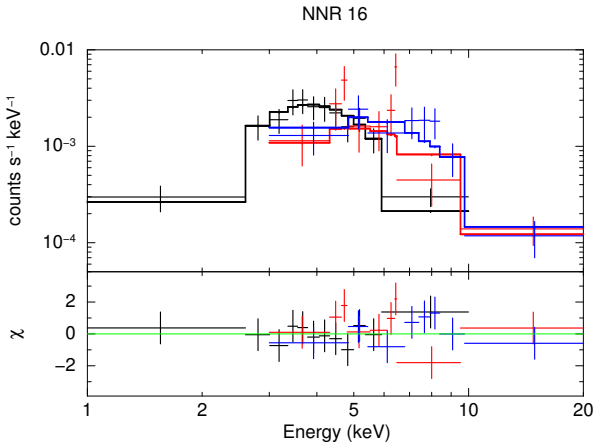
NNR 16
counts s⁻¹ keV⁻¹
χ
Energy (keV)

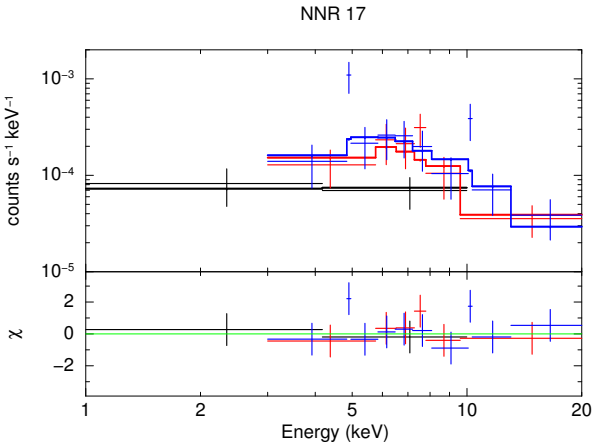
NNR 17
counts s⁻¹ keV⁻¹
χ
Energy (keV)

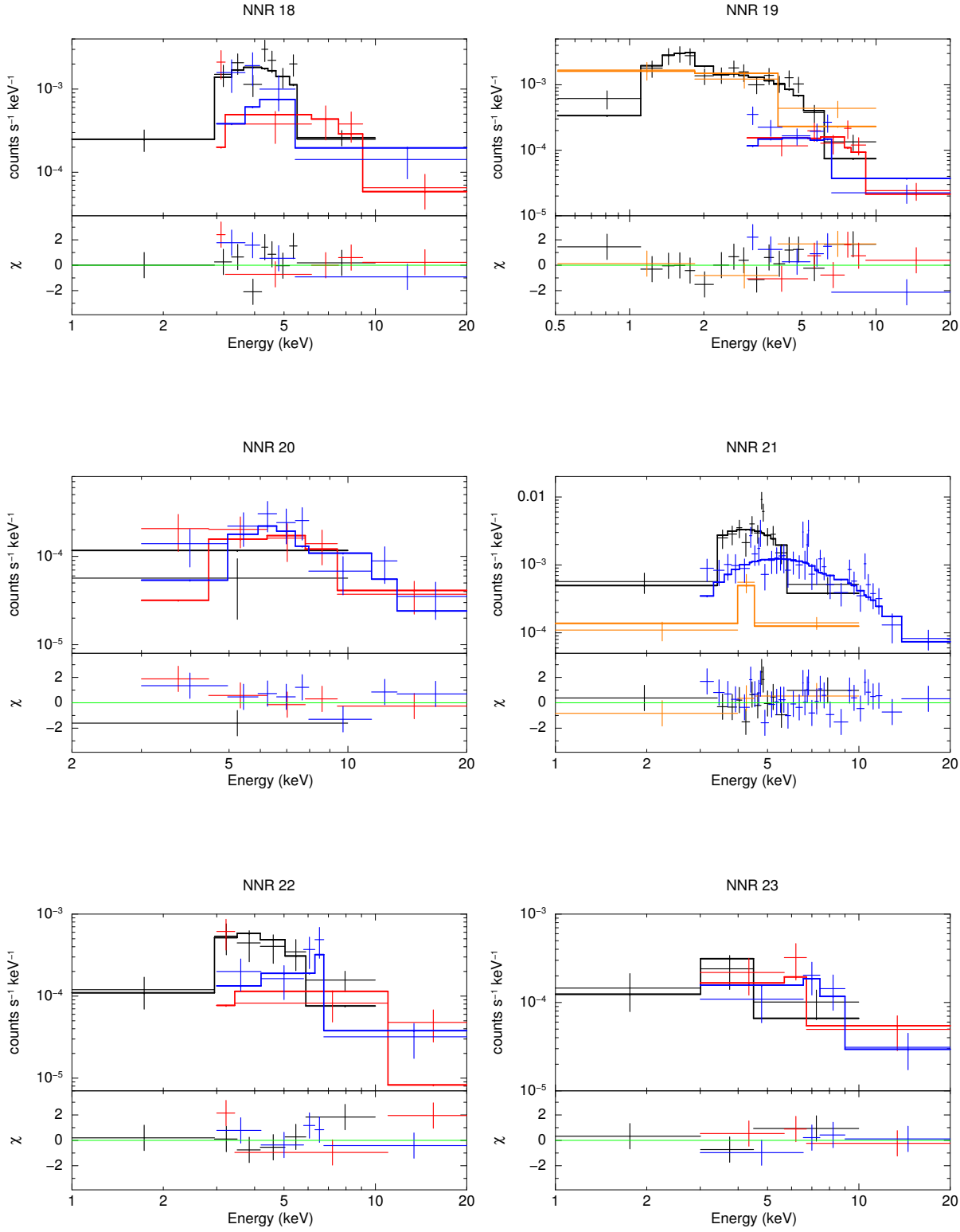
NNR 18
NNR 19
NNR 20
NNR 21
NNR 22
NNR 23
counts s⁻¹ keV⁻¹
χ
Energy (keV)

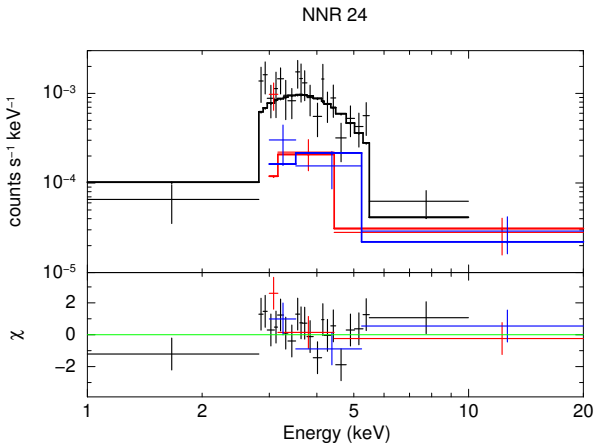
NNR 24
counts s⁻¹ keV⁻¹
10⁻³
10⁻⁴
10⁻⁵
χ
2
0
−2
1
2
5
10
20
Energy (keV)

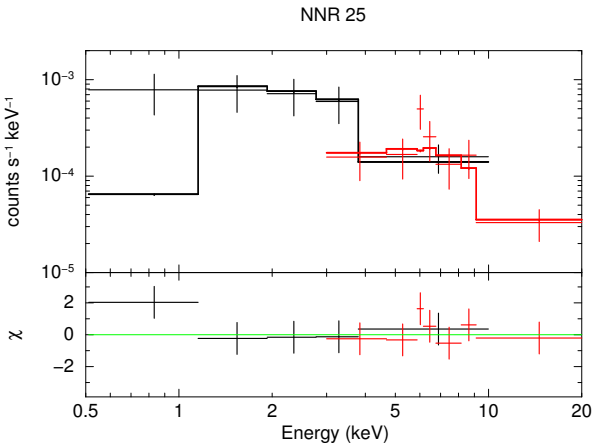
NNR 25
counts s⁻¹ keV⁻¹
10⁻³
10⁻⁴
10⁻⁵
χ
2
0
−2
0.5
1
2
5
10
20
Energy (keV)

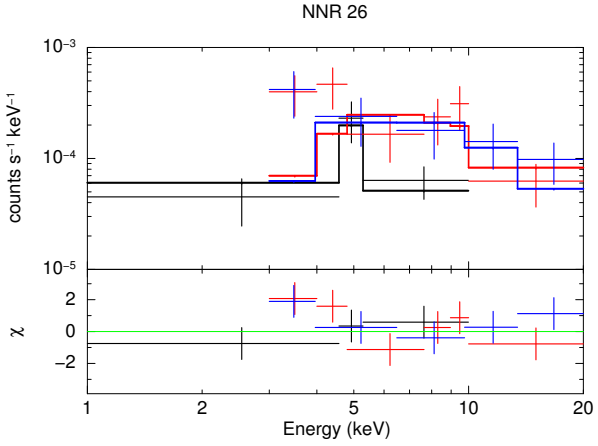
NNR 26
counts s⁻¹ keV⁻¹
10⁻³
10⁻⁴
10⁻⁵
χ
2
0
−2
1
2
5
10
20
Energy (keV)

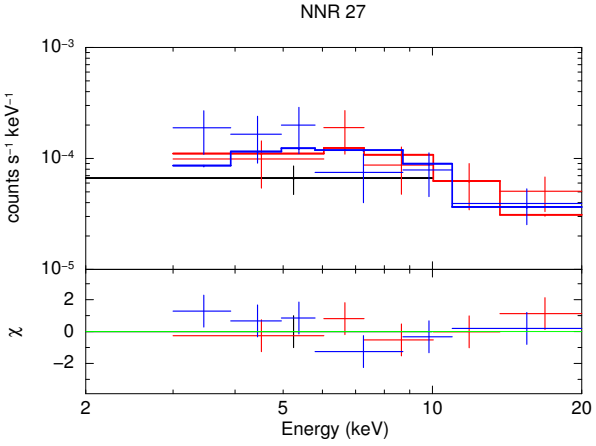
NNR 27
counts s⁻¹ keV⁻¹
10⁻³
10⁻⁴
10⁻⁵
χ
2
0
−2
2
5
10
20
Energy (keV)